

**The biophysical effects of nanosized particles
in contact with alveolar lung surfactant**

María Miguel Díez M.Sc.

2017

Thesis presented for the degree of Doctor of Philosophy (PhD)
Lung Cell Biology, National Heart and Lung Institute, Imperial College London

Author's Declaration

The work described in this thesis was carried out between October 2011 and December 2014, under the supervision of Professor Terry Tetley, Dr. Alison Buckley and Dr. Rachel Smith. Except where indicated by specific reference in the text, all the work is that of the author.

Signed: María Miguel Díez

Copyright

The copyright of this thesis rests with the author and is made available under a Creative Commons Attribution Non-Commercial No Derivatives licence. Researchers are free to copy, distribute or transmit the thesis on the condition that they attribute it, that they do not use it for commercial purposes and that they do not alter, transform or build upon it. For any reuse or redistribution, researchers must make clear to others the licence terms of this work.

DEDICATION

To my grandparents

Matilde, Prescencio, Alejandra and Julio,

who due to economic hardship did not have access to higher education

Acknowledgements

I would like to express my sincere thanks and gratitude to my supervisors Professor Terry Tetley, Dr. Alison Buckley and Dr. Rachel Smith for having given me the opportunity to undertake this PhD and for their continuous help and support.

I would also like to thank Chris Gregory from Public Health England for building the exposure chamber in such a brilliant way, Dr. Joanna Seiffert, Dr. Judith Thei, Dr. Sarah Fearn and Ecaterina Ware from Imperial College London for their help with the enzymatic-colorimetric assay, SEM, ToF-SIMS and TEM respectively and Dr. Nick Hardy from Biolin Scientific for his support with the LWB system.

Grateful thanks to Dr. Valeria Garbin from Imperial College London and James Warren from Public Health England for their very valuable advice. Also to Neil Galloway-Phillipps from Imperial College London for his support during the writing-up period.

A special thanks to Public Health England for funding the project.

Finally, but by no means least, I would like to thank my family for their unfailing support, love and encouragement.

Abstract

The effects of engineered nanoparticles (NPs) on the biophysical properties of lung surfactant is a topic of increasing interest due to the rapid expansion of nanotechnologies and the potential for human exposure to airborne NPs. Langmuir monolayers of dipalmitoylphosphatidylcholine (DPPC), the major component of the lung surfactant, at the air/liquid interface represent a good model to investigate the lung surfactant behaviour and its interactions with NPs. Here, the effects of CeO₂ and Carbon Black (CB) NPs on DPPC monolayers were investigated by the analysis of surface pressure-Mma (*II*-Mma) compression isotherms recorded at experimental conditions similar to those found in human lungs using a Langmuir-Wilhelmy Balance (LWB) in parallel with the visualisation of the interface using SEM and ToF-SIMS. In previous studies, NPs were deposited from liquid suspensions, usually for ease of application. In this work, a method for aerosol NP deposition onto DPPC monolayers was developed and compared with depositions from liquid suspensions. To date, there are no other studies of NP deposition onto a surfactant monolayer in aerosol form using a LWB. CeO₂ NPs were first suspended in chloroform and deposited onto a DPPC monolayer located at the air/PBS interface, which had no effect on the *II*-Mma isotherm for any of the NP mass deposited due to the instability of CeO₂ NPs in this medium which rapidly agglomerated to form large, dense clusters that eventually detached from the interface and sedimented into the subphase hence, only small CeO₂ NPs remained at the surface at levels too low to affect the isotherm. In the second deposition method, NPs were mixed with DPPC in chloroform and deposited onto a clean PBS subphase. The coating of the NPs with DPPC increased the stability of the NPs in PBS. SEM and ToF-SIMS images showed that large agglomerates were present at the interface that had a remarkable effect on the *II*-Mma isotherms by shifting them towards larger areas with NP mass deposited. Thirdly, CeO₂ NPs in aerosol form were deposited onto a DPPC monolayer. Results showed that the presence of agglomerates of a similar size homogeneously spread across the surface during the compression of the interface improved the film containment causing an increase in the slope of the isotherm starting at a *II* ~ 30 mN/m and in the collapse *II* with NP mass deposited. Aerosolised CB NPs were also distributed uniformly across the surface and improved the stability of the monolayer in a similar way to aerosolised CeO₂ NPs. These experiments showed that the NP deposition method onto the air/PBS interface differentially affected the DPPC isotherm and that the degree of NP agglomeration is probably one of the most important determining factors of the NP effects on the DPPC isotherm. It is concluded that the deposition of NPs in aerosol form is the most appropriate experimental model to study inhaled NP interactions with lung surfactant using a LWB.

Table of Contents

Author's Declaration	3
Dedication	4
Acknowledgements	5
Abstract	6
List of figures	16
List of tables	32
Glossary of nomenclature and abbreviations	43
CHAPTER 1 – INTRODUCTION AND BACKGROUND INFORMATION	49
1.1 Rationale and strategy	49
1.2 Surface science, surface tension, surfactant and particle monolayers and colloids	50
1.2.1 Surface science, surfaces and interfaces	50
1.2.2 Surface tension.....	52
1.2.2.1 Concept and thermodynamics of surface tension.....	52
1.2.2.2 Dependence of surface tension on temperature.....	56
1.2.2.3 Methods to measure surface tension	57
1.2.3 Surfactant monolayers, particle monolayers and colloids	58
1.2.3.1 Surfactant monolayers.....	58
1.2.3.1.1 Surfactants	58
1.2.3.1.2 Techniques for studying the surface pressure behaviour and structure of surfactant monolayers.....	60
1.2.3.1.3 Insoluble surfactant monolayers	68
1.2.3.2 Particle monolayers	77
1.2.3.3 Colloids and colloidal stability.....	81
1.3 Lung surfactant	85
1.3.1 Introduction.....	85

1.3.2 Function of lung surfactant	87
1.3.3 Biophysical properties of lung surfactant	88
1.3.4 Composition and function of lung surfactant components	91
1.3.5 Lung surfactant and the near zero surface tension.....	99
1.3.6 Lung surfactant dysfunction and exogenous lung surfactant therapy.....	100
1.3.7 <i>In vitro</i> methods to investigate the surface properties of exogenous lung surfactant mixtures.....	102
1.4 Engineered nanoparticles.....	103
1.4.1 Nanotechnology and engineered nanomaterials	103
1.4.1.1 Introduction	103
1.4.1.2 Nanomaterial characterisation.....	107
1.4.2 Human inhalation exposure to nanoparticles: deposition, clearance and retained dose	109
1.4.2.1 Introduction	109
1.4.2.2 Inhalation exposure and particle deposition.....	111
1.4.2.3 Clearance mechanisms and retained dose	112
1.4.3 Human toxicity of engineered nanomaterials	113
1.4.3.1 Introduction	113
1.4.3.2 Toxic effects of ambient nanoparticles	114
1.4.3.3 Nanoparticle and lung surfactant interactions.....	115
1.5 Research objectives	117
1.6 Hypothesis	118

CHAPTER 2 – STUDY OF THE DPPC ISOTHERM USING A LANGMUIR-WILHELMY BALANCE (LWB) AND OPTIMISATION OF EXPERIMENTAL CONDITIONS FOR FUTURE EXPERIMENTS..... 119

2.1 Rationale.....	119
2.2 Hypothesis	121

2.3 Methodology.....	121
2.3.1 Reagents and materials	121
2.3.2 Cleaning of glassware	121
2.3.3 Determination of the concentration of a reference DPPC solution by enzymatic-colorimetric assay of the level of choline	121
2.3.4 LWB system.....	123
2.3.4.1 Main parts and accessories of a LWB system.....	123
2.3.4.2 Experiments performed using a LWB system.....	128
2.3.4.3 Cleaning of a LWB system and its accessories.....	130
2.3.4.4 Filling the trough with subphase liquid.....	130
2.3.4.5 Deposition of the DPPC solution	130
2.3.4.6 Further information for the dipping experiment	131
2.4 Results and discussion	131
2.4.1 Study of the DPPC isotherm using a LWB system.....	131
2.4.1.1 Derivation of relevant parameters to describe a DPPC isotherm.....	131
2.4.1.2 Rule to accept or reject measured isotherms to calculate an average DPPC isotherm.....	137
2.4.1.3 Determination of the lift-off M_{ma} of the DPPC isotherm and calculation of the concentration of DPPC solutions	139
2.4.1.3.1 Determination of the concentration of a reference DPPC solution by enzymatic-colorimetric assay of the level of choline	139
2.4.1.3.2 Determination of the lift-off M_{ma} using a reference DPPC solution.....	139
2.4.1.3.3 Determination of the concentration of any DPPC solution based on the lift-off M_{ma}	141
2.4.1.3.4 Determination of the lift-off M_{ma} under other experimental conditions.	142
2.4.1.4 Variability when measuring DPPC isotherms.....	143
2.4.1.5 Establishment of criteria to compare isotherms measured under different experimental conditions based on reference isotherm parameter variability values...	149

2.4.1.6 Study of DPPC isotherms with different deposited masses of DPPC.....	150
2.4.2 Measurement of the DPPC isotherm under experimental conditions close to those occurring <i>in vivo</i>	155
2.4.2.1 Effect of barrier speed on the DPPC isotherm	157
2.4.2.2 Effect of subphase composition on the DPPC isotherm	164
2.4.2.3 Effect of subphase temperature on the DPPC isotherm	167
2.4.2.4 Effect of relative humidity on the DPPC isotherm	175
2.4.2.5 Effect of subphase volume on the DPPC isotherm	177
2.5 Summary discussion and conclusion.....	181

CHAPTER 3 – STUDY OF HOW THE METHOD OF DEPOSITION OF CeO₂ NANOPARTICLES AFFECTS THE BEHAVIOUR OF A DPPC MONOLAYER..... 186

3.1 Rationale.....	186
3.2 Introduction	188
3.2.1 Literature studies that have investigated the interactions between lung surfactant and NPs with the aid of a spreading solvent.....	188
3.2.1.1 Literature studies that have investigated the interactions between DPPC and NPs with the aid of a spreading solvent.....	188
3.2.1.2 Literature studies that have investigated the interactions between lung surfactant models other than DPPC and NPs with the aid of a spreading solvent.....	193
3.2.2 Literature studies that have investigated the interactions between lung surfactant and NPs by depositing NPs in aerosol form	194
3.2.3 CeO ₂ nanoparticles.....	195
3.2.3.1 Properties, structure and uses of CeO ₂ nanoparticles.....	195
3.2.3.2 CeO ₂ nanoparticle exposure data.....	196
3.2.3.3 Health effects of CeO ₂ nanoparticles	197
3.3 Hypothesis	197
3.4 Methodology.....	198

3.4.1 Reagents and materials	198
3.4.2 Cleaning of glassware	198
3.4.3 Deposition method 1: Liquid deposition of CeO ₂ nanoparticles	198
3.4.3.1 Preparation of CeO ₂ nanoparticle suspensions and samples	198
3.4.3.2 Nanoparticle characterisation pre-CeO ₂ nanoparticle administration	198
3.4.3.2.1 Size and zeta potential of CeO ₂ nanoparticles	198
3.4.3.2.2 Wettability and surface tension activity of CeO ₂ nanoparticles	199
3.4.3.3 CeO ₂ nanoparticle deposition	200
3.4.4 Deposition method 2: Liquid deposition of mixtures of CeO ₂ nanoparticles and DPPC	200
3.4.4.1 Preparation of CeO ₂ nanoparticle and DPPC suspensions and samples	200
3.4.4.2 Nanoparticle characterisation pre-CeO ₂ nanoparticle administration	200
3.4.4.3 Deposition of CeO ₂ nanoparticle and DPPC suspensions	200
3.4.5 Deposition method 3: Deposition of CeO ₂ nanoparticles in aerosol form	200
3.4.5.1 Aerosol exposure system	200
3.4.5.2 Preparation of CeO ₂ nanoparticle suspensions for the constant output atomiser and samples	204
3.4.5.3 Nanoparticle characterisation pre-CeO ₂ nanoparticle administration	204
3.4.5.3.1 Size distribution and number concentration of aerosolised CeO ₂ nanoparticles	204
3.4.5.3.2 Mass concentration of aerosolised CeO ₂ nanoparticles	205
3.4.5.3.3 Determination of the aerosolised CeO ₂ nanoparticle mass deposited onto a Langmuir trough	207
3.4.5.3.4 Measurement of the spatial distribution and size of aerosolised CeO ₂ nanoparticles upon deposition	210
3.4.5.3.5 Wettability and surface tension activity of aerosolised CeO ₂ nanoparticles	211
3.4.5.4 CeO ₂ nanoparticle deposition	211

3.4.6 Measurement of the surface pressure–Mma isotherm	211
3.4.6.1 Relevant parameters used to describe a surface pressure-Mma isotherm.....	211
3.4.6.2 Criteria to compare surface pressure-Mma isotherms measured under different experimental conditions	211
3.4.7 Interfacial layer characteristics post-CeO ₂ nanoparticle administration - Langmuir- Blodgett films.....	212
3.5 Results and discussion	212
3.5.1 Deposition method 1: Liquid deposition of CeO ₂ nanoparticles	212
3.5.1.1 Nanoparticle characterisation pre-CeO ₂ nanoparticle administration	212
3.5.1.1.1 Size and zeta potential of CeO ₂ nanoparticles.....	212
3.5.1.1.2 Wettability and surface tension activity of CeO ₂ nanoparticles.....	214
3.5.1.2 Effect of the exposure of a DPPC monolayer to CeO ₂ nanoparticles on the surface pressure–Mma isotherm measured in PBS at 37°C and 21°C and interfacial layer characteristics post-CeO ₂ nanoparticle administration.....	222
3.5.2 Deposition method 2: Liquid deposition of mixtures of CeO ₂ nanoparticles and DPPC	243
3.5.2.1 Nanoparticle characterisation pre-CeO ₂ nanoparticle administration	243
3.5.2.1.1 Size and zeta potential of CeO ₂ nanoparticles.....	243
3.5.2.1.2 Wettability and surface tension activity of CeO ₂ nanoparticles.....	247
3.5.2.2 Effect of the deposition of different CeO ₂ nanoparticle and DPPC mass ratios on the surface pressure–Mma isotherm measured in PBS at 37°C and 21°C and interfacial layer characteristics post-CeO ₂ nanoparticle administration.....	247
3.5.3 Deposition method 3: Deposition of CeO ₂ nanoparticles in aerosol form.....	276
3.5.3.1 Nanoparticle characterisation pre-CeO ₂ nanoparticle administration	276
3.5.3.1.1 Determination of the mass of aerosolised CeO ₂ nanoparticles deposited onto the Langmuir trough	276
3.5.3.1.2 Size of aerosolised CeO ₂ nanoparticles upon deposition	280
3.5.3.1.3 Measurement of the spatial distribution of aerosolised CeO ₂ nanoparticles upon deposition.....	281

3.5.3.1.4 Wettability and surface tension activity of aerosolised CeO ₂ nanoparticles	283
3.5.3.2 Effect of the exposure of a DPPC monolayer to aerosolised CeO ₂ nanoparticles on the surface pressure–Mma isotherm measured in PBS at 37°C and 21°C and interfacial layer characteristics post-CeO ₂ nanoparticle administration.....	291
3.5.3.2.1 Interfacial layer characteristics post-CeO ₂ nanoparticle administration...	292
3.5.3.2.2 Effect of the exposure of a DPPC monolayer to aerosolised ultrapure water over increasing exposure times on the surface pressure–Mma isotherm measured in PBS at 37°C and 21°C	302
3.5.3.2.3 Effect of the exposure of a DPPC monolayer to aerosolised CeO ₂ nanoparticles on the surface pressure–Mma isotherm measured in PBS at 37°C and 21°C	310
3.6 Summary discussion and conclusion	326
3.6.1 Comparison of the three deposition methods.....	326
3.6.2 Comparison of the results with those from other studies.....	337

CHAPTER 4 – EFFECTS OF THE EXPOSURE OF A DPPC MONOLAYER TO AEROSOLISED CARBON BLACK (CB) NANOPARTICLES..... 342

4.1 Rationale	342
4.2 CB nanoparticles.....	342
4.2.1 Properties, structure and uses of CB nanoparticles.....	342
4.2.2 CB nanoparticle exposure data	343
4.2.3 Health effects of CB nanoparticles	344
4.3 Hypothesis	344
4.4 Methodology.....	345
4.4.1 Reagents and materials	345
4.4.2 Cleaning of glassware	345
4.4.3 CB nanoparticles in aerosol form	345
4.4.3.1 Aerosol exposure system.....	345

4.4.3.2 Preparation of CB nanoparticle suspensions for the constant output atomiser and samples	345
4.4.3.3 Nanoparticle characterisation pre-CB nanoparticle administration	346
4.4.3.3.1 Primary particle size, size distribution, number concentration, mass concentration, wettability and surface tension activity of aerosolised CB nanoparticles	346
4.4.3.3.2 Determination of the mass of aerosolised CB nanoparticles deposited onto a Langmuir trough	346
4.4.3.3.3 Measurement of the spatial distribution and size of aerosolised CB nanoparticles upon deposition	346
4.4.3.4 CB nanoparticle deposition	346
4.4.4 Measurement of the surface pressure–Mma isotherm	347
4.4.4.1 Relevant parameters used to describe a surface pressure-Mma isotherm.....	347
4.4.4.2 Criteria to compare surface pressure-Mma isotherms measured under different experimental conditions	347
4.4.5 Interfacial layer characteristics post-CB nanoparticle administration - Langmuir-Blodgett films.....	347
4.5 Results and discussion	347
4.5.1 Nanoparticle characterisation pre-CB nanoparticle administration.....	347
4.5.1.1 Size of CB primary particles	348
4.5.1.2 Determination of the mass of aerosolised CB nanoparticles deposited onto a Langmuir trough.....	348
4.5.1.3 Size of aerosolised CB nanoparticles upon deposition	351
4.5.1.4 Measurement of the spatial distribution of aerosolised CB nanoparticles upon deposition	354
4.5.1.5 Wettability and surface tension activity of aerosolised CB nanoparticles	354
4.5.2 Effect of the exposure of a DPPC monolayer to aerosolised CB nanoparticles on the surface pressure–Mma isotherm measured in PBS at 21°C and interfacial layer characteristics post-CB nanoparticle administration	360

4.5.2.1 Effect of the exposure of a DPPC monolayer to compressed air over increasing exposure times on the surface pressure–Mma isotherm.....	360
4.5.2.2 Interfacial layer characteristics post-CB nanoparticle administration	360
4.5.2.3 Effect of the exposure of a DPPC monolayer to aerosolised CB nanoparticles on the surface pressure–Mma isotherm measured in PBS at 21°C	365
4.5.2.4 Comparison of the similarities and differences between aerosolised CeO ₂ nanoparticles and CB nanoparticles and of their effect on the surface pressure–Mma isotherm measured in PBS at 21°C	374
4.5.2.5 Comparison of the results of aerosolised CB nanoparticles with those from other studies.....	376
4.6 Summary discussion and conclusion.....	377
CHAPTER 5 – SUMMARY CONCLUSION, RECOMMENDATIONS AND FUTURE STUDIES.....	381
5.1 Summary conclusion	381
5.2 Potential effects of the inhalation of nanoparticles on lung surfactant function <i>in vivo</i>	386
5.3 Recommendations and future studies	387
5.4 Scientific results for publication in peer-reviewed journals.....	393
REFERENCES.....	396
APPENDICES	426

List of figures

Figure 1. Illustration of the effect of subdivision of a two metre cube into smaller cubic particles. When divided into cubes one eighth of the original, the total surface area and area to volume ratio is eight times the respective value for the original cube. Adapted from Stoffer, 2013.	52
Figure 2. Schematic illustration for explaining the phenomenon of surface tension. The dashed line represents the interface between a liquid and a gas. Adapted from Ibrahim, 2000.	54
Figure 3. Schematic of a water drop onto a solid surface. Molecules inside the water drop are attracted in all directions. Molecules on the surface are attracted to the sides and inwards (NASA, 2011).	55
Figure 4. Graphical representation of the changes in water surface tension as a function of temperature (Department-of-Interfacial-Phenomena, 2013).	56
Figure 5. Three dimensional phase diagram of temperature (T), pressure (P) and volume (V) for water. Adapted from Walton, 1983.	57
Figure 6. Illustration of the surfactant classification according to the ionic nature of the polar group. Adapted from Abd-Elhady et al., 2011.	59
Figure 7. Illustration of a surfactant layer at the air/water interface. The polar group (in red) is immersed in the water phase whereas the hydrophobic tail (in blue) is located in the vapour phase (Lower, 2015).	60
Figure 8. BAM images of a calf lung surfactant at different surface pressure values. Liquid condensed domains (bright areas) were dispersed in a liquid expanded phase (dark areas) (Piknova et al., 2001).	64
Figure 9. Fluorescence images of DPPC liquid condensed domains (dark areas) dispersed in a liquid expanded phase (bright areas) obtained at 4.2 mN/m (image a), 4.3 mN/m (image b), 5.0 mN/m (image c) and 7.5 mN/m (image d). Adapted from McConlogue and Vanderlick, 1997.	65
Figure 10. ToF-SIMS images showing the distribution of all film constituents in a DPPC/d62-DPPG/SP-B (4:1:0.2 mol %) model system. For each film component, one main colour is shown. Additionally, an image overlay is displayed (Seifert et al., 2007).	67

Figure 11. Graphical representation of the theoretical Π -Mean Molecular Area isotherm obtained by compressing an insoluble monolayer at an air/water interface. Monolayer phases and orientation of the surfactant in different phases are also shown. The red arrow shows the direction of isotherm formation. Adapted from Kaganer et al., 1999.....	73
Figure 12. Schematic representation of the mechanism of monolayer collapse. Upon lateral compression and beyond a certain threshold the monolayer becomes unstable and collapse begins with buckling and folding into a bilayer at the water subphase (a-c). The bilayer folds bend into a semi-vesicle (d-e) and can transform into a vesicle and detach from the monolayer (f) (Baoukina et al., 2008).	74
Figure 13. Π -Mma isotherms for DPPC at five different subphase temperatures. Curve 1, 30°C; curve 2, 25°C; curve 3, 20°C; curve 4, 15°C; curve 5, 10°C (Toimil et al., 2010).....	76
Figure 14. BAM images of a DPPC monolayer for a mean molecular area value of 60 Å ² /molecule at different subphase temperatures (23°C, 32°C and 37°C). Liquid condensed domains (bright areas) were dispersed in a liquid expanded phase (dark areas). Adapted from Telesford, 2012.....	77
Figure 15. Illustration of the surface tension forces (F_s) acting on a floating sphere located at the air/liquid interface. θ is the contact angle. Adapted from Liu et al., 2009.....	78
Figure 16. Schematic of the position of a particle according to its hydrophobicity at a fluid/fluid interface. θ is the contact angle (Maestro et al., 2014).....	78
Figure 17. Π -A isotherm for 2.6 µm diameter monodisperse spherical polystyrene particles at the octane/water interface. Letters A, B and C and numbers 1, 2 and 3 represent different regions in the isotherm (Aveyard et al., 2000b).....	80
Figure 18. Graphical representation of the coexistence of long and short ripples with wavelengths λ_1 and λ_2 found in monolayers of fumed silica particles at the octane/water interface after collapse (Horozov et al., 2006).	81
Figure 19. Schematic representation of the electrical double layer around a spherical colloidal particle and the electric potential (Alias, 2013).	82
Figure 20. Schematic of the respiratory system and alveoli. Adapted from Dorland's-Medical-Dictionary-for-Health-Consumers, 2007.	85
Figure 21. Schematic of the structure of the alveoli. The lung surfactant is a mixture of phospholipids, neutral lipids and proteins located at the air/liquid interface of the entire alveolar region. Adapted from Hawgood and Clements, 1990.....	87
Figure 22. Illustration of the monolayer to multilayer transition plateau at a Π around ~ 45 mN/m in a compression isotherm of Curosurf®, a natural lung surfactant.	91

Figure 23. Graphical representation of the lung surfactant composition, the major phospholipids being DPPC – dipalmitoylphosphatidylcholine (the most abundant component of lung surfactant), UPC – unsaturated phosphatidylcholine and PG – Phosphatidylglycerol.	92
Figure 24. Chemical structure of DPPC. The complete chemical formula of a molecule of palmitic acid is $\text{CH}_3(\text{CH}_2)_{14}\text{COOH}$.	93
Figure 25. Scale axis of cells, viruses, biological structures, molecules and atoms. Adapted from Purves et al., 2003.	104
Figure 26. Graphical representation of the deposition of inhaled particles in the human respiratory tract. The model splits the respiratory tract into three regions: nasopharyngeal region, tracheobronchial region and alveolar region. Adapted from ICRP, 1994.	112
Figure 27. Schematic of nanoparticle deposition at the alveolar air/liquid interface and the possibility of translocation of nanoparticles across the alveolar epithelium and into the lymphatic and circulatory system and accumulation in various secondary organs. For example, some inhaled nanoparticles have been shown to be excreted by the kidneys into the urine (Kreyling et al., 2010).	115
Figure 28. Illustration of the KSV Nima [®] Langmuir-Wilhelmy balance system: 1. Trough; 2. Subphase;	123
Figure 29. Illustration of the temperature measurement probe (left) and Julabo circulator/water bath (right) used to regulate the subphase temperature of a Langmuir trough. Adapted from KSV-Nima, 2014.	124
Figure 30. Graphical representation of the available surface area in a Langmuir trough which is the area between the barriers and the edges of the trough.	125
Figure 31. Illustration of the dipping mechanism in a Langmuir-Wilhelmy Balance system. Adapted from KSV-Nima, 2014.	126
Figure 32. Illustration of the experimental set-up data screen. The experimental set-up data were entered before each experiment with information related to the Wilhelmy plate dimensions, trough area, subphase composition/temperature, surfactant used and substrate (KSV-Nima, 2010).	127
Figure 33. Illustration of the trough control window used to select the type of experiment as well as the barrier speed before each experiment performed using the Langmuir-Wilhelmy balance (KSV-Nima, 2010).	128
Figure 34. Illustration of the deposition of a monolayer onto a solid substrate by vertically passing the substrate through the monolayer, also called Langmuir-Blodgett deposition. Adapted from KSV-Nima, 2010.	129

Figure 35. DPPC Π -Mma isotherm for Π values between 1-5 mN/m and equation of line of best fit to calculate the lift-off Mma of the isotherm. The isotherm was measured in water at 21°C. This method was also used for DPPC isotherms measured at 37°C..... 133

Figure 36. DPPC Π -Mma isotherm (black line) measured in water at 21°C (top) and at 37°C (bottom) with the lines of best fit in different regions of the isotherm. C_m was calculated for each region from the slopes of the lines of best fit. For the isotherm measured at 21°C, the regions should correspond to the following monolayer phases: LE (purple line), LE-LC transition plateau (green line), LC (red line) and S (blue line). For the isotherm measured at 37°C, the entire isotherm was in LE phase for Π above 0 mN/m and thus, C_m was evaluated in different parts of the isotherm indicated by the purple, green and red line. n = 5 experiments/condition. 135

Figure 37. Graphical representation of derivation of the collapse Π and collapse Mma of a DPPC Π -Mma isotherm measured in water at 21°C. n = 5 experiments. This method was also used for DPPC isotherms measured at 37°C..... 136

Figure 38. Π -Mma isotherms measured under ostensibly the same experimental conditions (6 μ g of DPPC, PBS subphase at 37°C) but resulting in different lift-off Mma. The table shows the lift-off Mma of each isotherm as well as the average lift-off Mma value, standard deviation of this and the relative standard deviation. n = 1 experiment per isotherm measured under the same conditions. 138

Figure 39. Π -A isotherm of the reference DPPC solution measured under the following experimental conditions: ultrapure water subphase at 21°C, trough area of 76 cm² and compression barrier speed of..... 141

Figure 40. Π -Mma isotherms measured in PBS at 37°C to investigate the variability between DPPC isotherms measured under ostensibly the same experimental conditions. The DPPC mass deposited for each experiment was 6 μ g. n = 1 experiment per isotherm measured under the same conditions. 145

Figure 41. Π -Mma isotherms measured in PBS at 21°C to investigate the variability between DPPC isotherms measured under ostensibly the same experimental conditions. The DPPC mass deposited for each experiment was 7 μ g. n = 1 experiment per isotherm measured under the same conditions. 147

Figure 42. Π -A isotherms measured in PBS at 37°C after depositing a DPPC mass of 5.25 μ g, 6.00 μ g and 6.75 μ g. The table shows the lift-off area, collapse area, collapse Π and length of the isotherm from the lift-off area to the collapse area for each DPPC mass. n = 3 experiments/condition. 151

Figure 43. <i>II</i> -Mma isotherms determined by normalising the <i>II</i> -A isotherms measured in PBS at 37°C after depositing a DPPC mass of 5.25 µg, 6.00 µg and 6.75 µg to the DPPC mass content. n = 3 experiments/condition.	153
Figure 44. Effect of barrier speed (5, 40, 90 and 270 mm/min) on the <i>II</i> -Mma isotherm measured for DPPC in water at 21°C. The DPPC mass deposited for each experiment was 8 µg. n = 5 experiments/condition.	157
Figure 45. <i>II</i> -A isotherms of a DPPC monolayer compressed and expanded 2 times from 0 to ~ 52 mN/m measured in PBS at 21°C (experiment 1). The table shows the lift-off area for each compression isotherm.	161
Figure 46. <i>II</i> -A isotherms of a DPPC monolayer compressed and expanded 2 times, from 0 to ~ 57 mN/m in the first cycle, measured in PBS at 21°C (experiment 2). The table shows the lift-off area for each compression isotherm. n = 1 experiment/cycle.	162
Figure 47. <i>II</i> -Mma isotherms of DPPC obtained with a conventional Langmuir trough and a ribbon barrier trough (KSV-Nima, 2012).	163
Figure 48. Effect of subphase composition, water or PBS, on the <i>II</i> -Mma isotherm measured for DPPC at 21°C. The DPPC mass deposited for each experiment was 7 µg. n = 4 experiments/condition.	165
Figure 49. Effect of subphase temperature, 37°C or 21°C, on the <i>II</i> -Mma isotherm measured for DPPC in PBS. The DPPC mass deposited for each experiment was 7 µg. n = 4 experiments/condition.	168
Figure 50. Monolayer phases of a <i>II</i> -Mma isotherm measured for DPPC in PBS at 37°C. .	169
Figure 51. Effect of the trough size/surface area, small (76 cm ²) or medium (238 cm ²), on the <i>II</i> -Mma isotherm measured for DPPC in PBS at 37°C. The table shows the area of the trough, the DPPC mass deposited, the barrier speed and the collapse <i>II</i> . n = 5 experiments for small trough and n = 3 experiments for medium trough.	171
Figure 52. Effect of relative humidity, ambient (~ 45%) or high (> 87%), on the <i>II</i> -Mma isotherm, measured for DPPC in PBS at 37°C. The DPPC mass deposited for each experiment was 6 µg. n = 5 experiments for ambient relative humidity and n = 4 experiments for high relative humidity.	175
Figure 53. Effect of subphase volume, normal (62 mL) or low (50 mL), on the <i>II</i> -Mma isotherm measured for DPPC in PBS at 21°C. The DPPC mass deposited was 11 µg for the low subphase volume and 7 µg for the normal subphase volume. n = 3 experiments/condition.	178
Figure 54. Illustration of the fluorite structure of a unit cell of CeO ₂ (Vyas, 2005).	195

Figure 55. Illustration of the aerosol exposure system developed for the deposition of nanoparticles in aerosol form onto a Langmuir trough. It consisted of a TSI® Constant Output Atomiser (COA), an exposure chamber and an airflow system that distributed the aerosolised nanoparticles through the system. A Scanning Mobility Particle Sizer (SMPS) Spectrometer sampled the aerosolised nanoparticles within the exposure chamber. 201

Figure 56. Illustration of the TSI® Constant Output Atomiser Model 3076 used to generate aerosolised nanoparticles and its different parts: air filter, pressure control, bottle with nanoparticle suspension, atomiser assembly block and diffusion dryer. Adapted from TSI, 2005. 202

Figure 57. Illustration of the aerosol exposure chamber used to deposit nanoparticles in aerosol form onto a Langmuir trough. It had a gas inlet connected to the TSI COA and four gas outlets to promote a homogeneous distribution of the aerosol within the chamber. 203

Figure 58. Schematic diagram of the airflow system that distributed the aerosolised nanoparticles through the aerosol exposure system. 204

Figure 59. Illustration of the equipment used to sample aerosolised nanoparticles onto a filter membrane (located inside the filter holder) using a pump preceded by a flow meter. This equipment was used to determine the aerosol mass concentration within the chamber. 205

Figure 60. Illustration of the quartz crystal microbalance placed inside the exposure chamber at a similar height as the Langmuir trough and used to determine an average aerosol deposition velocity. 209

Figure 61. Illustration of the set-up of six EMFAB® filter membranes used to determine an average aerosol deposition velocity. The filters were placed on top of the Langmuir trough together with four TEM grids for nanoparticle imaging purposes. 210

Figure 62. TEM images of CeO₂ primary particles at different magnifications. The scale bar in the left image is 20 nm and in the right image is 5 nm. 213

Figure 63. TEM images of CeO₂ nanoparticle agglomerates. The scale bar is 200 nm for both images. 213

Figure 64. SEM images of the same area at two magnifications from a dipping experiment performed after depositing 60 µg of CeO₂ nanoparticles suspended in chloroform onto PBS at 21°C and compressing the interface to the smallest area technically feasible. The box area in the left image indicates the region displayed in the right image at higher magnification. In the right image, CeO₂ nanoparticle agglomerates (indicated by a blue arrow) were covered in some cases by a layer of salt (indicated by a red arrow). The dotted scale bar in the left image is 50 µm and in the right image is 10 µm. 216

Figure 65. SEM images of the same area at two magnifications from a dipping experiment performed after depositing 60 μg of CeO_2 nanoparticles suspended in chloroform onto PBS at 21°C and compressing the interface to the smallest area technically feasible. The box area in the left image indicates the region displayed in the right image at higher magnification. The dotted scale bar in the left image is 50 μm and in the right image is 5 μm 216

Figure 66. ToF-SIMS (left) and SEM (right) images from a dipping experiment performed by submerging a mica sheet in a clean PBS solution at 21°C. The areas imaged with each technique were different. ToF-SIMS image is 100 μm x 100 μm and the presence of sodium ions (Na^+) is indicated by the green colour scale located at the right side of the image. In the SEM image, the dotted scale bar is 50 μm 217

Figure 67. Graphical representation of the influence of pH on the θ . The maximum θ occurs at the isoelectric point decreasing symmetrically on either side. Adapted from Hanly et al., 2011. 218

Figure 68. SEM images of CeO_2 nanoparticle agglomerates. The dipping experiment was performed after depositing 60 μg of CeO_2 nanoparticles suspended in chloroform onto a water subphase at 21°C and compressing the interface to the smallest area technically feasible. The dotted scale bar is 50 μm for both images. 219

Figure 69. ToF-SIMS images of CeO_2 nanoparticle agglomerates. The dipping experiment was performed after depositing 60 μg of CeO_2 nanoparticles suspended in chloroform onto a water subphase at 21°C and compressing the interface to the smallest area technically feasible. The presence of CeO_2 nanoparticles is indicated by the green colour scale located at the right side of each image. Images are 100 μm x 100 μm 219

Figure 70. Π -A isotherm recorded after depositing 60 μg of CeO_2 nanoparticles suspended in chloroform onto a clean PBS subphase at 21°C and compressing the interface to the smallest area technically feasible. The Π -A isotherm of PBS was first measured to ensure that the subphase was clean. The table shows the maximum Π value reached for each isotherm. n = 1 experiment/condition. 221

Figure 71. Effect of the exposure of a DPPC monolayer to different CeO_2 nanoparticle masses on the DPPC 223

Figure 72. Effect of the exposure of a DPPC monolayer to different CeO_2 nanoparticle masses on the Π -Mma isotherm measured in PBS at 21°C. CeO_2 nanoparticles were suspended in chloroform and deposited onto a DPPC monolayer using a microsyringe. n = 3 experiments/condition. 226

Figure 73. SEM and ToF-SIMS images of LB films of pure DPPC (left image) and DPPC exposed to CeO₂ nanoparticles suspended in chloroform (3.20/1 CeO₂/DPPC mass ratio, right image) produced in PBS at 21°C during the initial compression of the monolayer at three different Π values: 20 (A), 40 (B) and 70 (C) mN/m. The areas imaged with each technique were different. In the SEM images, the dotted scale bar is 50 μm . ToF-SIMS images are 100 μm x 100 μm and the presence of CeO₂ nanoparticles is indicated by the green colour scale located at the right side of each image. 229

Figure 74. SEM and ToF-SIMS images of LB films of pure DPPC (left image) and DPPC exposed to CeO₂ nanoparticles suspended in chloroform (3.20/1 CeO₂/DPPC mass ratio, right image) produced at a Π value of 40 mN/m after three compression-expansion cycles performed at normal barrier speed in PBS at 21°C. The areas imaged with each technique were different. In the SEM images, the dotted scale bar is 50 μm . ToF-SIMS images are 100 μm x 100 μm and the presence of CeO₂ nanoparticles is indicated by the green colour scale located at the right side of each image. 232

Figure 75. SEM and ToF-SIMS images of LB films of pure DPPC (left image) and DPPC exposed to CeO₂ nanoparticles suspended in chloroform (3.20/1 CeO₂/DPPC mass ratio, right image) produced at a Π value of 40 mN/m after three compression-expansion cycles performed at maximum barrier speed in PBS at 21°C. The areas imaged with each technique were different. In the SEM images, the dotted scale bar is 50 μm . ToF-SIMS images are 100 μm x 100 μm and the presence of CeO₂ nanoparticles is indicated by the green colour scale located at the right side of each image. 233

Figure 76. SEM images of pure DPPC (left) and DPPC exposed to CeO₂ nanoparticles suspended in chloroform (right) at a Π value of 20 mN/m from a dipping experiment performed after depositing CeO₂ nanoparticles suspended in chloroform onto a DPPC monolayer at a 3/1 CeO₂/DPPC mass ratio measured in water at 21°C. The dotted scale bar is 50 μm for both images. 236

Figure 77. SEM images of CeO₂ nanoparticle agglomerates with different surface concentration. Voids are seen in the agglomerate with higher surface concentration (right image) and indicated by red arrows. These images correspond to the dipping experiment performed at a Π value of 40 mN/m after depositing CeO₂ nanoparticles suspended in chloroform onto a DPPC monolayer located at the air/PBS interface at a 3.20/1 CeO₂/DPPC mass ratio and cycling the interface 3 times at normal barrier speed. The dotted scale bar is 5 μm for both images. 237

Figure 78. Π -A compression isotherms measured after depositing 60 μg of CeO_2 nanoparticles suspended in chloroform onto a water subphase (left) and onto a PBS subphase (right) at 21°C and compressing the interface five times to the smallest area technically feasible. The tables show the lift-off area and the maximum Π reached after each compression. $n = 1$ experiment/cycle. 239

Figure 79. AFM height images of an LB film of a DPPC monolayer when deposited onto a water subphase at 21°C (left) and when deposited onto a PBS subphase at 21°C (right), taken at a Π value of 40 mN/m. AFM was operated in tapping mode. The height of the interface is indicated by the scale located at the right side of each image. The scale bar in the left image ranges from -0.2 nm to 0.2 nm and in the right image from -69.3 nm to 89.3 nm. These images illustrate the presence of large salt crystals across the monolayer when using a PBS subphase compared to a water subphase. 242

Figure 80. TEM images of CeO_2 nanoparticle agglomerates that correspond to the 1.25/1 CeO_2 /DPPC mass ratio suspension in chloroform (left image) and to the CeO_2 nanoparticle suspension in chloroform (right image). The scale bar is 200 nm for both images. 245

Figure 81. TEM image of a CeO_2 nanoparticle agglomerate probably coated with DPPC (indicated by a red arrow). This image corresponds to the 1.25/1 CeO_2 /DPPC mass ratio suspension in chloroform. The scale bar is 20 nm. 246

Figure 82. SEM and ToF-SIMS images of LB films of pure DPPC (left) and DPPC mixed with CeO_2 nanoparticles in chloroform at a 3/1 CeO_2 /DPPC mass ratio (right) produced in PBS at 21°C during the initial compression of the monolayer at four different Π values: 20 (A), 40 (B), 60 (C) and 70 (D) mN/m. The areas imaged with each technique were different. In the SEM images, the dotted scale bar is 50 μm . ToF-SIMS images are 100 μm x 100 μm and the presence of CeO_2 nanoparticles is indicated by the green colour scale located at the right side of each image. 249

Figure 83. SEM and ToF-SIMS images of LB films of pure DPPC (left image) and DPPC mixed with CeO_2 nanoparticles in chloroform (3/1 CeO_2 /DPPC mass ratio, right image) produced at a Π value of 40 mN/m after 3 compression-expansion cycles performed at normal barrier speed in PBS at 21°C . The areas imaged with each technique were different. In the SEM images, the dotted scale bar is 50 μm . ToF-SIMS images are 100 μm x 100 μm and the presence of CeO_2 nanoparticles is indicated by the green colour scale located at the right side of each image. 253

Figure 84. SEM and ToF-SIMS images of LB films of pure DPPC (left image) and DPPC mixed with CeO ₂ nanoparticles in chloroform (3/1 CeO ₂ /DPPC mass ratio, right image) produced at a Π value of 40 mN/m after 3 compression-expansion cycles performed at maximum barrier speed in PBS at 21°C. The areas imaged with each technique were different. In the SEM images, the dotted scale bar is 50 μ m. ToF-SIMS images are 100 μ m x 100 μ m and the presence of CeO ₂ nanoparticles is indicated by the green colour scale located at the right side of each image.	254
Figure 85. Normalised count of CeO ⁺ ions derived from the ToF-SIMS image data at Π values of 20, 40, 60 and 70 mN/m during the initial compression of the monolayer. The dipping experiments were performed after depositing a 3/1 CeO ₂ /DPPC mass ratio suspension in chloroform onto a clean PBS subphase at 21°C. Two different sample areas were analysed per Π	257
Figure 86. SEM images of LB films of DPPC mixed with CeO ₂ nanoparticles in chloroform at a 3/1 CeO ₂ /DPPC mass ratio produced in water at 21°C during the initial compression of the monolayer at four different Π values: 20, 40, 60 and 70 mN/m. The dotted scale bar is 50 μ m.	259
Figure 87. Effect of the deposition of different CeO ₂ /DPPC mass ratio mixtures suspended in chloroform onto a PBS subphase on the Π -Mma isotherm measured at 37°C. n = 4 experiments/condition.	261
Figure 88. Effect of the deposition of different CeO ₂ /DPPC mass ratio mixtures suspended in chloroform onto a PBS subphase on the Π -Mma isotherm measured at 21°C. n = 5 experiments/condition.	264
Figure 89. Graphical representation of the effect of the deposition of different CeO ₂ /DPPC mass ratio suspensions in chloroform onto a PBS subphase at 21°C on the C_m	266
Figure 90. Graphical representation of the effect of the deposition of different CeO ₂ /DPPC mass ratio suspensions in chloroform on the lift-off Mma of the Π -Mma isotherms measured in PBS at 37°C (blue) and at 21°C (red).	267
Figure 91. Graphical representation of the effect of the deposition of different CeO ₂ /DPPC mass ratios in chloroform on the Mma of the Π -Mma isotherms at different Π values. The experiments were performed in PBS at 37°C (left) and 21°C (right). Note the reduced segment of the y axis. The lines are representative of the trend.....	273
Figure 92. Π -Mma isotherms corresponding to the 0.05/1 and 3.00/1 CeO ₂ /DPPC mass ratio suspensions in chloroform measured in PBS at 21°C using a low subphase volume of 50 mL. n = 1 experiment/condition.	274

Figure 93. TEM images of aerosol CeO₂ nanoparticle agglomerates upon deposition onto a TEM grid located on the Langmuir trough over 6 hours. The scale bar is 0.5 μm for all the images..... 281

Figure 94. Illustration of the set-up of 4 TEM grids used in the 6 hour experiment to determine the spatial distribution of aerosol CeO₂ nanoparticle agglomerates upon deposition. The TEM grids are numbered sequentially from left to right. 282

Figure 95. SEM images of the same area at two magnifications of CeO₂ nanoparticle agglomerates. The dipping experiment was performed after depositing approximately 33 μg of aerosolised CeO₂ nanoparticles onto a PBS subphase at 21°C and compressing the interface to the smallest area technically feasible. The box area in the left image indicates the region displayed in the right image at higher magnification. In the right image, CeO₂ nanoparticle agglomerates (indicated by a blue arrow) were covered in some cases by a layer of salt (indicated by a red arrow). The dotted scale bar in the left image is 50 μm and in the right image is 10 μm. 284

Figure 96. ToF-SIMS images of CeO₂ nanoparticle agglomerates (left) and sodium (right). The dipping experiment was performed after depositing approximately 33 μg of aerosolised CeO₂ nanoparticles onto a PBS subphase at 21°C and compressing the interface to the smallest area technically feasible. The presence of CeO₂ nanoparticles and sodium is indicated by the green colour scale located at the right side of each image. Images are 100 μm x 100 μm..... 285

Figure 97. Normalised count of CeO⁺ ions derived from the ToF-SIMS image data. The dipping experiments were performed after depositing approximately 33 μg of aerosolised CeO₂ nanoparticles (aerosol deposition method) and 60 μg of CeO₂ nanoparticles suspended in chloroform (liquid deposition method 1) onto a clean PBS subphase at 21°C and compressing the interface to the smallest area technically feasible. Two different sample areas were analysed per deposition method. 286

Figure 98. SEM images of CeO₂ nanoparticle agglomerates. The dipping experiments were performed after depositing approximately 33 μg of aerosolised CeO₂ nanoparticles (aerosol deposition method) and 60 μg of CeO₂ nanoparticles suspended in chloroform (liquid deposition method 1) onto a clean PBS subphase at 21°C and compressing the interface to the smallest area technically feasible. The dotted scale bar is 100 μm for both images..... 287

Figure 99. Π -A isotherm recorded after depositing approximately 33 μg of aerosolised CeO_2 nanoparticles onto a clean PBS subphase at 21°C and compressing the interface to the smallest area technically feasible. The Π -A isotherm of PBS was first measured to ensure that the subphase was clean. The table shows the maximum Π value reached for each isotherm. $n = 1$ experiment/condition..... 288

Figure 100. Π -A compression isotherms measured after depositing approximately 33 μg of aerosolised CeO_2 nanoparticles (aerosol deposition method) and 60 μg of CeO_2 nanoparticles suspended in chloroform (liquid deposition method 1) onto a clean PBS subphase at 21°C and compressing the interface five times to the smallest area technically feasible. The tables show the lift-off area and the maximum Π reached after each compression. $n = 1$ experiment/cycle. 290

Figure 101. SEM and ToF-SIMS images of LB films of pure DPPC (left) and DPPC exposed to CeO_2 nanoparticles (deposited by aerosol, right) at a 1.12/1 CeO_2 /DPPC mass ratio, produced in PBS at 21°C during the initial compression of the monolayer at two different Π values: 40 (A) and 70 (B) mN/m . The areas imaged with each technique were different. In the SEM images, the dotted scale bar is 50 μm . ToF-SIMS images are 100 μm x 100 μm and the presence of CeO_2 nanoparticles is indicated by the green colour scale located at the right side of each image. 294

Figure 102. SEM and ToF-SIMS images of LB films of pure DPPC (left image) and DPPC exposed to CeO_2 nanoparticles (deposited by aerosol, 1.12/1 CeO_2 /DPPC mass ratio, right image) produced at a Π value of 40 mN/m after 3 compression-expansion cycles performed at normal barrier speed in PBS at 21°C . The areas imaged with each technique were different. In the SEM images, the dotted scale bar is 50 μm . ToF-SIMS images are 100 μm x 100 μm and the presence of CeO_2 nanoparticles is indicated by the green colour scale located at the right side of each image. 296

Figure 103. SEM and ToF-SIMS images of LB films of pure DPPC (left) and DPPC exposed to CeO_2 nanoparticles (deposited by aerosol, right) at a 2.42/1 CeO_2 /DPPC mass ratio, produced in PBS at 21°C during the initial compression of the monolayer at a Π value of 20 mN/m . The areas imaged with each technique were different. In the SEM images, the dotted scale bar is 50 μm . ToF-SIMS images are 100 μm x 100 μm and the presence of CeO_2 nanoparticles is indicated by the green colour scale located at the right side of each image. 298

Figure 104. SEM and ToF-SIMS images of LB films of pure DPPC (left image) and DPPC exposed to CeO₂ nanoparticles (deposited by aerosol, 2.42/1 CeO₂/DPPC mass ratio, right image) produced at a Π value of 40 mN/m after 3 compression-expansion cycles performed at maximum barrier speed in PBS at 21°C. The areas imaged with each technique were different. In the SEM images, the dotted scale bar is 50 μ m. ToF-SIMS images are 100 μ m x 100 μ m and the presence of CeO₂ nanoparticles is indicated by the green colour scale located at the right side of each image. 299

Figure 105. Normalised count of CeO⁺ ions derived from the ToF-SIMS image data at Π values of 40 and 70 mN/m during the initial compression of the monolayer (experiment 1). The dipping experiment was performed in PBS at 21°C after depositing aerosolised CeO₂ nanoparticles onto a DPPC monolayer at a 1.12/1 NP/DPPC mass ratio. Two different sample areas were analysed per Π 301

Figure 106. Effect of the exposure of a DPPC monolayer to aerosolised ultrapure water over increasing exposure times on the Π -Mma isotherm measured in PBS at 37°C. n = 3 experiments for control (0 minute exposure experiment) and n = 1 experiment for 30, 90 and 180 minute exposure experiments. 303

Figure 107. Graphical representation of the effect of the exposure of a DPPC monolayer to aerosolised ultrapure water over increasing exposure times on the lift-off Mma of the Π -Mma isotherms measured in PBS at 37°C. 305

Figure 108. Effect of the exposure of a DPPC monolayer to aerosolised ultrapure water over increasing exposure times on the Π -Mma isotherm measured in PBS at 21°C. n = 3 experiments for control (0 minute exposure experiment) and n = 1 experiment for 10, 90 and 150 minute exposure experiments. 306

Figure 109. DPPC Π -Mma isotherm measured after leaving the monolayer undisturbed for 15 minutes (blue isotherm) and 80 minutes (red isotherm) measured in PBS at 21°C. n = 4 experiments for the 15 minute experiment and n = 2 experiments for the 80 minute experiment. 308

Figure 110. TEM images taken from TEM grids placed onto the Langmuir trough and exposed to aerosolised ultrapure water over 120 minutes. The scale bar is 0.2 μ m for both images. . 309

Figure 111. Graphical representation of the CeO₂ aerosol size distribution for an experiment performed to study the effect of the exposure of a DPPC monolayer to aerosolised water, compressed air flow and aerosolised CeO₂ nanoparticles over 60 minutes measured in PBS at 37°C. 311

Figure 112. Effect of the exposure of a DPPC monolayer to aerosolised water, compressed air flow and aerosolised CeO₂ nanoparticles over 60 minutes (4.53/1 CeO₂/DPPC mass ratio) on the *II*-Mma isotherm measured in PBS at 37°C. n = 1 experiment/condition. 312

Figure 113. Effect of the exposure of a DPPC monolayer to aerosolised water, compressed air flow and aerosolised CeO₂ nanoparticles over 45 minutes (3.09/1 CeO₂/DPPC mass ratio) on the *II*-Mma isotherm measured in PBS at 37°C. n = 1 experiment/condition. 315

Figure 114. Graphical representation of the CeO₂ aerosol size distribution for each of the four experiments performed to study the effects of the exposure of a DPPC monolayer to increasing amounts of aerosolised CeO₂ nanoparticles measured in PBS at 37°C. 318

Figure 115. Effect of the exposure of a DPPC monolayer to increasing amounts of aerosolised CeO₂ nanoparticles over increasing exposure times on the *II*-Mma isotherm measured in PBS at 37°C. n = 3 experiments for 0 minute exposure experiment and n = 1 experiment for 10, 30, 60 and 150 minute exposure experiments. 319

Figure 116. Graphical representation of the effect of the exposure of a DPPC monolayer to increasing amounts of aerosolised CeO₂ nanoparticles (0.15/1, 0.93/1, 2.98/1 and 13.48/1 CeO₂/DPPC mass ratios) on the collapse *II* of the *II*-Mma isotherms measured in PBS at 37°C. 319

Figure 117. Graphical representation of the CeO₂ aerosol size distribution for the 10 and 90 minute experiments performed to study the effects of the exposure of a DPPC monolayer to increasing aerosolised CeO₂ nanoparticle mass measured in PBS at 21°C. 321

Figure 118. Effect of the exposure of a DPPC monolayer to aerosolised CeO₂ nanoparticles over 10 minutes (0.10/1 CeO₂/DPPC mass ratio, left image) and over 90 minutes (2.31/1 CeO₂/DPPC mass ratio, right image) on the *II*-Mma isotherm measured in PBS at 21°C. The control isotherm was measured after exposing a DPPC monolayer to compressed air flow for the same duration. n = 1 experiment/condition. 323

Figure 119. Comparison of the effects of the three different CeO₂ nanoparticle deposition methods used in the present work on the DPPC *II*-Mma isotherm, using the most similar NP/DPPC mass ratios. Deposition method 1 refers to the deposition of CeO₂ nanoparticles suspended in chloroform onto a preformed DPPC monolayer. Deposition method 2 refers to the deposition of CeO₂ nanoparticles and DPPC mixtures in the same chloroform suspension onto a clean subphase. Deposition method 3 refers to the deposition of aerosolised CeO₂ nanoparticles onto a preformed DPPC monolayer. The CeO₂ NP/DPPC mass ratios were 3.64/1 for deposition method 1, 3.75/1 for deposition method 2 and 4.53/1 for deposition method 3. For deposition methods 1 and 2, the control isotherm was measured after leaving a DPPC

monolayer undisturbed for 15 minutes. For deposition method 3, the control isotherm was measured after exposing a DPPC monolayer to compressed air flow for the same exposure duration as the aerosol CeO₂ nanoparticle experiment. The subphase used was PBS at 37°C.

.....	335
Figure 120. Illustration of the structure of a carbon black agglomerate (left) and spherical carbon black particle (right). Adapted from Deshmukh et al., 2010 and Liu, 2013.	343
Figure 121. TEM images of CB primary particles.	348
Figure 122. Graphical representation of the CB aerosol size distribution for the 5 and 6 hour experiments performed to calculate an average deposition velocity for aerosolised CB nanoparticles using four EMFAB filters.	349
Figure 123. Size distribution of aerosolised CB nanoparticle agglomerates upon deposition onto the Langmuir trough obtained by analysing two TEM grids used in the 6 hour experiment.	352
Figure 124. TEM images of aerosolised CB nanoparticle agglomerates upon deposition onto a TEM grid located on the Langmuir trough over 6 hours. The scale bar is 0.5 μm for all the images.	353
Figure 125. Graphical representation of the CB aerosol size distribution for an experiment performed to study the wettability and surface tension activity of aerosolised CB nanoparticles when deposited onto a clean PBS subphase at 21°C.	356
Figure 126. SEM images of the same area at two magnifications of CB nanoparticle agglomerates. The dipping experiment was performed after depositing approximately 33 μg of aerosolised CB nanoparticles onto a PBS subphase at 21°C and compressing the interface to the smallest area technically feasible. The box area in the left image indicates the region displayed in the right image at higher magnification. The dotted scale bar in the left image is 100 μm and in the right image is 5 μm	356
Figure 127. Π -A isotherm recorded after depositing approximately 33 μg of aerosolised CB nanoparticles onto a clean PBS subphase at 21°C and compressing the interface to the smallest area technically feasible. The Π -A isotherm of PBS was first measured to ensure that the subphase was clean. The table shows the maximum Π value reached for each isotherm. n = 1 experiment/condition.	358
Figure 128. Π -A compression isotherms measured after depositing approximately 33 μg of aerosolised CB nanoparticles onto a PBS subphase at 21°C and compressing the interface five times to the smallest area technically feasible. The table shows the lift-off area and the maximum Π reached after each compression. n = 1 experiment/cycle.	359

Figure 129. Graphical representation of the CB aerosol size distribution for a dipping experiment performed in PBS at 21°C after exposing a DPPC monolayer to aerosolised CB nanoparticles to investigate the presence of CB nanoparticles at the interface during the initial compression of the monolayer and after three compression-expansion cycles at maximum barrier speed.	362
Figure 130. SEM images of LB films of pure DPPC (left) and DPPC exposed to CB nanoparticles (deposited by aerosol, right) at a 1/3.22 CB/DPPC mass ratio, produced in PBS at 21°C during the initial compression of the monolayer at three different Π values: 20, 40 and 70 mN/m. The dotted scale bar is 50 μm for all the images.	363
Figure 131. SEM images of LB films of pure DPPC (left image) and DPPC exposed to CB nanoparticles (deposited by aerosol, 1/3.22 CB/DPPC mass ratio, right image) produced at a Π value of 40 mN/m after 3 compression-expansion cycles performed at maximum barrier speed in PBS at 21°C. The dotted scale bar is 50 μm for all the images.	364
Figure 132. Graphical representation of the CB aerosol size distribution for the 10, 90 and 150 minute experiments performed to study the effects of the exposure of a DPPC monolayer to varying amounts of aerosolised CB nanoparticles.	366
Figure 133. Effect of the exposure of a DPPC monolayer to aerosolised CB nanoparticles over 10 minutes (0.02/1 CB/DPPC mass ratio) on the Π -Mma isotherm measured in PBS at 21°C. The control isotherm was measured after exposing a DPPC monolayer to compressed air flow for the same duration. n = 1 experiment/condition.	367
Figure 134. Effect of the exposure of a DPPC monolayer to aerosolised CB nanoparticles over 90 minutes (1.58/1 CB/DPPC mass ratio) on the Π -Mma isotherm measured in PBS at 21°C. The control isotherm was measured after exposing a DPPC monolayer to compressed air flow for the same duration. n = 1 experiment/condition.	369
Figure 135. Effect of the exposure of a DPPC monolayer to aerosolised CB nanoparticles over 150 minutes (1.01/1 CB/DPPC mass ratio) on the Π -Mma isotherm measured in PBS at 21°C. The control isotherm was measured after exposing a DPPC monolayer to compressed air flow for the same duration. n = 1 experiment/condition.	371
Figure 136. Comparison of the effects of the exposure of a DPPC monolayer to aerosolised CeO ₂ and CB nanoparticles on the Π -Mma isotherm. In both experiments the aerosol nanoparticles were deposited over 90 minutes and the NP/DPPC mass ratio was 2.31/1 and 1.58/1 for CeO ₂ and CB nanoparticles respectively. The control isotherm was measured after exposing a DPPC monolayer to compressed air flow for the same duration. The subphase used was PBS at 21°C.	376

List of tables

Table 1. Effect of subdivision of a two metre cube into smaller cubic particles on the area to volume ratio per particle and on the total surface area and total area to volume ratio.....	52
Table 2. Phospholipid composition and chemical structure of lung surfactant (Parent, 1992).	94
Table 3. Neutral lipid composition of lung surfactant (Parent, 1992).	96
Table 4. Clinical surfactant preparations obtained from animal sources (Fox and Sothinathan, 2005).....	102
Table 5. Application and estimated global production of some ENMs (The Royal Society and The Royal Academy of Engineering, 2004).....	106
Table 6. Relevant physicochemical properties of ENMs and their respective associated measurement techniques (Hassellöv et al., 2008, Baalousha et al., 2012a, Baalousha et al., 2012b).....	108
Table 7. Main sources of NMs in the environment (Farré et al., 2011).	110
Table 8. Regions of the DPPC isotherm defined by their lower and upper II range value for which the C_m was determined for isotherms generated at 21°C and 37°C.	136
Table 9. Lift-off M_{ma} of DPPC isotherms generated under different experimental conditions using the LWB as reported in the literature.	139
Table 10. Lift-off M_{ma} value of the II - M_{ma} isotherm measured under different experimental conditions and consequent equation used to determine the DPPC mass deposited onto the subphase.	143
Table 11. Lift-off M_{ma} , C_m , collapse II and collapse M_{ma} of five II - M_{ma} isotherms measured in PBS at 37°C after depositing a DPPC mass of 6 μg . The average value, standard deviation, relative standard deviation and % change from midpoint in each of the parameters are also shown.	146
Table 12. Lift-off M_{ma} , C_m , collapse II and collapse M_{ma} of five II - M_{ma} isotherms measured in PBS at 21°C after depositing a DPPC mass of 7 μg . The average value, standard deviation, relative standard deviation and % change from midpoint in each of the parameters are also shown.	148
Table 13. Compression rate per DPPC molecule for three different monolayers formed after depositing a DPPC mass of 5.25 μg , 6.00 μg and 6.75 μg onto a PBS subphase at 37°C and compressed with the barriers at a speed of 5 mm/min (2.5 cm^2/min).	152

Table 14. Effect of the DPPC mass deposited (5.25 μg , 6.00 μg and 6.75 μg) on the lift-off M_{ma} , C_m , collapse Π and collapse M_{ma} of the Π - M_{ma} isotherms measured in PBS at 37°C. The corresponding values in each of these parameters measured for DPPC masses 6.00 μg and 6.75 μg were compared with those measured for 5.25 μg (control) by calculating the difference in each of the parameters for the experimental isotherm and the control expressed as a % of the control value and dividing them by the reference % change from midpoint values for the relevant reference isotherm (Table 11). This approach assumes similar levels of uncertainties on the control and experimental isotherm parameters to those of the reference isotherm parameters. 154

Table 15. Commonly used and quasi-physiological conditions under which a DPPC monolayer was tested using a LWB system to determine the differences and hence the importance of measuring isotherms under conditions as close as possible to those occurring *in vivo* and to set up the relevant conditions for future experiments..... 156

Table 16. Effect of barrier speed (5, 40, 90 and 270 mm/min) on the lift-off M_{ma} , C_m , collapse Π and collapse M_{ma} of the Π - M_{ma} isotherms measured for DPPC in water at 21°C. The corresponding values in each of these parameters for barrier speeds 40, 90 and 270 mm/min were compared with those for barrier speed 5 mm/min (control) by calculating the difference in each of the parameters for the experimental isotherm and the control expressed as a % of the control value and dividing them by the reference % change from midpoint values for the relevant reference isotherm (Table 12). This approach assumes similar levels of uncertainties on the control and experimental isotherm parameters to those of the reference isotherm parameters. 158

Table 17. Effect of subphase composition, water or PBS, on the lift-off M_{ma} , C_m , collapse Π and collapse M_{ma} of the Π - M_{ma} isotherms measured for DPPC at 21°C. The corresponding values in each of these parameters for PBS subphase were compared with those for water subphase (control) by calculating the difference in each of the parameters for the experimental isotherm and the control expressed as a % of the control value and dividing them by the reference % change from midpoint values for the relevant reference isotherm (Table 12). This approach assumes similar levels of uncertainties on the control and experimental isotherm parameters to those of the reference isotherm parameters. 166

Table 18. Effect of subphase temperature, 37°C or 21°C, on the lift-off M_{ma} , C_m , collapse II and collapse M_{ma} of the II - M_{ma} isotherms measured for DPPC in PBS. As the isotherm measured at 37°C was shorter than that measured at 21°C, the C_m was calculated for the isotherm regions 1-5, 10-25 and 31 mN/m – lowest collapse II . The corresponding values for subphase temperature of 37°C were compared with those for subphase temperature of 21°C (control) by calculating the difference in each of the parameters for the experimental isotherm and the control expressed as a % of the control value and dividing them by the reference % change from midpoint values for the relevant reference isotherm (Table 11). This approach assumes similar levels of uncertainties on the control and experimental isotherm parameters to those of the reference isotherm parameters. 173

Table 19. Effect of relative humidity, ambient (~ 45%) or high (> 87%), on the lift-off M_{ma} , C_m , collapse II and collapse M_{ma} of the II - M_{ma} isotherms measured for DPPC in PBS at 37°C. The corresponding values in each of these parameters for high relative humidity were compared with those for ambient relative humidity (control) by calculating the difference in each of the parameters for the experimental isotherm and the control expressed as a % of the control value and dividing them by the reference % change from midpoint values for the relevant reference isotherm (Table 11). This approach assumes similar levels of uncertainties on the control and experimental isotherm parameters to those of the reference isotherm parameters. 176

Table 20. Effect of subphase volume, normal (62 mL) or low (50 mL), on the lift-off M_{ma} , C_m , collapse II and collapse M_{ma} of the II - M_{ma} isotherms measured for DPPC in PBS at 21°C. The corresponding values in each of these parameters for low subphase volume were compared with those for normal subphase volume (control) by calculating the difference in each of the parameters for the experimental isotherm and the control expressed as a % of the control value and dividing them by the reference % change from midpoint values for the relevant reference isotherm (Table 12). This approach assumes similar levels of uncertainties on the control and experimental isotherm parameters to those of the reference isotherm parameters. 179

Table 21. Literature studies on DPPC and nanoparticle interactions at the air/liquid interface using a LWB and some of their most relevant characteristics. In these studies nanoparticles were delivered onto the air/liquid interface with the aid of a spreading solvent as described. 192

Table 22. CeO₂ nanoparticle masses and CeO₂/DPPC mass ratios of four experiments performed in PBS at 37°C to study the effects of the exposure of a DPPC monolayer to varying amounts of CeO₂ nanoparticles suspended in chloroform. 223

Table 23. Effect of the exposure of a DPPC monolayer to different CeO₂ nanoparticle masses suspended in chloroform on the lift-off Mma, C_m , collapse Π and collapse Mma of the Π -Mma isotherms measured in PBS at 37°C. The corresponding values in each of these parameters for each CeO₂/DPPC mass ratio were compared with those of pure DPPC (control) by calculating the difference in each of the parameters for the experimental isotherm and the control expressed as a % of the control value and dividing them by the reference % change from midpoint values for the relevant reference isotherm (Table 11). This approach assumes similar levels of uncertainties on the control and experimental isotherm parameters to those of the reference isotherm parameters. 224

Table 24. CeO₂ nanoparticle masses and CeO₂/DPPC mass ratios of four different experiments performed in PBS at 21°C to study the effects of the exposure of a DPPC monolayer to varying amounts of CeO₂ nanoparticles suspended in chloroform. 225

Table 25. Effect of the exposure of a DPPC monolayer to different CeO₂ nanoparticle masses suspended in chloroform on the lift-off Mma, C_m , collapse Π and collapse Mma of the Π -Mma isotherms measured in PBS at 21°C. The corresponding values in each of these parameters for each CeO₂/DPPC mass ratio were compared with those of pure DPPC (control) by calculating the difference in each of the parameters for the experimental isotherm and the control expressed as a % of the control value and dividing them by the reference % change from midpoint values for the relevant reference isotherm (Table 12). This approach assumes similar levels of uncertainties on the control and experimental isotherm parameters to those of the reference isotherm parameters. 227

Table 26. CeO₂/DPPC mass ratios, CMD, GSD and Z-average diameter for each of the suspensions in chloroform used in the experiments performed in PBS at 37°C to study the effect of the deposition of different CeO₂/DPPC mass ratios on the Π -Mma isotherm..... 243

Table 27. CeO₂/DPPC mass ratios and zeta potential for each of the suspensions in chloroform used in the experiments performed in PBS at 21°C to study the effect of the deposition of different CeO₂/DPPC mass ratios on the Π -Mma isotherm. 244

Table 28. CeO₂/DPPC mass ratios, Z-average diameter, zeta potential and pH for each of the suspensions in PBS..... 247

Table 29. Area covered by the CeO₂ nanoparticle agglomerates at Π values of 20, 40, 60 and 70 mN/m during the initial compression of the monolayer. The dipping experiments were performed after depositing a 3/1 CeO₂/DPPC mass ratio suspension in chloroform onto a clean PBS subphase at 21°C. The area covered by the CeO₂ nanoparticles was determined by analysing representative SEM images and expressed as a percentage of the total image area. One sample area per Π was analysed. 256

Table 30. CeO₂ nanoparticle and DPPC masses deposited onto a clean PBS subphase at 37°C for the DPPC solution (control) and each CeO₂/DPPC mass ratio suspension in chloroform for a set of experiments performed to study the effect of the deposition of different CeO₂/DPPC mass ratio mixtures on the Π -Mma isotherm. 260

Table 31. Effect of the deposition of different CeO₂/DPPC mass ratio suspensions in chloroform onto a PBS subphase at 37°C on the lift-off Mma, C_m , collapse Π and collapse Mma of the Π -Mma isotherms. The corresponding values in each of these parameters for each CeO₂/DPPC mass ratio mixture were compared with those of pure DPPC (control) by calculating the difference in each of the parameters for the experimental isotherm and the control expressed as a % of the control value and dividing them by the reference % change from midpoint values for the relevant reference isotherm (Table 11). This approach assumes similar levels of uncertainties on the control and experimental isotherm parameters to those of the reference isotherm parameters. 262

Table 32. CeO₂ nanoparticle and DPPC masses deposited onto a clean PBS subphase at 21°C for the DPPC solution (control) and each CeO₂/DPPC mass ratio suspension in chloroform for a set of experiments performed to study the effect of the deposition of different CeO₂/DPPC mass ratio mixtures on the Π -Mma isotherm. 264

Table 33. Effect of the deposition of different CeO₂/DPPC mass ratio suspensions in chloroform onto a PBS subphase at 21°C on the lift-off Mma, C_m , collapse Π and collapse Mma of the Π -Mma isotherms. The corresponding values in each of these parameters for each CeO₂/DPPC mass ratio mixture were compared with those of pure DPPC (control) by calculating the difference in each of the parameters for the experimental isotherm and the control expressed as a % of the control value and dividing them by the reference % change from midpoint values for the relevant reference isotherm (Table 12). This approach assumes similar levels of uncertainties on the control and experimental isotherm parameters to those of the reference isotherm parameters 265

Table 34. Lift-off area of the <i>I</i> -A isotherms for each CeO ₂ /DPPC mass ratio suspension in chloroform measured in PBS at 37°C.	270
Table 35. Lift-off area of the <i>I</i> -A isotherms for each CeO ₂ /DPPC mass ratio suspension in chloroform measured in PBS at 21°C.	270
Table 36. Hypothetical surface area covered by the CeO ₂ nanoparticles determined for different NP/DPPC mass ratio in two ways: (a) using the size of the CeO ₂ nanoparticle agglomerates and (b) using the primary particle size. The calculations were based on the total mass of CeO ₂ nanoparticles deposited in each experiment and a density value of 7.215 g/cm ³ . For comparative purposes, the effect of the presence of the nanoparticles was also determined by subtracting from the lift-off area of the DPPC + NP isotherm the lift-off area of the DPPC only isotherm. Experiments were performed by depositing the NP/DPPC mass ratio mixture suspended in chloroform onto a PBS subphase at 21°C.	272
Table 37. Average aerosol CMD, GSD and number concentration of all the scans run for each of the seven experiments performed to calculate an average deposition velocity for aerosolised CeO ₂ nanoparticles using a QCM.	276
Table 38. Calculation of an average deposition velocity for aerosolised CeO ₂ nanoparticles by performing seven experiments in the exposure chamber using a QCM.	277
Table 39. Average aerosol CMD, GSD and number concentration of all the scans run for each of the two experiments performed to calculate an average deposition velocity for aerosolised CeO ₂ nanoparticles using six EMFAB filters.	278
Table 40. Calculation of an average <i>mda</i> value for each of the two experiments performed to determine an average deposition velocity for aerosolised CeO ₂ nanoparticles using six EMFAB filters.....	278
Table 41. Calculation of an average deposition velocity for aerosolised CeO ₂ nanoparticles by performing two experiments in the exposure chamber using six EMFAB filters.....	279
Table 42. Spatial distribution of aerosol CeO ₂ nanoparticle agglomerates upon deposition calculated for each of the four TEM grids placed onto the Langmuir trough during the 6 hour experiment. The average number of agglomerates per μm ² as well as the SD and RSD are also shown. Number of particles counted per TEM grid: TEM grid 1 = 168, TEM grid 2 = 64, TEM grid 3 = 315, TEM grid 4 = 74.	282
Table 43. Average aerosol CMD, GSD, number concentration, mass concentration and estimated CeO ₂ nanoparticle mass deposited for an experiment performed to study the wettability and surface tension activity of aerosolised CeO ₂ nanoparticles when deposited onto a clean PBS subphase at 21°C.....	283

Table 44. Average aerosol CMD, GSD, number concentration, mass concentration, estimated CeO ₂ nanoparticle mass deposited and CeO ₂ /DPPC mass ratio for a dipping experiment performed in PBS at 21°C.....	293
Table 45. Average aerosol CMD, GSD, number concentration, mass concentration, estimated CeO ₂ nanoparticle mass deposited and CeO ₂ /DPPC mass ratio for a dipping experiment performed in PBS at 21°C.....	297
Table 46. Area covered by the CeO ₂ nanoparticle agglomerates at <i>II</i> values of 40 and 70 mN/m during the initial compression of the monolayer (experiment 1). The dipping experiment was performed in PBS at 21°C after depositing aerosolised CeO ₂ nanoparticles onto a DPPC monolayer at a 1.12/1 NP/DPPC mass ratio. The area covered by the CeO ₂ nanoparticles was determined by analysing representative SEM images and expressed as a percentage of the total image area. Two different sample areas were analysed per <i>II</i>	300
Table 47. Effect of the exposure of a DPPC monolayer to aerosolised ultrapure water over increasing exposure times on the lift-off <i>M_{ma}</i> , <i>C_m</i> , collapse <i>II</i> and collapse <i>M_{ma}</i> of the <i>II</i> - <i>M_{ma}</i> isotherms measured in PBS at 37°C. The corresponding values in each of these parameters measured for each exposure time were compared with those of no exposure (control) by calculating the difference in each of the parameters for the experimental isotherm and the control expressed as a % of the control value and dividing them by the reference % change from midpoint values for the relevant reference isotherm (Table 11). This approach assumes similar levels of uncertainties on the control and experimental isotherm parameters to those of the reference isotherm parameters.	304
Table 48. Effect of the exposure of a DPPC monolayer to aerosolised ultrapure water over increasing exposure times on the lift-off <i>M_{ma}</i> , <i>C_m</i> , collapse <i>II</i> and collapse <i>M_{ma}</i> of the <i>II</i> - <i>M_{ma}</i> isotherm measured in PBS at 21°C. The corresponding values measured in each of these parameters for each exposure time were compared with those of no exposure (control) by calculating the difference in each of the parameters for the experimental isotherm and the control expressed as a % of the control value and dividing them by the reference % change from midpoint values for the relevant reference isotherm (Table 12). This approach assumes similar levels of uncertainties on the control and experimental isotherm parameters to those of the reference isotherm parameters.	307
Table 49. Average aerosol CMD, GSD, number concentration, mass concentration, estimated CeO ₂ nanoparticle mass deposited and CeO ₂ /DPPC mass ratio for an experiment performed to study the effect of the exposure of a DPPC monolayer to aerosolised water, compressed air flow and aerosolised CeO ₂ nanoparticles over 60 minutes measured in PBS at 37°C.....	310

Table 50. Effect of the exposure of a DPPC monolayer to aerosolised water, compressed air flow and aerosolised CeO₂ nanoparticles over 60 minutes (4.53/1 CeO₂/DPPC mass ratio) on the lift-off M_{ma} , C_m , collapse H and collapse M_{ma} of the H - M_{ma} isotherms measured in PBS at 37°C. The corresponding values in each of these parameters measured for water and CeO₂ nanoparticles were compared with those of compressed air flow (control) by calculating the difference in each of the parameters for the experimental isotherm and the control expressed as a % of the control value and dividing them by the reference % change from midpoint values for the relevant reference isotherm (Table 11). This approach assumes similar levels of uncertainties on the control and experimental isotherm parameters to those of the reference isotherm parameters. 313

Table 51. Average aerosol CMD, GSD, number concentration, mass concentration, estimated CeO₂ nanoparticle mass deposited and CeO₂/DPPC mass ratio for an experiment performed to study the effect of the exposure of a DPPC monolayer to aerosolised water, compressed air flow and aerosolised CeO₂ nanoparticles over 45 minutes measured in PBS at 37°C..... 315

Table 52. Exposure time, average aerosol CMD, GSD and number concentration of four different experiments performed to study the effects of the exposure of a DPPC monolayer to increasing amounts of aerosolised CeO₂ nanoparticles measured in PBS at 37°C..... 317

Table 53. Exposure time, aerosol mass concentration, estimated CeO₂ nanoparticle mass deposited, CeO₂/DPPC mass ratio and collapse H of the H - M_{ma} isotherms for each of the four experiments performed to study the effects of the exposure of a DPPC monolayer to increasing amounts of aerosolised CeO₂ nanoparticles measured in PBS at 37°C. 318

Table 54. Exposure time, average aerosol CMD, GSD and number concentration of two experiments performed to study the effects of the exposure of a DPPC monolayer to increasing aerosolised CeO₂ nanoparticle mass measured in PBS at 21°C..... 321

Table 55. Exposure time, aerosol mass concentration, estimated CeO₂ nanoparticle mass deposited and CeO₂/DPPC mass ratio of two experiments performed to study the effects of the exposure of a DPPC monolayer to increasing aerosolised CeO₂ nanoparticle mass measured in PBS at 21°C..... 322

Table 56. Effect of the exposure of a DPPC monolayer to aerosolised CeO₂ nanoparticles over 10 minutes (0.10/1 CeO₂/DPPC mass ratio) on the C_m for the region 30-45 mN/m and the collapse H of the H - M_{ma} isotherms measured in PBS at 21°C. The corresponding values in each of the parameters measured for CeO₂ nanoparticles were compared with those of compressed air flow (control) by calculating the difference in each of the parameters for the experimental isotherm and the control expressed as a % of the control value and dividing them

by the reference % change from midpoint values for the relevant reference isotherm (Table 12). This approach assumes similar levels of uncertainties on the control and experimental isotherm parameters to those of the reference isotherm parameters. Additionally, the assumption was made that for the reference isotherm, the uncertainty values for the C_m for the region 25-45 mN/m would be similar for the region 30-45 mN/m. 324

Table 57. Effect of the exposure of a DPPC monolayer to aerosolised CeO₂ nanoparticles over 90 minutes (2.31/1 CeO₂/DPPC mass ratio) on the C_m for the region 30-45 mN/m and the collapse H of the H -Mma isotherm measured in PBS at 21°C. The corresponding values in each of the parameters measured for CeO₂ nanoparticles were compared with those of compressed air flow (control) by calculating the difference in each of the parameters for the experimental isotherm and the control expressed as a % of the control value and dividing them by the reference % change from midpoint values for the relevant reference isotherm (Table 12). This approach assumes similar levels of uncertainties on the control and experimental isotherm parameters to those of the reference isotherm parameters. Additionally, the assumption was made that for the reference isotherm, the uncertainty values for the C_m for the region 25-45 mN/m would be similar for the region 30-45 mN/m. 325

Table 58. Summary of the experimental conditions for the three different CeO₂ nanoparticle deposition methods used in the present work and their effects on the DPPC isotherm. 336

Table 59. Average aerosol CMD, GSD and number concentration of all the scans run for each of the two experiments performed to calculate an average deposition velocity for aerosolised CB nanoparticles using four EMFAB filters. 349

Table 60. Calculation of an average mda value for each of the two experiments performed to determine an average deposition velocity for aerosolised CB nanoparticles using four EMFAB filters. 350

Table 61. Calculation of an average deposition velocity for aerosolised CB nanoparticles by performing two experiments in the exposure chamber using four EMFAB filters. 351

Table 62. Spatial distribution of the aerosol CB nanoparticle agglomerates upon deposition calculated for each of the mica sheets placed onto the Langmuir trough during the 5 and 6 hour experiments. The average number of agglomerates per μm^2 as well as the SD and RSD are also shown. Number of particles counted per mica sheet: 5 hour experiment mica sheet 1 = 192 particles, 5 hour experiment mica sheet 2 = 127 particles, 6 hour experiment mica sheet 1 = 132 particles, 6 hour experiment mica sheet 2 = 124 particles. 354

Table 63. Average aerosol CMD, GSD, number concentration, mass concentration and estimated CB nanoparticle mass deposited for an experiment performed to study the wettability and surface tension activity of aerosolised CB nanoparticles when deposited onto a clean PBS subphase at 21°C. Note that the CMD is expected to be underestimated as the full aerosol size range could not be measured. 355

Table 64. Average aerosol CMD, GSD, number concentration, mass concentration, estimated CB nanoparticle mass deposited and CB/DPPC nanoparticle mass ratio for a dipping experiment performed in PBS at 21°C after exposing a DPPC monolayer to aerosolised CB nanoparticles to investigate the presence of CB nanoparticles at the interface during the initial compression of the monolayer and after three compression-expansion cycles at maximum barrier speed. 361

Table 65. Area covered by the CB nanoparticle agglomerates at Π values of 20, 40 and 70 mN/m during the initial compression of the monolayer. The dipping experiment was performed in PBS at 21°C after depositing aerosolised CB nanoparticles onto a DPPC monolayer at a 1/3.22 CB/DPPC mass ratio. The area covered by the CB nanoparticles was determined by analysing representative SEM images and expressed as a percentage of the total image area. At least two different sample areas were analysed per Π 364

Table 66. Exposure time, average aerosol CMD, GSD and number concentration of three different experiments performed in PBS at 21°C to study the effects of the exposure of a DPPC monolayer to varying amounts of aerosolised CB nanoparticles. Note that the CMD for the 90 and 150 minute exposure experiments are expected to be underestimated as the full aerosol size range could not be measured. 366

Table 67. Exposure time, aerosol mass concentration, estimated CB nanoparticle mass deposited and CB/DPPC mass ratio of three different experiments performed in PBS at 21°C to study the effects of the exposure of a DPPC monolayer to varying amounts of aerosolised CB nanoparticles. 367

Table 68. Effect of the exposure of a DPPC monolayer to aerosolised CB nanoparticles over 10 minutes (0.02/1 CB/DPPC mass ratio) on the C_m for the region 30-45 mN/m and the collapse Π of the Π -Mma isotherm measured in PBS at 21°C. The corresponding values in each of the parameters measured for CB nanoparticles were compared with those of compressed air flow (control) by calculating the difference in each of the parameters for the experimental isotherm and the control expressed as a % of the control value and dividing them by the reference % change from midpoint values for the relevant reference isotherm (Table 12). This approach assumes similar levels of uncertainties on the control and experimental isotherm parameters to

those of the reference isotherm parameters. Additionally, the assumption was made that for the reference isotherm, the uncertainty values for the C_m for the region 25-45 mN/m would be similar for the region 30-45 mN/m. 368

Table 69. Effect of the exposure of a DPPC monolayer to aerosolised CB nanoparticles over 90 minutes (1.58/1 CB/DPPC mass ratio) on the C_m for the region 30-45 mN/m and the collapse Π of the Π -Mma isotherm measured in PBS at 21°C. The corresponding values in each of the parameters measured for CB nanoparticles were compared with those of compressed air flow (control) by calculating the difference in each of the parameters for the experimental isotherm and the control expressed as a % of the control value and dividing them by the reference % change from midpoint values for the relevant reference isotherm (Table 12). This approach assumes similar levels of uncertainties on the control and experimental isotherm parameters to those of the reference isotherm parameters. Additionally, the assumption was made that for the reference isotherm, the uncertainty values for the C_m for the region 25-45 mN/m would be similar for the region 30-45 mN/m. 370

Table 70. Effect of the exposure of a DPPC monolayer to aerosolised CB nanoparticles over 150 minutes (1.01/1 CB/DPPC mass ratio) on the C_m for the region 30-45 mN/m and the collapse Π of the Π -Mma isotherm measured in PBS at 21°C. The corresponding values in each of the parameters measured for CB nanoparticles were compared with those of compressed air flow (control) by calculating the difference in each of the parameters for the experimental isotherm and the control expressed as a % of the control value and dividing them by the reference % change from midpoint values for the relevant reference isotherm (Table 12). This approach assumes similar levels of uncertainties on the control and experimental isotherm parameters to those of the reference isotherm parameters. Additionally, the assumption was made that for the reference isotherm, the uncertainty values for the C_m for the region 25-45 mN/m would be similar for the region 30-45 mN/m. 372

Table 71. Comparison of the similarities and differences between CeO₂ nanoparticles and CB nanoparticles. 374

Glossary of nomenclature and abbreviations

Nomenclature

Π	Surface pressure
Π_{disp}	Surface pressure due to dispersive (van der Waals) forces
Π_e	Equilibrium spreading pressure
γ	Surface tension
θ	Contact angle
ρ	Density
π	Pi number
θ	Contact angle
\emptyset	Correction factor to calculate the surface tension of a liquid using the drop weight or volume method
A	Area
C_f	Sensitivity factor for a quartz crystal
d	Depth
dv	Aerosol deposition velocity
E_d	Activation energy of an atom to diffuse from the bulk of a liquid to the surface
E_d'	Activation energy of an atom to diffuse from the surface of a liquid to the bulk of the liquid
f	Frequency
F	Force
$F(r_s)$	Attractive forces experienced by atoms present at the liquid/gas interface
F_s	Force due to surface tension
g	Gravitational constant
G	Gibbs free energy

G	Gas
h	Height
k_B	Boltzmann constant
l	Length
L	Liquid
m	Mass
mc	Aerosol mass concentration
mda	Aerosol mass deposited per unit area over the exposure time
mdt	Aerosol mass deposited onto a Langmuir trough
n	Number of replicates
£	Pound sterling
P	Pressure
r	Radius
r_s	Interatomic distance of atoms present at the liquid/gas interface
S	Solid
S	Entropy
S^{LS}	Spreading coefficient
T	Temperature
T_c	Critical point temperature
t	Thickness
v	Vapour
V	Volume
V_A	Van der Waals attractive forces
V_R	Electrical double layer repulsive forces
V_S	Potential energy due to the solvent

V_T	Total potential energy
W	Work
w	Width

Abbreviations

ADSA	Axisymmetric drop shape analysis
AFM	Atomic force microscopy
ARDS	Acute respiratory distress syndrome
ATR	Attenuated total reflection
BAL	Bronchoalveolar lavage
BAM	Brewster angle microscopy
BET	Brunauer, Emmett and Teller
BLES	Bovine lipid extract surfactant
CA	Compressed air
CB	Carbon black
CDS	Constrained drop surfactometer
CMD	Count median diameter
CNM	Carbonaceous nanomaterials
COA	Constant output atomiser
COPD	Chronic obstructive pulmonary disease
DLS	Dynamic light scattering
DMA	Differential mobility analyser
DOPC	Dioleoylphosphatidylcholine
DPPC	Dipalmitoylphosphatidylcholine
DPPE	Phosphatidylethanolamine

DPPG	Dipalmitoylphosphatidylglycerol
EELS	Electron energy loss spectroscopy
ELS	Electrophoretic light scattering
EM	Electron microscopy
ENM	Engineered nanomaterial
ENP	Engineered nanoparticle
FFF	Field flow fractionation
FTIR	Fourier transform infrared spectroscopy
FTIR-RAS	Fourier transform infrared - reflection absorption spectroscopy
GIR	Grazing incidence reflection
GIXD	Grazing incidence X-ray diffraction
GNPs	Graphene nanoplatelets
GSD	Geometric standard deviation
ICRP	International Commission on Radiological Protection
ICP-MS	Inductively coupled plasma mass spectrometry
IR	Infrared
IRDS	Infant respiratory distress syndrome
IUPAC	International Union of Pure and Applied Chemistry
LB	Langmuir-Blodgett
LC	Liquid-condensed
LE	Liquid-expanded
LMWCNT	Long multiwalled carbon nanotube
lpm	Litre per minute
LRT	Lower respiratory tract
LWB	Langmuir-Wilhelmy balance

Mma	Mean molecular area
MWCNT	Multiwalled carbon nanotube
NASA	National Aeronautics and Space Administration
NM	Nanomaterial
NP	Nanoparticle
OECD	Organisation for Economic Co-operation and Development
OELs	Occupational exposure limits
PA	Palmitic acid
PBS	Phosphate buffered saline
PC	Personal computer
PG	Phosphatidylglycerol
PI	Phosphatidylinositol
PLD	Phospholipase D
PM	Particulate matter
POM	Polyoxymethylene
POPG	Palmitoyl-oleoyl-phosphatidylglycerol
PP	Polypropylene
Psig	Pounds per square inch gauge
PTFE	Polytetrafluoroethylene
QCM	Quartz crystal microbalance
SCENIHR	Scientific Committee on Emerging and Newly Identified Health Risks
SEM	Scanning electron microscope
SD	Standard deviation
RSD	Relative standard deviation
SI	International system of units

SMPS	Scanning mobility particle sizer [®]
SMWCNT	Short multiwalled carbon nanotube
SP	Surfactant protein
TEM	Transmission electron microscope
ToF-SIMS	Time of flight secondary ion mass spectrometry
UFP	Ultrafine particle
UPC	Unsaturated phosphatidylcholine
URT	Upper respiratory tract
UV	Ultraviolet
X-EDS	Energy-dispersive X-ray spectroscopy
XPS	X-ray photoelectron spectroscopy

CHAPTER 1 – INTRODUCTION AND BACKGROUND INFORMATION

1.1 Rationale and strategy

Nanosized materials including nanoparticles (NPs) are typically defined as having at least one dimension smaller than 100 nm. Nanotechnology - which is the creation and/or manipulation of nanosized materials, often referred to as engineered or manufactured nanomaterials - is a relatively new area of science and technology but, however, one of the fastest developing technologies of the 21st century. Engineered NPs (ENPs) provide the potential for a wide range of benefits due to their unique properties and they are being rapidly developed for many technological uses. However, concerns based on the findings from research into the health effects of air pollutants, asbestos and other particulate matter have been raised about their potential impact on human health. Inhalation will be a significant exposure route for ENPs suspended in the air and a high proportion of inhaled NPs will deposit in the alveolar region; the first biological barrier is lung surfactant which consists of a mixture of phospholipids and proteins that covers the entire alveolar region located at the air/liquid interface. The main physiological function of lung surfactant is to reduce surface tension during exhalation to near zero values in order to prevent the collapse of the lungs and, thus, it is absolutely essential for life. Lung surfactant also has a host defence function against inhaled objects, including microbes, organic and inorganic materials, and aerosols such as NPs. The main component of lung surfactant is dipalmitoylphosphatidylcholine (DPPC), a disaturated phospholipid capable of reaching very low surface tensions which has been demonstrated on compression with a Langmuir-Willhelmy balance (LWB). Several studies have shown that NPs are able to interact with lung surfactant components and impede the ability of surfactant to reduce surface tension. This interaction may also modify the NP properties and therefore, any toxic effects or bioreactivity. In addition to all this, some studies indicate that surfactant displaces particles into the alveolar subphase fluid where they can come into contact with the alveolar epithelium and macrophages. Some *in vivo* studies indicate that a low percentage of some types of NPs that deposit in the alveoli have the potential to translocate across the alveolar epithelium and into the lymphatic and circulatory system and accumulate in various secondary organs. Little is known of the interactions between ENPs and lung surfactant but this is crucial to gain a full understanding of how NPs might enter the body and cause systemic health problems.

In this work, two commonly used ENPs – CeO₂ and carbon black (CB) – have been studied. CeO₂ NPs have a wide range of applications, including coating surfaces and as a polishing

material. One important use is as a diesel fuel additive to increase fuel combustion efficiency and reduce the emission of unburned hydrocarbons, soot and nitrogen oxides. On the other hand, CB NPs are predominantly employed as a reinforcement and filling agent in automotive tyres. Of particular interest was to examine possible effects of these NPs on the function of lung surfactant by measuring the Π -Mma isotherm using DPPC monolayers within a LWB system; in addition, the effect of DPPC on particle behaviour was studied using a range of imaging techniques in parallel with particle characterisation before and during the individual experiments. Phase 1 of the project focused on the study of the DPPC isotherm and optimising experimental conditions for future experiments in order to study and test exogenous lung surfactant under relevant physiological conditions. These studies are reported in chapter 2. Phase 2 focused on the development of a realistic air-to-surfactant particle deposition model and the investigation of the effect of different NP deposition methods on the DPPC isotherm. In other, previous studies, NPs have been delivered onto the air/liquid interface from liquid suspensions, mostly for ease of application. This is not representative of *in vivo* deposition of NPs, as in the alveoli NPs would be expected to deposit onto the alveolar surfactant layer by diffusion. A method to deposit aerosolised NPs (CeO₂) was developed and compared with deposition from liquid suspensions. To date, there are no other studies of NP deposition onto a surfactant monolayer in aerosol form using a LWB, thus, these data are novel. This study is described in chapter 3. Phase 3 of the work focused on the use of the deposition model developed in phase 2 to compare the effects of aerosolised CB NPs with that of CeO₂ NPs on the functional activity of DPPC. This component of the study is reported in chapter 4. These three chapters are preceded by a general introduction that contains relevant background information related to (a) surface science focusing on surface tension, surfactant and particle monolayers and colloids; (b) lung surfactant, focusing on its function, biophysical properties, composition, dysfunction and methods to investigate the surface properties of lung surfactant and (c) ENPs, focusing on nanomaterial characterisation, particle deposition in the lungs, exposure, toxic effects and lung surfactant and NP interactions.

1.2 Surface science, surface tension, surfactant and particle monolayers and colloids

1.2.1 Surface science, surfaces and interfaces

Surface science is the study of physical and chemical phenomena that occur at the interface of two phases. It is one of the fastest growing areas of research in the fields of science, biology

and engineering and its relevance is increasing due to the emergence of nanoscience. It has a variety of applications including catalysis, nanotechnology, inhibition of corrosion, microelectronics, food safety, biological surfaces or modification of surface properties for example, friction, wear, stickiness or wetting (Jonas, 2009).

A **surface** is defined as the few top layers of a phase of matter (solid or a liquid) in contact with its environment.

An **interface** is an area where two different homogeneous phases of matter meet and interact with each other. It is a non-uniform and inhomogeneous area whose properties are different from the properties of the phases (IUPAC, 2001). Interfaces can occur between an insoluble solid and liquid, insoluble solid and gas, insoluble liquid and gas, two immiscible liquids or two solids. A triple interface is a line where three bulk phases meet (Bothe and Prüss, 2015). The physical, electrical, optical, mechanical and thermal properties at the interfaces are strongly influenced by the composition, structure, topology and morphology of the material surface (Nalwa, 2001). Sometimes, the presence of an interface does not influence the behaviour of the system but in many cases, it does have an effect or dominates the behaviour. The importance of the interface depends on the type of system: the bigger the surface area to volume ratio, the higher the effect the surface phenomena will have on the system (Ma and Kim, 2011). The breakdown of an object in smaller pieces will increase the total surface area and the surface area to volume ratio as shown in Figure 1 and Table 1. A cube of side 2 m has a volume of 8 m³, a surface area of 24 m² and an area to volume ratio of 3. If we divide this cube into pieces that are one eighth of the original size, the total surface area and the area to volume ratio per particle are 8 times the respective values for the original cube.

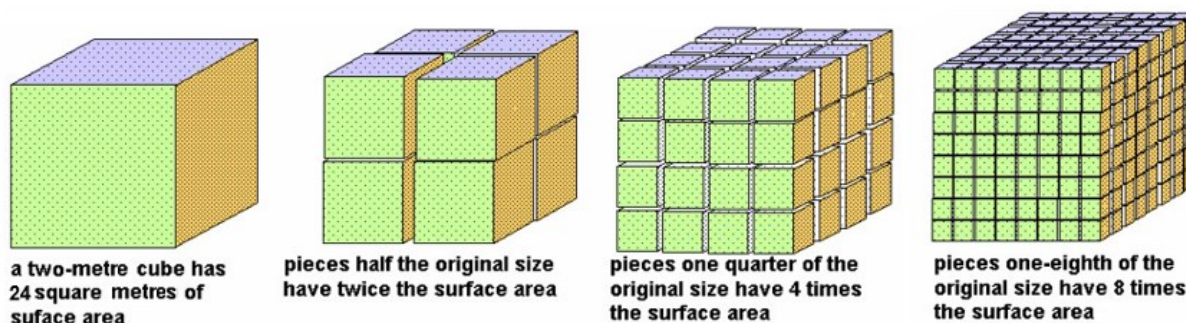


Figure 1. Illustration of the effect of subdivision of a two metre cube into smaller cubic particles. When divided into cubes one eighth of the original, the total surface area and area to volume ratio is eight times the respective value for the original cube. Adapted from Stoffer, 2013.

Table 1. Effect of subdivision of a two metre cube into smaller cubic particles on the area to volume ratio per particle and on the total surface area and total area to volume ratio.

Number of particles	Length of particle edge (m)	Particle area (m ²)	Particle volume (m ³)	Area to volume ratio per particle	Total surface area (m ²)	Total area to volume ratio
1	2	24	8	3	24	3
8	1	6	1	6	48	6
64	0.50	1.50	0.13	12	96	12
512	0.25	0.38	0.02	19	195	24

1.2.2 Surface tension

1.2.2.1 Concept and thermodynamics of surface tension

Many of the phenomena that occur in systems containing an interface in which one of the phases is a liquid can be understood through the concept of surface tension (γ). Thus, surface tension is a property of the liquid's interface with another medium.

Adhesive forces are molecular attractive interactions between two different media whereas cohesive forces are molecular attractive interactions within a phase which cause a tendency in the media to resist separation. In a liquid, molecules which are located within the bulk of a liquid experience equal forces of attraction in all directions. These cohesive forces between the molecules are shared with all the neighbouring atoms. The molecules on the surface have however no atoms above and experience stronger and unbalanced attractive forces that pulls

them from the surface to the interior part of the liquid. Surface tension is the force acting at right angles required to break a line of unit length on the liquid surface. Its SI unit is Newton per m but the unit of Dyne per cm or Joule per m² is also used.

Figure 2 can be used to explain the phenomenon of surface tension simplistically from the perspective of the energy states of the molecules/atoms in the bulk and surface of a material. Atoms 1, 2, 3 and 4 are present in the interface between a liquid and a gas phases. Atoms 6, 7, 8, 9, 10 and 11 are present in the bulk of a liquid. Atoms 12, 13, 14, 15 and 16 are present in the bulk of a gas. Atom 2 present in the interface requires some energy called activation energy to diffuse from the interface to the bulk of the liquid (E_d') by separating atoms 6 and 7 and overcoming the weak attractive forces with gas atoms. Attractive forces between atom 2 and atom 7 present in the bulk of the liquid are stronger than between atom 2 and atom 13 present in the gas phase. This is because gas atoms are well separated with no regular arrangement. Atom 7 requires some activation energy to diffuse from the bulk of the liquid to the surface (E_d). E_d' is lower than E_d as the magnitude of the forces to overcome in the liquid bulk is greater than in the interfacial region hence, it is easier for an atom to move from the surface to the bulk of the liquid than in the reverse direction. The magnitude of E_d' is continuously increasing with time till diffusion rates from both phases are equal, $E_d' = E_d$, and an equilibrium is reached. If atoms 1, 2 and 3 are taken as examples, atom 2 experience attractive forces with atoms 1 and 3. Atoms in the surface have an average interatomic distance r_s . Surface tension is the force per unit length of the surface as shown in the following equation (Walton, 1983):

$$\gamma = \frac{F(r_s)}{r_s}$$

Equation 1

where γ is surface tension; r_s is the average interatomic distance of atoms present at the liquid/gas interface; $F(r_s)$ are the attractive forces experienced by atoms present at the liquid/gas interface

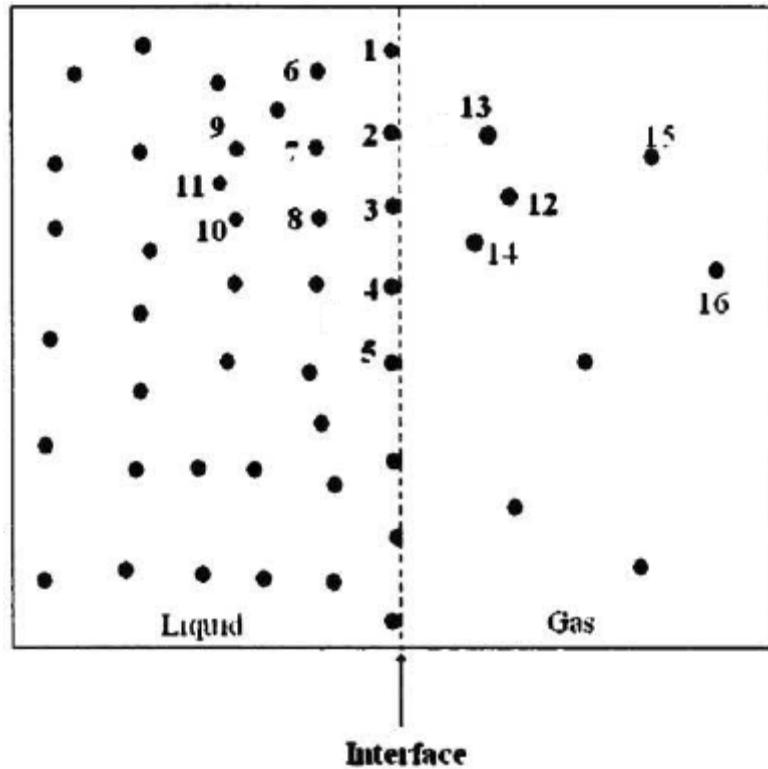


Figure 2. Schematic illustration for explaining the phenomenon of surface tension. The dashed line represents the interface between a liquid and a gas. Adapted from Ibrahim, 2000.

Surface tension can also be considered mathematically from a detailed thermodynamic perspective. Surface tension is the energy that must be brought into the system to extend it. Thus, surface tension is the mechanical work required to increase the area of a surface by unit amount (Equation 2). The work required is proportional to the number of molecules that must be brought up to the surface.

$$\gamma = \frac{\partial w}{\partial A}$$

Equation 2

where γ is surface tension; W is mechanical work and A is surface area

The Gibbs free energy (G) is the energy associated with a chemical reaction that can be used to do work. The Gibbs free energy for a reversible process is shown in the following equation:

$$\partial G = V\partial P + \gamma \partial A - S\partial T$$

Equation 3

where G is the Gibbs free energy; V is volume; P is pressure; γ is surface tension; A is surface area; S is entropy and T is temperature

At constant pressure and temperature the work of extension is equivalent to the Gibbs free energy, and therefore, surface tension will contribute to this free energy and it will be a function of the surface area:

$$\partial G = \gamma \partial A$$

Equation 4

where G is the Gibbs free energy; γ is surface tension and A is surface area

The minimum Gibbs free energy principle states that at constant temperature and pressure any closed system (work and heat can be transferred but not matter) is at equilibrium when its Gibbs free energy is at a minimum. Thus, liquids will tend to minimise their surface area by the transport of surface molecules to the interior of the liquid and therefore, the surface will contract spontaneously (Duncan, 1980). This explains why drops of a liquid in air, and bubbles, are spherical (Figure 3). Processes that lower the value of the surface tension would also be thermodynamically favoured, for example, the adsorption or concentration of a surfactant at the interface.

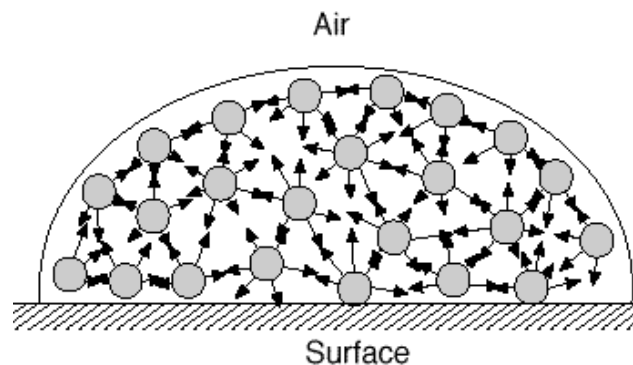


Figure 3. Schematic of a water drop onto a solid surface. Molecules inside the water drop are attracted in all directions. Molecules on the surface are attracted to the sides and inwards (NASA, 2011).

Surface tension must be positive as, if it was negative, the system could lower its free energy by increasing its surface area. The surface area would spontaneously expand which would lead to the dissolving of one phase in the other (Barnes and Gentle, 2011).

Further key concepts related to surface tension including (a) the Laplace equation for spherical interfaces; (b) contact angle; (c) wetting; (d) spreading coefficient and (e) floating are discussed in Appendix 1.

1.2.2.2 Dependence of surface tension on temperature

The surface tension of a pure liquid in contact with air depends on the temperature of the liquid. Surface tension decreases almost linearly with temperature. For example, for water, surface tension at 25°C is ~ 71.99 mN/m whereas at 37°C surface tension is ~ 70 mN/m (Vargaftik et al., 1983, Pallas and Harrison, 1990) (Figure 4).

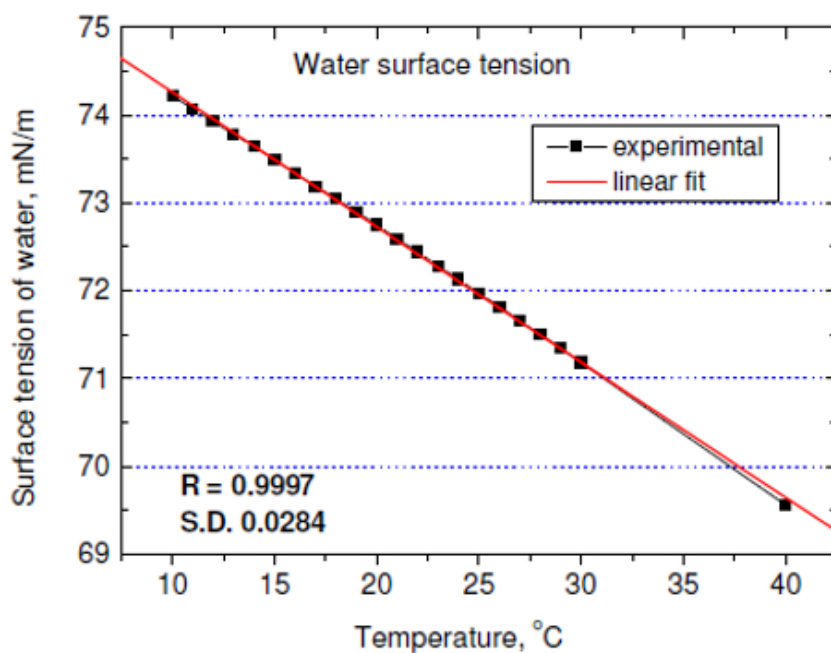


Figure 4. Graphical representation of the changes in water surface tension as a function of temperature (Department-of-Interfacial-Phenomena, 2013).

The relationship between surface tension and temperature can be explained using the three dimensional phase diagram of pressure, volume and temperature for water shown in Figure 5. For a liquid in equilibrium with its vapour, as the temperature increases, the state of the liquid will move along the saturated liquid line (ac), the vapour state will move along the vapour-

saturated line (bc) and eventually both states will approach the critical point (c). At the critical point temperature, T_c , the two phases will be indistinguishable and the surface tension will tend to zero. This is because atoms that were at the interface governed by the attractive forces with atoms in the bulk liquid will be moving loosely in the gas phase and interacting with gas atoms. Subsequently, the unbalanced downwards attraction that causes the surface tension will be compensated (Walton, 1983).

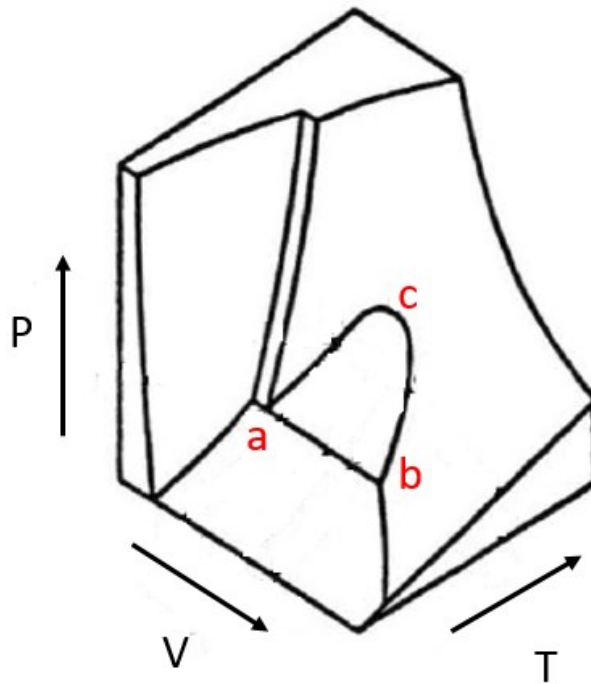


Figure 5. Three dimensional phase diagram of temperature (T), pressure (P) and volume (V) for water. Adapted from Walton, 1983.

1.2.2.3 Methods to measure surface tension

There are several ways of measuring the surface tension of a liquid. Each has its advantages and limitations. The reason why there are different methods is that surface tension is a very complicated property of a liquid and depends upon variables such as temperature and composition of the liquid. One category of methods is based on the contact angle a liquid makes to a solid surface which may be a vertical plate or the walls of a thin tube (capillary). A common limitation of these methods is that it is difficult to measure the contact angle accurately. A second category of methods is based on the shape of a drop of the liquid that may be hanging stationary, dripping or resting on a flat surface. A common limitation of these methods is that

the analysis of the shape of the drop and surface tension of the liquid is complicated and must be solved numerically. Each of these methods can also be a static measurement of surface tension, in which the liquid is not moving and the system is in thermodynamic equilibrium independent of time, or a dynamic measurement of surface tension, in which the liquid is moving or the size of the interface changes during measurement (O'Lenick, 2009). The static and dynamic surface tension can thus also be referred to as equilibrium surface tension and nonequilibrium surface tension respectively. In addition to all this, if the change of the interface is sufficiently slow, an equilibrium value can be measured. This is referred to as a quasi-static measurement of surface tension. For a particular interface, there is only one value for the static surface tension. The dynamic surface tension however can take a whole range of values depending on the dynamic process under which it is measured (Tricot, 1997). A detailed description of the methods for measuring surface tension including (a) the capillary rise method; (b) Wilhelmy plate; (c) drop weight or volume; (d) maximum bubble pressure; (e) pendant and sessile drop profile method and (f) indicator oils is discussed in Appendix 2.

1.2.3 Surfactant monolayers, particle monolayers and colloids

1.2.3.1 Surfactant monolayers

1.2.3.1.1 Surfactants

By definition, a surfactant is a substance that reduces surface tension. Surfactant or surface active agents are usually organic compounds that are amphiphilic. A typical amphiphilic substance combines a segment that exhibits a strong affinity for polar solvents, particularly water and an apolar part that is water insoluble (or oil soluble). The hydrophilic part (“head”) consists of a polar or ionic group whereas the hydrophobic part (“tail”) usually consists of a hydrocarbon chain of the alkyl or alkylbenzene type (Salager, 2002).

There are four classes of surfactants according to the ionic nature of the hydrophilic or polar group (Figure 6) (Salager, 2002, Abd-Elhady et al., 2011):

- a) Anionic surfactants** contain a negatively charged ion or anion at their polar group. Examples of anionic functional groups are sulfonate, sulphate, carboxylates and phosphate. They are the most commonly used surfactants.

- b) Cationic surfactants** contain a positively charged ion or cation at their polar group. A very large proportion of this class corresponds to nitrogen compounds such as fatty amine salts and quaternary ammonium ions.
- c) Zwitterionic surfactants** have both cationic and anionic centers attached to the same molecule. Examples of these types of surfactants are synthetic products like betaines or sulfobetaines and natural substances such as aminoacids and some phospholipids like phosphatidylcholine.
- d) Non-ionic surfactants** contain a polar group that does not ionize in aqueous solution such as alcohol, phenol, ether, ester, or amide.

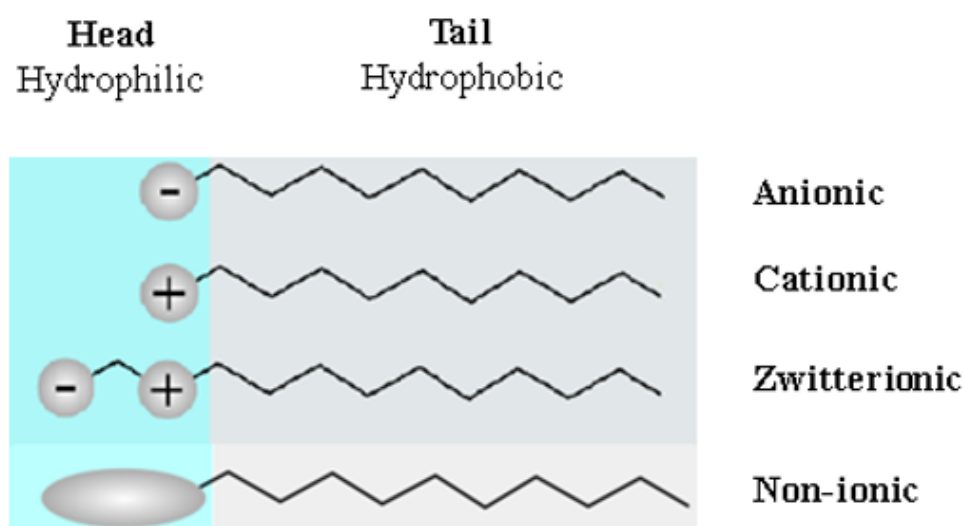


Figure 6. Illustration of the surfactant classification according to the ionic nature of the polar group. Adapted from Abd-Elhady et al., 2011.

Due to their amphiphilic nature, molecules do not feel “at ease” in any solvent, be it polar or non-polar, as one of the groups of the molecule does not exhibit affinity for the medium. Therefore, surfactants have a strong tendency to concentrate or adsorb at interfaces, effectively creating a new surface. For example, in an air/water interface, the polar group is immersed in the water phase whereas the hydrophobic tail is located in the vapour phase (Figure 7). The adsorption of surfactants to interfaces is a process that is energetically favourable and reduces the surface tension or free energy of the system. These adsorbed layers are one molecule thick

which gives a thickness of 1-3 nm and therefore, they can be described as nanofilms or monolayers. The lower bulk phase is usually called a subphase.

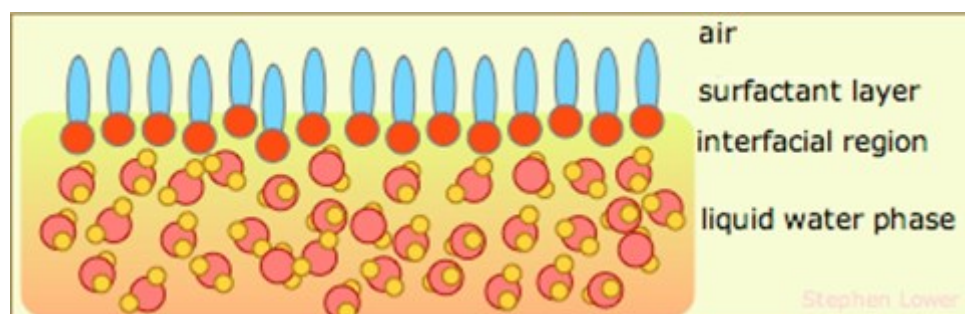


Figure 7. Illustration of a surfactant layer at the air/water interface. The polar group (in red) is immersed in the water phase whereas the hydrophobic tail (in blue) is located in the vapour phase (Lower, 2015).

Surface pressure (Π) is a concept frequently used in situations where the surface tension has been decreased by events such as the adsorption or concentration of a surfactant at the interface. It is the difference between the surface tension of a liquid and the surface tension of the liquid with a surfactant monolayer present at the air/liquid interface.

$$\Pi = \gamma_0 - \gamma \quad \text{Equation 5}$$

where Π is the surface pressure; γ_0 is the surface tension in absence of the monolayer and γ is the surface tension with the monolayer present

1.2.3.1.2 Techniques for studying the surface pressure behaviour and structure of surfactant monolayers

For almost a century, the main source of data regarding the structure of surfactant monolayers was the measurement of Π -A isotherms and no direct structural information was available. Currently, there are different improved and novel techniques that allow the study of the film structure and composition in much more detail. Some of the techniques currently used to study floating monolayers are described below.

Measurement of the Π -A isotherm

There are a number of methods for measuring surface tension but there are few techniques that enable the measurement of Π -A isotherms (Putz et al., 1998, Dillow and Lowman, 2002):

a) Surface film balance. It is a basic technique used to measure the γ of a liquid with a surfactant monolayer spread onto its surface during the compression or expansion of the monolayer by two barriers. An example of a surface film balance is the Langmuir-Wilhelmy balance.

b) Pulsating bubble surfactometer. It is a basic technique used to measure changes in surface tension during dynamic oscillation of an air bubble that is suspended at the end of a capillary with surfactant film adsorbed at the bubble surface.

c) Captive bubble surfactometer. It is a technique invented to address some of the problems of the pulsating bubble surfactometer.

Further details on these techniques are provided in Appendix 6.

Surface film structure and composition

Advanced techniques have made it possible to investigate surfactant film structure *in situ* or to analyse the surfactant film transferred to a solid substrate. Some of the techniques currently used to study floating monolayers are (Peng et al., 2001, Pérez-Morales et al., 2005, Keating et al., 2011, Ala'a et al., 2012):

a) Grazing Incidence X-ray Diffraction (GIXD). It is the primary technique used to obtain information on the monolayer structure with angstrom resolution (Tamam et al., 2009). It may require the transfer of the monolayer onto a solid substrate or the technique can be used *in situ*. This technique is based on observing the scattered intensity of an X-ray beam hitting a sample as a function of incident and scattered angle, polarization and wavelength. Because monolayers are so thin compared to the substrate on which they are deposited, it is necessary to use X-rays at a very low incident angle (grazing incidence). Very bright sources that give a good signal to noise ratio are also needed and thus, the brightness of synchrotron X-ray sources are normally used (Helm et al., 1987). In the literature, GIXD has been used to investigate the area covered by a DPPC molecule at a certain surface pressure. For example, Watkins et al, 2009 found that the area of a DPPC molecule at 30, 40 and 50 mN/m was 47.43 Å², 46.97 Å² and 45.36 Å² respectively. GIXD has also been used to investigate structural changes in the packing of the lipid film at the molecular level, information not obtainable using other methods. For example, You et al., 2016 found that the presence of gold NPs restricted the freedom of the hydrophobic

tails to attain a more tilted state as seen in the absence of NPs. Miller et al., 2008 used GIXD to study the structure of two monolayer systems: the ganglioside GT1b receptor and DPPC and GT1b and dipalmitoyl phosphatidylethanolamine (DPPE) and found that at 20 and 40 mN/m GT1b was intercalated within the DPPC/DPPE, the presence of GT1b condensed DPPC but slightly expanded the DPPE matrix and no phase separation of the two components occurred in each monolayer system.

b) Neutron Reflectometry. It is a neutron diffraction technique with a nanometre scale resolution (Lin et al., 2002) and a very useful method that gives information about the thickness and the scattering length density of each layer. In this technique, neutrons at thermal energies are incident on a surface at a grazing angle less than 3° (NIST-Center-for-Neutron-Research, 1999). As with X-rays, the wavelength or the incident angle is scanned and the reflectivity pattern compared with that of a likely layer model. With a neutron beam the scattering centres are the atomic nuclei. In the literature Miller et al., 2004 used neutron reflectometry to characterise the structure of mixed 1,2-dipalmitoyl-D62-snglycero-3-phosphoethanolamine (DPPE) and ganglioside GM₁ (80:20 mol%) lipid monolayers before and during the binding of a protein. Results showed that the density of the lipid layer slightly decreased upon protein binding due to geometrical constraints imposed by the protein which decreased the packing of the lipids. Qi et al., 2008 investigated the phase miscibility and escaping tendency of mixed palmitic and stearic acid monolayers using a combination of techniques including neutron reflectivity. Results showed a marked selective dissolution of palmitic acid into an alkali subphase with time and allowed quantification of the rate of dissolution of this species.

c) Scanning Electron Microscopy (SEM). It requires the transfer of the monolayer onto a solid substrate and it is a technique used to image the monolayer. An SEM scans a focused high-energy beam of electrons over a surface. The electrons in the beam interact with the sample producing secondary electrons, backscattered electrons and characteristic X-rays. The electron beam can penetrate the sample to a depth of a few microns, depending on the density of the sample and the accelerating voltage. These signals are collected by appropriate detectors to obtain information about a defined area on the sample and form images which are then displayed on the computer screen. The resolution obtained in an SEM depends on several factors such as the interaction volume of the electron beam with the sample and the electron spot size. Typically, modern full-sized SEMs provide a resolution between 1-20 nm

(NanoScience-Instruments, 2016). In the present work, SEM was used to visualise NP agglomerates in a NP-DPPC system.

d) Ellipsometry. It is a long established, non-destructive, light optical analysis technique to measure the thickness and refractive index of thin films and that can achieve angstrom resolution (Richter et al., 2001). It requires the transfer of the monolayer onto a solid substrate. With this technique a beam of a narrow monochromatic laser light is plane polarised and directed at the surface being studied. Ellipsometry is based on the fact that light undergoes some change in polarization when it is reflected off the surface of the material. The polarization change is characteristic of the surface structure of the sample and by analysing the reflected light beam various types of information can be obtained such as the aforementioned film thickness and refractive index. In the literature, ellipsometry has been used to study the effect of NPs on the DPPC monolayer thickness. Tatur and Badia, 2011 found that the addition of C₁₆SAu NPs at concentrations of up to 0.2 mol % to DPPC did not influence the monolayer thickness.

e) Brewster Angle Microscopy (BAM). This is the technique most commonly used to characterise the monolayer film structure and dynamics *in situ* with a micrometre scale resolution. The principle of BAM is based on the Brewster's law and the Brewster angle. According to the Brewster's law, no reflection occurs from a clean and perfect interface illuminated under a unique angle of incidence with *p*-polarised light i.e., light is entirely transmitted. This so-called Brewster angle is 53° for the air/water interface. Any subsequent changes of the optical properties at the interface will lead to reflection. For example, when a surfactant film with refractive index different from that of water is present, a substantial fraction of the light is reflected at the interface and can be used to generate an image. Image contrast can provide information about film morphology and dynamics. It is desirable to have contrast between areas where condensed monolayer domains are present and areas where there is relatively little monolayer material. The technique is thus mostly used in the transition regions between expanded and condensed phases. For example, Piknova et al., 2001 used BAM to study the phase behaviour of calf lung surfactant and found that at low and high surface pressure values an expanded phase coexisted with a condensed phase. The relative area occupied by each phase barely changed with increasing surface pressure; the area covered by the expanded phase was approximately 70% of the interfacial area. BAM images of the surfactant film at surface pressures between 45 mN/m and 56 mN/m are show in Figure 8.

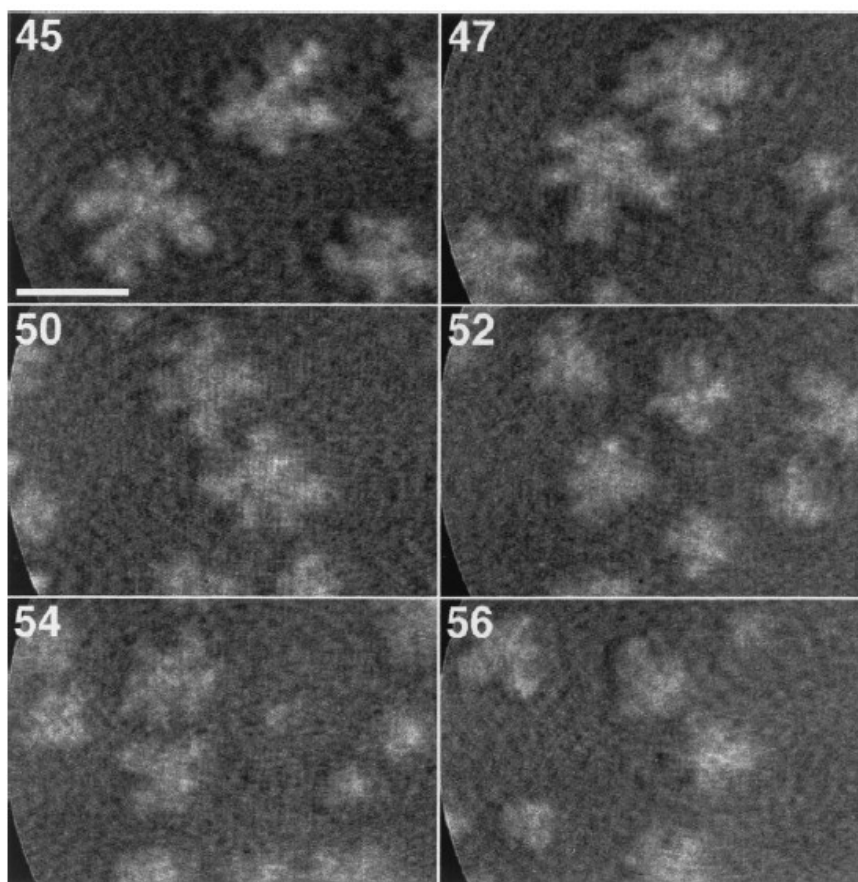


Figure 8. BAM images of a calf lung surfactant at different surface pressure values. Liquid condensed domains (bright areas) were dispersed in a liquid expanded phase (dark areas) (Piknova et al., 2001).

f) Fluorescence Microscopy. This technique allows the observation of structures of the monolayer *in situ* with a micrometre scale resolution. The principle of this type of microscopy is based on fluorescence. In this technique the film absorbs light of a specific wavelength and emits light of longer wavelength that can be used to generate an image. Similar information may be obtained with BAM and this technique. However, fluorescence microscopy requires the mix of a highly fluorescing amphiphilic dye with the monolayer material before spreading it, which may alter the pattern of the monolayer structures although comparison with BAM data shows that this is not usually a problem. The solubility of the dye should be different in different phases so that when the monolayer is illuminated by a suitable intense light source a difference in fluorescence intensity can be seen through a microscope. In the literature, studies have used this technique to visualise DPPC domains of the liquid expanded (LE)-liquid condensed (LC) phase coexistence that typically occurs at surface pressures between ~ 3.6 mN/m and ~ 7.5 mN/m. In this phase, the LC domains are dispersed in the less ordered LE phase. For example, McConlogue and Vanderlick, 1997 found that the basic domain shape was “an asymmetric bean

with a flattened lobe and a distinct cavity” and that domains grew with compression occupying all the available area (Figure 9).

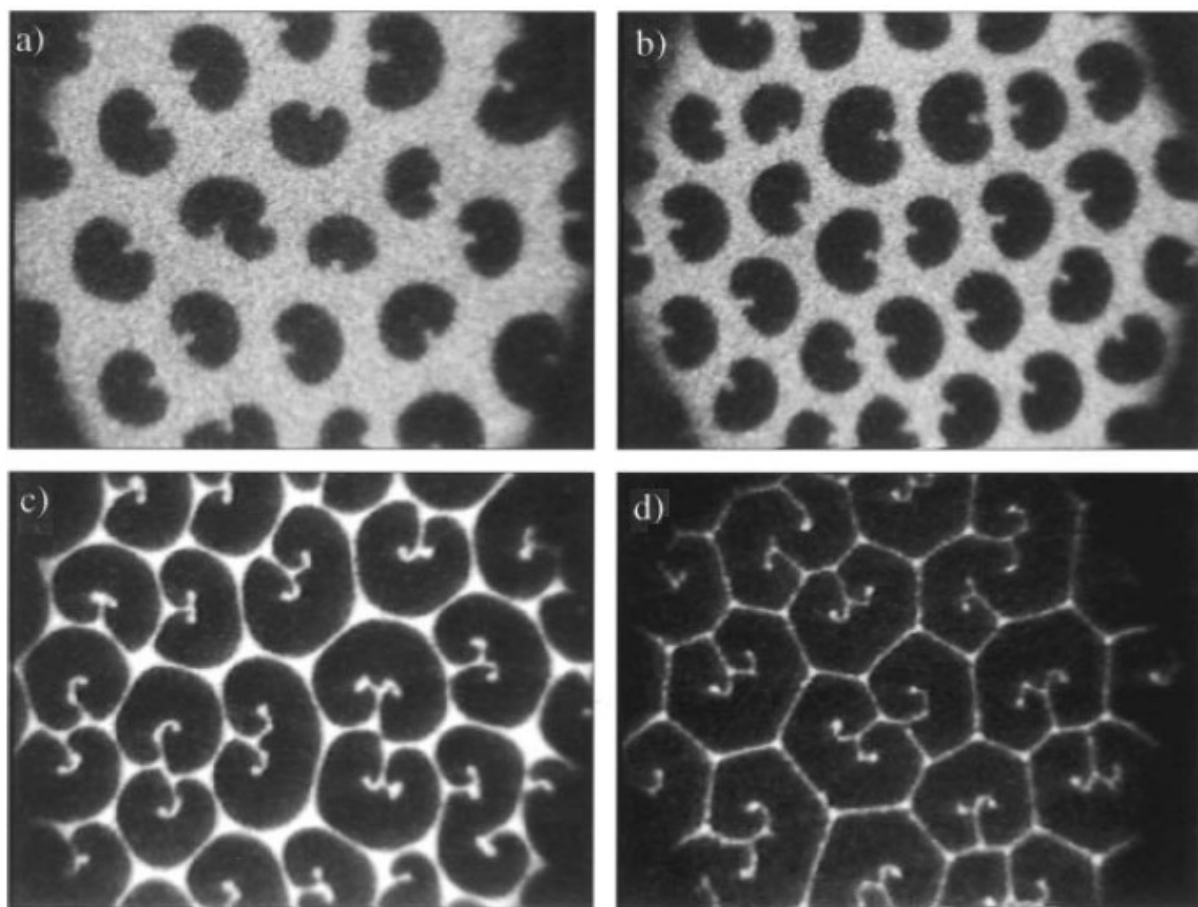


Figure 9. Fluorescence images of DPPC liquid condensed domains (dark areas) dispersed in a liquid expanded phase (bright areas) obtained at 4.2 mN/m (image a), 4.3 mN/m (image b), 5.0 mN/m (image c) and 7.5 mN/m (image d). Adapted from McConlogue and Vanderlick, 1997.

g) Atomic Force Microscopy (AFM). It is a very high resolution type of scanning probe microscopy. It requires the transfer of the monolayer onto a solid substrate and gives information about the morphology or topography of the film surface with a nanometre scale resolution. An AFM operates by using a cantilever with a very sharp tip to scan over a sample surface and correlating the deflections of the probe with the underlying surface morphology. As the tip approaches the surface, the attractive force between the surface and the tip cause the cantilever to deflect towards the surface. However, if the tip makes contact with the surface, increasingly repulsive forces cause the cantilever to deflect away from the surface. An incident laser beam off the flat top of the cantilever is used to detect cantilever deflections towards or away from the surface. An AFM image of a sample is obtained by scanning the cantilever over

a region of interest (Park-systems, 2016). In the literature, this technique has been used to image surfactant monolayers and bilayers and study phase transition and separation. For example, Zuo et al., 2008a used AFM to investigate a natural lung surfactant (BLES) at different surface pressure values. Results showed phospholipid phase separation with compression and a monolayer to multilayer transition plateau at a surface pressure of 40-50 mN/m. The liquid condensed phase was embedded uniformly in the liquid expanded phase and consisted of domains on the micrometre and nanometre scale. On compression, the microdomains broke up into nanodomains. Nanodomains can not be detected by other techniques with a micrometre scale resolution such as fluorescence microscopy or BAM, hence, AFM is ideal for studying surfactant films. AFM was used in the present studies to investigate DPPC domains at the air/water interface although results of this work are not shown in this thesis as the images were difficult to interpret due to the presence of materials from the subphase, such as NaCl crystals, attached to the monolayer. This is further discussed in section 3.5.1.2.

h) Time of Flight – Secondary Ion Mass Spectrometry (ToF-SIMS). It requires the transfer of the monolayer onto a solid substrate. It enables the molecular identification and chemical imaging of a monolayer and can achieve a lateral resolution of ~ 100 nm (Sodhi, 2004). For a TOF-SIMS analysis, a solid sample surface is bombarded with a pulsed primary ion beam of some keV energy. The primary ion energy is transferred to target atoms via atomic collisions and a so-called collision cascade is generated. The interaction of the collision cascade with surface molecules allow the extraction and emission of both atomic and molecular ions from the outer layers of the surface (one or two monolayers depth). The mass of the emitted ions is measured by their time of flight to the detector which provides a detailed spatial information on the elemental and molecular composition of the surface. Time of flight mass spectrometry is based on the fact that ions with the same energy but different masses travel with different velocities. The lighter ions fly with a higher velocity and arrive at the detector before the heavier ions (IONTOF, 2016). In the literature, ToF-SIMS has been used to visualise the lateral organisation and localisation of surfactant components in a monolayer. For example, Seifert et al., 2007 studied the distribution of all film constituents in a DPPC/deuterated dipalmitoylphosphatidylglycerol (d62-DPPG)/SP-B (4:1:0.2 mol %) model system. Figure 10 shows ToF-SIMS images for each film component and an overlay image. Each film component has a background colour (green for d62-DPPG, red for SP-B and blue for DPPC). The overlay of all images shows the formation of separated rigid condensed d62-DPPG domains with a diameter of less than $5 \mu\text{m}$ (green region) in a DPPC/SP-B surface film (pink region as an

overlay of red and blue). In the present work, ToF-SIMS was used to chemically identify and localise NP agglomerates in a NP-DPPC system.

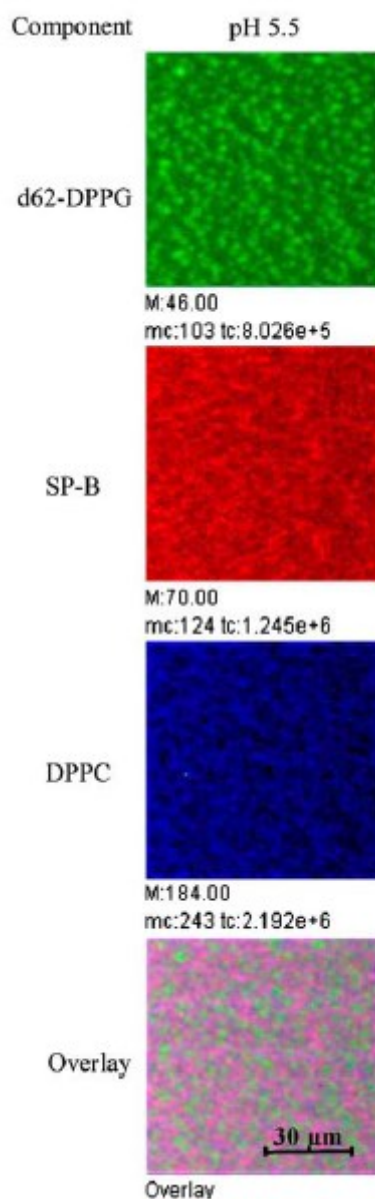


Figure 10. ToF-SIMS images showing the distribution of all film constituents in a DPPC/d62-DPPG/SP-B (4:1:0.2 mol %) model system. For each film component, one main colour is shown. Additionally, an image overlay is displayed (Seifert et al., 2007).

i) Fourier Transform Infrared Spectroscopy (FTIR). This technique identifies the chemical composition and structure of a sample using the molecules' characteristic adsorption of infrared (IR) radiation. First, the sample is exposed to different wavelengths of IR light. When IR

radiation is passed through a sample some radiation is absorbed by the sample and some passes through or is transmitted. The resulting signal at the detector is converted into an interpretable absorbance spectrum that represents the molecular “fingerprint” of the sample using the Fourier Transform. This spectrum can then be compared to a library of spectra to find a match (ThermoFisher-Scientific, 2015). For floating monolayers, FTIR has been developed as a reflection-absorption technique (Fourier Transform Infrared - Reflection Absorption Spectroscopy (FTIR-RAS)). In this technique, the IR beam is incident on the surface at an angle between 30° and 60° to the normal, and the beam reflected at the same angle is measured. Good signals from the alkyl chains are usually observed as opposed to the head group which are often obscured due to the strong absorption of the surrounding water vapour in the optical path. This problem can be overcome by polarization modulation (Blaudez et al., 1996). For transferred monolayers onto a solid substrate, grazing incidence reflection (GIR) and attenuated total reflection (ATR) are often used. For GIR, a highly reflective metal substrate is required. For ATR, the film is deposited on both sides of a suitable crystal and the IR beam is reflected from both sides several times before entering the detector. An example of a study that has used this technique to study monolayers at the air/water interface is that of Sinnamon et al., 1999. FTIR-RAS was used to measure *in situ* the molecular level structure of pentadecanoic acid monolayers at the air/water interface as a function of the surface pressure. Results showed that when the monolayer was in an expanded state, acyl chains were disordered and possessed high concentration of *gauche* defects whereas when the monolayer was more condensed the acyl chains were highly ordered and adopted an all-*trans* conformation.

1.2.3.1.3 Insoluble surfactant monolayers

Two-dimensional insoluble monolayers are formed at the air/water interface by amphiphiles that have a hydrocarbon chain long enough to make the molecule insoluble in water while the polar group has sufficient attraction to water to anchor the molecules to the water surface. As a rule of thumb, the hydrocarbon chain of the amphiphilic substance should have more than 12 hydrocarbons in the chain ((CH₂)_n, n >12) (Ghosh, 2009). The most common way to form a monolayer onto a water surface is to dissolve the surfactant in a solvent and spread a measured volume of the solution onto the surface. The solvent must have a positive spreading coefficient so that the solution spreads rapidly to cover the available water area. The solvent should also be insoluble in the subphase and volatile so that it will not mix with the subphase and evaporate easily. Commonly used spreading solvents include hexane, benzene and chloroform (Rosoff,

2001, Roberts, 2013). These monolayers, also known as Langmuir films, represent an extreme case when considering adsorption at liquid surfaces as all the molecules are concentrated at the interface in contrast to monolayers which are formed by adsorption from solution. Thus, the surface concentration of insoluble monolayers are directly known from the amount of material spread onto the surface (Duncan, 1980). The equilibrium spreading pressure (Π_e) is the highest Π obtained by spreading an amphiphile molecule onto the surface. At this point, the monolayer is in equilibrium with the subphase. Π_e can only be increased at a fixed temperature by lateral film compression (Zuo et al., 2008c, Goto and Caseli, 2013).

One of the most important indicators of monolayer properties is the measurement of the Π as a function of the available surface area to each molecule (mean molecular area, M_{ma}) or simply as a function of the available surface area (A). Measurements are carried out at constant temperature and are represented by a so-called isotherm. Usually an isotherm is recorded by continuously monitoring changes in Π during the expansion or compression (increment or reduction of the available surface area respectively) of a surfactant monolayer at a constant rate. At low monolayer surface density, the surfactant does not alter the surface tension and Π is zero. An increase in monolayer surface density achieved by monolayer lateral compression results in formation of phases that are more ordered and a decrease in surface tension or increase in Π . These monolayer phases are different physical states that bear some resemblance to the gaseous, liquid and solid states in the three-dimensional matter (Duncan, 1980, Satake et al., 2003, Shinoda et al., 2013) (see Appendix 3). They are related to the level of conformational order of the molecules at the interface due to the presence of intermolecular interactions within the monolayer (Eeman and Deleu, 2010) but especially due to the packing of the hydrophobic tails (Guzmán et al., 2012c). The term “phase” refers to a thermodynamic equilibrium state. Phases above the Π_e are however in a metastable state as with time they may change to an equilibrium state. Because they are stable relative to the experimental timescale, they are still considered as phases (Peng et al., 2001). Monolayer phases can be identified as a number of distinct regions or discontinuities in the compression isotherm. There are four principal monolayer phases (Figure 11) (Duncan, 1980, Kaganer et al., 1999, Zuo et al., 2008c, Barnes and Gentle, 2011). This classification was proposed by W. D. Harkins as early as 1952 (Harkins, 1952):

- **Gaseous (G):** This phase is rarely observed as it requires equipment of higher sensitivity than that usually available. It occurs at very large areas (extremely low Π) in the range of

hundreds of square angstroms per molecule. The molecules are widely separated and move independently like a two-dimensional gas. Molecules can collide with one another but because the distance between molecules is sufficiently large not to induce any interaction with neighbouring molecules they tend to remain separated. There is however sufficient interaction between the polar head group and the subphase to make the monolayer non-volatile and insoluble (Telesford, 2012). The molecules in the gas phase have an average kinetic energy, $\frac{1}{2}k_B T$ for each degree of freedom, where k_B is the Boltzmann constant. A gaseous monolayer usually obeys a two dimensional version of the equation for an ideal gas (MacRitchie, 2012):

$$\Pi A = k_B T$$

Equation 6

where Π is the surface pressure; A is the area per molecule; k_B is the Boltzmann constant and T is the temperature

- **Liquid-expanded (LE):** Reducing the area available to each molecule increases the surface concentration; molecules start to interact and Π begins to rise leading to the formation of a liquid like state. Molecules however have relatively weak chain-chain attraction which impedes them to be closely packed. The chains of the molecules are disordered, as in a liquid, and transitions from condensed phases to the LE phase are described as chain melting. The area or Mma at which Π begins to rise is called lift-off area or lift-off Mma respectively. Lipid monolayers in the liquid states usually obey van der Waals-like equation of state (MacRitchie, 2012, Chattoraj, 2012):

$$(\Pi - \Pi_{disp}(A_0))(A - A_0) = k_B T$$

Equation 7

where Π is the surface pressure; Π_{disp} is the surface pressure due to dispersive (van der Waals) forces; $A_0 = \pi d^2/2$ is twice the area defined by the distance, d , of closest approach; k_B is the Boltzmann constant and T is the temperature

- **Liquid-condensed (LC):** As the film is further compressed, molecules become more closely packed to generate a more ordered phase. Chains are fully extended but tilted at an

angle to the vertical. For this reason, this phase is also called tilted-condensed. The monolayer is less compressible than in the LE state. Recent GIXD measurements on some alkanolic acids and alkanols indicate rectangular structures with the chains tilted either to the nearest neighbour or the next nearest neighbour. It appears to be a rotator phase, i.e., chains nearly fully extended with no restrictions on the orientation of the zigzag plane relative to the crystallographic axes. GIXD studies on surfactant DPPC performed at a surface pressure of 20 mN/m found that the area covered by a DPPC molecule was 49.7 \AA^2 . The chain area measured as the cross sectional area of the chains in the direction perpendicular to the chains was 20.3 \AA^2 and the tilt angle of the alkane chains with respect to the liquid surface was 35.4° . GIXD results also indicated a rectangular two molecular unit cell of dimensions 5.77 \AA and 8.61 \AA , consistent with a hexagonal packing of the alkane chains (Choi et al., 2014).

- **Solid phase (S):** Upon further compression, a solid state is reached, characterised by a very steep and fast linear increase in the Π at low areas. In this S phase molecules are very closely packed and form a rigid layer. The molecules strongly interact via van der Waals forces between the chains, steric forces between the headgroups and hydrogen bonding between the polar group and the subphase. For simple amphiphiles such as the straight-chain alkanolic acids and alkanols, the hydrocarbon chains are fully extended in a planar zigzag of the carbon atoms repeating at 0.254 nm intervals, with the long axis perpendicular to the interface. For this reason, this phase is also called untilted condensed. The monolayer is less compressible than in the LC state. The in-plane structure revealed by GIXD is usually a rectangular structure with a herringbone orientation of the alkyl chains (Kenn et al., 1991). BAM shows that the monolayer is an array of randomly orientated domains, like a two-dimensional powder. The area per surfactant molecule at high Π corresponds to the cross-sectional molecular area and can be obtained in the compression isotherm by extrapolating a linear line through this S phase to zero Π . GIXD studies on surfactant DPPC performed at a surface pressure of 50 mN/m found that the area covered by a DPPC molecule was 45.36 \AA^2 (Watkins et al., 2009). Monolayers in the solid phase obey an equation of state of the form (Chattoraj, 2012):

$$a\Pi = b - A$$

Equation 8

where Π is the surface pressure; A is the area per molecule and a and b are constants

A **phase transition or phase coexistence** is a region where two different phases coexist. First order phase transitions appear as almost constant pressure regions in the compression isotherm as shown in Figure 11. In this coexistence region the two phases are in equilibrium with one another, the density is intermediate between the two phases and the Gibbs free energy for both phases is equal to zero (Telesford, 2012). The Π at which a first order phase transition occurs depends on the type of molecule, the hydrocarbon chain length and the subphase temperature. Second order phase transitions appear as abrupt changes in the slope of the isotherm. The transition from LE to LC phase is a first order transition. The transition from LC to S phase is usually a second order transition.

Reduction of surface tension is possible until a certain threshold which corresponds to the cross-sectional molecular area. After this point, if the monolayer is further compressed, it will eventually lead to a situation where packing is restricted by the head group of the amphiphile molecule. The monolayer can then fracture and break, buckle at constant area or lose material. The propensity of a monolayer to reach these particular attributes is dependent on the elastic and solubility properties of the monolayer. This minimum surface pressure achieved by a particular monolayer is known as **monolayer collapse** and in the isotherm is generally seen as a rapid decrease in the Π or as a horizontal break. Physicochemical studies show that for fluid monolayers at physiological temperatures, collapse occurs rapidly by the ejection of materials to the subphase when Π is higher than Π_e . Monolayers that collapse in the S phase are rigid enough to sustain higher Π values. Collapse in this case occurs by the formation of bilayer or multilayer agglomerates at the air or water side of the interface or by fracturing, followed by a loss of material in the subphase (Lipp et al., 1998, Lee, 2008, Baoukina et al., 2014). The formation of multilayers near the air phase occurs for fatty acid monolayers whereas for phospholipids such as DPPC, this happens at the water phase (Goto and Caseli, 2013). The mechanism of monolayer collapse is not fully understood. A molecular dynamics simulation study investigated the molecular mechanism of monolayer collapse using binary lipid mixtures of DPPC and palmitoyl-oleoyl-phosphatidylglycerol (POPG) and simulating a collapse that proceeds by buckling and folding of the monolayer into a bilayer at the water side of the

interface (Baoukina et al., 2008). They found that immediately after collapse, the bilayer folds have a flat semielliptical shape that can transform into a flat circular bilayer or vesicle and detach from the monolayer (Figure 12). For the particular case of pure DPPC monolayers, it is likely that the 3D structures formed remain attached to the interface below the monolayer (Goto and Caseli, 2013).

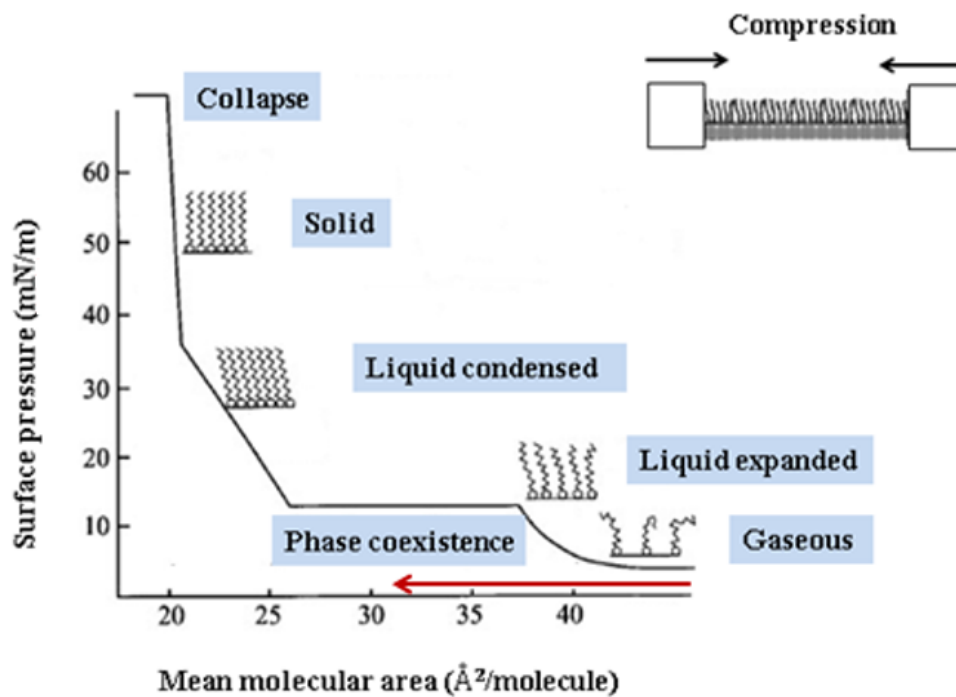


Figure 11. Graphical representation of the theoretical Π -Mean Molecular Area isotherm obtained by compressing an insoluble monolayer at an air/water interface. Monolayer phases and orientation of the surfactant in different phases are also shown. The red arrow shows the direction of isotherm formation. Adapted from Kaganer et al., 1999.

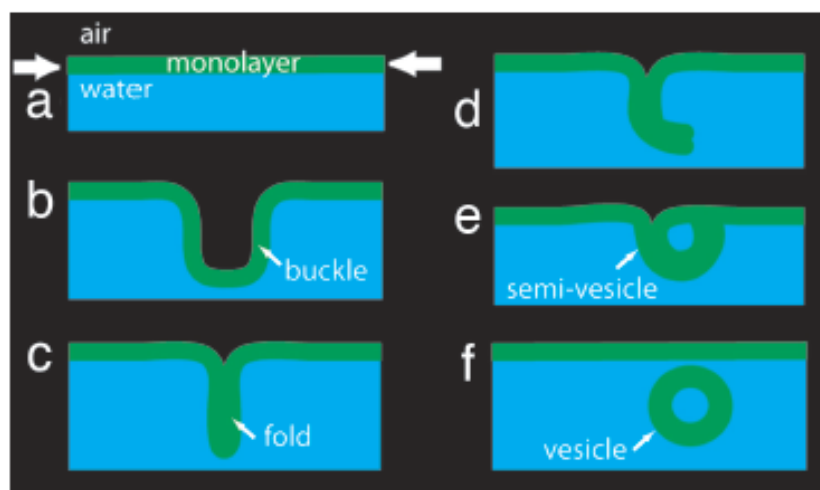


Figure 12. Schematic representation of the mechanism of monolayer collapse. Upon lateral compression and beyond a certain threshold the monolayer becomes unstable and collapse begins with buckling and folding into a bilayer at the water subphase (a-c). The bilayer folds bend into a semi-vesicle (d-e) and can transform into a vesicle and detach from the monolayer (f) (Baoukina et al., 2008).

Monolayer phases are mainly determined by the physical and chemical properties of the amphiphile, the subphase composition and the subphase temperature (KSV-Nima, 2010, Shinoda et al., 2013). With regards to the nature of the amphiphile, this dictates the magnitude of the forces acting in a monolayer for example dispersive (van der Waals) forces between the alkyl chains of the molecules, electrostatic (coulombic) repulsive forces between the polar headgroups, kinetic forces, steric forces between the headgroup and other interactions such as hydrogen bonding between the polar headgroup and molecules from the liquid subphase. The interplay of these forces determines the surface pressure and ultimately the shape of the isotherm (Telesford, 2012). The balance between the hydrophobic and hydrophilic segments of the molecule is a measure of the degree to which the surfactant is hydrophilic or lipophilic ranging from molecules that are almost completely insoluble in water to ones that are highly soluble. This is referred to as the hydrophilic-lipophilic balance (Barnes and Gentle, 2011). Surfactant films can be tightly or loosely packed depending on the area occupied by each molecule resulting in very different interfacial properties. For instance, straight chains and large head groups relative to the tail cross section favour close packing, while branched, bulky, or multiple hydrophobic chains give rise to steric hindrance at the interface (Nave, 2001). The electric charge amount of the polar head group and its distribution along the surfactant molecule including the hydrophobic tail influence the physicochemical properties of surfactant systems (Zhao et al., 2008). There is evidence that increasing surface charge density leads to a greater

structural ordering and rigidity of surfactant bilayers as well as increased viscosity (Bradbury and Nagao, 2016). When surfactants adsorb at liquid interfaces, they not only decrease the surface tension but also confer rheological properties to the surface such as compressibility. In contrast to bulk fluids which are incompressible, surfactant monolayers are rather compressible. A low compressibility indicates high resistance to compression and therefore, high rigidity and vice versa.

Regarding the subphase composition, dissolved electrolytes in the subphase can have a profound effect on the state of the film. For example, Ca^{2+} ions form insoluble calcium soaps with fatty acid films, thus making the film more condensed (Duncan, 1980). Ions in the subphase can also screen the charges of the polar head groups of the surfactant monolayer (KSV-Nima, 2010). Ionisable fatty acid monolayers, when spread on alkaline subphases, form gaseous or liquid expanded films at much lower temperatures due to the ionisation and consequent repulsion between the carboxyl groups (Duncan, 1980). The pH of the subphase is also important for those zwitterionic surfactants that are pH sensitive. This means that the pH determines if they are positively or negatively charged or if they carry no charge. Non-ionic surfactants on the other side are very unstable to pH variations (Mehta et al., 2006).

With regards to the effect of subphase temperature on the monolayer phases, Figure 13 shows the effect of temperature (10°C, 15°C, 20°C, 25°C and 30°C) on the Π -Mma isotherm of the surfactant phospholipid dipalmitoylphosphatidylcholine (DPPC) measured in water (Toimil et al., 2010). As can be seen in this figure, the isotherm shifts to higher Mma values with temperature. This behaviour is likely caused by an increase in the thermal motion of the chain at higher temperature, leading to an increase in Π (Yun et al., 2003). At high temperatures (20°C, 25°C and 30°C), the isotherm follows the sequence of monolayer phases G, G-LE, LE, LE-LC, LC and S. Collapse occurs at a Π value of ~ 60 mN/m although other studies have reported a collapse Π value of ~ 70 mN/m (i.e., near zero surface tension values) (Crane et al., 1999, Duncan and Larson, 2008). The Π value corresponding to the onset of the LE-LC phase transition increases and the plateau becomes shorter and less horizontal with temperature. At lower temperatures (10°C and 15°C), the LE-LC transition plateau disappears and a G-LC phase transition takes place directly without the existence of a LE phase. Typical experimental values of C_m for DPPC monolayers are 0.02-0.1 (mN/m)⁻¹ for LE films, 0.004-0.01 (mN/m)⁻¹ for LC films and < 0.004 (mN/m)⁻¹ for S films (Kodama et al., 2004, Vitovič et al., 2006). Although limited, there is some evidence that indicates that subphase temperature also affects

the shape, size and number of DPPC condensed domains. Telesford, 2012 investigated the effect of subphase temperature on the DPPC domains at a certain area per molecule using BAM. As can be seen in Figure 14, at a mean molecular area value of $60 \text{ \AA}^2/\text{molecule}$, an increase in subphase temperature from 23°C to 37°C decreased the size of the condensed domains, changed their shape, increased their number and decreased the area covered by them. Similar results have been described elsewhere (Ibrahim, 2000).

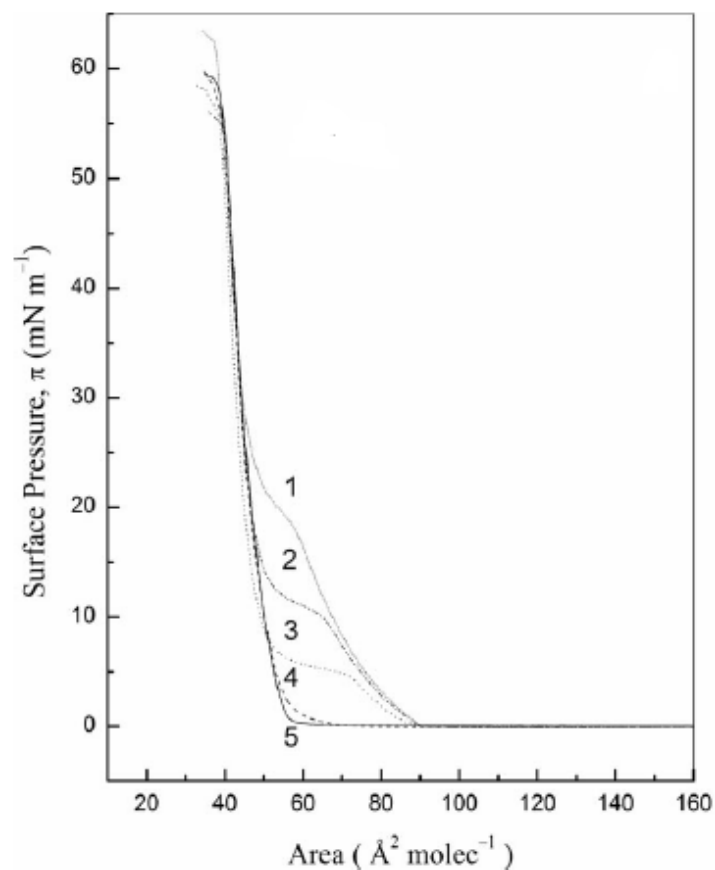


Figure 13. *II*-Mma isotherms for DPPC at five different subphase temperatures. Curve 1, 30°C ; curve 2, 25°C ; curve 3, 20°C ; curve 4, 15°C ; curve 5, 10°C (Toimil et al., 2010).

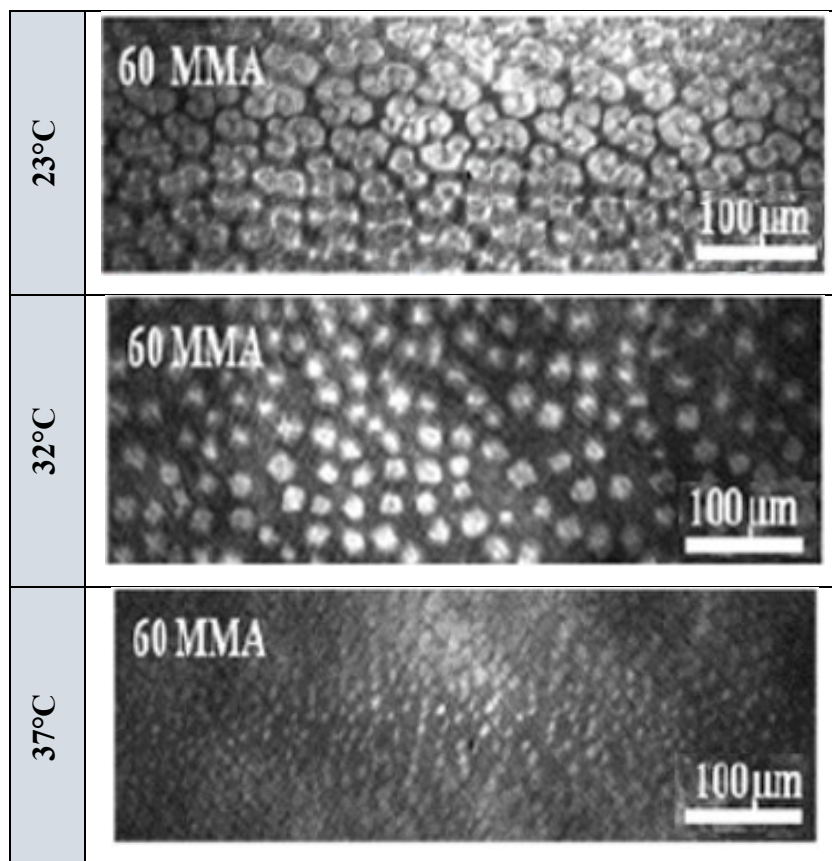


Figure 14. BAM images of a DPPC monolayer for a mean molecular area value of $60 \text{ \AA}^2/\text{molecule}$ at different subphase temperatures (23°C, 32°C and 37°C). Liquid condensed domains (bright areas) were dispersed in a liquid expanded phase (dark areas). Adapted from Telesford, 2012.

1.2.3.2 Particle monolayers

Solid particles, similar to surfactant molecules, can accumulate and strongly attach to an air/liquid interface forming particle monolayers with well-ordered structures (Albrecht et al., 1986, Aveyard et al., 2000a, Binks, 2002, Horozov et al., 2005). Particle monolayers can be fabricated using appropriate solvents such as chloroform or propanol (Aveyard et al., 2000b, Huang et al., 2001a, Huang et al., 2004, Horozov et al., 2006). When a particle is brought into contact with the liquid surface, a meniscus forms around the edge of the object and a triple interface between solid, liquid and gas is formed (Figure 15). The force due to surface tension of a liquid (F_s) acts on the circular contact line and has to provide a buoyant force large enough to float particles denser than the liquid (Liu et al., 2007). For this, the contact angle (θ) at the air-liquid-solid interface has to be above a minimum critical value (Chipfunhu et al., 2011). This means that the material is hydrophobic enough to provide a buoyant force that makes it float in the liquid.

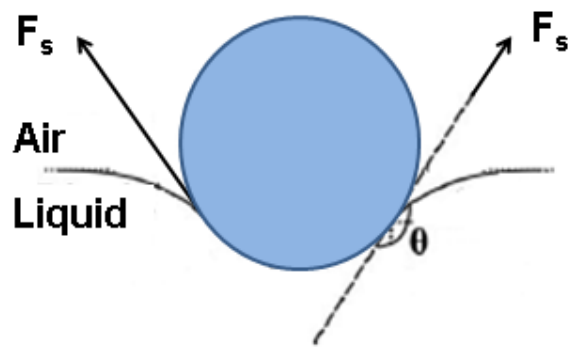


Figure 15. Illustration of the surface tension forces (F_s) acting on a floating sphere located at the air/liquid interface. θ is the contact angle. Adapted from Liu et al., 2009.

The attached amount of particles to a fluid/fluid interface during the spreading process strongly depends on particle hydrophobicity or wettability. It is larger for particles with intermediate hydrophobicity ($\theta \sim 90^\circ$) but rapidly decreases for particles with higher hydrophobicity ($\theta > 90^\circ$) or lower hydrophobicity ($\theta < 90^\circ$). The most hydrophilic particles will be pushed irreversibly into the liquid phase and the most hydrophobic particles will collapse and form a multilayer, with the particles with intermediate hydrophobicity being the most stable in the system (Binks, 2002). A graphical representation of the position of a particle according to its hydrophobicity is shown in Figure 16. Particles with $\theta = 0^\circ$ - 10° and $\theta = 170^\circ$ - 180° are preferentially located in one of the two fluid phases (Horozov et al., 2006, Maestro et al., 2014, Maestro et al., 2015). The wettability of the particle is also a key factor in controlling its behaviour at a fluid interface (Maestro et al., 2010).

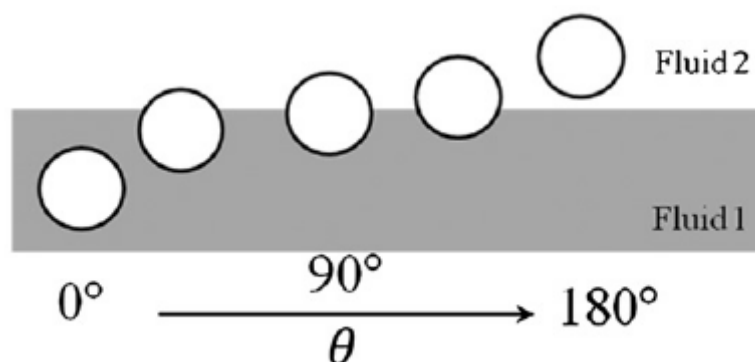


Figure 16. Schematic of the position of a particle according to its hydrophobicity at a fluid/fluid interface. θ is the contact angle (Maestro et al., 2014).

Measuring the θ is challenging due to the difficulties associated with monitoring a single particle adsorbed at a fluid interface. At the same time, the mechanisms that govern the θ are poorly understood due to the multiple variables, associated with the physicochemical nature of the particle and the fluid phases, which are involved in the wetting process of particles by fluid interfaces. Thus, the development of a theory that establishes the role of the θ in the attachment of particles to a fluid/fluid interface is still needed (Maestro et al., 2014).

Similar to surfactant monolayers, repulsive forces between particles can lead to a reduction of γ at the fluid/fluid interface. A Π -A isotherm can therefore be measured during the compression of a particle monolayer in a surface film balance (Aveyard et al., 2000a, Ji et al., 2005, Horozov et al., 2006). During this compression, particle agglomeration occurs through encounters between different clusters (Robinson and Earnshaw, 1992a, Robinson and Earnshaw, 1992b, Stankiewicz et al., 1993). In general, the forces responsible for the interactions between particles in bulk also operate in particle monolayers (Aveyard et al., 2000a, Binks, 2002). The monolayer structure can also be studied *in situ* or after transferring it onto a solid substrate using a variety of techniques including transmission electron microscopy (TEM), scanning electron microscopy (SEM), AFM or BAM (Kotov et al., 1994, Heath et al., 1997, Grabar et al., 1997, Huang et al., 2004).

An example of a Π -A isotherm is that measured by Aveyard et al., 2000b for 2.6 μm diameter monodisperse spherical polystyrene particles at the octane/water interface (Figure 17). A Langmuir trough placed on the stage of a microscope was used in this study for the microscopic observation of the structure of particle monolayers during compression. There were three distinct regions in the isotherm: at high areas from around 80 cm^2 to 45 cm^2 (region A) the surface pressure rose slowly, the particles were hexagonally packed and repulsive interparticle forces were long range. As the monolayer was further compressed, the surface pressure rose more steeply and some distortion of the lattice occurred (region B). Dominance of particle-particle repulsion on compression led to collapse which was seen as a horizontal break in the isotherm (region C). The collapse pressure of the monolayer was equal to the surface tension at the octane/water interface. Just below collapse, the monolayer was hexagonally closely packed (point 1). Upon further compression, the monolayer folded without particles being expelled from the monolayer (point 2). Further compression led to the formation of large corrugations of the monolayer or ripple phases with the surface pressure remaining nearly constant (point 3). Repulsive interparticle forces at points 1, 2, and 3 were short range.

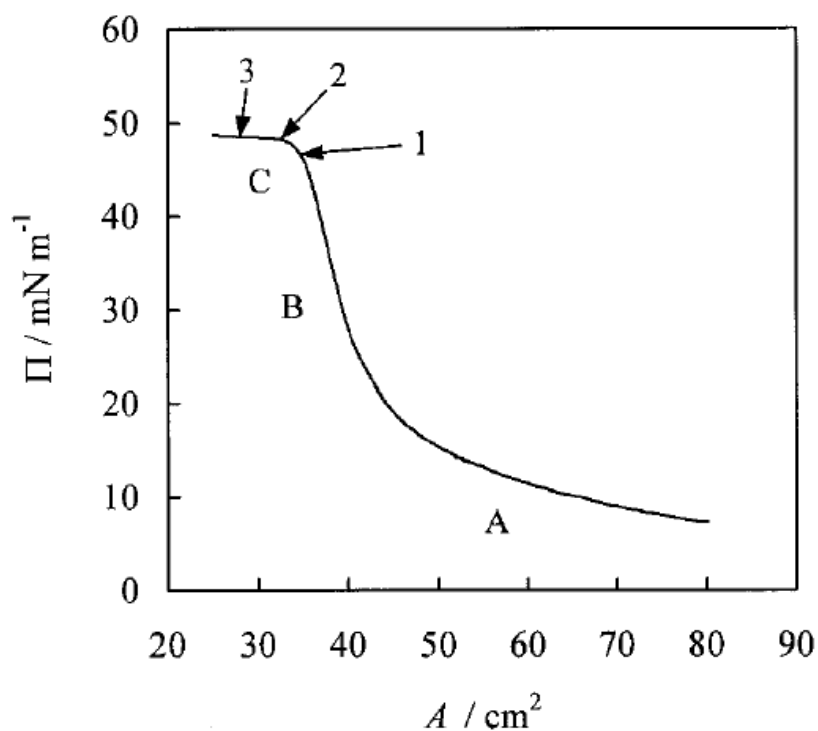


Figure 17. Π - A isotherm for 2.6 μm diameter monodisperse spherical polystyrene particles at the octane/water interface. Letters A, B and C and numbers 1, 2 and 3 represent different regions in the isotherm (Aveyard et al., 2000b).

Other studies such as that of Horozov et al., 2006 found that for fumed silica particles located at the octane/water interface, buckling began well before the collapse point and that there was a coexistence of ripples with two different wavelengths (λ_1 and λ_2) after collapse (Figure 18). Molecular dynamics simulation studies have shown similar particulate collapse mechanisms (Fenwick et al., 2001, Powell et al., 2002).

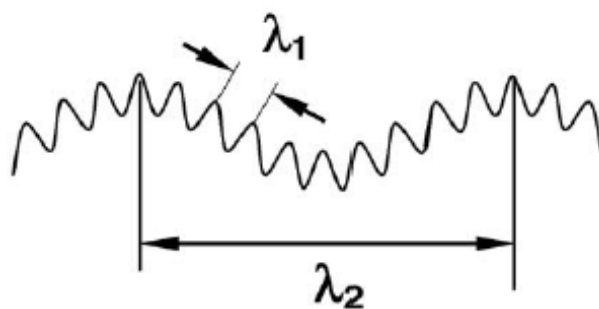


Figure 18. Graphical representation of the coexistence of long and short ripples with wavelengths λ_1 and λ_2 found in monolayers of fumed silica particles at the octane/water interface after collapse (Horozov et al., 2006).

Other studies, however, have made the assumption that particles are expelled from the monolayer on collapse (Clint and Taylor, 1992, Máté et al., 1998). The mode of monolayer collapse may therefore be dependent on the contact angle and size of the particles as well as on the surface tension at the fluid/fluid interface although strong evidence of the buckling collapse suggests that this monolayer collapse mode is probably a general feature of an array of particles (Aveyard et al., 2000b).

1.2.3.3 Colloids and colloidal stability

The properties of the interface are particularly important in systems where one phase is dispersed (called dispersed phase) as many very small particles in the other phase (called continuous phase or dispersant) as such systems have a very large interfacial area. These systems include heterogeneous mixtures in which the dispersed phase is insoluble in the continuous phase. Examples include colloidal dispersions which are systems where the dispersed material has at least one dimension within the range of about 1 nm to 1 μm .

An example of a colloidal dispersion is the dispersion of solid particles (e.g. nanoparticles) in a liquid medium. Most of these particles carry an electric charge due to different mechanisms such as the ionisation of surface groups, loss of ions from the crystal lattice or the adsorption of charged species on the surface of the particle. The development of a net charge at the particle surface results in an increased concentration of ions of opposite charge to that of the particle close to the surface and the appearance of an electrical double layer. This layer exists as two

parts: an inner region where the ions are strongly bound called Stern layer and an outer region where they are less firmly associated called diffuse layer. Any ions within this boundary will move with the particle when it moves in the liquid. The electric potential on the external boundary of the Stern layer versus the bulk electrolyte is called Stern potential and the electric potential on the external boundary of the diffuse layer versus the bulk electrolyte is called zeta potential. All this is shown in Figure 19:

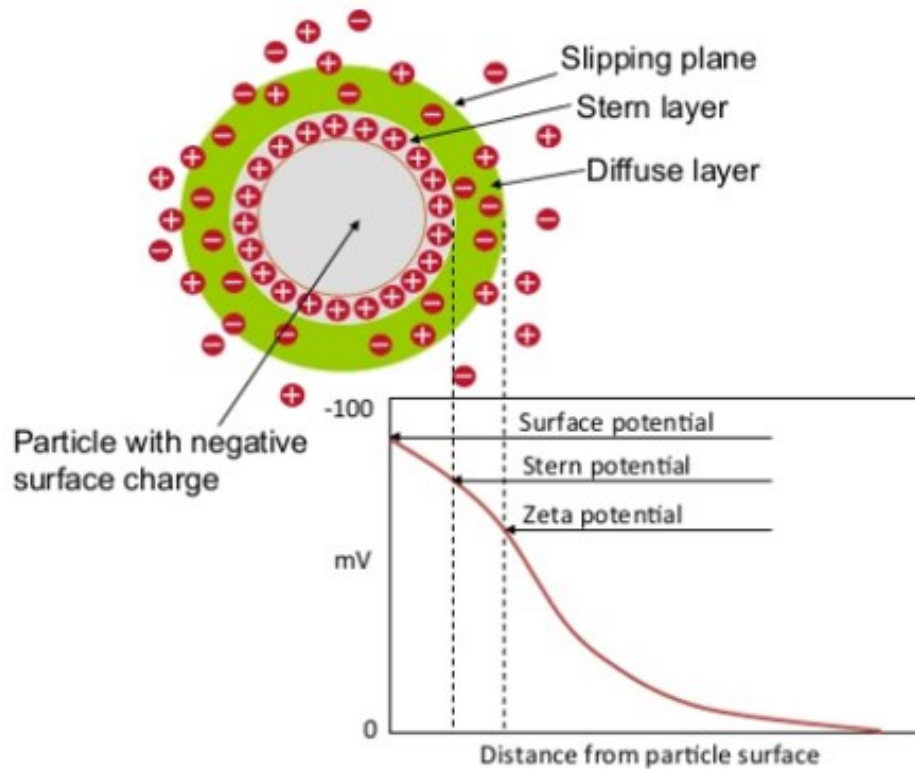


Figure 19. Schematic representation of the electrical double layer around a spherical colloidal particle and the electric potential (Alias, 2013).

The major issue in colloidal systems is the strong tendency of the particles to agglomerate and sediment. The stability of a colloidal system is defined by particles remaining suspended in the dispersion medium at equilibrium. The DVLO theory is the classical explanation of the stability of colloids in suspension and states that the stability is dependent upon its total potential energy function (V_T) which is the sum of three variables as shown in the following equation (Liu and Bashir, 2015):

$$V_T = V_S + V_A + V_R$$

Equation 9

where V_T is the total potential energy; V_S is the potential energy due to the solvent; V_A are the van der Waals attractive forces and V_R are the electrical double layer repulsive forces

V_S only makes a marginal contribution to the total potential energy whereas V_A and V_R are much larger and operate over a much larger distance. As the particles approach each other due to Brownian motion, if there is sufficiently high repulsion, the dispersion will be stable. However, if a repulsion mechanism does not exist flocculation or coagulation will eventually take place. Therefore, to maintain the stability of a colloidal system the repulsive forces must be dominant. In this sense, the magnitude of the zeta potential gives an indication of the potential stability of the colloidal system. As a rule of thumb, particles that have a zeta potential more positive than + 30mV or more negative than - 30mV are considered strongly cationic and strongly anionic respectively. They tend to repel each other and the system will be stable. If zeta potential is between + 30 mV and - 30 mV, the system will be unstable and particles will adhere to one another to form agglomerates (Clogston and Patri, 2011). If the density of the agglomerates is higher than that of the suspending medium, they will eventually sediment.

The pH of the sample is one of the factors that most affects the zeta potential as the magnitude of the surface charge depends on the pH of the solution. The isoelectric point is the pH at which zeta potential is zero. This means that the particle exhibits no net charge and represents the point where the colloidal system is least stable. Thus, zeta potential measurements should always be reported along with the sample pH. Zeta potential is also a function of concentration and type of salts present in the dispersant (Salgın et al., 2012). The specific adsorption of inorganic ions onto a particle surface can have a dramatic effect on the zeta potential of the particle dispersion and even lead to charge reversal of the surface. For example, if acid is added to a suspension where particles have a positive zeta potential, the particles tend to acquire more positive charge. If an alkali is added to the suspension, then a point will be reached where the charge will be neutralised and further addition of alkali will cause a build-up of negative charge. Hence, aggregation of colloidal particles can be induced by adding salts to the suspension (Robinson and Earnshaw, 1992a). The use of buffer solutions will have a strong influence on the charge of the particles due to the adsorption of specific buffer ions to the surface of the particle (Burns and Zydney, 2000). Buffer solutions have a resistance to pH change because of the presence of an equilibrium between the acid and its conjugate base (or the base and its

conjugate acid). Moreover, the higher the concentration of ions in solution (calculated from the ionic strength of the medium) and the higher the valence of the ions, the more compressed the double layer becomes (Malvern-Instruments, 2015).

The hydrophobicity of particles in a suspending medium can also be modified by the adsorption of surfactants to the surface of the particles (Maestro et al., 2012, Maestro et al., 2015). The adsorption of anionic surfactants leads to a negatively charged surface and of cationic surfactants to a positively charged surface and can prevent aggregation and enhance dispersion stability by increasing surface charge (Hotze et al., 2010). Surfactants can also neutralise the particle surface charge which is associated with the maximum value for the contact angle of the particles and the greater instability of the system. Other surface coatings such as polymers or polyelectrolytes can also enhance dispersion stability as they provide electrosteric repulsions that prevent particle aggregation.

In the particular case of nanomaterials, which have one or more external dimensions in the size range 1 nm to 100 nm (e.g. nanoparticles), colloid science is fundamental to understanding and developing theories for nanomaterial systems. However, due to the unique physical and chemical properties of these materials, theories in colloid science such as the DLVO theory are not always applicable as they do not accurately predict aggregation behavior (Hotze et al., 2010). For example, as a particle decreases in size, a greater percentage of its atoms are present on the surface which can alter the electronic structure, surface charge behavior and surface reactivity (Hochella et al., 2008). The DLVO theory also assumes that particles are spherical. Nanoparticles, however, have a variety of nonspherical shapes and electrical double layer forces are affected by changes in shape (Montgomery et al., 2000). Much work still needs to be done to fully understand nanoparticle aggregation (Hotze et al., 2010).

The most popular method to measure zeta potential is electrophoretic light scattering (ELS) in which particles move under an external electric field passed through the suspension; charged particles will be attracted towards the electrode of opposite charge. The velocity of the particle will be measured and is dependent on the strength of the electric field, the dielectric constant and viscosity of the medium and the zeta potential. Zeta potential is subsequently derived from the theoretical model. Electrophoretic determination of zeta potential is most commonly made in aqueous media. Particles suspended in a non-polar solvent can still be attracted to each other and form larger particles. However, since it is difficult to pass an electric current through low

polarity to non-polar solvents, i.e., low dielectric constants, this will result in a very low particle velocity and the need of instruments able to detect mobilities orders of magnitude smaller than those usually encountered in aqueous dispersants (Malvern-Instruments, 2016).

1.3 Lung surfactant

1.3.1 Introduction

The respiratory system is a complex set of specific organs and structures. It consists of the upper respiratory tract and the lower respiratory tract (Figure 20). The upper respiratory tract contains the organs and structures located outside the chest cavity and it consists of nose, nasal cavity, pharynx and larynx. The lower respiratory tract contains organs and structures located in the chest cavity and it consists of: trachea, two bronchial tubes, bronchi, bronchioles and alveoli (see Appendix 4 for further details on the respiratory system and the breathing process).

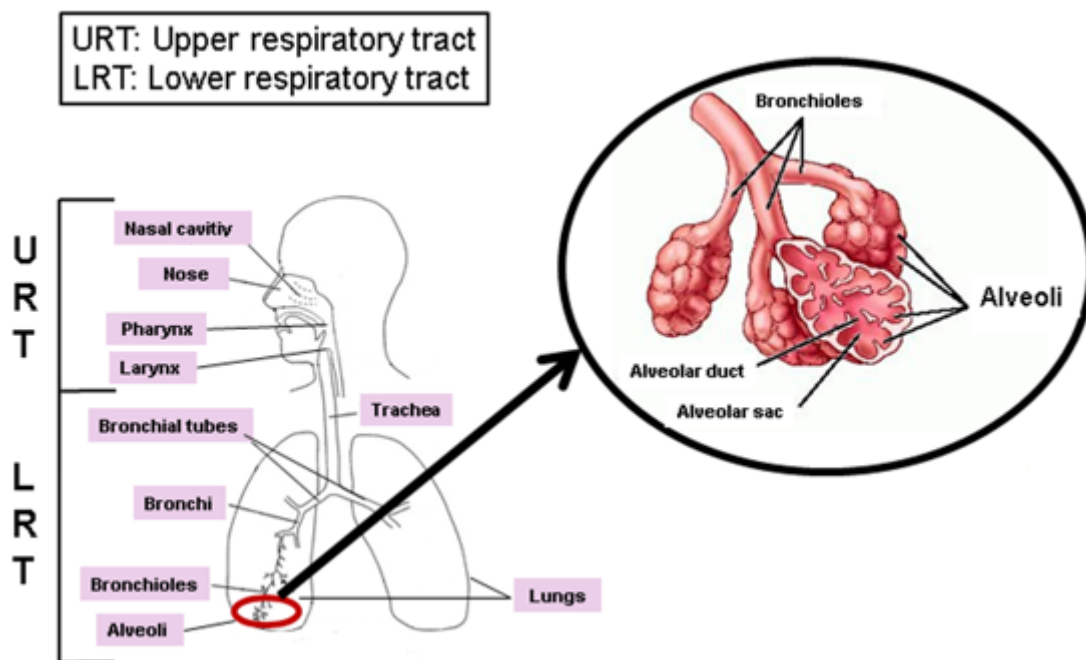


Figure 20. Schematic of the respiratory system and alveoli. Adapted from Dorland's-Medical-Dictionary-for-Health-Consumers, 2007.

There are about 300 million alveoli per human lung each 0.3 mm in diameter (Gottschlich, 2001, West, 2012). The alveolar epithelium is one cell thick and consists of type I alveolar epithelial cells and type II alveolar epithelial cells. Type I cells cover 95% of the alveolar surface area (Ng et al., 2004). Type II cells constitute about 60% of the alveolar epithelial cell

number but they cover less than 5% of the alveolar surface area of adult human lungs (Crapo et al., 1982). The epithelial surface area in the alveoli is lined with a thin continuous fluid called the alveolar lining layer (West, 2012) of about $\sim 0.1 - 0.2 \mu\text{m}$ in thickness. This lining consists of alveolar subphase fluid and lung surfactant (Ng et al., 2004) (Figure 21).

Lung surfactant - also known as pulmonary surfactant - is a surfactant film of $\sim 5 \text{ nm}$ in thickness that covers the entire alveolar region at the air/liquid interface consisting of a mixture of phospholipids, neutral lipids and four surfactant proteins (SP-A, SP-B, SP-C and SP-D) (Pattle, 1966, Zuo et al., 2008c). Lung surfactant was discovered by Richard Pattle in 1955 (Halliday, 2008, Zuo et al., 2008c).

The alveolar subphase fluid is a watery phase with $\text{pH} \sim 6.9$ and buffering capacity that contains a number of ions such as H^+ , Na^+ , Ca^{+2} or Cl^+ as well as a sizable population of resident immune cells, the alveolar macrophages being the most abundant (Ross et al., 2002, Ng et al., 2004). Because the alveolar subphase fluid is continuous to the surfactant layer, the subphase may have a number of important effects on surfactant structure, function, and metabolism (Nielson et al., 1981). For example Ca^{+2} facilitates a rapid surfactant adsorption to the air/liquid interface (Benson et al., 1984, Ross et al., 2002).

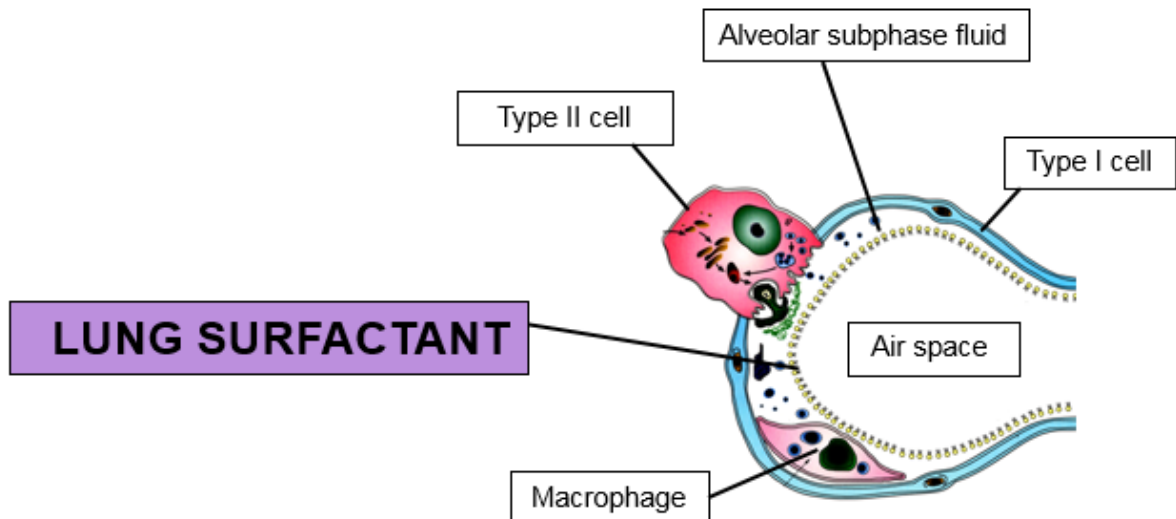


Figure 21. Schematic of the structure of the alveoli. The lung surfactant is a mixture of phospholipids, neutral lipids and proteins located at the air/liquid interface of the entire alveolar region. Adapted from Hawgood and Clements, 1990.

1.3.2 Function of lung surfactant

The reduction of the alveolar surface area during exhalation causes the compression of the lung surfactant film (Piknova et al., 2002). During this compression, lung surfactant reduces the surface tension of the alveolar subphase fluid that lines the alveolar epithelium at the air/liquid interface. Lung surfactant has a number of physiological functions which are surface tension related:

- It reduces the likelihood of alveolar collapse (also known as atelectasis) which would result in reduced or absent gas exchange by decreasing the elastic recoil of the lungs. This is the main physiological function of lung surfactant (Pattle, 1966, Frerking et al., 2001).
- It reduces the energy required to inflate the lungs with each breath and therefore, it increases pulmonary compliance (Orgeig et al., 2007, West, 2012).
- It maintains a large surface area to promote gas exchange (Pison et al., 1996, Orgeig et al., 2007).

- It stabilises the alveoli during tidal breathing (Ingenito et al., 2000). During exhalation, the rate of shrinking is more regular because of the stability of surface area caused by surfactant (Possmayer et al., 2010). During inhalation, it promotes uniform lung inflation (Alonso et al., 2005).
- It prevents transudation of fluid from the capillaries (also known as pulmonary oedema) as surface tension forces tend to suck fluid from the capillaries into the alveolar spaces (Pattle, 1966, West, 2012).
- It improves the mucociliary transport (Brown and Pattishall, 1993). Mucociliary clearance is an important self-clearing mechanism of the conducting airways (Munkholm and Mortensen, 2014).

Lung surfactant also has a number of physiological functions which are non-surface tension related:

- It has a host defence function against inhaled pathogens and particles, thus protecting the lungs from injuries and infections (Ng et al., 2004, Wright, 2005).
- It slows down local evaporation and protects the cells against excessive drying (Bourbon, 1991).

1.3.3 Biophysical properties of lung surfactant

From a surface active point of view, three are the biophysical properties that a functional lung surfactant should have for normal respiratory physiology (King and Clements, 1972, Notter, 2000, Serrano and Pérez-Gil, 2006):

- a) Rapid film formation through adsorption of surface active molecules from the alveolar subphase fluid into the air/liquid interface.** The rate of change of surface tension reflects the adsorption rate of the surface active material to the air/liquid interface (King and Clements, 1972). A functional lung surfactant should adsorb within a few seconds or faster (Schürch et al., 2001, Zuo et al., 2008c) and evidence suggests that this process consists of two sequential steps (Walters et al., 2000, Ross et al., 2002):

1. Surfactant vesicles diffuse from the alveolar subphase fluid to the interface and remain closely adjacent to the film. This process depends on material concentration on the subphase and is regulated by the surface charge of surfactant components, the surfactant proteins SP-B and SP-C and Ca^{+2} ions in solution.
2. Rupture of surfactant vesicles and fusion with the interfacial film. This process depends on the surface concentration of the monolayer and is facilitated by the surfactant proteins SP-B and SP-C.

During film adsorption at 37°C , surfactant can decrease surface tension from ~ 70 mN/m to a maximum of ~ 25 mN/m (Polin et al., 2011) or reach a Π of ~ 45 mN/m which corresponds to the Π_e , although this region has no physiological relevance as described below.

- b) Surface tension reduction to near zero values upon film compression during exhalation.** Although limited, some evidence suggests that surface tension at the alveolar surface falls to near zero (~ 1 mN/m) at the end of exhalation (Schürch, 1982, Bachofen et al., 1987). This low surface tension should be achieved by a slight film compression, particularly by no more than 20-30 % alveolar area reduction which is the maximum area variation during normal tidal breathing (Bachofen et al., 1987, Bachofen and Schürch, 2001). It should also remain constant in static lungs for tens of minutes (Horie and Hildebrandt, 1971, Schürch et al., 1978) and thus, it is not necessary to continuously compress the film to maintain the low surface tension value (Nag, 2005).
- c) Effective re-spreading of the surface active material to cover the expanded area during inhalation in order to maintain the low surface tension.** Upon expansion during inhalation surface tension should only increase slightly and remain close to the Π_e (Schürch et al., 1978). Thus, the physiologically relevant Π range in healthy lungs is confined to between Π_e and the collapse pressure of the film, i.e., from ~ 45 mN/m to ~ 70 mN/m respectively (Piknova et al., 2002, Zuo et al., 2008c). AFM studies have shown that upon compression, modified and natural surfactants are in monolayers at Π lower than ~ 45 mN/m. In normal healthy lungs, this region has no significant physiological relevance. At a Π around ~ 45 mN/m they undergo a monolayer to multilayer transition in which Π increases slightly with significant film compression (Figure 22) (Zhang et al., 2011a, Zhang

et al., 2011b). At Π above Π_e and before the collapse pressure, the surfactant film is a multilayer structure: it consists of a monolayer at the air/liquid interface with squeeze-out multilayers attached to it and located in the aqueous subphase. This is a surface-associated surfactant reservoir that can also be formed during adsorption of novo material. Several studies have shown the existence of this excessive lung surfactant material (Yu and Possmayer, 2003, Follows et al., 2007). It is identical in composition and morphology to the interfacial monolayer and functionally associated with it (Takamoto et al., 2001, Piknova et al., 2002, Zuo et al., 2008c). Fluorescence microscopy studies have shown that there is a LE and LC phase coexistence that persists at Π values approaching 70 mN/m. The LC domains contain mostly DPPC and other small amounts of disaturated phospholipids such as DPPG while the LE domains contain mostly unsaturated components and cover about 60% of the area, thus accounting for most of the surface (Piknova et al., 2001, Piknova et al., 2002, Harbottle et al., 2003). Although not fully understood, it is evident that SP-B and SP-C contribute to reservoir formation. Once this surface-associated surfactant reservoir is created, it can exchange surface active material with the interfacial surfactant film during film expansion or inhalation to cover the expanded area. This process is much faster than the adsorption of novo material from the subphase (Zuo et al., 2008c). The surface activity is still controlled by the interfacial monolayer (Zhang et al., 2011a). SP-B also plays a vital role in sustaining surfactant film stability at the most compressed states (Schürch et al., 2010).

Traditionally, the surfactant film has been considered to be a monolayer. However, experimental and morphological evidence observations show that at least part of this film consists of a multilayer (Schürch et al., 2001, Zuo et al., 2008c). In fact, the monolayer has not been sampled yet (Veldhuizen et al., 1998, Schürch et al., 2001).

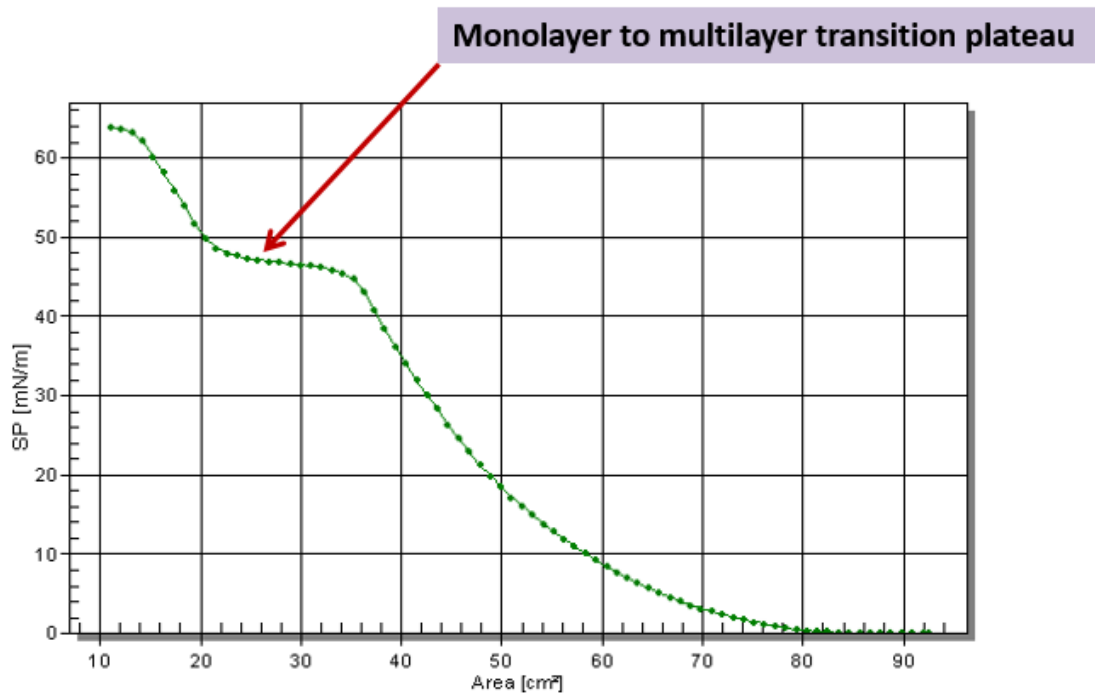


Figure 22. Illustration of the monolayer to multilayer transition plateau at a Π around ~ 45 mN/m in a compression isotherm of Curosurf®, a natural lung surfactant.

1.3.4 Composition and function of lung surfactant components

For most studies, the source of surfactant composition has been the analysis of fluid extracts obtained by bronchoalveolar lavage (BAL) (Creuwels et al., 1997, Frerking et al., 2001). Lung surfactant consists of $\sim 80\%$ weight phospholipids, $\sim 10\%$ weight neutral lipids and $\sim 10\%$ weight proteins (Goerke, 1998, Gupta et al., 2001, Ng et al., 2004) (Figure 23). The function of the individual components of lung surfactant have been difficult to unravel due to the complex nature of the system and the demanding circumstances under which lung surfactant operates (Barnes and Gentle, 2011). Details of the chemical structure of the lung surfactant components are provided in Appendix 5.

Lung surfactant composition

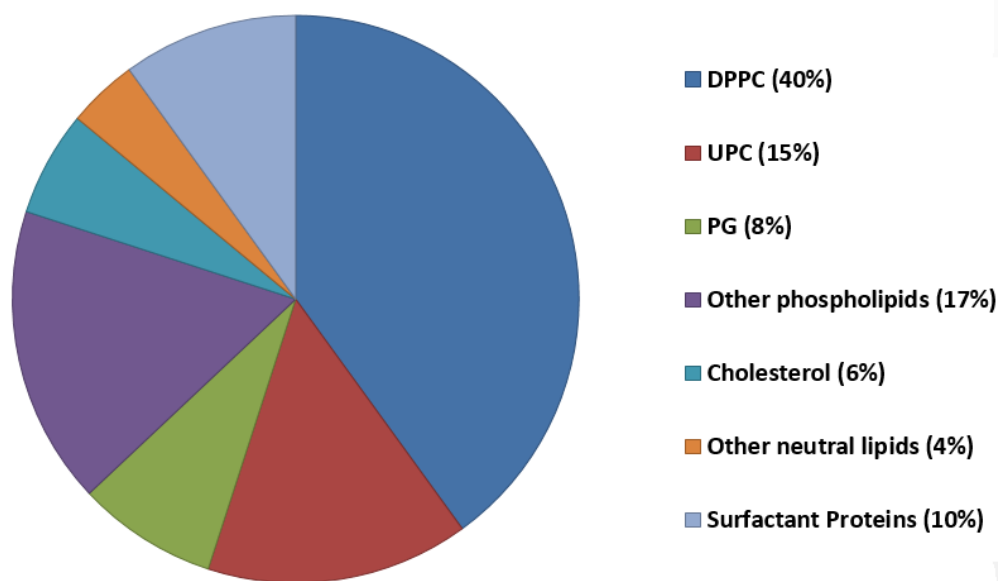


Figure 23. Graphical representation of the lung surfactant composition, the major phospholipids being DPPC – dipalmitoylphosphatidylcholine (the most abundant component of lung surfactant), UPC – unsaturated phosphatidylcholine and PG – Phosphatidylglycerol.

A. Phospholipids

Composition

Lung surfactant contains ~ 80% weight phospholipids. Table 2 shows the phospholipid composition of lung surfactant, their chemical structure and abundance. Phospholipids are amphiphilic molecules that belong to the class of lipids. They contain a polar phosphate group. They are also called “complex lipids” as they yield three or more products on hydrolysis (Fahy et al., 2005). The most abundant component of lung surfactant (~ 40% weight of lung surfactant content) is the disaturated phospholipid dipalmitoylphosphatidylcholine (DPPC). It consists of 2 molecules of palmitic acid, a molecule of glycerol (also called glycerin), a phosphate group and choline (Figure 24). The chemical formula of DPPC is $C_{40}H_{80}NO_8P$ and its molar mass 734.1 g/mol. DPPC is a zwitterionic surfactant as it has both cationic and anionic centers attached to the same molecule.

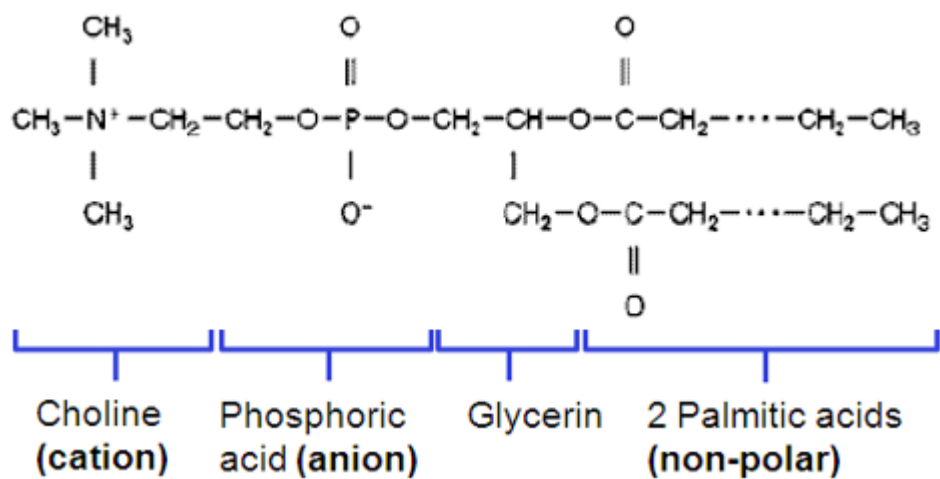


Figure 24. Chemical structure of DPPC. The complete chemical formula of a molecule of palmitic acid is $\text{CH}_3(\text{CH}_2)_{14}\text{COOH}$.

Table 2. Phospholipid composition and chemical structure of lung surfactant (Parent, 1992).

Type	Abbreviation	Name	Chemical structure	% of phospholipid content	% of lung surfactant content
Glycerophosphatides	DPPC	Dipalmitoylphosphatidylcholine (Saturated Phosphatidylcholine)	1,2-dipalmitoyl-sn-glycero-3-phosphocholine	49.3	39.4
	UPC	Unsaturated Phosphatidylcholine	1,2-diacyl-sn-glycerol-3-phosphocholine	18.2	14.6
	PG	Phosphatidylglycerol	1,2-diacyl-sn-glycerol-3-phosphoglycerol	10	8.0
	PE	Phosphatidylethanolamine	1,2-diacyl-sn-glycerol-3-phosphoethanolamine	5.3	4.2
	PI	Phosphatidylinositol	1,2-diacyl-sn-glycerol-3-phosphoinositol	3.6	2.9
	LBPA	Lysobisphosphatidic acid	1,2-diacyl-sn-glycerol-3-phospho-1-acylglycerol	3.6	2.9
	PS	Phosphatidylserine	1,2-diacyl-sn-glycerol-3-phosphoserine	1.6	1.3
	CL	Cardiolipin	1,2-diacyl-sn-glycerol-3-phospho-hosphatidylglycerol	0.9	0.7
Sphingosyl phosphatides	Sph	Sphingomyelin	N-acylsphingosine-1-phosphorylcholine	4.0	3.2
Lysoglycerophosphatides	LPC	Lysophosphatidylcholine	1-acyl-sn-glycerol-3-phosphocholine	1.7	1.4
Others				1.8	1.4

Function of phospholipids

Phospholipids are the primary surface tension-lowering components of the lung surfactant and essential for its biophysical function. The surface properties of phospholipid species (including stability, surface tension reduction and spreading) are influenced by a number of factors including the chemical nature of the fatty acid chains. The degree of saturation of the hydrocarbon chains will alter the degree of packing of phospholipid molecules: species with double bonds will occupy a larger area and so they cannot be compressed to the same extent as species with single bonds such as DPPC. On the other hand, the carbon atoms of the acyl chain of saturated phospholipids are fully hydrogenated which promotes a dense packing thanks to the hydrophobic interactions of the acyl chains where most of the water molecules will be expelled from the interface. Thus, saturated phospholipids are more effective in reducing surface tension (Blanco and Pérez-Gil, 2007, Polin et al., 2011).

Surfactant phospholipids can be classified as (Takamoto et al., 2001, Ku et al., 2008):

- Low surface tension stabilisers: they are competent to produce low surface tensions and to be stable or remain at the interface at near zero surface tensions but however adsorb and re-spread poorly into the air/liquid interface.
- Film fluidisers: they are capable of adsorbing and re-spreading quickly into the air/liquid interface but are easily excluded from the interface at high pressures and thus, cannot achieve low surface tensions.

A single lung surfactant constituent is not able to perform both functions (King and Clements, 1972). DPPC is a low surface tension stabiliser and the only lung surfactant phospholipid capable of forming a LC phase and reach a near zero surface tension on compression with a Langmuir-Wilhelmy balance (LWB) (Smith and Berg, 1980, Zhang et al., 2011b). However, it is incapable of adsorbing and re-spreading quickly into the air/liquid interface (Walters et al., 2000). Fluid phospholipids, such as unsaturated PC, introduce some fluidity into the monolayer although it is the surfactant proteins SP-B and SP-C which play an important role in film adsorption (Veldhuizen et al., 1998, Blanco and Pérez-Gil, 2007).

Lung surfactant phospholipids can also be classified according to the charge of their polar head groups. PG and PI are biochemically unique as they are the only anionic phospholipids of lung

surfactant in contrast to the remainder surfactant phospholipids which are zwitterionic. There is evidence that anionic lung surfactant phospholipids impart stability to the interfacial films during dynamic compression-expansion cycling through interactions with non-lipidic surfactant components, particularly the surfactant proteins SP-B and SP-C (Ingenito et al., 2000, Takamoto et al., 2001). PG and PI also accelerate the adsorption of surfactant material into the air/liquid interface (Walters et al., 2000, Ross et al., 2002). However, some other studies show that zwitterionic phospholipids play a major role over anionic phospholipids in pulmonary surfactant function including stability, surface tension reduction and spreading. Thus, the precise role of PG and PI and its presence in most adult surfactants is still not understood and requires further research (Wang et al., 1997, Veldhuizen et al., 1998).

B. Neutral lipids

Composition of neutral lipids

Lung surfactant contains ~ 10% weight neutral lipids. Table 3 shows the neutral lipid composition of lung surfactant and abundance.

Table 3. Neutral lipid composition of lung surfactant (Parent, 1992).

Name	% of neutral lipid content	% of lung surfactant content
Cholesterol	59.9	6.0
Free fatty acids	16.8	1.7
Diacylglyceride	12.4	1.2
Tryacylglyceride	6.1	0.6
Cholesterol esters	2.6	0.3
Monoacylglyceride	2.2	0.2

Neutral lipids belong to the class of lipids. In general, they have a hydrophobic tail but no polar group. They are also called “simple lipids” as they yield at most two types of products on hydrolysis (Fahy et al., 2005).

Function of neutral lipids

The contribution of neutral lipids to surfactant performance has not been extensively studied except in the case of cholesterol which is the most important neutral lipid of lung surfactant (Blanco and Pérez-Gil, 2007).

There is evidence that monoacylglycerides, diacylglycerides, triacylglycerides and palmitic acid increase the interfacial adsorption rate of DPPC (Veldhuizen et al., 1998) and that palmitic acid makes a DPPC monolayer more viscous at high Π and fluid at low Π (Ding et al., 2001).

Regarding cholesterol, there is evidence that cholesterol content as low as 2-3% can significantly alter surfactant films in 3 ways:

- by inducing the formation of a new liquid-ordered phase whose degree of lipid chain order is intermediate between the LE and LC phases (Mouritsen and Zuckermann, 2004, de la Serna et al., 2004, Zuo et al., 2008c).
- by the variation of film fluidity (Zhang et al., 2011a).
- by the variation of the collapse mechanism (Zhang et al., 2011a). There is however some evidence that this may be related to the experimental methodology, particularly to leakage artifacts of the devices used to measure Π . This leakage might have been favoured in relatively more fluid cholesterol containing films which would have produced a film collapse at pressures lower than needed for a good surfactant to work properly (Blanco and Pérez-Gil, 2007).

Other studies show that cholesterol at physiological level or lower appears not to affect the surface tension lowering ability (Gunasekara et al., 2005, Keating et al., 2007) and that the physiological proportion of cholesterol is essential to organise the lateral structure of surface films in pulmonary surfactant (de la Serna et al., 2004). Further research is still required to unravel the mechanisms by which cholesterol modulates surfactant activity at physiological level (Blanco and Pérez-Gil, 2007). Cholesterol above the physiological level exhibits significant inhibition on surfactant function (Malcharek et al., 2005, Leonenko et al., 2007).

C. Surfactant proteins (SP)

Lung surfactant contains ~ 10% weight proteins although only 6-8% weight appear specifically associated with surfactant lipids (surfactant associated proteins) (Serrano and Pérez-Gil, 2006, Blanco and Pérez-Gil, 2007). They are also called apoproteins (Chung et al., 1998). Up to now, four surfactant proteins have been identified according to their chronological discovery: SP-A, SP-B, SP-C and SP-D (Possmayer, 1988). The surfactant proteins are either exclusively lung associated or predominantly found in the lung (Creuwels et al., 1997).

SP-A and SP-D

SP-A and SP-D are hydrophilic proteins. SP-A is the major protein in surfactant representing about 5–6% weight of lung surfactant content. It is strongly associated with surfactant phospholipids and hydrophobic proteins. SP-D represents ~ 0.5% weight of lung surfactant content. It does not appear associated with surfactant lipids. SP-A and SP-D play an important role in host immune defence (Wright, 2005). SP-A and SP-D do not have a direct role in the formation of a surfactant monolayer and/or surface tension reduction. However, there is evidence that SP-A enhances the adsorption of surface-active material to the air/liquid interface in the presence of SP-B (Schürch et al., 1992, Possmayer et al., 2001). SP-A also takes part in surfactant metabolism as it is needed to form and maintain the tubular myelin structure, which is an intermediate in interface film formation (Klein et al., 2002, Serrano and Pérez-Gil, 2006). On the other hand, SP-D promotes the formation of a surplus of surfactant phospholipids which may be needed in situations where surfactant performance is challenged (Blanco and Pérez-Gil, 2007).

SP-B and SP-C

SP-B and SP-C are small hydrophobic proteins. Each of them represents about 1-1.5% of lung surfactant content (Serrano and Pérez-Gil, 2006). They are strongly associated with surfactant lipids (Blanco and Pérez-Gil, 2007). Despite their relatively low abundance, they play critical roles in the formation of a surfactant monolayer at the air/liquid interface by accelerating the adsorption and surface spreading of phospholipids to cover the expanded area during inhalation and also maintenance of a functional interfacial film (Robertson and Halliday, 1998, Weaver and Conkright, 2001). Thus, these proteins contribute to the reduction of surface tension at the air/liquid interface. SP-B is the only surfactant protein essential for life (Vayrynen, 2003). Humans with SP-B deficiency suffer from lethal respiratory failure (Nogee et al., 1993, Klein et al., 1998b).

1.3.5 Lung surfactant and the near zero surface tension

Physicochemical studies show that for fluid monolayers at physiological temperatures, collapse occurs rapidly by the ejection of materials to the subphase when Π is higher than Π_e . Monolayers that collapse in the S phase are rigid enough to sustain higher Π values. Collapse in this case occurs by the formation of bilayer or multilayer agglomerates at the air or water side of the interface or by fracturing, followed by a loss of material in the subphase (Lipp et al., 1998, Lee, 2008, Baoukina et al., 2014). One of the most remarkable characteristics of pulmonary surfactant is that it remains in a metastable state at Π well above Π_e . Thus, this resistance to collapse indicates the presence of highly ordered structures with the rigidity of a solid film (Piknova et al., 2002). The detailed mechanism by which lung surfactant reaches a near zero surface tension value is however still not known (Lalchev et al., 2008, Zuo et al., 2008c, Possmayer et al., 2010). There are several models that try to explain how lung surfactant may function. The “squeeze-out” hypothesis is the classical model and it is based on the fact that DPPC is the only constituent capable of reaching near zero surface tension on compression with a LWB (Smith and Berg, 1980, Zhang et al., 2011b). A LWB is one of the most commonly used devices to study monolayers and was introduced by Clements (Clements, 1957 cited in Polin et al., 2011). This model states that during compression, less stable fluidising non-DPPC components are selectively removed from the interfacial monolayer, which would result in a pure DPPC monolayer at very low surface tensions (Watkins, 1968, Clements, 1977). This model has recently been updated by other studies that indicate that the removed surfactant material remains closely attached to the interfacial monolayer forming a multilayer structure known as lung surfactant reservoir (Lee, 2008, Zuo et al., 2008c). However, the presence of a pure DPPC film has never been demonstrated.

This theoretical model has been challenged in two ways that show that a monolayer of DPPC is not required for reaching very low surface tensions:

- Recent evidence demonstrates that there is a LE – LC phase coexistence in the phospholipid fraction of the interfacial monolayer at near zero surface tensions. The LC phase is located in nanoscale domains which are uniformly distributed in the LE phase. The LE domains cover about 60% of the area and thus, account for most of the surface (Piknova et al., 2001, Piknova et al., 2002, Harbottle et al., 2003, Yu and Possmayer, 2003). How these LE domains remain at high Π is still unknown (Zuo et al., 2008c).

- Other studies have shown that fluid non-DPPC phospholipids can reach very low surface tensions on compression at very high speeds at 37°C with a captive bubble surfactometer (Crane and Hall, 2001, Smith et al., 2003). Such rates have never been achieved with a LWB.

Thus, evidence suggests that the ability to reach near zero surface tension depends on the monolayer composition and the rate the monolayer is compressed (Polin et al., 2011).

1.3.6 Lung surfactant dysfunction and exogenous lung surfactant therapy

The absence, deficiency or inactivation of lung surfactant is associated with severe pulmonary diseases and therefore, lung surfactant is absolutely necessary (Griese, 1999). Infant Respiratory Distress Syndrome (IRDS) is the major disease of lung surfactant deficiency with great global incidence. It is suffered by premature infants who do not produce sufficient amounts of lung surfactant due to the immaturity of their lungs. The pathophysiological features of IRDS include stiff lungs (low compliance), increased work of breathing, areas of atelectasis with reduced functional residual capacity, impaired gas exchange and lung oedema (West, 2012). It is estimated that 10% of all premature infants in developed countries are affected by IRDS (Martin et al., 2003 cited in Zuo et al., 2008c).

Other severe disease that displays similar symptoms to IRDS is Acute Respiratory Distress Syndrome (ARDS). ARDS is not associated with a surfactant deficiency but with an impairment of surfactant due to the liberation or leakage of a variety of inhibitory substances such as plasma proteins, haemoglobin and certain lipids into the alveolar space. The pathological features of ARDS include lung inflammation, aspiration, trauma, sepsis, severe pulmonary infection, near drowning or pneumonia (Wauer, 1998, Ware and Matthay, 2000). ARDS affects patients of all ages and has a fatality rate of approximately 30-40% (McIntyre Jr. et al., 2000 cited in Zuo et al., 2008c).

Other biochemical surfactant abnormalities have been described in a variety of diseases including obstructive lung diseases (for example asthma or chronic obstructive pulmonary disease (COPD)), infectious and suppurative lung diseases (such as cystic fibrosis or pneumonia), interstitial lung diseases (sarcoidosis) and even in smokers or patients with cardiopulmonary bypass (Griese, 1999).

The application of exogenous lung surfactant to babies that suffer from IRDS has proved to be an efficient therapeutic intervention which has dramatically improved the survival of the premature babies (Zhang et al., 2004, Wright, 2005). Surfactant therapy, however, has shown limited positive effects with ARDS patients (Haitsma et al., 2004, Lewis and Veldhuizen, 2006) and needs further research for other surfactant abnormalities (Griese, 1999). Supplies of human lung surfactant to treat diseases are limited (Bringezu et al., 2002) and therefore, clinical surfactant preparations are necessary. Surfactant preparations can be divided based on their surfactant protein content:

- a) **First-generation protein-free synthetic surfactants.** The first synthetic surfactant trials used nebulised DPPC as exogenous surfactant. Results show that DPPC alone lacks the ability to restore the mechanical characteristics of the lungs due to its poor biophysical properties (Hall et al., 1992) and thus, was ineffective as a therapeutic agent for infants that suffered from IRDS (Robillard et al., 1964, Chu et al., 1967).
- b) **New generation synthetic surfactants** that contain simplified peptides or recombinant surfactant protein analogues. Peptide-containing synthetic surfactants, although promising, are still under development (Halliday, 2008).
- c) **Surfactant from human amniotic fluid.** It contains both the hydrophilic and the hydrophobic proteins. The used of this surfactant showed promising results (Merritt et al., 1986) but lacks commercial capacity due to its source limitation (Zuo et al., 2008c).
- d) **Surfactant preparations obtained from animal sources.** Animal sources are the surfactant preparations most commonly used. Surfactant can be extracted by bronchopulmonary lavage or lung mincing (Zhang et al., 2011a). During the manufacture, they undergo organic extraction which removes SP-A and SP-D and in some cases reduces the content of SP-B and SP-C (Bernhard et al., 2000). Additional procedures remove or reduce the neutral lipid content, mainly cholesterol, as it has traditionally been considered harmful in terms of surface activity (Blanco and Pérez-Gil, 2007, Zhang et al., 2011a). Table 4 shows natural surfactant preparations used in clinical trials and its composition. Clinical surfactant preparations differ in the concentration and profile of phospholipids, cholesterol, individual surfactant proteins and additives. Several studies show that the physiological

effect of these surfactant preparations may be influenced by their composition (Hall et al., 1992, Zhang et al., 2011a).

Table 4. Clinical surfactant preparations obtained from animal sources (Fox and Sothinathan, 2005).

Generic name	Trade name	Composition	Surfactant protein
Beractant	Survanta	Bovine minced lung + synthetic DPPC, tripalmitin and palmitic acid	B and C
Bovine Lipid Extract Surfactant	BLES	Bovine lung lavage	B and C
Bovactant	Alveofact	Bovine lung lavage	B and C
Calfactant	Infasurf	Bovine lung lavage	B and C
Poractant alfa	Curosurf	Porcine minced lung	B and C
Surfactant TA	Surfacten	Bovine minced lung + synthetic DPPC, tripalmitin and palmitic acid	B and C

1.3.7 *In vitro* methods to investigate the surface properties of exogenous lung surfactant mixtures

The composition of lung surfactant is very complex, and so many different surfactant mixtures have been studied to investigate lung surfactant properties. Five are the key components capable of mimicking many of the features of native lung surfactant: DPPC, PG and palmitic acid (PA) as the main lipid components and the surfactant proteins SP-B and SP-C (Johansson et al., 1994, Veldhuizen et al., 1998, Johansson et al., 1998). Some of the exogenous lung surfactant mixtures that have been investigated are:

- Clinical surfactant preparations obtained from animal sources - BLES, Survanta, Curosurf, Infasurf and Surfacten (Lu et al., 2003, Nakahara et al., 2008).
- Mixtures of DPPC/PG/PA/SP-B (Ding et al., 2001, Bringezu et al., 2002).
- Mixtures of PA/SP-B (Lipp et al., 1997, Flanders et al., 2002).
- Mixtures of DPPC/PA (Guzmán et al., 2012c).

- Mixtures of DPPC/Cholesterol (Chou and Chang, 2000, Yuan and Johnston, 2002).
- DPPC (Wen and Franses, 2001, Stuart et al., 2006, Guzmán et al., 2011).

The most common *in vitro* techniques used to investigate the surface properties of exogenous lung surfactant mixtures are the Langmuir-Wilhelmy balance, pulsating bubble surfactometer and the captive bubble surfactometer (Notter and Morrow, 1975, Tabak and Notter, 1977, Putz et al., 1994, Prokop and Neumann, 1996, Schürch et al., 2001, Zuo et al., 2008c). A detail description of each of these techniques as well as its advantages and disadvantages are shown in Appendix 6.

1.4 Engineered nanoparticles

1.4.1 Nanotechnology and engineered nanomaterials

1.4.1.1 Introduction

The European Commission defines nanomaterials (NMs) as "*a natural, incidental or manufactured material containing particles, in an unbound state or as an aggregate or as an agglomerate and where, for 50 % or more of the particles in the number size distribution, one or more external dimensions is in the size range 1 nm - 100 nm*" (European-Commission, 2011). Thus, NMs are typically defined based on particle size solely. To put things into perspective, the diameter of a human hair is 100,000 nm. Plant and animal cell size varies between 10,000-100,000 nm in diameter. A DNA double helix is 2 nm wide. 1 nm is only 10 times the diameter of a single hydrogen atom (Mou et al., 1995, Purves et al., 2003, Beaumont, 2005). Figure 25 shows a scale axis of cells, viruses, biological structures, molecules and atoms.

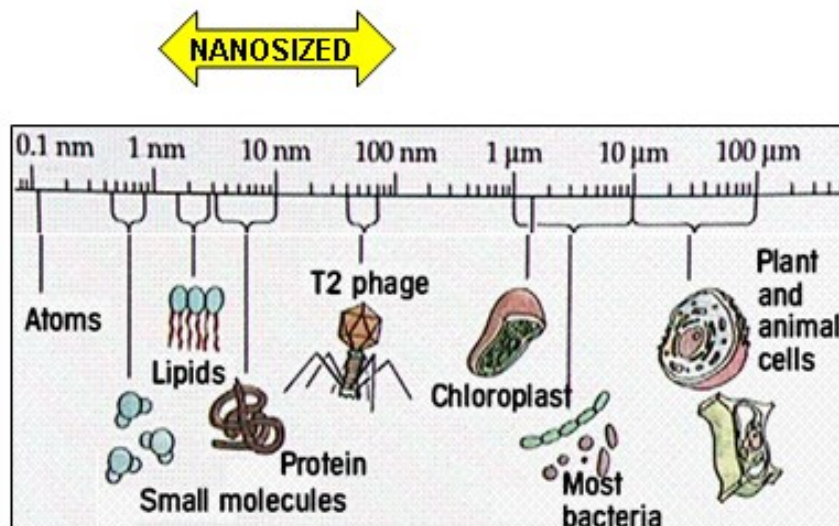


Figure 25. Scale axis of cells, viruses, biological structures, molecules and atoms. Adapted from Purves et al., 2003.

Naturally occurring NMs have been present on earth for millions of years (Nowack and Bucheli, 2007). NMs have also been inadvertently formed since the industrial revolution as a by-product of industrial and/or combustion processes such as automobile engines (Schleh et al., 2009, Farré et al., 2011). Other NMs such as titanium dioxide, iron oxides or amorphous silica have been intentionally produced by industry for decades in applications such as pigments, resins and cosmetics (Borm et al., 2006). In addition to all this, engineered nanomaterials (ENMs) are materials whose atomic, molecular and macromolecular scales have been manipulated to confer unique properties and applications to the material (Borm et al., 2006, Stone et al., 2007). Engineered NMs, devices and systems are produced by a relatively new area of science called nanotechnology, which is nevertheless, one of the fastest developing technologies of the 21st century with a global market worth \$10.5 billion in 2006 (BCC, 2006 cited in Crane et al., 2008) and estimated to reach more than \$ 1 trillion by 2015 (SCENIHR, 2006 cited in Rossi et al., 2010). It is expected that nanotechnology will change the way everything is made and designed in society. The potential of nanotechnology includes the decrease of waste and pollution during material fabrication, the detection and treatment of diseases at earliest stages or the improvement of the performance of electronic devices (Sen et al., 1999).

Typical ENMs include carbon NMs (e.g. carbon black and carbon nanotubes), metal-oxide nanoparticles (e.g. cerium dioxide nanoparticles), zero-valence metals (e.g. silver or gold nanoparticles) and quantum dots or dendrimers (Farré et al., 2011). In the particular case of

nanoparticles (NPs), these are currently defined as single particles with a nominal diameter smaller than 100 nm. Aggregates and agglomerates can be larger than 100 nm and are not included in this definition. However, they are usually taken into consideration when investigating the nanosubstance as they may break down or deagglomerate by mechanical forces or in solvents (Borm et al., 2006).

ENMs exhibit enhanced or novel physicochemical properties compared to the same material in larger bulk form including strong surface reactivity, strength, conductivity and electrical properties or optical characteristics. Two are the main factors that cause the properties of ENMs to be unique: large surface to volume ratio and quantum effects (Stone et al., 2007, Auffan et al., 2009b, Farré et al., 2011).

The list of uses for ENMs is already substantial and is predicted to exponentially increase in the future (Lanone et al., 2009). For example, ENPs have already been implemented in sunscreens, cosmetics, food additives, self-cleaning paints and glass, clothing, disinfectants, fuel additives, batteries and other products (Bakand et al., 2012). The potential benefits of nanotechnology are therefore considerable with applications in a wide variety of areas such as electronics, biomedicine, pharmaceuticals, cosmetics, energy, environmental, catalysts and material applications (Nowack and Bucheli, 2007). The application and estimated global production of some ENMs are presented in Table 5.

Table 5. Application and estimated global production of some ENMs (The Royal Society and The Royal Academy of Engineering, 2004).

Application	Nanomaterial/device	Estimated global production (tonnes per year)		
		2003/04	2010	2020
Structural applications	Ceramics, catalysts, films & coatings, composites, metals	10	10 ³	10 ⁴ -10 ⁵
Skincare products	Metal oxides (e.g. TiO ₂ , ZnO)	10 ³	10 ³	10 ³
Information & Communication Technologies	Single walled carbon nanotubes, nanoelectronic and optoelectronic materials (excluding chemical mechanical planarization slurries), organic light emitters and electronics, nanophosphors	10	10 ²	>10 ³
Biotechnology	Nanocomposites & encapsulates, targeted drug delivery, diagnostic markers, biosensors	<1	1	10
Environmental	Nanofiltration, membranes	10	10 ²	10 ³ -10 ⁴

1.4.1.2 Nanomaterial characterisation

The importance of ENM characteristics in relation to their toxic effects means that appropriate characterisation of NMs is a key issue. Table 6 shows relevant physicochemical properties of ENMs and their measurement techniques. It is recommended to use more than one method to characterise a property and to clearly state the method used as different techniques often produce contrasting results. There is a need to establish minimum characterisation requirements of ENMs at production and also take into account the changes that can occur to the ENM when it is delivered to, or during its lifetime in the environment or a living system (Bouwmeester et al., 2011). In the absence of this information it is difficult to set environmental quality standards and guidelines or perform risk assessments for ENMs (Crane et al., 2008).

Table 6. Relevant physicochemical properties of ENMs and their respective associated measurement techniques (Hassellöv et al., 2008, Baalousha et al., 2012a, Baalousha et al., 2012b).

Physicochemical property	Measurement technique
Size and size distribution	<ul style="list-style-type: none"> • Dynamic Light Scattering (DLS) as hydrodynamic size • Differential Mobility Analyser (DMA) as mobility size • Electron Microscopy (EM) • Atomic Force Microscopy (AFM) • Flow-Field Flow Fractionation (Flow-FFF)
Shape and morphology	<ul style="list-style-type: none"> • Electron Microscopy (EM) • Atomic Force Microscopy (AFM)
Surface area	<ul style="list-style-type: none"> • Brunauer, Emmett and Teller (BET)
Surface charge	<ul style="list-style-type: none"> • Zeta potential • Electrophoretic mobility
Surface chemistry	<ul style="list-style-type: none"> • Raman spectroscopy • Energy-dispersive X-ray spectroscopy (X-EDS) • Electron energy loss spectroscopy (EELS) • X-ray photoelectron spectroscopy (XPS)
Crystal structure	<ul style="list-style-type: none"> • X-ray diffraction • High resolution transmission electron microscope (High resolution TEM)
Aggregation state	<ul style="list-style-type: none"> • Dynamic Light Scattering (DLS) • Electron Microscopy (EM) • Atomic Force Microscopy (AFM)

1.4.2 Human inhalation exposure to nanoparticles: deposition, clearance and retained dose

1.4.2.1 Introduction

Human beings have been exposed to naturally occurring NPs throughout their evolutionary stages. Exposures to unintentionally generated NPs have increased dramatically since the industrial revolution. In addition to this, the intentional production of NPs and newly developed ENPs coming from nanotechnology represents a potential source for human exposure to NPs (Schleh et al., 2009). The main sources of NMs in the environment are summarised in Table 7.

The rapid development and production of NMs worldwide could lead to human exposure to NPs through various routes (inhalation, ingestion, dermal and injection) (Oberdörster et al., 2005) during material fabrication, handling, usage and waste disposal (Wiesner et al., 2006). However, measurement techniques to determine exposures are not fully developed (Kaluza et al., 2009).

Table 7. Main sources of NMs in the environment (Farré et al., 2011).

	Natural origin	Incidental origin	Engineered nanoparticles
Air	<ul style="list-style-type: none"> • Volcanic eruption • Hydrothermal vent systems • Physicochemical wearing of rocks and dust volatilisation • Biological processes • UV degradation from aquatic systems • Nucleation processes 	<ul style="list-style-type: none"> • Combustion processes • Industrial emissions 	<ul style="list-style-type: none"> • Nanotechnology-production processes
Water	<ul style="list-style-type: none"> • Metal-sulfide nanoclusters • Hydrous iron • Manganese oxide 	<ul style="list-style-type: none"> • Deposition from atmosphere 	<ul style="list-style-type: none"> • Spillage from nanotechnology
Soil	<ul style="list-style-type: none"> • Nanominerals (e.g. ferrihydrite) • Natural organic-material aggregates • Biogenic origin (e.g. uraninite) 	<ul style="list-style-type: none"> • Deposition from atmosphere • Sorption and transport from aquatic systems 	<ul style="list-style-type: none"> • Spillage from nanotechnology

1.4.2.2 Inhalation exposure and particle deposition

Inhalation may be the most important route for human exposure to NPs (Hoet et al., 2004, Oberdörster et al., 2005, Sharifi et al., 2012) and therefore, it is likely to be a significant entry route for ENPs. A fraction of the inhaled material is filtered by the respiratory system and exhaled out of the body and the rest deposits in the respiratory tract (Möller et al., 2004, Bailey and Puncher, 2007). The behaviour of airborne particles in the respiratory tract depends on particle-related parameters (size, shape and density), breathing patterns and airway anatomy (Bailey and Puncher, 2007, Park et al., 2008). There are 5 main mechanisms for deposition of inhaled particles (Oberdörster et al., 2005, Bailey and Puncher, 2007, Scott, 2015):

- **Impaction.** Important for particle sizes $> 0.5 \mu\text{m}$ where deposition occurs by rapid changes in airflow direction which deviate the particle from the air streamline due to inertial motion.
- **Sedimentation.** Important for particle sizes $> 0.5 \mu\text{m}$ where deposition is caused by gravity.
- **Interception.** Important for particle sizes $> 0.5 \mu\text{m}$ where deposition occurs when the particle contacts the airway wall because of its high ratio of length to width which affects the aerodynamics of the particle.
- **Electrostatic precipitation.** Important when particles carry significant electric charges. Electrostatic precipitation occurs from the image charges induced on the surface of the airways by the charged particles.
- **Diffusion.** Important for particle sizes $< 0.5 \mu\text{m}$ and the main deposition mechanism of inhaled NPs. In this type of deposition submicron particles move randomly due to the collision with gas molecules surrounding the medium. This is known as Brownian motion which increases with decreasing particle size.

The respiratory system is a very complex environment and thus, the theoretical prediction of particulate deposition is challenging. Instead, empirically derived models are generally used (Hinds, 2012) being the current standard model the International Commission on Radiological Protection (ICRP) which predicts deposition as a function of size (ICRP, 1994). The model

splits the respiratory tract into three regions: nasopharyngeal (nasal, pharynx and larynx) region, tracheobronchial region and alveolar region (Figure 26). According to this model, particles < 100 nm (0.1 μm) are deposited in all regions of the respiratory tract:

- ➔ 90% of particles of ~ 1 nm (0.001 μm) in size would deposit in the nasopharyngeal region
- ➔ Particles of ~ 5 nm (0.005 μm) in size would deposit equally throughout the respiratory tract
- ➔ Particles of ~ 20 nm (0.02 μm) in size have the greatest deposition efficiency (~ 50%) in the alveolar region

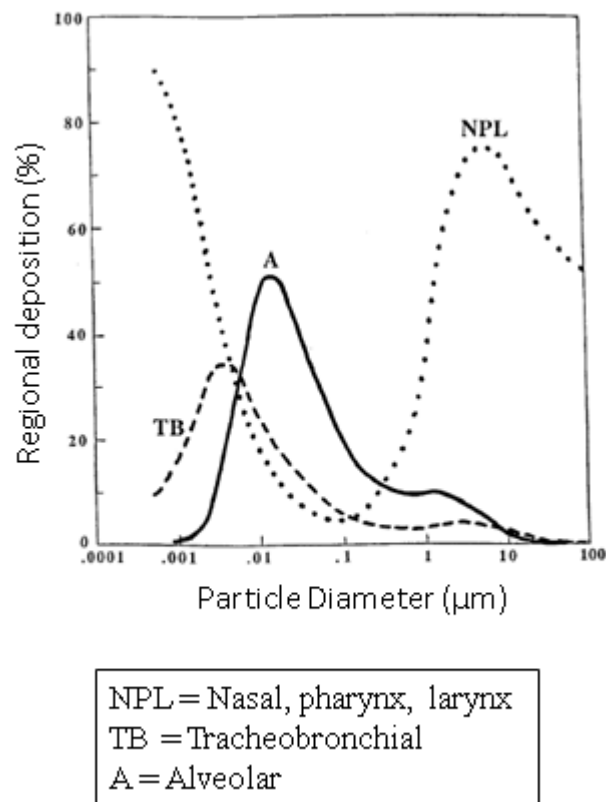


Figure 26. Graphical representation of the deposition of inhaled particles in the human respiratory tract. The model splits the respiratory tract into three regions: nasopharyngeal region, tracheobronchial region and alveolar region. Adapted from ICRP, 1994.

1.4.2.3 Clearance mechanisms and retained dose

Upon deposition, the process of particle clearance starts (Peters et al., 2006). The length of time the particle clearance takes is inversely proportional to the particle size (Gehr et al., 1996).

Particle clearance is highly correlated with the region where they have been deposited and is achieved by different routes (Möller et al., 2004, Bailey and Puncher, 2007):

- **Nasopharyngeal region:** particles are removed by nose blowing and wiping.
- **Tracheobronchial region:** particles are transported out of the lung towards the gastrointestinal tract by mucociliary clearance which takes a matter of hours. When particle-laden mucus (also containing airway macrophages that have phagocytosed particles) reaches the throat, it is expectorated or swallowed.
- **Alveolar region:** particles are cleared more slowly, largely by alveolar macrophages which phagocytose and attempt to digest the particles. Macrophages then migrate to the mucociliary clearance system or into the lymphatic system, removing particles from the alveolar region. A small fraction of particles deposited in the alveoli (< 1%) pass through the thin alveolar epithelium into the bloodstream.

Particles of low solubility can be retained in the lungs for longer times; although acid hydrolysis in macrophages can dispose of many particulate materials (Möller et al., 2004), at high doses, some particles escape normal clearance mechanisms and can remain in the lung for many months and years. The alveolar retained dose is the amount of particles that remain in the alveoli under continuous deposition and clearance. It is this dose that is directly related to the potential adverse effects of the particles (Park et al., 2008).

1.4.3 Human toxicity of engineered nanomaterials

1.4.3.1 Introduction

NPs can exhibit different physicochemical properties compared to the same conventional material at a larger scale. Thus, the central question is: are the toxic effects of NPs different from those shown by larger particles of identical composition? This remains an open question and therefore it is critical to recognise the potential risks of NP exposure (Auffan et al., 2009a, Bakand et al., 2012).

Up to now, the potential toxic effects of ENMs are largely unknown and are being investigated under a new discipline called nanotoxicology (Bakand et al., 2012). Several physicochemical

properties such as size, surface area, surface chemistry or oxidation status have been proposed to be critical in NM toxicity; however, a single parameter responsible for NM toxicity has not yet been identified (Crane et al., 2008, Lanone et al., 2009). Small, hydrophobic and positively charged NPs have been found to be more toxic than their counterparts (Torrano et al., 2013).

The potential adverse effects of ENMs have become a top priority in governments, the private sector and the public across the world (Roco, 2005, Helland et al., 2006, Siegrist et al., 2007).

1.4.3.2 Toxic effects of ambient nanoparticles

Some concerns about the potential toxicity of inhaled ENMs arise from perceived similarities with ambient air pollution particles. Ambient particulate matter (PM) is often categorised as PM₁₀ (diameter less than 10 µm), PM_{2.5} (diameter less than 2.5 µm) and PM_{0.1} (diameter less than 100 nm, often referred to as ultrafine particles, UFPs) which comprise the greatest number of particles but the least mass (Atkinson et al., 2010). Numerous epidemiological and toxicological studies have found a strong correlation between PM levels and lung cancer, cardiopulmonary morbidity and mortality (Pope III et al., 2002, Stone et al., 2007, Kleinman et al., 2008). Moreover, several epidemiological studies have shown that UFPs were more potent than larger particles at driving negative health effects (Seaton et al., 1995, Oberdörster, 2001). Until now, however, it is not known if the hazards and risks found with unintentionally generated UFPs, which are relatively polydispersed and with a chemically complex nature, can be extrapolated to ambient ENPs, which are comparatively monodispersed with precise chemical characteristics (Bakand et al., 2012). Experimental toxicological studies with carbon black or titanium dioxide NPs have shown that these NPs can cause the adverse effects of UFPs at lower doses (Borm et al., 2006).

Ambient ENPs are considered relevant with respect to health effects because of their large surface to volume ratio, chemical composition (Donaldson et al., 2001), very high alveolar deposition fraction (Oberdörster et al., 2005), ability to induce inflammation (Donaldson et al., 2001, Renwick et al., 2004) and potential to translocate across the alveolar epithelium and into the lymphatic and circulatory system and the accumulation in various secondary organs as shown in Figure 27 (Oberdörster et al., 2002, Kreyling et al., 2002).

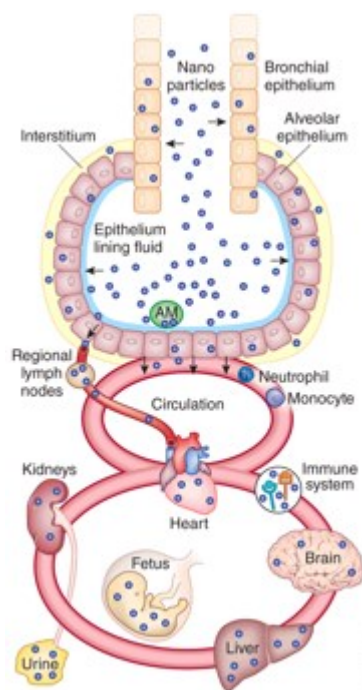


Figure 27. Schematic of nanoparticle deposition at the alveolar air/liquid interface and the possibility of translocation of nanoparticles across the alveolar epithelium and into the lymphatic and circulatory system and accumulation in various secondary organs. For example, some inhaled nanoparticles have been shown to be excreted by the kidneys into the urine (Kreyling et al., 2010).

1.4.3.3 Nanoparticle and lung surfactant interactions

When NPs deposit in the alveolar region, they first come into contact with the lung surfactant (Peters et al., 2006, Schleh and Hohlfield, 2009, Schleh et al., 2011). It has been shown that NPs are able to interact with lung surfactant components which can affect the biophysical surfactant properties. This interaction may also modify the NP properties and therefore, its toxic effects. In addition to all this, surfactant displaces particles into the alveolar subphase fluid where they can come into contact with the alveolar epithelium:

- Bakshi et al., 2008 found that gold NPs sequestered lung surfactant phospholipids and impeded surfactant adsorption, the surfactants' ability to reduce surface tension and the function of the surfactant proteins. Schleh et al., 2009 found that titanium dioxide NPs induced biophysical and structural alterations of lung surfactant. Guzmán et al., 2011 showed that silica NPs present in the aqueous subphase were incorporated into the surfactant monolayer.

- Lung surfactant may also affect NP properties. For example, Maynard, 2002 found that titanium dioxide NPs suspended in lung surfactant (DPPC) were deagglomerated. Deagglomeration increases the number of individual particles, decreases their size and increases the surface area which could modify the particle toxicological effects. On the other hand, Maier et al., 2006 found that titanium dioxide NPs suspended in a lung surfactant (DPPC) agglomerated and aggregated. More work is therefore needed to understand the effect of lung surfactant on the agglomeration state of NPs. Harishchandra et al., 2010 showed that polyorganosiloxane NPs remained at the air/liquid interface probably by coating themselves in lipids and thus, exhibiting hydrophobic surface properties. Hu et al., 2013 showed evidence of the formation of a pulmonary surfactant lipoprotein corona on inhaled NPs.
- Several studies found that micron-sized particles were wetted by the surfactant and displaced into the alveolar subphase fluid (Schürch et al., 1990, Geiser et al., 2003). The lower the surface tension, the greater the immersion of the particles into the liquid phase. A similar process is suggested to occur with NPs, although so far little research has been done on the subject. A molecular dynamics simulation study showed that hydrophobic fullerene C60 NPs did not spontaneously translocate across a surfactant monolayer (DPPC) and remained inside the lipid tail region. However, adding a hydroxyl group to the surface made the NP hydrophilic and able to translocate across the monolayer (Schneemilch and Quirke, 2010).

To date, not many studies have systematically investigated the physicochemical properties that govern the deposition of NPs onto the lung surfactant, the displacement of NPs into the lung surfactant and the translocation of NPs across the lung surfactant. This is crucial to gain a full understanding of how NPs might enter the body and cause systemic health problems. For example, Hu et al., 2013 investigated the physicochemical properties of NPs that regulate translocation across the pulmonary surfactant monolayer and the formation of a lipoprotein corona. The authors found that hydrophilic NPs generally translocated quickly across the surfactant film (Infasurf) but a high proportion of hydrophobic NPs were present in the film and encapsulated in lipid protrusions upon film compression. The study of lung nanotoxicology and NP-based lung drug delivery should consider the lipoprotein corona. Valle et al. 2014, investigated the effect of the degree of NP hydrophobicity on lung surfactant inhibition and particle retention. The authors concluded that increasing the degree of NP hydrophobicity led

to a higher degree of surfactant inhibition and a higher NP retention in the surfactant monolayer (Infasurf). Other studies have investigated the adsorption of phospholipids and surfactant proteins onto the nanomaterial surface which has important implications for predicting the potential reactivity of the NPs in the lung and the environment. Leo et al., 2013 found that silver NPs were coated with DPPC which served as a semipermeable layer and Theodorou et al., 2015 found that both phospholipids and protein components modified the dissolution kinetics of silver nanowires due to the formation of a lipid corona. Moreover, most of the literature studies investigated the effects of NPs on the surface tension reduction of lung surfactant but did not focus on other biophysical properties that a functional lung surfactant should have for normal respiratory physiology. This includes the rapid film formation through adsorption of surface active molecules from the subphase into the interface or the effective re-spreading of the surface active material to cover the expanded area during inhalation.

A more detailed literature review of the studies that have investigated *in vitro* NP-lung surfactant interactions is included later in the thesis (sections 3.2.1 and 3.2.2).

1.5 Research objectives

The objectives of this study were:

- To study the compression isotherm of the major phospholipid component of pulmonary surfactant, DPPC, using a Langmuir-Wilhelmy balance system and to set up the relevant experimental conditions to work with in future experiments.
- To set up, optimise and verify an aerosol exposure system in which to test and compare the effects of aerosolised NPs (CeO₂ and CB) on DPPC function.
- To compare the effects of aerosolised CeO₂ NPs with that of CeO₂ NPs applied as suspensions on the functional activity of DPPC.
- To determine the significance of CeO₂ NP mass and subphase temperature on DPPC function in parallel with changes in CeO₂ NP format and relocation within the DPPC monolayer.

- To compare the effects of aerosolised CB NPs with that of aerosolised CeO₂ NPs on the functional activity of DPPC.

1.6 Hypothesis

We hypothesised that the interactions of CeO₂ and CB NPs with monolayers of DPPC would alter the functional activity of DPPC. We further hypothesised that the effects of CeO₂ and CB NPs on the DPPC isotherm would depend on the method of delivery of NPs to the DPPC monolayer, the physicochemical characteristics of the NPs, the NP mass and the subphase temperature as well as changes in the NPs during NP-DPPC interactions.

CHAPTER 2 – STUDY OF THE DPPC ISOTHERM USING A LANGMUIR-WILHELMY BALANCE (LWB) AND OPTIMISATION OF EXPERIMENTAL CONDITIONS FOR FUTURE EXPERIMENTS

2.1 Rationale

DPPC was chosen as the model lung surfactant for this study. The main physiological function of lung surfactant is the reduction of surface tension during exhalation to near zero values in order to prevent the collapse of the lungs, and there is evidence that DPPC is the only lung surfactant phospholipid capable of forming a LC phase and reaching a near zero γ on compression with a LWB (Smith and Berg, 1980, Zhang et al., 2011b) hence the importance of studying DPPC. DPPC monolayer properties and phase states have also been widely investigated for many years for lung surfactant and other biological system studies (Tatur and Badia, 2011, Guzmán et al., 2011, Dwivedi et al., 2014, Melbourne et al., 2015). Moreover, it was expected that as DPPC is the major component of lung surfactant, alteration in its phase behaviour would consequently cause alteration in the phase behaviour of the lung surfactant (Dwivedi et al., 2014).

We hypothesised that a DPPC isotherm measured under conditions similar to those occurring in the alveoli would differ from a DPPC isotherm measured under more commonly used experimental conditions. For this reason, two main issues were chosen to be addressed in this chapter. Firstly, the reproducibility of measurement of the DPPC isotherm using a LWB system was determined. Secondly, the DPPC isotherm was measured under relevant quasi-physiological conditions and compared to that obtained under more commonly used experimental conditions, in order to fully comprehend the importance of measuring isotherms under conditions as close as possible to those occurring *in vivo*. Ultimately, the aim of work in this chapter was to optimise and establish physiologically relevant conditions to work with in future experiments.

- **Reproducible measurement of the DPPC isotherm:** The issues that might result in unreproducible isotherms include: the presence of impurities in the DPPC solution or in the subphase; surfactant weighing errors when preparing the solutions; differences in DPPC solution concentration due to the evaporation of chloroform; trough overflow; barrier

leakage problems or material loss after DPPC spreading. The specific aims in this respect were to determine/establish:

- a) The relevant parameters to describe a DPPC isotherm.
 - b) A rule to reject or accept measured isotherms to calculate an average DPPC isotherm.
 - c) An accurate lift-off M_{ma} for the DPPC isotherm for the most common experimental conditions to use in future experiments. The accurate lift-off M_{ma} values would then be used to estimate the amount of DPPC material deposited onto the air/liquid interface, together with determination of the lift-off area of the isotherm.
 - d) The expected variability when measuring DPPC isotherms to establish parameter uncertainty values which would be valid for all the experiments performed in these studies.
 - e) Criteria to compare isotherms measured under different experimental conditions based on the aforementioned uncertainty values.
 - f) The comparative study of DPPC isotherms with different deposited masses of DPPC, which would result in different lift-off areas and would potentially also give some indication of the overall effect of other factors which result in differences in lift-off areas.
- **Physiological conditions important in the measurement of the DPPC isotherm:** It is well known that the shape of a DPPC isotherm is dependent on many conditions. Some of the most relevant conditions present in the alveoli of healthy lungs during the breathing cycle are: frequency of the inhalation-exhalation breathing cycle: 10-15 times per minute; alveolar subphase fluid composition: a watery phase containing a number of ions such as H^+ , Na^+ , Ca^{+2} or Cl^+ ; subphase temperature: $37^{\circ}C$; relative humidity: 100%; surface tension reached at the end of exhalation: near zero values. Bearing this in mind, the aim here was to test DPPC under different relevant physiological conditions in order to understand how each of these factors affected the DPPC isotherm compared to the most commonly used experimental conditions and to set up the most relevant experimental conditions to work with in future experiments.

2.2 Hypothesis

As detailed above, we hypothesised that a DPPC isotherm measured under commonly used conditions would not be the same as that measured under more physiologically relevant conditions that exist *in vivo*.

2.3 Methodology

2.3.1 Reagents and materials

1,2-dipalmitoyl-*sn*-glycero-3-phosphocholine (DPPC, semisynthetic, $\geq 99\%$) was purchased from Sigma-Aldrich and used without further purification. DPPC was suspended in chloroform (purchased from Sigma-Aldrich) to form stock solutions with a concentration of 0.5 mg/mL unless otherwise specified. Solutions were stored in glass bottles with polypropylene (PP) screw caps and polytetrafluoroethylene (PTFE) bottles at -20°C until use. Glass, PP and PTFE were used as these materials are compatible with chloroform and to avoid contamination of the solution by the container. For the same reason, glass pipettes were used to prepare the chloroform solutions. DPPC was weighed using a Sartorius M-power balance with a resolution of 0.1 mg. Solutions of DPPC were shaken in a Vortex Genoe[®] 2 model G-560E. The water used was Milli-Q[®] ultrapure water with a resistivity of $18\text{ m}\Omega\text{cm}^{-1}$ at 25°C . Water was stored in glass bottles. All the solvents were HPLC grade.

2.3.2 Cleaning of glassware

All the glassware and bottles were cleaned with ethanol (purchased from Fisher Scientific) and chloroform. Afterwards, they were rinsed three times with ultrapure water. In order to avoid contamination of the solvents in beakers, beakers were covered with aluminium foil. All the cleaning procedures that involved the use of chloroform and ethanol were performed in a fume cupboard.

2.3.3 Determination of the concentration of a reference DPPC solution by enzymatic-colorimetric assay of the level of choline

The DPPC content of a chloroform stock solution was determined using an enzymatic-colorimetric phospholipid assay kit purchased from Sigma-Aldrich. This consisted of an assay buffer, an enzyme mix, a phosphatidylcholine standard (2 mM), a phospholipase D (PLD) enzyme and a dye reagent. In this assay, DPPC is hydrolysed by the PLD enzyme which releases the choline group. Choline is then oxidised by choline oxidase into betaine and hydrogen

peroxide, which, in the presence of peroxidase reacts with 4-aminoantipyrine and a phenol-derivative forming a red compound. The colour intensity of this compound is directly proportional to the DPPC concentration in the sample as there is one choline within each DPPC molecule. The concentration range of detection is 3-200 μM .

100 μL of a DPPC solution in chloroform with an approximate concentration of ~ 0.25 mg/mL was evaporated and diluted in 5,000 μL of water (using a sonicating water bath) to make a concentration of ~ 0.005 mg/mL which is equivalent to ~ 6.812 μM . A phosphatidylcholine standard curve was prepared: 24 μL of the phosphatidylcholine standard (2 mM) was added to 216 μL of water to prepare a 200 μM standard solution. From this solution, 0, 60, 120 and 200 μM standards were prepared.

Reaction mixes of the experimental sample of unknown DPPC concentration and standards were prepared in an identical manner in a 96-well flat-bottom cell culture plate (Corning[®] Costar[®]). 20 μL of the sample and each standard were transferred in duplicate into separate wells. The assay buffer, enzyme mix, PLD enzyme and dye reagent were mixed in the following proportion: 96.6%, 1.14%, 1.14% and 1.14% respectively and 80 μL of this mix was added to each well that contained the sample and standards. The plate was then covered in aluminium foil to protect it from the light and incubated for 30 minutes at room temperature. The sample and standards absorbance were measured at 570 nm using a Luminex[®] 100 system. Each sample and standard absorbance was measured in duplicate and an average of the duplicate values taken. The absorbance of the 0 standard was subtracted from the absorbance of the sample and standards. The standard concentrations and absorbance values were plotted to generate a standard curve. The original concentration of the experimental sample was obtained from the standard curve from its absorbance value, taking into account the dilution factor.

2.3.4 LWB system

2.3.4.1 Main parts and accessories of a LWB system

The LWB system (KSV Nima[®]) used in these experiments is shown in Figure 28.

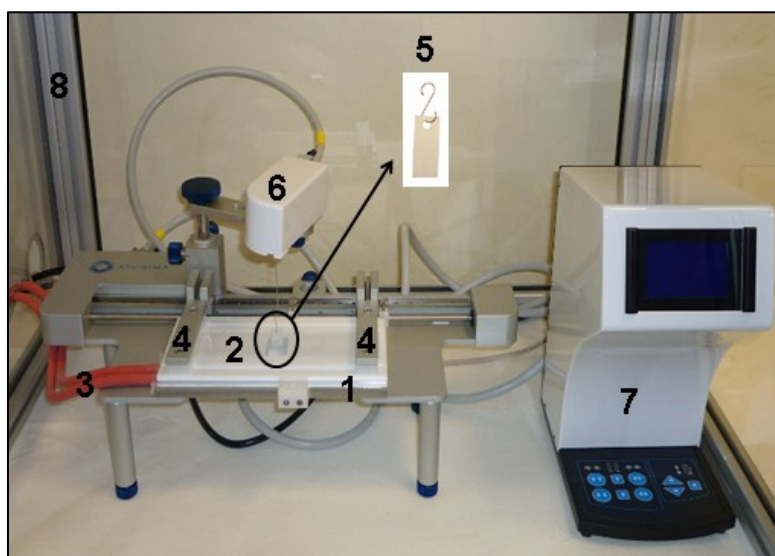
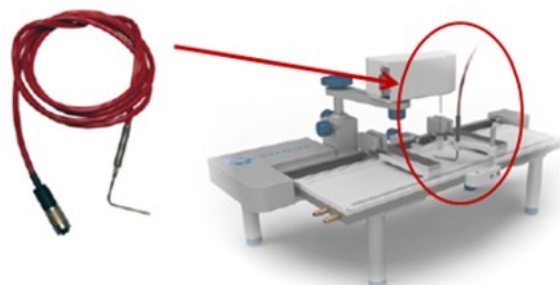


Figure 28. Illustration of the KSV Nima[®] Langmuir-Wilhelmy balance system: 1. Trough; 2. Subphase; 3. Rubber tubes to water bath; 4. Barriers; 5. Plate; 6. Electrobalance; 7. Interface unit; 8. Cabinet.

The LWB system consisted of the following parts and accessories:

- a) **A trough** made of Teflon[®] (best-known brand name of PTFE) that held the liquid subphase. PTFE is a hydrophobic material that reduced any leakage of the subphase over the edges of the trough. The trough was attached to a metallic frame to prevent its deformation. Two trough sizes were used in these experiments: small with dimensions 19.5 cm x 5 cm x 0.4 cm (l, w, h) and medium with dimensions 36.4 cm x 7.5 cm x 0.4 cm (l, w, h). Unless otherwise specified, the trough used in these experiments was the small one. The subphase temperature was regulated by circulating water from a water bath through channels placed in the metallic frame. The water bath (Julabo[®] F12-MA Refrigerated/Heating Circulator) was connected to the metallic frame by two rubber tubes. The computer-controlled target subphase temperature was reached by adjusting the temperature of the water bath measured using a temperature probe that was submerged in the subphase (Figure 29).

Temperature
measurement probe



Water bath



Figure 29. Illustration of the temperature measurement probe (left) and Julabo circulator/water bath (right) used to regulate the subphase temperature of a Langmuir trough. Adapted from KSV-Nima, 2014.

- b) **Two barriers** made of Delrin[®] (brand name of polyoxymethylene - POM), a hydrophilic material that reduces any leakage of the lipid monolayer beneath the barriers. These two barriers were movable and the available surface area of the trough was varied (see Figure 30) by closing them (compression/reduction of the surface area) or opening them (expansion/increase of the surface area). For the small and medium trough the available surface area was 76 cm² and 238 cm² respectively when the barriers were fully open.

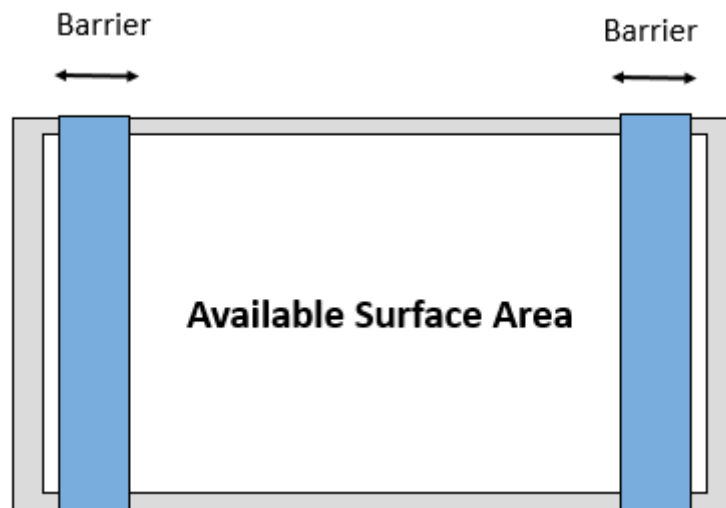


Figure 30. Graphical representation of the available surface area in a Langmuir trough which is the area between the barriers and the edges of the trough.

Barrier speed could vary from a minimum of 1 mm/min to a maximum of 270 mm/min, the most commonly used barrier speeds being between 5-20 mm/min. Unless otherwise specified, the barrier speeds used in these experiments were 5 mm/min (2.5 cm²/min) for the small trough and 10 mm/min (7.5 cm²/min) for the medium trough.

- c) The Wilhelmy plate** hung from a sensitive electrobalance to measure the change in surface pressure. Both platinum and paper plates were used in these experiments. Paper plates with dimensions 1 cm x 2 cm (*w*, *l*) were self-cut from a roll of chromatography paper (Whatman[®]). The material used is irrelevant as long as the surface of these materials are perfectly wetted by the liquid ($\theta = 0^\circ$). Platinum plates have the advantage of accuracy and ease of cleaning and re-use. The disadvantage of this material is that after one compression, some of the monolayer deposits onto the plate which will no longer be completely wetted by the liquid hence, when performing compression-expansion experiments, results will be skewed after one compression. In this case, a paper plate gives more accurate and reproducible results. Further details on the Wilhelmy plate are shown in Appendix 2b.
- d) A dipping mechanism** consisted of a dipping arm attached to a horizontal dipping clamp that held a solid substrate (Figure 31), which allowed for vertical deposition of the monolayer on the solid substrate.

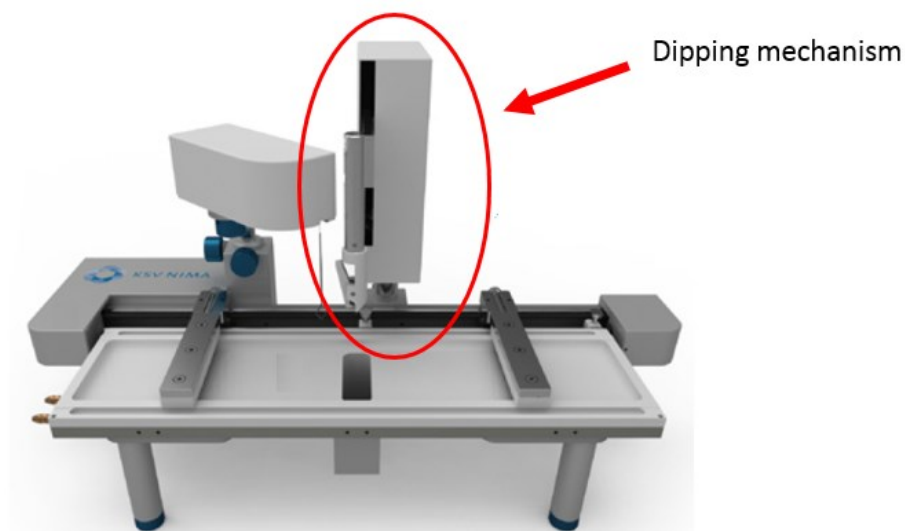


Figure 31. Illustration of the dipping mechanism in a Langmuir-Wilhelmy Balance system. Adapted from KSV-Nima, 2014.

- e) A **KSV Nima[®] Cabinet** was made of clear acrylic glass panels with an aluminium frame, in this case with dimensions 712 mm x 450 mm x 500 mm (l, w, h). It protected the LWB from dust or air conditioning which might have had an impact on the measurements.
- f) A **traceable Jumbo[®] Humidity/Temperature Meter** was used to monitor ambient humidity within the cabinet where the LWB system was placed.
- g) An **interface unit** formed the nexus point between the computer and other devices that comprised the LWB system. The experiments were performed using the KSV Nima LB software, version 3.5. Before each experiment, an experimental set-up window was filled (Figure 32) with information related to the Wilhelmy plate, trough, subphase, surfactant and substrate. The type of experiment as well as the barrier speed was then selected in a trough control window (Figure 33). When the experiment was completed, the data were transferred to an excel sheet for further analysis.

Experimental Setup

Name: Example Isotherm User: KSV NIMA Date: 8.6.2007 15:40:42

Probe for Balance1
Name: Wilhelmy Perim.: 39,240 mm

Probe for Balance2
Name: Wilhelmy Perim.: 39,800 mm

Trough
Name: Mini Width: 75,0 mm Area: 24300,0 mm² Symmetric Barriers

Subphase
Name: water Mixed with:
T: °C pH: Conc: Unit: Unknown

Substance1
Name: stearic acid
Conc: 1,04 Unit: mg/ml
MW: 284,5 Volume: 25,00 µl

Substance2
Name:
Conc: Unit: Unknown
MW: Volume: ml

Substrate
Name:
Shape: Rectangle Height: mm
Width: mm Thickness: mm

Comments

Accept Edits Cancel Edit Data Base

Figure 32. Illustration of the experimental set-up data screen. The experimental set-up data were entered before each experiment with information related to the Wilhelmy plate dimensions, trough area, subphase composition/temperature, surfactant used and substrate (KSV-Nima, 2010).

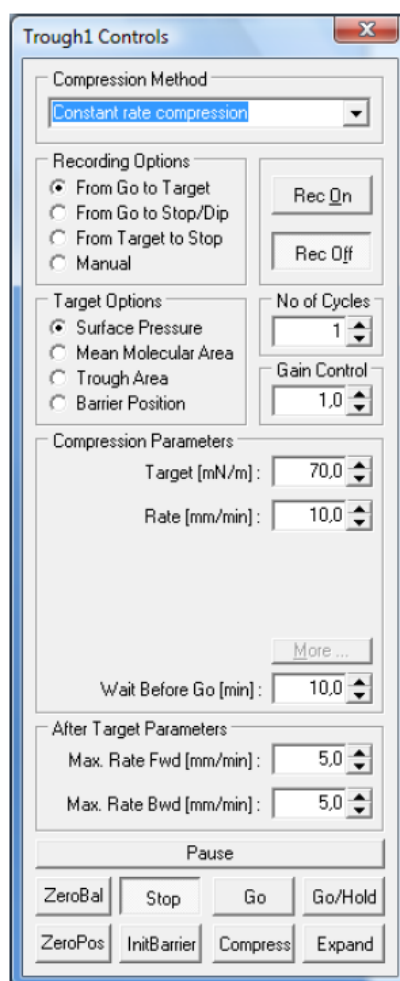


Figure 33. Illustration of the trough control window used to select the type of experiment as well as the barrier speed before each experiment performed using the Langmuir-Wilhelmy balance (KSV-Nima, 2010).

2.3.4.2 Experiments performed using a LWB system

This system was used to perform the following experiments:

a) Measurement of the Π -Mma or Π -A isotherm

A LWB measures changes in Π during the compression or expansion of a surfactant monolayer spread onto a liquid surface. Π is usually measured as a function of the available surface area to each molecule (mean molecular area, Mma) or simply as a function of the available surface area (A). The Mma can be determined by monitoring the distance the barriers have moved and known dimensions of the trough. Measurements were carried out at a constant temperature and represented by a so-called isotherm.

b) Vertical deposition of a surfactant monolayer on a solid substrate (Langmuir-Blodgett deposition)

A LWB with a dipping mechanism enables the vertical deposition of a surfactant monolayer on a solid substrate at constant Π forming a so-called Langmuir-Blodgett (LB) film. This is performed by vertical passage of the substrate through the floating monolayer which will adsorb onto the substrate (Figure 34). As the deposition is performed at a constant Π the monolayer area needs to decrease as material is being removed from the surface to maintain the target Π value. LB films are usually deposited at high Π (≥ 20 mN/m) (Peng et al., 2001).

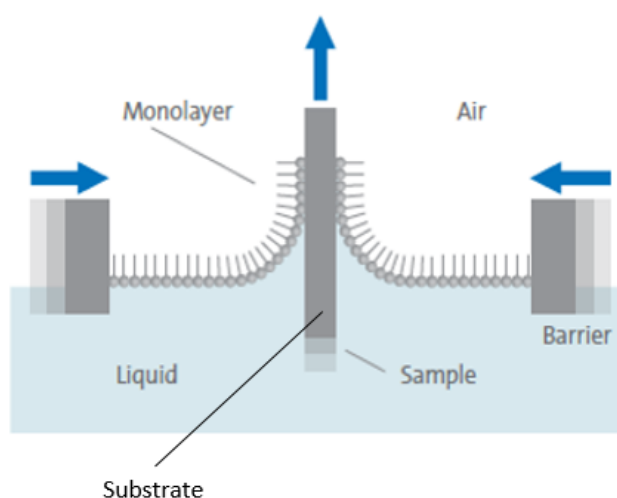


Figure 34. Illustration of the deposition of a monolayer onto a solid substrate by vertically passing the substrate through the monolayer, also called Langmuir-Blodgett deposition. Adapted from KSV-Nima, 2010.

The speed of solid substrate movement should be low enough to ensure smooth transfer of the monolayer (Peng et al., 2001), being 1 mm/min the speed used in the present studies. The substrate material used depends on the eventual use of the LB film (Barnes and Gentle, 2011). For example, mica is often used for AFM, quartz for optical studies or silicon for X-ray diffraction. When the solid substrate is hydrophobic, the first layer is deposited by lowering the substrate into the subphase whereas if the solid substrate is hydrophilic, the first layer is deposited by raising the previously submerged solid substrate. Mica substrates were used in this study which is a hydrophilic material. The LB film was oriented with the polar heads facing the substrate and the hydrocarbon chain outwards as shown in Figure 34.

In this chapter, the LWB system was used only to measure the Π -A isotherms. In chapter 3 and 4 the LWB system was also used to produce LB films for further examination.

2.3.4.3 Cleaning of a LWB system and its accessories

Cleaning the trough, barriers, temperature probe and plate thoroughly before each experiment was of utmost importance. Powder free nitrile gloves (Fisherbrand[®]) were used to minimise the contamination of the apparatus with oils from the skin. Trough, barriers and temperature probe were cleaned by wiping them with lint-free tissues (Kimcare[®] medical wipes) using ethanol and chloroform and then rinsing them with ultrapure water. The platinum plate was cleaned by rinsing the plate with ethanol, chloroform and ultrapure water. When not in use, the plate was stored in ethanol. Paper plates were soaked in a glass bottle with subphase liquid for at least 30 minutes prior to the experiment to dissolve any contaminants from the plate. A new paper plate was used for each experiment. The 50 μ L microsyringe (Hamilton[®]) used to deposit the surfactant solution was cleaned by filling and emptying with chloroform approximately ten times.

Additional cleaning for the dipping experiment: The dipping clamp was cleaned by rinsing it with ethanol, chloroform and ultrapure water. Mica was cleaved immediately before use which left a clean and flat surface ready to be used. The cleaving was performed by inserting the edge of a razor into the corner of the mica sheet and gently separating the natural layers of the mica.

2.3.4.4 Filling the trough with subphase liquid

Two subphase liquids were used, Milli-Q[®] ultrapure water and Dulbecco's phosphate buffered saline (PBS) with calcium chloride (133 mg/L) and magnesium chloride (100 mg/L) which mimics physiological conditions, purchased from Sigma-Aldrich. The purity of the liquid subphase was checked by zeroing the value of the balance when the barriers were fully open and then moving the barriers closer together. The subphase was considered sufficiently clean if the Π did not go above 0.3 mN/m.

2.3.4.5 Deposition of the DPPC solution

The DPPC solution was first equilibrated to room temperature. Immediately before use, it was heavily vortexed for 30 seconds. Surfactant was delivered to the surface via a microsyringe

needle. Surfactant was left undisturbed for 15 minutes to allow complete evaporation of the solvent.

2.3.4.6 Further information for the dipping experiment

When the monolayer was compressed to the target Π it was left undisturbed to stabilise for 15 minutes. The mica sheet containing the LB film was stored in a clean petri dish and left to dry in a Scienceware[®] vacuum desiccator for at least 12 hours.

2.4 Results and discussion

2.4.1 Study of the DPPC isotherm using a LWB system

The experiments were carried out using the equipment, principles and conditions described above and the results are shown in Figure 35, Figure 36 and Figure 37 and Table 8.

2.4.1.1 Derivation of relevant parameters to describe a DPPC isotherm

There are no exact guidelines regarding the parameters that are used to describe and compare isotherms generated for different surfactant materials, and under different experimental conditions. In the literature, studies describe measured Π -Mma isotherms using some of the following parameters which focus on the molecular packing of the monolayer:

- Lift-off Mma determined by extrapolating the first linear steep region to zero Π (Bringezu et al., 2002, Tatur and Badia, 2011).
- Onset of the LE-LC transition plateau described by the Mma at which it occurs (Yu et al., 2002, Nakahara et al., 2008, Tatur and Badia, 2011).
- Π at which the LE-LC transition plateau occurs (McConlogue and Vanderlick, 1997, Bringezu et al., 2002, Yu et al., 2002, Nakahara et al., 2008).
- Mean limiting molecular area, determined by extrapolating the final steep region of the isotherm to zero Π , which should be comparable to the cross-sectional molecular area (Tatur and Badia, 2011).
- Collapse Π and collapse Mma (Bringezu et al., 2002, Zuo et al., 2008a, Nakahara et al., 2008, Tatur and Badia, 2011).
- Two-dimensional compressibility.

Moreover, in this field, experimental results are usually reported without an associated measurement of the uncertainty or variability. The differences between isotherms for different experimental conditions are typically described qualitatively (e.g. with reference to isotherm shape) (Bringezu et al., 2002, Harishchandra et al., 2010, Tatur and Badia, 2011, Guzmán et al., 2011) and only very rarely are statistical tests of significance used (Melbourne et al., 2015, Valle et al., 2015).

In the present studies, DPPC Π -Mma isotherms were systematically described taking into account four different characteristics of the curve: the lift-off Mma, the two-dimensional compressibility, the collapse Π and the collapse Mma. The methods for determining these parameter values are described below. The treatment of variability is described in detail in section 2.4.1.4.

a) Lift-off Mma: The lift-off Mma was determined by extrapolating the first linear steep region at which an initial increase in Π was observed, to zero Π . The equation of the line of best fit was used to calculate the value of the lift-off Mma when Π was 0 mN/m as shown in Figure 35. This method was also used to calculate the lift-off area of the Π -A isotherms.

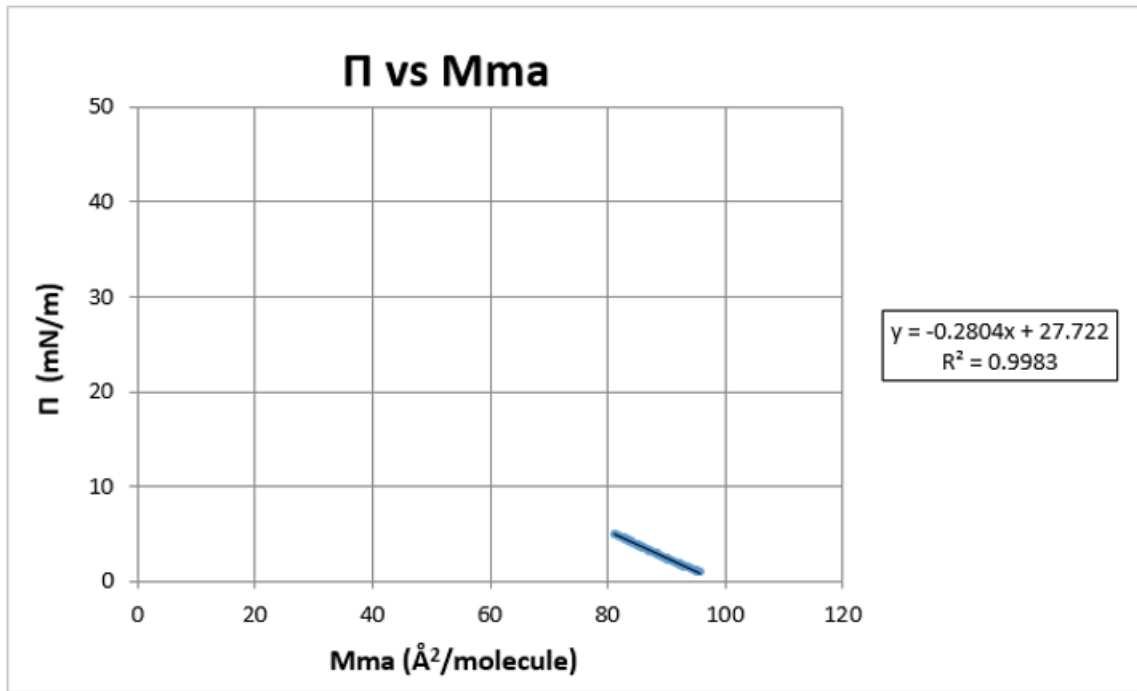


Figure 35. DPPC Π -Mma isotherm for Π values between 1-5 mN/m and equation of line of best fit to calculate the lift-off Mma of the isotherm. The isotherm was measured in water at 21°C. This method was also used for DPPC isotherms measured at 37°C.

b) Two-dimensional compressibility (C_m): C_m can be calculated from the inverse of the slope of the Π -A isotherm as follows:

$$C_m = -\frac{1}{A} \frac{\partial A}{\partial \Pi} \quad \text{Equation 10}$$

where C_m is the two-dimensional compressibility; Π is the surface pressure and A is the available surface area

A low C_m indicates high resistance to compression and therefore, high rigidity and vice versa. Typical experimental values of C_m for DPPC monolayers are 0.02-0.1 (mN/m)⁻¹ for LE films, 0.004-0.01 (mN/m)⁻¹ for LC films and < 0.004 (mN/m)⁻¹ for S films (Kodama et al., 2004, Vitovič et al., 2006).

C_m can be calculated at any point on the isotherm (Yu et al., 2002, Zhang et al., 2011b) or for the different monolayer phases by using a linear regression of the curve in that region (Duncan and Larson, 2008, DeVries et al., 2011). In the present studies, C_m was determined for the

different monolayer phases from the slope of the line of best fit. Each linear regression gave an R^2 value greater than 0.9. To illustrate this, Figure 36 shows a DPPC Π -Mma isotherm measured in water at 21°C and at 37°C (trough area and barrier speed were 76 cm² and 5 mm/min (2.5 cm²/min) respectively in all the experiments unless otherwise specified) with the lines of best fit for different regions of the isotherm. As can be seen in this figure, the DPPC isotherm measured at 21°C differed from that measured at 37°C. This is further discussed in section 2.4.2.3. For the isotherm measured at 21°C, the identified regions should correspond to the following monolayer phases: LE, LE-LC transition plateau, LC and S. At 37°C however, the entire isotherm was in LE phase for Π above 0 mN/m and thus, C_m was evaluated in different parts of the isotherm. Table 8 shows the regions of the DPPC isotherm - defined by their lower and upper Π range value - for which the C_m was determined for isotherms generated at 21°C and 37°C.

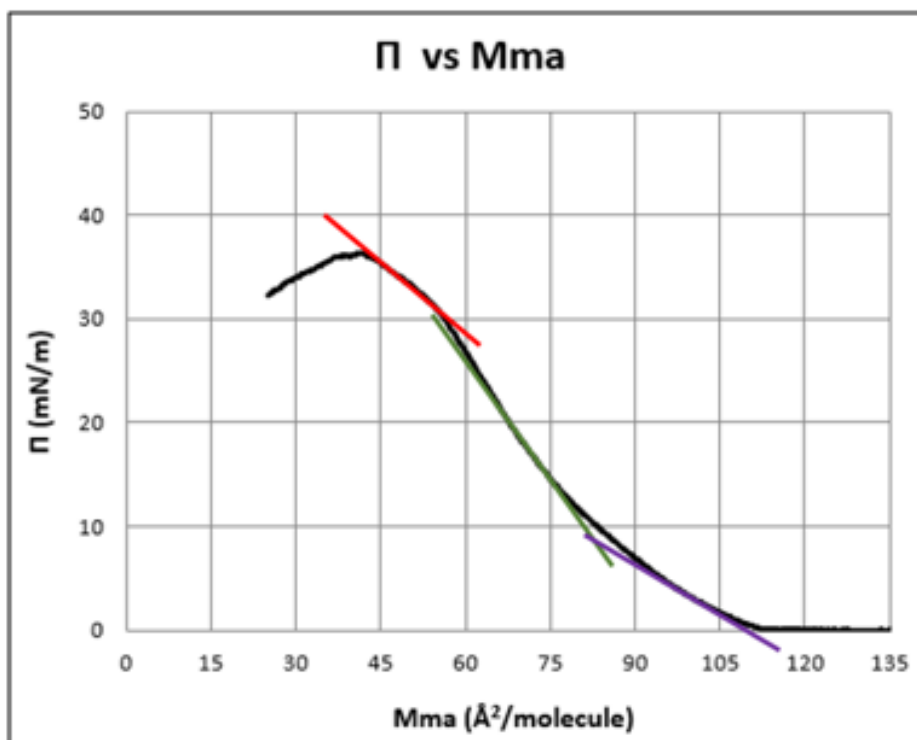
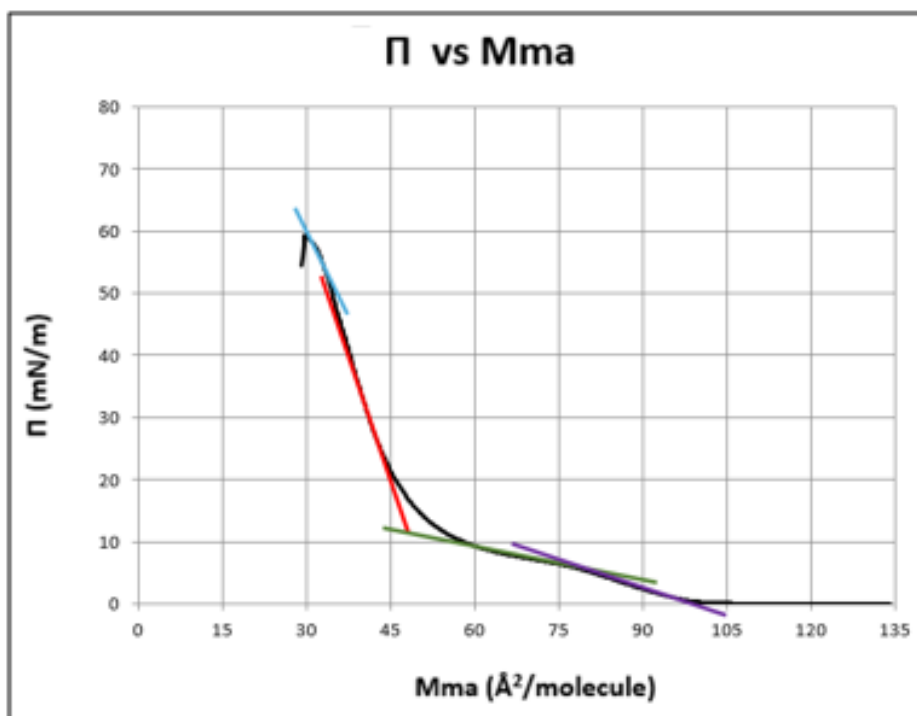


Figure 36. DPPC Π -Mma isotherm (black line) measured in water at 21°C (top) and at 37°C (bottom) with the lines of best fit in different regions of the isotherm. C_m was calculated for each region from the slopes of the lines of best fit. For the isotherm measured at 21°C, the regions should correspond to the following monolayer phases: LE (purple line), LE-LC transition plateau (green line), LC (red line) and S (blue line). For the isotherm measured at 37°C, the entire isotherm was in LE phase for Π above 0 mN/m and thus, C_m [was evaluated in different parts of the isotherm indicated by the purple, green and red line. $n = 5$ experiments/condition.

Table 8. Regions of the DPPC isotherm defined by their lower and upper Π range value for which the C_m was determined for isotherms generated at 21°C and 37°C.

Subphase temperature	Π range of the DPPC isotherm regions for which the C_m was calculated			
21°C	1-5 mN/m	5-10 mN/m	25-45 mN/m	50 mN/m – collapse Π
37°C	1-5 mN/m	10-25 mN/m	31 mN/m – collapse Π	

c) **Collapse Π and collapse Mma:** the method by which the collapse Π and collapse Mma of a DPPC Π -Mma isotherm was derived is shown graphically in Figure 37.

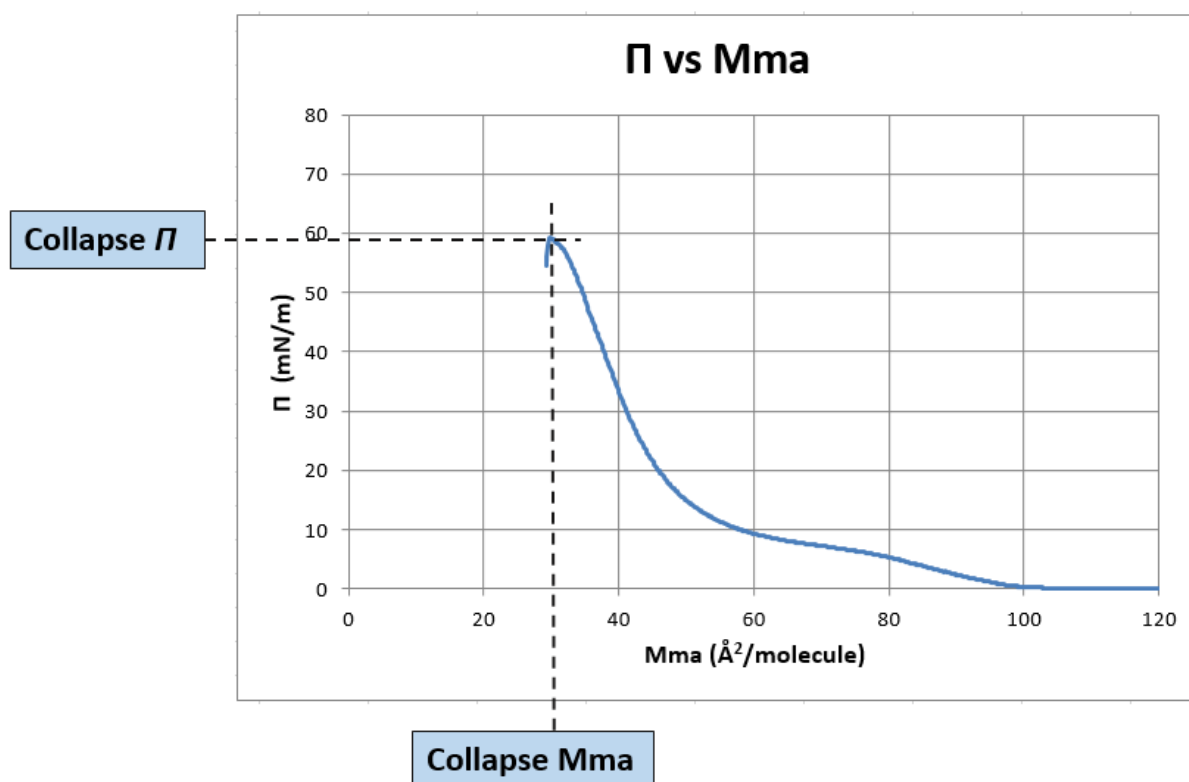
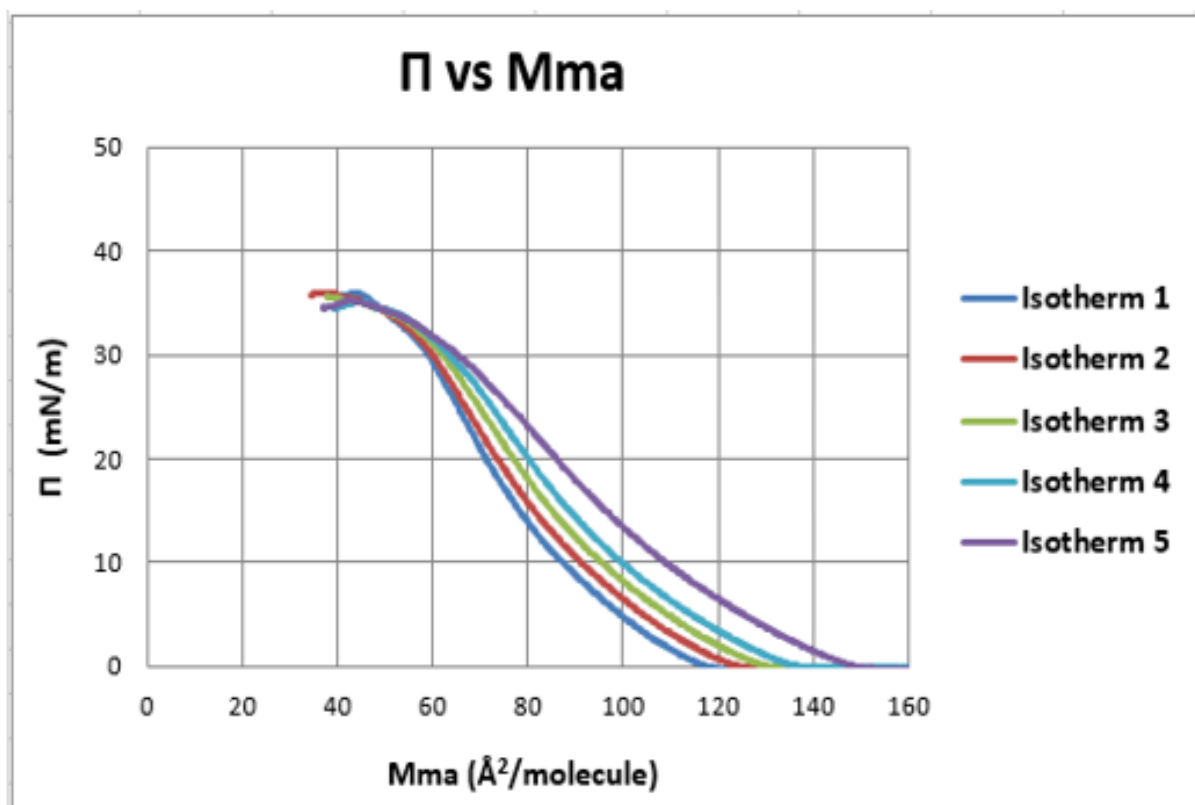


Figure 37. Graphical representation of derivation of the collapse Π and collapse Mma of a DPPC Π -Mma isotherm measured in water at 21°C. $n = 5$ experiments. This method was also used for DPPC isotherms measured at 37°C.

2.4.1.2 Rule to accept or reject measured isotherms to calculate an average DPPC isotherm

The LWB system is a very sensitive apparatus and it was difficult to obtain reproducible results. The presence of impurities in the DPPC solution or on the subphase, small surfactant weighing errors when preparing the solutions, differences in DPPC solution concentration due to the evaporation of chloroform, trough overflow, barrier leakage problems or material loss after spreading from solution could lead to very different Π -Mma isotherms. To illustrate this, Figure 38 shows five isotherms measured under ostensibly the same experimental conditions on different occasions (6 μg of DPPC, PBS subphase at 37°C). However the resulting lift-off Mma of each isotherm was different and unrelated to the order in which the experiments were carried out. The table shows the lift-off Mma of each isotherm as well as the average value, standard deviation (SD) and relative standard deviation (RSD). The RSD is the ratio of the SD to the average lift-off Mma expressed as a percentage. As can be seen in this figure, the average lift-off Mma was 129 $\text{\AA}^2/\text{molecule}$ with a SD of 12 and a RSD of 9%.

Chosen criteria: Consistent with those used in other studies and the recommendations of the device manual (Crane et al., 1999, Stuart et al., 2006, KSV-Nima, 2010), it was decided that a Mma of $\pm 1 \text{ \AA}^2/\text{molecule}$ between experiments performed under the same conditions was acceptable; values outside of this were considered to reflect artefacts and were rejected. Thus, here, and in the following chapters, repeated measurements of Π -Mma isotherms were performed under each set of experimental conditions investigated, using a minimum of three experiments per condition wherever possible, where the isotherms had a lift-off Mma that only deviated by $\pm 1 \text{ \AA}^2/\text{molecule}$. If the deviation was greater than this, more experiments were performed until the desired criteria were met. The isotherms that satisfied the criteria were then used to calculate an average isotherm.



Isotherm	Lift-off Mma (Å ² /molecule)
1	115
2	122
3	128
4	134
5	146
Average	129
SD	12
RSD (%)	9

Figure 38. *II*-Mma isotherms measured under ostensibly the same experimental conditions (6 µg of DPPC, PBS subphase at 37°C) but resulting in different lift-off Mma. The table shows the lift-off Mma of each isotherm as well as the average lift-off Mma value, standard deviation of this and the relative standard deviation. n = 1 experiment per isotherm measured under the same conditions.

2.4.1.3 Determination of the lift-off Mma of the DPPC isotherm and calculation of the concentration of DPPC solutions

2.4.1.3.1 Determination of the concentration of a reference DPPC solution by enzymatic-colorimetric assay of the level of choline

In order to obtain an accurate lift-off Mma value, the concentration of the reference DPPC solution was determined by enzymatic-colorimetric assay, described previously in section 2.3.3. In this experiment the mass concentration of the solution was determined to be 0.24 mg/mL.

2.4.1.3.2 Determination of the lift-off Mma using a reference DPPC solution

Depending on the set of experimental conditions, the lift-off Mma of a DPPC isotherm varies. Several lift-off Mma values have been described in the literature for DPPC as measured using the LWB under a number of conditions, shown in Table 9.

Table 9. Lift-off Mma of DPPC isotherms generated under different experimental conditions using the LWB as reported in the literature.

Subphase composition and temperature	Trough area (cm ²)	Rate of compression (cm ² /min)	Lift-off Mma (Å ² /molecule)	References
Purified water at 25°C	-	7.5	87	Yun et al., 2003
Ultrapure water at 20°C	500	15	90	Toimil et al., 2010
Ultrapure water at 20°C	768	6	92	Tatur and Badia, 2011
Ultrapure water at room temperature	243	3.75	100	KSV-Nima, 2010
Triply distilled water at 22°C	-	56 Å ² /molecule/min	104	Notter et al., 1982
Ultrapure water at 25°C	37	5	107	Stuart et al., 2006

Thus, one of the first steps in this research was to determine the lift-off M_{ma} of a DPPC isotherm using an ultrapure water subphase at 21°C and the reference DPPC solution. The II - M_{ma} isotherm is calculated by dividing the available surface area during the compression of the monolayer by the number of DPPC molecules deposited onto the subphase. In the same way, the lift-off M_{ma} is calculated by dividing the lift-off area by the number of DPPC molecules deposited onto the subphase as shown in the following equation:

$$\text{Lift-off } M_{ma} = \frac{\text{Lift-off Area}}{\text{Number of DPPC molecules}} \quad \text{Equation 11}$$

This equation can also be expressed as a function of the DPPC mass deposited onto the subphase:

$$\text{Lift-off } M_{ma} = \frac{\text{Lift-off Area} \times M_{DPPC}}{\text{MASS}_{DPPC} \times N_A} \quad \text{Equation 12}$$

where M_{DPPC} is the molecular mass of DPPC; MASS_{DPPC} is the DPPC mass deposited onto the subphase and N_A is Avogadro's number

Taking into account that the molecular mass of DPPC is 734.1 g/mol, the equation can be simplified as follows:

$$\text{Lift-off } M_{ma} (\text{\AA}^2 \cdot \text{molecule}^{-1}) = 12.19 \times \frac{\text{Lift-off Area (cm}^2\text{)}}{\text{MASS}_{DPPC}(\mu\text{g})} \quad \text{Equation 13}$$

Figure 39 shows the DPPC II - A isotherm of the reference solution obtained after depositing 29 μL of the solution onto the water subphase. The lift-off area value of the isotherm was 57 cm^2 .

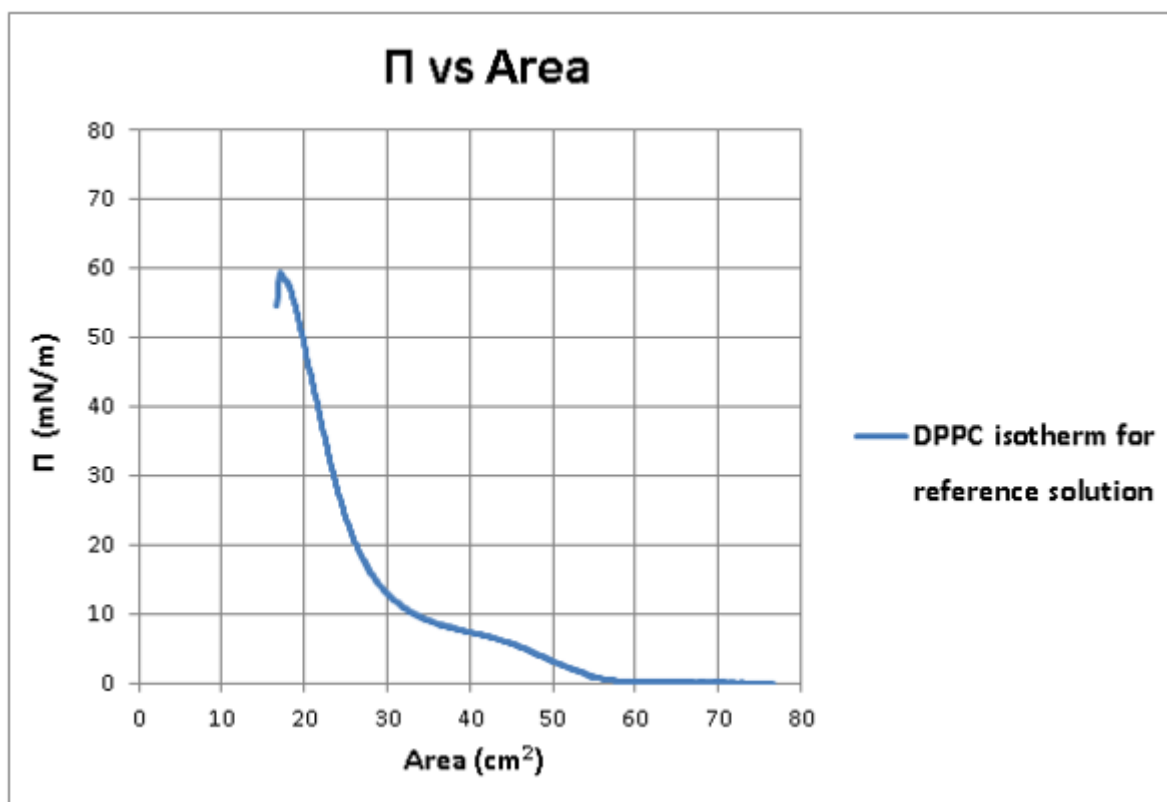


Figure 39. Π -A isotherm of the reference DPPC solution measured under the following experimental conditions: ultrapure water subphase at 21°C, trough area of 76 cm² and compression barrier speed of 5 mm/min (2.5 cm²/min). The lift-off area of the isotherm was 57 cm². n = 5 experiments.

In order to get an accurate M_{ma} , it is necessary to know the number of DPPC molecules deposited on the surface and therefore, the solution concentration (assuming that all the DPPC material remains at the air/liquid interface). The concentration of the reference solution calculated with an enzymatic-colorimetric assay was 0.24 mg/mL. As the volume deposited onto the subphase was 29 μ L, the mass of DPPC deposited was 7 μ g.

Thus, using Equation 13, the lift-off M_{ma} of the Π - M_{ma} isotherm for the reference DPPC solution measured in ultrapure water at 21°C was 99 \AA^2 /molecule. This value is similar to that reported in the LWB manufacturer's manual (100 \AA^2 /molecule).

2.4.1.3.3 Determination of the concentration of any DPPC solution based on the lift-off M_{ma}

It has been mentioned previously that knowing the DPPC mass deposited onto a subphase, and therefore the solution concentration, is of utmost importance to get an accurate lift-off M_{ma} .

DPPC mass was weighed and solutions in chloroform were prepared manually which introduced an error factor for the solution concentration. Besides, chloroform is a very volatile solvent that evaporates with time increasing the solution concentration. Unfortunately, it was not possible to calculate the solution concentration of each new DPPC solution prepared using the enzymatic-colorimetric assay and thus a method to calculate the amount of DPPC material deposited onto the air/liquid was developed. As the lift-off M_{ma} is a unique value depending on experimental conditions, whenever a DPPC isotherm was measured under that same experimental conditions (in the present case water subphase at 21°C, which corresponds to a lift-off M_{ma} of 99 Å²/molecule), the mass of DPPC deposited onto the subphase could be determined by simply calculating the lift-off area of the Π -A DPPC isotherm and using the following equation which is derived from Equation 13:

$$Mass_{DPPC}(\mu g) = 0.123 \times \text{Lift-off Area} (cm^2) \quad \text{Equation 14}$$

If the mass of DPPC deposited was known, then the solution concentration could be calculated as follows:

$$\text{Solution concentration} \left(\frac{\mu g}{\mu L} \right) = \frac{Mass_{DPPC} (\mu g)}{\text{Syringe volume} (\mu L)} \quad \text{Equation 15}$$

2.4.1.3.4 Determination of the lift-off M_{ma} under other experimental conditions

The lift-off M_{ma} was also determined for ultrapure water at 37°C and PBS at 21°C and 37°C. Π -A isotherms for each set of experimental conditions were measured using the same reference DPPC solution of known concentration and depositing the same DPPC mass. Table 10 summarises the lift-off M_{ma} values obtained for each set of experimental conditions. These lift-off M_{ma} values were also used to calculate the mass of DPPC deposited onto the subphase when working with each set of experimental conditions.

Table 10. Lift-off Mma value of the *H*-Mma isotherm measured under different experimental conditions and consequent equation used to determine the DPPC mass deposited onto the subphase.

Experimental conditions	Lift-off Mma (Å²/molecule)	Equation to determine the DPPC mass deposited onto the subphase (µg)
Ultrapure water 21°C	99	$0.123 \times \text{Lift-off Area (cm}^2\text{)}$
PBS 21°C	100	$0.122 \times \text{Lift-off Area (cm}^2\text{)}$
Ultrapure water 37°C	112	$0.108 \times \text{Lift-off Area (cm}^2\text{)}$
PBS 37°C	123	$0.099 \times \text{Lift-off Area (cm}^2\text{)}$

2.4.1.4 Variability when measuring DPPC isotherms

As already mentioned, typically in the literature results for similar studies are presented without an associated indication of the uncertainty/variability and consequently comparisons between isotherms for different experimental conditions are discussed in a broadly qualitative manner rather than quantitatively. As such, it was considered important in the present work to try to adopt a more quantitative approach. The extent to which this could be done was however limited for a number of reasons. The LWB is a very sensitive apparatus and it was difficult to obtain reproducible results. These problems are encountered by all researchers that work with a LWB system. Also in some experiments shown in chapter 3 and chapter 4 of the present studies, isotherms could only be determined for a single measurement, and hence, for these experiments it was not possible to calculate values expressing the variability (e.g. the SD, RSD or range) on each of the parameters that describe the isotherm.

To address these issues it was decided to determine values representing the variability on DPPC isotherm parameters for the two most common set of experimental conditions used in the present work (PBS at 37°C and 21°C) and assume that the levels of variability seen would be indicative of those for the other experiments for which direct derivation of variability on isotherm parameters was not undertaken.

To do this, isotherms were measured for the aforementioned two reference conditions until five good isotherms each were recorded (PBS subphase at 37°C (Figure 40) and PBS subphase at 21°C (Figure 41)) using the rejection criteria described previously in section 2.4.1.2. For each

set of five isotherms, the average, SD and RSD in the lift-off M_{ma} , C_m , collapse II and collapse M_{ma} were calculated (Table 11 and Table 12 for each experimental condition respectively). For each parameter, a measure of the experimental range, expressed in terms of a percentage difference from the midpoint of the whole range was also evaluated; this is termed the ‘% change from midpoint’ and is determined as follows:

$$\% \text{ change from midpoint} = \frac{(\text{maximum} - \text{minimum})/2}{\text{midpoint}} \times 100$$

where midpoint = (maximum + minimum)/2

Due to the fact that the isotherms collapsed at different II values, in order to be able to compare the C_m for the last region of the isotherm (31 mN/m – collapse II for subphase temperature of 37°C and 50 mN/m – collapse II for subphase temperature of 21°C) the lowest collapse II value of all the isotherms was taken as a reference point; for each isotherm the C_m was then determined for the region between 31 mN/m and the lowest collapse II value (when working at 37°C) or between 50 mN/m and the lowest collapse II value (when working at 21°C).

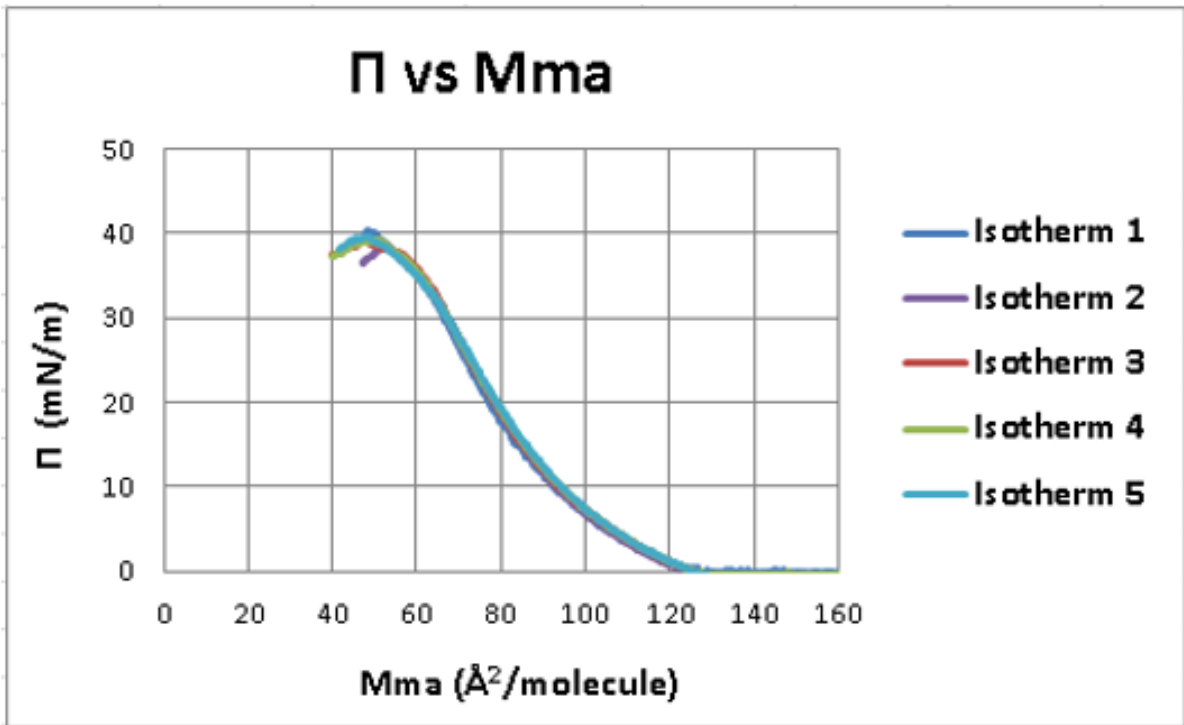


Figure 40. Π -Mma isotherms measured in PBS at 37°C to investigate the variability between DPPC isotherms measured under ostensibly the same experimental conditions. The DPPC mass deposited for each experiment was 6 μg . n = 1 experiment per isotherm measured under the same conditions.

Table 11. Lift-off Mma, C_m , collapse Π and collapse Mma of five Π -Mma isotherms measured in PBS at 37°C after depositing a DPPC mass of 6 μg . The average value, standard deviation, relative standard deviation and % change from midpoint in each of the parameters are also shown.

Isotherm	Lift-off Mma ($\text{\AA}^2/\text{molecule}$)	C_m 1-5 mN/m (mN/m)⁻¹	C_m 10-25 mN/m (mN/m)⁻¹	C_m 31 mN/m – lowest collapse Π (mN/m)⁻¹	Collapse Π (mN/m)	Collapse Mma ($\text{\AA}^2/\text{molecule}$)
1	123	0.0312	0.0153	0.0259	40.42	48
2	123	0.0294	0.0150	0.0349	39.21	48
3	124	0.0296	0.0151	0.0278	39.27	50
4	122	0.0292	0.0146	0.0290	38.61	52
5	124	0.0296	0.0150	0.0292	39.49	48
Average	123	0.0298	0.0150	0.0294	39.40	49
SD	1	0.0008	0.0003	0.0034	0.66	2
RSD (%)	1	3	2	12	2	4
% change from midpoint	1	3	2	15	2	4

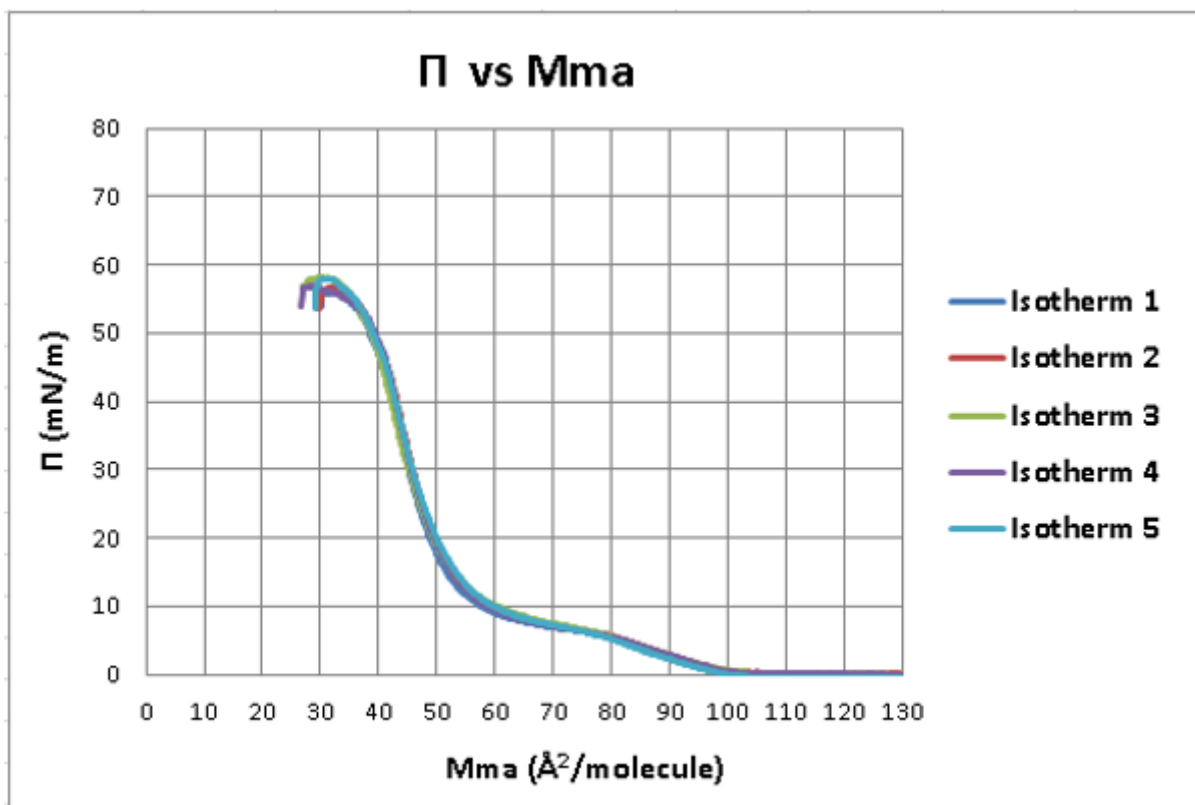


Figure 41. Π -Mma isotherms measured in PBS at 21°C to investigate the variability between DPPC isotherms measured under ostensibly the same experimental conditions. The DPPC mass deposited for each experiment was 7 μg . n = 1 experiment per isotherm measured under the same conditions.

Table 12. Lift-off Mma, C_m , collapse Π and collapse Mma of five Π -Mma isotherms measured in PBS at 21°C after depositing a DPPC mass of 7 μg . The average value, standard deviation, relative standard deviation and % change from midpoint in each of the parameters are also shown.

Isotherm	Lift-off Mma ($\text{\AA}^2/\text{molecule}$)	C_m 1-5 mN/m (mN/m)⁻¹	C_m 5-10 mN/m (mN/m)⁻¹	C_m 25-45 mN/m (mN/m)⁻¹	C_m 50 mN/m – lowest collapse Π (mN/m)⁻¹	Collapse Π (mN/m)	Collapse Mma ($\text{\AA}^2/\text{molecule}$)
1	99	0.0370	0.0691	0.0062	0.0317	56.02	32
2	100	0.0373	0.0669	0.0060	0.0206	56.82	32
3	101	0.0393	0.0594	0.0067	0.0168	58.16	30
4	101	0.0384	0.0643	0.0060	0.0359	56.93	29
5	98	0.0371	0.0582	0.0064	0.0184	57.95	31
Average	100	0.0378	0.0636	0.0063	0.0247	57.17	31
SD	1	0.0010	0.0047	0.0003	0.0086	0.88	1
RSD (%)	1	3	7	5	35	2	3
% change from midpoint	2	3	9	6	36	2	5

As can be seen in Table 11, the average lift-off M_{ma} was $123 \text{ \AA}^2/\text{molecule}$ with a SD of 1 and a RSD of 1% when experiments were performed in PBS at 37°C . The average $C_m (\text{mN/m})^{-1}$ for the regions 1-5, 10-25 and 31-lowest collapse II were 0.0298, 0.0150 and 0.0294 with RSD of 3%, 2% and 12% respectively. The average collapse II value was 39.40 mN/m with a RSD of 2% and the average collapse M_{ma} was $49 \text{ \AA}^2/\text{molecule}$ with a RSD of 4%. Thus, the C_m for the region 31-lowest collapse II , which is the last region of the isotherm, had the highest variability.

Table 12 shows that the average lift-off M_{ma} was $100 \text{ \AA}^2/\text{molecule}$ with a SD of 1 and a RSD of 1% when experiments were performed in PBS at 21°C . The average $C_m (\text{mN/m})^{-1}$ for the regions 1-5, 5-10, 25-45 and 50-lowest collapse II was 0.0378, 0.0636, 0.0063 and 0.0247 with RSD of 3%, 7%, 5% and 35% respectively. The average collapse II value was 57.17 mN/m with a RSD of 2% and the collapse M_{ma} was $31 \text{ \AA}^2/\text{molecule}$ with a RSD of 3%. Thus, the highest variability was found in the C_m for the region 50-lowest collapse II , which is the last region of the isotherm, in agreement with the results at 37°C .

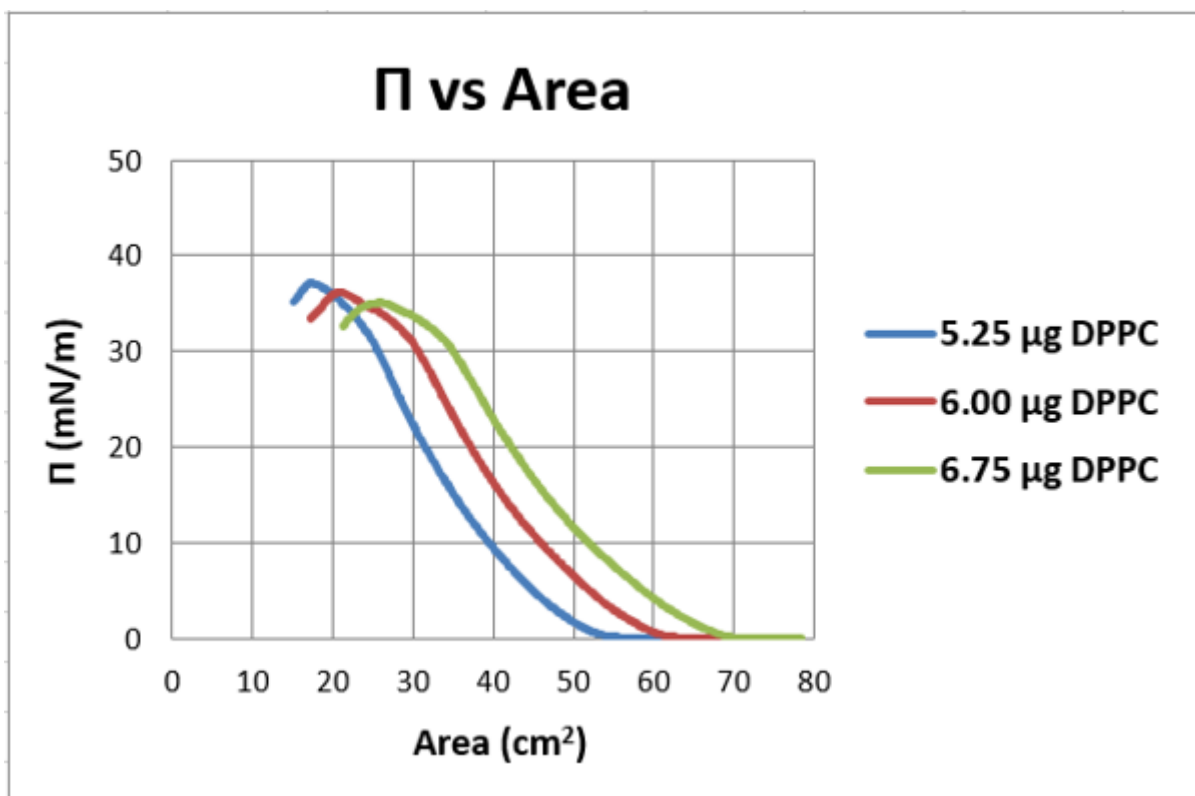
2.4.1.5 Establishment of criteria to compare isotherms measured under different experimental conditions based on reference isotherm parameter variability values

As already mentioned, typically in the literature results for similar studies are presented without an associated indication of the uncertainty/variability and consequently comparisons between isotherms for different experimental conditions are discussed in a broadly qualitative manner rather than quantitatively. In the present work we used the following criteria to compare an experimental isotherm with its associated control isotherm in a quantitative and consistent way for all experiments. In the initial step, an experimental and a control isotherm were determined for a set of experimental conditions, typically by averaging 3 isotherms in both cases, but in some instances (see chapters 3 and 4) it was only possible to generate single isotherms. The lift-off M_{ma} , C_m , collapse II and collapse M_{ma} were subsequently calculated for the ‘average’ isotherm for both the experimental and control case. The difference between the experiment and control parameter value, expressed as a % of the control parameter value was also determined for each parameter. This is termed the ‘% difference between experiment and control’.

The assumption was then made that the variability on both the control and experiment isotherm parameter values was approximately the same as that represented by the % change from midpoint values for the relevant reference DPPC isotherm (i.e. 37°C or 21°C) shown previously in Table 11 and Table 12. These reference % change from midpoint values were then used to indicate quantitatively if there were any differences between an experimental isotherm and the control. Essentially the ‘% difference between experiment and control’ for each of the parameters (lift-off M_{ma} , C_m , collapse II and collapse M_{ma}) was divided by the ‘% change from midpoint’ for the relevant reference isotherm. If the ratio was greater than 1, then this suggested that those experimental conditions affected the profile of the isotherm for that parameter when compared to the control. The greater the ratio between the two values the more potentially significant this difference was, especially for values above 3. This is clearly not a strict quantitative measure of the statistical significance of the difference between the control and experiment but nonetheless within the limitations of the experimental conditions provides a useful indication of this.

2.4.1.6 Study of DPPC isotherms with different deposited masses of DPPC

In the present experiments, different amounts of DPPC were deposited onto the subphase. Although the lift-off M_{ma} remained the same for a set of experimental conditions, this was clearly not the case for the lift-off area, which shifted to higher or lower area values depending on the DPPC mass deposited. It was considered important to investigate whether this had any impact on other parts of the isotherm. It is also very common for other changes in experimental conditions to result in the shifting of the lift-off area even if the same DPPC mass was deposited onto the subphase. It was thought that investigating the effect of different DPPC masses, which result in different lift-off areas, would potentially also give some indication of the overall effect of other factors which result in differences in lift-off areas. To investigate what happened to the DPPC isotherm when the deposited mass was different, 7, 8 and 9 μL of a DPPC solution with concentration 0.75 mg/mL were deposited onto a PBS subphase at 37°C and the II -A isotherms measured. Figure 42 shows the II -A isotherm for each DPPC mass deposited (5.25 μg , 6.00 μg and 6.75 μg) as well as the lift-off area, collapse area, collapse II and length of the isotherm that was calculated by determining the distance from the lift-off area to the collapse area.



DPPC mass (µg)	Lift-off area (cm ²)	Collapse Area (cm ²)	Collapse Π (mN/m)	Length of the isotherm (cm ²)
5.25	53	17	37.14	36
6.00	61	21	36.16	39
6.75	68	26	35.12	42

Figure 42. *II-A* isotherms measured in PBS at 37°C after depositing a DPPC mass of 5.25 µg, 6.00 µg and 6.75 µg. The table shows the lift-off area, collapse area, collapse Π and length of the isotherm from the lift-off area to the collapse area for each DPPC mass. $n = 3$ experiments/condition.

These data show that the isotherm with the highest DPPC mass deposited is the longest one. The lift-off area is the point where the surface concentration of DPPC is the same for each isotherm and DPPC molecules start to interact decreasing the surface tension. It also represents the area under which the isotherm will be measured. The more the isotherm shifts to the right, the higher the lift-off area and thus, as the barrier speed is constant, the lower the compression rate per DPPC molecule and vice versa. The experiment will take longer and the isotherm will

be more elongated. The compression rate is defined as the area by which each DPPC molecule is compressed per unit time with units $\text{\AA}^2/\text{min}/\text{molecule}$. For a barrier speed of 5 mm/min or $2.5 \text{ cm}^2/\text{min}$ used in these experiments, the compression rate was calculated as follows:

$$\text{Compression rate } (\text{\AA}^2/\text{min}/\text{molecule}) = \frac{2.5E + 16 (\text{\AA}^2/\text{min})}{\text{Number of DPPC molecules (molecule)}}$$

Equation 16

Table 13 shows the compression rate for each of the experiments. As can be seen in the table, the compression rate decreased in relation to the amount of DPPC mass deposited.

Table 13. Compression rate per DPPC molecule for three different monolayers formed after depositing a DPPC mass of 5.25 μg , 6.00 μg and 6.75 μg onto a PBS subphase at 37°C and compressed with the barriers at a speed of 5 mm/min ($2.5 \text{ cm}^2/\text{min}$).

Volume (μL)	DPPC mass (μg)	Number of DPPC molecules (molecule)	Compression rate ($\text{\AA}^2/\text{min}/\text{molecule}$)
7	5.25	4.29E+15	5.83
8	6.00	4.91E+15	5.10
9	6.75	5.51E+15	4.54

Finally, *II*-A isotherms were normalised to the DPPC mass content, i.e., the *II*-Mma isotherms were plotted (Figure 43) and the lift-off Mma, C_m , collapse *II* and collapse Mma of the *II*-Mma isotherms were determined (Table 14). The corresponding values of each of these parameters measured for DPPC masses 6.00 μg and 6.75 μg were compared with those measured for DPPC mass 5.25 μg (control) by calculating the % difference between experiment and control for each of the parameters and dividing them by the reference % change from midpoint values, i.e., as indicated earlier, assuming similar levels of uncertainties on the parameters to those of the reference isotherms (see section 2.4.1.5).

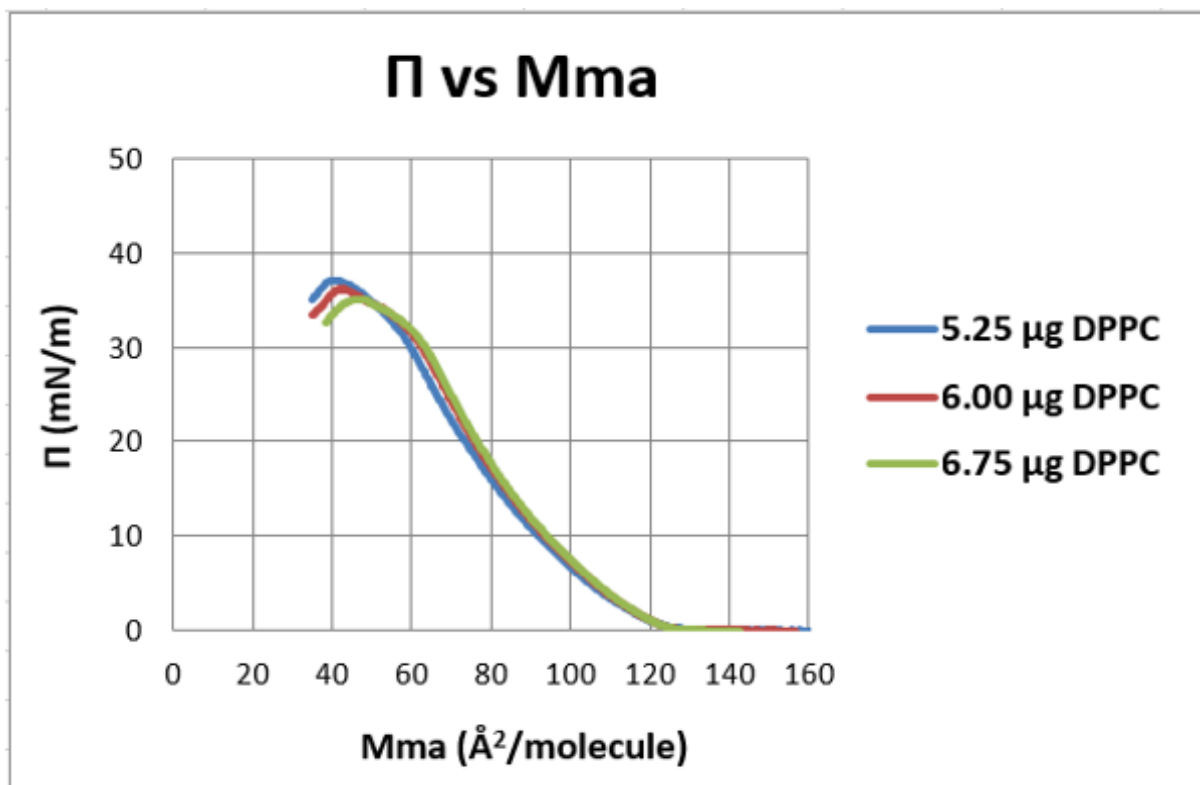


Figure 43. Π - M_{ma} isotherms determined by normalising the Π - A isotherms measured in PBS at 37°C after depositing a DPPC mass of 5.25 μg , 6.00 μg and 6.75 μg to the DPPC mass content. $n = 3$ experiments/condition.

Table 14. Effect of the DPPC mass deposited (5.25 μg , 6.00 μg and 6.75 μg) on the lift-off M_{ma} , C_m , collapse Π and collapse M_{ma} of the Π - M_{ma} isotherms measured in PBS at 37°C. The corresponding values in each of these parameters measured for DPPC masses 6.00 μg and 6.75 μg were compared with those measured for 5.25 μg (control) by calculating the difference in each of the parameters for the experimental isotherm and the control expressed as a % of the control value and dividing them by the reference % change from midpoint values for the relevant reference isotherm (Table 11). This approach assumes similar levels of uncertainties on the control and experimental isotherm parameters to those of the reference isotherm parameters.

DPPC mass (μg)	Lift-off M_{ma} ($\text{\AA}^2/\text{molecule}$)	(% difference experiment and control)/(reference % change from midpoint)	C_m 1-5 mN/m (mN/m) ⁻¹	(% difference experiment and control)/(reference % change from midpoint)	C_m 10-25 mN/m (mN/m) ⁻¹	(% difference experiment and control)/(reference % change from midpoint)
<i>Reference isotherm</i>	123	1.0 (% change from midpoint)	0.0298	3.0 (% change from midpoint)	0.0150	2.0 (% change from midpoint)
5.25 (control)	123		0.0323		0.0187	
6.00	123	0.0	0.0299	2.3	0.0176	3.0
6.75	123	0.0	0.0290	3.3	0.0172	4.0

DPPC mass (μg)	C_m 31 mN/m – lowest collapse Π (mN/m) ⁻¹	(% difference experiment and control)/(reference % change from midpoint)	Collapse Π (mN/m)	(% difference experiment and control)/(reference % change from midpoint)	Collapse M_{ma} ($\text{\AA}^2/\text{molecule}$)	(% difference experiment and control)/(reference % change from midpoint)
<i>Reference isotherm</i>	0.0294	15.0 (% change from midpoint)	39.40	2.0 (% change from midpoint)	49	4.0 (% change from midpoint)
5.25 (control)	0.0380		37.14		41	
6.00	0.0546	2.9	36.16	1.5	43	1.3
6.75	0.0596	3.8	35.12	2.5	47	3.8

As can be seen in the previous tables, the lift-off M_{ma} for each isotherm was $123 \text{ \AA}^2/\text{molecule}$. This means that depositing 6.00 \mu g and 6.75 \mu g of DPPC did not have an effect on the lift-off M_{ma} compared to the control. This is expected as the lift-off M_{ma} is the lift-off area normalised to the DPPC content and should be the same when the isotherm is measured under the same experimental conditions. Depositing 6.00 \mu g and 6.75 \mu g of DPPC however had an effect on all the other parameters compared to the control, most significantly for the C_m for the region 10-25. The effects were DPPC mass-dependant. In particular, the C_m of the isotherm decreased in the regions 1-5 and 10-25, increased in the region 31 mN/m – lowest collapse Π , and the collapse Π decreased whereas the collapse M_{ma} increased with DPPC mass deposited. It is therefore clearly important for any set of experiments to use similar DPPC masses.

These differences might have been caused by the different compression rates at which DPPC molecules were compressed in each experiment. In order to investigate the effect of compression rate on the DPPC isotherm, a set of experiments was performed where a DPPC monolayer was compressed under different barrier speeds and the effect on the lift-off M_{ma} , C_m , collapse Π and collapse M_{ma} determined. The isotherms were measured in water at 21°C . Results showed that barrier speed did have an effect on the DPPC isotherm. This is shown later in the chapter (section 2.4.2.1).

2.4.2 Measurement of the DPPC isotherm under experimental conditions close to those occurring *in vivo*

The shape of an isotherm is of utmost importance to understand what is occurring at the molecular level and its physiological implications. It is well known that the shape of a DPPC isotherm is dependent on many conditions including subphase temperature or subphase composition (Duncan and Larson, 2008). Some of the most relevant conditions present in the alveoli of healthy lungs during the breathing cycle have been mentioned in the introduction and include:

- Frequency of the inhalation-exhalation breathing cycle: 10-15 times per minute.
- Alveolar subphase fluid: a watery phase that contains a number of ions such as H^+ , Na^+ , Ca^{+2} or Cl^+ .
- Temperature: 37°C .
- Relative humidity: 100%.

- Surface tension reached at the end of exhalation: falls to near zero values at the end of exhalation.

Bearing this in mind, DPPC was tested under different relevant quasi-physiological conditions in order to understand how each of these factors affected the DPPC isotherm compared to that obtained under more common experimental conditions and to set up the most relevant experimental conditions to work with in future experiments. Table 15 shows the conditions under which DPPC was tested using a LWB system to illustrate the difference and hence the importance of measuring isotherms under conditions as close as possible to those occurring *in vivo* and to set up the relevant conditions to work with in future experiments.

Table 15. Commonly used and quasi-physiological conditions under which a DPPC monolayer was tested using a LWB system to determine the differences and hence the importance of measuring isotherms under conditions as close as possible to those occurring *in vivo* and to set up the relevant conditions for future experiments.

	Common condition	Quasi-physiological condition
Frequency of the inhalation-exhalation cycle	Barrier speed of 5 mm/min	Barrier speed of 40, 90 and 270 mm/min
Subphase fluid	Ultrapure water	Phosphate buffered saline
Subphase temperature	21°C	37°C
Relative humidity	~ 45% (ambient)	> 87%
Surface tension (γ) reached at the end of exhalation	Higher than near zero values	Near zero values

2.4.2.1 Effect of barrier speed on the DPPC isotherm

Figure 44 shows the effect of barrier speed on the DPPC Π -Mma isotherm. The isotherms were measured in water at a temperature of 21°C. The DPPC mass deposited for each experiment was 8 μg . The compression barrier speeds were 5 (control), 40, 90 and 270 mm/min which is the maximum barrier speed for the LWB system. Table 16 shows the lift-off Mma, C_m , collapse Π and collapse Mma of the Π -Mma isotherms. The corresponding values in each of these parameters for barrier speeds 40, 90 and 270 mm/min were compared with those for barrier speed 5 mm/min (control) by calculating the % difference between experiment and control for each of the parameters and dividing them by the reference % change from midpoint values, i.e., assuming similar levels of uncertainties on the parameters to those of the reference isotherms (see section 2.4.1.5). The C_m of the isotherm measured at 270 mm/min is only shown for the region 1-5 mN/m as there were not enough points in the curve to calculate it for the other regions of the isotherm. Collapse Π and collapse Mma for this barrier speed are indicated in the table but strictly speaking cannot be considered a collapse as no plateau or rapid decrease in Π occurred.

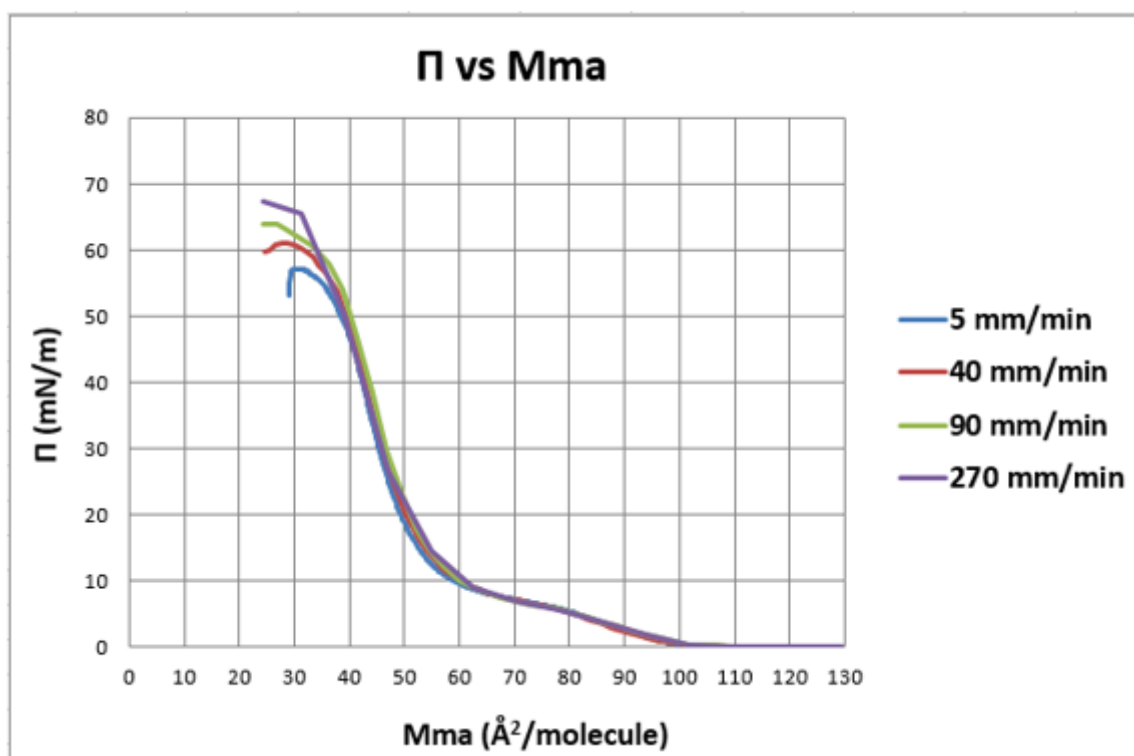


Figure 44. Effect of barrier speed (5, 40, 90 and 270 mm/min) on the Π -Mma isotherm measured for DPPC in water at 21°C. The DPPC mass deposited for each experiment was 8 μg . $n = 5$ experiments/condition.

Table 16. Effect of barrier speed (5, 40, 90 and 270 mm/min) on the lift-off M_{ma} , C_m , collapse Π and collapse M_{ma} of the Π - M_{ma} isotherms measured for DPPC in water at 21°C. The corresponding values in each of these parameters for barrier speeds 40, 90 and 270 mm/min were compared with those for barrier speed 5 mm/min (control) by calculating the difference in each of the parameters for the experimental isotherm and the control expressed as a % of the control value and dividing them by the reference % change from midpoint values for the relevant reference isotherm (Table 12). This approach assumes similar levels of uncertainties on the control and experimental isotherm parameters to those of the reference isotherm parameters.

Speed (mm/min)	Lift-off M_{ma} ($\text{\AA}^2/\text{molecule}$)	(% difference experiment and control)/(reference % change from midpoint)	C_m 1-5 mN/m (mN/m^{-1})	(% difference experiment and control)/(reference % change from midpoint)	C_m 5-10 mN/m (mN/m^{-1})	(% difference experiment and control)/(reference % change from midpoint)
<i>Reference isotherm</i>	100	2.0 (% change from midpoint)	0.0378	3.0 (% change from midpoint)	0.0636	9.0 (% change from midpoint)
5 (control)	99		0.0380		0.0631	
40	99	0.0	0.0391	1.0	0.0562	1.2
90	101	1.0	0.0408	2.3	0.0559	1.2
270	101	1.0	0.0436	5.0	-	

Speed (mm/min)	C_m 25-45 mN/m (mN/m^{-1})	(% difference experiment and control)/(reference % change from midpoint)	C_m 50 mN/m – lowest collapse Π (mN/m^{-1})	(% difference experiment and control)/(reference % change from midpoint)	Collapse Π (mN/m)	(% difference experiment and control)/(reference % change from midpoint)	Collapse M_{ma} ($\text{\AA}^2/\text{molecule}$)	(% difference experiment and control)/(reference % change from midpoint)
<i>Reference isotherm</i>	0.0063	6.0 (% change from midpoint)	0.0247	36.0 (% change from midpoint)	57.17	2.0 (% change from midpoint)	31	5.0 (% change from midpoint)
5 (control)	0.0065		0.0211		57.20		31	
40	0.0066	0.3	0.0138	0.9	60.65	3.0	30	0.6
90	0.0067	0.5	0.0116	1.3	64.05	6.0	27	2.6
270	-		-		67.44	9.0	24	4.6

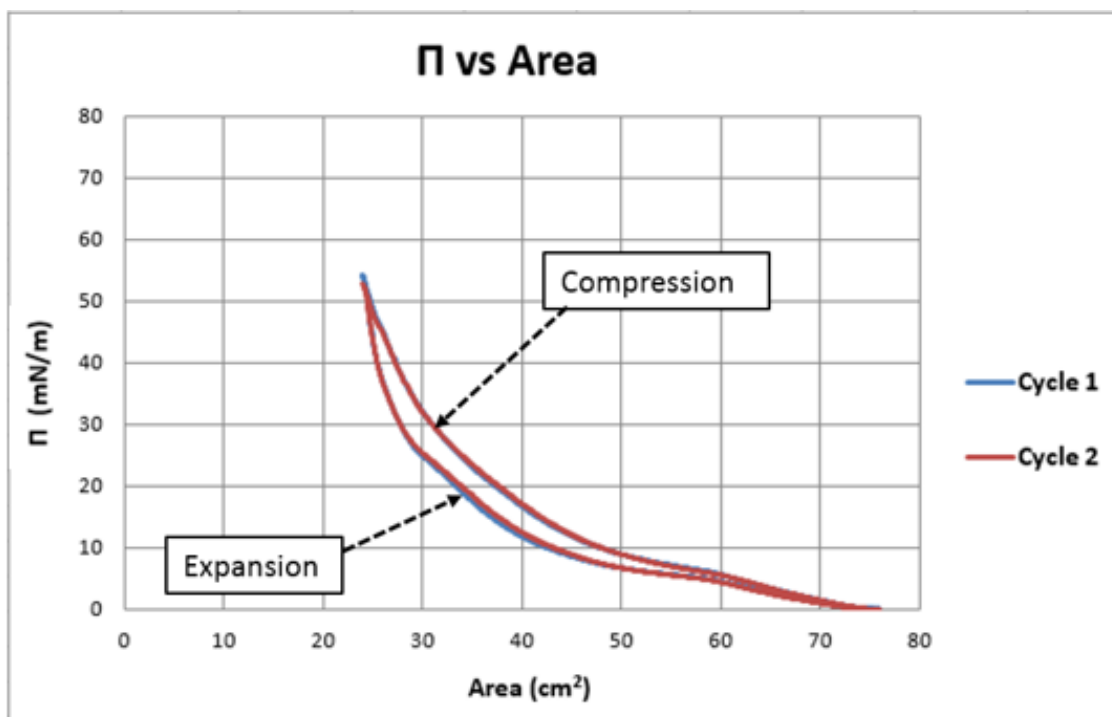
As can be seen from Table 16, the barrier speed did not have an effect on the lift-off M_{ma} and the C_m for the region 25-45 mN/m. Moreover, compressing the interface at 40 mm/min did not affect the C_m for the regions 1-5 and 50-lowest collapse II and the collapse M_{ma} . The barrier speed had an effect on all the other parameters of the isotherm that were generally more pronounced with barrier speed. For each barrier speed, the isotherm parameter that was most significantly affected was the collapse II which increased with barrier speed, while the collapse M_{ma} decreased. It is difficult to compare these results with those shown previously in Table 14 for the different deposited DPPC masses, as the subphase temperature used was different for each set of experiments. However, those experiments also showed a clear decrease in the collapse II and increase in the collapse M_{ma} with DPPC mass and no effect on the lift-off M_{ma} which suggests that the effects might have been caused by the different compression rates per DPPC molecule.

It has been reported in the literature that the compression rate has very little or no influence on the shape of the isotherm (Nag et al., 1991, Jyoti et al., 1996). However, in the present study the compression rate had a clear effect on the collapse II and collapse M_{ma} . Higher collapse II values were reached at lower collapse M_{ma} values. As previously mentioned in the introduction (section 1.2.3.1.3), in the LC phase the tails of the DPPC molecule are fully extended but tilted at an angle to the vertical, whereas in the S phase chains are fully extended and nearly perpendicular to the surface. Energy must be put into the system for the DPPC tails to become vertical. Thus, the higher the compression rate, the higher the energy available to make the tails vertical and the range of area per molecule over which the compression occurs increases (Jyoti et al., 1996). The monolayer is capable of resisting collapse at a lower M_{ma} , and as a result, a higher collapse II is reached. In fact, there is some evidence in the literature which supports the current study and suggests that the higher the rate at which the monolayer is compressed, the higher the collapse II value reached (Crane and Hall, 2001, Smith et al., 2003).

In the present work, the collapse II reached at a barrier speed of 5 mm/min was 57.20 mN/m; however, there is evidence that DPPC is capable of reaching near zero γ on compression using a LWB at a similar barrier speed (Smith and Berg, 1980, Zhang et al., 2011b). It is possible that the low collapse II in this study was caused by surfactant leakage problems. Leakage in LWB systems is a problem that typically happens at II around ~ 50 mN/m when working at 21°C and is greater at high subphase temperatures (Zuo et al., 2008c, Duncan and Larson, 2008) probably due to an increase in the thermal motion of the molecules (Yun et al., 2003). Surfactant material

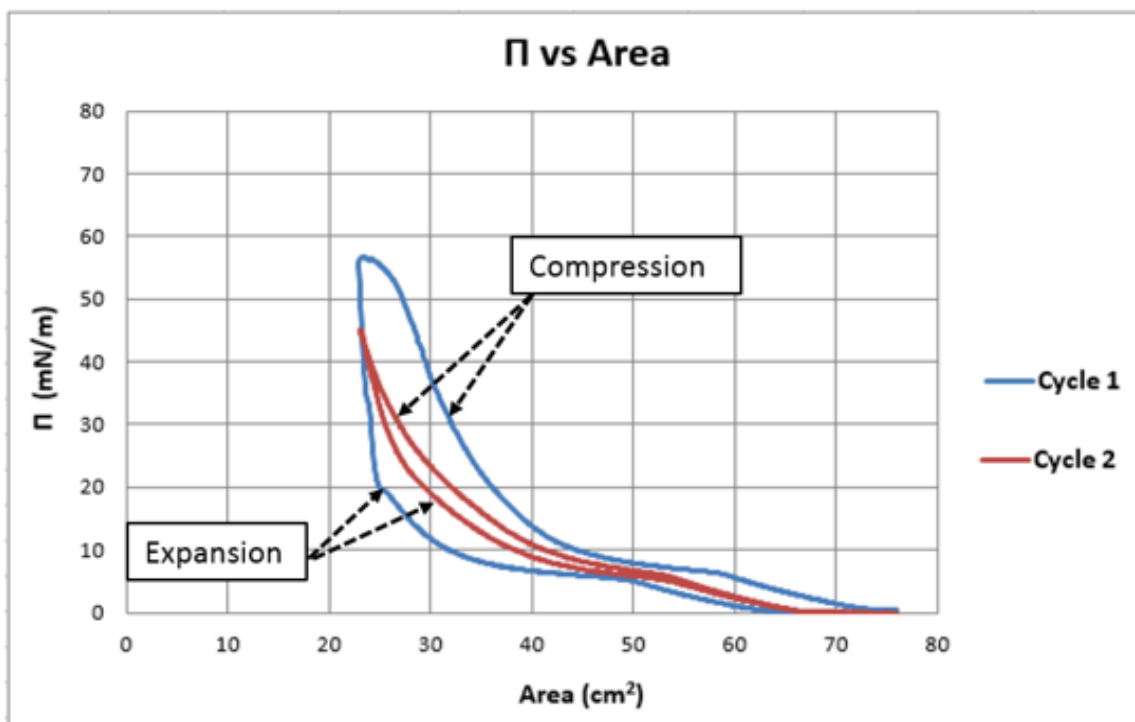
tends to spread onto the trough sidewalls, floor, barriers, Wilhelmy plate and into the subphase. In an experiment performed with a ^{14}C -labeled DPPC, the monolayer was compressed in stages over a 3 hour period and then samples collected from various parts of the trough for radioactivity assay. It was found that 14.3% of the surfactant was lost onto the following parts of the system: 8.8% sides and barriers, 0.1% floor, 3.9% Wilhelmy plate and 1.5% subphase (Goerke and Gonzales, 1981). Due to this leakage, the area per molecule, as well as the compression rate, can be erroneous. The ability to reach very high Π values is also greatly compromised as premature film collapse can occur. Leakage can sometimes be seen in the isotherm as a kink and a decrease in its slope just prior to the monolayer collapse (Tabak and Notter, 1977, Duncan and Larson, 2008, Zuo et al., 2008c). In the current experiments, and taking into account experimental values of C_m for the DPPC monolayer phases from the literature (i.e. $0.02\text{-}0.1 \text{ (mN/m)}^{-1}$ for LE films, $0.004\text{-}0.01 \text{ (mN/m)}^{-1}$ for LC films and $< 0.004 \text{ (mN/m)}^{-1}$ for S films (Kodama et al., 2004, Vitovič et al., 2006)), the isotherm measured at barrier speed 5 mm/min was in LE state in the region 1-5 mN/m, in a LC state in the region 25-45 mN/m, and again in a LE state in the region 50 mN/m - lowest collapse Π . The isotherms measured at barrier speeds 40 and 90 mm/min were however in a LC state in the region 50 mN/m - lowest collapse Π . This suggests possible surfactant material loss at Π above ~ 50 mN/m when compressing the interface at 5 mm/min.

To investigate this, two different experiments were performed. 9 μg of DPPC was deposited onto PBS at 21°C. The DPPC monolayer was then compressed and expanded 2 times at a barrier speed of 5 mm/min and the isotherms recorded. In the first experiment, the monolayer was compressed from a Π value of 0 to ~ 52 mN/m (Figure 45) and in the second experiment from a Π value of 0 to ~ 57 mN/m, just before the collapse of the monolayer (Figure 46). The lift-off area was calculated for each compression isotherm.



	Lift-off area (cm ²)
Compression 1 (cycle 1)	73
Compression 2 (cycle 2)	73

Figure 45. *Π*-*A* isotherms of a DPPC monolayer compressed and expanded 2 times from 0 to ~ 52 mN/m measured in PBS at 21°C (experiment 1). The table shows the lift-off area for each compression isotherm. n = 1 experiment/cycle.



	Lift-off area (cm ²)
Compression 1 (cycle 1)	73
Compression 2 (cycle 2)	66

Figure 46. Π -A isotherms of a DPPC monolayer compressed and expanded 2 times, from 0 to ~ 57 mN/m in the first cycle, measured in PBS at 21°C (experiment 2). The table shows the lift-off area for each compression isotherm. $n = 1$ experiment/cycle.

As can be seen in Figure 45, the lift-off area was 73 cm² for each compression isotherm and both the compression and expansion isotherms were very similar. In the second experiment however (Figure 46) the lift-off area decreased from 73 cm² for the first compression isotherm to 66 cm² for the second compression isotherm which suggests loss of surfactant material during the first cycle as the lift-off area is directly related to the DPPC mass present at the interface (Equation 13). This confirmed the suggestion that possible surfactant material loss occurred at Π above ~ 50 mN/m when compressing the interface at 5 mm/min.

Leakage of test samples has been ignored by most investigators and thus, could have led to incorrect assessment of the intrinsic properties of lung surfactant (Blanco and Pérez-Gil, 2007,

Duncan and Larson, 2008). The use of a ribbon trough, which uses a ribbon barrier instead of conventional barriers for perfect film containment, minimises or eliminates leakage problems (Tabak and Notter, 1977, Duncan and Larson, 2008, KSV-Nima, 2012) as shown in Figure 47. Although this is a more expensive apparatus compared to the conventional LWB system (according to the manufacturer Biolin Scientific), in retrospect this may have proven more effective. A captive bubble surfactometer is also a leak-proof system but the composition and structure of the monolayer cannot be further examined using microscopic and spectroscopic techniques as is possible with the LWB system. Taking all this into account, it is anticipated that if the present experiments had been performed in a system where no leakage occurred, the collapse Π value would have been the same for any barrier speed and thus, barrier speed would have had very little effect on the DPPC isotherm, as other studies have shown (Nag et al., 1991, Jyoti et al., 1996). There is however evidence that compression rate has an effect on the size (Nag et al., 1991) and morphology (Klopfer and Vanderlick, 1996, Blanchette et al., 2008) of the LE and LC domains of a DPPC monolayer.

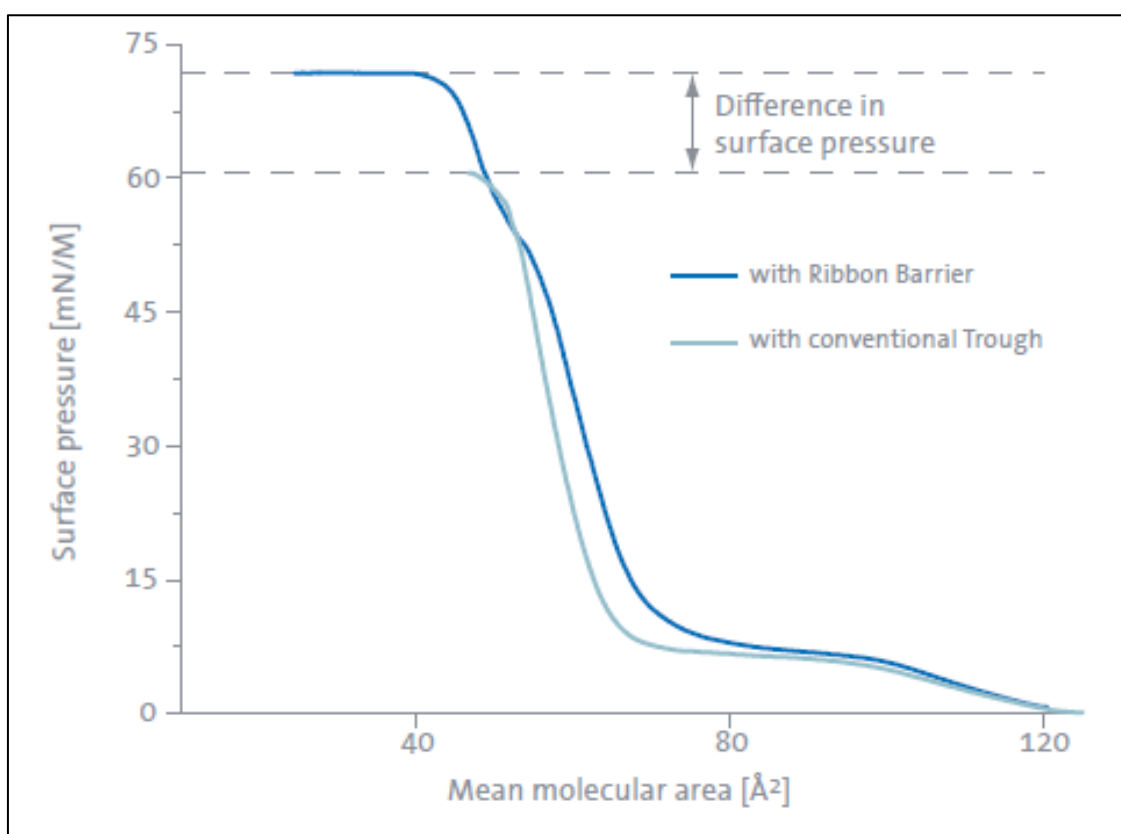


Figure 47. Π -Mma isotherms of DPPC obtained with a conventional Langmuir trough and a ribbon barrier trough (KSV-Nima, 2012).

A LWB system requires low barrier speeds to allow the monolayer to reorganise itself but also to avoid the creation of waves at the interface which may interfere with the Π measurements (Zuo et al., 2008c). In the literature, different compression rates have been used to measure a DPPC isotherm using a LWB as shown previously in Table 9. The manufacturer of the LWB system recommends working with barrier speeds between 5-20 mm/min (KSV-Nima, 2010). For this reason, a barrier speed of 5 mm/min (2.5 cm²/min) was chosen in all the experiments in the present studies when performed in a small trough (unless otherwise specified). The normal cycle of respiration in man occurs approximately about 10-15 times per minute. When using a LWB system with a small trough and maximum barrier speed, it is only possible to complete two full compression-expansion cycles in a minute. Thus, even if the monolayer had been compressed at maximum barrier speed (270 mm/min) it would still not reflect what happens *in vivo*.

2.4.2.2 Effect of subphase composition on the DPPC isotherm

Figure 48 shows the effect of subphase composition on the DPPC Π -Mma isotherm. The isotherms were measured in ultrapure water and PBS, which mimics physiological conditions, at a temperature of 21°C. The DPPC mass deposited for each experiment was 7 µg. Table 17 shows the lift-off Mma, C_m , collapse Π and collapse Mma of the Π -Mma isotherms. The corresponding values in each of these parameters for PBS subphase were compared with those for water subphase (control) by calculating the % difference between experiment and control for each of the parameters and dividing them by the reference % change from midpoint values, i.e., assuming similar levels of uncertainties on the parameters to those of the reference isotherms (see section 2.4.1.5).

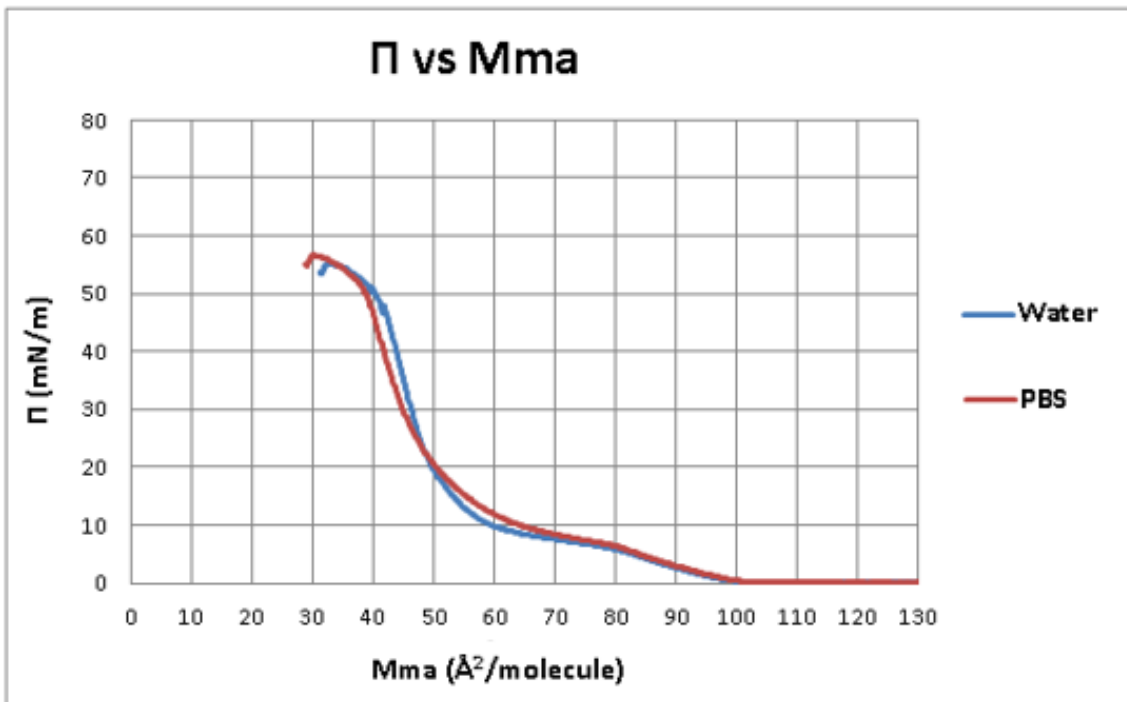


Figure 48. Effect of subphase composition, water or PBS, on the Π - M_{ma} isotherm measured for DPPC at 21°C. The DPPC mass deposited for each experiment was 7 μg . n = 4 experiments/condition.

Table 17. Effect of subphase composition, water or PBS, on the lift-off Mma, C_m , collapse II and collapse Mma of the II -Mma isotherms measured for DPPC at 21°C. The corresponding values in each of these parameters for PBS subphase were compared with those for water subphase (control) by calculating the difference in each of the parameters for the experimental isotherm and the control expressed as a % of the control value and dividing them by the reference % change from midpoint values for the relevant reference isotherm (Table 12). This approach assumes similar levels of uncertainties on the control and experimental isotherm parameters to those of the reference isotherm parameters.

Subphase composition	Lift-off Mma ($\text{\AA}^2/\text{molecule}$)	(% difference experiment and control)/(reference % change from midpoint)	C_m 1-5 mN/m (mN/m) ⁻¹	(% difference experiment and control)/(reference % change from midpoint)	C_m 5-10 mN/m (mN/m) ⁻¹	(% difference experiment and control)/(reference % change from midpoint)
<i>Reference isotherm</i>	100	2.0 (% change from midpoint)	0.0378	3.0 (% change from midpoint)	0.0636	9.0 (% change from midpoint)
Water (control)	99		0.0340		0.0651	
PBS	100	0.5	0.0341	0.0	0.0526	2.1

Subphase composition	C_m 25-45 mN/m (mN/m) ⁻¹	(% difference experiment and control)/(reference % change from midpoint)	C_m 50 mN/m – lowest collapse II (mN/m) ⁻¹	(% difference experiment and control)/(reference % change from midpoint)	Collapse II (mN/m)	(% difference experiment and control)/(reference % change from midpoint)	Collapse Mma ($\text{\AA}^2/\text{molecule}$)	(% difference experiment and control)/(reference % change from midpoint)
<i>Reference isotherm</i>	0.0063	6.0 (% change from midpoint)	0.0247	36.0 (% change from midpoint)	57.17	2.0 (% change from midpoint)	31	5.0 (% change from midpoint)
Water (control)	0.0052		0.0356		55.27		33	
PBS	0.0070	5.8	0.0259	0.8	56.50	1.0	31	1.2

Table 17 shows the impact of using PBS subphase instead of water on 3 parameters of the isotherm: the C_m for the regions 5-10 and 25-45 and the collapse M_{ma} . The parameter that was most significantly affected by the PBS subphase was the C_m for the region 25-45. The C_m for the region 5-10 was higher for water because, in PBS, the LE-LC transition plateau became less horizontal. Moreover, as shown previously in Table 10, when working at 37°C, the lift-off M_{ma} for water and PBS was 112 Å²/molecule and 123 Å²/molecule respectively. Thus, the subphase composition also had an effect on the lift-off M_{ma} when working at this subphase temperature.

It has been reported that the phase behaviour of a monolayer is dependent on many conditions including subphase composition (McConnell, 1991, Zuo et al., 2008a, KSV-Nima, 2010). There is evidence that metal cations interact with the negatively charged moieties of the lipid head groups (Herrmann et al., 1986, Binder and Zschörnig, 2002) and that the presence of calcium ions affects the monolayer structure (Lee et al., 2006, Sovago et al., 2007, Casillas-Ituarte et al., 2010). However, other studies show that spreading films onto a saline solution instead of water led to no detectable differences in the isotherm (Zuo et al., 2008a, Zuo et al., 2008b) and that the presence of small concentrations of ions led to little or no change in the isotherm shape of zwitterionic monolayers (Zaitsev et al., 1996, Shapovalov, 1998). Exogenous lung surfactant activity has been tested using a subphase of saline solution (Lipp et al., 1997, Ding et al., 2001, Bringezu et al., 2002, Flanders et al., 2002) and also ultrapure water (Hifeda and Rayfield, 1992, Jyoti et al., 1996, Klopfer and Vanderlick, 1996, Zuo et al., 2008b, Zhang et al., 2011b). In the present studies, it was found that the use of PBS had a different impact on the DPPC isotherm when compared with water. Thus, PBS was chosen as the subphase composition for use in all the following experiments as it is more physiologically relevant.

2.4.2.3 Effect of subphase temperature on the DPPC isotherm

Figure 49 shows the effect of subphase temperature on the DPPC Π - M_{ma} isotherm. The isotherms were measured in PBS at a temperature of 21°C and 37°C. The DPPC mass deposited for each experiment was 7 µg. At 21°C the isotherm followed the sequence of monolayer phases shown previously in Figure 11, i.e. G, LE-LC transition plateau and LC with collapse occurring at 56.50 mN/m. At 37°C however, the sequence of monolayer phases was G, LE and a possible LE-LC transition plateau with collapse occurring at 40.50 mN/m. Monolayer phases at 37°C are shown in Figure 50. The isotherm measured at 37°C also shifted to higher M_{ma} values compared to that measured at 21°C. This behaviour was likely caused by an increase in the

thermal motion of the chain at higher temperature, leading to an increase in Π (Yun et al., 2003). Similar effects of subphase temperature on the DPPC isotherm have been reported in the literature (Tchoreloff et al., 1991, Crane et al., 1999, Duncan and Larson, 2008, Mohammad-Aghaie et al., 2009, Toimil et al., 2010).

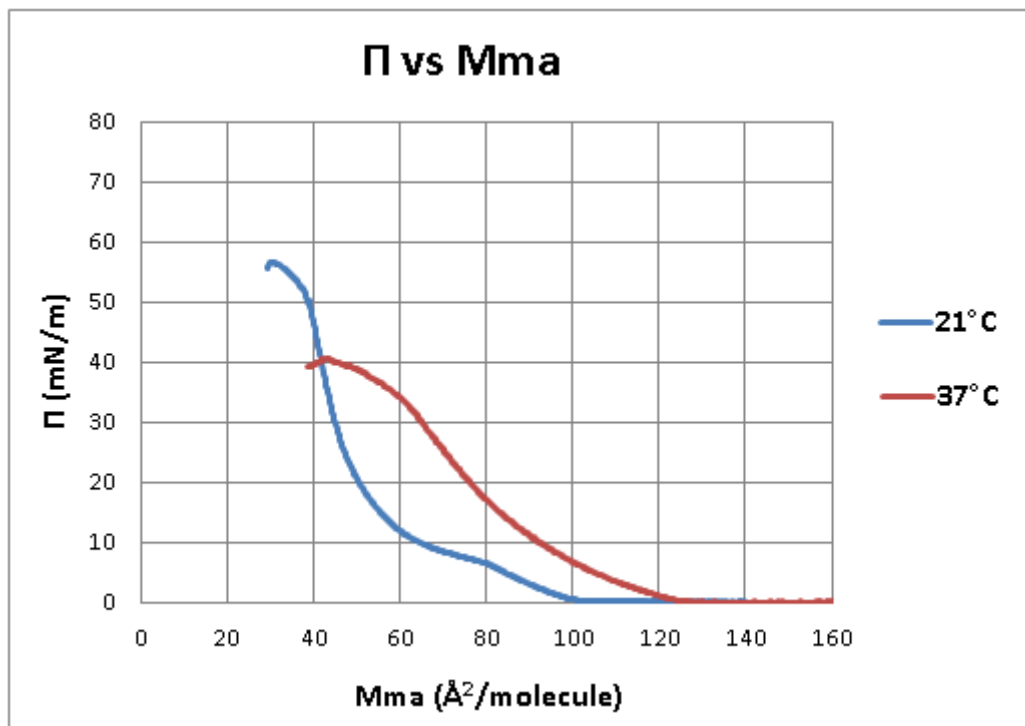


Figure 49. Effect of subphase temperature, 37°C or 21°C, on the Π -Mma isotherm measured for DPPC in PBS. The DPPC mass deposited for each experiment was 7 μg . n = 4 experiments/condition.

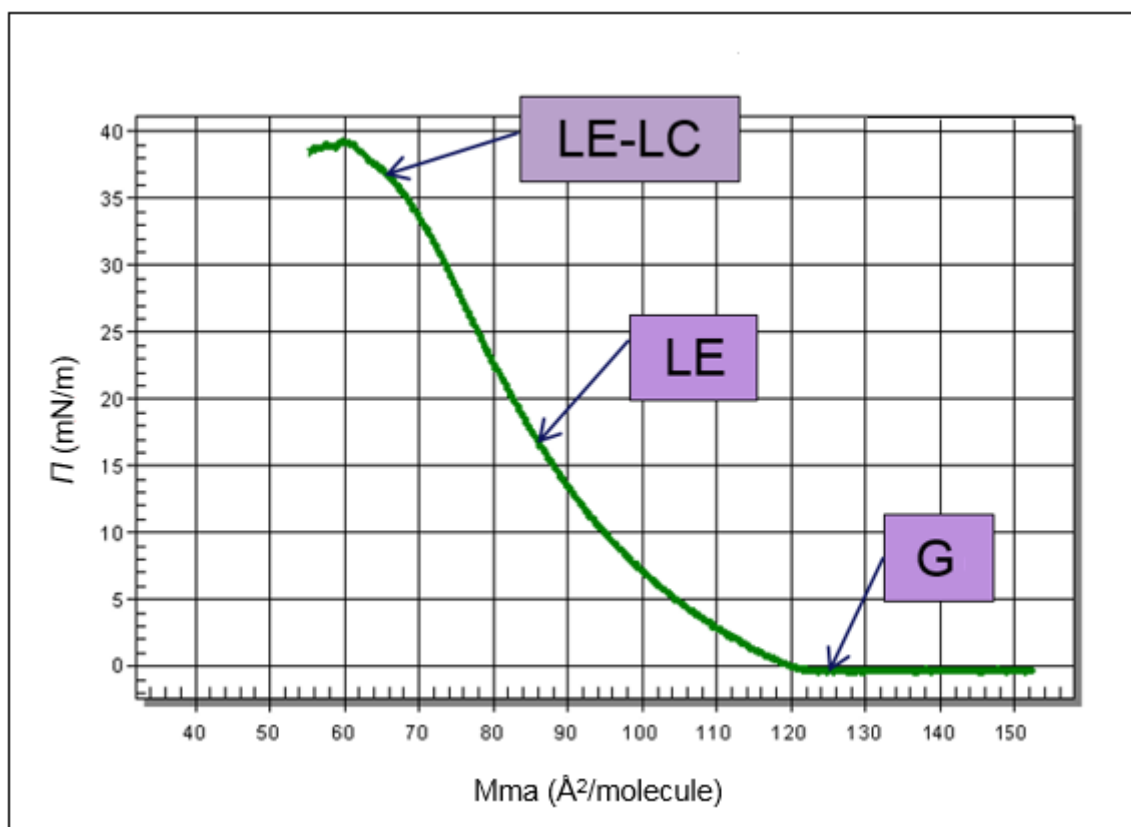
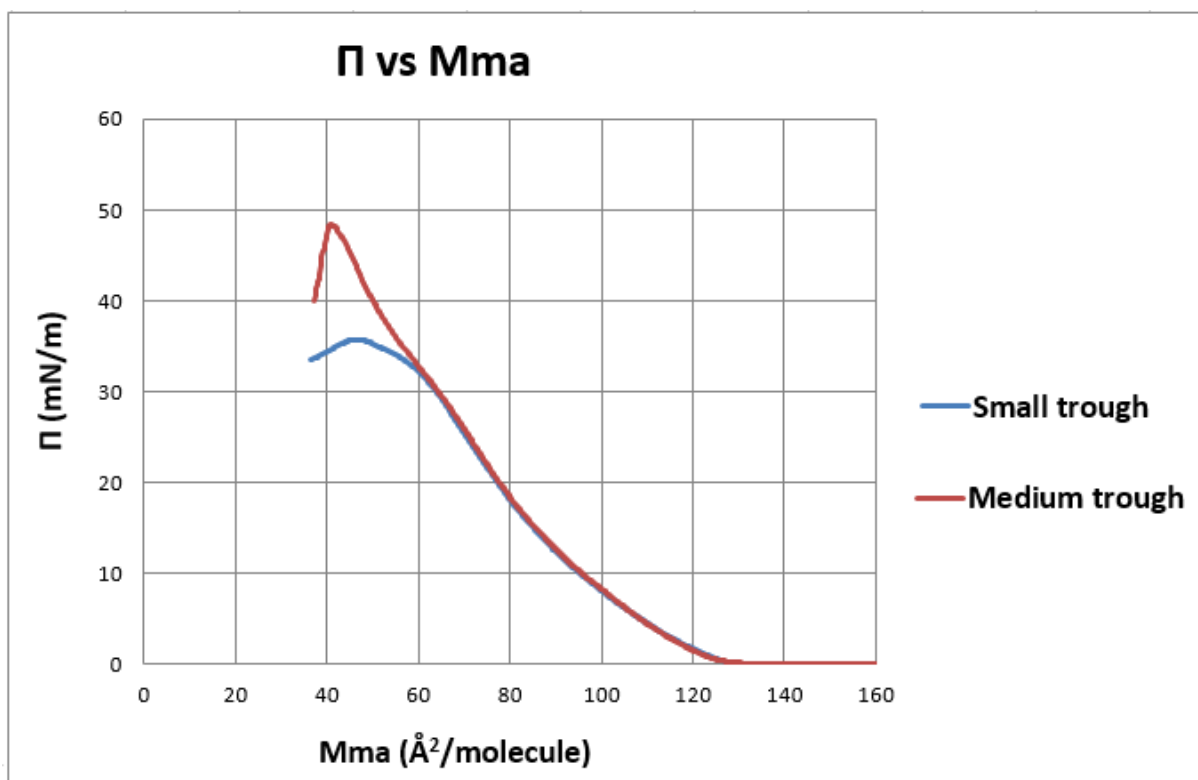


Figure 50. Monolayer phases of a Π -Mma isotherm measured for DPPC in PBS at 37°C.

The previous figures show that the onset of the LE-LC transition plateau occurred at a Π value ~ 6 mN/m at 21°C, whereas at 37°C it occurred at a Π value ~ 35 mN/m. Thus, higher subphase temperature favoured the existence of expanded films. As the physiologically relevant Π range is confined to between ~ 45 to ~ 70 mN/m in normal healthy lungs, a DPPC monolayer would only be expected to exist in the LC and S phase in the alveoli. The premature collapse observed in this study at 37°C suggests that 1) the achievement of a high collapse Π was greatly compromised and 2) collapse probably occurred in the LE or LE-LC transition plateau. This may be explained by 1) monolayers tend to become more unstable (collapse faster) as the temperature is raised, 2) the high compressibility commonly associated with phase transitions facilitates a more rapid monolayer collapse (Goerke and Gonzales, 1981) and 3) monolayers in the LE phase typically collapse near the Π_e (Baoukina et al., 2014) which for DPPC is $\sim 40 - 45$ mN/m at physiological temperatures (Veldhuizen et al., 1998, Chou and Chang, 2000, Piknova et al., 2002). There are studies, however, that show that DPPC is capable of reaching near zero γ values at 37°C (Crane et al., 1999, Duncan and Larson, 2008). Thus, leakage problems could have also played a role in the premature collapse of DPPC at 37°C described here. In fact, and as previously mentioned in section 2.4.2.1 the potential for leakage is greatest

at high subphase temperatures (Zuo et al., 2008c, Duncan and Larson, 2008) probably due to an increase in the thermal motion of the molecules (Yun et al., 2003). In order to investigate this, a DPPC isotherm was measured at 37°C in a medium trough that had a surface area approximately three times that of a small trough when the barriers were fully open (238 cm² and 76 cm² respectively), as it was expected that proportionally, the amount of surfactant lost from the interface would be lower in a medium trough compared to a small trough. The reason for this is that surfactant is mostly lost onto the barriers, trough side walls and Wilhelmy plate during a compression experiment as shown by Goerke and Gonzales, 1981. The size of the barriers used in a medium and small trough were the same, as was the Wilhelmy plate. Additionally, the perimeter of the small trough was 49 cm, whereas the perimeter of the medium trough was 87.8 cm, i.e. 1.79 times the perimeter of a small trough. However, the area was 3 times bigger. Hence, the amount of surfactant lost from the interface would be proportionally lower in a medium trough compared to a small trough. The results of these experiments are shown in Figure 51. The DPPC mass deposited when using a medium trough was three times that of the mass deposited when using a small trough to reflect the increased surface area. DPPC was compressed at a barrier speed of 10 mm/min (7.5 cm²/min) in the medium trough, i.e., three times the barrier speed used in a small trough to keep the compression rate per DPPC molecule constant. The subphase used was PBS.



Trough	Surface area (cm ²)	DPPC mass (μg)	Barrier speed (cm ² /min)	Collapse Π (mN/m)
Small	76	6	2.5	35.73
Medium	238	17	7.5	48.37

Figure 51. Effect of the trough size/surface area, small (76 cm²) or medium (238 cm²), on the Π -Mma isotherm measured for DPPC in PBS at 37°C. The table shows the area of the trough, the DPPC mass deposited, the barrier speed and the collapse Π . n = 5 experiments for small trough and n = 3 experiments for medium trough.

As can be seen in Figure 51, the isotherm reached a higher collapse Π in a medium trough (48.37 mN/m) compared to a smaller trough (35.73 mN/m), which was an indication of lower surfactant leakage in the medium trough. The collapse Π however was still low as DPPC was not capable of reaching near zero γ values. As the first experiments for this study were performed in a small trough, for comparative purposes, it was decided to use this size in all the following experiments.

Finally, Table 18 (below) shows the lift-off Mma, C_m , collapse Π and collapse Mma of the Π -Mma isotherms. The corresponding values in each of these parameters for subphase

temperature of 37°C were compared with those for subphase temperature of 21°C (control) by calculating the % difference between experiment and control for each of the parameters and dividing them by the reference % change from midpoint values, i.e., assuming similar levels of uncertainties on the parameters to those of the reference isotherms (see section 2.4.1.5). Due to the fact that the isotherm measured at 37°C was shorter than that measured at 21°C, the C_m was calculated for the isotherm regions 1-5, 10-25 and 31 mN/m – lowest collapse *II*.

Table 18. Effect of subphase temperature, 37°C or 21°C, on the lift-off Mma, C_m , collapse Π and collapse Mma of the Π -Mma isotherms measured for DPPC in PBS. As the isotherm measured at 37°C was shorter than that measured at 21°C, the C_m was calculated for the isotherm regions 1-5, 10-25 and 31 mN/m – lowest collapse Π . The corresponding values for subphase temperature of 37°C were compared with those for subphase temperature of 21°C (control) by calculating the difference in each of the parameters for the experimental isotherm and the control expressed as a % of the control value and dividing them by the reference % change from midpoint values for the relevant reference isotherm (Table 11). This approach assumes similar levels of uncertainties on the control and experimental isotherm parameters to those of the reference isotherm parameters.

Temperature (°C)	Lift-off Mma (Å ² /molecule)	(% difference experiment and control)/(reference % change from midpoint)	C_m 1-5 mN/m (mN/m) ⁻¹	(% difference experiment and control)/(reference % change from midpoint)	C_m 10-25 mN/m (mN/m) ⁻¹	(% difference experiment and control)/(reference % change from midpoint)
<i>Reference isotherm</i>	123	1.0 (% change from midpoint)	0.0298	3.0 (% change from midpoint)	0.0150	2.0 (% change from midpoint)
21 (control)	100		0.0341		0.0185	
37	123	23.0	0.0319	2.0	0.0158	7.5

Temperature (°C)	C_m 31 mN/m – lowest collapse Π (mN/m) ⁻¹	(% difference experiment and control)/(reference % change from midpoint)	Collapse Π (mN/m)	(% difference experiment and control)/(reference % change from midpoint)	Collapse Mma (Å ² /molecule)	(% difference experiment and control)/(reference % change from midpoint)
<i>Reference isotherm</i>	0.0294	15.0 (% change from midpoint)	39.40	2.0 (% change from midpoint)	49	4.0 (% change from midpoint)
21 (control)	0.0068		56.50		31	
37	0.0358	28.4	40.50	14.0	43	9.8

Table 18 shows that working at 37°C resulted in a markedly different isotherm compared to that of the control isotherm, performed at 21°C, being different for all measured parameters. The parameter that was most significantly affected by an increase in the subphase temperature was the C_m for the region 31 mN/m – lowest collapse II followed by the collapse II . The lift-off M_{ma} at 21°C and 37°C was 100 and 123 Å²/molecule respectively. Thus, subphase temperature increased the lift-off M_{ma} . C_m was higher at 21°C for the regions 1-5 and 10-25, whereas the C_m was higher at 37°C for the region 31 mN/m – lowest collapse II . C_m values for all the regions of the isotherm measured at 37°C were between 0.02-0.1 (mN/m)⁻¹. This indicates that the isotherm was not in a condensed state. In addition, the C_m for the region 41 to 45 mN/m of the isotherm measured in a medium trough at 37°C was calculated. This value was 0.01 (mN/m)⁻¹. Thus, when the DPPC II - M_{ma} isotherm was measured in a medium trough in PBS at 37°C it was in LC state past the II_e . Finally, the collapse II decreased significantly with increasing subphase temperature going from 56.50 mN/m at 21°C to 40.50 mN/m at 37°C. The collapse M_{ma} increased with subphase temperature rising from 31 Å²/molecule at 21°C to 43 Å²/molecule at 37°C.

Exogenous lung surfactant has previously been tested at a subphase temperature of 20°C (Bringezu et al., 2002, Zhang et al., 2011b), 24°C (Zuo et al., 2008b), 25°C (Stuart et al., 2006), 30°C (Ding et al., 2001) and 37°C (Lu et al., 2003, Zuo et al., 2005, Zuo et al., 2006). The results of the present work indicated that subphase temperature had a significant effect on the isotherm and it was chosen to work primarily with a temperature of 37°C as it is body temperature and thus more physiologically relevant. However, as in the literature most of the experiments are performed at a temperature of ~ 20°C, which may be due to the fact that working at 37°C has multiple technical problems such as subphase evaporation or thermal disequilibrium between the air, liquid and solid support (Cruz et al., 2004), in the present studies, experiments were additionally performed at 21°C, primarily for comparative purposes, but also because a LC phase was only found in the isotherm measured at 21°C and not in that measured at 37°C, which would provide further information.

2.4.2.4 Effect of relative humidity on the DPPC isotherm

Figure 52 shows the effect of relative humidity on the DPPC *II*-Mma isotherm. The isotherms were measured at ambient relative humidity ($\sim 45\%$) and high relative humidity ($> 87\%$) in PBS at 37°C . A high relative humidity was generated by placing the trough in a chamber that was perfectly sealed. When working at 37°C , the evaporation of the subphase led to an increase in the ambient relative humidity to values above 87% . The DPPC mass deposited for each experiment was $6\ \mu\text{g}$. Table 19 shows the lift-off Mma, C_m , collapse *II* and collapse Mma of the *II*-Mma isotherms. The corresponding values in each of these parameters for high relative humidity were compared with those for ambient relative humidity (control) by calculating the % difference between experiment and control for each of the parameters and dividing them by the reference % change from midpoint values, i.e., assuming similar levels of uncertainties on the parameters to those of the reference isotherms (see section 2.4.1.5).

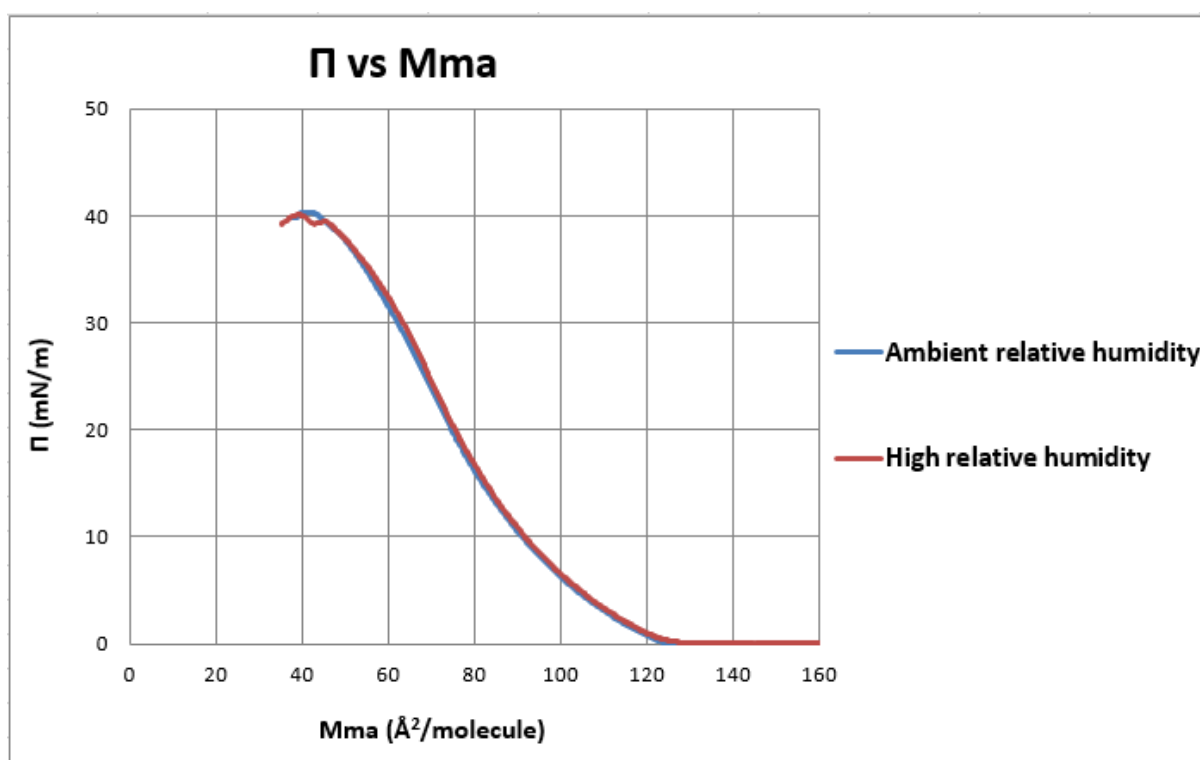


Figure 52. Effect of relative humidity, ambient ($\sim 45\%$) or high ($> 87\%$), on the *II*-Mma isotherm, measured for DPPC in PBS at 37°C . The DPPC mass deposited for each experiment was $6\ \mu\text{g}$. $n = 5$ experiments for ambient relative humidity and $n = 4$ experiments for high relative humidity.

Table 19. Effect of relative humidity, ambient (~ 45%) or high (> 87%), on the lift-off M_{ma} , C_m , collapse Π and collapse M_{ma} of the Π - M_{ma} isotherms measured for DPPC in PBS at 37°C. The corresponding values in each of these parameters for high relative humidity were compared with those for ambient relative humidity (control) by calculating the difference in each of the parameters for the experimental isotherm and the control expressed as a % of the control value and dividing them by the reference % change from midpoint values for the relevant reference isotherm (Table 11). This approach assumes similar levels of uncertainties on the control and experimental isotherm parameters to those of the reference isotherm parameters.

Relative humidity (%)	Lift-off M_{ma} ($\text{\AA}^2/\text{molecule}$)	(% difference experiment and control)/(reference % change from midpoint)	C_m 1-5 mN/m (mN/m^{-1})	(% difference experiment and control)/(reference % change from midpoint)	C_m 10-25 mN/m (mN/m^{-1})	(% difference experiment and control)/(reference % change from midpoint)
<i>Reference isotherm</i>	123	1.0 (% change from midpoint)	0.0298	3.0 (% change from midpoint)	0.0150	2.0 (% change from midpoint)
~ 45 (ambient, control)	123		0.0326		0.0165	
> 87 (high)	123	0.0	0.0323	0.3	0.0161	1.0

Relative humidity (%)	C_m 31 mN/m – lowest collapse Π (mN/m^{-1})	(% difference experiment and control)/(reference % change from midpoint)	Collapse Π (mN/m)	(% difference experiment and control)/(reference % change from midpoint)	Collapse M_{ma} ($\text{\AA}^2/\text{molecule}$)	(% difference experiment and control)/(reference % change from midpoint)
<i>Reference isotherm</i>	0.0294	15.0 (% change from midpoint)	39.40	2.0 (% change from midpoint)	49	4.0 (% change from midpoint)
~ 45 (ambient, control)	0.0292		40.59		41	
> 87 (high)	0.0314	0.5	40.03	0.5	39	1.3

Table 19 shows that a high relative humidity only slightly affected the collapse M_{ma} compared to the control. As such, it was concluded that a relative humidity above 87% did not have an appreciable effect on the DPPC isotherm compared to an ambient relative humidity. As such, all the subsequent experiments were measured at ambient relative humidity.

In the literature, the effect of humidity is poorly understood (Zuo et al., 2005). Some studies have reported that high relative humidity increases the minimum γ reached during the compression of a DPPC monolayer at 37°C (Wildeboer-Venema, 1980, Zuo et al., 2006). Other studies have shown that DPPC films at 37°C can reach very low γ at a high relative humidity under certain conditions such as a low subphase pH but prevents the attainment of zero γ at subphase pH between 6.5 and 8.0. (Colacicco et al., 1976). Zuo et al., 2005 showed that 100% relative humidity impaired the surfactant adsorption kinetics to the air/liquid interface, although this is not relevant for the present work as this surfactant property was not studied. Exogenous lung surfactant properties have been investigated at both room relative humidity (Zuo et al., 2008a, Zhang et al., 2011b) and physiological relative humidity (100%) (Colacicco et al., 1976, Wildeboer-Venema, 1980, Zuo et al., 2005).

2.4.2.5 Effect of subphase volume on the DPPC isotherm

Figure 53 shows the effect of subphase volume on the DPPC Π - M_{ma} isotherm. The isotherms were measured in PBS at a temperature of 21°C. The subphase volumes used were 62 mL (normal volume) and 50 mL (low volume). The DPPC mass deposited was higher for the low subphase volume (11 μg) compared to the normal subphase volume (7 μg). Table 20 shows the lift-off M_{ma} , C_m , collapse Π and collapse M_{ma} of the Π - M_{ma} isotherms. The corresponding values in each of these parameters for low subphase volume were compared with those for normal subphase volume (control) by calculating the % difference between experiment and control for each of the parameters and dividing them by the reference % change from midpoint values, i.e., assuming similar levels of uncertainties on the parameters to those of the reference isotherms (see section 2.4.1.5).

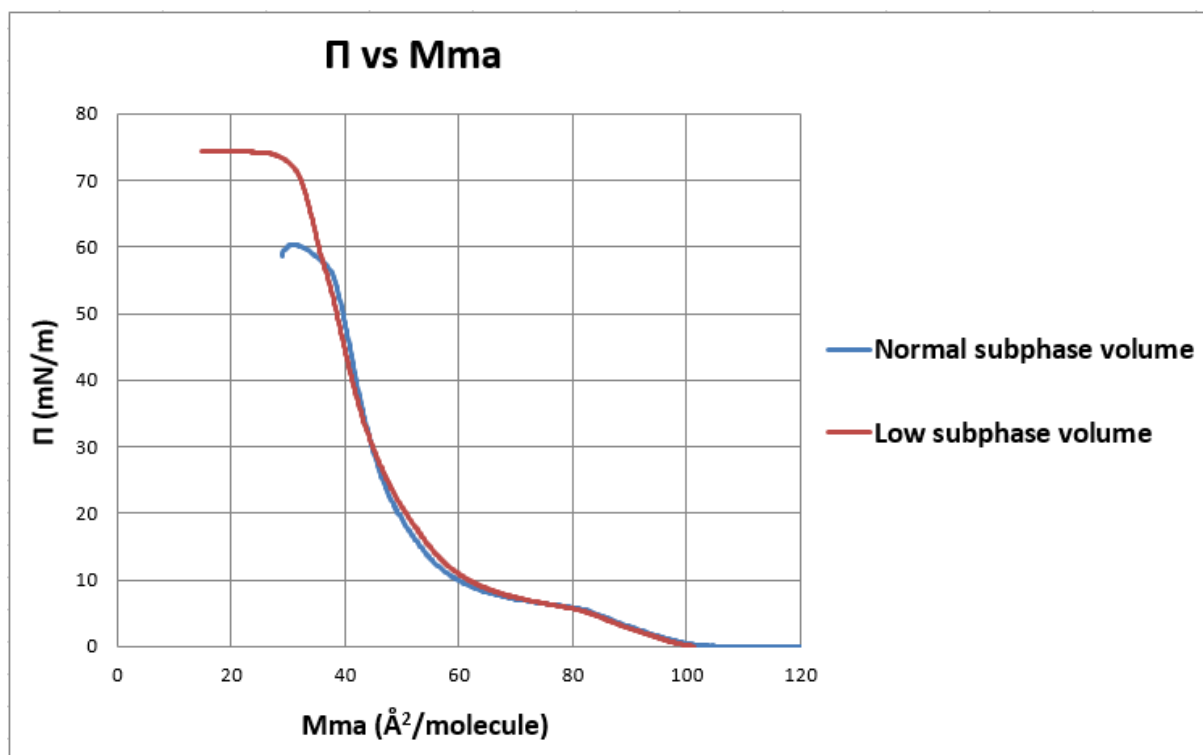


Figure 53. Effect of subphase volume, normal (62 mL) or low (50 mL), on the Π - M_{ma} isotherm measured for DPPC in PBS at 21°C. The DPPC mass deposited was 11 μg for the low subphase volume and 7 μg for the normal subphase volume. $n = 3$ experiments/condition.

Table 20. Effect of subphase volume, normal (62 mL) or low (50 mL), on the lift-off M_{ma} , C_m , collapse Π and collapse M_{ma} of the Π - M_{ma} isotherms measured for DPPC in PBS at 21°C. The corresponding values in each of these parameters for low subphase volume were compared with those for normal subphase volume (control) by calculating the difference in each of the parameters for the experimental isotherm and the control expressed as a % of the control value and dividing them by the reference % change from midpoint values for the relevant reference isotherm (Table 12). This approach assumes similar levels of uncertainties on the control and experimental isotherm parameters to those of the reference isotherm parameters.

Subphase volume (mL)	Lift-off M_{ma} ($\text{\AA}^2/\text{molecule}$)	(% difference experiment and control)/(reference % change from midpoint)	C_m 1-5 mN/m (mN/m) ⁻¹	(% difference experiment and control)/(reference % change from midpoint)	C_m 5-10 mN/m (mN/m) ⁻¹	(% difference experiment and control)/(reference % change from midpoint)
<i>Reference isotherm</i>	100	2.0 (% change from midpoint)	0.0378	3.0 (% change from midpoint)	0.0636	9.0 (% change from midpoint)
62 (normal, control)	100		0.0348		0.0680	
50 (low)	101	0.5	0.0348	0.0	0.0586	1.6

Subphase volume (mL)	C_m 25-45 mN/m (mN/m) ⁻¹	(% difference experiment and control)/(reference % change from midpoint)	C_m 50 mN/m – lowest collapse Π (mN/m) ⁻¹	(% difference experiment and control)/(reference % change from midpoint)	Collapse Π (mN/m)	(% difference experiment and control)/(reference % change from midpoint)	Collapse M_{ma} ($\text{\AA}^2/\text{molecule}$)	(% difference experiment and control)/(reference % change from midpoint)
<i>Reference isotherm</i>	0.0063	6.0 (% change from midpoint)	0.0247	36.0 (% change from midpoint)	57.17	2.0 (% change from midpoint)	31	5.0 (% change from midpoint)
62 (normal, control)	0.0062		0.0262		60.41		31	
50 (low)	0.0082	5.3	0.0084	1.9	74.39	11.5	17	9.0

As can be seen from Table 20, a low subphase volume did not affect the lift-off M_{ma} and the C_m for the region 1-5 compared to the control. It however affected all the other parameters and most significantly the collapse Π followed by the collapse M_{ma} . The C_m for the regions 5-10 and 50-lowest collapse Π was higher for the normal subphase volume, whereas the C_m for the region 25-45 was higher for the low subphase volume. It is important to bear in mind that these differences might have been caused by the fact that the DPPC mass deposited in each experiment was different (and thus, the lift-off area of each isotherm was different and with it, the compression rate per DPPC molecule, see section 2.4.1.6). Moreover, at normal subphase volume collapse Π was 60.41 mN/m, whereas at low subphase volume collapse Π was 74.39 mN/m. This means that the γ was reduced to near zero values when reducing the subphase volume from 62 to 50 mL. It is believed that this was caused by an improvement in the film containment within the trough area as the probability of losing material onto the sides of the trough by trough overflow was reduced. In fact, this isotherm was very similar to that measured by the manufacturer using a ribbon trough (KSV-Nima, 2012) and others shown in the literature in which near zero γ values were reached (Zhang et al., 2011a, Zhang et al., 2011b). The γ value of 74.39 mN/m is higher than that of water at 20°C which is ~ 72.8 mN/m (Vargaftik et al., 1983, Pallas and Harrison, 1990). The γ of PBS at 20°C is not known. However, there is evidence that an increase in the electrolyte concentration or the presence of salts such as NaCl increases the γ of water (Liu et al., 2009, Zhang and Carloni, 2012). On the other hand, collapse M_{ma} increased in relation to the subphase volume from 17 Å²/molecule at low subphase volume to 31 Å²/molecule at normal subphase volume. Moreover, the pattern of collapse was different for each isotherm: when working at normal subphase volume the isotherm collapse occurred as a decrease in Π , whereas at low subphase volume collapse was seen as a horizontal break. This might have been related to the monolayer phase where this process occurred. The C_m for the last part of the isotherm for normal subphase volume was 0.03 (mN/m)⁻¹. The C_m for the region 60-74 mN/m for low subphase volume was 0.01 (mN/m)⁻¹. Thus, at normal subphase volume, collapse occurred in the LE phase, whereas at low subphase volume, collapse occurred in the LC phase.

To date, there are no data in the literature about the effect of subphase volume on the DPPC isotherm. Normal subphase volume (62 mL) was used to measure DPPC Π - M_{ma} isotherms in the first set of experiments of the present work and in order to be coherent, all the following experiments were performed in the same way. LB monolayer deposition experiments at Π

values below 40 mN/m were also performed at normal subphase volumes, however, to enable the production of LB monolayers at higher Π values low subphase volumes were used.

2.5 Summary discussion and conclusion

In this research, DPPC Π -Mma isotherms were systematically described in terms of four different characteristics of the curve: the lift-off Mma, the two-dimensional compressibility (C_m) of different regions of the isotherm, the collapse Π and the collapse Mma.

A LWB system is a very sensitive apparatus and factors such as the presence of impurities in the DPPC solution or on the subphase, material loss after spreading from solution or barrier leakage problems could lead to very different Π -Mma isotherms. In these experiments, it was decided that a Mma of $\pm 1 \text{ \AA}^2/\text{molecule}$ between experiments performed under the same conditions was acceptable; values outside of this were considered to reflect artefacts and were rejected. Thus, here, and in the following chapters, repeated measurements of Π -Mma isotherms were performed under each set of experimental conditions investigated, using a minimum of three experiments per condition wherever possible, where the isotherms had a lift-off Mma that only deviated by $\pm 1 \text{ \AA}^2/\text{molecule}$. If the deviation was greater than this, more experiments were performed until the desired criteria were met. The isotherms that satisfied the criteria were then used to calculate an average isotherm.

An accurate lift-off Mma for the DPPC isotherm measured in water at 21°C was calculated by determining the concentration of a DPPC solution using an enzymatic-colorimetric assay and dividing the lift-off area of the isotherm by the number of DPPC molecules deposited onto the subphase, assuming that all the DPPC material remained at the air/liquid interface. This value was 99 $\text{\AA}^2/\text{molecule}$. The lift-off Mma was also determined for the DPPC isotherm measured in PBS at 21°C and in water and PBS at 37°C using the same DPPC solution of known concentration. These values were 100, 112 and 123 $\text{\AA}^2/\text{molecule}$ respectively. As the lift-off Mma was a unique value for each set of experimental conditions, an equation to calculate the DPPC mass deposited onto the subphase was developed based on the aforementioned lift-off Mma values and the lift-off area of the isotherm. If the DPPC mass deposited was known, it was possible to calculate the concentration of any new DPPC solution prepared by derivation from Equation 15.

Typically in the literature results for similar studies are presented without an associated indication of the uncertainty/variability and consequently comparisons between isotherms for different experimental conditions are discussed in a broadly qualitative manner rather than quantitatively. As such, it was considered important in the present work to try to adopt a more quantitative approach. To address these issues it was decided to determine values representing the variability on DPPC isotherm parameters for the two most common set of experimental conditions used in this work (PBS at 21°C and 37°C) and assume that the levels of variability seen would be indicative of those for the other experiments for which direct derivation of variability on isotherm parameters was not undertaken. To do this, isotherms were measured for the aforementioned two reference conditions until five good isotherms each were recorded using the rejection criteria described above. For each set of five isotherms, the average, SD, RSD and % change from midpoint in the lift-off M_{ma} , C_m , collapse II and collapse M_{ma} were calculated. The RSD values showed that at 21°C, the C_m for the region 50-lowest collapse II had the highest variability whereas at 37°C the highest variability was found in the C_m for the region 31-lowest collapse II . These reference % change from midpoint values for subphase temperatures of 21°C and 37°C were used in the later experiments to compare an experimental isotherm with its associated control isotherm in a quantitative and consistent way for all experiments. For this, the % difference between experiment and control was calculated for each isotherm parameter and divided by the reference % change from midpoint value for the relevant reference isotherm. If the ratio was greater than 1, then this suggested that those experimental conditions affected the profile of the isotherm for that parameter when compared to the control. The greater the ratio between the two values the more potentially significant this difference was, especially for values above 3.

Isotherms with different lift-off areas were also studied as this was a relevant issue to take into account in future experiments. The lift-off area is the point at which surface tension starts to decrease and also represents the area under which the isotherm will be measured. Changes in experimental conditions or the deposition of different DPPC masses can result in the shifting of the lift-off area to higher or lower area values. In this study, three different DPPC masses were deposited and the isotherms measured. As expected, the lift-off area increased with DPPC mass. For higher lift-off areas, as the barrier speed was constant, the compression rate per DPPC molecule was lower. In this particular case, increasing the DPPC mass content (and thus decreasing the compression rate per DPPC molecule) affected the C_m of the isotherm, decreased

the collapse Π and increased the collapse M_{ma} . It is therefore clearly important for any set of experiments to use similar DPPC masses.

Finally, DPPC was tested under different relevant quasi-physiological conditions in order to understand how each of these factors affected the DPPC isotherm compared to those obtained under more common experimental conditions, and to set up the most relevant experimental conditions to work with in future experiments. Five different variables were tested: barrier speed, subphase composition, subphase temperature, relative humidity and subphase volume.

- **Barrier speed:** in the present studies, barrier speeds of 5, 40, 90 and 270 mm/min were tested and it was found that barrier speed significantly affected the collapse Π value of the DPPC isotherm, which increased with barrier speed, and the collapse M_{ma} , which decreased with barrier speed. The higher the barrier speed, the higher the energy available to push the tails of the DPPC molecule into a vertical position (Jyoti et al., 1996); the area per molecule over which compression occurred increased and as a result, a higher collapse Π was reached at a lower collapse M_{ma} . It is necessary to be cautious when talking about collapse Π , though. The collapse Π reached at a barrier speed of 5 mm/min was 57.20 mN/m but there is evidence that DPPC is capable of reaching near zero γ on compression with a LWB (Smith and Berg, 1980, Zhang et al., 2011b). This low collapse Π was probably caused by surfactant leakage problems, which cannot be ignored when interpreting results. If these experiments had been performed in a system where no leakage occurred, it is postulated that the collapse Π value would have been the same for any barrier speed and thus, barrier speed would have had very little effect on the DPPC isotherm, as other studies have shown (Nag et al., 1991, Jyoti et al., 1996). However, even if barrier speed had no effect on the shape of the isotherm, there is evidence in the literature that the compression rate has an effect on the size (Nag et al., 1991) and shape (Klopfer and Vanderlick, 1996, Blanchette et al., 2008) of the LE and LC domains of a DPPC monolayer. A LWB system requires low barrier speeds and for this reason, a barrier speed of 5 mm/min (2.5 cm²/min) was chosen in all the experiments in the present studies when performed in a small trough (unless otherwise specified). This cycle rate does not simulate the inhalation-exhalation cycle of breathing as it is significantly slower but was a necessary, practical limitation.
- **Subphase composition:** in the literature, both saline solutions and water have been used to study exogenous lung surfactant. Here, it was discovered that measuring a DPPC isotherm

in PBS instead of water (control) had an effect on the C_m for the regions 5-10 and 25-45 and the collapse M_{ma} . Particularly, for the isotherm measured in PBS, the C_m for the region 5-10 and collapse M_{ma} was lower than the control whereas the C_m for the region 25-45 was higher than the control. The parameter that was most significantly affected by the PBS subphase was the C_m for the region 25-45. Moreover, when working at 37°C the subphase composition also had an effect on the lift-off M_{ma} . Thus, PBS was the subphase composition used in all the subsequent experiments of this study as it is more physiologically relevant.

- **Subphase temperature:** both 21°C and 37°C were tested and it was found that subphase temperature had a significant effect on all the measured parameters of the isotherm. The lift-off M_{ma} increased with temperature. C_m was higher at 21°C for the regions 1-5 and 10-25 whereas C_m was higher at 37°C for the region 31 mN/m – lowest collapse Π . Taking into account experimental values of C_m for the DPPC monolayer phases from the literature (i.e. 0.02-0.1 (mN/m)⁻¹ for LE films, 0.004-0.01 (mN/m)⁻¹ for LC films and < 0.004 (mN/m)⁻¹ for S films (Kodama et al., 2004, Vitovič et al., 2006)), the whole isotherm at 37°C was in an expanded state. It was however possible to reach a LC phase past the Π_e by measuring the isotherm in a medium trough where proportionally less surfactant material was lost due to leakage problems associated with the LWB. Moreover, the collapse Π decreased significantly from 56.50 mN/m at 21°C to 40.50 mN/m at 37°C whereas the collapse M_{ma} increased with subphase temperature. The achievement of a high collapse Π at 37°C was greatly compromised as monolayers tend to become more unstable as the temperature is raised but also due to the aforementioned leakage problems. As the physiologically relevant Π range is confined to between ~ 45 to ~ 70 mN/m, a DPPC monolayer would only exist in the LC and S phase in the alveoli. From these experiments it was concluded that the preferred subphase temperature to work with was 37°C as it is body temperature and thus more physiologically relevant. In the present studies, experiments were additionally performed at 21°C primarily for comparative purposes, but also because a LC phase was only found in the isotherm measured at 21°C and not in that measured at 37°C when working with a small trough, which was the size used in these experiments.
- **Relative humidity:** In the literature, the effect of humidity is poorly understood. In the present studies, ambient (~ 45%) and high (> 87%) relative humidity were tested and it was

found that relative humidity did not have an appreciable effect on the DPPC isotherm. As such, all the subsequent experiments were measured at ambient relative humidity.

- **Subphase volume:** decreasing the subphase volume from 62 mL (normal volume) to 50 mL (low volume) had an effect on C_m for the regions 5-10, 25-45 and 50-lowest collapse II . This however might have been caused by the fact that the DPPC mass deposited was different for each experiment. Collapse II followed by the collapse M_{ma} were the parameters most significantly affected by the subphase volume. Collapse M_{ma} increased in relation to the subphase volume whereas collapse II decreased with subphase volume. At low subphase volume, collapse II was 74.39 mN/m and thus, γ was reduced to near zero values. It is believed that this was caused by an improvement in the film containment within the trough area. The pattern of collapse was also different for each isotherm and this might have been related to the monolayer phase where it occurred: at normal subphase volume the isotherm collapse occurred as a decrease in II , whereas at low subphase volume collapse was seen as a horizontal break. To date, there are no data in the literature about the effect of subphase volume on the DPPC isotherm. In this study, normal subphase volume (62 mL) was used to measure DPPC II - M_{ma} isotherms. LB monolayer deposition experiments at II values below 40 mN/m were also performed at normal subphase volumes, however, to enable the production of LB monolayers at higher II values low subphase volumes were used.

CHAPTER 3 – STUDY OF HOW THE METHOD OF DEPOSITION OF CeO₂ NANOPARTICLES AFFECTS THE BEHAVIOUR OF A DPPC MONOLAYER

3.1 Rationale

Several studies have recently been performed using a LWB to study the effects of NPs on the properties of lung surfactant films at an air/liquid interface. The conditions by which the NPs were applied to the surfactant have varied significantly. For example, in one study hydrophobic NPs were suspended in a volatile solvent and deposited onto a preformed surfactant monolayer at the air/liquid interface using a microsyringe (Guzmán et al., 2011), whereas in other studies, the NPs were mixed with the surfactant in the same volatile solvent prior to being deposited onto a clean liquid subphase using a microsyringe (Stuart et al., 2006, Harishchandra et al., 2010, Tatur and Badia, 2011, Fan et al., 2011, Dwivedi et al., 2014). In other studies using hydrophilic NPs, these were suspended in the subphase solution and the surfactant monolayer was subsequently deposited onto this NP-containing subphase solution (Guzmán et al., 2011, Guzmán et al., 2012a, Guzmán et al., 2012b, Guzmán et al., 2012c, Guzmán et al., 2013).

The main mechanism for deposition of inhaled airborne NPs is diffusion. In this type of deposition particles move randomly due to the collision with gas molecules surrounding the medium. This is known as Brownian motion which increases with decreasing particle size (see section 1.4.2.2). Aerosol NP deposition onto the alveolar region will be spatially uniform (Bahk and Isawa, 1994). Once deposited, it is expected that NPs will not be able to interact with each other because of the large inter-particle distances. In fact, particles tend to interact with the fluids, cells and tissues while being retained in the alveolar region (Sturm, 2010). Using NP suspensions as described above may not be representative of *in vivo* deposition of inhaled NPs and might lead to processes that are unlikely to occur during inhaled NP exposures *in vivo*. For example:

- Suspending NPs in liquids is likely to change the size and surface chemistry of the NPs. For example, there might be increased NP agglomeration due to the surface charge the NPs acquire in the suspending medium. Moreover, the surface of the NPs may contain impurities from the dispersed liquid which could affect the θ at the air-liquid-solid interface and in turn affect the behaviour of the NPs at the interface (Roth et al., 2004, Messing et al., 2009, Maestro et al., 2010).
- Using premixed suspensions of NPs and surfactant presumes that interactions between NPs and surfactant occur in solution and not at the air/liquid interface. Coating the NPs with surfactant could also modify the surface chemistry of the NPs and, with it, the θ at the air-liquid-solid interface (Maestro et al., 2012, Maestro et al., 2015).
- There is evidence that after depositing particles onto an air/liquid interface the evaporation of the spreading solvent causes attraction between the particles, leading to the formation of particle agglomerates prior to the compression of the monolayer (Huang et al., 2001a, Huang et al., 2001b).

In the literature there are studies where cultured lung cells were grown at an air/liquid interface and exposed to either aerosolised NPs or NPs suspended in the tissue culture medium. These studies found that the impact of NPs on the cells was different for each deposition method. The use of NP suspensions applied directly to cell cultures was not considered a realistic exposure method. For example, Holder et al., 2008 exposed human bronchial epithelial cells to aerosolised diesel exhaust particles at the air/liquid interface and to suspensions of collected particles. Exposure to aerosolised particles caused a slight decrease in cell viability and induced IL-8 secretion, which was a similar response to the conventional particle suspension exposure but at a quarter of the dose, suggesting that particles deposited by aerosol were significantly less toxic. However, they believed that this was caused by artefacts introduced during the collection and resuspension of particles for the conventional suspension exposure. Lenz et al., 2009 exposed a human alveolar epithelial-like cell line (A549) to aerosolised and liquid suspended ZnO NPs. They found a dose-response change, showing significant differences in mRNA expression of pro-inflammatory and oxidative stress markers when comparing between exposure methods. Xie et al., 2012 exposed mouse alveolar type II epithelial cells (C10) to aerosolised and suspended ZnO NPs. Results showed that different patterns of oxidative stress over 24 hours were observed in the two exposure methods. A relatively small and transient

increase in oxidative stress was observed in those cells exposed to aerosolised ZnO NPs. In contrast, a robust increase, more than tenfold, in oxidative stress two hours post exposure was observed in those cells exposed to suspended ZnO NPs. This suggested that the toxicity of aerosolised ZnO NPs originated from direct interactions of cellular structures with the intact NP or with locally dissolved Zn^{2+} at the contact site of the NP with the cell respectively. Although these are cellular studies, they indicate the significance of the method of delivery to the bioreactivity of the NPs with biological interfaces. These studies suggest that to determine the effect of NPs on lung surfactant the most relevant results would be those generated using aerosolised NPs. Thus one aim of the work in this chapter was to compare the impact of aerosolised NPs with that of the same NPs applied using the other methods described above.

3.2 Introduction

To date, there are a limited number of studies that have investigated the effects of ENPs on the physicochemical properties of lung surfactant. A detailed description of some of the studies that have investigated NP and lung surfactant interactions using DPPC or other more complex lung surfactant preparations such as those obtained from animal sources is shown in sections 3.2.1 and 3.2.2. This introduction also contains relevant information on CeO_2 NPs focusing on their properties, structures and uses, exposure data and health effects, included in section 3.2.3.

3.2.1 Literature studies that have investigated the interactions between lung surfactant and NPs with the aid of a spreading solvent

3.2.1.1 Literature studies that have investigated the interactions between DPPC and NPs with the aid of a spreading solvent

In the literature, most of the studies that have investigated the interactions between DPPC and NPs using a LWB system delivered the NPs onto the air/liquid interface with the aid of a spreading solvent. Details of the most relevant studies are shown in Table 21.

Study 1: Carbon black (CB) NPs 15-20 nm in diameter (primary particle size) were suspended in chloroform (no information on agglomerate size was provided) and deposited onto a preformed DPPC monolayer at DPPC/NP w/w ratios 10/1, 2/1 and 1/3. The subphase used was water at 22°C and isotherms were recorded during one compression. Results showed that the isotherm shifted to higher areas per DPPC molecule with NP mass deposited. The authors believed this was caused by a penetration of the NPs into the lipid layer and the reduction of

the available area per DPPC molecule which favoured an earlier molecular packing at the interface. NPs did not affect the LE-LC transition plateau. It was assumed that the compression led to the packing of the DPPC molecules around the NPs without affecting the reorientation of the lipid molecules. In fact, BAM images showed that NPs did not affect the nucleation of the LC domains. NPs however increased the C_m of the monolayer at Π values above ~ 10 mN/m and decreased the collapse Π value. This was attributed to the cohesive interactions between DPPC molecules and NPs at the interface which reduced the relative packing density of DPPC. It is suggested that the NPs were irreversibly attached at the interface and that there was no loss of NP material into the subphase with compression, although this was not proven.

Study 2: The purpose of this study was to investigate if pulmonary NP delivery was a possible route of administration for drugs. Two different gelatin based NPs with an average agglomerate diameter of 187 nm and 313 nm were mixed with DPPC in chloroform at DPPC/NP w/w ratios 18/1, 12/1 and 6/1 for the smaller size and 21/1, 11/1 and 7/1 for the larger size. The mixtures were deposited onto a clean water subphase and the isotherm recorded during one compression. Results showed that as the NP content increased the isotherm shifted to larger areas per DPPC molecule. The increase in area showed a linear correlation with the increase in NP content for Π values up to 40 mN/m which indicated an accumulation of the NPs at the interface with no significant squeeze out of the larger particles from the monofilm into the subphase. The LE-LC transition plateau obscured with NP mass i.e. the plateau became less horizontal with increase in mass deposited. These effects were slightly more pronounced for the larger NP size. The collapse Π was slightly lower than that of pure DPPC (~ 54 mN/m) with an average collapse Π value of ~ 52 mN/m for the 187 nm NP and ~ 53 mN/m for the 313 nm NP which meant that the NPs did not destabilise the monolayer. This was an important finding because a concentration-dependent reduction in the collapse Π would have limited the dose of inhalable NPs. Moreover, it was concluded that inhalation of NPs was a feasible route for drug delivery.

Study 3: Polyorganosiloxane NPs 22 nm in diameter (primary particle size) were mixed with DPPC in chloroform/methanol solution at DPPC/NP w/w ratios 10/1, 1/1, 0.5/1, 0.1/1. No information on agglomerate size was provided. The mixtures were deposited onto a clean water subphase at 20°C and the isotherms recorded during one compression. Results showed that with increasing NP content, isotherms slightly shifted to larger molecular areas and the LE-LC transition plateau gradually disappeared. A discontinuity in the isotherm was seen at a Π value of ~ 25 mN/m which was attributed to the squeeze out of material into the subphase. This effect

was greater the higher the NP content. It was concluded that NPs were coated by lipids thus becoming an integral part of the monolayer and had an effect on the surfactant function during film compression.

Study 4: Pure DPPC (99.9-99.5 mol %) and alkylated gold NPs 2 nm in diameter (primary particle size) were mixed in chloroform (0.1-0.5 mol %). No information on particle agglomerate size was provided. The mixtures were deposited onto a clean water subphase at 20°C and the isotherms recorded during one compression. Results showed that the addition of up to 0.2 mol % of NPs did not affect the isotherm. At NP concentrations above 0.3 mol %, the isotherm shifted to higher mean molecular areas especially at $\sim \Pi$ above 5 mN/m. The LE-LC transition plateau became shorter and less horizontal. At higher Π values a ‘rollover’ in the slope of the isotherm appeared, which the authors believed was caused by a wrinkling of aggregated NPs in the monolayer. Moreover, the addition of 0.2 mol % of NPs altered the nucleation, growth and morphology of the condensed domains visualised by BAM and AFM. From these results, the authors concluded that the NPs had an impact on the biophysical properties of the surfactant monolayer.

Study 5: Two different polyorganosiloxane NPs with an average agglomerate diameter of 12 nm and 136 nm were mixed with DPPC (1 mg/mL) in chloroform/methanol solution at concentrations 1, 10, 20, 50 and 100 $\mu\text{g/mL}$ for both sizes. The number of NPs in the case of 12 nm NPs was 1,000 times greater than that of the 136 nm NPs. These mixtures were then sonicated and deposited onto a buffered subphase at 20°C and the isotherm recorded during one compression. Results showed that in the presence of 12 nm NPs no change in the isotherm occurred for any of the NP masses deposited. Epifluorescence microscopy showed however that NPs caused disruption of the domain morphology of the LE phase. In the presence of 136 nm NPs the isotherm shifted to higher areas per DPPC molecule and the LE-LC transition plateau became shorter and less horizontal. C_m values were calculated in the LC phase for the 136 nm NPs and increased with the NP mass deposited. Fewer numbers of 136 nm NPs had a much more structural and functional damaging effect than the comparatively higher number of 12 nm NPs.

Study 6: Short (1,100 nm length) and long (2,100 nm length) multiwalled carbon nanotubes (SMWCNTs and LMWCNTs respectively) of 25 and 26 nm in diameter respectively (primary size) were mixed with DPPC in chloroform at DPPC/NP w/w ratios 50/1, 20/1, 2/1 and 1/1 for

the SMWCNTs and 50/1 and 1/1 for the LMWCNTs. The mixtures were then sonicated for 10 minutes and deposited onto a water subphase at 20°C and the isotherm recorded during one compression. Results showed that for the SMWCNTs the isotherm shifted to higher mean molecular areas with NP content. At 1/1 ratio however the shift reduced due to the aggregation of the SMWCNTs. SMWCNTs did not affect the LE-LC transition plateau but reduced the collapse *II*. Particularly for the 20/1 and 1/1 mass ratio there was a significant concentration-dependant reduction linked to the reduced relative packing density of the DPPC as more SMWCNTs were incorporated into the film. The LMWCNTs also shifted the isotherm to higher mean molecular areas but the LE-LC transition plateau was lost, causing more disruption than the SMWCNTs. Hence, changes in the DPPC isotherm were found to be MWCNT length-dependent.

Table 21. Literature studies on DPPC and nanoparticle interactions at the air/liquid interface using a LWB and some of their most relevant characteristics. In these studies nanoparticles were delivered onto the air/liquid interface with the aid of a spreading solvent as described.

Study	References	NP	NP size (nm)	Subphase/ Temperature	NP suspension deposition method/Solvent	Summary of the results
1	Guzmán et al., 2011	Carbon black	15-20 (primary particle size)	Water, 22°C	Deposition method 1/ Chloroform	NPs shifted the isotherm to higher areas with NP content, did not affect the LE-LC transition plateau, increased the C_m of the monolayer at Π values above ~ 10 mN/m and decreased the collapse Π
2	Stuart et al., 2006	Gelatin	2 sizes: 187 and 313 (agglomerate size)	Water, room temperature	Deposition method 2/ Chloroform	NPs shifted the isotherm to higher areas with NP content for Π values up to 40 mN/m. The LE-LC transition plateau obscured with NP mass. These effects were slightly more pronounced for the larger NP size. The collapse Π value was slightly lower than that of pure DPPC
3	Harishchandra et al., 2010	Polyorganosiloxane	22 (primary particle size)	Water, 20°C	Deposition method 2/ Chloroform/methanol	NPs slightly shifted the isotherm to higher areas with NP content and the LE-LC transition plateau gradually disappeared. A discontinuity in the isotherm was seen at a Π value of ~ 25 mN/m
4	Tatur and Badia, 2011	Alkylated gold	2 ± 0.5 (primary particle size)	Water, 20°C	Deposition method 2/ Chloroform	The addition of up to 0.2 mol % of NPs did not affect the isotherm but altered the nucleation, growth and morphology of the condensed domains. At NP concentrations above 0.3 mol %, the isotherm shifted to higher areas especially at $\sim \Pi$ above 5 mN/m. The LE-LC transition plateau became less horizontal. At higher Π values a ‘rollover’ in the slope of the isotherm appeared
5	Dwivedi et al., 2014	Polyorganosiloxane	2 sizes: 12 and 136 (agglomerate size)	Buffered subphase, 20°C	Deposition method 2/ Chloroform/methanol	In the presence of 12 nm NPs no change in the isotherm occurred for any of the NP mass deposited but caused disruption of the domain morphology of the LE phase. In the presence of 136 nm NPs the isotherm shifted to higher areas and the LE-LC transition plateau became less horizontal. C_m increased with the NP mass deposited. Fewer numbers of 136 nm NPs had a much more damaging effect than the comparatively higher number of 12 nm NPs
6	Melbourne et al., 2015	Short and long multiwalled carbon nanotubes (SMWCNT and LMWCNT)	Short: length 1,100, diameter 25 ± 0.7 Long: length 2,100, diameter 26 ± 0.6 (primary size)	Water, $\sim 20^\circ\text{C}$	Deposition method 2/ Chloroform	SMWCNTs shifted the isotherm to higher areas with NP content. At 1/1 ratio however the shift reduced due to the aggregation of the SMWCNTs. SMWCNTs reduced the collapse Π . The LMWCNTs shifted the isotherm to higher areas and removed the LE-LC transition plateau, causing more disruption than the SMWCNTs

3.2.1.2 Literature studies that have investigated the interactions between lung surfactant models other than DPPC and NPs with the aid of a spreading solvent

In view of the highly complex and dynamic nature of the natural lung surfactant film, other studies have investigated lung surfactant and NP interactions using lung surfactant models other than DPPC. For example, Guzmán et al., 2012a studied DOPC and mixtures of DOPC and DPPC in the presence of hydrophilic silica NPs and found that NPs incorporated into the lipid monolayer and affected the phase behaviour of the lipid system and the formation of domains due to an increase in the structural disorder of the monolayer and the modification of the miscibility between the two lipid components. This effect was also observed in previous studies for DPPC alone. Guzmán et al., 2012c investigated the interactions between mixtures of DPPC and palmitic acid and hydrophilic silica NPs and found that NPs incorporated into the lipid monolayer, hindering the ordering of the monolayer and affecting the phase behaviour as well as modifying the quasi-equilibrium dilational elasticity. Similar results were found by Guzmán et al., 2013 who investigated the interactions between cholesterol and mixtures of cholesterol and DPPC and hydrophilic silica NPs: NPs incorporated into the lipid monolayer and modified the cohesive interactions of lipid components, subsequently affecting the phase behaviour and structural properties of the monolayer. Tatur and Badia, 2011 on the other side investigated both DPPC and Survanta and showed that the presence of hydrophobic alkylated gold NPs in amounts that did not influence the isotherm altered the nucleation, growth and morphology of the condensed domains in monolayers of DPPC but not of those of Survanta. Fan et al., 2011 studied the effect of hydroxyapatite NPs on Infasurf and found a time-dependant inhibitory effect of NPs on the lung surfactant function due to the protein adsorption onto the NPs. Sachan et al., 2012 investigated the effects of hydrophobic polyorganosiloxane NPs on a mixture of DPPC, DPPG and SP-C and found that NPs did not significantly destabilise the film and up to a certain concentration did not affect the structural properties and functioning of the film, but however, more dramatic effects were seen at higher NP concentrations. NPs selectively partitioned at lower surface pressures in the fluid phase of the film and interacted with surface-associated structures at higher surface pressures; this interaction could possibly affect the regeneration of the surfactant. NPs were also unable to translocate into the subphase due to their interactions with the surfactant components.

3.2.2 Literature studies that have investigated the interactions between lung surfactant and NPs by depositing NPs in aerosol form

To date, there are no studies of NP deposition onto a surfactant monolayer in aerosol form using a LWB. The only published study that has investigated *in vitro* inhaled NP and lung surfactant interactions at the air/liquid interface by depositing NPs in aerosol form, Valle et al., 2015, used a novel methodology called the constrained drop surfactometer (CDS). In this study, the biophysical influence of airborne carbonaceous NMs (CNMs) on Infasurf was investigated. The CNMs investigated were MWCNTs with a length of 1-5 μm and diameter of 30 ± 15 nm and graphene nanoplatelets (GNPs) with a sheet length of 5 μm and a thickness of 6-8 nm. Their aerosol aerodynamic diameter was less than 2.5 μm and most particles were in the submicron range (300-500 nm). The CNM aerosol concentrations used were comparable to those defined in international occupational exposure limits (OELs), as opposed to the large NP concentrations typically used with LWBs when depositing NPs from liquid suspensions. The CDS was capable of simulating respiration by the compression and expansion of the interface at quick cycle rates and the achievement of near zero γ values by no more than a 20% variation in surface area. The Π range studied was from ~ 40 to ~ 70 mN/m. This device also minimised the hysteresis area loop by gradually increasing the γ during expansion. The subphase temperature used was 37°C and the relative humidity 85%. The CDS also allowed the film to be transferred to a solid substrate for visualisation of the interface.

Results showed that for both CNMs, increasing the aerosol concentration increased the minimum γ and increased the hysteresis area loop which suggests that CNMs induced a concentration-dependent surfactant inhibition. The compression isotherms shifted to lower areas per molecule with increasing aerosol concentration. This characteristic has also been observed in other studies that have investigated lung surfactant models that contained surfactant proteins (Harishchandra et al., 2010, Fan et al., 2011, Hu et al., 2013, Dwivedi et al., 2014, Valle et al., 2014); as opposed to those that used DPPC or other mixtures without the presence of surfactant proteins in which the isotherm shifted to higher molecular areas with NP mass deposited. This suggests that surfactant proteins may have an important role in NP-lung surfactant interactions. AFM images showed that this inhibition was caused by the adsorption of the airborne CNMs onto the surfactant film, which disturbed its morphology and structure. The aggregate size was within the aerosol size range suggesting limited agglomeration of the NPs upon deposition. This study also demonstrates that NP doses that would not affect lung

surfactant properties when deposited from liquid suspensions do have an effect when deposited by aerosol.

3.2.3 CeO₂ nanoparticles

3.2.3.1 Properties, structure and uses of CeO₂ nanoparticles

Cerium (Ce) is a lanthanide metal and a member of the rare earth metals. The level of cerium in the crust of the earth is estimated to be 20-60 ppm (Casseo et al., 2011). It is very reactive and a strong oxidising agent: it rapidly oxidises when in contact with oxygen. It also absorbs ultraviolet (UV) radiation strongly. The most common form of cerium is as cerium (IV) oxide (CeO₂) also known as cerium dioxide or ceria. It is a yellow-white powder with molar mass of 172.115 g/mol and density 7.215 g/cm³. CeO₂ is a hydrophobic material due to its electronic structure. The 4f orbitals of rare-earth atoms are shielded by the full octet electrons (5s² p⁶) which inhibit polar interactions with interfacial water molecules (Azimi et al., 2013). CeO₂ has a fluorite structure (Figure 54) which consists of a simple cubic oxygen sub-lattice with the cerium ions occupying alternate cube centres. The oxygen - oxygen distance is 2.705 Å which is half the lattice parameter. The oxygen ions have a formal charge of -2. The cerium ions have a formal charge of +4.

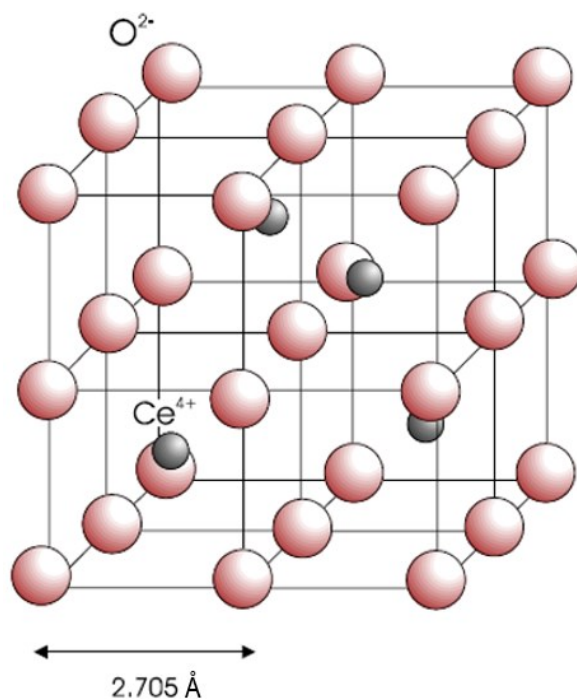


Figure 54. Illustration of the fluorite structure of a unit cell of CeO₂ (Vyas, 2005).

CeO₂ is a commonly manufactured ENP, being one of the 14 reference ENMs on the OECD list (Bouwmeester et al., 2011). It has a wide range of applications, including coating surfaces due to its UV-filtering properties and hardness, and as a polishing material for glass mirrors, plate glass or television tubes. One important use is as a diesel fuel additive due to its surface reactive properties. CeO₂ NPs have been commercially used as a diesel additive since 1999 (Cassee et al., 2011, Yokel et al., 2014). Envirox™, for example, is the trade name of a cerium based diesel fuel additive currently used in the United Kingdom. It acts as an oxygen-donating catalyst that increases fuel combustion efficiency and therefore reduces the emission of unburned hydrocarbons, soot and nitrogen oxides (NO_x), which are converted to harmless gases, as well as reducing the fuel consumption by 5 - 8% (Park et al., 2008).

3.2.3.2 CeO₂ nanoparticle exposure data

The use of CeO₂ NPs, especially as a diesel additive, has led to ongoing human exposure. Despite efficiently reducing the emissions of PM, a small amount of CeO₂ is emitted in the exhaust in the particulate phase. The most likely route of exposure is through inhalation (Cassee et al., 2011). Park et al., 2008, estimated potential future exposures to CeO₂ NPs based on data from modelling studies. Two models developed under contract for the European Commission, COPERT (Computer Programme to calculate Emissions from Road Traffic) and TRENDS (Transport and Environmental Database System), were used to estimate future CeO₂ exposure levels based on various scenarios for the future use of CeO₂ additives in vehicles in Europe, using baseline statistical data from the Eurostat database New Cronos in the TRENDS model. Based on these projections it was estimated that the exposure of the EU urban population to CeO₂ in 2020 would be in the range 0.2-2.9 g/capita/year (best and worst case scenario respectively). These emission estimates were used to derive atmospheric concentrations in urban environments and thus lung depositions. The Aristotle University of Thessaloniki also performed a modelling study for a street canyon and based on the worst-case scenario of CeO₂ atmospheric concentration levels of 80 ng/m³, they predicted a pulmonary retention dose of 30,000 ng over 20 year exposure (7h/day, 7 days/week) (Park et al., 2008).

Estimates of lung deposition of CeO₂ have also been made based on measurement data. Envirox™ was introduced into the diesel fuel used to supply all the buses operated in Newcastle by the bus company Stagecoach during 2005. Cerium levels in airborne particulates were measured at an airborne monitoring site adjacent to the route where the buses using Envirox™ passed. Park et al., 2008 used a validated computer model and the measured airborne cerium

levels to estimate the dose of cerium that would be retained in the lungs, which was calculated and predicted to be 230 ng over a period of 20 years (7h/day, 7 days/week).

3.2.3.3 Health effects of CeO₂ nanoparticles

Until recently, there has been little exploration of the potential health effects of CeO₂ NPs on humans. Indications of potential adverse effects of CeO₂ NPs exposures are primarily gathered from *in vitro* studies; there are limited *in vivo* studies in the literature on acute, sub-chronic or chronic inhalation exposure to CeO₂ NPs. Moreover, most studies are performed on microscale, and not nanoscale, CeO₂ particles. Finally, studies differ in terms of particle size used, concentration, duration and end-point measures (Cassee et al., 2011, Yokel et al., 2014). Thus, there is still much to discover regarding human exposure to CeO₂ NPs and possible adverse effects. In the following study, nano-CeO₂ has been used to address the working hypothesis.

3.3 Hypothesis

We hypothesised that the method by which CeO₂ NPs are deposited on/introduced to a DPPC monolayer located at the air/liquid interface would differentially affect the nature and profile of the DPPC isotherm. We further hypothesised that the effects of CeO₂ NPs on the DPPC isotherm would be mass-dependant and modified by the subphase temperature.

Specific aims:

- To examine whether the method used to deliver CeO₂ NPs to a DPPC surfactant monolayer differentially affected surfactant function as measured using a LWB.
- To develop an exposure system to deposit CeO₂ NPs by aerosol onto a DPPC surfactant monolayer and to compare the results with delivery using liquid suspensions: 1) CeO₂ NPs alone suspended in a volatile solvent and deposited onto a preformed DPPC surfactant monolayer or 2) CeO₂ NPs mixed with the surfactant in a volatile solvent prior to being deposited onto a liquid subphase. These two liquid deposition methods will be referred to as deposition method 1 and deposition method 2, respectively. The deposition of CeO₂ NPs by aerosol onto a DPPC surfactant monolayer will be referred to as deposition method 3.

3.4 Methodology

3.4.1 Reagents and materials

For reagents and materials, see section 2.3.1.

Additional information for this chapter: cerium dioxide (CeO_2) NPs (nominal size < 25 nm determined by BET, manufacturer's data) were purchased from Sigma-Aldrich. CeO_2 NPs were weighed using a Sartorius M-power balance with a resolution of 0.1 mg. Suspensions of CeO_2 NPs in chloroform were sonicated in an ultrasonic water bath (Ultrawave Ltd, model number F0001602). CeO_2 NP samples were collected onto transmission electron microscopy (TEM) grids (300-mesh copper with carbon support film, purchased from Agar Scientific) for imaging purposes.

3.4.2 Cleaning of glassware

Glassware was cleaned as described previously (see section 2.3.2).

3.4.3 Deposition method 1: Liquid deposition of CeO_2 nanoparticles

3.4.3.1 Preparation of CeO_2 nanoparticle suspensions and samples

CeO_2 NPs were suspended in chloroform to form stock solutions with a concentration of 0.5 mg/mL and stored in PTFE bottles at -20°C until use. Suspensions were sonicated for 30 minutes in the ultrasonic water bath before use. A drop of the CeO_2 NP suspension was deposited with a glass pipette onto a TEM grid and air-dried for imaging purposes.

3.4.3.2 Nanoparticle characterisation pre- CeO_2 nanoparticle administration

3.4.3.2.1 Size and zeta potential of CeO_2 nanoparticles

NPs are usually not a perfect sphere and size is reported as the diameter of a sphere that is equivalent in the selected property to the particle measured. Primary particle size and agglomerate size were determined by TEM, using a JEOL 3000F microscope. TEM images were analysed using the software Image J and the diameter obtained was the diameter of a sphere with the same projected surface area as the particle under examination. The NP size distribution was described using the count median diameter (CMD) and the geometric standard deviation (GSD). The CMD and the GSD are the two parameters that describe a lognormal distribution (Kulkarni et al., 2011). The CMD is the median of a lognormal distribution. The GSD indicates the spread of values within the distribution and thus, the degree of polydispersity.

GSD is always greater than 1. A value of ≤ 1.3 indicates a monodisperse distribution whereas a value >1.3 indicates a polydisperse distribution. TEM images were taken by Dr. Kerstin Jurkschat from the Oxford Materials Characterisation Service, University of Oxford. Particle agglomerate size in dispersion was also determined by DLS using a Zetasizer Nano (Malvern Instruments) and described by the Z-average diameter as recommended by the manufacturer. The Z-average diameter is a hydrodynamic diameter i.e., the diameter of a sphere that moves through a liquid medium with the same speed as the particle under examination. A good agreement between sizes measured by TEM and DLS can only be obtained for stable, monodisperse, single crystals and spheres. Deviation from these criteria will lead to variability in the measured sizes (Baalousha et al., 2012a).

Zeta potential was determined using a Zetasizer Nano (Malvern Instruments). Measurements were performed using a disposable capillary cell for aqueous suspensions and a dip cell for non-aqueous suspensions as recommended by the manufacturer. Along with the zeta potential measurements, the pH of the solution was measured using a S20 SevenEasy® pH meter by Mettler Toledo.

3.4.3.2.2 Wettability and surface tension activity of CeO₂ nanoparticles

Particle hydrophobicity or wettability was determined qualitatively by the capacity of the NPs to remain at the air/liquid interface as the θ at the air-liquid-solid interface was not measured in this study. To visualise the NPs at the interface, a dipping experiment was performed by compressing the interface to the smallest area technically feasible and subsequently vertically passing a previously submerged mica sheet through the interface using a LWB. The film was analysed using two techniques:

a) Time of Flight – Secondary Ion Mass Spectrometry (ToF-SIMS): Chemical identification of the monolayer components was determined using an IONTOF ToF-SIMSV instrument. Images were analysed using the software SurfaceLab 6. ToF-SIMS images were taken with the help of Dr. Sarah Fearn from the Department of Materials, Faculty of Engineering, Imperial College London.

b) Scanning Electron Microscopy (SEM): Imaging of the monolayer was performed using a Hitachi S-3400N microscope. SEM images were analysed using the software image J.

The surface tension activity of the NPs was determined by depositing the NPs onto a clean PBS subphase at 21°C and subsequently measuring the Π -A isotherm during the compression of the interface to the smallest area technically feasible using a LWB.

3.4.3.3 CeO₂ nanoparticle deposition

CeO₂ NP suspensions were deposited onto a preformed DPPC monolayer located at the air/liquid interface, using a microsyringe. The trough was left undisturbed for 15 minutes to allow complete evaporation of the solvent. Experiments were performed in PBS at 37°C and 21°C.

3.4.4 Deposition method 2: Liquid deposition of mixtures of CeO₂ nanoparticles and DPPC

3.4.4.1 Preparation of CeO₂ nanoparticle and DPPC suspensions and samples

CeO₂ NPs and DPPC were mixed in chloroform to form stock suspensions with different CeO₂/DPPC mass concentration ratios. Suspensions were stored in PTFE bottles at -20°C until use. A drop of the CeO₂/DPPC suspension was deposited using a glass pipette onto a TEM grid and air-dried for imaging purposes.

3.4.4.2 Nanoparticle characterisation pre-CeO₂ nanoparticle administration

The size, zeta potential, wettability and surface tension activity of the CeO₂ NPs were determined as described previously (see sections 3.4.3.2.1 and 3.4.3.2.2).

3.4.4.3 Deposition of CeO₂ nanoparticle and DPPC suspensions

CeO₂/DPPC suspensions in chloroform were first equilibrated to room temperature before use and deposited onto a clean liquid subphase using a microsyringe. The trough was left undisturbed for 15 minutes to allow complete evaporation of the solvent. Experiments were performed in PBS at 37°C and 21°C.

3.4.5 Deposition method 3: Deposition of CeO₂ nanoparticles in aerosol form

3.4.5.1 Aerosol exposure system

A novel aerosol exposure system was developed to deposit NPs in aerosol form onto the Langmuir trough. It consisted of three main components (Figure 55): a TSI[®] Constant Output

Atomiser (COA) Model 3076 that generated the aerosolised NPs, an exposure chamber containing the Langmuir trough and an airflow system that distributed the aerosolised NPs through the system. A Scanning Mobility Particle Sizer[®] (SMPS) Spectrometer (Classifier 3080, Differential Mobility Analyzer 3081, Condensation Particle Counter 3775, TSI[®]) sampled the aerosolised NPs within the exposure chamber. This aerosol exposure system was developed with the help of Dr. Alison Buckley. The exposure chamber was built by Mr Chris Gregory from Public Health England.

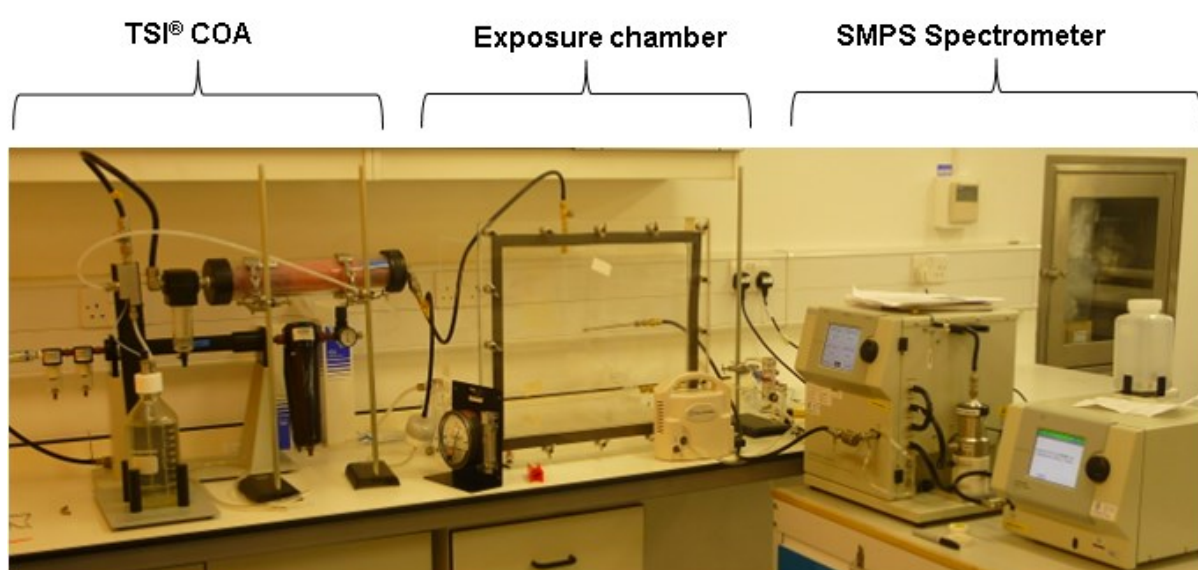


Figure 55. Illustration of the aerosol exposure system developed for the deposition of nanoparticles in aerosol form onto a Langmuir trough. It consisted of a TSI[®] Constant Output Atomiser (COA), an exposure chamber and an airflow system that distributed the aerosolised nanoparticles through the system. A Scanning Mobility Particle Sizer (SMPS) Spectrometer sampled the aerosolised nanoparticles within the exposure chamber.

a) TSI[®] COA Model 3076: This device generated aerosols of constant particle size by atomising a NP suspension. It was a collision-type atomiser (Figure 56). Compressed air was first cleaned by passing it through a filter and then entered an atomiser assembly block where it expanded to form a high-velocity jet. The pressure at which the compressed air entered the atomiser assembly block was regulated with a pressure control. The NP suspension was drawn from a glass bottle into the atomising section through a vertical passage and was then atomised by the high-velocity jet. Excess liquid was drained at the bottom of the atomiser assembly block back into the glass bottle. The aerosolised NPs coming out of the atomiser were still wet and had to be dried. This was done by passing the aerosol through a diffusion dryer which contained

silica gel that absorbed the water vapour as aerosol passed through. The aerosol was then expelled into the exposure chamber.

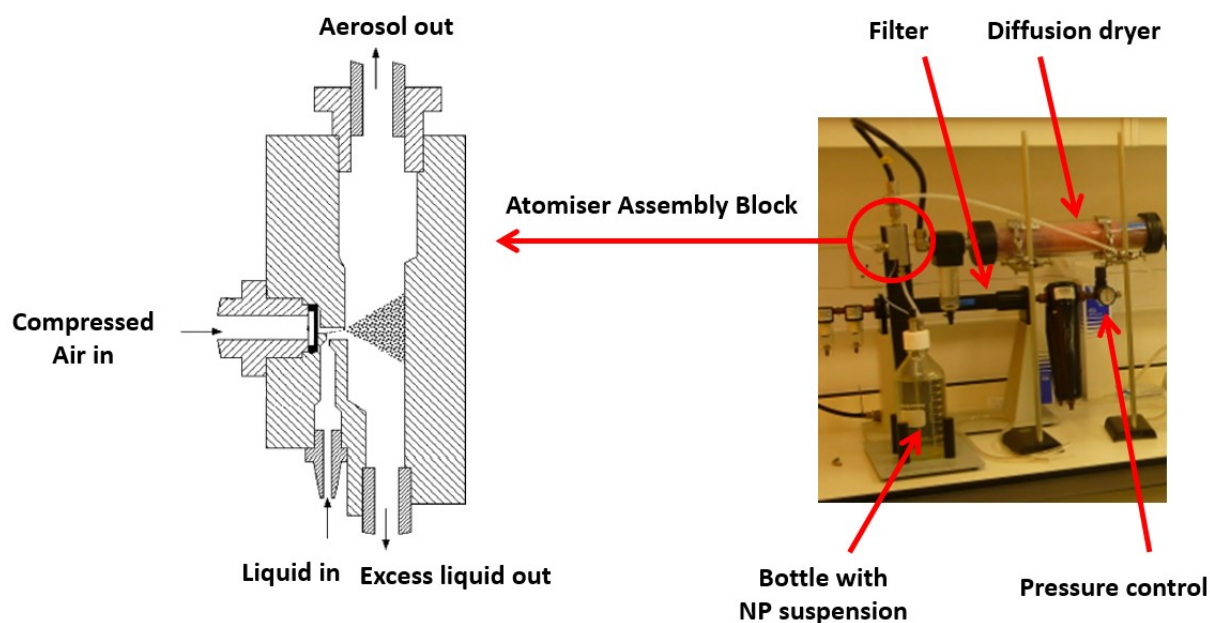


Figure 56. Illustration of the TSI® Constant Output Atomiser Model 3076 used to generate aerosolised nanoparticles and its different parts: air filter, pressure control, bottle with nanoparticle suspension, atomiser assembly block and diffusion dryer. Adapted from TSI, 2005.

b) Exposure chamber: The aerosol exposure chamber was made of acrylate with dimensions 48 (l) x 35 (w) x 40 (h) cm. The chamber was wrapped with a sticky transparent film for safety reasons. The chamber opened at the front and was sealed with gasket and 16 screws. It had a gas inlet connected to the TSI COA and four gas outlets to promote a homogeneous distribution of the aerosol within the chamber. The Langmuir trough was placed inside the chamber as shown in Figure 57.

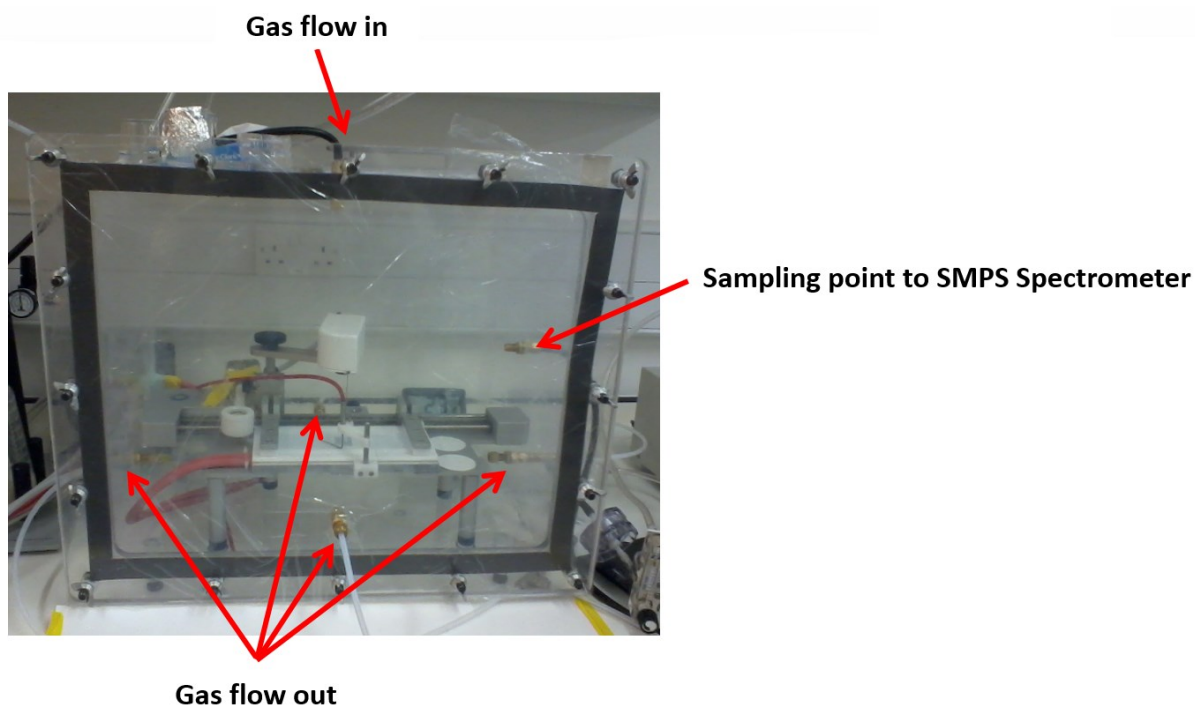


Figure 57. Illustration of the aerosol exposure chamber used to deposit nanoparticles in aerosol form onto a Langmuir trough. It had a gas inlet connected to the TSI COA and four gas outlets to promote a homogeneous distribution of the aerosol within the chamber.

c) Airflow system: Figure 58 shows a schematic diagram of the airflow system. The gas flow in was 3 litres per minute (lpm) which corresponded to 30 psig in the TSI COA pressure control. A pump preceded by an air filter and regulated by a chamber exhaust valve and a pump excess valve extracted air in order to achieve a slight negative pressure within the chamber of ~ -0.3 inch of water measured with a differential pressure meter. This avoided any leakage of aerosolised NPs if there was a crack in the chamber but did not affect the aerosol size distribution. There were 2 extra sampling points in the chamber: one to the SMPS Spectrometer which measured aerosol number concentration and aerosol mobility size distribution, and one to a pump that was pulling air through a filter membrane that was used to calculate the aerosol mass concentration.

Once the experiment was completed, the aerosol number concentration had to drop to near zero values before opening the exposure chamber. The TSI COA valve was closed and compressed air was circulated inside the chamber through a dilution gas valve while the pumps were still running. A negative pressure within the chamber was also maintained while the chamber was flushed with compressed air.

The tubing used in the airflow system was usually made of an electrically conductive material which reduced the loss of particles onto the walls of the tube due to static electricity.

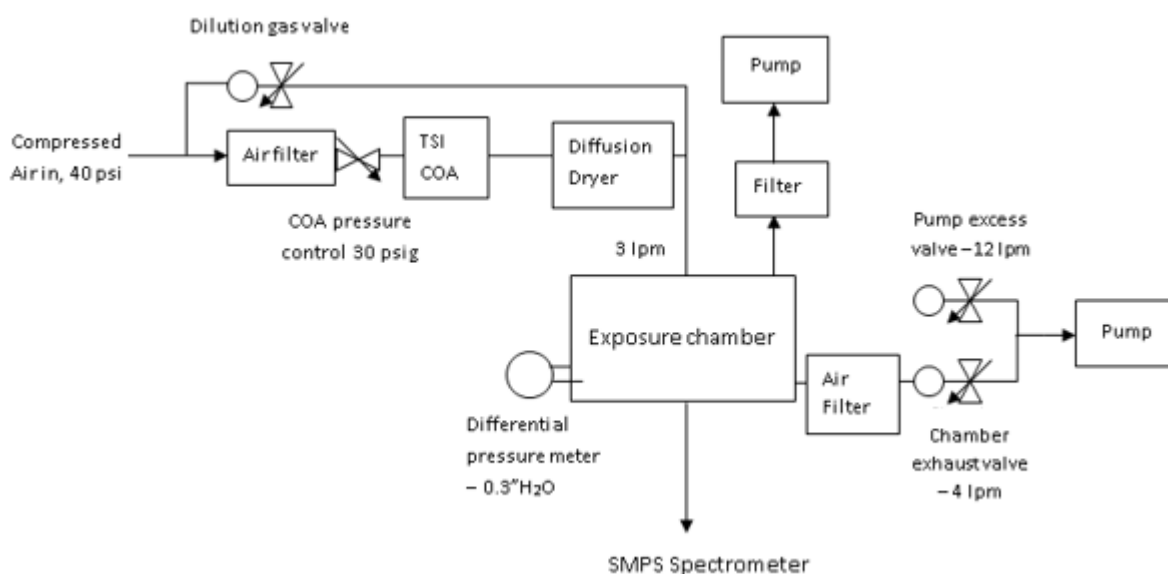


Figure 58. Schematic diagram of the airflow system that distributed the aerosolised nanoparticles through the aerosol exposure system.

3.4.5.2 Preparation of CeO₂ nanoparticle suspensions for the constant output atomiser and samples

CeO₂ NPs were suspended in ultrapure water to form stock suspensions with a concentration of 10 mg/mL and stored in the fridge in glass bottles with PP screw caps until use. Suspensions were sonicated for ~ 5 minutes in an ultrasonic water bath before use in the TSI COA. Samples of aerosolised CeO₂ NPs were collected onto TEM grids placed on a horizontal surface while performing an experiment, for later characterisation by TEM imaging.

3.4.5.3 Nanoparticle characterisation pre-CeO₂ nanoparticle administration

3.4.5.3.1 Size distribution and number concentration of aerosolised CeO₂ nanoparticles

The aerosol mobility size is the diameter of a sphere with unit charge that diffuses with the same speed as the particle under examination. The aerosol number concentration refers to the number of aerosol particles per unit volume of air. Aerosol mobility size distribution and number concentration were determined using an SMPS Spectrometer by TSI®. The SMPS Spectrometer was configured to measure multiple scans each of 3 minutes in length. The aerosol

NP size and number concentration were described by the average CMD and GSD and by the average number concentration respectively of all the scans run for that experiment. In some cases, the aerosol particle size distribution was plotted.

3.4.5.3.2 Mass concentration of aerosolised CeO₂ nanoparticles

Aerosol mass concentration refers to the mass of aerosol particles per unit volume of air. The density of the aerosol CeO₂ NP agglomerates was not known and, therefore, it was not possible to convert the number concentration into mass concentration using the aerosol size distribution data provided by the SMPS Spectrometer. Thus, the aerosol mass concentration was determined by sampling onto a filter membrane using a pump preceded by a flow meter as shown in Figure 59.

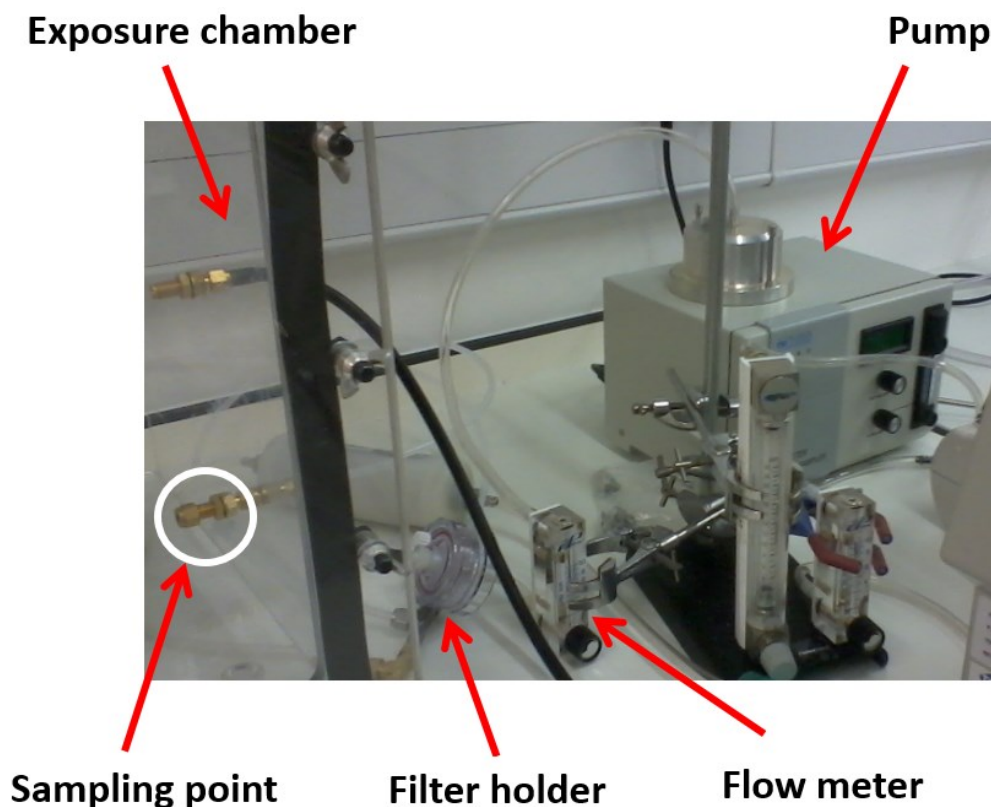


Figure 59. Illustration of the equipment used to sample aerosolised nanoparticles onto a filter membrane (located inside the filter holder) using a pump preceded by a flow meter. This equipment was used to determine the aerosol mass concentration within the chamber.

The aerosol mass concentration was calculated using the following equation:

$$mc = \frac{mfa - mfb}{sr \times t}$$

Equation 17

where mc is the aerosol mass concentration (ng/cm^3); mfa is the mass of the filter after being exposed to the aerosol (ng); mfb is the mass of the filter before being exposed to the aerosol (ng); sr is the sampling rate of the aerosol through the filter (ml/min) and t the exposure time (min)

The sampling rate of the aerosol through the filter (sr) was 1 lpm. PTFE filter membranes of 47 mm diameter were used (purchased from Pall Corporation). The filters were weighed using a Sartorius ultra-microbalance model SE2-F with a resolution of 0.1 μg which was calibrated before each weighing session. Before weighing the filter, the electrostatic charges were neutralised using a filter static charge neutraliser (Sartorius YIB01-0UR Ionizing Blower) by holding the filter in the ion stream of the blower for a few seconds. This operation was necessary as the presence of charge on the material being weighed builds up an electric field between the material and the non-moving parts of the balance. Electrostatic forces can interact with the lightweight mechanisms of the scale or provoke the movement of the material being weighed which may result in measurement inaccuracies (Gumkowski et al., 2014).

The alteration of the air temperature and/or humidity also affects the mass of the filters (Su et al., 2008). In order to determine the effect of these two parameters on the filter mass, a blank filter was continuously placed in an open petri dish inside a fume cupboard and next to the balance. The sample filter was conditioned in the fume cupboard for at least 24 hours before and after the aerosol exposure experiment so that both the blank and sample filter were weighed under the same temperature and humidity conditions. The sample filter was weighed before and after being exposed to the aerosol together with the blank filter. The aerosol mass deposited onto the sample filter was corrected as follows:

$$mf = (mfa - mfb) - (mfa_b - mfb_b) \quad \text{Equation 18}$$

where mf is the corrected aerosol mass deposited onto the sample filter; mfa is the mass of the sample filter after being exposed to the aerosol (ng); mfb is the mass of the filter before being exposed to the aerosol (ng); mfa_b is the mass of the blank filter after the aerosol exposure experiment (ng) and mfb_b is the mass of the blank filter before the aerosol exposure experiment (ng)

3.4.5.3.3 Determination of the aerosolised CeO₂ nanoparticle mass deposited onto a Langmuir trough

Aerosol deposition refers to the process by which aerosol particles deposit onto a surface. If you make the simplifying assumption of a constant aerosol in the chamber during any exposure (i.e. constant in mass concentration, number concentration and size distribution) that is also uniform throughout the chamber, then the aerosol mass deposited onto a Langmuir trough (mdt) can be derived using the following simplified equation:

$$mdt = mc \times dv \times t \times tarea \quad \text{Equation 19}$$

where mdt is the aerosol mass deposited onto a Langmuir trough (ng); mc is the aerosol mass concentration (ng/cm³); dv is the aerosol deposition velocity (cm/min); t is the exposure time (min) and $tarea$ is the area of the trough (cm²)

The **aerosol mass concentration** for each experiment was calculated as described previously in section 3.4.5.3.2.

The **trough area** refers to the available surface area when the barriers were fully open.

The **exposure time** refers to the duration the trough was exposed to the aerosol particles.

The **aerosol deposition velocity** is the ratio of deposition rate to air concentration. Because its unit is length per unit time, it represents an effective velocity. In the present studies, the deposition velocity was calculated using the following equation:

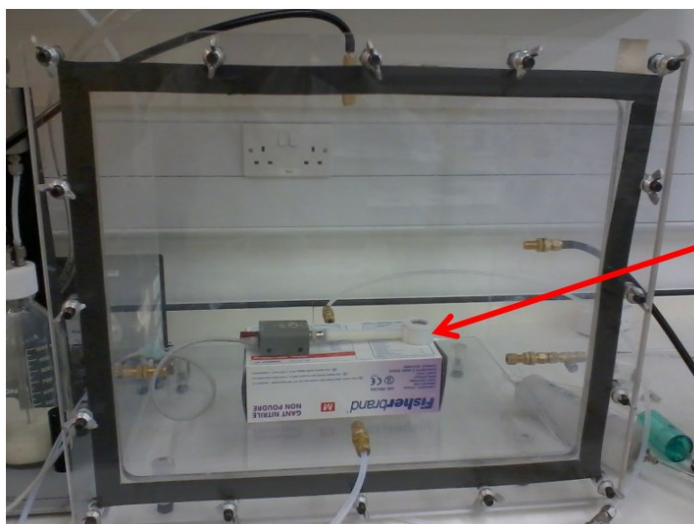
$$dv = \frac{mda}{mc \times t}$$

Equation 20

where dv is the aerosol deposition velocity (cm/min); mda is the total mass deposited per unit area over the exposure time (ng/cm²); mc is the aerosol mass concentration (ng/cm³) and t is the exposure time (min)

Neither mda nor dv for aerosolised CeO₂ NPs could be determined directly in each of the experiments performed in the presence of a DPPC monolayer. Thus, an average aerosol dv value was calculated by performing several experiments in the exposure chamber without the presence of a DPPC monolayer using Equation 20. Two different methods were employed to calculate mda : for the first set of experiments a quartz crystal microbalance (QCM) was used. As the QCM subsequently ceased to operate effectively, a method based on filter membranes was developed. mc was calculated as described previously in section 3.4.5.3.2. This average dv value was afterwards used to calculate mdt in each of the experiments performed in the presence of a DPPC monolayer using Equation 19.

a) Measurement of mda using a QCM: mda was directly measured using a QCM200 purchased from Stanford Research Systems. In this set of experiments (seven in total), the QCM was placed inside the exposure chamber at a similar height as the Langmuir trough as shown in Figure 60 so that the measurement of mda was as accurate as possible. The mda value was used to calculate a dv for aerosolised CeO₂ NPs in each of the seven experiments. The average dv of all the experiments was then used to determine mdt in the experiments performed in the presence of a DPPC monolayer at a subphase temperature of 37°C. Results are shown later in the chapter (section 3.5.3.1.1).



Quartz Crystal Microbalance

Figure 60. Illustration of the quartz crystal microbalance placed inside the exposure chamber at a similar height as the Langmuir trough and used to determine an average aerosol deposition velocity.

b) Measurement of *mda* using filter membranes: The filter membranes used were EMFAB[®] filters of 47 mm diameter (purchased from Pall Corporation). Six filters were placed onto the Langmuir trough together with four TEM grids for NP imaging purposes as shown in Figure 61.

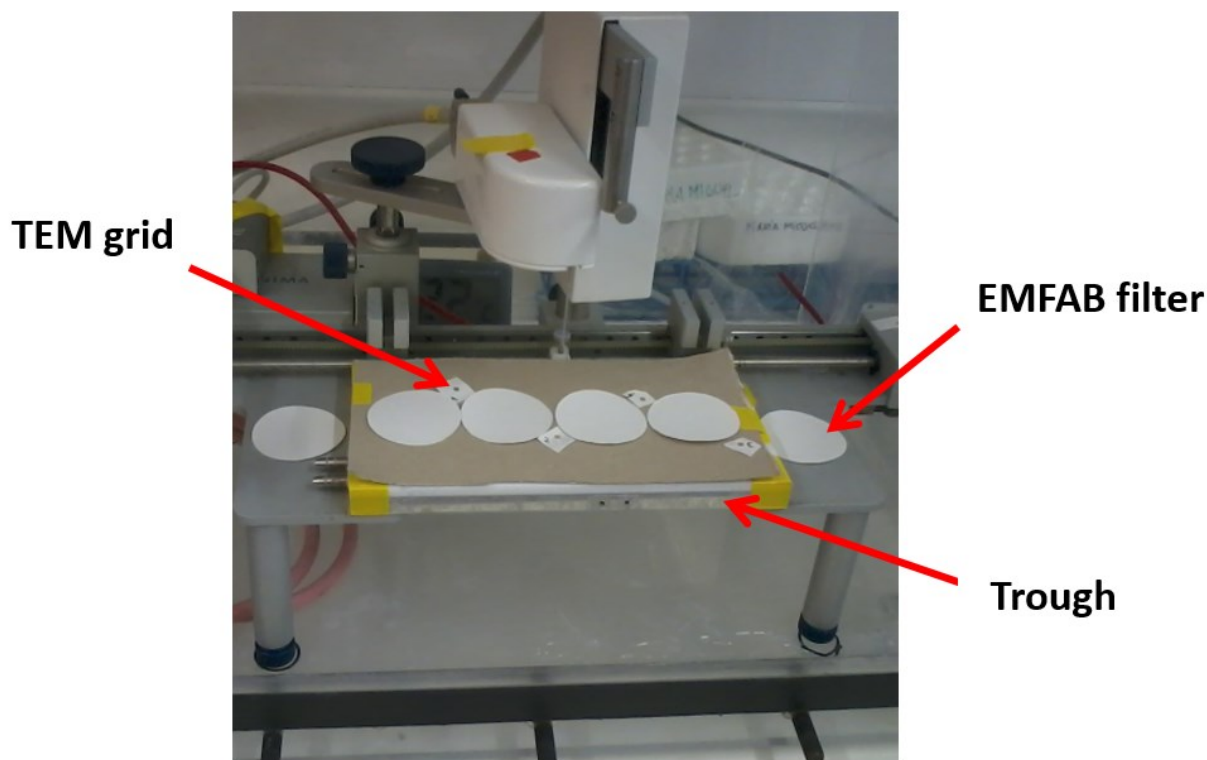


Figure 61. Illustration of the set-up of six EMFAB® filter membranes used to determine an average aerosol deposition velocity. The filters were placed on top of the Langmuir trough together with four TEM grids for nanoparticle imaging purposes.

Five and six hour experiments were performed inside the exposure chamber. The duration of these experiments was longer than usual to make sure that enough material deposited onto the filters in order to get an *mda* as accurate as possible. Each EMFAB® filter was weighed as described previously in section 3.4.5.3.2. The *mda* value was calculated for each EMFAB filter by dividing the mass deposited onto the filter by the filter area. The average *mda* value for all the filters was then used to determine a *dv* for aerosolised CeO₂ NPs for that experiment. The average *dv* of both experiments was used to determine *mdt* in the experiments performed in the presence of a DPPC monolayer at a subphase temperature of 21°C. Results are shown later in the chapter (section 3.5.3.1.1).

3.4.5.3.4 Measurement of the spatial distribution and size of aerosolised CeO₂ nanoparticles upon deposition

The samples collected onto TEM grids during the six hour experiment were used to determine the spatial distribution and size of aerosol CeO₂ NP agglomerates upon deposition. The spatial distribution was determined by TEM, using a JEM – 2000FX II microscope. Random areas of

four TEM grids were imaged. Afterwards, the number of aerosol agglomerates per image were counted by eye and divided by the image area. The size of aerosol CeO₂ NP agglomerates upon deposition was determined using TEM. TEM images were analysed using the software Image J and the CeO₂ NP size was described using the CMD of the agglomerate projected area and the GSD. TEM images were taken by Mrs Ecaterina Ware from the Department of Materials, Faculty of Engineering, Imperial College London.

3.4.5.3.5 Wettability and surface tension activity of aerosolised CeO₂ nanoparticles

The wettability and surface tension activity of the aerosolised CeO₂ NPs were determined as described previously (see section 3.4.3.2.2).

3.4.5.4 CeO₂ nanoparticle deposition

Aerosolised CeO₂ NPs were deposited onto a preformed DPPC monolayer located at the air/liquid interface over different exposure times, as detailed in the results section. Experiments were performed in PBS at 37°C and 21°C.

3.4.6 Measurement of the surface pressure–Mma isotherm

For each of the deposition methods (deposition method 1, 2 and 3), measurement of Π –Mma isotherms was performed using a LWB system as described previously (see section 2.3.4).

3.4.6.1 Relevant parameters used to describe a surface pressure–Mma isotherm

Π –Mma isotherms were described in terms of four different characteristics of the curve: lift-off Mma, two-dimensional compressibility, collapse Π and collapse Mma as described previously (see section 2.4.1.1).

3.4.6.2 Criteria to compare surface pressure–Mma isotherms measured under different experimental conditions

An experimental isotherm was compared with its associated control isotherm using reference % change from midpoint values as described previously (see section 2.4.1.5).

3.4.7 Interfacial layer characteristics post-CeO₂ nanoparticle administration - Langmuir-Blodgett films

For each of the deposition methods (deposition method 1, 2 and 3), LB film deposition was performed using a LWB system as described previously (see section 2.3.4) at 21°C, as working at 37°C has multiple technical problems such as subphase evaporation or thermal disequilibrium between the air, liquid and solid support (Cruz et al., 2004) and, as previously mentioned, the achievement of high *IT* at 37°C was greatly compromised when working with a small trough. The solid substrate used to produce the LB film was mica (9.9 mm diameter, 0.1 mm thick, purchased from Agar Scientific). The LB film was analysed using ToF-SIMS and SEM. ToF-SIMS images were taken with the help of Dr. Sarah Fearn from the Department of Materials, Faculty of Engineering, Imperial College London. SEM images were analysed using the software image J.

Further information for the aerosol deposition method: To perform an LB deposition the aerosol number concentration within the chamber needed to be close to zero to avoid any NP deposition onto the solid substrate when taken out of the subphase. Thus, compressed air was first flushed within the chamber as described previously in section 3.4.5.1 before starting the LB deposition.

3.5 Results and discussion

3.5.1 Deposition method 1: Liquid deposition of CeO₂ nanoparticles

3.5.1.1 Nanoparticle characterisation pre-CeO₂ nanoparticle administration

3.5.1.1.1 Size and zeta potential of CeO₂ nanoparticles

NPs should be characterised before administration both outside the biological environment and within the biological environment as changes can occur when they are delivered to the biological environment (Powers et al., 2006). Hence, the present work characterised the primary particle and agglomerate size and zeta potential of CeO₂ NPs in both chloroform, which was the suspension medium, and PBS, which was the subphase medium onto which CeO₂ NPs were deposited.

A. Chloroform

CeO₂ NP suspensions in chloroform were water bath-sonicated for 30 minutes before characterisation.

Size: Figure 62 shows TEM images of CeO₂ primary particles and Figure 63 shows TEM images of CeO₂ NP agglomerates. For the primary particle, the CMD was 19 nm with a GSD of 1.8. The size determined was within the particle size range stated by the manufacturer, i.e., nominal size < 25 nm. A GSD of 1.8 indicates that the sample was polydisperse. For the NP agglomerates, the CMD was 158 nm with a GSD of 1.5. Thus, NP agglomerates were ~ 8 times larger than the primary particle. A GSD of 1.5 indicates that the sample was polydisperse.

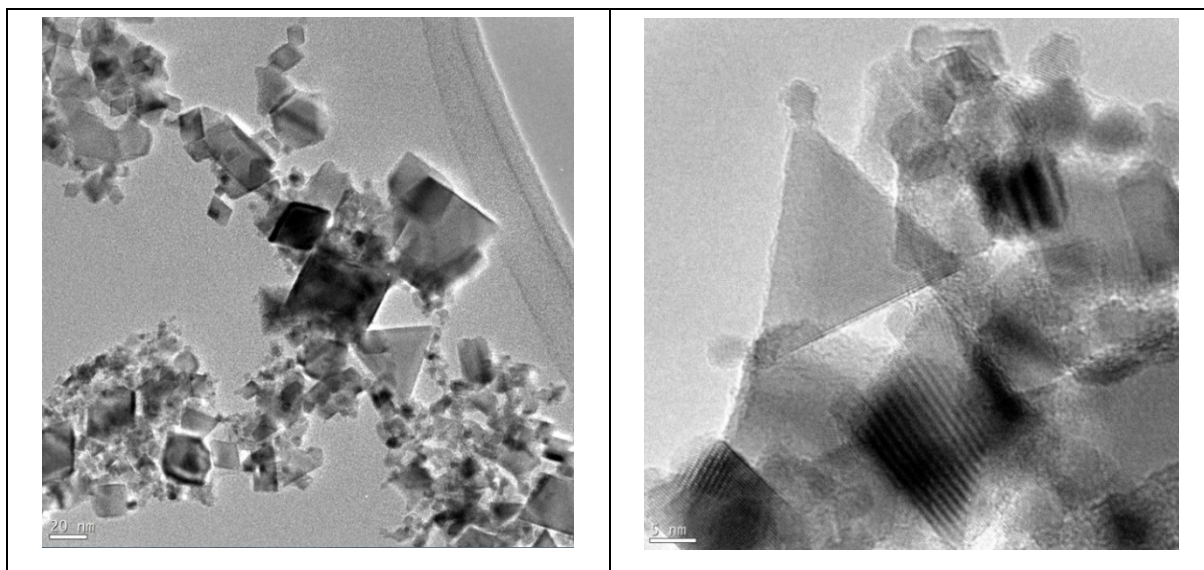


Figure 62. TEM images of CeO₂ primary particles at different magnifications. The scale bar in the left image is 20 nm and in the right image is 5 nm.

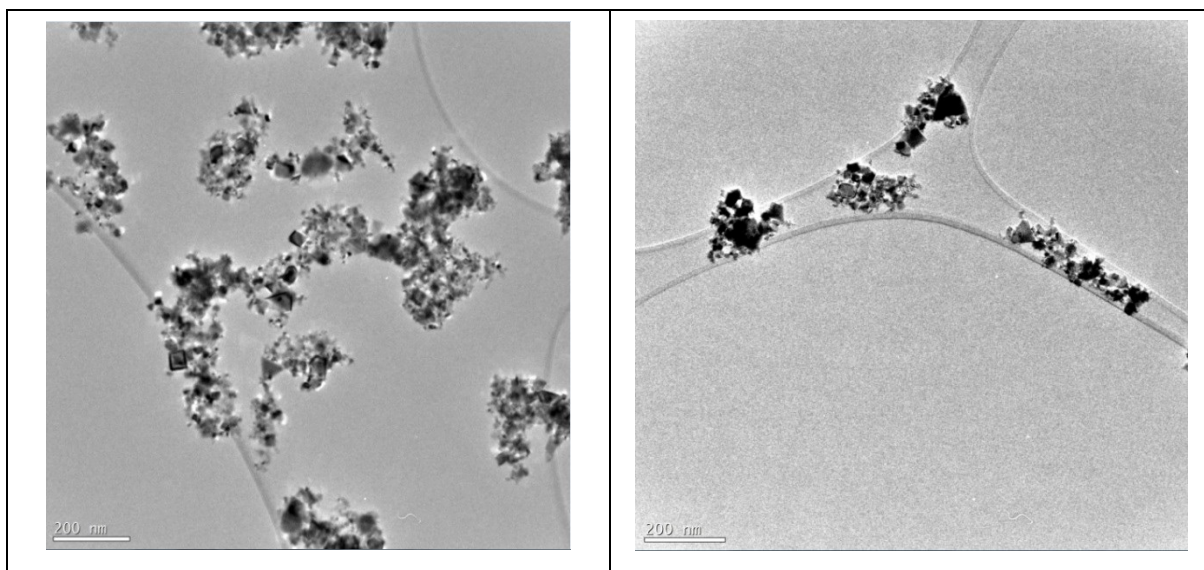


Figure 63. TEM images of CeO₂ nanoparticle agglomerates. The scale bar is 200 nm for both images.

The size of the CeO₂ NP agglomerates was also measured using DLS. The Z-average diameter of the CeO₂ NP agglomerates under investigation was 222 nm.

Zeta potential: The zeta potential of the CeO₂ NP suspensions under investigation was -70.2 mV. This means that CeO₂ NPs were strongly anionic and the system stable. The pH of the solution was not measured as chloroform is a non-polar solvent that does not dissociate in water to form hydrogen ions (H⁺).

B. PBS

CeO₂ NPs suspended in PBS agglomerated and settled at the bottom of the bottle within seconds. This means that this colloidal system was very unstable. It has been reported in the literature that the isoelectric point of CeO₂ NPs is approximately 8 (Baalousha et al., 2012b) which explains the instability of these NPs in aqueous media such as PBS which has a pH of ~ 7. As such, it was not possible to measure the size of the CeO₂ NP agglomerates in this medium. It is also relevant to mention that in general, the forces responsible for the interactions between particles in bulk also operate in particle monolayers (Aveyard et al., 2000a, Binks, 2002).

3.5.1.1.2 Wettability and surface tension activity of CeO₂ nanoparticles

CeO₂ is a material seven times denser than water. In this study, the capacity of CeO₂ NPs to remain at the air/liquid interface was investigated. 60 µg of CeO₂ NPs suspended in chloroform were deposited onto a clean PBS subphase at 21°C and compressed with the barriers to the smallest area technically feasible. To visualise the NPs on the surface, a dipping experiment was performed. Numerous SEM images were processed and examined. In a few images, CeO₂ NPs were clearly visible as can be seen in Figure 64. SEM images also show that some of the areas of CeO₂ NPs were covered with a white crust which was probably solidified salt formed after the dipping experiment was performed due to the evaporation of PBS. The non CeO₂ NP control performed by dipping a mica sheet into a clean PBS solution also shows the presence of salt crystals (sodium ions) (Figure 66). Taking into consideration that the dipping experiment was performed by vertically passing a previously submerged mica sheet through the interface, if sodium ions and NP agglomerates had interacted at the interface it is expected that the layer of salt would have been formed around or underneath the CeO₂ NP agglomerates.

However, the vast majority of images did not indicate the presence of CeO₂ NPs. A representative image of this situation is shown in Figure 65. As mentioned earlier, a non CeO₂ NP control experiment was performed (Figure 66), and although this illustrates how salt can deposit on the sheet, this was not always a feature of the CeO₂ NP experiments: as can be seen in both images, the pattern of salt distribution was very different for each experiment, with small salt crystals of around 900 nm in diameter spread across the surface for the CeO₂ NP experiment and large clusters of salt for the control experiment. It is possible that the CeO₂ NP agglomerates were small and located beneath the salt crystals and impeded the formation of large salt crystal layers as those shown in Figure 66. This pattern could also be an indication of early stages of agglomeration of the CeO₂ NP clusters as found elsewhere (Alves et al., 2008, Trefalt et al., 2013). Furthermore, other areas of the same sample were analysed using ToF-SIMS and CeO₂ NP agglomerates were not detected. This suggests that the areas imaged did not contain any NP, or that NPs were not detected because they were located beneath the salt crystals or that the size of the NP agglomerates was below the detection limit of this technique (~ 300 nm, manufacturer's data).

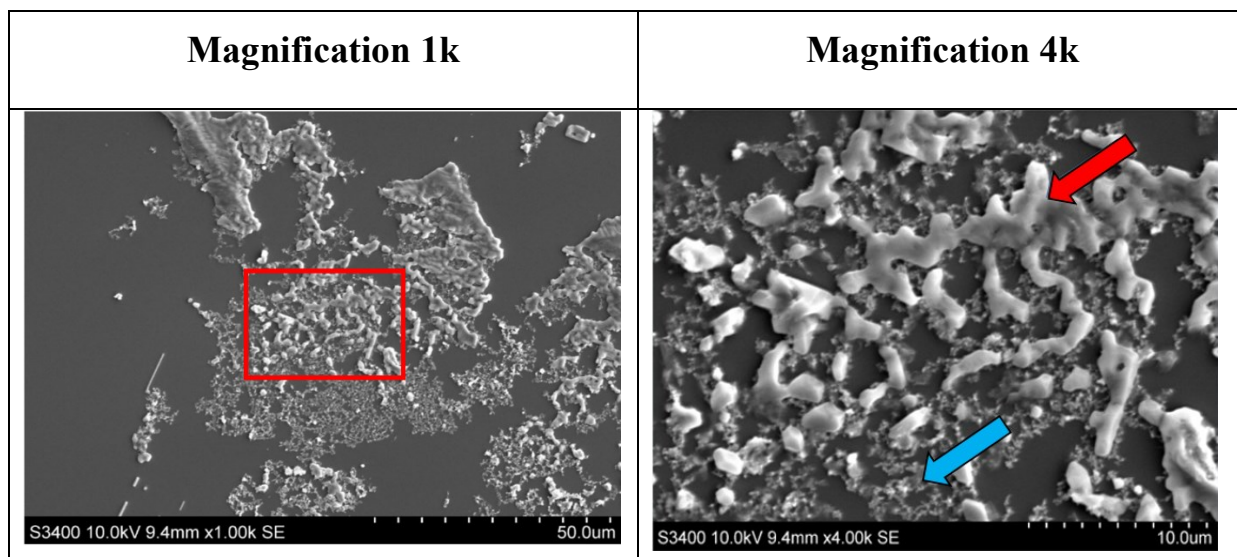


Figure 64. SEM images of the same area at two magnifications from a dipping experiment performed after depositing 60 μg of CeO_2 nanoparticles suspended in chloroform onto PBS at 21°C and compressing the interface to the smallest area technically feasible. The box area in the left image indicates the region displayed in the right image at higher magnification. In the right image, CeO_2 nanoparticle agglomerates (indicated by a blue arrow) were covered in some cases by a layer of salt (indicated by a red arrow). The dotted scale bar in the left image is 50 μm and in the right image is 10 μm .

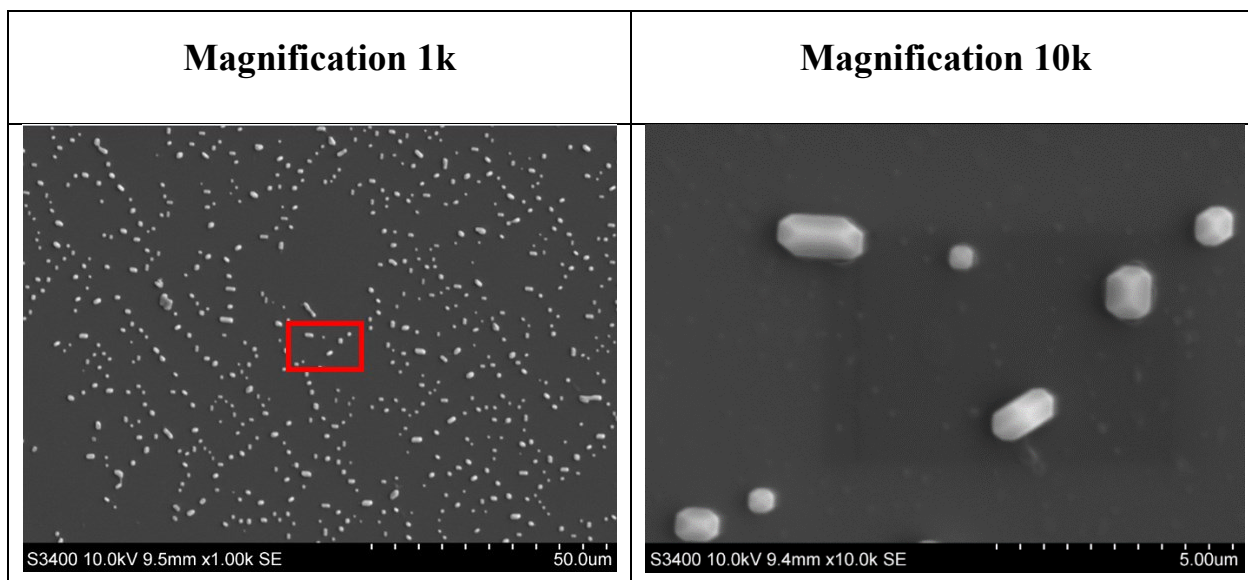


Figure 65. SEM images of the same area at two magnifications from a dipping experiment performed after depositing 60 μg of CeO_2 nanoparticles suspended in chloroform onto PBS at 21°C and compressing the interface to the smallest area technically feasible. The box area in the left image indicates the region displayed in the right image at higher magnification. The dotted scale bar in the left image is 50 μm and in the right image is 5 μm .

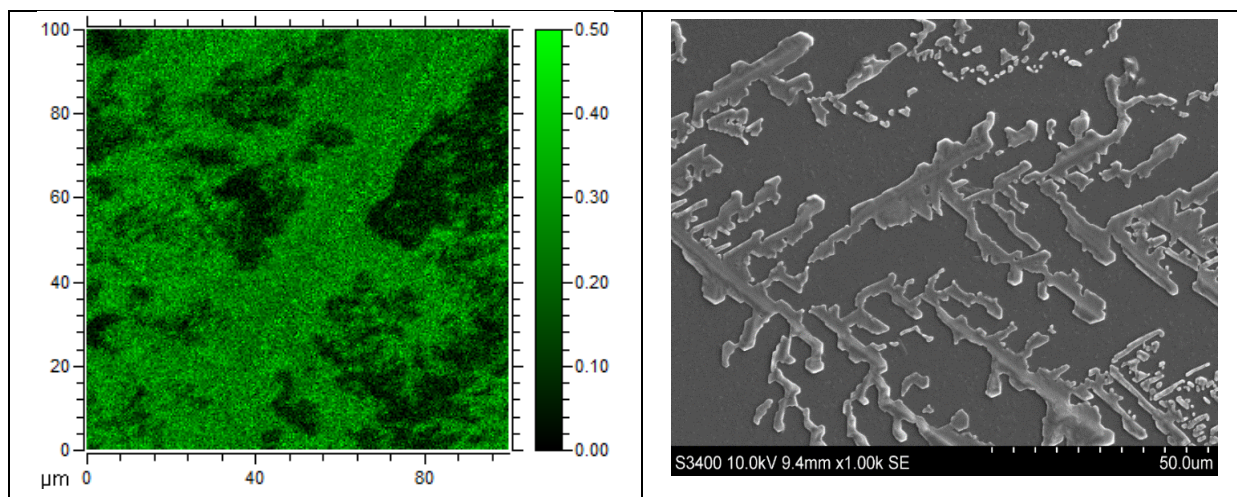


Figure 66. ToF-SIMS (left) and SEM (right) images from a dipping experiment performed by submerging a mica sheet in a clean PBS solution at 21°C. The areas imaged with each technique were different. ToF-SIMS image is 100 μm x 100 μm and the presence of sodium ions (Na⁺) is indicated by the green colour scale located at the right side of the image. In the SEM image, the dotted scale bar is 50 μm.

As already mentioned in the introductory chapter, the amount of particles at the air/liquid interface strongly depends on particle wettability. Particles with $\theta = 0^\circ$ - 10° and $\theta = 170^\circ$ - 180° are preferentially located in one of the two fluid phases (Horozov et al., 2006, Maestro et al., 2014, Maestro et al., 2015). There are several methods to determine the θ of particles at the air-liquid-solid interface such as the pendant drop profile method discussed in Appendix 2e which is also used for measuring γ , but this was not performed in this study. There is however evidence that the water θ of rare-earth oxide metals such as CeO₂ range between 100° and 115° (Azimi et al., 2013) and that pH and θ are related, with the maximum θ occurring at the isoelectric point, decreasing symmetrically on either side as shown in Figure 67 (Puah et al., 2010, Hanly et al., 2011).

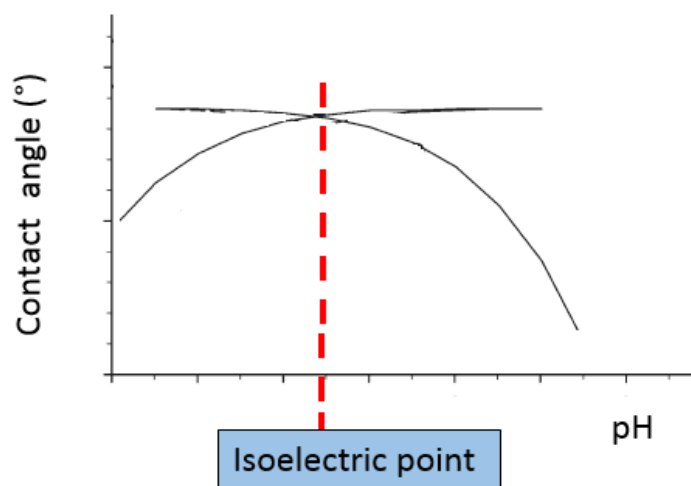


Figure 67. Graphical representation of the influence of pH on the θ . The maximum θ occurs at the isoelectric point decreasing symmetrically on either side. Adapted from Hanly et al., 2011.

In order to investigate the degree of particle attachment to the air/PBS interface, the behaviour of CeO₂ NPs in water was studied and results compared with those obtained in PBS. CeO₂ NPs were first suspended in water to determine the stability of the NPs in this suspending medium. As previously mentioned, in general the forces responsible for the interactions between particles in bulk also operate in particle monolayers (Aveyard et al., 2000a, Binks, 2002). A solution with a NP concentration of 0.5 mg/mL was prepared. After sonicating the solution for 15 minutes the zeta potential was measured. This value was +42 mV for a pH = 5.5 and the dispersion was visually much more stable than with PBS. Based on Figure 67, this suggests that the PBS θ of CeO₂ NPs was higher than the water θ hence, the ability of CeO₂ NPs to remain on the surface compared to water should also be higher. The capacity of CeO₂ NPs to remain at the air/water interface was investigated by depositing 60 μ g of CeO₂ NPs suspended in chloroform onto a water subphase at 21°C and performing a dipping experiment after compressing the interface with the barriers to the smallest area technically feasible. Representative SEM and ToF-SIMS images of this system are shown in Figure 68 and Figure 69 respectively. The areas imaged with each technique were different.

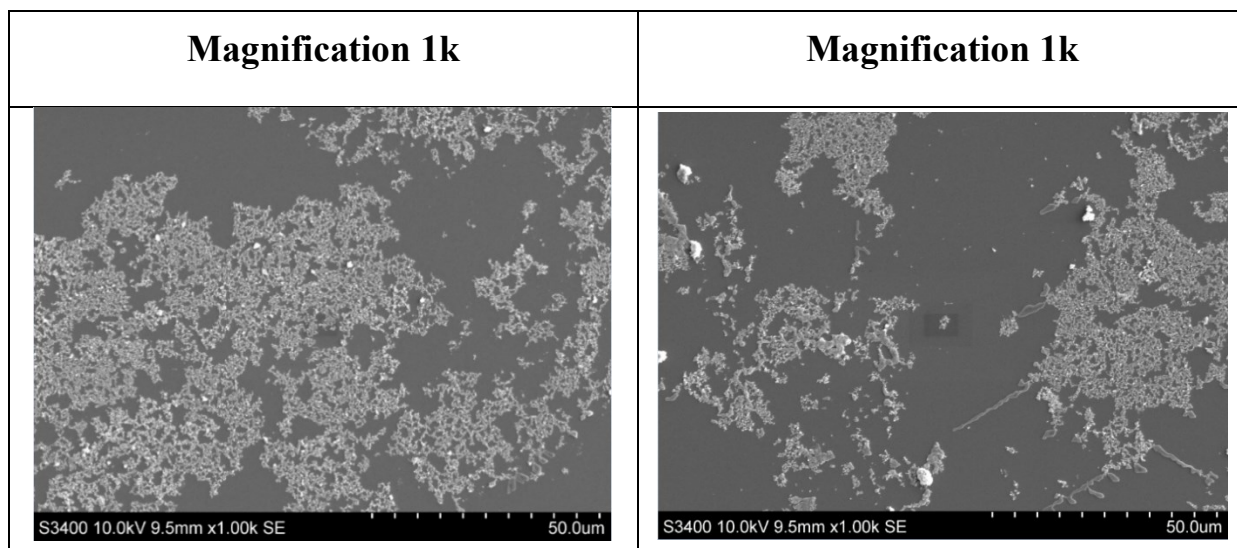


Figure 68. SEM images of CeO₂ nanoparticle agglomerates. The dipping experiment was performed after depositing 60 µg of CeO₂ nanoparticles suspended in chloroform onto a water subphase at 21°C and compressing the interface to the smallest area technically feasible. The dotted scale bar is 50 µm for both images.

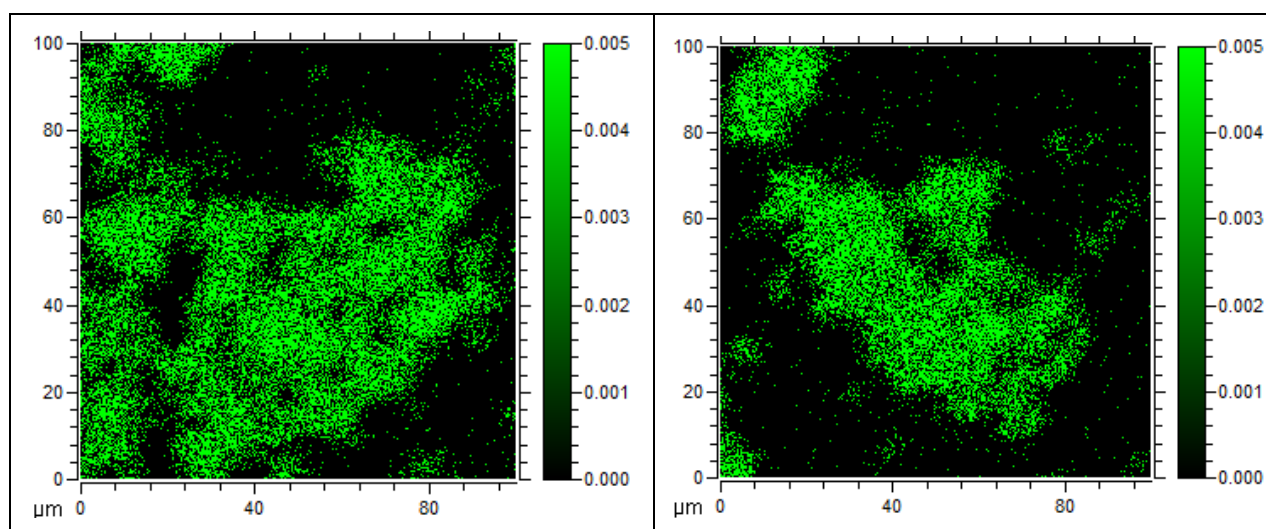
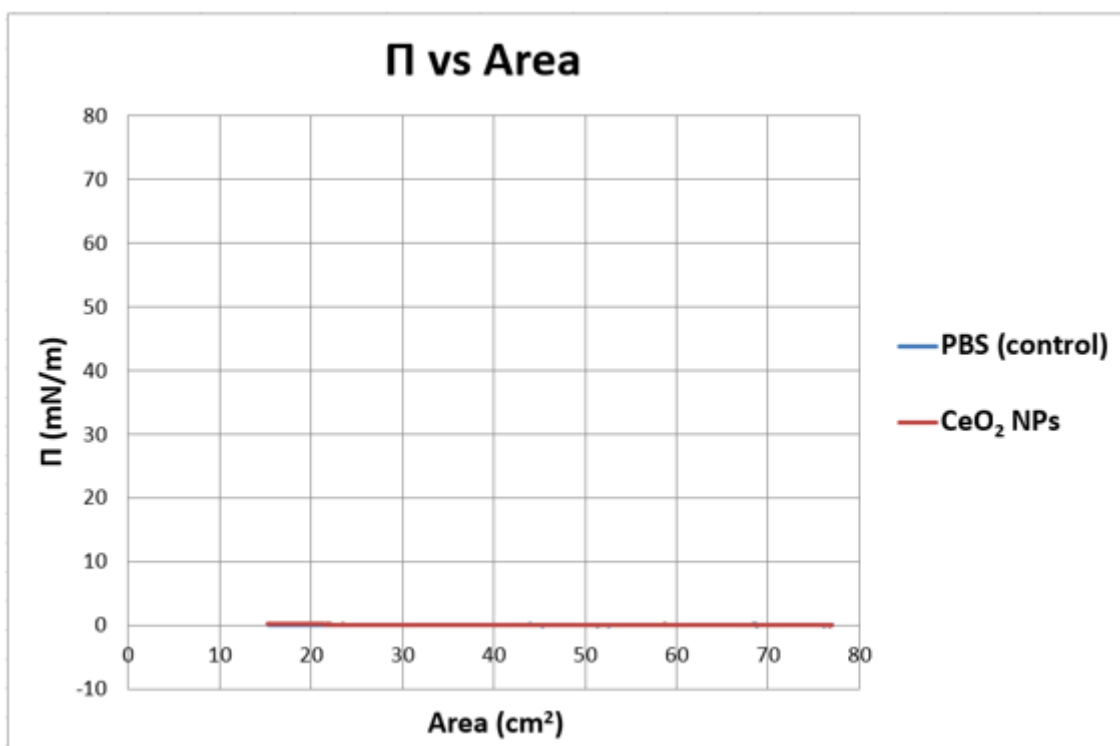


Figure 69. ToF-SIMS images of CeO₂ nanoparticle agglomerates. The dipping experiment was performed after depositing 60 µg of CeO₂ nanoparticles suspended in chloroform onto a water subphase at 21°C and compressing the interface to the smallest area technically feasible. The presence of CeO₂ nanoparticles is indicated by the green colour scale located at the right side of each image. Images are 100 µm x 100 µm.

As can be seen in Figure 68 and Figure 69, using a water subphase, CeO₂ NP agglomerates were large and easily visualised throughout the mica surface as opposed to the experiment performed in PBS, where the vast majority of images did not indicate the presence of CeO₂ NPs (Figure 65). This was not in agreement with the expectations as the ability of CeO₂ NPs to remain onto

a PBS subphase compared to water should be higher as mentioned previously. Consequently, it is hypothesised that, due to the instability of CeO₂ NPs in PBS compared to water, they rapidly agglomerated to form large, dense clusters that eventually detached from the interface and sedimented into the subphase, hence, mainly small agglomerates remained at the interface. Preliminary studies on CeO₂ NP translocation were performed by taking samples of the subphase with a pipette and analysing them using quadrupole inductively coupled plasma mass spectrometry (ICP-MS) which is a technique used to detect and quantify elements in liquid samples. Unfortunately, the data produced were not reproducible and thus not robust enough to be presented in this thesis. One of the possible reasons for this is that once in the subphase, CeO₂ NPs rapidly sedimented to the bottom of the trough and hence, samples did not contain a representative amount of CeO₂ NPs for that experiment. This is clearly an area in which further work would be useful.

Finally, the surface tension activity of the CeO₂ NPs suspended in chloroform was investigated by recording the Π - A isotherm during the compression of the interface with the barriers to the smallest area technically feasible. This is shown in Figure 70. The Π - A isotherm of PBS was first measured to ensure that the subphase was clean. The isotherms were determined using only one measurement per condition. The table shows the maximum Π value for each isotherm.



Isotherm	Maximum Π value (mN/m)
PBS (control)	0.09
CeO ₂ NPs	0.21

Figure 70. Π - A isotherm recorded after depositing 60 μg of CeO₂ nanoparticles suspended in chloroform onto a clean PBS subphase at 21°C and compressing the interface to the smallest area technically feasible. The Π - A isotherm of PBS was first measured to ensure that the subphase was clean. The table shows the maximum Π value reached for each isotherm. $n = 1$ experiment/condition.

As can be seen in this figure, following application of CeO₂ NPs, Π only increased slightly at the very late stage of compression from 0.09 to 0.21 mN/m. Hence, the effect on the Π - A isotherm was small after one compression although it is important to take into consideration that most likely not all the NP mass deposited remained at the interface. The effect of chloroform alone on the Π - A isotherm was not measured in the present work but in this experiment 120 μL of chloroform was deposited onto the air/liquid interface and Figure 70 shows that the solvent had no or limited effect on the surface tension. This however contrasts with other studies that indicate that polar solvents are surface active (Wen et al., 2006, Duncan and Larson, 2008).

3.5.1.2 Effect of the exposure of a DPPC monolayer to CeO₂ nanoparticles on the surface pressure–Mma isotherm measured in PBS at 37°C and 21°C and interfacial layer characteristics post-CeO₂ nanoparticle administration

In this set of experiments, a DPPC monolayer located at the air/PBS interface was exposed to different CeO₂ NP masses suspended in chloroform at 37°C and the *II*–Mma isotherm recorded during one compression. The CeO₂ NP masses deposited and the CeO₂/DPPC mass ratios for each experiment are shown in Table 22. The effect of the exposure of a DPPC monolayer to different CeO₂ NP masses on the *II*–Mma isotherm is shown in Figure 71, which shows minimal changes with CeO₂ NP deposition. Table 23 shows the lift-off Mma, C_m , collapse *II* and collapse Mma of the *II*–Mma isotherms. The corresponding values in each of these parameters measured for each CeO₂/DPPC mass ratio were compared with those of pure DPPC (control) by calculating the % difference between experiment and control for each of the parameters and dividing them by the reference % change from midpoint values, i.e., assuming similar levels of uncertainties on the parameters to those of the reference isotherms (see section 2.4.1.5). As can be seen from Table 23, depositing 0.35 µg of CeO₂ NPs (0.06/1 NP/DPPC mass ratio) increased the lift-off Mma; depositing 7 µg of CeO₂ NPs (1.21/1 NP/DPPC mass ratio) induced a small decrease in the C_m for the region 31 mN/m – lowest collapse *II* and depositing 21 µg of CeO₂ NPs (3.64/1 NP/DPPC mass ratio) induced a small decrease in the collapse Mma, based on the principal of the 1.0 % difference from control described previously. However, these effects were neither very significant nor showed any trends relating to the CeO₂ NP mass deposited. It was therefore concluded that depositing up to 21 µg of CeO₂ NPs suspended in chloroform did not have an appreciable effect on the DPPC isotherm measured in PBS at 37°C.

Table 22. CeO₂ nanoparticle masses and CeO₂/DPPC mass ratios of four experiments performed in PBS at 37°C to study the effects of the exposure of a DPPC monolayer to varying amounts of CeO₂ nanoparticles suspended in chloroform.

Experiment	CeO ₂ NP mass (μg)	CeO ₂ /DPPC mass ratio
1 (DPPC, control)	0.00	0
2	0.35	0.06/1
3	7.00	1.21/1
4	21.00	3.64/1

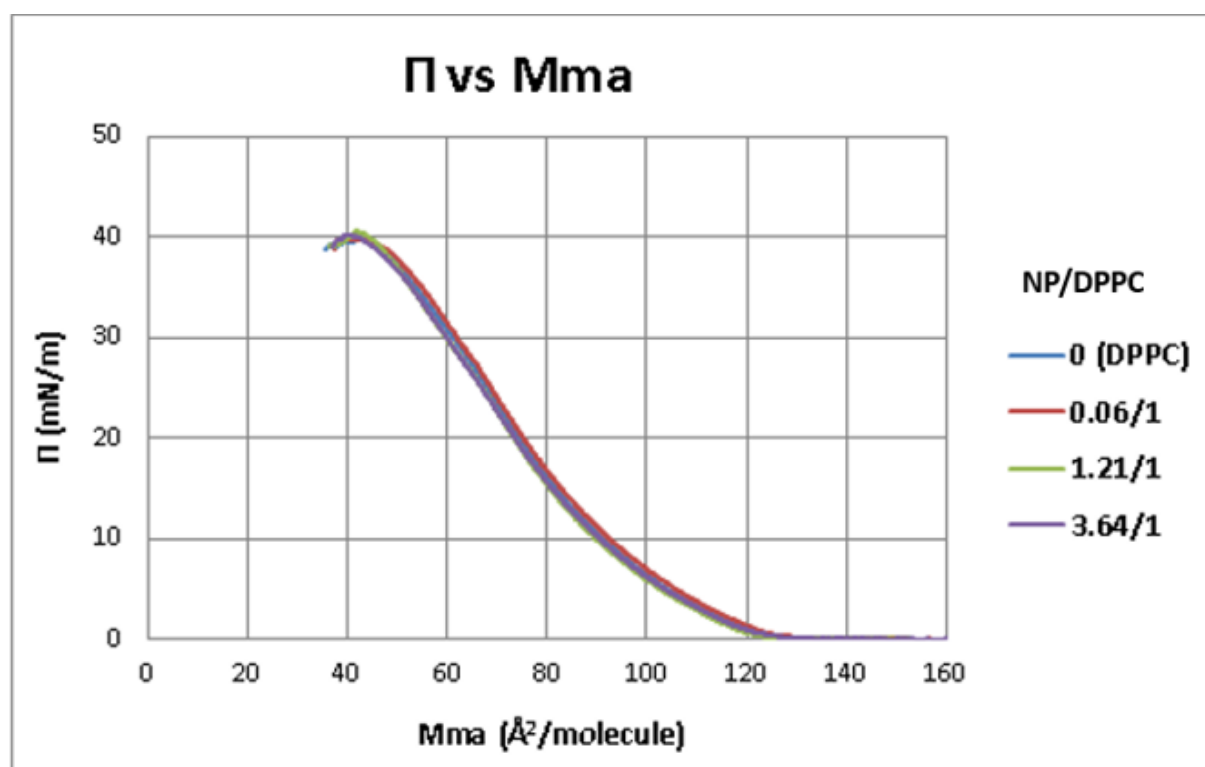


Figure 71. Effect of the exposure of a DPPC monolayer to different CeO₂ nanoparticle masses on the DPPC Π - M_{ma} isotherm measured in PBS at 37°C. CeO₂ nanoparticles were suspended in chloroform and deposited onto a DPPC monolayer using a microsyringe. n = 4 experiments/condition.

Table 23. Effect of the exposure of a DPPC monolayer to different CeO₂ nanoparticle masses suspended in chloroform on the lift-off Mma, C_m, collapse II and collapse Mma of the II-Mma isotherms measured in PBS at 37°C. The corresponding values in each of these parameters for each CeO₂/DPPC mass ratio were compared with those of pure DPPC (control) by calculating the difference in each of the parameters for the experimental isotherm and the control expressed as a % of the control value and dividing them by the reference % change from midpoint values for the relevant reference isotherm (Table 11). This approach assumes similar levels of uncertainties on the control and experimental isotherm parameters to those of the reference isotherm parameters.

CeO ₂ /DPPC mass ratio	Lift-off Mma (Å ² /molecule)	(% difference experiment and control)/ (reference % change from midpoint)	C _m 1-5 mN/m (mN/m) ⁻¹	(% difference experiment and control)/ (reference % change from midpoint)	C _m 10-25 mN/m (mN/m) ⁻¹	(% difference experiment and control)/ (reference % change from midpoint)
<i>Reference isotherm</i>	123	1.0 (% change from midpoint)	0.0298	3.0 (% change from midpoint)	0.0150	2.0 (% change from midpoint)
0 (control)	123		0.0334		0.0220	
0.06/1	125	2.0	0.0329	0.3	0.0220	0.0
1.21/1	122	1.0	0.0327	0.7	0.0218	0.5
3.64/1	123	0.0	0.0334	0.0	0.0223	0.5

CeO ₂ /DPPC mass ratio	C _m 31 mN/m – lowest collapse II (mN/m) ⁻¹	(% difference experiment and control)/(reference % change from midpoint)	Collapse II (mN/m)	(% difference experiment and control)/(reference % change from midpoint)	Collapse Mma (Å ² /molecule)	(% difference experiment and control)/(reference % change from midpoint)
<i>Reference isotherm</i>	0.0294	15.0 (% change from midpoint)	39.40	2.0 (% change from midpoint)	49	4.0 (% change from midpoint)
0 (control)	0.0303		39.78		43	
0.06/1	0.0331	0.6	39.78	0.0	42	0.5
1.21/1	0.0256	1.1	40.55	1.0	42	0.5
3.64/1	0.0300	0.1	40.20	0.5	41	1.3

A similar set of experiments was performed at 21°C for comparative purposes. The CeO₂ NP masses (suspended in chloroform) deposited and the CeO₂/DPPC mass ratios for each experiment are shown in Table 24. The effect of the exposure of a DPPC monolayer to different CeO₂ NP masses on the *II*-Mma isotherm is shown in Figure 72. Table 25 shows the lift-off Mma, *C_m*, collapse *II* and collapse Mma of the *II*-Mma isotherms. The corresponding values in each of these parameters measured for each CeO₂/DPPC mass ratio were compared with those of pure DPPC (control) by calculating the % difference between experiment and control for each of the parameters and dividing them by the reference % change from midpoint values, i.e., assuming similar levels of uncertainties on the parameters to those of the reference isotherms (see section 2.4.1.5). Data in Table 25 indicates that CeO₂ NPs had no effect on any of the parameters of the DPPC isotherm for any of the NP masses deposited.

Table 24. CeO₂ nanoparticle masses and CeO₂/DPPC mass ratios of four different experiments performed in PBS at 21°C to study the effects of the exposure of a DPPC monolayer to varying amounts of CeO₂ nanoparticles suspended in chloroform.

Experiment	CeO ₂ NP mass (µg)	CeO ₂ /DPPC mass ratio
1 (DPPC, control)	0.0	0
2	0.4	0.06/1
3	8.0	1.16/1
4	24.0	3.49/1

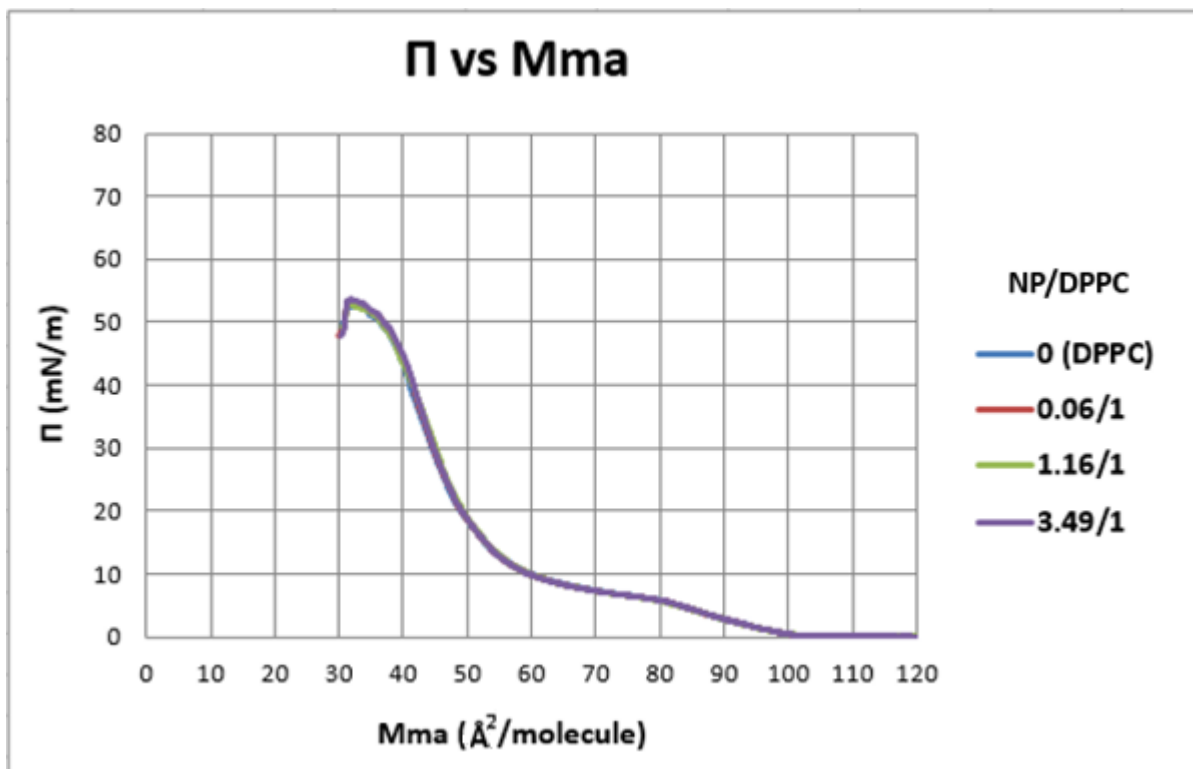


Figure 72. Effect of the exposure of a DPPC monolayer to different CeO_2 nanoparticle masses on the Π - Mma isotherm measured in PBS at 21°C . CeO_2 nanoparticles were suspended in chloroform and deposited onto a DPPC monolayer using a microsyringe. $n = 3$ experiments/condition.

Table 25. Effect of the exposure of a DPPC monolayer to different CeO₂ nanoparticle masses suspended in chloroform on the lift-off Mma, C_m, collapse *II* and collapse Mma of the *II*-Mma isotherms measured in PBS at 21°C. The corresponding values in each of these parameters for each CeO₂/DPPC mass ratio were compared with those of pure DPPC (control) by calculating the difference in each of the parameters for the experimental isotherm and the control expressed as a % of the control value and dividing them by the reference % change from midpoint values for the relevant reference isotherm (Table 12). This approach assumes similar levels of uncertainties on the control and experimental isotherm parameters to those of the reference isotherm parameters.

CeO ₂ /DPPC mass ratio	Lift-off Mma (Å ² /molecule)	(% difference experiment and control)/(reference % change from midpoint)	C _m 1-5 mN/m (mN/m) ⁻¹	(% difference experiment and control)/(reference % change from midpoint)	C _m 5-10 mN/m (mN/m) ⁻¹	(% difference experiment and control)/(reference % change from midpoint)
<i>Reference isotherm</i>	100	2.0 (% change from midpoint)	0.0378	3.0 (% change from midpoint)	0.0636	9.0 (% change from midpoint)
0 (control)	100		0.0361		0.0637	
0.06/1	100	0.0	0.0361	0.0	0.0647	0.2
1.16/1	100	0.0	0.0363	0.3	0.0636	0.0
3.49/1	100	0.0	0.0361	0.0	0.0652	0.2

CeO ₂ /DPPC mass ratio	C _m 25-45 mN/m (mN/m) ⁻¹	(% difference experiment and control)/(reference % change from midpoint)	C _m 50 mN/m – lowest collapse <i>II</i> (mN/m) ⁻¹	(% difference experiment and control)/(reference % change from midpoint)	Collapse <i>II</i> (mN/m)	(% difference experiment and control)/(reference % change from midpoint)	Collapse Mma (Å ² /molecule)	(% difference experiment and control)/(reference % change from midpoint)
<i>Reference isotherm</i>	0.0063	6.0 (% change from midpoint)	0.0247	36.0 (% change from midpoint)	57.17	2.0 (% change from midpoint)	31	5.0 (% change from midpoint)
0 (control)	0.0075		0.0452		52.63		32	
0.06/1	0.0072	0.6	0.0349	0.6	53.25	0.5	32	0.0
1.16/1	0.0079	0.8	0.0476	0.1	53.27	0.5	31	0.6
3.49/1	0.0071	0.8	0.0343	0.7	53.58	1.0	32	0.0

The presence of CeO₂ NP agglomerates at the interface was investigated during the initial compression of the monolayer, after three compression-expansion cycles performed at normal barrier speed and after three compression-expansion cycles performed at maximum barrier speed (270 mm/min) for comparative purposes. For these experiments, 60 μg of CeO₂ NPs suspended in chloroform were deposited onto a DPPC monolayer located at the air/PBS interface at 21°C. The CeO₂/DPPC mass ratio was 3.20/1. A dipping experiment was performed at three different Π values during the initial compression of the monolayer: 20, 40 and 70 mN/m. SEM and ToF-SIMS images of pure DPPC and DPPC exposed to CeO₂ NPs are shown in Figure 73. After one compression, the layer was expanded and compressed for a total of 3 compression-expansion cycles from 0 mN/m to 70 mN/m at normal barrier speed and a dipping experiment performed at a Π value of 40 mN/m. SEM and ToF-SIMS images of pure DPPC and DPPC exposed to CeO₂ NPs are shown in Figure 74. A further experiment was performed by depositing the same CeO₂ NP and DPPC masses with the monolayer compressed from 0 mN/m to 70 mN/m and expanded at maximum barrier speed for a total of 3 compression-expansion cycles. A dipping experiment was then performed at a Π value of 40 mN/m. SEM and ToF-SIMS images of pure DPPC and DPPC exposed to CeO₂ NPs are shown in Figure 75. The areas imaged with each technique were different for each sample. In the ToF-SIMS images, the presence of CeO₂ NPs is indicated by the green colour scale located at the right side of each image.

Figure 73. SEM and ToF-SIMS images of LB films of pure DPPC (left image) and DPPC exposed to CeO₂ nanoparticles suspended in chloroform (3.20/1 CeO₂/DPPC mass ratio, right image) produced in PBS at 21°C during the initial compression of the monolayer at three different Π values: 20 (A), 40 (B) and 70 (C) mN/m. The areas imaged with each technique were different. In the SEM images, the dotted scale bar is 50 μ m. ToF-SIMS images are 100 μ m x 100 μ m and the presence of CeO₂ nanoparticles is indicated by the green colour scale located at the right side of each image.

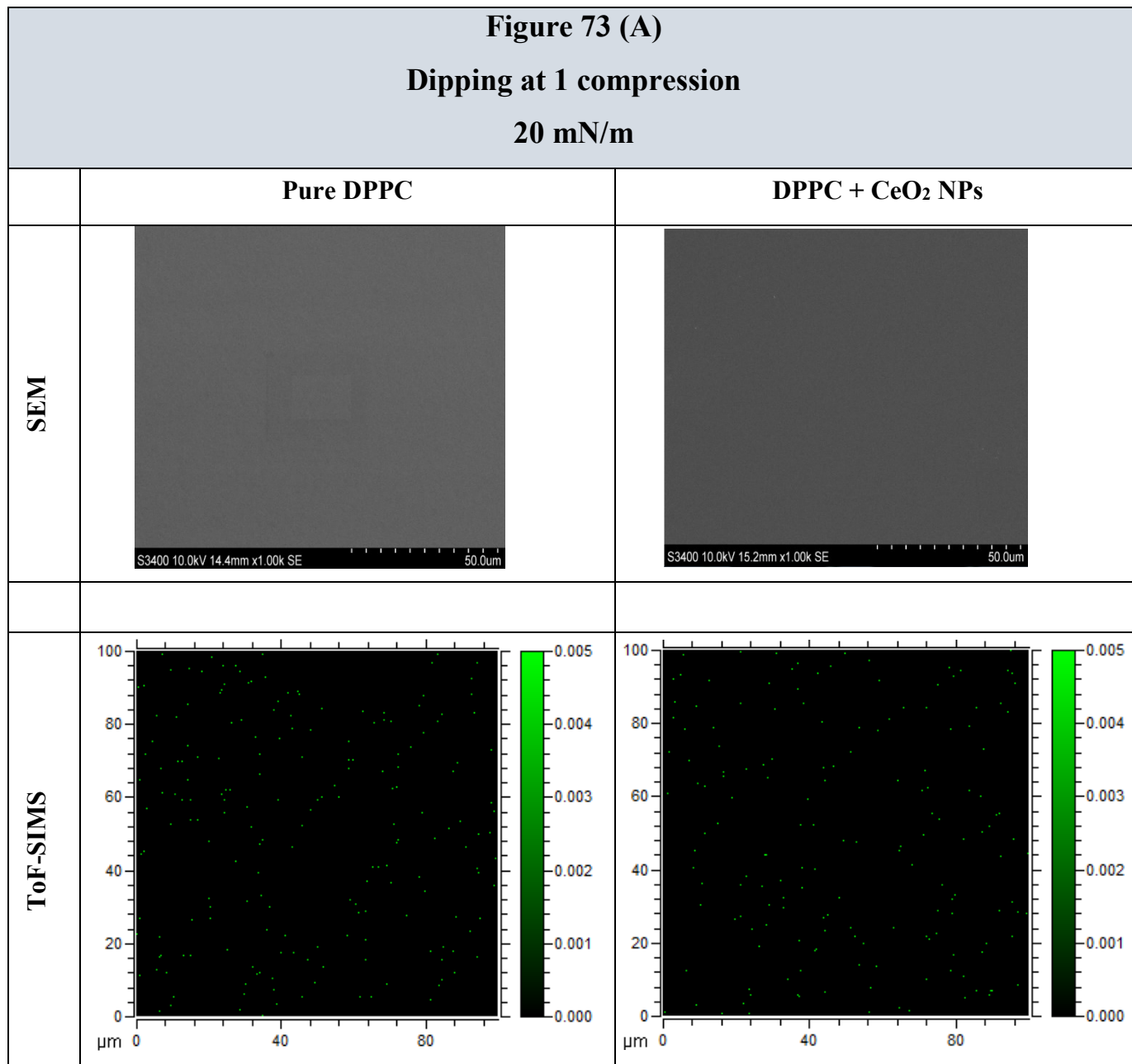


Figure 73 (B)
Dipping at 1 compression
40 mN/m

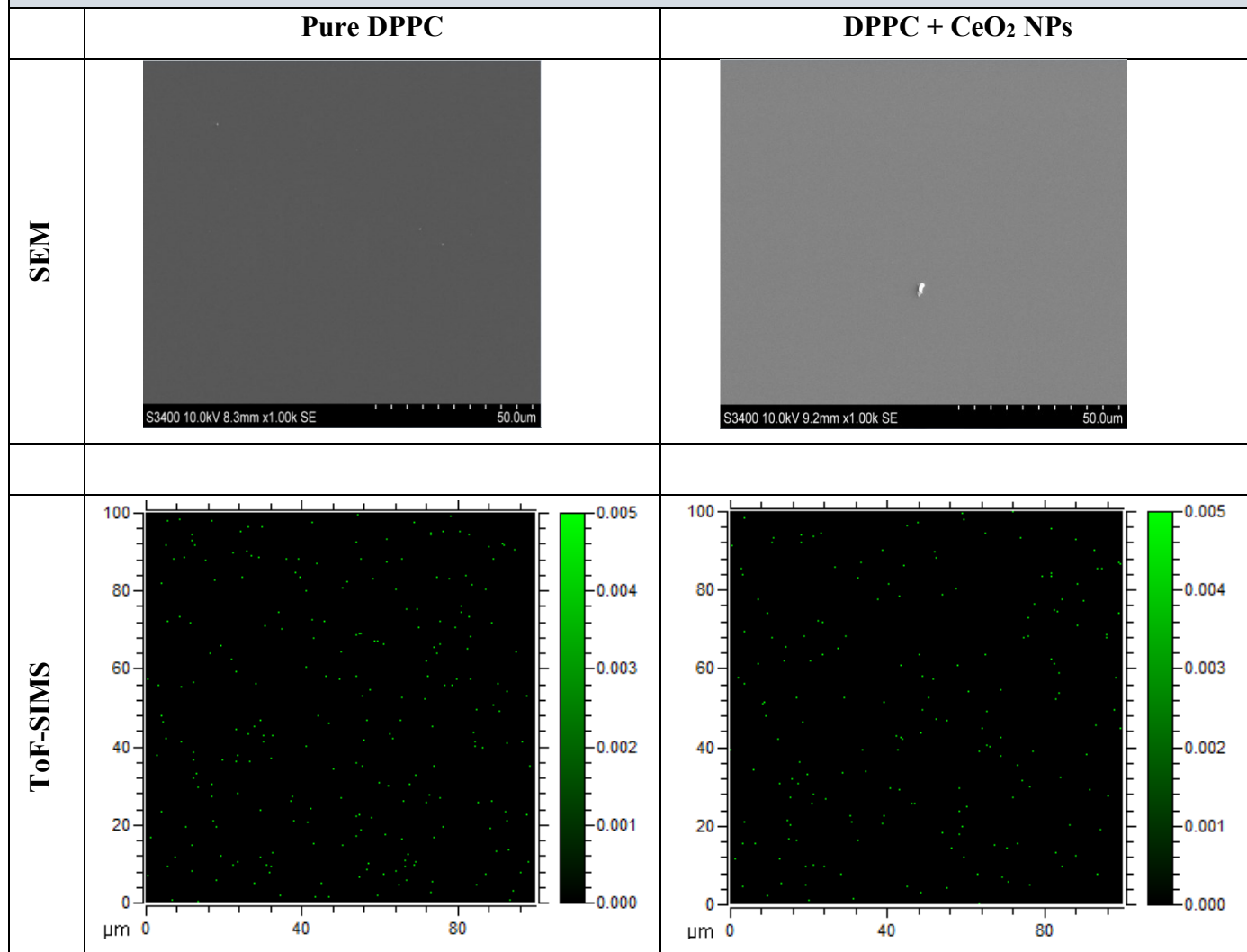


Figure 73 (C)
Dipping at 1 compression
70 mN/m

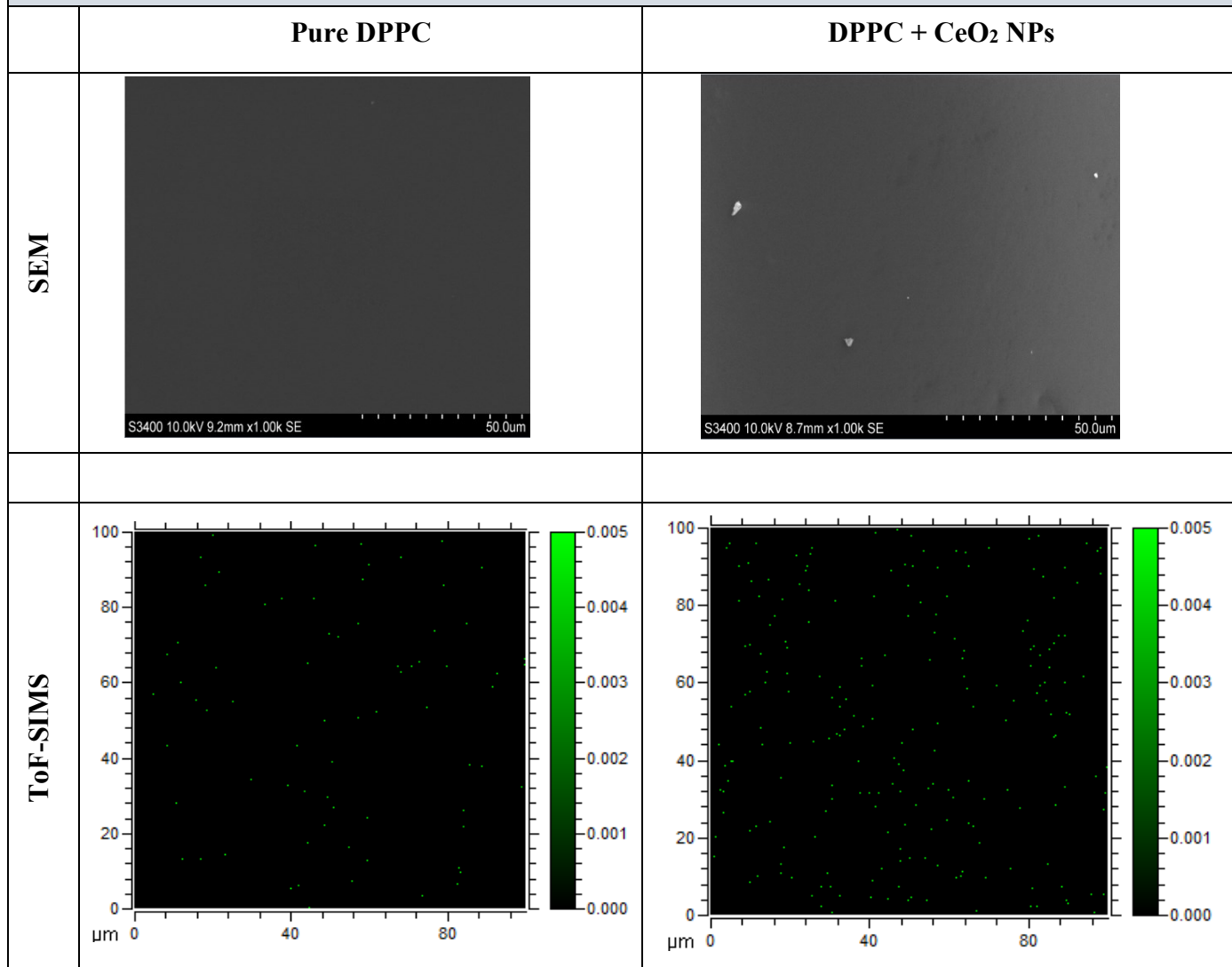


Figure 74. SEM and ToF-SIMS images of LB films of pure DPPC (left image) and DPPC exposed to CeO₂ nanoparticles suspended in chloroform (3.20/1 CeO₂/DPPC mass ratio, right image) produced at a Π value of 40 mN/m after three compression-expansion cycles performed at normal barrier speed in PBS at 21°C. The areas imaged with each technique were different. In the SEM images, the dotted scale bar is 50 μ m. ToF-SIMS images are 100 μ m x 100 μ m and the presence of CeO₂ nanoparticles is indicated by the green colour scale located at the right side of each image.

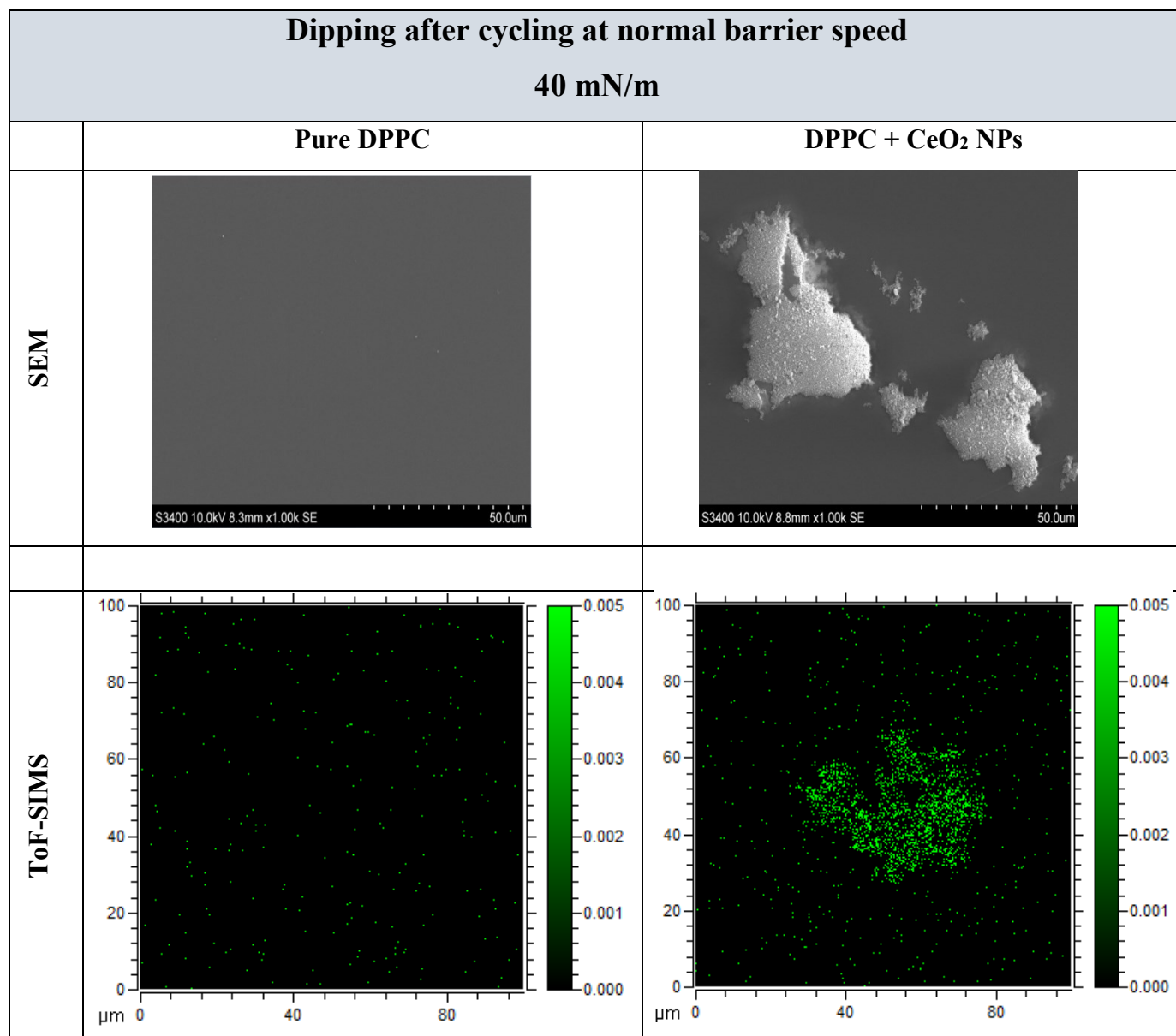
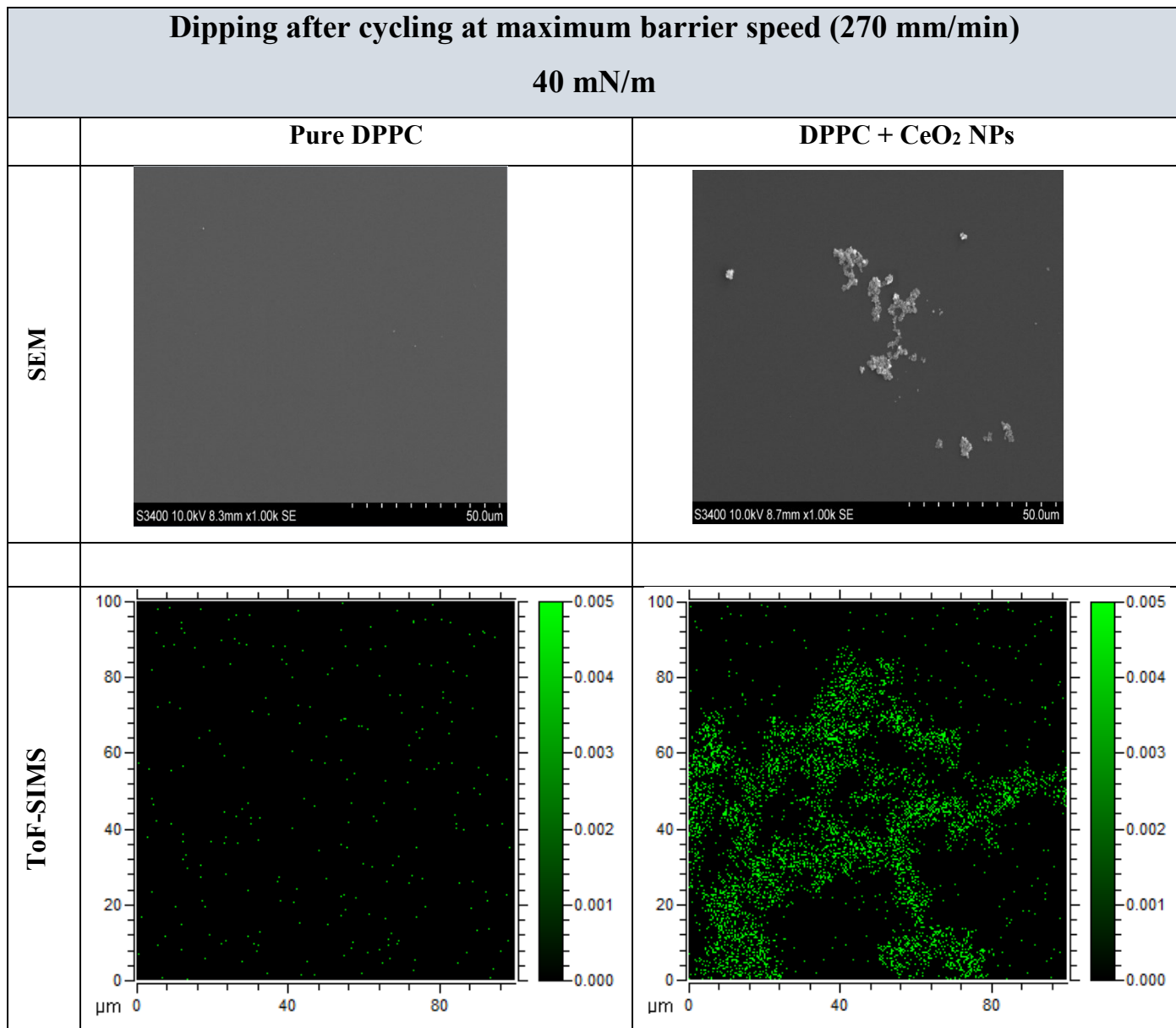


Figure 75. SEM and ToF-SIMS images of LB films of pure DPPC (left image) and DPPC exposed to CeO₂ nanoparticles suspended in chloroform (3.20/1 CeO₂/DPPC mass ratio, right image) produced at a Π value of 40 mN/m after three compression-expansion cycles performed at maximum barrier speed in PBS at 21°C. The areas imaged with each technique were different. In the SEM images, the dotted scale bar is 50 μ m. ToF-SIMS images are 100 μ m x 100 μ m and the presence of CeO₂ nanoparticles is indicated by the green colour scale located at the right side of each image.



As can be seen in the previous figures, some CeO₂ NPs were clearly present at the interface after 3 compression-expansion cycles performed at normal and maximum barrier speed. This is shown in both SEM and ToF-SIMS images. During the first compression, however, only small objects of around 3 μm in diameter could be visualised and as cerium was not identified by ToF-SIMS, it is not possible to confirm that they were CeO₂ NPs. One possible explanation for these results is that during the first compression, CeO₂ NP agglomerates were too small to visualise (i.e. agglomerates were below the minimum detectable size of approximately 300 nm) but after several compression-expansion cycles they agglomerated further and became larger and thus visible. If this were the case the isotherms would suggest that small agglomerates had no effect on the monolayer behaviour. Based on the results shown previously for CeO₂ NPs deposited onto a clean PBS subphase (section 3.5.1.1.2), it is also possible that large CeO₂ NP agglomerates quickly formed at the interface at the very early stages of compression and detached into the subphase leaving only a small number of smaller agglomerates which subsequently agglomerated during cycling. If this were the case then only small quantities of CeO₂ NPs would remain on the surface and the isotherms would suggest that the amount remaining was insufficient to have any effect on monolayer behaviour. It is difficult to interpret these results further without additional quantitative information on the amount of CeO₂ at the interface (or in the subphase). Preliminary studies on CeO₂ NP translocation across the DPPC monolayer were performed by taking samples of the subphase with a pipette and analysing those using ICP-MS. As previously mentioned, the data produced were not robust enough to be presented in this thesis. This is clearly an area in which further work would be useful. Furthermore, the presence of large and dense CeO₂ NP agglomerates at the interface after 3 compression-expansion cycles could be an indication that DPPC coated the CeO₂ NP agglomerates and increased their wettability, making them more stable at the air/PBS interface. There is evidence that the wettability of particles in a suspending medium can be modified by the adsorption of surfactant to the surface of the particles (Maestro et al., 2012, Maestro et al., 2015). In fact, the effect of DPPC on the wettability of the CeO₂ NP agglomerates was studied for the liquid deposition method 2 where DPPC was mixed with CeO₂ NPs in the same volatile solvent, probably coating the surface of the CeO₂ NPs. Results showed that the presence of DPPC increased the wettability of the CeO₂ NPs. This is shown later in the chapter (section 3.5.2). Finally, it is important to mention that for all dipping experiments there could be the potential for CeO₂ NP deposition onto the submerged mica substrate from the subphase prior to the dipping experiment, which could explain the presence of CeO₂ NP agglomerates.

However, it is believed that this effect is negligible. Mica is a hydrophilic material, with an excess negative surface charge (Bailey, 1984) and with a zeta potential in water that varies from + 40 to + 50 mV at a pH of 5.6 (Sides et al., 2009). When submerged in PBS, it is expected that ions of opposite charge will adsorb onto the mica surface; however, the zeta potential of mica in PBS is not known. CeO₂ NPs on the other hand were very unstable in PBS and as already mentioned agglomerated and settled within seconds. For this reason and the fact that NPs were deposited throughout the trough area and far from the Wilhelmy plate and mica substrate, it is believed that any CeO₂ NPs entering the PBS subphase settled at the bottom of the trough very quickly with minimal potential for interaction with the mica substrate.

For comparison, the same experiment was performed by depositing CeO₂ NPs suspended in chloroform onto a DPPC monolayer using a water subphase, instead of PBS, at 21°C. The CeO₂/DPPC mass ratio was 3/1. A dipping experiment was performed during one compression at 20 mN/m. Representative SEM images of pure DPPC and DPPC exposed to CeO₂ NPs suspended in chloroform are shown in Figure 76:

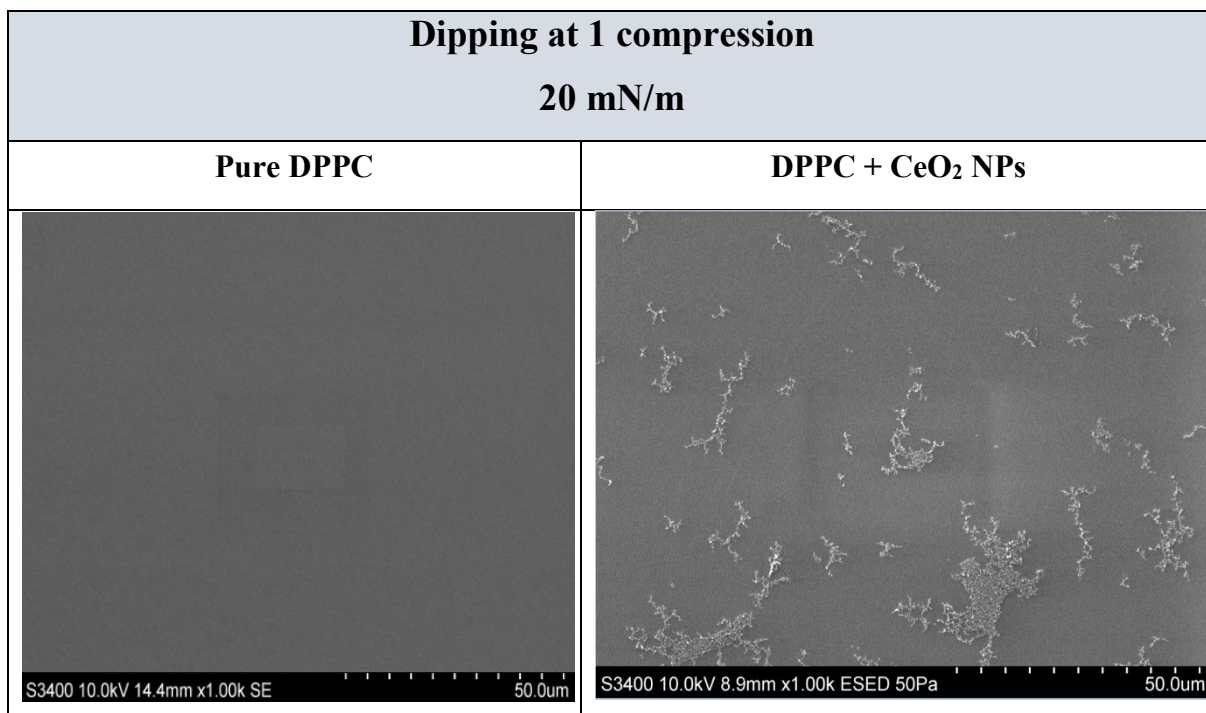


Figure 76. SEM images of pure DPPC (left) and DPPC exposed to CeO₂ nanoparticles suspended in chloroform (right) at a Π value of 20 mN/m from a dipping experiment performed after depositing CeO₂ nanoparticles suspended in chloroform onto a DPPC monolayer at a 3/1 CeO₂/DPPC mass ratio measured in water at 21°C. The dotted scale bar is 50 μ m for both images.

As can be seen in Figure 76, CeO₂ NP agglomerates were present across the surface when deposited onto a DPPC monolayer using a water subphase. This is very different from what was seen when using a PBS subphase, where during the first compression, cerium was not identified by ToF-SIMS (Figure 73). These results and those obtained using a PBS subphase in the presence of a DPPC monolayer parallel those shown previously for CeO₂ NPs deposited onto a clean water and PBS subphase respectively (section 3.5.1.1.2) which showed that CeO₂ NP agglomerates could be easily visualised throughout the mica surface when using a water subphase as opposed to a PBS subphase. This suggests that a key factor that dictated the CeO₂ NP behaviour at an air/liquid interface in the presence of a DPPC monolayer was the subphase composition. It is therefore hypothesised that in the presence of a PBS subphase large and dense agglomerates rapidly formed and detached from the interface into the subphase at early stages of compression and hence, only small agglomerates remained at the interface.

Small particle agglomerates with a large average interparticle distance have a minimal effect on the Π . However, as the particle domains get closer and agglomerate to a densely packed

monolayer, the Π increases (Huang et al., 2001a, Huang et al., 2001b). In fact, there is evidence that suggests that increments in Π are caused by the restructuring of the NP monolayer and elimination of voids during the compression of the monolayer (Huang et al., 2004). To visualise this, Figure 77 shows two CeO₂ NP agglomerates with different surface concentration. Voids are clearly seen in the agglomerate with higher NP surface concentration (right image) and indicated by red arrows. These images correspond to the dipping experiment performed at 40 mN/m after depositing CeO₂ NPs suspended in chloroform onto a DPPC monolayer located at the air/PBS interface at a 3.20/1 CeO₂/DPPC mass ratio and cycling the interface 3 times at normal barrier speed.

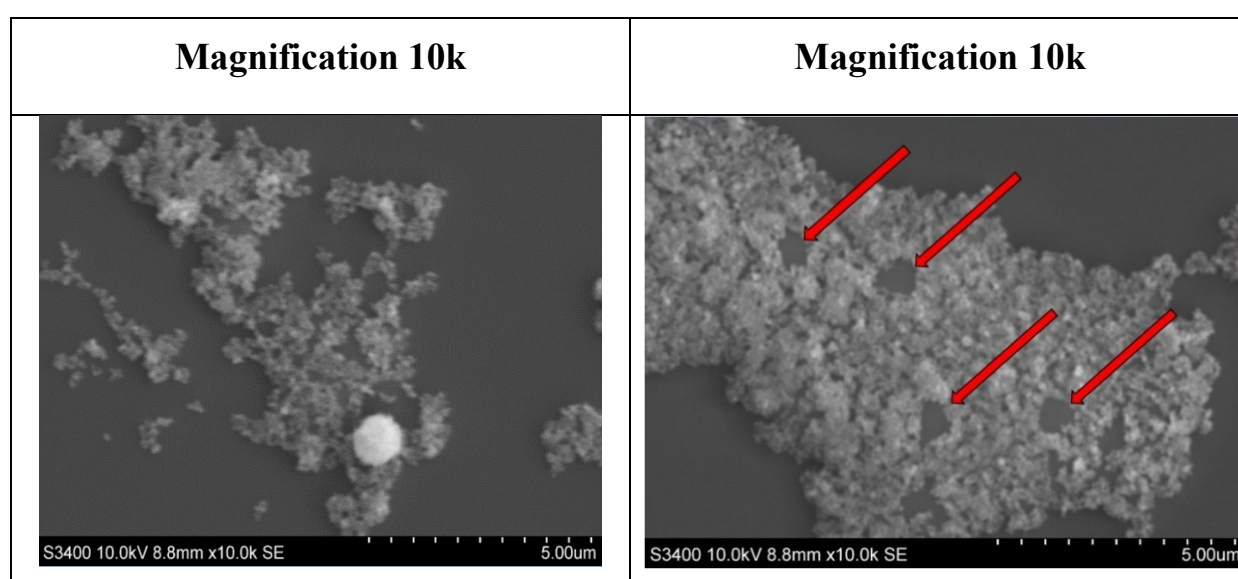
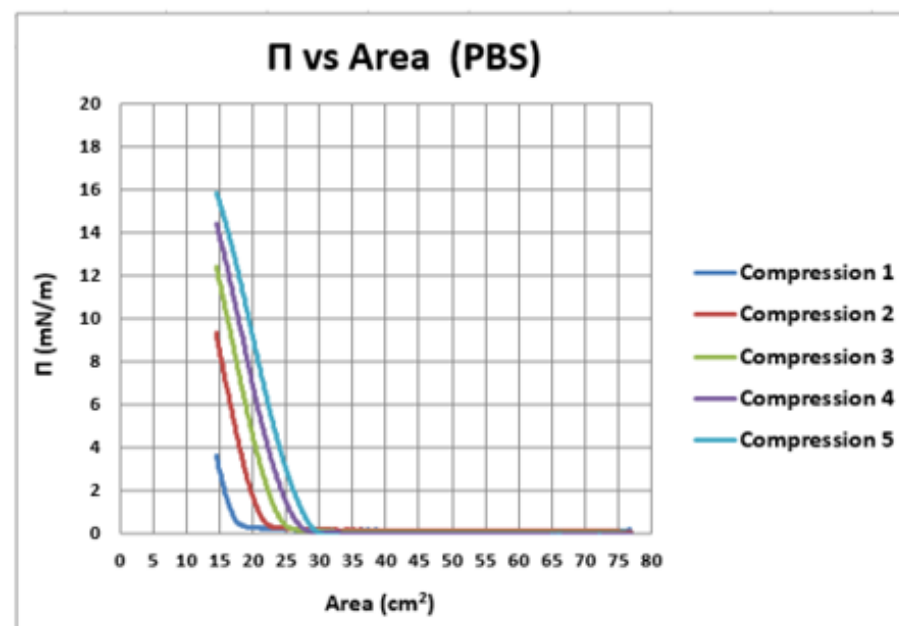
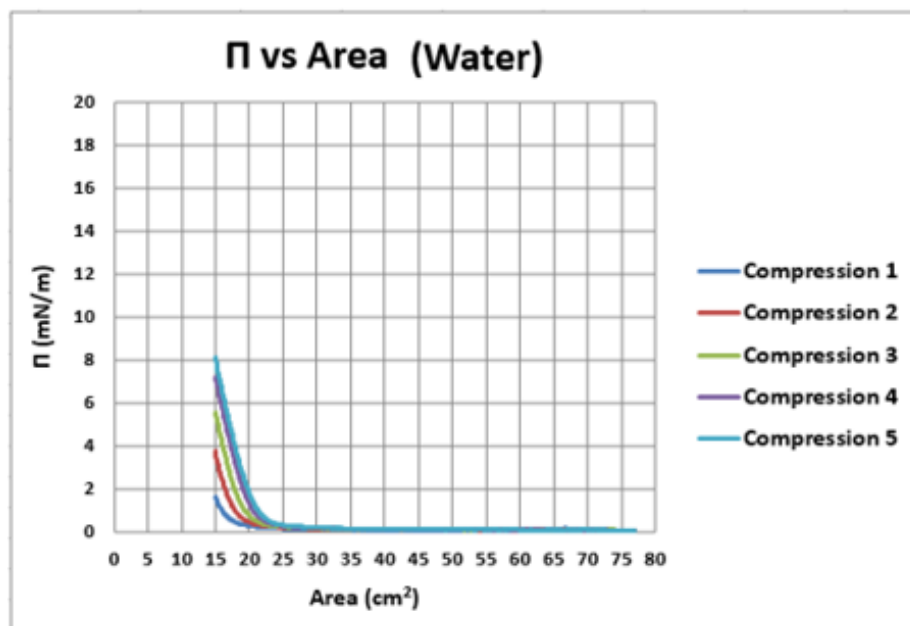


Figure 77. SEM images of CeO₂ nanoparticle agglomerates with different surface concentration. Voids are seen in the agglomerate with higher surface concentration (right image) and indicated by red arrows. These images correspond to the dipping experiment performed at a Π value of 40 mN/m after depositing CeO₂ nanoparticles suspended in chloroform onto a DPPC monolayer located at the air/PBS interface at a 3.20/1 CeO₂/DPPC mass ratio and cycling the interface 3 times at normal barrier speed. The dotted scale bar is 5 μ m for both images.

In order to understand how larger CeO₂ NP agglomerates affected Π , 60 μ g of CeO₂ NPs in chloroform were deposited onto a clean PBS subphase at 21°C and cycled five times at normal barrier speed as, based on the SEM and ToF-SIMS images shown previously in Figure 73, Figure 74 and Figure 75, it was expected that after each cycle larger and denser agglomerates would form at the interface. The same experiment was repeated using a water subphase for comparative reasons. Π -A compression isotherms were measured and the lift-off area and

maximum II reached after each compression recorded. The isotherms were determined using only one measurement per cycle. These data are shown in Figure 78.



Compression	Lift-off area (cm ²)	Maximum Π (mN/m)
1	18	1.60
2	19	3.74
3	20	5.53
4	22	7.22
5	23	8.12

Compression	Lift-off area (cm ²)	Maximum Π (mN/m)
1	18	3.63
2	21	9.37
3	25	12.42
4	27	14.45
5	29	15.86

Figure 78. Π -A compression isotherms measured after depositing 60 μg of CeO_2 nanoparticles suspended in chloroform onto a water subphase (left) and onto a PBS subphase (right) at 21°C and compressing the interface five times to the smallest area technically feasible. The tables show the lift-off area and the maximum Π reached after each compression. n = 1 experiment/cycle.

As can be seen in the previous figure, Π started to increase at a similar area for both water and PBS but the Π reached after one compression was 1.60 mN/m for water and 3.63 mN/m for PBS. After 5 compressions, the lift-off area for water increased from 18 to 23 cm² and the Π from 1.60 to 8.12 mN/m. For PBS however, the lift-off area increased from 18 to 29 cm² and the Π from 3.63 to 15.82 mN/m which was almost the double of that of water. This suggests that after each compression, larger CeO₂ NP agglomerates were formed at the interface that had a greater effect on the Π -A isotherm described by higher lift-off areas, steeper isotherms and higher maximum Π values. In fact, Stuart et al., 2006 showed that the compression isotherm of two different sized gelatin NPs shifted to larger areas with NP size for a similar mass deposited. Moreover, due to the fact that the effect on Π was higher for PBS than for water, the surface concentration of the CeO₂ NP agglomerates probably played a key role in increasing Π as it is expected that due to the higher instability of CeO₂ NPs in PBS than in water, CeO₂ NP clusters agglomerated faster with each compression and had a higher surface concentration. This suggests that it was the size and surface concentration of the CeO₂ NP agglomerates and not the area covered by them that influenced Π ; these data support the concept that small NP agglomerates spread all over the interfacial area would not have an appreciable effect on the Π .

It has been shown in these studies that CeO₂ NPs did not have an appreciable effect on the DPPC isotherm after one compression when measured in PBS at both 21°C and 37°C. Based on the above data, two main hypotheses for this lack of effect have been developed:

- a) Following deposition there was a rapid agglomeration of CeO₂ NP clusters which detached from the surface and sedimented out in the subphase, thus the majority of the CeO₂ NPs were lost from the interface and the small mass remaining was insufficient to have any impact upon the isotherms (for the reasons outlined in (b)). These results could be investigated further by ICP-MS analysis of the subphase and also by quantitative measurement of CeO₂ NPs in the monolayer. It is important to note that in the literature, the majority of studies that investigate NP-lung surfactant interactions link dose with effects assuming that all the NPs remain at the interface and few studies have considered losses. In this context, the wettability of the particles within the system is an important determinant of loss.

- b) During the initial compression of the monolayer, the CeO₂ NP agglomerates present at the interface were of small size and large interparticle distance and therefore, did not affect the Π -MMA isotherm. This suggests a size and surface concentration-dependent effect of CeO₂ NP agglomerates on Π . At the same time, DPPC molecules would have packed around the NPs or rearranged themselves to fit in whatever space was available without influencing the isotherm shape (Jyoti et al., 1996, Guzmán et al., 2011).

Even if CeO₂ NPs did not affect the DPPC isotherm, the effect of NPs on the monolayer domains should also be studied. For example, Tatur and Badia, 2011 showed that depositing mixtures of 0.2 mol % of NPs and 99.8 mol % of DPPC onto a water subphase did not have an effect on the DPPC compression isotherm but altered the nucleation, growth and morphology of the condensed domains. Dwivedi et al, 2014 showed that the presence of polyorganosiloxane NPs of 12 nm did not change the isotherm for any of the NP mass deposited, but caused disruption of the domain morphology of the LE phase. In the present work, the effect of CeO₂ NPs on the DPPC domains was not investigated as the only technique available to us at the time to study the structure of films at the air/liquid interface, including those incorporating CeO₂ NPs, was AFM. This technique gives information about the topography of the film surface with a nanometre scale resolution, however it was not suitable for the present study as NPs could not be clearly differentiated from salt crystals formed during the evaporation of PBS and the presence of salt across the surface made it difficult to visualise the domains. To illustrate this, Figure 79 shows an AFM height image of a DPPC monolayer when deposited onto a water subphase and when deposited onto a PBS subphase, taken at a Π value of 40 mN/m. The AFM used was a Veeco Multimode, Model number MMAFMLZ, with a Bruker Nanoscope V controller and was operated in tapping mode. The height of the interface is indicated by the scale located at the right side of each image. This figure shows the salt crystals spread across the surface when using a PBS subphase compared to water. The height of these crystals was around 100 nm. These crystals could not be differentiated from CeO₂ NPs when imaging the interface after depositing CeO₂ NPs onto a PBS subphase and also impeded the study of the DPPC monolayer domains.

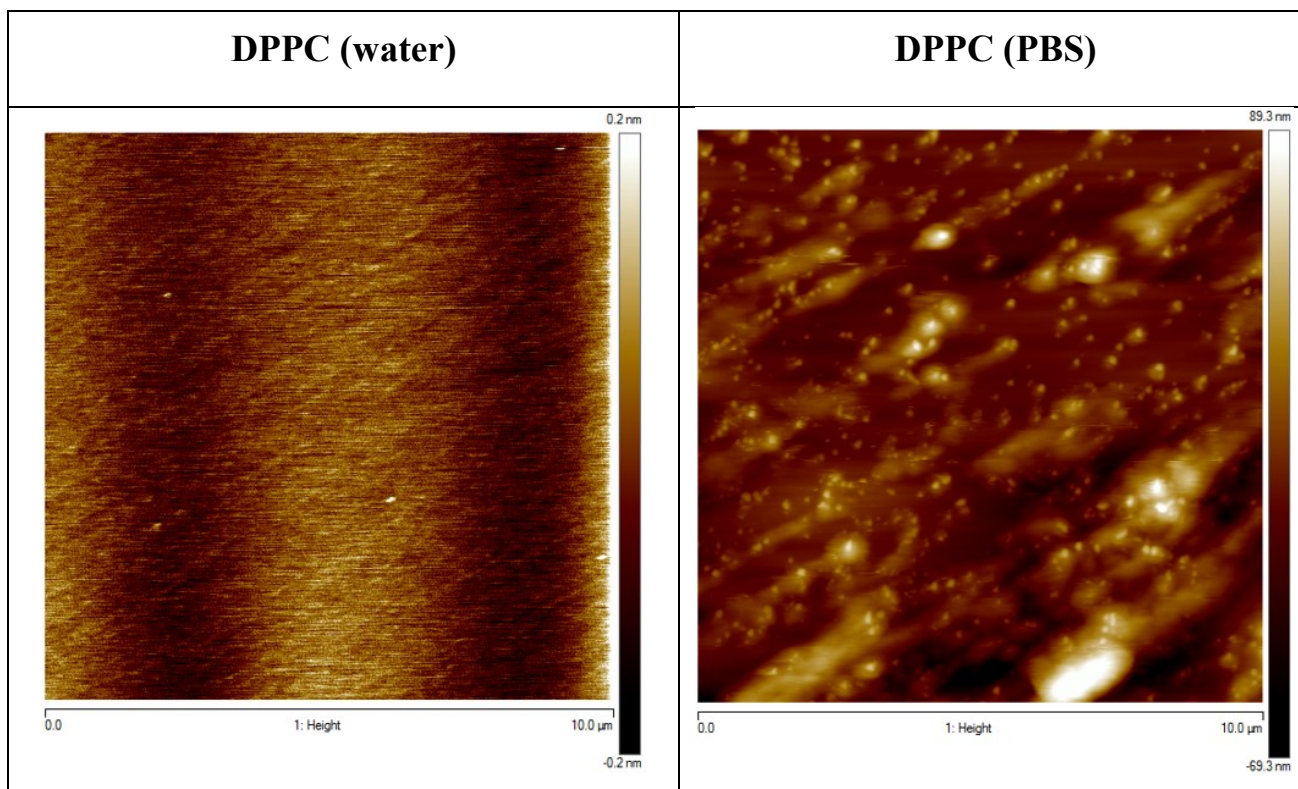


Figure 79. AFM height images of an LB film of a DPPC monolayer when deposited onto a water subphase at 21°C (left) and when deposited onto a PBS subphase at 21°C (right), taken at a Π value of 40 mN/m. AFM was operated in tapping mode. The height of the interface is indicated by the scale located at the right side of each image. The scale bar in the left image ranges from -0.2 nm to 0.2 nm and in the right image from -69.3 nm to 89.3 nm. These images illustrate the presence of large salt crystals across the monolayer when using a PBS subphase compared to a water subphase.

Finally, cycling experiments also showed that in the presence of DPPC and after several compression-expansion cycles, CeO₂ NP agglomerates became larger. These experiments are therefore key to understand how the system would evolve. In the literature however, cycling is not usually performed in those studies that investigate NP-lung surfactant interactions. The present work also emphasises the importance of working with subphases that mimic physiological conditions in order to get a better picture of what happens *in vivo* as the θ of particles at the air-liquid-solid interface and with it the particle behaviour depends on the subphase medium. In the literature, most of the studies that investigate NP-lung surfactant interactions used water as the subphase medium.

A detailed comparison of the results reported in the present section and those in the literature is included later in this chapter (section 3.6.2).

3.5.2 Deposition method 2: Liquid deposition of mixtures of CeO₂ nanoparticles and DPPC

3.5.2.1 Nanoparticle characterisation pre-CeO₂ nanoparticle administration

3.5.2.1.1 Size and zeta potential of CeO₂ nanoparticles

The present work characterised the NP agglomerate size and zeta potential of the premixed suspensions of CeO₂ NPs and DPPC under investigation in both chloroform, which was the suspension medium, and PBS which was the subphase medium onto which CeO₂ NPs were deposited.

A. Chloroform

Size and zeta potential: CeO₂ NPs and DPPC were mixed in chloroform at different mass ratios for the experiments performed in PBS at 37°C and 21°C. Table 26 shows the CeO₂/DPPC mass ratios, CMD, GSD and Z-average diameter for each of the suspensions used for the experiments performed at 37°C. Table 27 shows the CeO₂/DPPC mass ratios, Z-average diameter and zeta potential for each of the suspensions used for the experiments performed at 21°C.

Table 26. CeO₂/DPPC mass ratios, CMD, GSD and Z-average diameter for each of the suspensions in chloroform used in the experiments performed in PBS at 37°C to study the effect of the deposition of different CeO₂/DPPC mass ratios on the *I*-Mma isotherm.

CeO ₂ /DPPC mass ratio	CMD (nm)	GSD	Z-average diameter (nm)
0.06/1	42	1.7	154
1.25/1	40	2.0	132
3.75/1	38	2.2	131

Table 27. CeO₂/DPPC mass ratios and zeta potential for each of the suspensions in chloroform used in the experiments performed in PBS at 21°C to study the effect of the deposition of different CeO₂/DPPC mass ratios on the *I*-Mma isotherm.

CeO₂/DPPC mass ratio	Z-average diameter (nm)	Zeta potential (mV)
0.05/1	145	+ 37.53
1.00/1	122	+ 42.77
3.00/1	119	+ 52.47

As can be seen in Table 26 and Table 27, the CMD was smaller than the Z-average diameter for all the CeO₂/DPPC mass ratio suspensions in chloroform. The CMD and Z-average diameter were also smaller than those values reported previously for CeO₂ NPs alone suspended in chloroform whose CMD and Z-average diameter were 158 nm and 222 nm respectively (see section 3.5.1.1.1). This can be visualised in Figure 80 which shows two TEM images of CeO₂ NP agglomerates corresponding to the 1.25/1 CeO₂/DPPC mass ratio suspension (with smaller size) and to the CeO₂ NP suspension (with larger size).

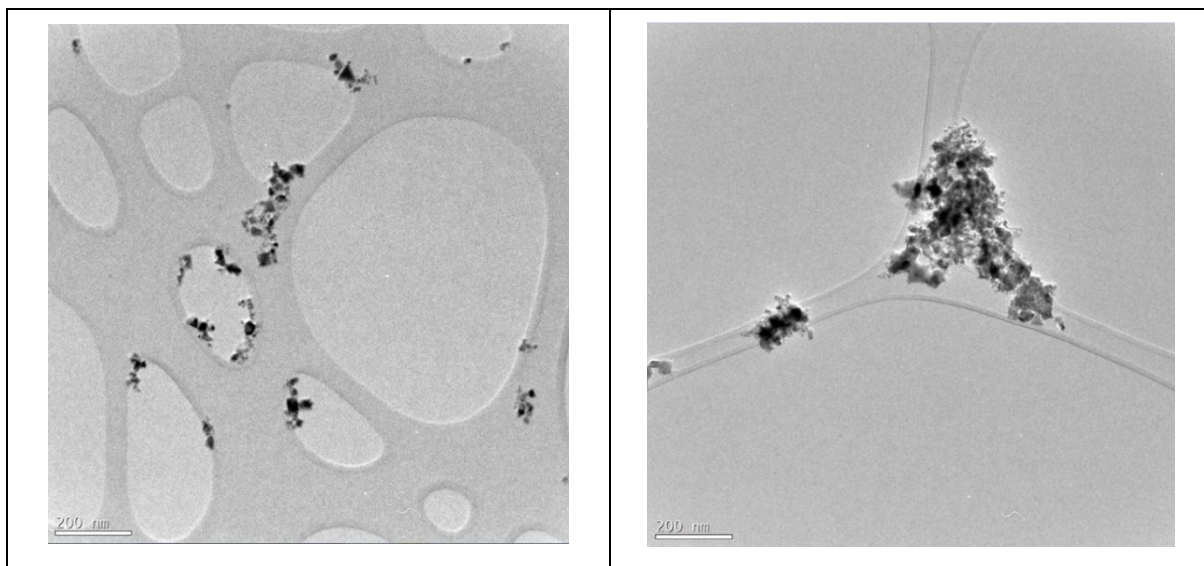


Figure 80. TEM images of CeO₂ nanoparticle agglomerates that correspond to the 1.25/1 CeO₂/DPPC mass ratio suspension in chloroform (left image) and to the CeO₂ nanoparticle suspension in chloroform (right image). The scale bar is 200 nm for both images.

As previously mentioned, there is evidence that the wettability or degree of hydrophobicity of particles in a suspending medium can be modified by the adsorption of surfactant to the surface of the particles (Maestro et al., 2012, Maestro et al., 2015). Thus, it is believed that the adsorption of DPPC onto the surface of CeO₂ NPs increased the wettability of the NPs and with it their stability in chloroform and decreased the NP agglomerate size. In fact, CeO₂ NP and DPPC suspensions in chloroform were much more stable than suspensions of CeO₂ NPs in chloroform and did not need to be sonicated prior to characterisation or use. Figure 81 shows a TEM image of CeO₂ NP agglomerates coated with a layer which was probably DPPC, as previously described for nanosilver and DPPC (Leo et al., 2013, Theodorou et al., 2015).

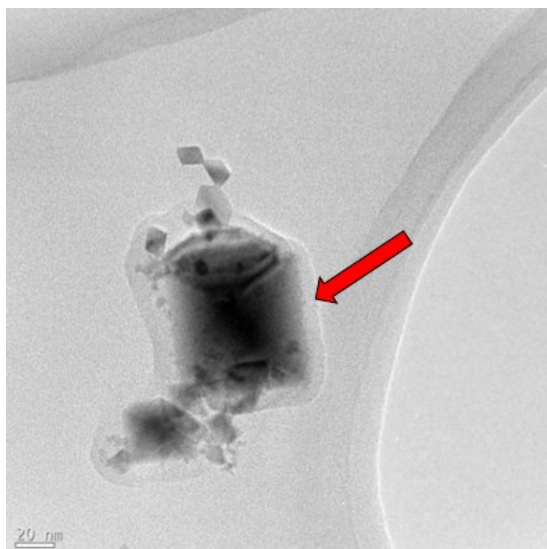


Figure 81. TEM image of a CeO₂ nanoparticle agglomerate probably coated with DPPC (indicated by a red arrow). This image corresponds to the 1.25/1 CeO₂/DPPC mass ratio suspension in chloroform. The scale bar is 20 nm.

It was also shown previously in Table 27 that as the CeO₂/DPPC mass ratio reduced (by increasing the DPPC mass) the size of the NP agglomerates increased whereas the zeta potential decreased, indicating lower stability. This suggests that the addition of surfactant to a chloroform medium decreased the CeO₂ NP agglomerate size up to a point after which, further increases in surfactant concentration led to an increase in the hydrophobicity of the CeO₂ NP agglomerates and therefore, an increase in their size. Zeta potential measurements are in good agreement with this as more unstable suspensions were those with a higher DPPC concentration.

B. PBS

Size and zeta potential: As previously mentioned in section 3.5.1.1.1, CeO₂ NPs suspended in PBS agglomerated and sedimented within seconds. The presence of DPPC enabled CeO₂ NPs to remain suspended in PBS and measurements of their size and zeta potential could be taken. CeO₂ NPs and DPPC were suspended in PBS at two different CeO₂/DPPC mass ratios: 0.2/1 and 3.0/1. Table 28 shows the Z-average diameter, zeta potential and pH for each of the suspensions.

Table 28. CeO₂/DPPC mass ratios, Z-average diameter, zeta potential and pH for each of the suspensions in PBS.

CeO ₂ /DPPC mass ratio	Z-average diameter (nm)	Zeta potential (mV)	pH
0.2/1	1,444	+ 2.11	7.30
3.0 /1	2,434	- 2.30	6.96

As can be seen from this table, increased DPPC concentration reduced the size of the agglomerates as they could remain suspended in the PBS medium. It is believed that the coating with DPPC changed the wettability of the NPs making them less hydrophobic compared to CeO₂ NPs alone in PBS. These sizes however were larger than those reported previously for suspensions in chloroform due to the higher instability of the current systems which have zeta potential values close to the zero net charge. Despite these low zeta potential values, it was observed that CeO₂ NP agglomerates with DPPC remained suspended in the PBS medium and did not easily settle at the bottom of the bottle.

3.5.2.1.2 Wettability and surface tension activity of CeO₂ nanoparticles

As already seen in section 3.5.2.1.1, the wettability of the CeO₂ NPs was probably modified by the adsorption of surfactant to the surface of the NP. Both the wettability and surface tension activity of CeO₂ NPs mixed with DPPC at different mass ratios were investigated in the next section (section 3.5.2.2).

3.5.2.2 Effect of the deposition of different CeO₂ nanoparticle and DPPC mass ratios on the surface pressure–Mma isotherm measured in PBS at 37°C and 21°C and interfacial layer characteristics post-CeO₂ nanoparticle administration

In this study, the capacity of CeO₂ NPs to remain at the air/liquid interface was investigated for the 3/1 CeO₂/DPPC mass ratio suspension in chloroform during the initial compression of the monolayer, after three compression-expansion cycles performed at normal barrier speed and after three compression-expansion cycles performed at maximum barrier speed (270 mm/min)

for comparative purposes. Figure 82 shows SEM and ToF-SIMS images of pure DPPC and DPPC mixed with CeO₂ NPs from a dipping experiment performed at four different Π values during the initial compression of the monolayer: 20, 40, 60 and 70 mN/m. Figure 83 shows SEM and ToF-SIMS images of pure DPPC and DPPC mixed with CeO₂ NPs from a dipping experiment performed at a Π value of 40 mN/m after three compression-expansion cycles at normal barrier speed. Figure 84 shows SEM and ToF-SIMS images of pure DPPC and DPPC mixed with CeO₂ NPs from a dipping experiment performed at a Π value of 40 mN/m after three compression-expansion cycles at maximum barrier speed. The areas imaged with each technique were different for each sample. In the ToF-SIMS images, the presence of CeO₂ NPs is indicated by the green colour scale located at the right side of each image.

Figure 82. SEM and ToF-SIMS images of LB films of pure DPPC (left) and DPPC mixed with CeO₂ nanoparticles in chloroform at a 3/1 CeO₂/DPPC mass ratio (right) produced in PBS at 21°C during the initial compression of the monolayer at four different *II* values: 20 (A), 40 (B), 60 (C) and 70 (D) mN/m. The areas imaged with each technique were different. In the SEM images, the dotted scale bar is 50 μm. ToF-SIMS images are 100 μm x 100 μm and the presence of CeO₂ nanoparticles is indicated by the green colour scale located at the right side of each image.

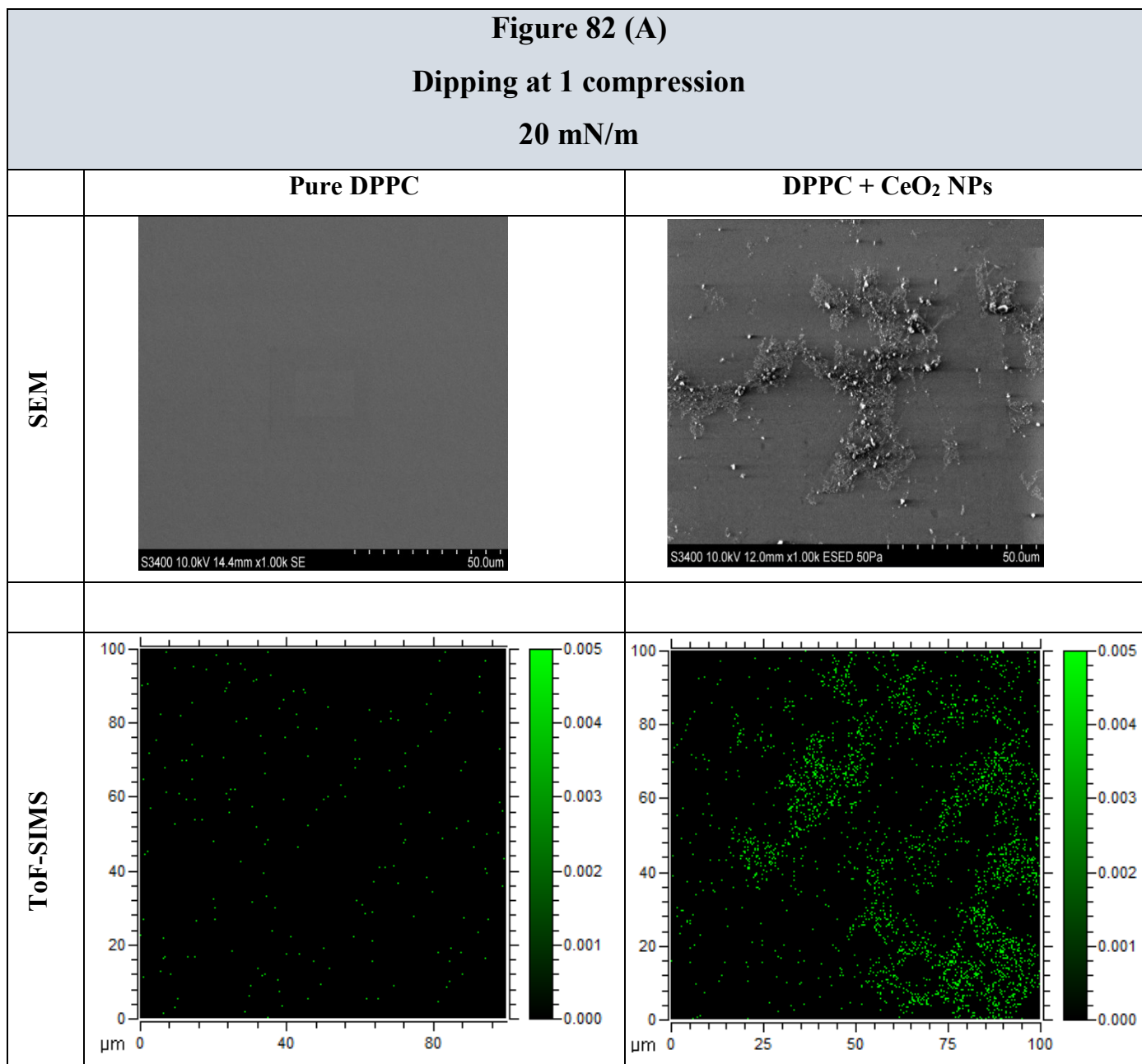


Figure 82 (B)
Dipping at 1 compression
40 mN/m

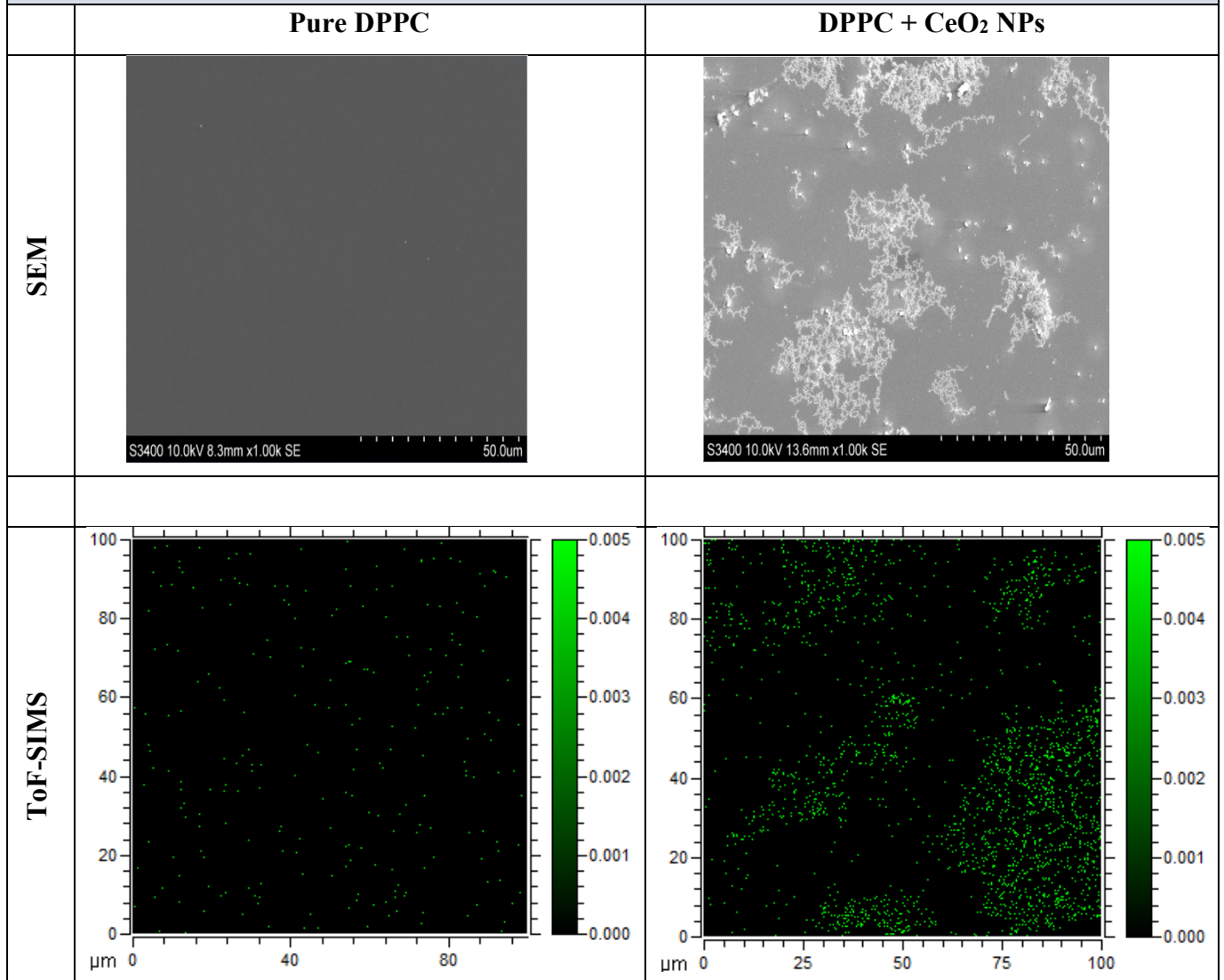


Figure 82 (C)
Dipping at 1 compression
60 mN/m

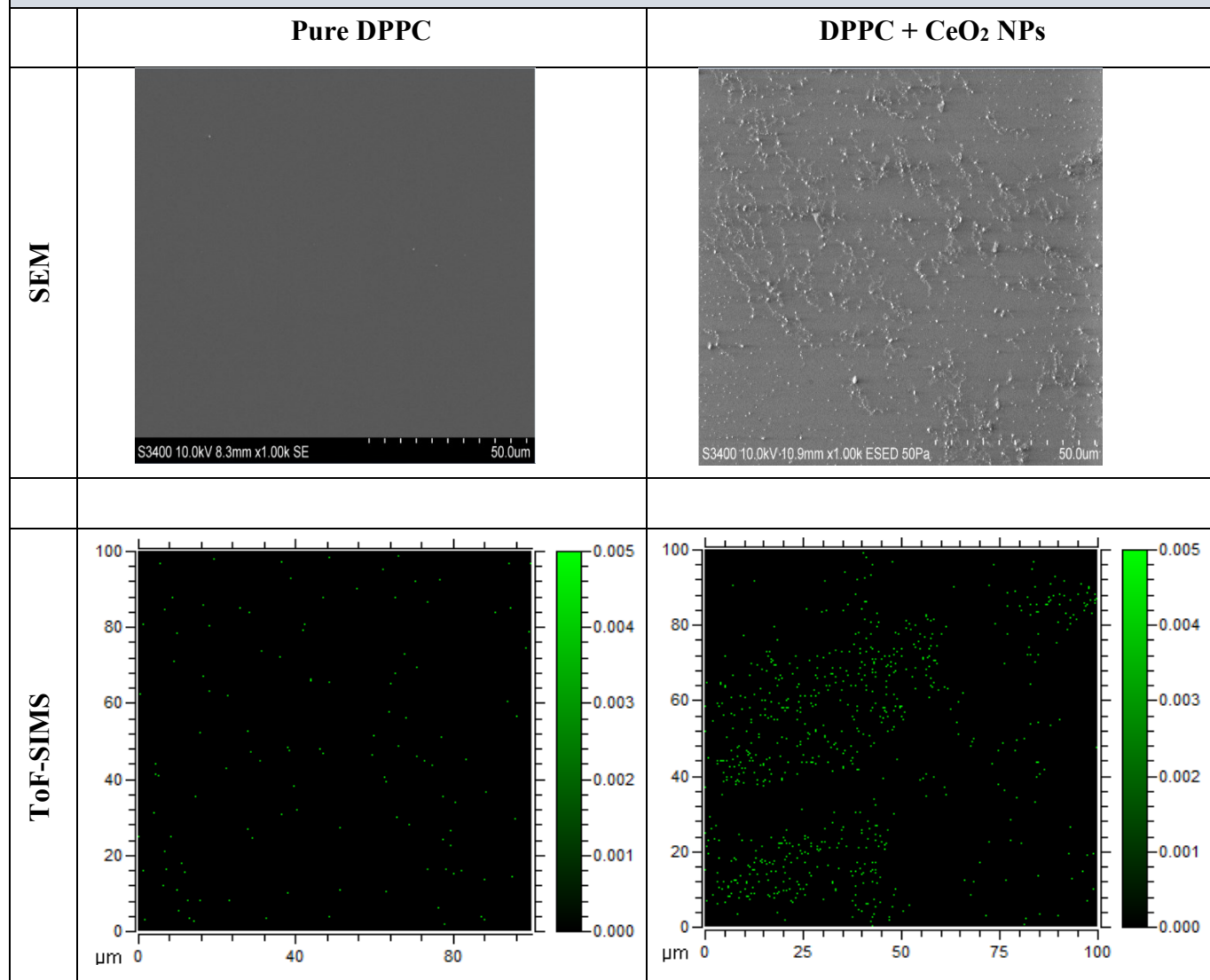


Figure 82 (D)
Dipping at 1 compression
70 mN/m

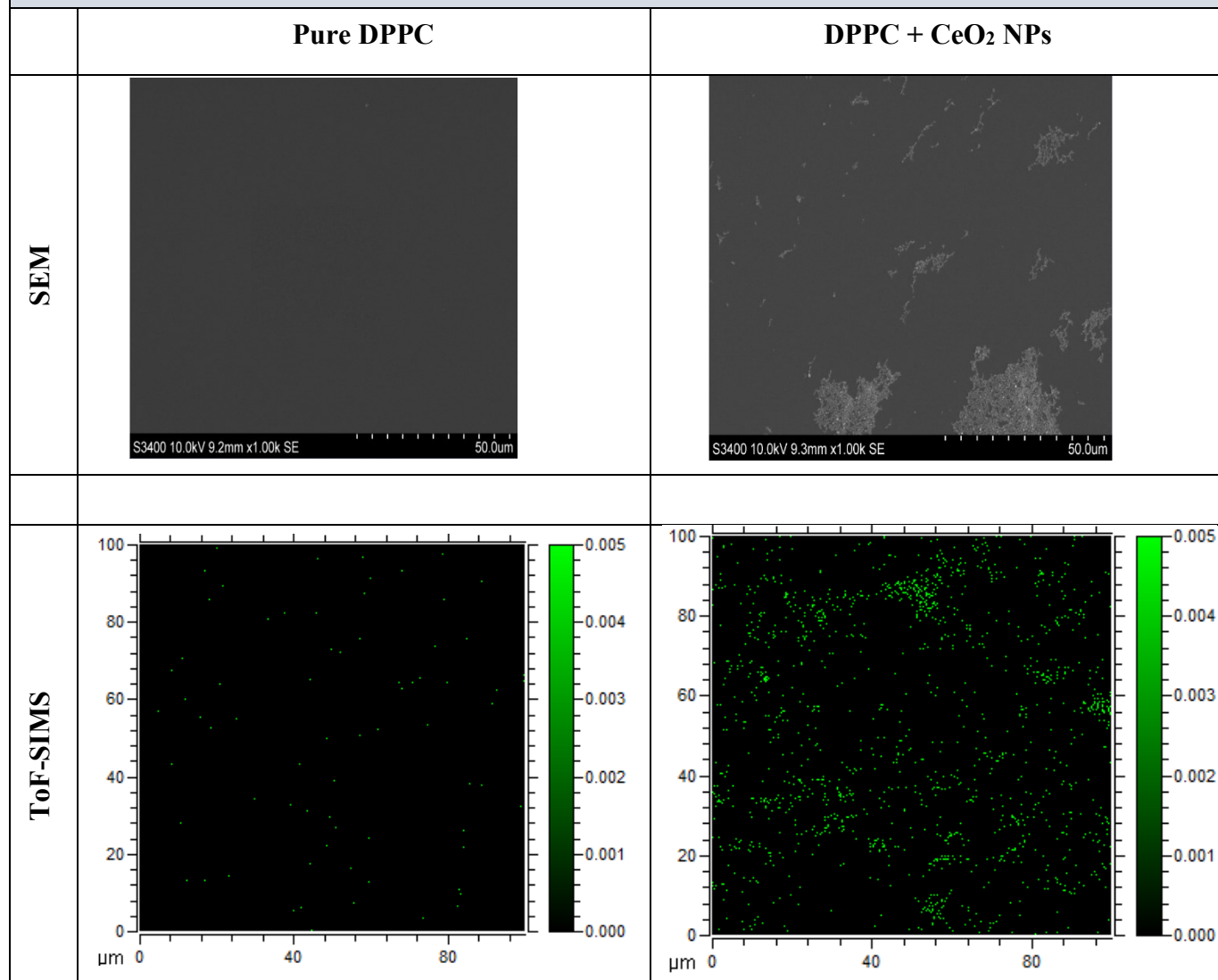


Figure 83. SEM and ToF-SIMS images of LB films of pure DPPC (left image) and DPPC mixed with CeO₂ nanoparticles in chloroform (3/1 CeO₂/DPPC mass ratio, right image) produced at a Π value of 40 mN/m after 3 compression-expansion cycles performed at normal barrier speed in PBS at 21°C. The areas imaged with each technique were different. In the SEM images, the dotted scale bar is 50 μ m. ToF-SIMS images are 100 μ m x 100 μ m and the presence of CeO₂ nanoparticles is indicated by the green colour scale located at the right side of each image.

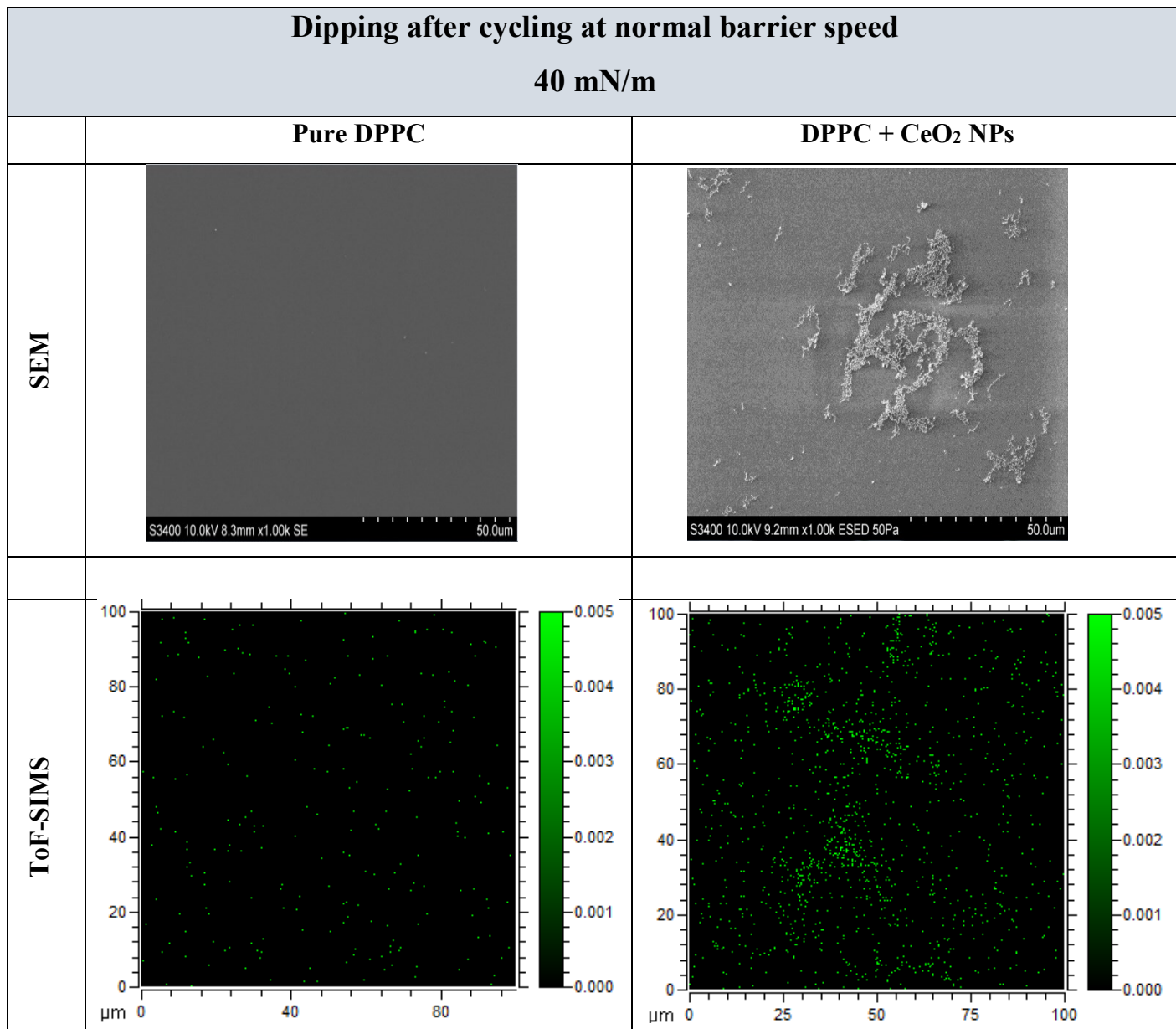


Figure 84. SEM and ToF-SIMS images of LB films of pure DPPC (left image) and DPPC mixed with CeO₂ nanoparticles in chloroform (3/1 CeO₂/DPPC mass ratio, right image) produced at a Π value of 40 mN/m after 3 compression-expansion cycles performed at maximum barrier speed in PBS at 21°C. The areas imaged with each technique were different. In the SEM images, the dotted scale bar is 50 μ m. ToF-SIMS images are 100 μ m x 100 μ m and the presence of CeO₂ nanoparticles is indicated by the green colour scale located at the right side of each image.

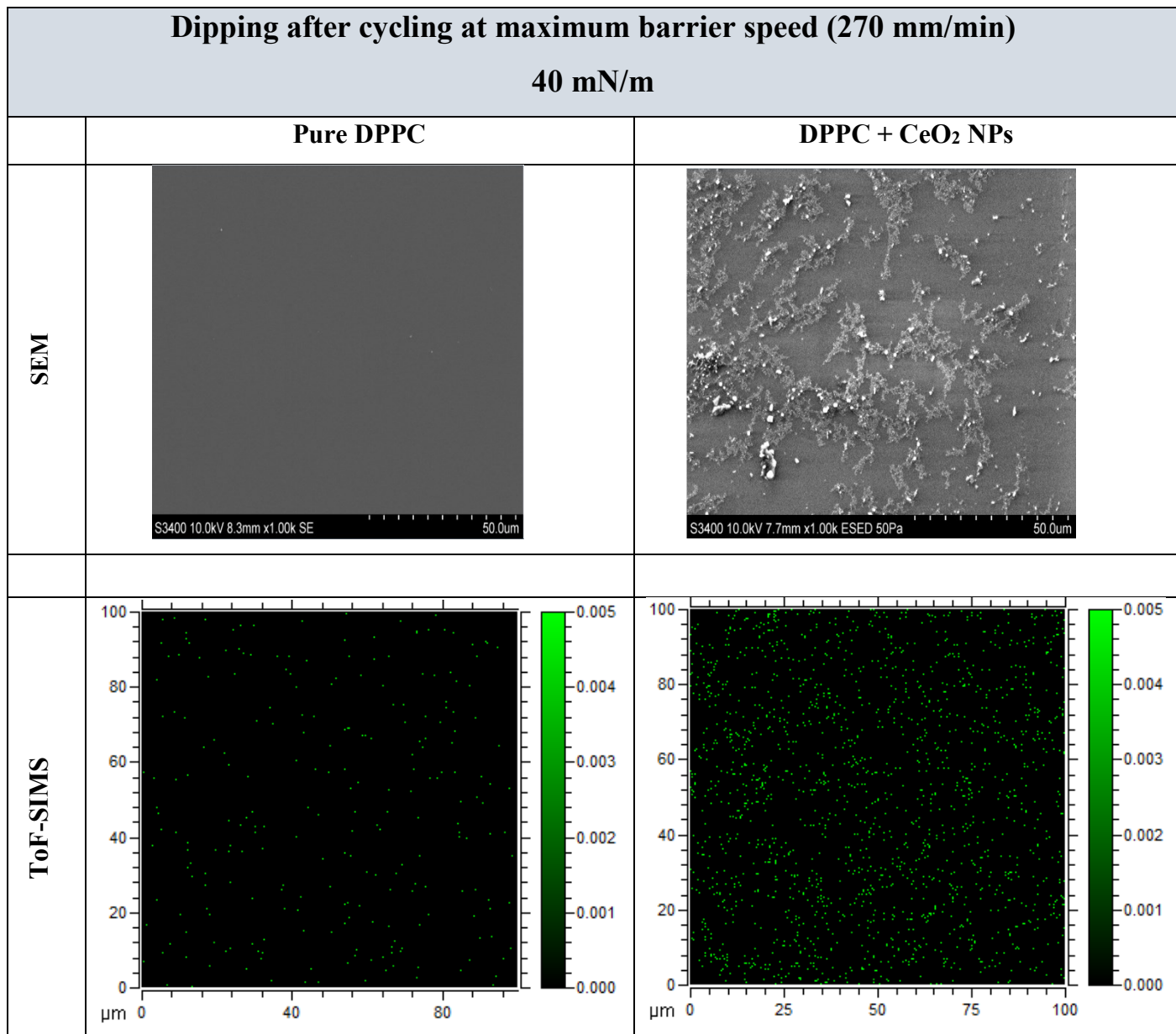


Figure 82 shows that during one compression CeO₂ NP agglomerates were present across the interface at Γ values of 20, 40, 60 and 70 mN/m. This suggests that the coating of CeO₂ NPs with DPPC decreased the degree of hydrophobicity and increased the stability of the NPs compared to CeO₂ NPs alone deposited onto a PBS subphase from chloroform suspensions (deposition method 1) which, it is hypothesised, rapidly agglomerated to form large, dense clusters that eventually sedimented into the subphase hence, mainly small agglomerates remained at the interface during one compression. This was shown previously in section 3.5.1.1.2. It is important to also bear in mind that the CMD and Z-average diameter for CeO₂/DPPC mixtures were smaller than those values reported previously for CeO₂ NPs alone and that the size is an important factor in the wetting process of particles by fluid interfaces. In fact, for most particles, θ increases with particle size till a plateau value. The surface charge of the particle is also a critical parameter to control the θ (Maestro et al., 2014, Maestro et al., 2015). Figure 83 and Figure 84 show that after 3 compression-expansion cycles performed at normal and maximum barrier speed there were still some CeO₂ NP agglomerates at the interface.

The areas covered by the CeO₂ NPs at the interface at various Γ values during one compression were determined by analysing the SEM images and expressed as a percentage of the total image area. Only one representative SEM image per Γ was analysed as it was necessary to have a very good contrast between the particles and the background and this was not the case for most of the SEM images. Results are shown in Table 29. As can be seen in this table, the area covered by the CeO₂ NP agglomerates increased up to 40 mN/m and then decreased with further compression.

Table 29. Area covered by the CeO₂ nanoparticle agglomerates at *H* values of 20, 40, 60 and 70 mN/m during the initial compression of the monolayer. The dipping experiments were performed after depositing a 3/1 CeO₂/DPPC mass ratio suspension in chloroform onto a clean PBS subphase at 21°C. The area covered by the CeO₂ nanoparticles was determined by analysing representative SEM images and expressed as a percentage of the total image area. One sample area per *H* was analysed.

Surface pressure (mN/m)	Area covered by CeO ₂ NP agglomerates (area covered/total image area, %)
20	12
40	19
60	5
70	4

Semi-quantitative analysis of the ToF-SIMS images was undertaken by counting the number of CeO⁺ ions at each position and normalising it to the total count of ions recorded per sample area (pixel-by-pixel division) to remove topographic and secondary ion yield effects (Yamada et al., 2003, Magnusson et al., 2008, Kempson et al., 2010). The higher the count, the higher the amount of material at the interface or surface concentration. In order to investigate the evolution of the CeO₂ surface concentration with compression, the count of CeO⁺ ions per sample area obtained for each *H* (20, 40, 60 and 70 mN/m) was plotted and is shown in Figure 85. Two different sample areas were analysed per *H*.

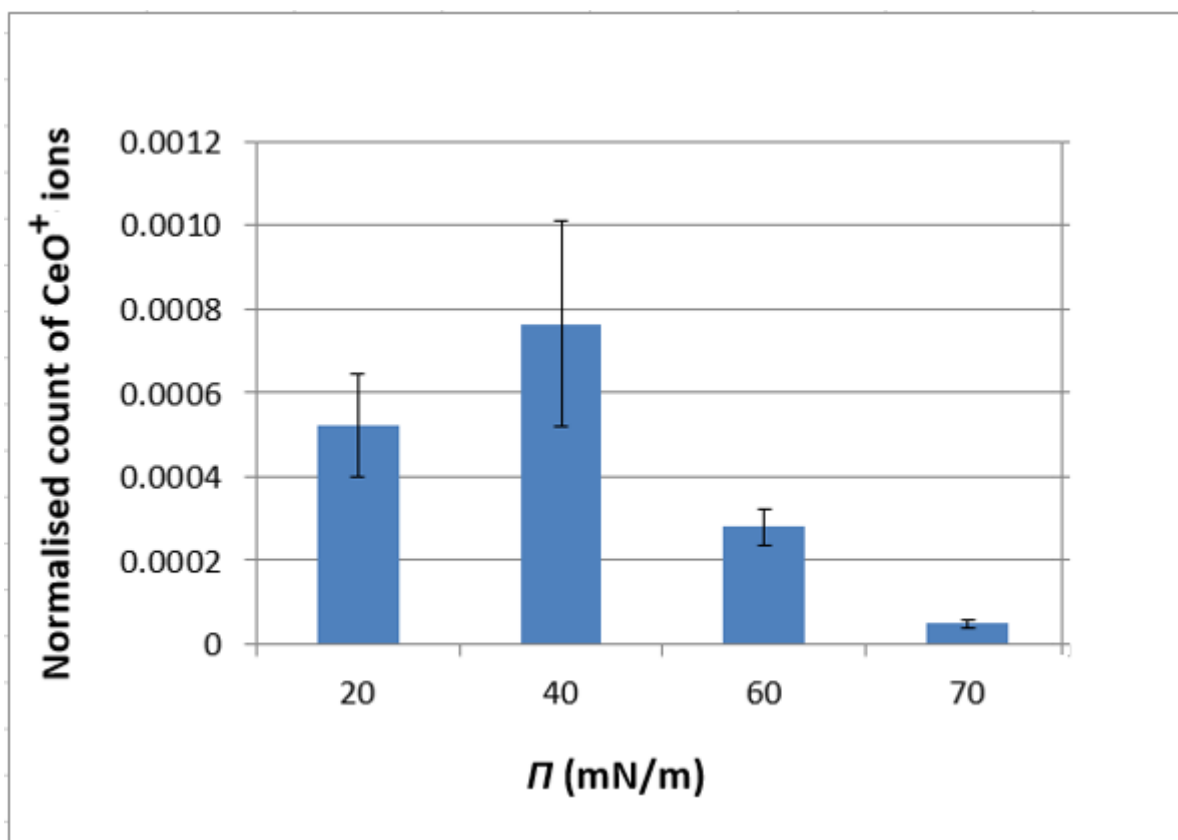


Figure 85. Normalised count of CeO^+ ions derived from the ToF-SIMS image data at Π values of 20, 40, 60 and 70 mN/m during the initial compression of the monolayer. The dipping experiments were performed after depositing a 3/1 CeO_2 /DPPC mass ratio suspension in chloroform onto a clean PBS subphase at 21°C. Two different sample areas were analysed per Π .

As can be seen in Figure 85, the CeO_2 surface concentration increased up to 40 mN/m and then decreased with further compression. Based on these results and those shown previously in Table 29, it is believed that this was caused by the formation of large and dense agglomerates with compression that eventually detached from the interface and sedimented into the subphase. This was investigated further by taking samples of the subphase with a pipette and analysing those using ICP-MS but the data produced were not robust enough to be presented in this thesis. These results contrast with other literature studies performed by spreading NPs onto an octane/water interface (Aveyard et al., 2000b, Horozov et al., 2006) and molecular simulation studies (Fenwick et al., 2001, Powell et al., 2002) that show that the particle monolayer folded with compression and led to the formation of large corrugations without particles being expelled from the interface (see section 1.2.3.2). In order to investigate this further, the same experiment was performed by depositing a 3/1 CeO_2 /DPPC mass ratio suspension onto a clean water

subphase and compressing the interface. Figure 86 shows SEM images of DPPC mixed with CeO₂ NPs at four different Π values during the compression of the monolayer: 20, 40, 60 and 70 mN/m. Unfortunately, the area covered by the NPs at the interface could not be determined because there was not a good contrast between the particles and the background to analyse the images with the software image J. However, it is clear from this figure that CeO₂ NPs agglomerated with compression up to 70 mN/m and possibly did not leave the interface. This contrasts with the present work when using a PBS subphase which suggests that agglomerates detached from the interface and sedimented into the subphase (see Figure 85). It also agrees with other studies in the literature (Aveyard et al., 2000b, Horozov et al., 2006). Thus, this supports the hypothesis that a key factor that dictates the CeO₂ NP behaviour at an air/liquid interface is the subphase composition.

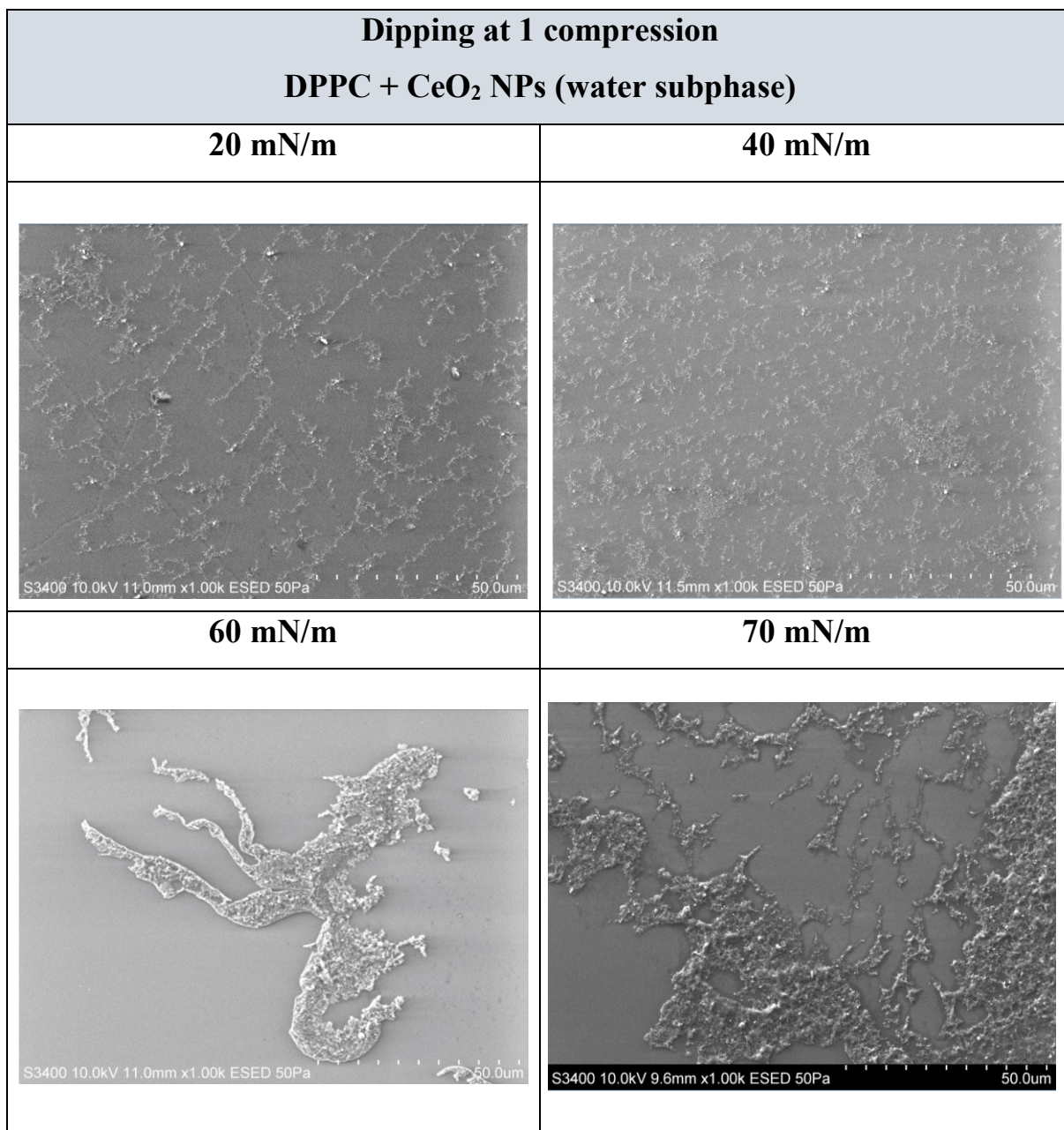


Figure 86. SEM images of LB films of DPPC mixed with CeO₂ nanoparticles in chloroform at a 3/1 CeO₂/DPPC mass ratio produced in water at 21°C during the initial compression of the monolayer at four different Π values: 20, 40, 60 and 70 mN/m. The dotted scale bar is 50 μ m.

The effect of each CeO₂/DPPC mass ratio suspension on the Π -M_{ma} isotherm during one compression was also measured in PBS and compared with that of DPPC alone at both 37°C and 21°C. Results obtained at 37°C are shown first. Table 30 shows the DPPC and CeO₂ NP masses deposited for each CeO₂/DPPC mass ratio suspension as well as the DPPC mass deposited for the control experiment. Figure 87 shows the effect of the deposition of different

CeO₂/DPPC mass ratio suspensions onto a PBS subphase on the *II*-Mma isotherm. *II* was measured as a function of the available surface area to each DPPC molecule. Table 31 shows the lift-off Mma, C_m , collapse *II* and collapse Mma of the *II*-Mma isotherms. The corresponding values in each of these parameters measured for each CeO₂/DPPC mass ratio suspension were compared with those of pure DPPC (control) by calculating the % difference between experiment and control for each of the parameters and dividing them by the reference % change from midpoint values, i.e., assuming similar levels of uncertainties on the parameters to those of the reference isotherms (see section 2.4.1.5). As can be seen from Table 31, depositing 0.33 µg of CeO₂ NPs (0.06/1 NP/DPPC mass ratio) increased the lift-off Mma but not the other isotherm parameters; depositing 7.00 µg of CeO₂ NPs (1.25/1 NP/DPPC mass ratio) had an effect on all the parameters of the isotherm and most markedly increased the lift-off Mma; depositing 13.13 µg of CeO₂ NPs (3.75/1 NP/DPPC mass ratio) altered all the isotherm parameters except the C_m for the region 31-lowest collapse *II*. The parameter that was most significantly affected by this NP mass was the lift-off Mma. Therefore all the CeO₂ NP masses deposited had a significant effect on the lift-off Mma that increased with NP mass. Moreover, for the 1.25/1 NP/DPPC mass ratio the collapse *II* value was significantly lower than that of the control. This will be discussed later in the chapter.

Table 30. CeO₂ nanoparticle and DPPC masses deposited onto a clean PBS subphase at 37°C for the DPPC solution (control) and each CeO₂/DPPC mass ratio suspension in chloroform for a set of experiments performed to study the effect of the deposition of different CeO₂/DPPC mass ratio mixtures on the *II*-Mma isotherm.

CeO ₂ /DPPC mass ratio	CeO ₂ NP mass deposited (µg)	DPPC mass deposited (µg)
0 (DPPC, control)	-	5.60
0.06/1	0.33	5.33
1.25/1	7.00	5.60
3.75/1	13.13	3.50

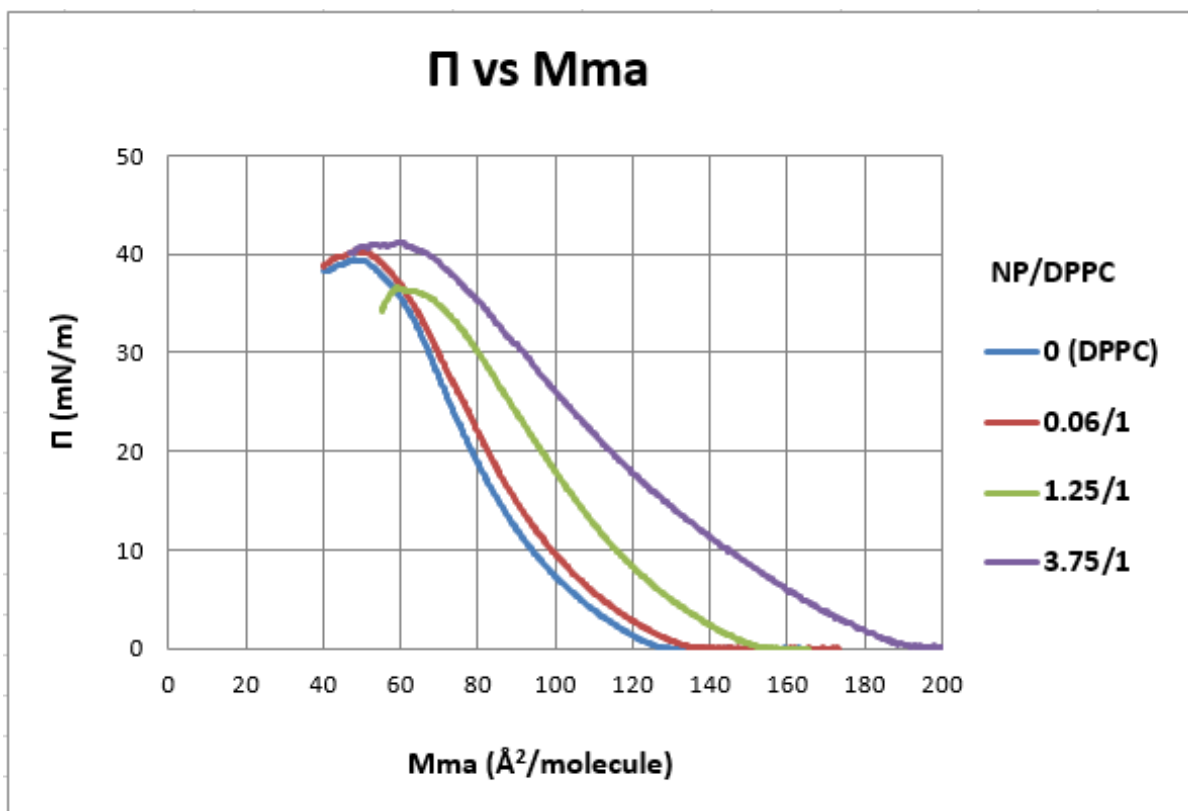


Figure 87. Effect of the deposition of different CeO₂/DPPC mass ratio mixtures suspended in chloroform onto a PBS subphase on the Π - Mma isotherm measured at 37°C. n = 4 experiments/condition.

Table 31. Effect of the deposition of different CeO₂/DPPC mass ratio suspensions in chloroform onto a PBS subphase at 37°C on the lift-off M_{ma}, C_m, collapse II and collapse M_{ma} of the II-M_{ma} isotherms. The corresponding values in each of these parameters for each CeO₂/DPPC mass ratio mixture were compared with those of pure DPPC (control) by calculating the difference in each of the parameters for the experimental isotherm and the control expressed as a % of the control value and dividing them by the reference % change from midpoint values for the relevant reference isotherm (Table 11). This approach assumes similar levels of uncertainties on the control and experimental isotherm parameters to those of the reference isotherm parameters.

CeO ₂ /DPPC mass ratio	Lift-off M _{ma} (Å ² /molecule)	(% difference experiment and control)/(reference % change from midpoint)	C _m 1-5 mN/m (mN/m) ⁻¹	(% difference experiment and control)/(reference % change from midpoint)	C _m 10-25 mN/m (mN/m) ⁻¹	(% difference experiment and control)/(reference % change from midpoint)
<i>Reference isotherm</i>	123	1.0 (% change from midpoint)	0.0298	3.0 (% change from midpoint)	0.0150	2.0 (% change from midpoint)
0 (control)	123		0.0309		0.0151	
0.06/1	132	7.0	0.0305	0.3	0.0150	0.5
1.25/1	151	23.0	0.0289	2.0	0.0157	2.0
3.75/1	189	54.0	0.0282	3.0	0.0195	14.5

CeO ₂ /DPPC mass ratio	C _m 31 mN/m – lowest collapse II (mN/m) ⁻¹	(% difference experiment and control)/(reference % change from midpoint)	Collapse II (mN/m)	(% difference experiment and control)/(reference % change from midpoint)	Collapse M _{ma} (Å ² /molecule)	(% difference experiment and control)/(reference % change from midpoint)
<i>Reference isotherm</i>	0.0294	15.0 (% change from midpoint)	39.40	2.0 (% change from midpoint)	49	4.0 (% change from midpoint)
0 (control)	0.0221		39.22		50	
0.06/1	0.0228	0.2	39.66	0.5	49	0.5
1.25/1	0.0446	6.8	36.61	3.5	59	4.5
3.75/1	0.0249	0.9	41.19	2.5	60	5.0

A similar experiment was performed in PBS at 21°C for comparative purposes. Table 32 shows the DPPC and CeO₂ NP masses deposited for each CeO₂/DPPC mass ratio suspension as well as the DPPC mass deposited for the control experiment. Figure 88 shows the effect of the deposition of different CeO₂/DPPC mass ratio suspensions onto a PBS subphase on the *II*-Mma isotherm. *II* was measured as a function of the available surface area to each DPPC molecule. Table 33 shows the lift-off Mma, *C_m*, collapse *II* and collapse Mma of the *II*-Mma isotherms. The corresponding values in each of these parameters measured for each CeO₂/DPPC mass ratio suspension were compared with those of pure DPPC (control) by calculating the % difference between experiment and control for each of the parameters and dividing them by the reference % change from midpoint values, i.e., assuming similar levels of uncertainties on the parameters to those of the reference isotherms (see section 2.4.1.5). As can be seen from Table 33, depositing 0.36 µg of CeO₂ NPs (0.05/1 NP/DPPC mass ratio) had a small, possibly unimportant effect on the lift-off Mma but not the other isotherm parameters; depositing 7.00 µg of CeO₂ NPs (1.00/1 NP/DPPC mass ratio) caused an increase in the lift-off Mma, a decrease in the *C_m* for the region 5-10 and an increase in the *C_m* for the region 25-45; depositing 18.75 µg of CeO₂ NPs (3.00/1 NP/DPPC mass ratio) most affected the lift-off Mma, which was increased, the *C_m* for the region 5-10, which was decreased, and the *C_m* for the region 25-45, which was increased. Thus, in agreement with those experiments performed at 37°C, the lift-off Mma increased with NP mass. A graphical representation of the effect of the different CeO₂/DPPC mass ratios on the *C_m*, collapse *II* and collapse Mma is shown in Figure 89.

Table 32. CeO₂ nanoparticle and DPPC masses deposited onto a clean PBS subphase at 21°C for the DPPC solution (control) and each CeO₂/DPPC mass ratio suspension in chloroform for a set of experiments performed to study the effect of the deposition of different CeO₂/DPPC mass ratio mixtures on the Π -Mma isotherm.

CeO ₂ /DPPC mass ratio	CeO ₂ NP mass deposited (μg)	DPPC mass deposited (μg)
0 (DPPC, control)	-	7.00
0.05/1	0.36	7.14
1.00/1	7.00	7.00
3.00/1	18.75	6.25

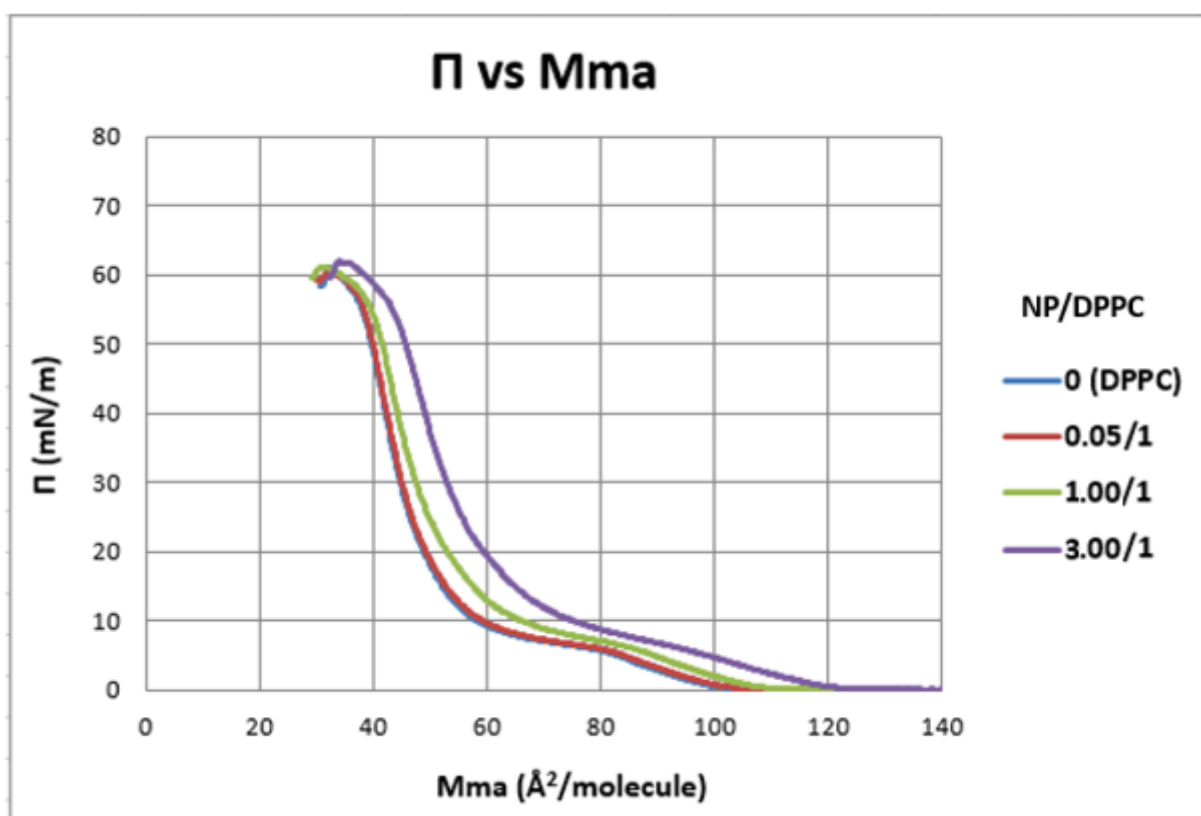


Figure 88. Effect of the deposition of different CeO₂/DPPC mass ratio mixtures suspended in chloroform onto a PBS subphase on the Π -Mma isotherm measured at 21°C. n = 5 experiments/condition.

Table 33. Effect of the deposition of different CeO₂/DPPC mass ratio suspensions in chloroform onto a PBS subphase at 21°C on the lift-off Mma, C_m, collapse II and collapse Mma of the II-Mma isotherms. The corresponding values in each of these parameters for each CeO₂/DPPC mass ratio mixture were compared with those of pure DPPC (control) by calculating the difference in each of the parameters for the experimental isotherm and the control expressed as a % of the control value and dividing them by the reference % change from midpoint values for the relevant reference isotherm (Table 12). This approach assumes similar levels of uncertainties on the control and experimental isotherm parameters to those of the reference isotherm parameters

CeO ₂ /DPPC mass ratio	Lift-off Mma (Å ² /molecule)	(% difference experiment and control)/(reference % change from midpoint)	C _m 1-5 mN/m (mN/m) ⁻¹	(% difference experiment and control)/(reference % change from midpoint)	C _m 5-10 mN/m (mN/m) ⁻¹	(% difference experiment and control)/(reference % change from midpoint)
<i>Reference isotherm</i>	100	2.0 (% change from midpoint)	0.0378	3.0 (% change from midpoint)	0.0636	9.0 (% change from midpoint)
0 (control)	100		0.0365		0.0704	
0.05/1	102	1.0	0.0369	0.3	0.0695	0.1
1.00/1	107	3.5	0.0373	0.7	0.0513	3.0
3.00/1	120	10.0	0.0378	1.3	0.0503	3.2

CeO ₂ /DPPC mass ratio	C _m 25-45 mN/m (mN/m) ⁻¹	(% difference experiment and control)/(reference % change from midpoint)	C _m 50 mN/m – lowest collapse II (mN/m) ⁻¹	(% difference experiment and control)/(reference % change from midpoint)	Collapse II (mN/m)	(% difference experiment and control)/(reference % change from midpoint)	Collapse Mma (Å ² /molecule)	(% difference experiment and control)/(reference % change from midpoint)
<i>Reference isotherm</i>	0.0063	6.0 (% change from midpoint)	0.0247	36.0 (% change from midpoint)	57.17	2.0 (% change from midpoint)	31	5.0 (% change from midpoint)
0 (control)	0.0057		0.0185		59.66		34	
0.05/1	0.0059	0.7	0.0144	0.6	60.30	0.5	32	1.2
1.00/1	0.0076	5.5	0.0170	0.2	61.02	1.0	32	1.2
3.00/1	0.0073	4.7	0.0164	0.3	61.90	2.0	34	0.0

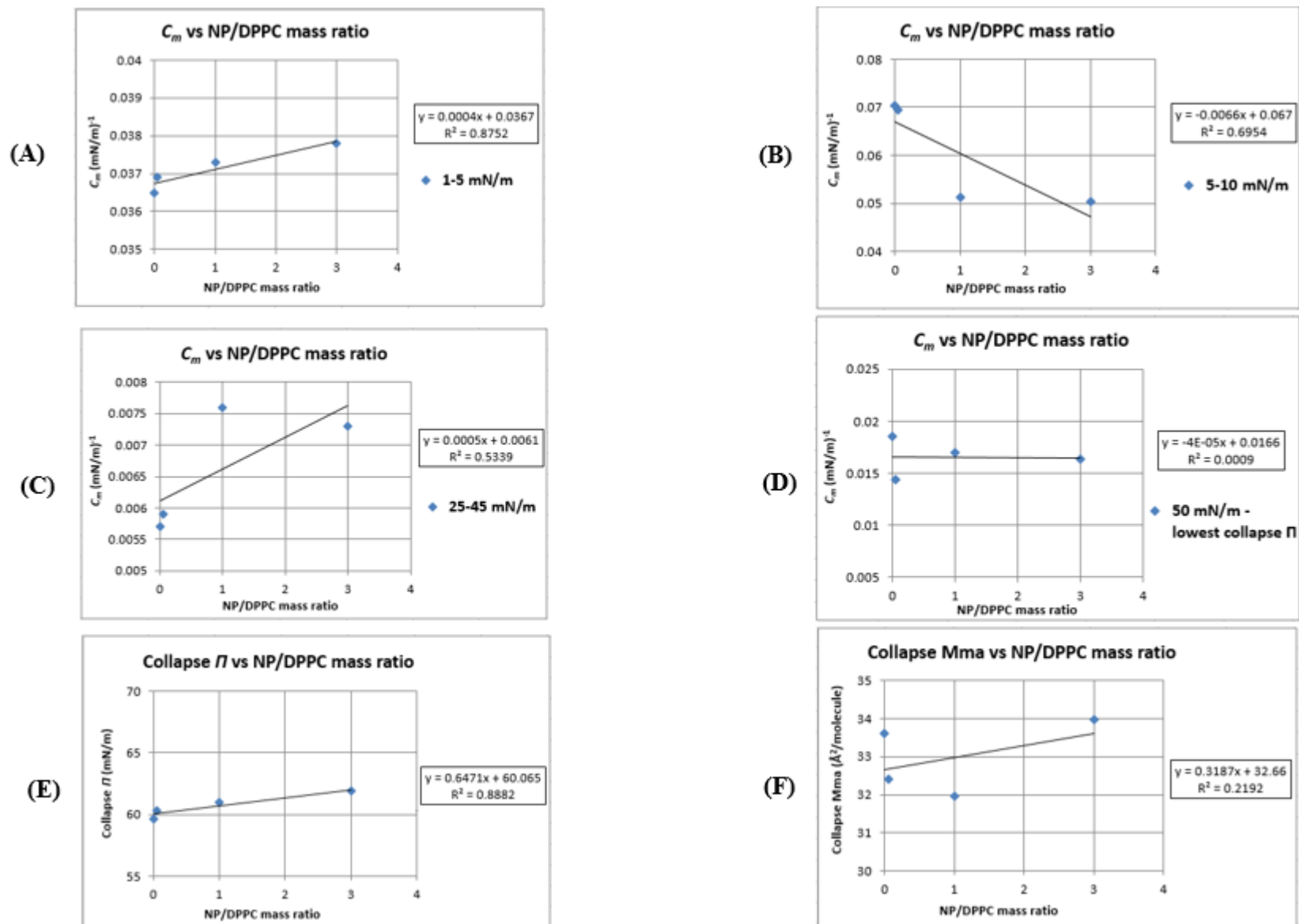


Figure 89. Graphical representation of the effect of the deposition of different CeO_2/DPPC mass ratio suspensions in chloroform onto a PBS subphase at 21°C on the C_m (A, B, C, D), collapse Π (E) and collapse Mma (F) of the Π -Mma isotherms. Note the reduced segment of the y axis. The lines are representative of the trend.

Results show that effects at 37°C were generally more pronounced than those at 21°C for similar CeO₂/DPPC mass ratios described by higher ratios of the % difference between experiment and control to the % change from midpoint in the isotherm parameters. For example, at 37°C, the lowest NP mass deposited had an effect on the lift-off Mma. This was not so pronounced at 21°C. Effects at 37°C were also larger for the collapse *II* compared to those determined at 21°C. Moreover, for each subphase temperature there was not a clear NP mass-dependant effect on most of the parameters of the *II*-Mma isotherms:

a) **Lift-off Mma**: the lift-off Mma increased with CeO₂ NP mass deposited. Figure 90 below shows a graphical representation of the effect of different CeO₂/DPPC mass ratio suspensions in chloroform on the lift-off Mma at 37°C and at 21°C.

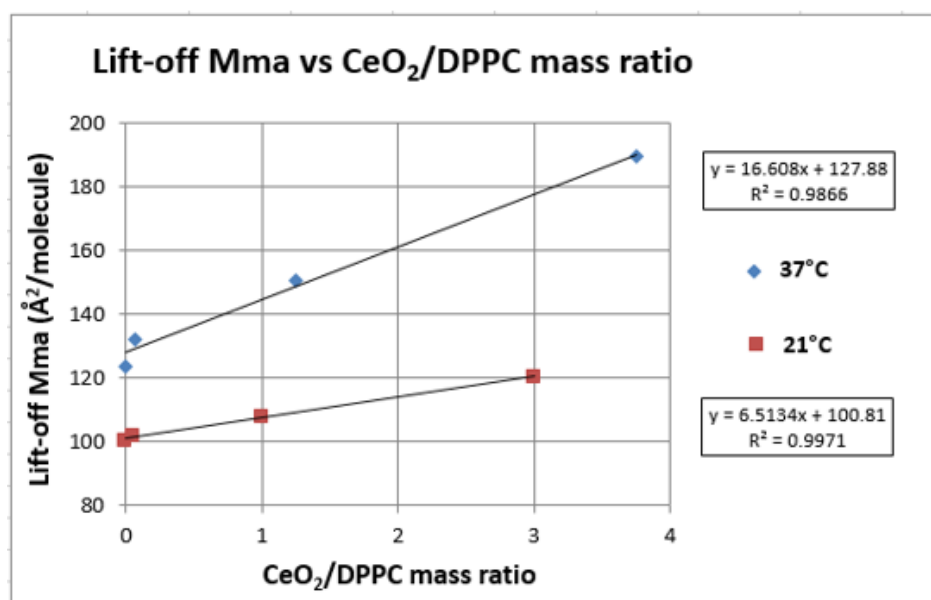


Figure 90. Graphical representation of the effect of the deposition of different CeO₂/DPPC mass ratio suspensions in chloroform on the lift-off Mma of the *II*-Mma isotherms measured in PBS at 37°C (blue) and at 21°C (red).

As can be seen in this figure, the effect of the different CeO₂/DPPC mass ratio suspensions on the lift-off Mma fitted a straight line with R² values of 0.98 for 37°C and 0.99 for 21°C. Based on the SEM and ToF-SIMS images shown previously in Figure 82, it is believed that this increase in the lift-off Mma was caused by the presence of a large number of CeO₂ NP agglomerates at the interface at early stages of compression large and dense enough to experience repulsive forces between them when compressed together (Huang et al., 2001a,

Huang et al., 2001b) and subsequently affect the isotherm. Thus, this effect was higher for the highest CeO₂ NP mass deposited. It is assumed that the presence of CeO₂ NPs in the lipid monolayer would have also reduced the available surface area per surfactant molecule enabling DPPC to increase the Π at an earlier stage of compression.

Finally, and as previously mentioned, the effect on the lift-off M_{ma} at 37°C was more pronounced than at 21°C. It was considered possible that this was due to temperature-dependent effects on agglomeration. In order to investigate the effect of temperature on the agglomerate size, the Z-average diameter of the CeO₂/DPPC agglomerates for the 3.00/1 mass ratio suspension in chloroform was measured at 21°C and 37°C. In both cases the diameter was 120 nm and thus, an increase in temperature from 21°C to 37°C did not have an effect on the initial size of the CeO₂ NP agglomerates. It is therefore unlikely that this was the reason for the overall temperature difference. The exact mechanism for the more pronounced effect of CeO₂/DPPC NP agglomerates on the lift-off M_{ma} at 37°C than at 21°C is currently unclear and worthy of further investigation.

b) C_m : at 37°C, the C_m for the region 1-5 decreased with NP mass whereas for the region 10-25 increased with NP mass. For the region 31-lowest collapse Π there was not a clear relationship between C_m and NP mass: the C_m was very high for the 1.25/1 CeO₂/DPPC mass ratio but similar to that of DPPC for the other CeO₂/DPPC mass ratios. At 21°C, the C_m for the region 1-5 was similar to that of DPPC for all the CeO₂/DPPC mass ratios. The C_m seemed to decrease with NP mass for the region 5-10 hence, the LE-LC transition plateau became less horizontal, and increased with NP mass for the region 25-45. This was shown previously in Figure 89. However, the effect of NP mass on C_m was not linear for the regions 5-10 and 25-45 (i.e. best fit R^2 values of 0.69 for the region 5-10 and 0.53 for the region 25-45). Finally, for the region 50-lowest collapse Π , none of the CeO₂/DPPC mass ratios deposited had an effect on the C_m .

c) Collapse Π and collapse M_{ma} : at 37°C, collapse Π was lower compared to that of pure DPPC for the 1.25/1 CeO₂/DPPC mass ratio whereas collapse Π was higher compared to that of pure DPPC for the 3.75/1 CeO₂/DPPC mass ratio. The collapse M_{ma} was however similar for both CeO₂/DPPC mass ratios but different to that of pure DPPC. The 0.06/1 CeO₂/DPPC mass ratio did not affect the collapse Π and collapse M_{ma} . At 21°C, collapse Π increased with NP mass and fitted a straight line as shown previously in Figure 89 with R^2 value of 0.89. There was however not a clear relationship between the NP mass and the collapse M_{ma} .

The lift-off M_{ma} was the only isotherm parameter affected by the CeO_2 NP mass in a similar way at both $37^\circ C$ and $21^\circ C$. For the other parameters, it is believed that several factors and not only the NP mass affected the isotherm which would explain the absence of a relationship between $CeO_2/DPPC$ mass ratios and effects seen. It is believed that the presence of CeO_2 NPs at the interface aided DPPC to decrease the γ at the air/liquid interface by decreasing the C_m in all the regions of the isotherm and increasing the collapse Π by decreasing the collapse M_{ma} . In fact, the shape of the isotherms was very similar to that of DPPC. During compression, larger agglomerates formed at the interface with repulsive forces between them that had a larger effect on the Π . The higher the CeO_2 NP mass deposited, the larger the agglomerates for the same compression stage. On the other hand, as NPs agglomerated with compression, the available surface area per DPPC molecule would have decreased leading to a higher compression rate per DPPC molecule as the barrier speed was constant. The effect of the compression rate on the isotherm was studied previously (see sections 2.4.1.6 and 2.4.2.1). The presence of NP agglomerates at the interface could have also increased the compression resistance of the DPPC monolayer and subsequently reduced the relative packing density of DPPC (Melbourne et al., 2015). The quantitative ToF-SIMS data suggests that once the agglomerates reached a certain size and surface concentration (i.e. mass), however, they detached from the interface and sedimented into the subphase. For the 3.00/1 $CeO_2/DPPC$ mass ratio this happened at a Π above 40 mN/m but for the other $CeO_2/DPPC$ mass ratios where the NP mass deposited was lower, this probably happened at later stages of compression. The detachment of NPs from the interface would have led to a higher available surface area per DPPC molecule and a lower compression rate. Moreover, the area at which DPPC started to decrease γ or lift-off area probably had an effect on the compression rate per DPPC molecule as shown previously in section 2.4.1.6. The lift-off area depends on the suspension volumes deposited onto the subphase. The lift-off area for the isotherms measured at $37^\circ C$ are shown in Table 34 and for those measured at $21^\circ C$ in Table 35.

Table 34. Lift-off area of the Π -A isotherms for each CeO₂/DPPC mass ratio suspension in chloroform measured in PBS at 37°C.

CeO₂/DPPC mass ratio	Lift-off Area (cm²)
0 (DPPC, control)	57
0.06/1	58
1.25/1	69
3.75/1	54

Table 35. Lift-off area of the Π -A isotherms for each CeO₂/DPPC mass ratio suspension in chloroform measured in PBS at 21°C.

CeO₂/DPPC mass ratio	Lift-off Area (cm²)
0 (DPPC, control)	58
0.05/1	60
1.00/1	62
3.00/1	62

Table 34 and Table 35 show that the lift-off area was especially different to that of the control for the 1.25/1 CeO₂/DPPC mass ratio corresponding to the experiments performed at 37°C. As shown previously in Table 30, the DPPC mass deposited for this mass ratio suspension was the same as that of the control experiment (5.6 μg) hence it is expected that the presence of CeO₂ NPs at the interface increased the lift-off area. Higher lift-off areas led to a lower compression rate per DPPC molecule which could explain the low collapse Π reached in the Π -Mma isotherms for this mass ratio (see Figure 87 and Table 31). Thus, the effect of CeO₂ NP mass on the different parameters of the isotherm were only clear for the lift-off Mma, which increased with NP mass deposited, whereas for the other parameters this effect could have depended on many factors such as the agglomerate size and surface concentration, compression rate per DPPC molecule or suspension volumes deposited onto the surface.

The hypothetical surface area covered by the CeO₂ NPs was determined for each NP/DPPC mass ratio. This area was the total projected area of the NPs assuming that all the NPs remained at the interface. It was determined in two ways, firstly using the CeO₂ NP agglomerate size pre-NP administration (measured using Zetasizer Nano, see Table 27) and secondly using the primary particle size. The calculations were based on the total mass of CeO₂ NPs deposited in each experiment (see Table 32) and a density of 7.215 g/cm³, which is the bulk density of CeO₂, was used for both the agglomerates and the primary particles. For comparative purposes, the effect of the presence of the NPs was also determined by subtracting from the lift-off area of the DPPC + NP isotherm the lift-off area of the DPPC only isotherm. These areas are shown in Table 36. As can be seen in this table, and as expected, the areas increased with NP/DPPC mass ratio. The primary particle based values were higher than the agglomerate based values. This was expected as the density value of 7.215 g/cm³ was more relevant for the primary particles; the density of the CeO₂ NP agglomerates would have been smaller than the bulk density of CeO₂, which would have increased the estimated area covered by the NP agglomerates. These values however were both significantly lower than the areas determined based on the lift-off area of the isotherm. This could indicate that the presence of CeO₂ NP agglomerates at the interface not only reduced the available surface area per surfactant molecule enabling DPPC to increase the Π at an earlier stage of compression but also contributed to the surface tension reduction possibly due to the repulsive forces experienced between them when compressed together.

Table 36. Hypothetical surface area covered by the CeO₂ nanoparticles determined for different NP/DPPC mass ratio in two ways: (a) using the size of the CeO₂ nanoparticle agglomerates and (b) using the primary particle size. The calculations were based on the total mass of CeO₂ nanoparticles deposited in each experiment and a density value of 7.215 g/cm³. For comparative purposes, the effect of the presence of the nanoparticles was also determined by subtracting from the lift-off area of the DPPC + NP isotherm the lift-off area of the DPPC only isotherm. Experiments were performed by depositing the NP/DPPC mass ratio mixture suspended in chloroform onto a PBS subphase at 21°C.

CeO ₂ /DPPC mass ratio	Area covered by the CeO ₂ NPs at the air/PBS interface		Change in lift-off area (cm ²)
	Primary particle based value (cm ²)	Agglomerate based value (cm ²)	
0.05/1	0.04	0.01	0.87
1.00/1	0.77	0.12	4.18
3.00/1	2.05	0.33	10.30

The effect of CeO₂ NP incorporation in the monolayer on the *II*-Mma isotherm was further analysed at subphase temperatures of 37°C and 21°C by plotting Mma values against the NP/DPPC mass ratio at different *II*. This is shown in Figure 91. As can be seen in this figure, for both subphase temperatures and *II* up to approximately 10 mN/m, the Mma increased in a similar way with the NP/DPPC mass ratio which indicates that the surface area was sufficient for the monolayer distribution as otherwise, multilayers of CeO₂ NPs would have formed at the interface decreasing the expected Mma (Lin et al., 2011, Guzmán et al., 2011). At higher *II* values however, the increase in Mma with the NP/DPPC mass ratio was not so pronounced; this was seen as a decrease in the gradient of the line of best fit. Results also show that the effect of CeO₂ NP agglomerates on the Mma at 37°C was greater (larger gradients of the line of best fit) compared to 21°C for similar CeO₂/DPPC mass ratios at a certain *II* value. As already mentioned, temperature did not affect the NP agglomerate size when measured in solution and currently it is unclear what caused the more pronounced effects of CeO₂ NP agglomerates on the isotherm at 37°C than at 21°C.

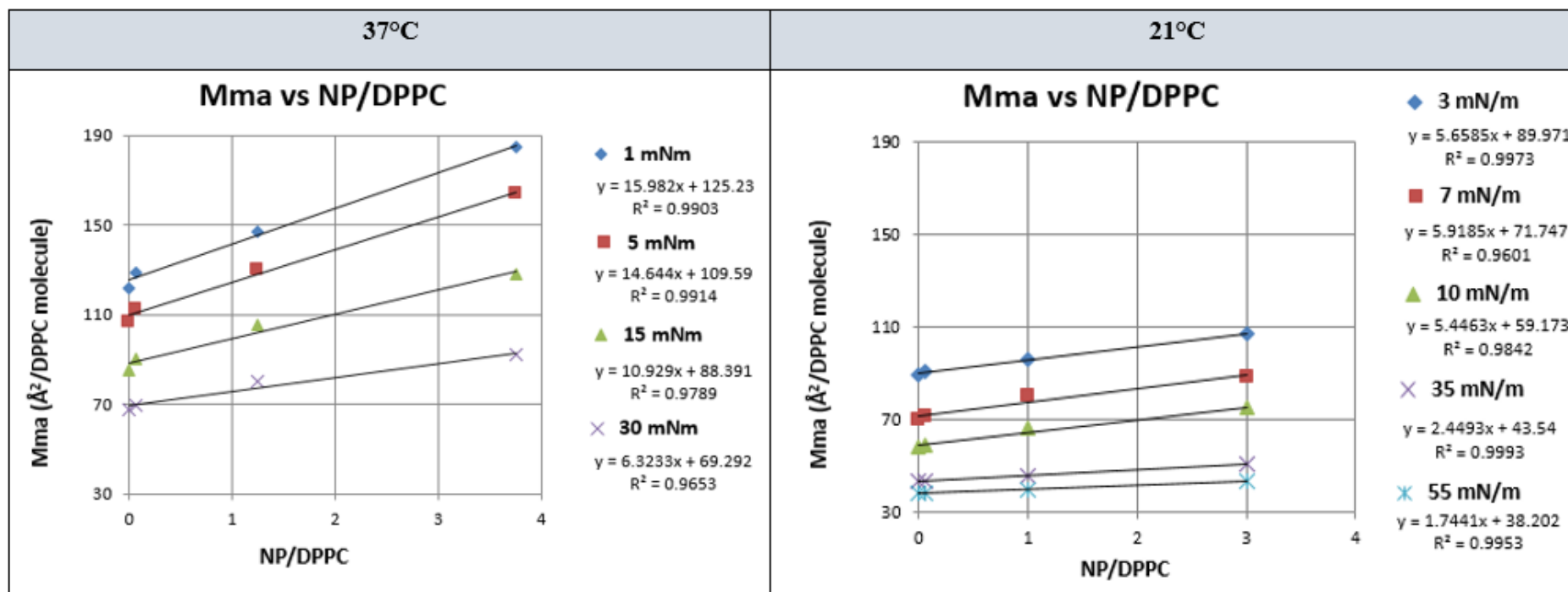


Figure 91. Graphical representation of the effect of the deposition of different CeO₂/DPPC mass ratios in chloroform on the Mma of the *II*-Mma isotherms at different *II* values. The experiments were performed in PBS at 37°C (left) and 21°C (right). Note the reduced segment of the y axis. The lines are representative of the trend.

Finally, Π - M_{ma} isotherms were measured for the 0.05/1 and 3.00/1 CeO_2 /DPPC mass ratio suspensions in PBS at 21°C using a lower subphase volume in order to achieve higher Π values. This is shown in Figure 92. The isotherms were determined using only one measurement per condition.

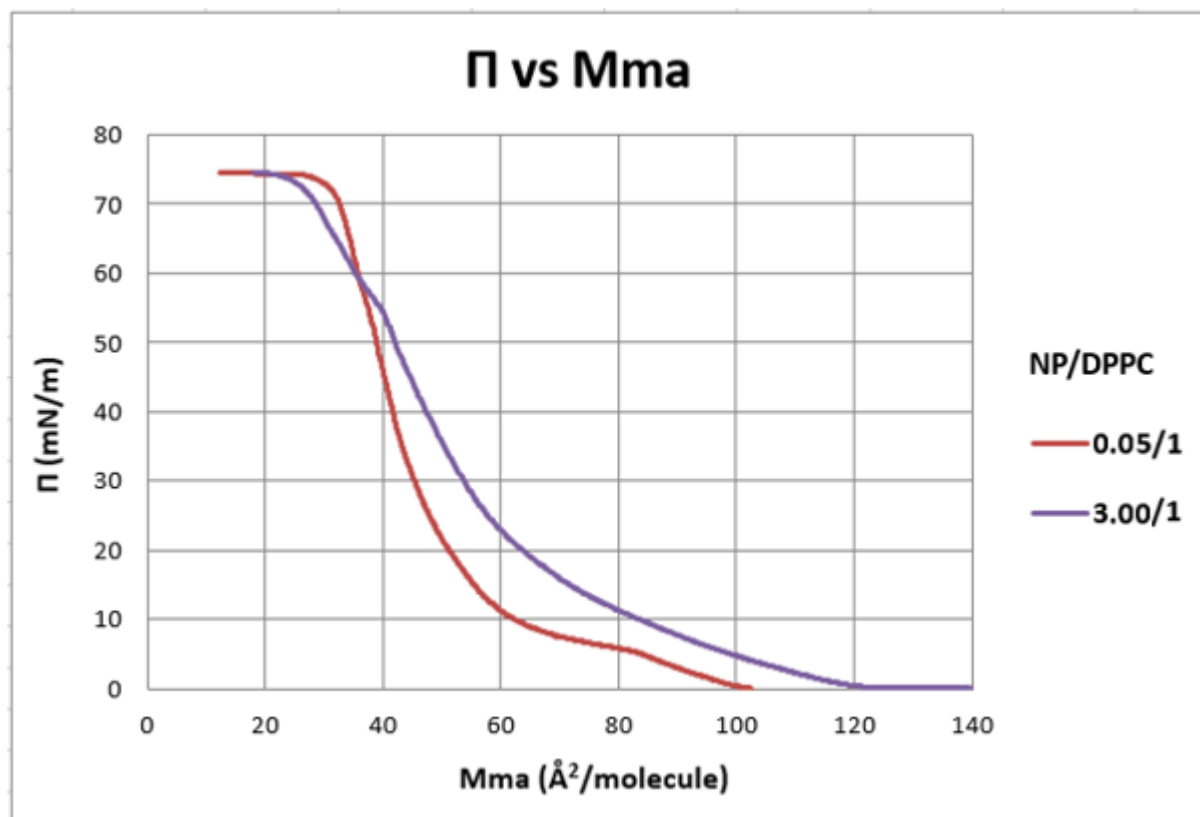


Figure 92. Π - M_{ma} isotherms corresponding to the 0.05/1 and 3.00/1 CeO_2 /DPPC mass ratio suspensions in chloroform measured in PBS at 21°C using a low subphase volume of 50 mL. $n = 1$ experiment/condition.

As discussed previously in section 2.4.2.1, working with normal subphase volumes led to surfactant leakage at Π above ~ 50 mN/m and a premature collapse of the monolayer. Hence, looking at this figure it is possible to understand that when working with normal subphase volumes the collapse M_{ma} for the 3.00/1 CeO_2 /DPPC mass ratio was higher compared to that for the 0.05/1 CeO_2 /DPPC mass ratio as the isotherm was shifted to higher M_{ma} values. However, when working with low subphase volumes, the C_m markedly increased from a $\Pi \sim 55$ mN/m to ~ 74 mN/m for the 3.00/1 CeO_2 /DPPC mass ratio compared to the 0.05/1 CeO_2 /DPPC mass ratio and collapse was reached at later stages of compression (or lower collapse M_{ma} values). Collapse Π for both isotherms was however the same. This increase in

C_m for the 3.00/1 CeO₂/DPPC mass ratio could have been caused by the detachment of large NP agglomerates from the interface at a Π above 40 mN/m in agreement with the SEM, ToF-SIMS images and graph shown previously in Figure 82 and Figure 85 which would have decreased the compression rate per DPPC molecule. The shift of the isotherm towards lower M_{ma} values attributed to the squeeze out of NPs into the subphase has been reported in other studies (Wang et al., 2009, Harishchandra et al., 2010, Stefaniu et al., 2012). A decrease in the compression rate in the last region of the isotherm would have led to an increase in the C_m for that region. Other studies have shown that the squeeze-out of particles would also remove DPPC (for example, adsorbed on the NP surface) from the interface and subsequently allow the compression of the monolayer to smaller areas than that for pure DPPC (Guzmán et al., 2011). In fact, if this was the case, the M_{ma} values of the isotherm would be erroneous as the DPPC content at the interface decreased with compression; the last region of the isotherm should actually shift towards higher M_{ma} values. Finally and to a lesser extent, the presence of some NPs at the interface could have increased the compression resistance of the DPPC monolayer and subsequently reduced the relative packing density of DPPC (Melbourne et al., 2015) which would have also contributed to the collapse of the monolayer at later stages of compression.

These experiments emphasise the importance of measuring isotherms under conditions as close as possible to those occurring *in vivo*. Measuring the Π - M_{ma} isotherm at a subphase temperature of 37°C and using leak-proof systems in order to reach lower γ values is key to gaining a better understanding of what happens in the alveoli. In the literature, reported isotherms do not reach the highest Π values (or lowest γ values), most probably due to leakage problems associated with conventional LWB systems. This is discussed later in the chapter (section 3.6.2). Furthermore, using mixtures of DPPC and NPs in chloroform to model the alveolar system implies that the most important interactions between surfactant and NPs occur in the suspending medium, which modifies the wettability of the NPs and therefore their behaviour, rather than at the air/liquid interface.

A detailed comparison of the results reported in the present section and those in the literature is included later in this chapter (section 3.6.2).

3.5.3 Deposition method 3: Deposition of CeO₂ nanoparticles in aerosol form

3.5.3.1 Nanoparticle characterisation pre-CeO₂ nanoparticle administration

In this study, a method to calculate the aerosol mass deposited onto the Langmuir trough was developed based on deriving the deposition velocity of the aerosolised CeO₂ NPs within the exposure chamber (Equation 19). The size, spatial distribution, wettability and surface tension activity of the aerosolised CeO₂ NP agglomerates upon deposition were also determined.

3.5.3.1.1 Determination of the mass of aerosolised CeO₂ nanoparticles deposited onto the Langmuir trough

a) **Measurement of dv using a QCM**: Seven experiments were performed in the exposure chamber in the presence of a QCM. The aerosol mobility size distribution and number concentration were determined using an SMPS Spectrometer which was configured to measure multiple scans each of 3 minutes in length. The average aerosol CMD, GSD and number concentration of all the scans run for each of the experiments are shown in Table 37. The average aerosol dv was calculated using Equation 20 and is shown in Table 38.

Table 37. Average aerosol CMD, GSD and number concentration of all the scans run for each of the seven experiments performed to calculate an average deposition velocity for aerosolised CeO₂ nanoparticles using a QCM.

Experiment	CMD \pm SD (nm)	GSD \pm SD	Number concentration \pm SD (particles/cm ³)
1	119 \pm 7	1.8 \pm 0.0	2.55E+05 \pm 8.53E+04
2	122 \pm 5	1.8 \pm 0.0	3.76E+05 \pm 5.40E+04
3	117 \pm 7	1.8 \pm 0.0	3.23E+05 \pm 1.00E+05
4	116 \pm 15	1.8 \pm 0.0	3.05E+05 \pm 8.38E+04
5	119 \pm 5	1.8 \pm 0.0	3.97E+05 \pm 8.84E+04
6	117 \pm 3	1.7 \pm 0.0	3.16E+05 \pm 7.70E+04
7	122 \pm 7	1.8 \pm 0.0	3.60E+05 \pm 6.71E+04

Table 38. Calculation of an average deposition velocity for aerosolised CeO₂ nanoparticles by performing seven experiments in the exposure chamber using a QCM.

Experiment	<i>mda</i> (ng/cm²)	Time (min)	<i>mc</i> (ng/cm³)	<i>dv</i> (cm/min)
1	310.60	43	7.30	0.99
2	906.35	250	8.84	0.41
3	508.30	117	6.72	0.65
4	496.46	123	7.01	0.58
5	647.70	78	8.25	1.01
6	289.75	60	4.59	1.05
7	417.31	129	8.96	0.36
Average <i>dv</i>				0.72
SD				0.29
RSD (%)				40.28

The average *dv* for aerosolised CeO₂ NPs was 0.72 cm/min with a SD of 0.29 cm/min. Having established a value for *dv*, *mdt* was estimated using the following equation for those experiments performed at a subphase temperature of 37°C as this was the first set of experiments performed in the exposure chamber in the presence of a QCM:

$$mdt = 0.72 \pm 0.29 (cm/min) \times mc \times t \times tarea \quad \text{Equation 21}$$

where *mdt* is the aerosol mass deposited onto the Langmuir trough (ng); *mc* is the aerosol mass concentration (ng/cm³); *t* is the exposure time (min) and *tarea* is the area of the trough (cm²)

b) Measurement of *dv* using filter membranes: As the QCM subsequently ceased to operate effectively, a method to calculate *mda* based on filter membranes was developed. Five and six hour experiments were performed in the exposure chamber in the presence of six EMFAB filter

membranes. The aerosol mobility size distribution and number concentration were determined using an SMPS Spectrometer which was configured to measure multiple scans each of 3 minutes in length. The average aerosol CMD, GSD and number concentration of all the scans run for each of the experiments are shown in Table 39. The average *mda* value for each experiment is shown in Table 40.

Table 39. Average aerosol CMD, GSD and number concentration of all the scans run for each of the two experiments performed to calculate an average deposition velocity for aerosolised CeO₂ nanoparticles using six EMFAB filters.

Experiment	CMD ± SD (nm)	GSD ± SD	Number concentration ± SD (particles/cm³)
1 (5 hour)	182 ± 13	1.9 ± 0.0	7.72E+05 ± 1.22E+05
2 (6 hour)	177 ± 10	2.0 ± 0.0	7.67E+05 ± 6.79E+04

Table 40. Calculation of an average *mda* value for each of the two experiments performed to determine an average deposition velocity for aerosolised CeO₂ nanoparticles using six EMFAB filters.

	5 hour experiment	6 hour experiment
<i>mda</i> filter 1 (ng/cm²)	1,730.60	1,402.54
<i>mda</i> filter 2 (ng/cm²)	497.13	1,152.77
<i>mda</i> filter 3 (ng/cm²)	718.08	1,095.14
<i>mda</i> filter 4 (ng/cm²)	737.30	1,114.35
<i>mda</i> filter 5 (ng/cm²)	871.79	1,075.92
<i>mda</i> filter 6 (ng/cm²)	1,167.66	1,075.92
Average <i>mda</i> (ng/cm²)	953.76	1,152.77
SD (ng/cm²)	439.74	125.69
RSD (%)	46.11	10.90

Table 39 show that the aerosol size distribution and number concentration were similar in both experiments. Table 40 shows however that the variability on the mass deposited per unit area was much greater for the 5 hour experiment, i.e., aerosolised CeO₂ NPs did not deposit homogeneously across the trough area in the 5 hour experiment, possibly due to a less uniform air flow in the system. Results on the spatial distribution of aerosol CeO₂ NP agglomerates upon deposition are shown in section 3.5.3.1.3 but were only determined for the 6 hour experiment. The average aerosol dv was calculated using Equation 20 and is shown in Table 41.

Table 41. Calculation of an average deposition velocity for aerosolised CeO₂ nanoparticles by performing two experiments in the exposure chamber using six EMFAB filters.

Experiment	mda (ng/cm ²)	Time (min)	mc (ng/cm ³)	dv (cm/min)
1	953.76 ± 439.74	300	24.40	0.13 ± 0.06
2	1,152.77 ± 125.69	363	25.66	0.12 ± 0.01
Average dv				0.13
SD				0.04
RSD (%)				34.68

The average dv for aerosolised CeO₂ NPs was 0.13 cm/min with a SD of 0.04 cm/min. Having established a value for dv , mdt was estimated using the following equation for those experiments performed at a subphase temperature of 21°C:

$$mdt = 0.13 \pm 0.04 (cm/min) \times mc \times t \times tarea \quad \text{Equation 22}$$

where mdt is the aerosol mass deposited onto the Langmuir trough (ng); mc is the aerosol mass concentration (ng/cm³); t is the exposure time (min) and $tarea$ is the area of the trough (cm²)

The estimated dv for aerosolised CeO₂ NPs was significantly different for each of the methods (0.72 cm/min for QCM method and 0.13 cm/min for EMFAB filter method). Table 37 and Table 39 show that both the aerosol sizes and number concentrations generated by the TSI COA

were higher for the experiments performed in the presence of EMFAB filters compared to those experiments where the QCM was used. The size of the aerosol particles depends on a number of factors including the solid material that is aerosolised, the pressure at which the compressed air enters the atomiser assembly block and the NP suspension concentration. As the material and pressure used in each experiment were similar, the concentration of the solutions used in each experiment might have been different leading to different aerosol size distributions. However, it is believed that the aerosol size and number concentration alone cannot explain the large differences in dv found for each method. A possible explanation for this is the different set-up of the experiments performed in the presence of a QCM compared to those using EMFAB filters. As shown previously, the electrobalance and dipping mechanism were located between the gas inlet and the trough in the experiments performed in the presence of EMFAB filters (Figure 61) but not in those where the QCM was used (Figure 60) hence, this could have affected the dv for aerosolised CeO₂ NPs. The set-up in each type of experiment was similar to that used for the actual aerosol to DPPC monolayer deposition experiments. An alternative explanation is that the QCM was not operating correctly for all or part of the experiment. It is not clear which explanation for the difference is more likely. Thus the QCM derived value was used for the 37°C experiments and the EMFAB derived value for the 21°C experiments, as the experimental set-ups in each case most closely mirrored those used for the dv derivations. It is worth noting that the dv derived for aerosolised carbon black NPs using EMFAB filter membranes (0.12 ± 0.06 cm/min) was very similar to that for the aerosolised CeO₂ NPs (0.13 ± 0.04 cm/min); this was expected as the experimental set-ups and the aerosol in each case were similar. This also means that it is reliable to use EMFAB filter membranes to calculate a dv . The measurement of dv for aerosolised CB NPs is shown later in chapter 4 (section 4.5.1.2).

3.5.3.1.2 Size of aerosolised CeO₂ nanoparticles upon deposition

In order to determine if aerosolised CeO₂ NPs agglomerated while they were settling from the air onto the trough, the average NP agglomerate size upon deposition was calculated by imaging and analysing two TEM grids used in the 6 hour experiment. The CMD of the CeO₂ aerosol NP agglomerates upon deposition was 220 nm with a GSD of 2.4. The CMD of the airborne CeO₂ NPs was 177 nm with a GSD of 2.0 (this was shown previously in Table 39). This indicates no or limited further agglomeration of airborne CeO₂ NPs during deposition. Finally, Figure 93 shows several TEM images of the aerosol CeO₂ NP agglomerates upon deposition onto the

TEM grid. As can be seen in these images, the smallest unit of the aerosol CeO₂ NP agglomerates had a broadly spherical shape.

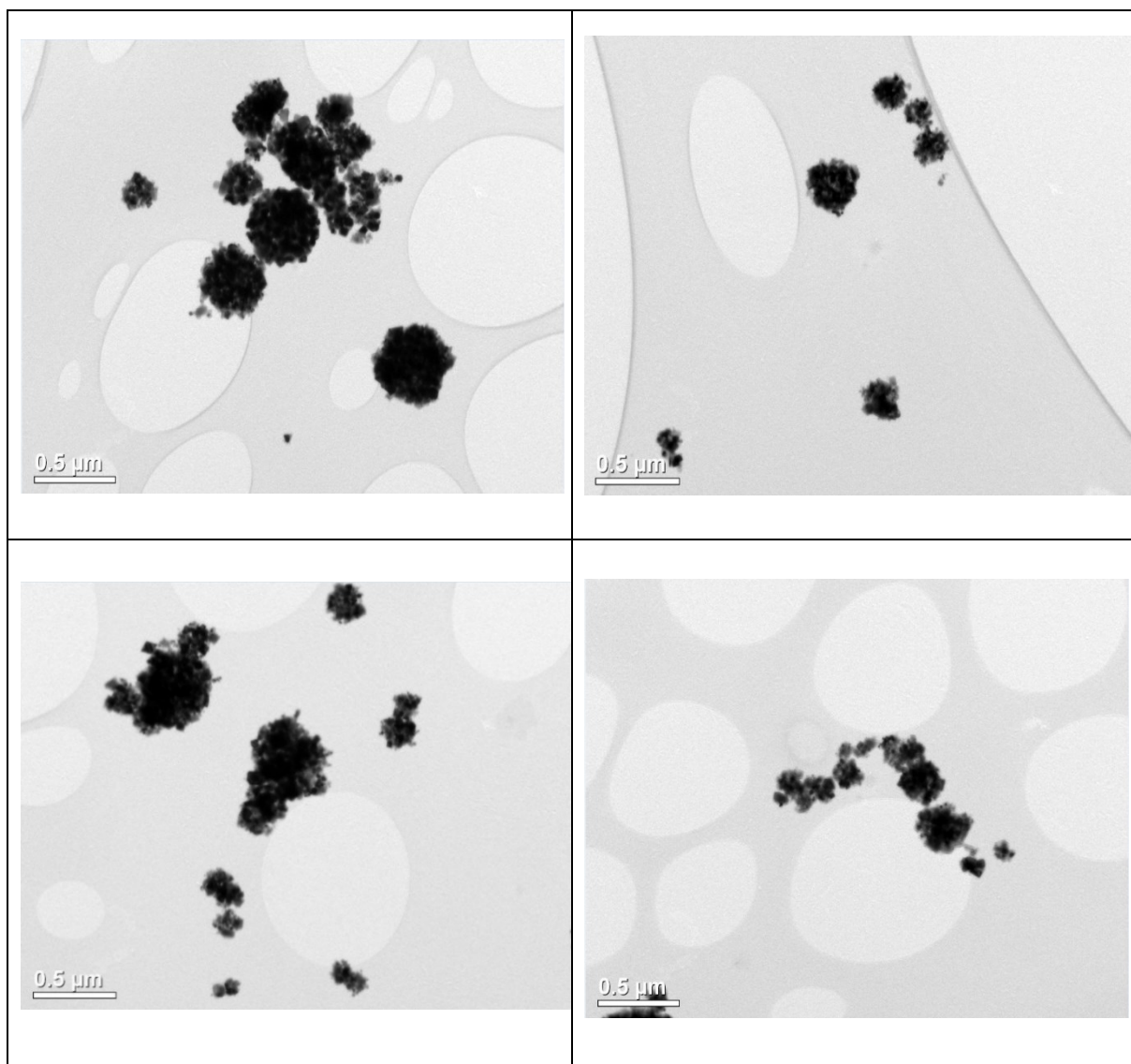


Figure 93. TEM images of aerosol CeO₂ nanoparticle agglomerates upon deposition onto a TEM grid located on the Langmuir trough over 6 hours. The scale bar is 0.5 μm for all the images.

3.5.3.1.3 Measurement of the spatial distribution of aerosolised CeO₂ nanoparticles upon deposition

The spatial distribution of the aerosolised CeO₂ NP agglomerates upon deposition, described by the number of agglomerates per μm², was determined for each of the four TEM grids placed onto the Langmuir trough during the 6 hour experiment and is shown in Table 42. Each value was obtained by analysing a minimum of 40 images. The average number of agglomerates per

μm^2 as well as the SD and RSD were also calculated. The TEM grids were placed next to EMFAB filters 2, 3, 4 and 5 during the 6 hour experiment as shown in Figure 94.

Table 42. Spatial distribution of aerosol CeO₂ nanoparticle agglomerates upon deposition calculated for each of the four TEM grids placed onto the Langmuir trough during the 6 hour experiment. The average number of agglomerates per μm^2 as well as the SD and RSD are also shown. Number of particles counted per TEM grid: TEM grid 1 = 168, TEM grid 2 = 64, TEM grid 3 = 315, TEM grid 4 = 74.

6 hour experiment	Agglomerate spatial distribution upon deposition (agglomerates/ μm^2)
TEM grid 1	0.45 ± 0.28
TEM grid 2	0.14 ± 0.07
TEM grid 3	0.95 ± 0.51
TEM grid 4	0.21 ± 0.17
Average \pm SD (RSD, %)	0.44 ± 0.37 (83.78)

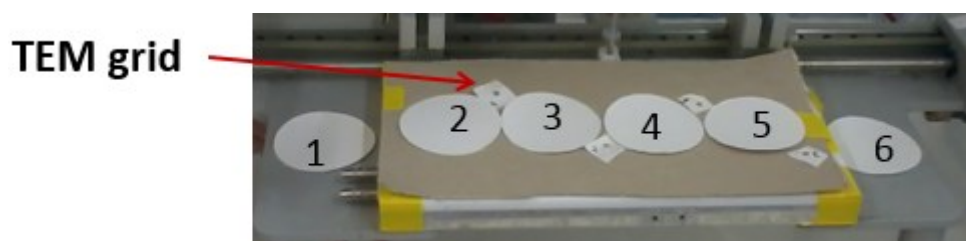


Figure 94. Illustration of the set-up of 4 TEM grids used in the 6 hour experiment to determine the spatial distribution of aerosol CeO₂ nanoparticle agglomerates upon deposition. The TEM grids are numbered sequentially from left to right.

This study showed that agglomerates did not deposit uniformly across the trough. This contrasts with the uniformity of the mass measurements per unit area for this experiment shown previously in Table 40 and suggests that the areas imaged for calculating the spatial distribution were not large enough or that a higher number of particles should have been counted to obtain more coherent results.

3.5.3.1.4 Wettability and surface tension activity of aerosolised CeO₂ nanoparticles

In this study, the capacity of aerosolised CeO₂ NPs to remain at the air/liquid interface was investigated. Approximately 33 µg of aerosolised CeO₂ NPs were deposited onto a clean PBS subphase at 21°C over 194 minutes and compressed with the barriers to the smallest area technically feasible. To visualise the CeO₂ NPs at the interface, a dipping experiment was performed. Table 43 shows the average aerosol CMD, GSD, number concentration, mass concentration and estimated CeO₂ NP mass deposited over the exposure time in this experiment. Figure 95 shows two SEM images of the surface at two magnifications. As can be seen in this figure, some CeO₂ NPs were present at the interface during one compression and some were covered with a white crust which was probably solidified salt. The presence of salt crystals (sodium ions) and CeO₂ NPs was chemically analysed using ToF-SIMS and images are shown in Figure 96. The areas imaged with each technique were different. In the ToF-SIMS images, the presence of CeO₂ NPs and sodium is indicated by the green colour scale located at the right side of each image. This figure shows that the pattern of the CeO₂ NP agglomerates was very similar to that of sodium which indicates that the agglomerates were covered with salt.

Table 43. Average aerosol CMD, GSD, number concentration, mass concentration and estimated CeO₂ nanoparticle mass deposited for an experiment performed to study the wettability and surface tension activity of aerosolised CeO₂ nanoparticles when deposited onto a clean PBS subphase at 21°C.

CMD ± SD (nm)	GSD ± SD	Number concentration ± SD (particles/cm³)	<i>mc</i> (ng/cm³)	CeO₂ NP mass deposited (µg)
171 ± 13	2.0 ± 0.0	7.55E+05 ± 1.11E+05	18.63	33 ± 11

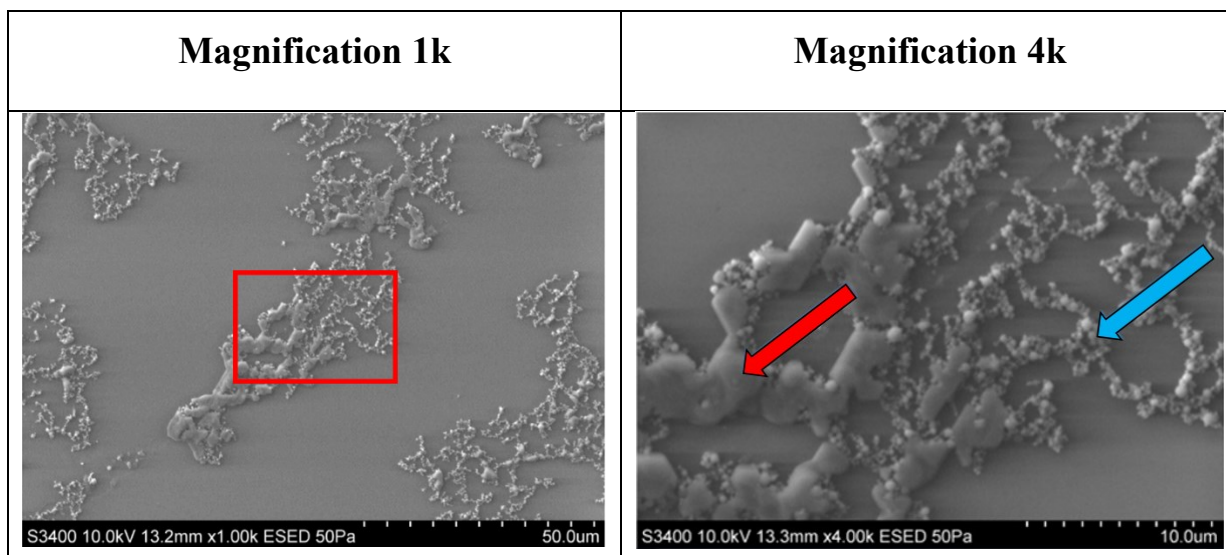


Figure 95. SEM images of the same area at two magnifications of CeO₂ nanoparticle agglomerates. The dipping experiment was performed after depositing approximately 33 μg of aerosolised CeO₂ nanoparticles onto a PBS subphase at 21°C and compressing the interface to the smallest area technically feasible. The box area in the left image indicates the region displayed in the right image at higher magnification. In the right image, CeO₂ nanoparticle agglomerates (indicated by a blue arrow) were covered in some cases by a layer of salt (indicated by a red arrow). The dotted scale bar in the left image is 50 μm and in the right image is 10 μm.

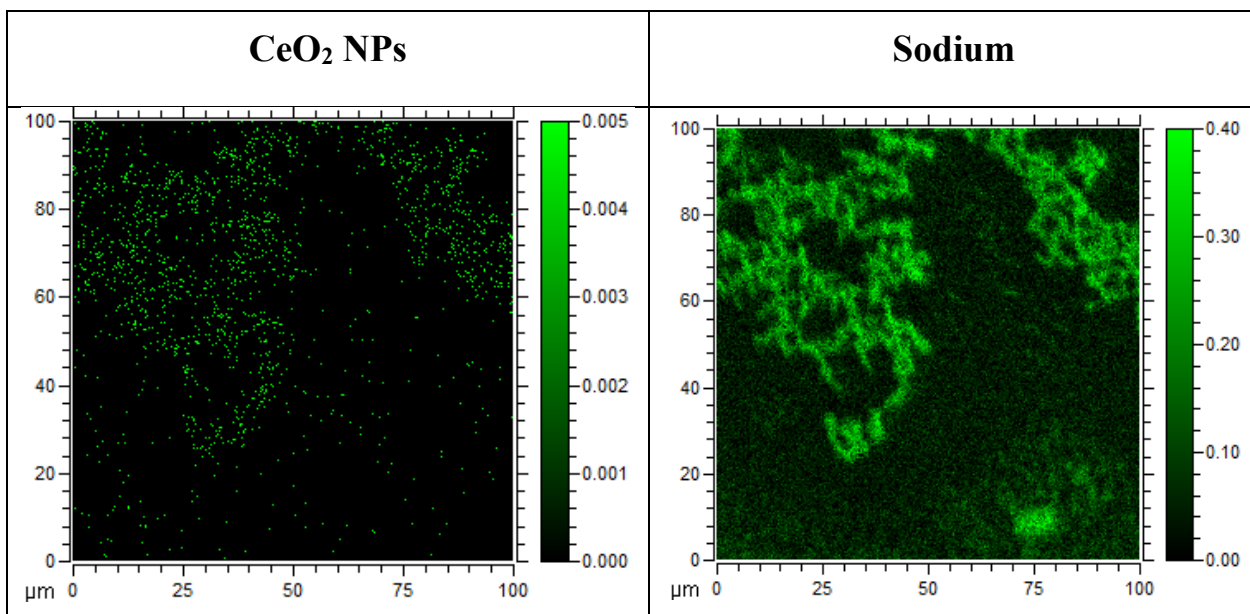


Figure 96. ToF-SIMS images of CeO₂ nanoparticle agglomerates (left) and sodium (right). The dipping experiment was performed after depositing approximately 33 μg of aerosolised CeO₂ nanoparticles onto a PBS subphase at 21°C and compressing the interface to the smallest area technically feasible. The presence of CeO₂ nanoparticles and sodium is indicated by the green colour scale located at the right side of each image. Images are 100 μm x 100 μm.

In order to compare the amount of CeO₂ NP material that remained at the interface in this experiment to that when CeO₂ NPs were deposited onto a clean PBS subphase from chloroform suspensions (deposition method 1, see section 3.5.1.1.2), the count of CeO⁺ ions (normalised to the total count of ions recorded) per sample area was derived from the ToF-SIMS image data for each deposition method and results are shown in Figure 97. Two different sample areas were analysed per deposition method.

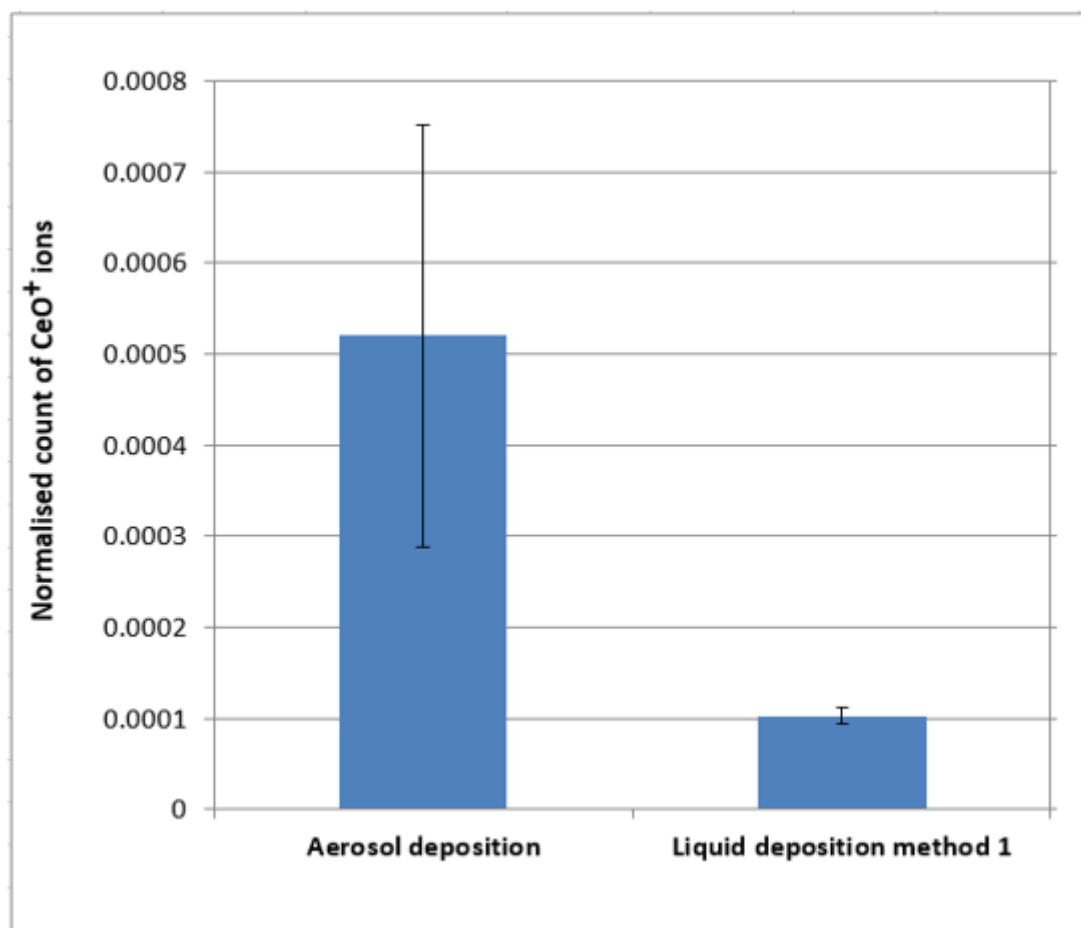


Figure 97. Normalised count of CeO⁺ ions derived from the ToF-SIMS image data. The dipping experiments were performed after depositing approximately 33 μg of aerosolised CeO₂ nanoparticles (aerosol deposition method) and 60 μg of CeO₂ nanoparticles suspended in chloroform (liquid deposition method 1) onto a clean PBS subphase at 21°C and compressing the interface to the smallest area technically feasible. Two different sample areas were analysed per deposition method.

Figure 97 shows that the amount of material at the interface was higher for the aerosol deposition method compared to the liquid deposition method 1. As the mass deposited was double for the liquid deposition method compared to the aerosol deposition method the difference is even more significant. The CMD was slightly larger for airborne CeO₂ NP agglomerates upon deposition onto the trough (approximately 171 nm) compared to that for CeO₂ NPs suspended in chloroform (158 nm). This suggests that aerosolised CeO₂ NPs did not agglomerate to the same extent as CeO₂ NPs deposited from chloroform suspensions, which it is hypothesised rapidly agglomerated to form large, dense clusters that eventually sedimented into the subphase, leaving mainly small agglomerates remaining at the interface (see section 3.5.1.1.2). This is further supported by Figure 98 which shows the uniform distribution of the

aerosolised CeO₂ NP agglomerates across the interface after deposition onto a PBS subphase (left image) as opposed to CeO₂ NP agglomerates deposited from chloroform suspensions (right image) which were fewer in number and had a higher surface density. The image corresponding to the liquid deposition method was shown previously in Figure 64 at higher magnification and is the only image where CeO₂ NPs were clearly seen at the interface.

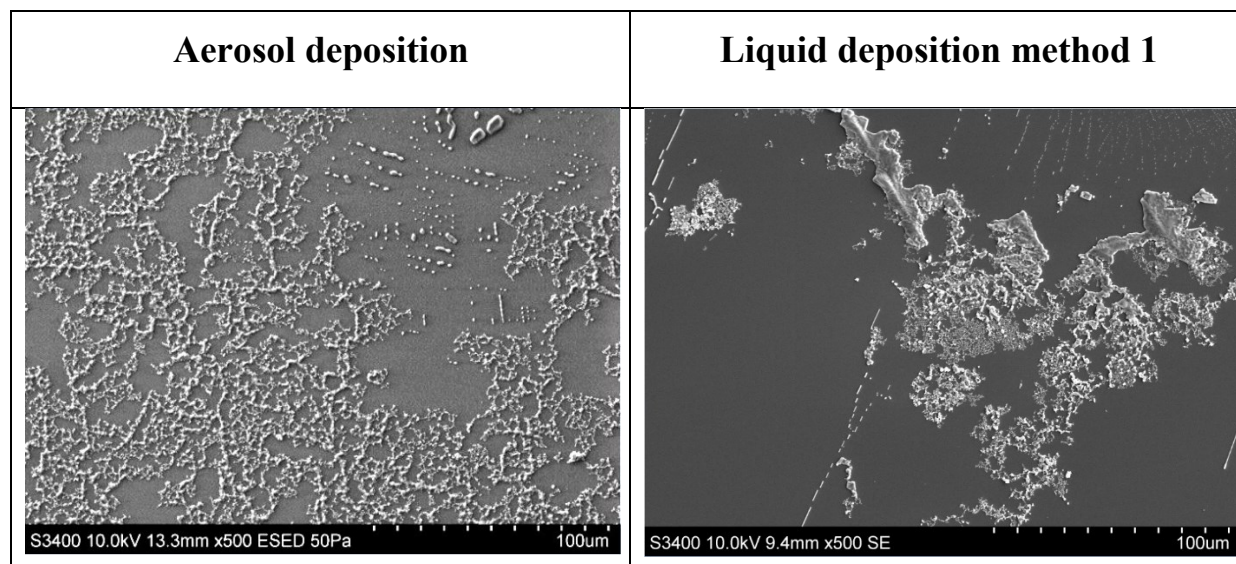
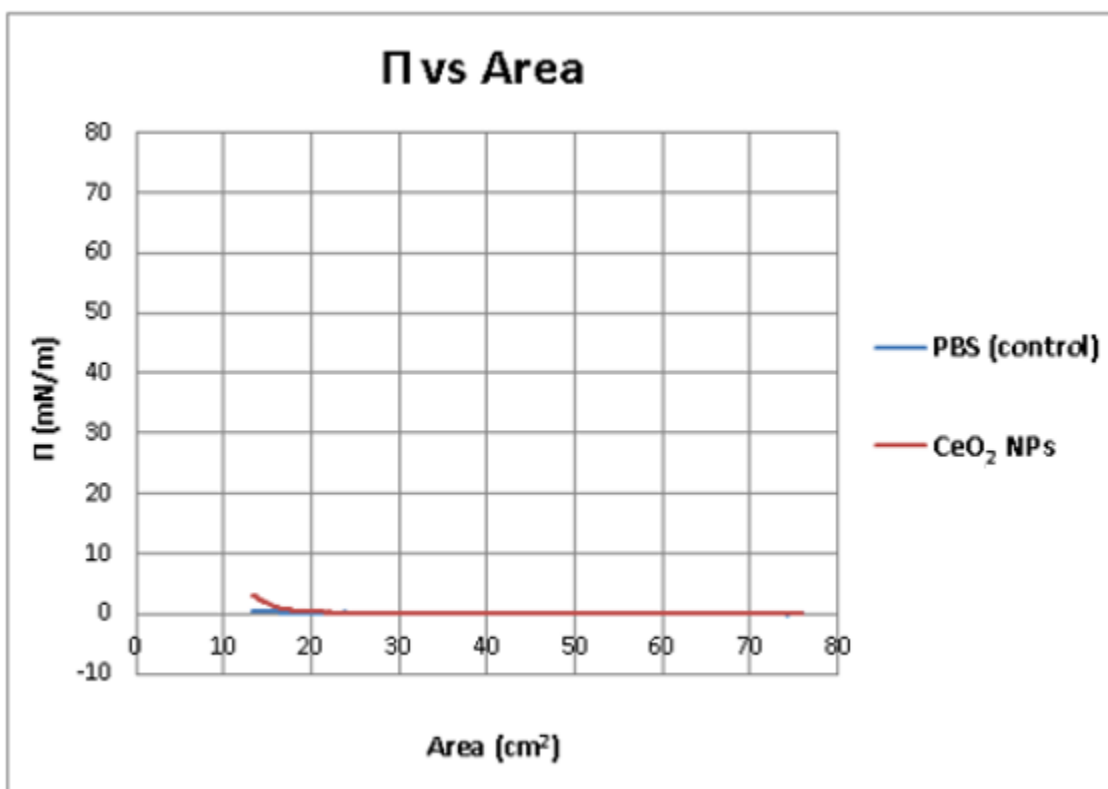


Figure 98. SEM images of CeO₂ nanoparticle agglomerates. The dipping experiments were performed after depositing approximately 33 μg of aerosolised CeO₂ nanoparticles (aerosol deposition method) and 60 μg of CeO₂ nanoparticles suspended in chloroform (liquid deposition method 1) onto a clean PBS subphase at 21°C and compressing the interface to the smallest area technically feasible. The dotted scale bar is 100 μm for both images.

The surface tension activity of the aerosolised CeO₂ NPs upon deposition onto the PBS subphase was investigated by recording the Π -A isotherm during the compression of the interface with the barriers to the smallest area technically feasible. This is shown in Figure 99. The Π -A isotherm of PBS was first measured to ensure that the subphase was clean. The isotherms were determined using only one measurement per condition. The table shows the maximum Π value for each isotherm.

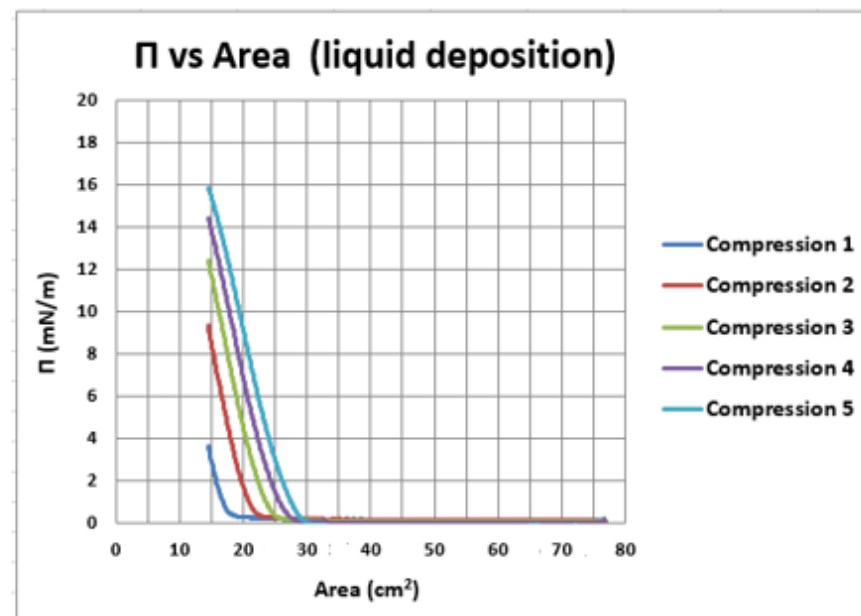
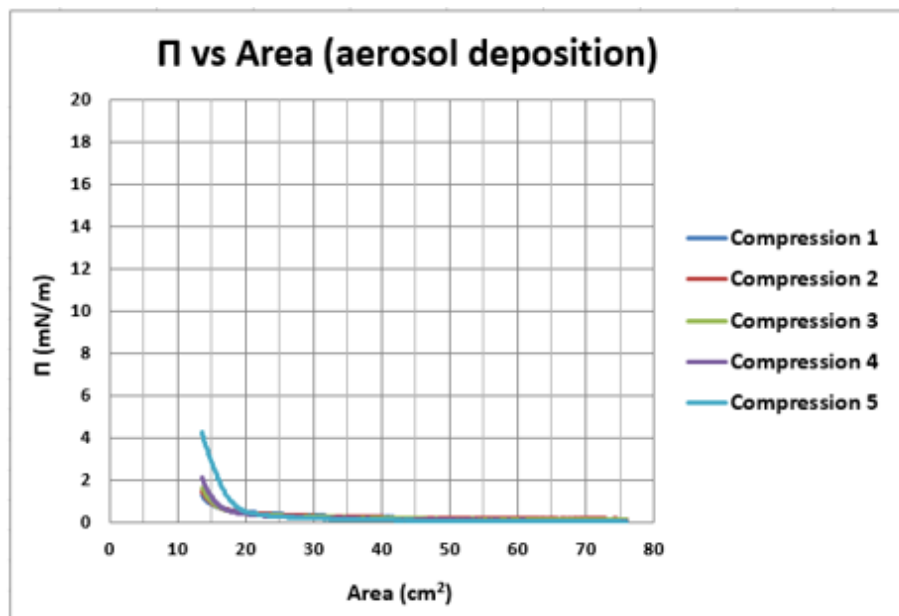


Isotherm	Maximum Π value (mN/m)
PBS (control)	0.38
CeO ₂ NPs	2.97

Figure 99. Π -A isotherm recorded after depositing approximately 33 μg of aerosolised CeO₂ nanoparticles onto a clean PBS subphase at 21°C and compressing the interface to the smallest area technically feasible. The Π -A isotherm of PBS was first measured to ensure that the subphase was clean. The table shows the maximum Π value reached for each isotherm. $n = 1$ experiment/condition.

Figure 99 shows that, following application of aerosolised CeO₂ NPs, Π only increased slightly at the very late stage of compression from 0.38 mN/m to 2.97 mN/m. In order to investigate how these aerosolised CeO₂ NPs affected Π after several compression-expansion cycles, the interface was compressed and expanded five times at normal barrier speed. Π -A compression isotherms were measured and the lift-off area and maximum Π reached after each compression recorded. The isotherms were determined using only one measurement per cycle. This experiment was compared to that performed when CeO₂ NPs were deposited onto a clean PBS

subphase from chloroform suspensions (deposition method 1), shown previously in Figure 78. These data are shown in Figure 100.



Compression	Lift-off area (cm ²)	Maximum Π (mN/m)
1	17	1.22
2	17	1.44
3	17	1.64
4	17	2.10
5	19	4.24

Compression	Lift-off area (cm ²)	Maximum Π (mN/m)
1	18	3.63
2	21	9.37
3	25	12.42
4	27	14.45
5	29	15.86

Figure 100. Π -A compression isotherms measured after depositing approximately 33 μg of aerosolised CeO₂ nanoparticles (aerosol deposition method) and 60 μg of CeO₂ nanoparticles suspended in chloroform (liquid deposition method 1) onto a clean PBS subphase at 21°C and compressing the interface five times to the smallest area technically feasible. The tables show the lift-off area and the maximum Π reached after each compression. n = 1 experiment/cycle.

As can be seen in the aerosol deposition graph, after 4 compressions, the Π increased slightly from 1.22 mN/m to 2.10 mN/m and the lift-off area remained the same (17 cm²). After 5 compressions, the lift-off area increased to 19 cm² and the maximum Π reached was 4.24 mN/m. In the liquid deposition experiment however, each compression had a more marked effect on both the lift-off area and the maximum Π . Even if the CeO₂ NP mass deposited was different for each deposition method, these experiments further support the hypothesis that aerosolised CeO₂ NPs did not agglomerate to the same extent as those CeO₂ NPs deposited from liquid suspensions which made them less surface active as larger and denser NP agglomerates would be expected to have a greater effect on the Π (Huang et al., 2001a, Huang et al., 2001b). One possible explanation for these results is that the wettability of the aerosolised CeO₂ NPs was higher than that of CeO₂ NPs deposited from chloroform suspensions, which increased the stability of the aerosolised CeO₂ NPs when deposited onto a PBS subphase. It is also possible that the use of a spreading solvent, such as chloroform, when depositing CeO₂ NPs onto the air/liquid interface would have induced the agglomeration of the particles to a greater extent compared to the aerosolised CeO₂ NPs. As already mentioned, there is evidence that the evaporation of the spreading solvent leads to the formation of particle agglomerates prior to the compression of the monolayer (Huang et al., 2001a, Huang et al., 2001b). This would have increased encounters between different CeO₂ NP clusters during the compression of the interface and hence, the agglomeration of the clusters. Furthermore, the deposition of aerosolised CeO₂ NPs was probably more spatially uniform across the surface compared to the liquid deposition method which would also have reduced the agglomeration of the aerosolised CeO₂ NPs with compression. This agrees well with what happens *in vivo* as inhaled airborne NPs deposit homogeneously onto the alveolar region (Bahk and Isawa, 1994).

3.5.3.2 Effect of the exposure of a DPPC monolayer to aerosolised CeO₂ nanoparticles on the surface pressure–Mma isotherm measured in PBS at 37°C and 21°C and interfacial layer characteristics post-CeO₂ nanoparticle administration

In this study, different aerosolised CeO₂ NP masses were deposited onto a DPPC monolayer and their effect investigated by visualising the particles at the interface as well as by measuring the Π –Mma isotherm. Aerosolised CeO₂ NPs were generated by atomising a suspension of CeO₂ NPs in ultrapure water and then transporting the aerosol particles into the exposure chamber using a gas flow. Ultrapure water can contain impurities that could be aerosolised

along with the CeO₂ NPs and potentially affect the DPPC isotherm. The deposition of higher aerosolised CeO₂ NP masses also required higher exposure times which could also have an effect on the DPPC monolayer. Thus, the effect of aerosolised ultrapure water and exposure time on the DPPC isotherm was also investigated.

3.5.3.2.1 Interfacial layer characteristics post-CeO₂ nanoparticle administration

Two experiments were performed to investigate the presence of aerosolised CeO₂ NPs at the interface during the initial compression of the monolayer, after 3 compression-expansion cycles performed at normal barrier speed and after 3 compression-expansion cycles performed at maximum barrier speed (270 mm/min) for comparative purposes.

Experiment 1

In this study, approximately 36 µg of aerosolised CeO₂ NPs were deposited onto a DPPC monolayer located at the air/PBS interface at 21°C over 222 minutes. Table 44 shows the average aerosol CMD, GSD, number concentration, mass concentration, estimated CeO₂ NP mass deposited over the exposure time and CeO₂/DPPC mass ratio for this experiment. A dipping experiment was performed at two different Π values during the initial compression of the monolayer: 40 mN/m and 70 mN/m. SEM and ToF-SIMS images of pure DPPC and DPPC exposed to CeO₂ NPs are shown in Figure 101. After one compression, the layer was expanded and compressed for a total of 3 compression-expansion cycles at normal barrier speed and a dipping experiment performed at a Π value of 40 mN/m. SEM and ToF-SIMS images of pure DPPC and DPPC exposed to CeO₂ NPs are shown in Figure 102. The areas imaged with each technique were different for each sample. In the ToF-SIMS images, the presence of CeO₂ NPs is indicated by the green colour scale located at the right side of each image.

Table 44. Average aerosol CMD, GSD, number concentration, mass concentration, estimated CeO₂ nanoparticle mass deposited and CeO₂/DPPC mass ratio for a dipping experiment performed in PBS at 21°C.

CMD ± SD (nm)	GSD ± SD	Number concentration ± SD (particles/cm³)	<i>mc</i> (ng/cm³)	CeO₂ NP mass deposited (µg)	CeO₂/DPPC mass ratio
176 ± 11	1.9 ± 0.0	7.69E+05 ± 4.64E+04	17.96	36 ± 12	1.12/1

Figure 101. SEM and ToF-SIMS images of LB films of pure DPPC (left) and DPPC exposed to CeO₂ nanoparticles (deposited by aerosol, right) at a 1.12/1 CeO₂/DPPC mass ratio, produced in PBS at 21°C during the initial compression of the monolayer at two different Π values: 40 (A) and 70 (B) mN/m. The areas imaged with each technique were different. In the SEM images, the dotted scale bar is 50 μm . ToF-SIMS images are 100 μm x 100 μm and the presence of CeO₂ nanoparticles is indicated by the green colour scale located at the right side of each image.

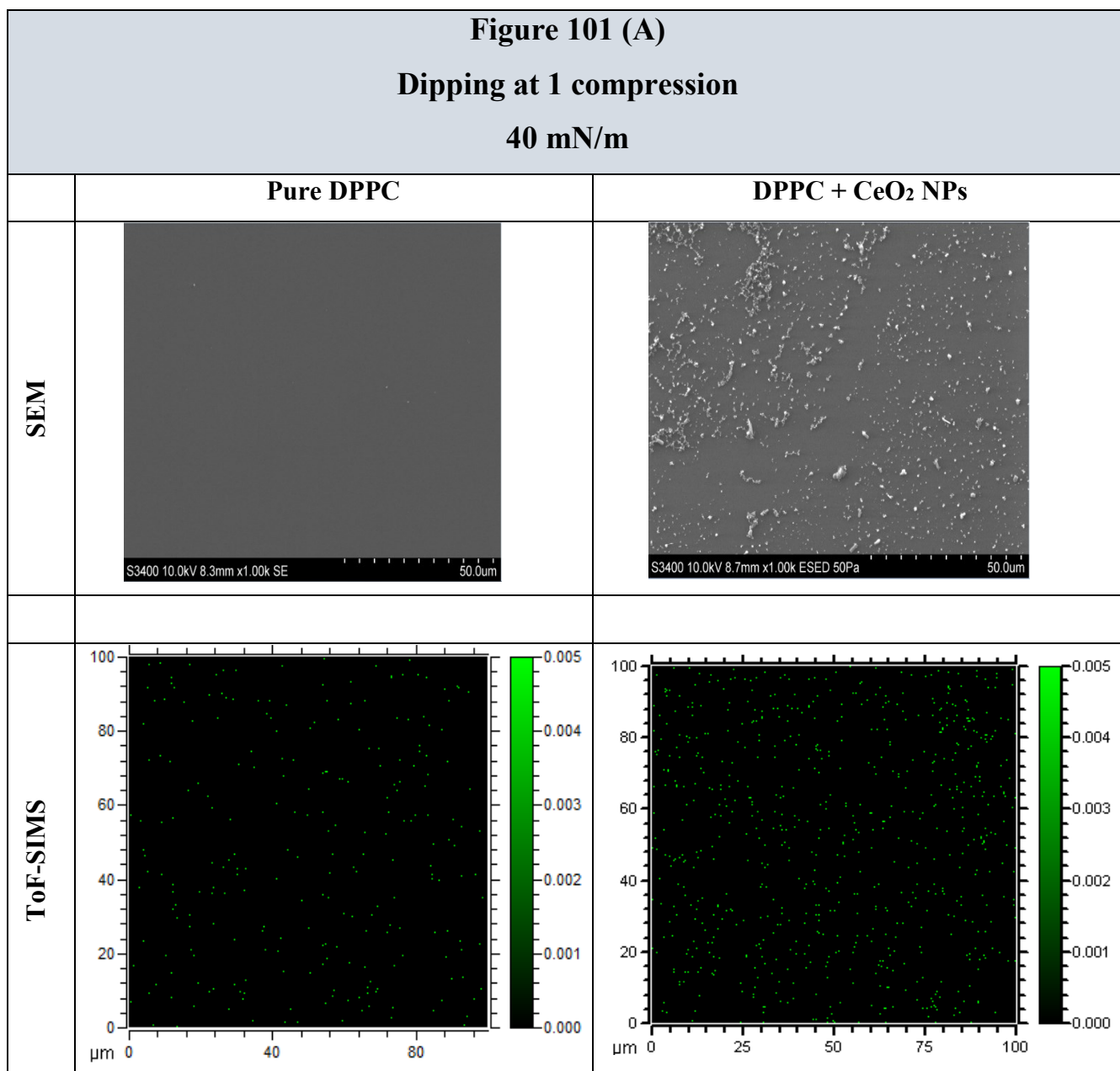


Figure 101 (B)
Dipping at 1 compression
70 mN/m

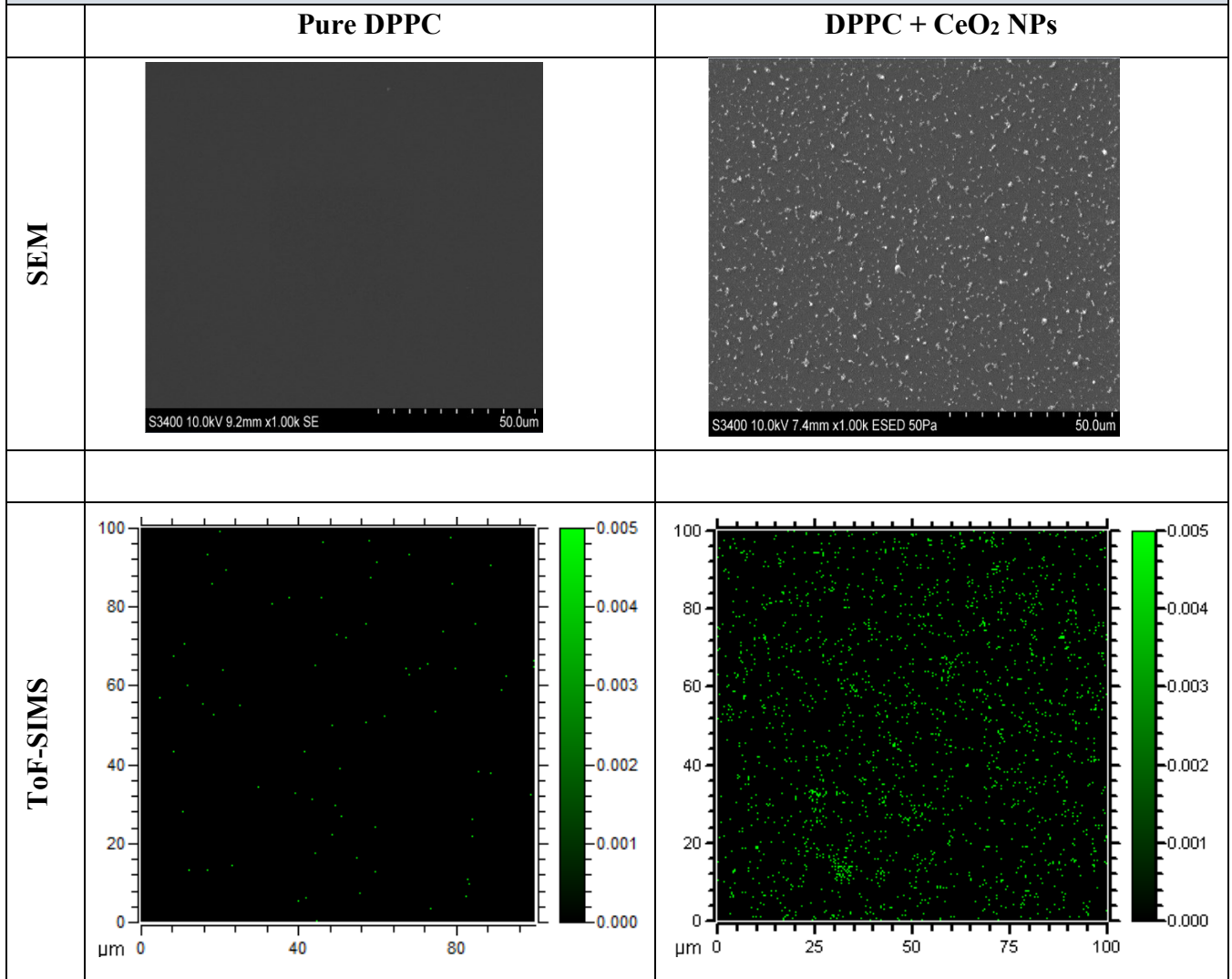
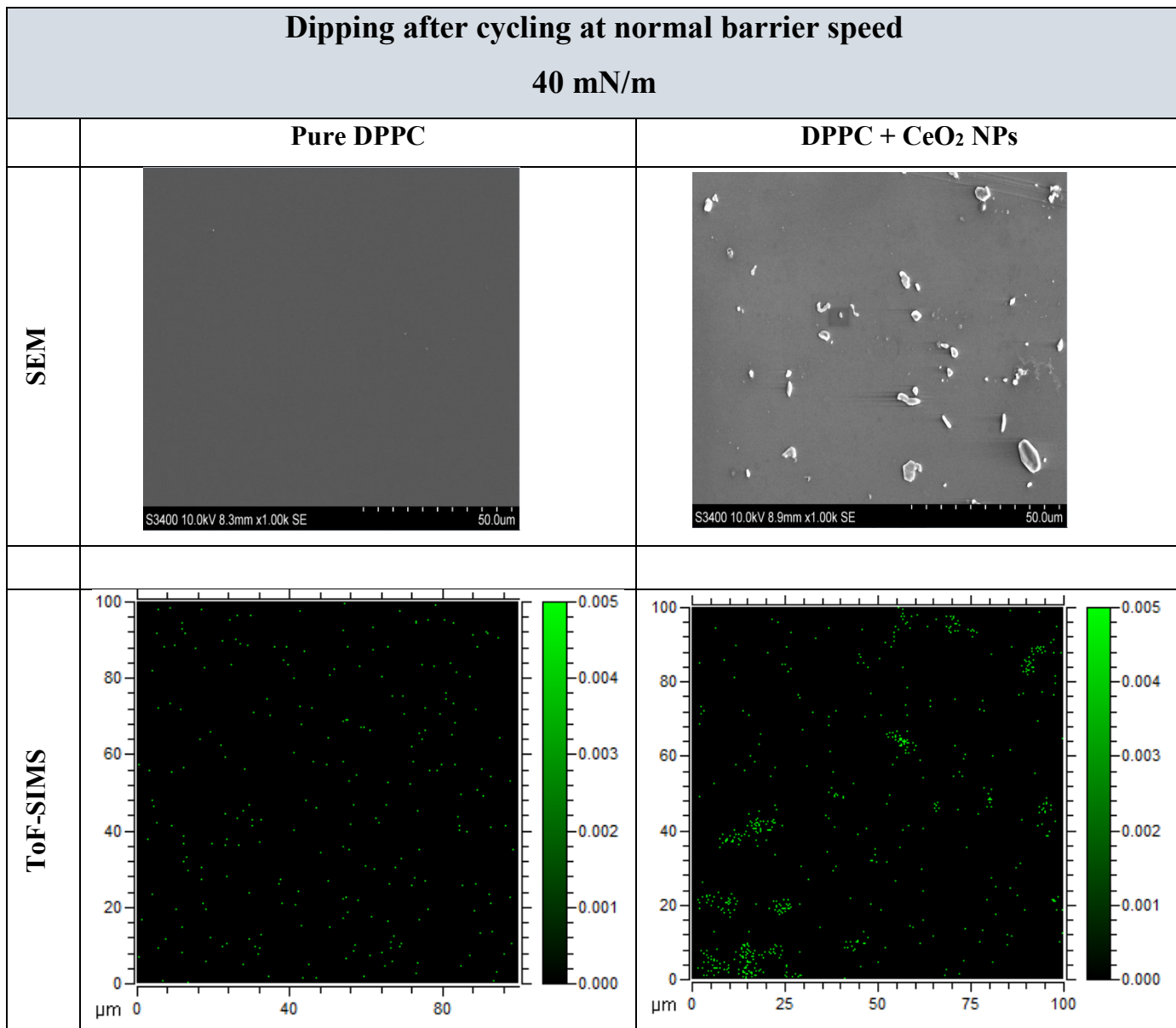


Figure 102. SEM and ToF-SIMS images of LB films of pure DPPC (left image) and DPPC exposed to CeO₂ nanoparticles (deposited by aerosol, 1.12/1 CeO₂/DPPC mass ratio, right image) produced at a Π value of 40 mN/m after 3 compression-expansion cycles performed at normal barrier speed in PBS at 21°C. The areas imaged with each technique were different. In the SEM images, the dotted scale bar is 50 μ m. ToF-SIMS images are 100 μ m x 100 μ m and the presence of CeO₂ nanoparticles is indicated by the green colour scale located at the right side of each image.



Experiment 2

In this study, approximately 35 μg of aerosolised CeO_2 NPs were deposited onto a DPPC monolayer located at the air/PBS interface at 21°C over 219 minutes. Table 45 shows the average aerosol CMD, GSD, number concentration, mass concentration, estimated CeO_2 NP mass deposited over the exposure time and CeO_2/DPPC mass ratio for this experiment. A dipping experiment was performed at a Π value of 20 mN/m during the initial compression of the monolayer. SEM and ToF-SIMS images of pure DPPC and DPPC exposed to CeO_2 NPs are shown in Figure 103. After one compression, the layer was expanded and compressed for a total of 3 compression-expansion cycles at maximum barrier speed and a dipping experiment performed at a Π value of 40 mN/m. SEM and ToF-SIMS images of pure DPPC and DPPC exposed to CeO_2 NPs are shown in Figure 104. The areas imaged with each technique were different for each sample. In the ToF-SIMS images, the presence of CeO_2 NPs is indicated by the green colour scale located at the right side of each image.

Table 45. Average aerosol CMD, GSD, number concentration, mass concentration, estimated CeO_2 nanoparticle mass deposited and CeO_2/DPPC mass ratio for a dipping experiment performed in PBS at 21°C .

CMD \pm SD (nm)	GSD \pm SD	Number concentration \pm SD (particles/cm³)	<i>mc</i> (ng/cm³)	CeO_2 NP mass deposited (μg)	CeO_2/DPPC mass ratio
166 \pm 11	2.0 \pm 0.0	7.77E+05 \pm 1.39E+05	17.42	35 \pm 12	2.42/1

Figure 103. SEM and ToF-SIMS images of LB films of pure DPPC (left) and DPPC exposed to CeO₂ nanoparticles (deposited by aerosol, right) at a 2.42/1 CeO₂/DPPC mass ratio, produced in PBS at 21°C during the initial compression of the monolayer at a Π value of 20 mN/m. The areas imaged with each technique were different. In the SEM images, the dotted scale bar is 50 μ m. ToF-SIMS images are 100 μ m x 100 μ m and the presence of CeO₂ nanoparticles is indicated by the green colour scale located at the right side of each image.

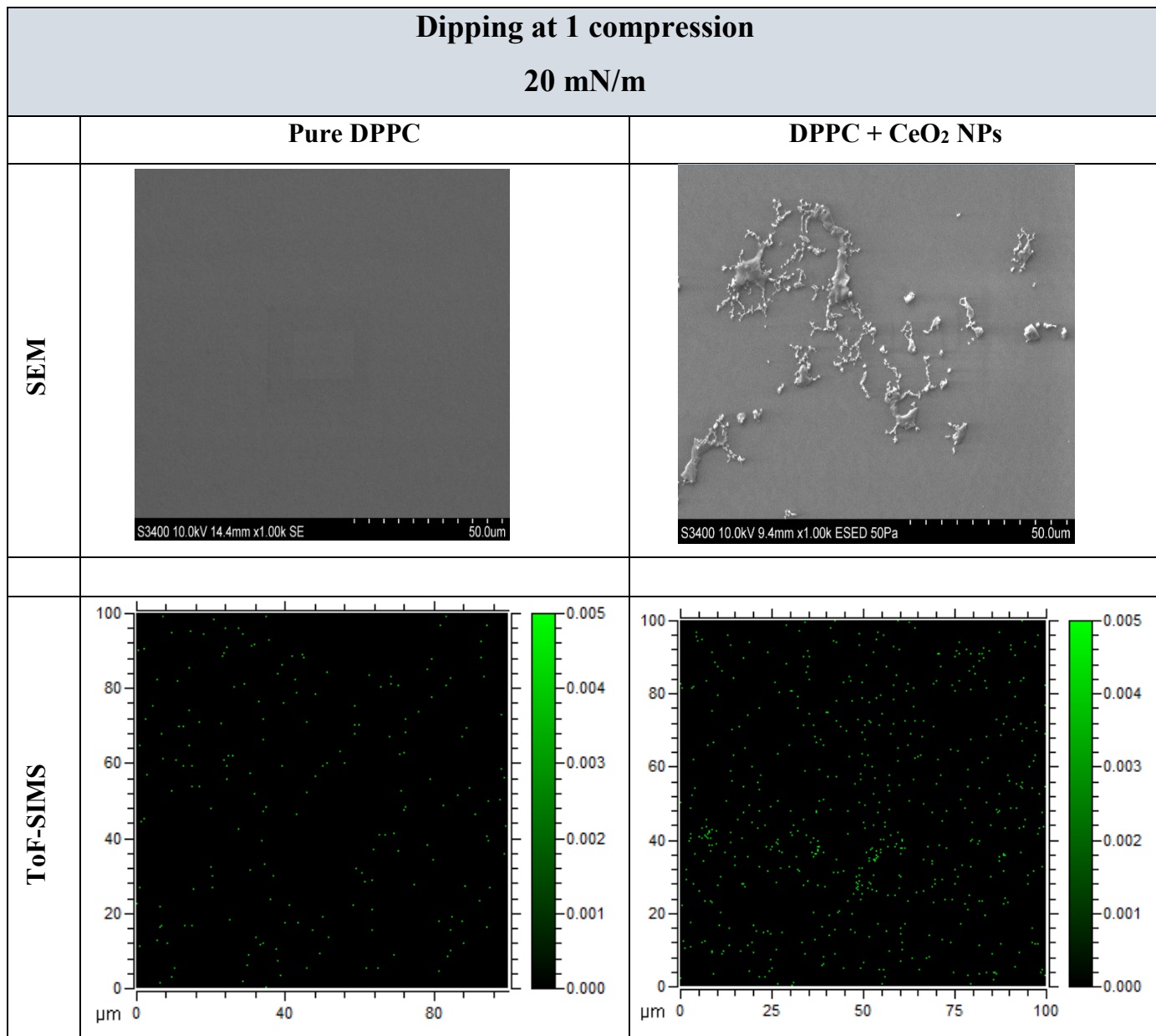


Figure 104. SEM and ToF-SIMS images of LB films of pure DPPC (left image) and DPPC exposed to CeO₂ nanoparticles (deposited by aerosol, 2.42/1 CeO₂/DPPC mass ratio, right image) produced at a Π value of 40 mN/m after 3 compression-expansion cycles performed at maximum barrier speed in PBS at 21°C. The areas imaged with each technique were different. In the SEM images, the dotted scale bar is 50 μ m. ToF-SIMS images are 100 μ m x 100 μ m and the presence of CeO₂ nanoparticles is indicated by the green colour scale located at the right side of each image.

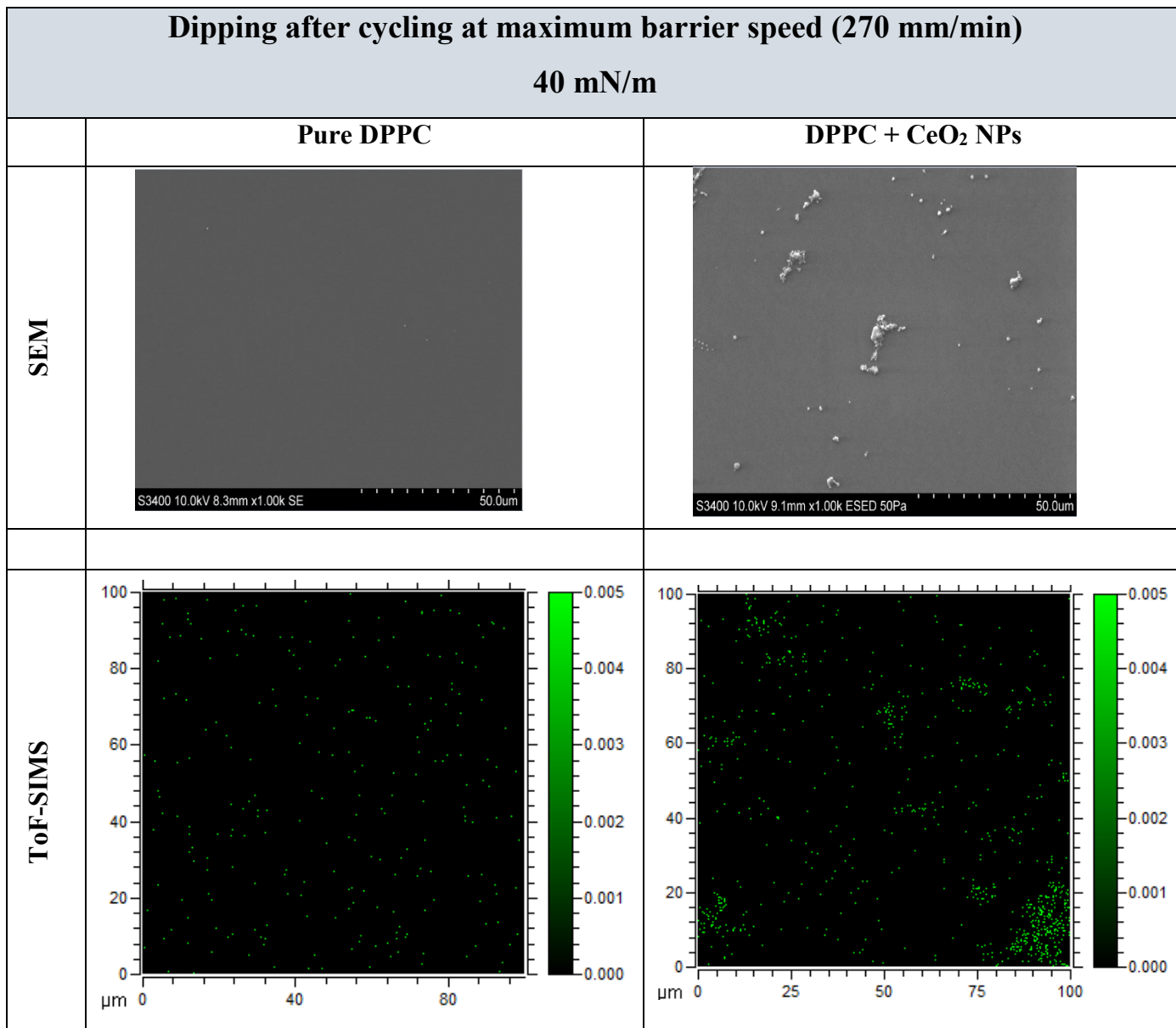


Figure 101 shows that CeO₂ NP agglomerates of a similar size were homogeneously spread across the surface during one compression at Π values of 40 and 70 mN/m. However, images taken at a Π value of 20 mN/m during one compression (Figure 103) showed that agglomerates were not so uniformly distributed. It is possible that this could have been related to aerosol CeO₂ NPs not depositing homogeneously across the trough area in this experiment. Interestingly, following three cycles at normal and maximum barrier speed, images show that compression-expansion cycles promoted the agglomeration of the CeO₂ NP clusters (Figure 102 and Figure 104) although their size was smaller compared to the liquid deposition methods (deposition methods 1 and 2, see Figure 74, Figure 75, Figure 83 and Figure 84).

The areas covered by the CeO₂ NPs at the interface at two Π values during one compression were determined by analysing representative SEM images of experiment 1 and expressed as a percentage of the total image area. Two different sample areas were analysed per Π . Results are shown in Table 46. As can be seen in this table, the area covered by the CeO₂ NP agglomerates increased with compression.

Table 46. Area covered by the CeO₂ nanoparticle agglomerates at Π values of 40 and 70 mN/m during the initial compression of the monolayer (experiment 1). The dipping experiment was performed in PBS at 21°C after depositing aerosolised CeO₂ nanoparticles onto a DPPC monolayer at a 1.12/1 NP/DPPC mass ratio. The area covered by the CeO₂ nanoparticles was determined by analysing representative SEM images and expressed as a percentage of the total image area. Two different sample areas were analysed per Π .

Surface pressure (mN/m)	Area covered by CeO₂ NP agglomerates \pm SD (area covered/total image area, %)
40	5 ± 1
70	8 ± 1

In order to investigate the evolution of the CeO₂ surface concentration with compression, the count of CeO⁺ ions (normalised to the total count of ions recorded) per sample area at various Π values (40 and 70 mN/m) was derived from the ToF-SIMS image data and results are shown in Figure 105. Two different sample areas were analysed per Π .

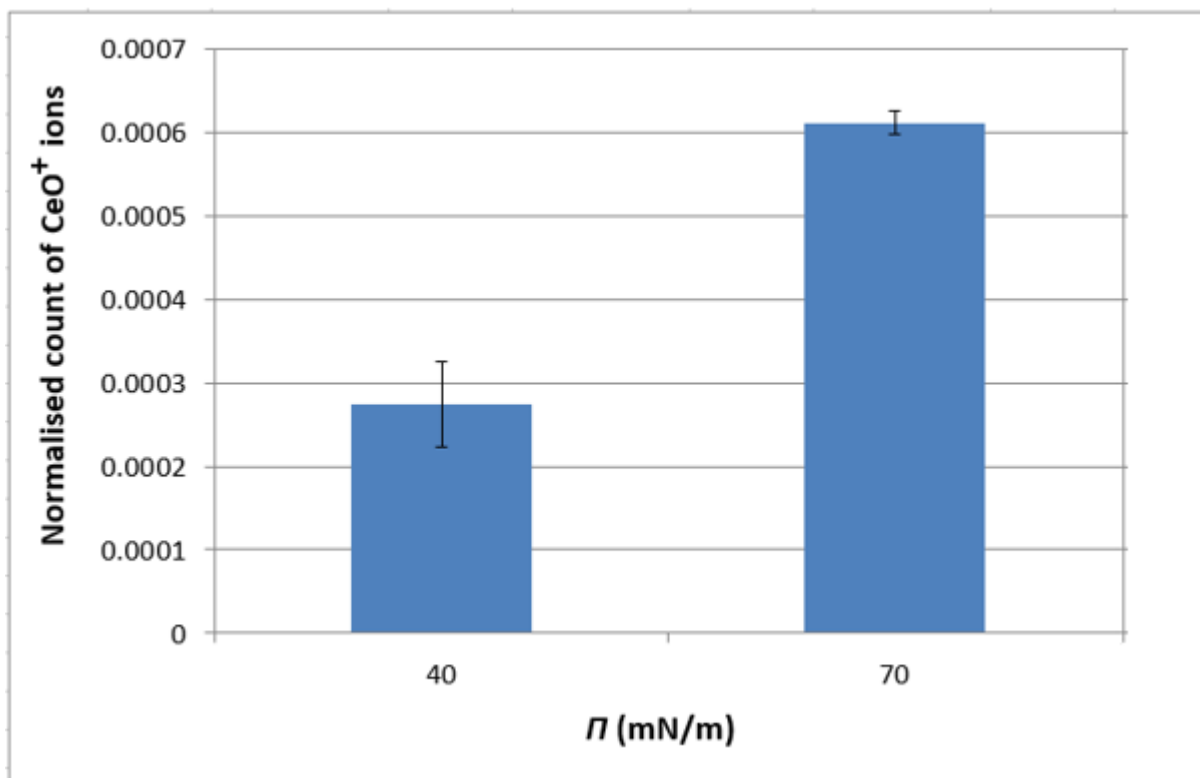


Figure 105. Normalised count of CeO^+ ions derived from the ToF-SIMS image data at Π values of 40 and 70 mN/m during the initial compression of the monolayer (experiment 1). The dipping experiment was performed in PBS at 21°C after depositing aerosolised CeO_2 nanoparticles onto a DPPC monolayer at a 1.12/1 NP/DPPC mass ratio. Two different sample areas were analysed per Π .

As can be seen in the previous bar chart, the surface concentration of aerosolised CeO_2 NPs at the interface increased with Π . Based on these results and those shown previously in Table 46, it is believed that limited or no loss of material from the interface into the subphase occurred during one compression, which was probably due to the low degree of agglomeration of CeO_2 NPs, hence, a higher surface concentration of material with compression. This was also investigated by taking samples of the subphase with a pipette and analysing them using ICP-MS but the data produced were not robust enough to be presented in this thesis. These results contrast with those obtained for the liquid suspension methods (deposition methods 1 and 2) in which it is hypothesised that, during one compression, CeO_2 NP agglomerates became large enough to detach from the interface into the subphase. The decrease in the amount of material present at the interface with compression for deposition method 2 was shown previously in Figure 85. It is hypothesised that this difference is due to different levels of agglomeration with particle loss from the interface increasing with the size and density of the agglomerates.

3.5.3.2.2 Effect of the exposure of a DPPC monolayer to aerosolised ultrapure water over increasing exposure times on the surface pressure–Mma isotherm measured in PBS at 37°C and 21°C

In order to investigate the effect of both aerosolised ultrapure water and exposure time on the DPPC isotherm, a DPPC monolayer located at the air/PBS interface at 37°C was exposed to aerosolised ultrapure water for increasing time periods (30, 45, 60, 90 and 180 minutes) and the Π -Mma isotherms recorded during one compression. For ease of presentation, only the isotherms corresponding to the 30, 90 and 180 minute exposure experiments are presented (Figure 106) although the other results followed the trend. Table 47 shows the lift-off Mma, C_m , collapse Π and collapse Mma of the Π -Mma isotherms. The corresponding values in each of these parameters measured for each exposure time were compared with those of no exposure (control) by calculating the % difference between experiment and control for each of the parameters and dividing them by the reference % change from midpoint values, i.e., assuming similar levels of uncertainties on the parameters to those of the reference isotherms (see section 2.4.1.5). Due to time limitations, the experiments were only performed once except for the 0 minute exposure isotherm which was obtained by averaging 3 measurements. As can be seen from Table 47, the isotherm parameter that was most significantly affected by the exposure to aerosolised ultrapure water was the lift-off Mma which increased with exposure time, with a smaller, but still marked increase in C_m in the region 10-25. A graphical representation of the effect of the exposure of a DPPC monolayer to aerosolised ultrapure water over increasing exposure times on the lift-off Mma is shown in Figure 107. The only isotherm parameter that was not at all affected by the exposure to aerosolised ultrapure water was the C_m for the region 1-5. Generally, the longer the exposure time, the greater the effect on the DPPC isotherm.

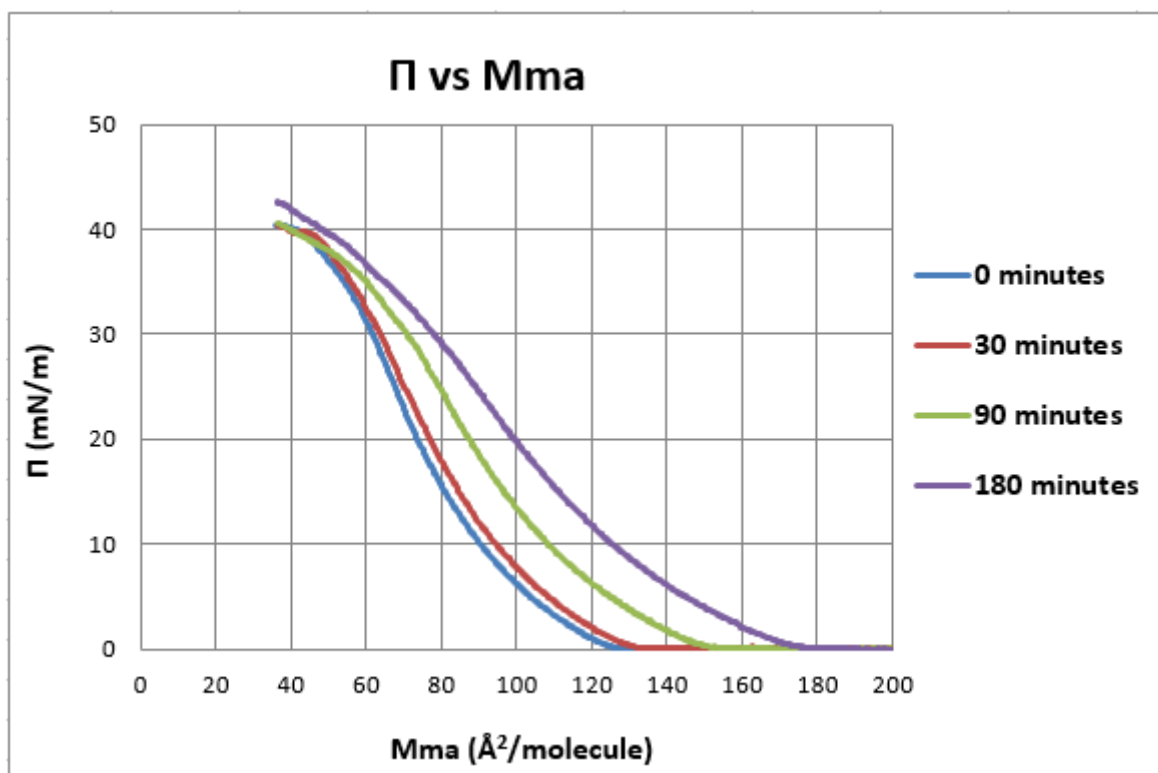


Figure 106. Effect of the exposure of a DPPC monolayer to aerosolised ultrapure water over increasing exposure times on the Π - Mma isotherm measured in PBS at 37°C. n = 3 experiments for control (0 minute exposure experiment) and n = 1 experiment for 30, 90 and 180 minute exposure experiments.

Table 47. Effect of the exposure of a DPPC monolayer to aerosolised ultrapure water over increasing exposure times on the lift-off M_{ma} , C_m , collapse Π and collapse M_{ma} of the Π - M_{ma} isotherms measured in PBS at 37°C. The corresponding values in each of these parameters measured for each exposure time were compared with those of no exposure (control) by calculating the difference in each of the parameters for the experimental isotherm and the control expressed as a % of the control value and dividing them by the reference % change from midpoint values for the relevant reference isotherm (Table 11). This approach assumes similar levels of uncertainties on the control and experimental isotherm parameters to those of the reference isotherm parameters.

Exposure time (min)	Lift-off M_{ma} ($\text{\AA}^2/\text{molecule}$)	(% difference experiment and control)/(reference % change from midpoint)	C_m 1-5 mN/m (mN/m) ⁻¹	(% difference experiment and control)/(reference % change from midpoint)	C_m 10-25 mN/m (mN/m) ⁻¹	(% difference experiment and control)/(reference % change from midpoint)
<i>Reference isotherm</i>	123	1.0 (% change from midpoint)	0.0298	3.0 (% change from midpoint)	0.0150	2.0 (% change from midpoint)
0 (control)	123		0.0340		0.0169	
30	129	5.0	0.0339	0.0	0.0170	0.5
90	149	21.0	0.0338	0.3	0.0179	3.0
180	172	40.0	0.0333	0.7	0.0192	7.0

Exposure time (min)	C_m 31 mN/m – lowest collapse Π (mN/m) ⁻¹	(% difference experiment and control)/(reference % change from midpoint)	Collapse Π (mN/m)	(% difference experiment and control)/(reference % change from midpoint)	Collapse M_{ma} ($\text{\AA}^2/\text{molecule}$)	(% difference experiment and control)/(reference % change from midpoint)
<i>Reference isotherm</i>	0.0294	15.0 (% change from midpoint)	39.40	2.0 (% change from midpoint)	49	4.0 (% change from midpoint)
0 (control)	0.0368		40.23		40	
30	0.0421	0.9	40.43	0.0	37	2.0
90	0.0492	2.3	40.62	0.5	36	2.5
180	0.0402	0.6	42.39	2.5	38	1.3

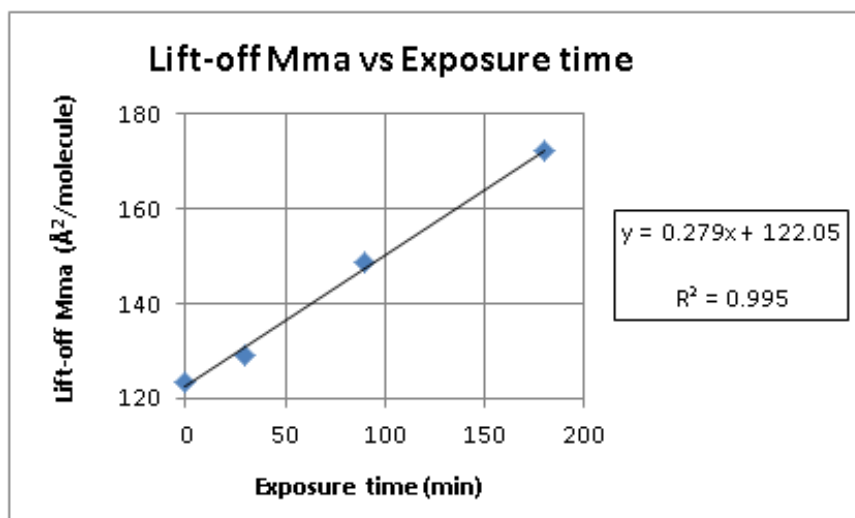


Figure 107. Graphical representation of the effect of the exposure of a DPPC monolayer to aerosolised ultrapure water over increasing exposure times on the lift-off Mma of the Π -Mma isotherms measured in PBS at 37°C.

A similar set of experiments was performed at a subphase temperature of 21°C, for comparative purposes. For this, a DPPC monolayer located at the air/PBS interface was exposed to aerosolised ultrapure water for various time periods (10, 90 and 150 minutes) and the Π -Mma isotherms recorded. This is shown in Figure 108. Table 48 shows the lift-off Mma, C_m , collapse Π and collapse Mma of the Π -Mma isotherms. The corresponding values in each of these parameters measured for each exposure time were compared with those of no exposure (control) by calculating the % difference between experiment and control for each of the parameters and dividing them by the reference % change from midpoint values, i.e., assuming similar levels of uncertainties on the parameters to those of the reference isotherms (see section 2.4.1.5). Due to time limitations, the experiments were only performed once except for the 0 minute exposure isotherm which was obtained by averaging 3 measurements. As can be seen from Table 48, the isotherm parameter that was most significantly affected by the exposure to aerosolised ultrapure water was the C_m for the region 25-45 followed by the lift-off Mma. In agreement with those studies performed at 37°C, the lift-off Mma increased with exposure time. C_m for the region 25-45 also increased with time. Generally, the longer the exposure time, the greater the effect on the DPPC isotherm. Moreover, taking into account experimental values of C_m for the DPPC monolayer phases from the literature (i.e. 0.02-0.1 (mN/m)⁻¹ for LE films, 0.004-0.01 (mN/m)⁻¹ for LC films and < 0.004 (mN/m)⁻¹ for S films (Kodama et al., 2004, Vitovič et al., 2006)), the

90 and 150 minute exposure isotherms were in a LE state in the region 25-45 mN/m and for the 10 minute exposure experiment, the isotherm was also somewhere between the LE and LC state instead of the expected LC phase. This suggests that the exposure of DPPC to aerosolised ultrapure water reduced the nucleation of the LE phases.

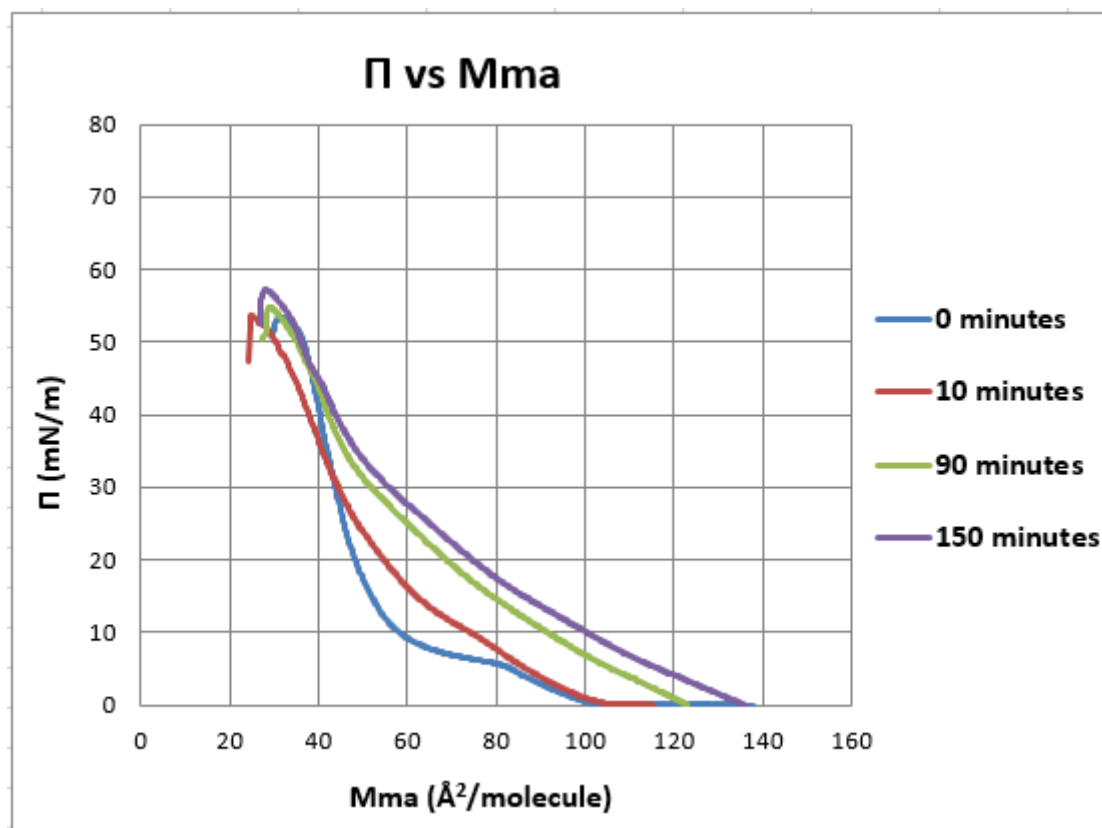


Figure 108. Effect of the exposure of a DPPC monolayer to aerosolised ultrapure water over increasing exposure times on the Π -Mma isotherm measured in PBS at 21°C. n = 3 experiments for control (0 minute exposure experiment) and n = 1 experiment for 10, 90 and 150 minute exposure experiments.

Table 48. Effect of the exposure of a DPPC monolayer to aerosolised ultrapure water over increasing exposure times on the lift-off M_{ma} , C_m , collapse Π and collapse M_{ma} of the Π - M_{ma} isotherm measured in PBS at 21°C. The corresponding values measured in each of these parameters for each exposure time were compared with those of no exposure (control) by calculating the difference in each of the parameters for the experimental isotherm and the control expressed as a % of the control value and dividing them by the reference % change from midpoint values for the relevant reference isotherm (Table 12). This approach assumes similar levels of uncertainties on the control and experimental isotherm parameters to those of the reference isotherm parameters.

Exposure time (min)	Lift-off M_{ma} ($\text{\AA}^2/\text{molecule}$)	(% difference experiment and control)/(reference % change from midpoint)	C_m 1-5 mN/m (mN/m^{-1})	(% difference experiment and control)/(reference % change from midpoint)	C_m 5-10 mN/m (mN/m^{-1})	(% difference experiment and control)/(reference % change from midpoint)
<i>Reference isotherm</i>	100	2.0 (% change from midpoint)	0.0378	3.0 (% change from midpoint)	0.0636	9.0 (% change from midpoint)
0 (control)	100		0.0366		0.0713	
10	103	1.5	0.0330	3.3	0.0282	6.7
90	123	11.5	0.0286	7.3	0.0271	6.9
150	136	18.0	0.0293	6.7	0.0276	6.8

Exposure time (min)	C_m 25-45 mN/m (mN/m^{-1})	(% difference experiment and control)/(reference % change from midpoint)	C_m 50 mN/m – lowest collapse Π (mN/m^{-1})	(% difference experiment and control)/(reference % change from midpoint)	Collapse Π (mN/m)	(% difference experiment and control)/(reference % change from midpoint)	Collapse M_{ma} ($\text{\AA}^2/\text{molecule}$)	(% difference experiment and control)/(reference % change from midpoint)
<i>Reference isotherm</i>	0.0063	6.0 (% change from midpoint)	0.0247	36.0 (% change from midpoint)	57.17	2.0 (% change from midpoint)	31	5.0 (% change from midpoint)
0 (control)	0.0076		0.0437		53.43		32	
10	0.0141	14.3	0.0498	0.4	53.63	0.0	25	4.4
90	0.0183	23.5	0.0301	0.9	54.88	1.5	29	1.8
150	0.0202	27.7	0.0193	1.6	57.20	3.5	28	2.6

In both the above studies, due to time constraints, only one isotherm was generated for each exposure duration. It must be recognised, therefore, that the uncertainties on these isotherm parameters were greater than those produced using the liquid deposition methods and thus any conclusions regarding effects must be drawn with more caution. However, the evidence of a trend of increasing changes with duration under both conditions is considered compelling.

To investigate possible causes of the effects seen on the DPPC monolayer, an experiment was performed to explore the effect of time on the behaviour of the DPPC monolayer in the absence of any aerosol (i.e. TSI COA switched off). The Π -Mma isotherm was measured after leaving a DPPC monolayer (on PBS at 21°C) undisturbed for 80 minutes instead of the conventional 15 minutes. Results are shown in Figure 109.

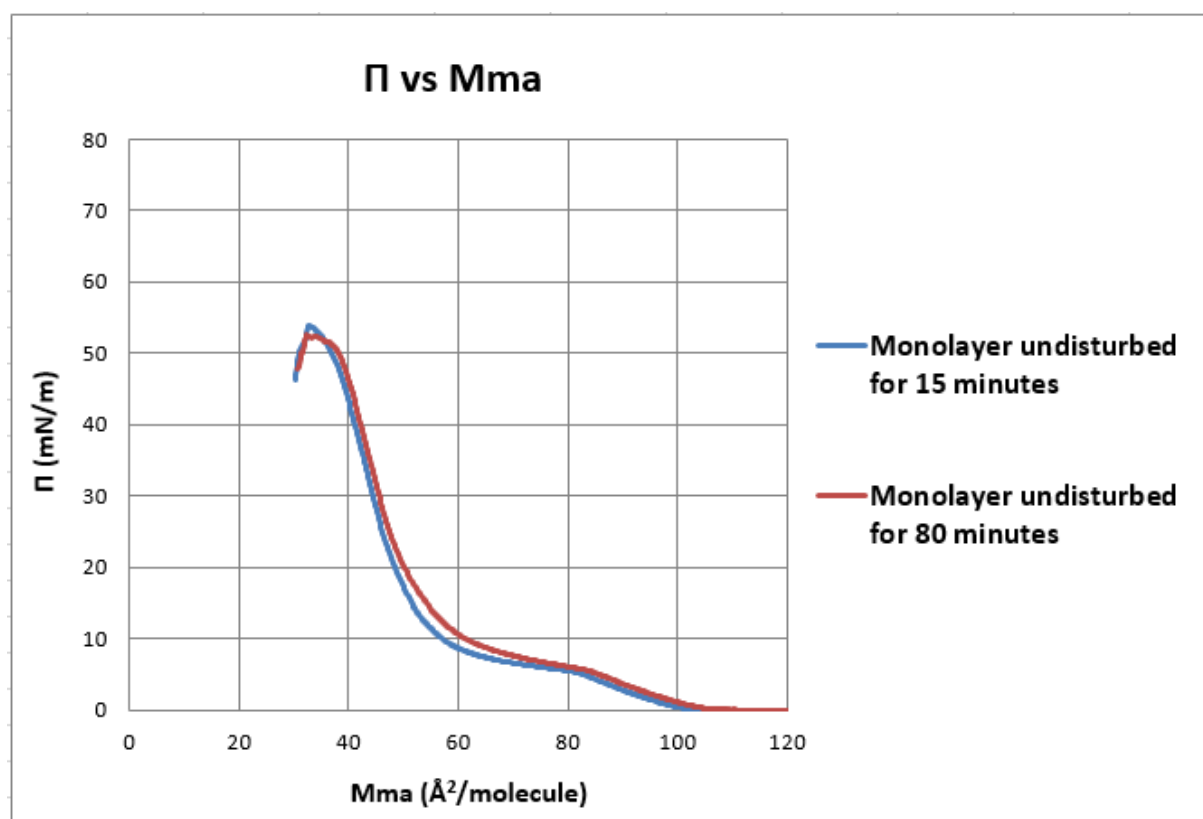


Figure 109. DPPC Π -Mma isotherm measured after leaving the monolayer undisturbed for 15 minutes (blue isotherm) and 80 minutes (red isotherm) measured in PBS at 21°C. $n = 4$ experiments for the 15 minute experiment and $n = 2$ experiments for the 80 minute experiment.

Thus, leaving a DPPC monolayer undisturbed for 80 minutes resulted in only minor differences in the DPPC isotherm by shifting the isotherm only slightly to higher Mma values, reducing the

nucleation of the LE phases and reducing the collapse Π value. It was therefore considered unlikely that the effects seen following exposure to aerosolised ultrapure water were due simply to potential ‘ageing’ effects on the DPPC monolayer.

It was further hypothesised that the change in the DPPC isotherm with exposure duration might have been due to impurities present in the water being deposited upon and affecting the DPPC monolayer. In order to investigate this, TEM grids were placed onto the Langmuir trough for imaging purposes and exposed to aerosolised ultrapure water for 120 minutes. Once the experiment was completed, several areas of the TEM grids were imaged. Two representative images of this situation are shown in Figure 110.

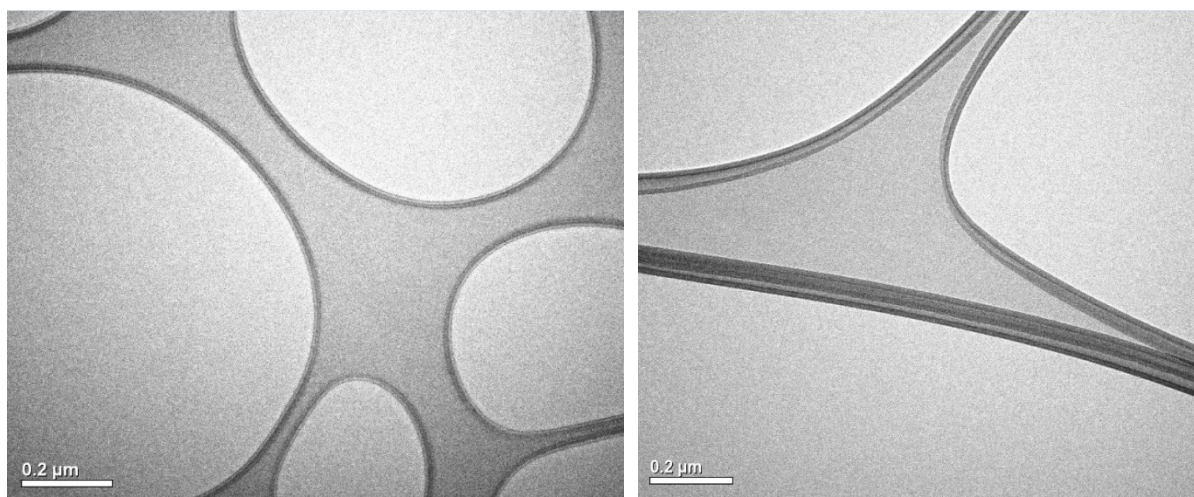


Figure 110. TEM images taken from TEM grids placed onto the Langmuir trough and exposed to aerosolised ultrapure water over 120 minutes. The scale bar is 0.2 μm for both images.

As can be seen from Figure 110, TEM images showed the carbon mesh structure with no particles indicating very low levels of impurities. Based on these results, it was hypothesised that the effects seen previously on the DPPC isotherm were probably caused by the exposure of the monolayer to the compressed air flow rather than aerosolised ultrapure water. To further investigate this, a DPPC monolayer was exposed to both aerosolised ultrapure water and compressed air flow over the same exposure time and effects on the DPPC isotherm were found to be similar. These results are shown in the next section (section 3.5.3.2.3).

3.5.3.2.3 Effect of the exposure of a DPPC monolayer to aerosolised CeO₂ nanoparticles on the surface pressure–Mma isotherm measured in PBS at 37°C and 21°C

To investigate the effect of aerosolised ultrapure water, compressed air (CA) flow and aerosolised CeO₂ NPs on the DPPC isotherm, a DPPC monolayer deposited onto a PBS subphase at 37°C was exposed over 60 minutes to aerosolised ultrapure water, CA flow and aerosolised CeO₂ NPs and the Π –Mma isotherm recorded during one compression. Table 49 shows the average aerosol CMD, GSD, number concentration, mass concentration, estimated CeO₂ NP mass deposited over the exposure time and CeO₂/DPPC mass ratio for the CeO₂ NP experiment. Figure 111 shows a graphical representation of the aerosol size distribution. This indicates that the CeO₂ aerosol size distribution was a uni-modal normal distribution with a CMD of 111 nm and a GSD of 1.8.

Figure 112 shows the effect of the exposure of a DPPC monolayer to aerosolised ultrapure water, CA flow and aerosolised CeO₂ NPs on the Π –Mma isotherm. Table 50 shows the lift-off Mma, C_m , collapse Π and collapse Mma of the Π –Mma isotherms. The corresponding values in each of these parameters measured for water and CeO₂ NPs were compared with those of CA (control) by calculating the % difference between experiment and control for each of the parameters and dividing them by the reference % change from midpoint values, i.e., assuming similar levels of uncertainties on the parameters to those of the reference isotherms (see section 2.4.1.5). The isotherms were determined only once for each condition.

Table 49. Average aerosol CMD, GSD, number concentration, mass concentration, estimated CeO₂ nanoparticle mass deposited and CeO₂/DPPC mass ratio for an experiment performed to study the effect of the exposure of a DPPC monolayer to aerosolised water, compressed air flow and aerosolised CeO₂ nanoparticles over 60 minutes measured in PBS at 37°C.

CMD ± SD (nm)	GSD ± SD	Number concentration ± SD (particles/cm ³)	mc (ng/cm ³)	CeO ₂ NP mass deposited (µg)	CeO ₂ /DPPC mass ratio
111 ± 4	1.8 ± 0.0	3.10E+05 ± 6.96E+04	7.58	25 ± 10	4.53/1

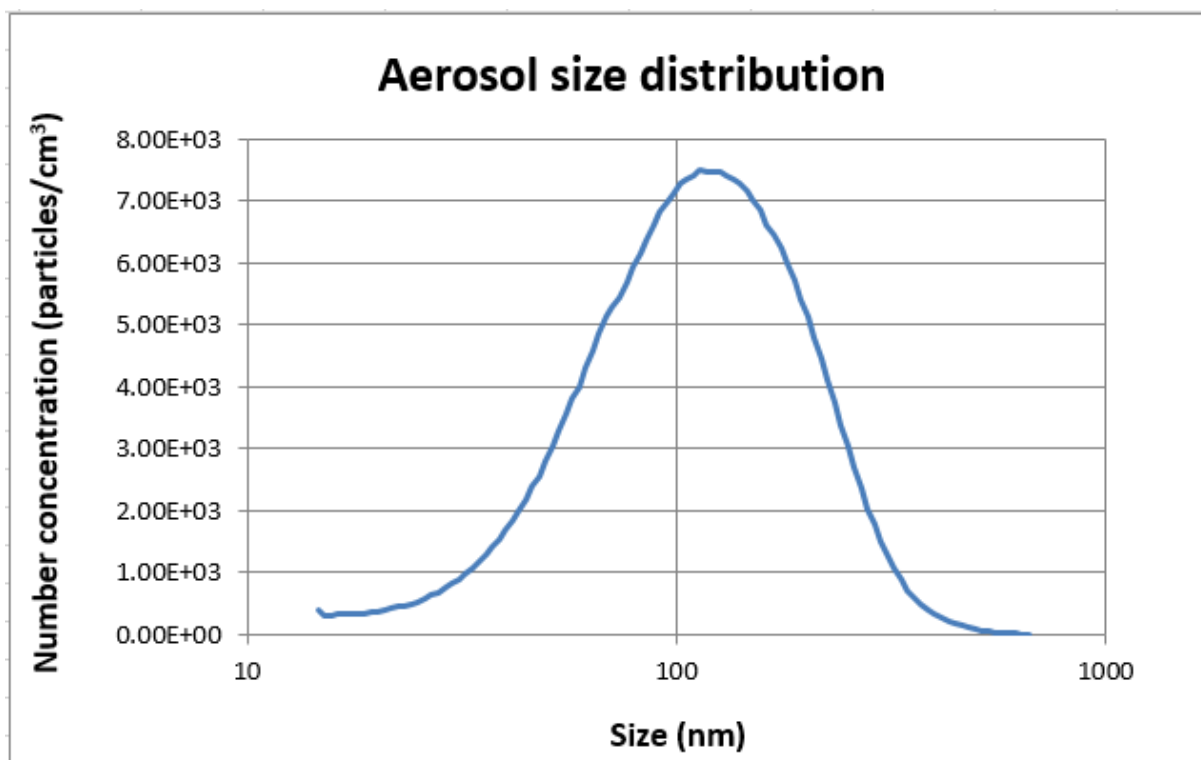


Figure 111. Graphical representation of the CeO₂ aerosol size distribution for an experiment performed to study the effect of the exposure of a DPPC monolayer to aerosolised water, compressed air flow and aerosolised CeO₂ nanoparticles over 60 minutes measured in PBS at 37°C.

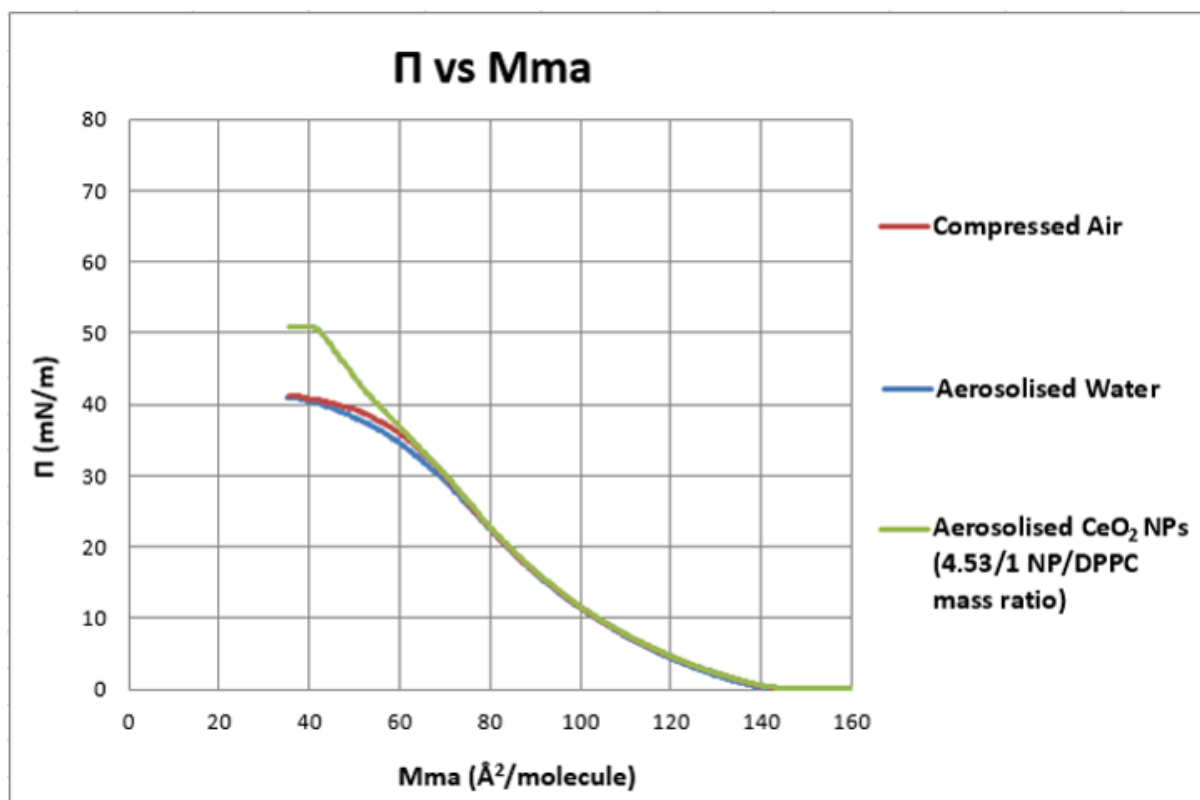


Figure 112. Effect of the exposure of a DPPC monolayer to aerosolised water, compressed air flow and aerosolised CeO_2 nanoparticles over 60 minutes (4.53/1 CeO_2 /DPPC mass ratio) on the Π - M_{ma} isotherm measured in PBS at 37°C . $n = 1$ experiment/condition.

Table 50. Effect of the exposure of a DPPC monolayer to aerosolised water, compressed air flow and aerosolised CeO₂ nanoparticles over 60 minutes (4.53/1 CeO₂/DPPC mass ratio) on the lift-off Mma, C_m , collapse Π and collapse Mma of the Π -Mma isotherms measured in PBS at 37°C. The corresponding values in each of these parameters measured for water and CeO₂ nanoparticles were compared with those of compressed air flow (control) by calculating the difference in each of the parameters for the experimental isotherm and the control expressed as a % of the control value and dividing them by the reference % change from midpoint values for the relevant reference isotherm (Table 11). This approach assumes similar levels of uncertainties on the control and experimental isotherm parameters to those of the reference isotherm parameters.

Deposition	Lift-off Mma (Å ² /molecule)	(% difference experiment and control)/(reference % change from midpoint)	C_m 1-5 mN/m (mN/m) ⁻¹	(% difference experiment and control)/(reference % change from midpoint)	C_m 10-25 mN/m (mN/m) ⁻¹	(% difference experiment and control)/(reference % change from midpoint)
<i>Reference isotherm</i>	123	1.0 (% change from midpoint)	0.0298	3.0 (% change from midpoint)	0.0150	2.0 (% change from midpoint)
CA (control)	141		0.0335		0.0175	
Water	139	1.0	0.0323	1.3	0.0174	0.5
CeO₂ NPs	141	0.0	0.0334	0.0	0.0174	0.5

Deposition	C_m 31 mN/m – lowest collapse Π (mN/m) ⁻¹	(% difference experiment and control)/(reference % change from midpoint)	Collapse Π (mN/m)	(% difference experiment and control)/(reference % change from midpoint)	Collapse Mma (Å ² /molecule)	(% difference experiment and control)/(reference % change from midpoint)
<i>Reference isotherm</i>	0.0294	15.0 (% change from midpoint)	39.40	2.0 (% change from midpoint)	49	4.0 (% change from midpoint)
CA (control)	0.0407		40.61		42	
Water	0.0423	0.3	40.48	0.0	41	0.5
CeO₂ NPs	0.0219	3.1	51.02	13.0	40	1.3

As can be seen from Table 50, the isotherms measured when a DPPC monolayer was exposed to CA flow and aerosolised water were very similar. The only isotherm parameter that was slightly different was the C_m for the region 1-5. Hence, the effects of aerosolised water on the DPPC isotherm seen in the previous section were most likely caused by the exposure of the monolayer to the CA flow. On the other hand, the isotherm measured after depositing aerosolised CeO₂ NPs onto a DPPC monolayer showed some differences compared to the CA and water aerosol isotherms with the most obvious being an increased collapse Π value. The lift-off M_{ma} , C_m for the regions 1-5 and 10-25 and collapse M_{ma} were similar to the control. The C_m for the region 31-lowest collapse Π and the collapse Π value were however different to the control; the C_m for the region 31-lowest collapse Π was lower than the control whereas the collapse Π value was higher than the control. A change in the C_m of the isotherm occurred at a $\Pi \sim 30$ mN/m compared to the control.

These experiments were repeated for an exposure time of 45 minutes. Table 51 shows the average aerosol CMD, GSD, number concentration, mass concentration, estimated CeO₂ NP mass deposited over the exposure time and CeO₂/DPPC mass ratio for the CeO₂ NP experiment. Figure 113 shows the effect of the exposure of a DPPC monolayer to aerosolised water, CA flow and aerosolised CeO₂ NPs on the Π - M_{ma} isotherm. The isotherms were determined using only one measurement per condition. The graphical representation of the aerosol size distribution as well as the lift-off M_{ma} , C_m , collapse Π and collapse M_{ma} of the Π - M_{ma} isotherms are shown in Appendix 7. The aerosol size distribution was a uni-modal size distribution with a peak at 107 nm and therefore very similar to that for the 60 minute exposure experiment, although the aerosol number concentration was lower for the 45 minute exposure experiment. Results showed that the isotherms measured when a DPPC monolayer was exposed to CA flow and aerosolised water over 45 minutes were very similar. Moreover, aerosolised CeO₂ NPs affected the C_m for the region 31-lowest collapse Π and the collapse Π in a similar way as for the 60 minute experiment. However, the effects were slightly smaller for this lower deposited mass (14 μ g for the 45 minute exposure experiment compared to 25 μ g for the 60 minute exposure experiment) described by a higher C_m for the region 31-lowest collapse Π and a lower collapse Π suggesting that the effect of aerosolised CeO₂ NPs on the DPPC monolayer might have been mass-dependant.

Table 51. Average aerosol CMD, GSD, number concentration, mass concentration, estimated CeO₂ nanoparticle mass deposited and CeO₂/DPPC mass ratio for an experiment performed to study the effect of the exposure of a DPPC monolayer to aerosolised water, compressed air flow and aerosolised CeO₂ nanoparticles over 45 minutes measured in PBS at 37°C.

CMD ± SD (nm)	GSD ± SD	Number concentration ± SD (particles/cm ³)	<i>mc</i> (ng/cm ³)	CeO ₂ NP mass deposited (µg)	CeO ₂ /DPPC mass ratio
107 ± 7	1.8 ± 0.0	1.80E+05 ± 1.61E+05	5.47	14 ± 5	3.09/1

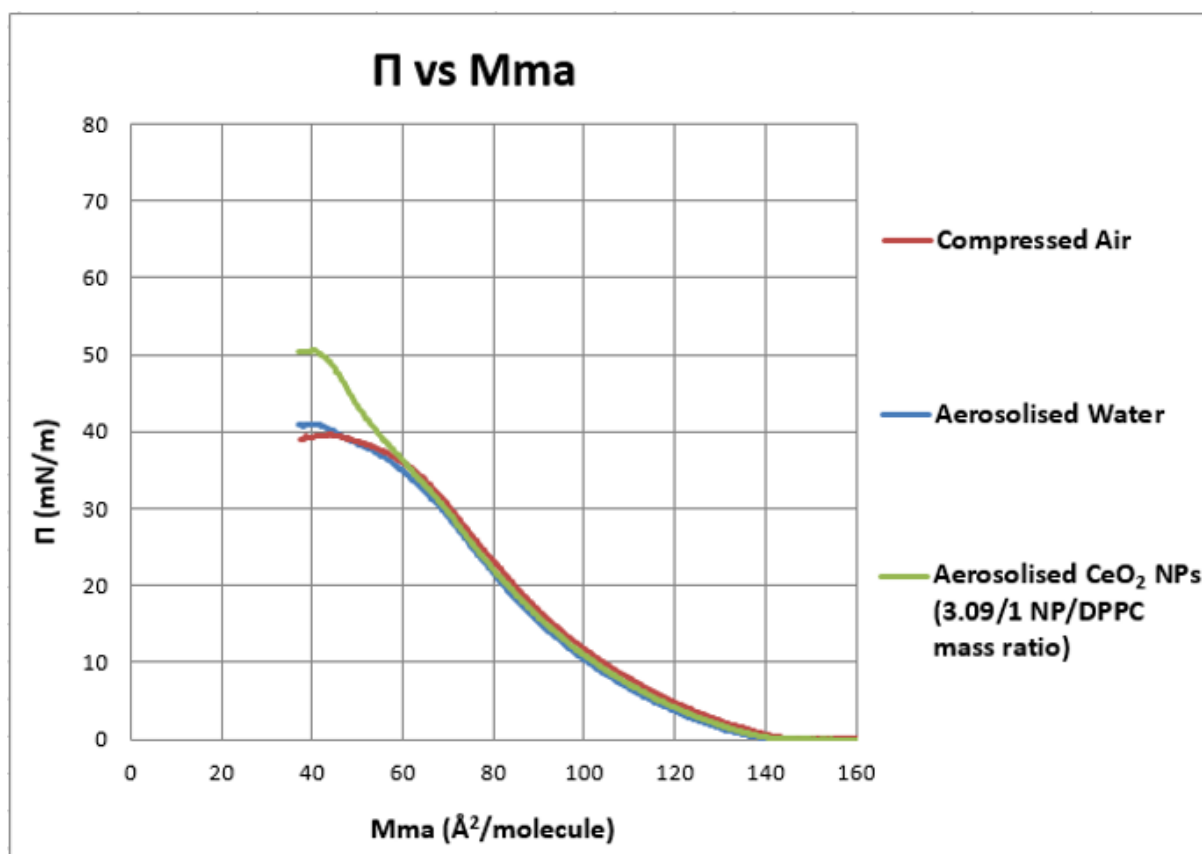


Figure 113. Effect of the exposure of a DPPC monolayer to aerosolised water, compressed air flow and aerosolised CeO₂ nanoparticles over 45 minutes (3.09/1 CeO₂/DPPC mass ratio) on the Π - M_{ma} isotherm measured in PBS at 37°C. n = 1 experiment/condition.

These results indicated a clear effect of the CA flow on the DPPC isotherm, which increased with the exposure duration. It is however not clear what was causing this. There are various possibilities, for example, the CA flow could have been physically deforming the monolayer thereby changing its properties. The CA flow could have also increased the temperature at the liquid surface possibly due to friction forces. The effect on the 21°C DPPC isotherm of increasing exposures to CA flow (with aerosolised water) as illustrated in Figure 108, showed some similarities to the change induced by an increase in subphase temperature as shown previously in section 2.4.2.3, especially the shift in the lift-off M_{ma} to larger areas and the effect on the LE-LC transition plateau which became steeper with temperature. Further investigation of this issue is clearly required to identify the cause of the effects of CA flow on the DPPC isotherm and could be explored by reducing the flow rate and/or changing the flow path of the gas within the exposure chamber.

Given these uncertainties, for the remaining parts of the present study, which was focussed on exploring the effects of deposited aerosol particle mass on DPPC monolayer behaviour, it was decided to focus on the parameters of the isotherm, particularly the C_m for II values above 30 mN/m and the collapse II , for which the above experiments indicated an effect of deposited aerosolised CeO₂ NP mass (e.g. Figure 112 and Figure 113) and also that the isotherm for the DPPC monolayer exposed to aerosol CeO₂ NPs would be compared with a control isotherm for the DPPC monolayer exposed to CA flow or aerosolised water for the same duration.

In order to further investigate the effect of deposited aerosolised CeO₂ NP mass on the collapse II , DPPC monolayers were exposed to a CeO₂ NP aerosol for the following exposure times: 10, 30, 60, 75, 90, 120 and 150 minutes. The 30, 60, 75, 90 and 120 minute experiments were performed in duplicate. For ease of presentation, only one set of experiments for the 10, 30, 60 and 150 minute exposure experiments are shown although the other results showed a similar trend, since for those experiments that were performed in duplicate results could not be averaged because the mass deposited in each experiment was different. A detailed description of the other experiments is shown in Appendix 8. Table 52 shows the exposure time, average aerosol CMD, GSD and number concentration for the 10, 30, 60 and 150 minute exposure experiments. Figure 114 shows a graphical representation of the aerosol size distribution for each of these four experiments. Thus, the profile of the aerosol size distribution was very similar for all the experiments, being a uni-modal normal distribution with a peak at a diameter of ~

110 nm. The aerosol number concentration and thus also the mass concentration increased with exposure time. Table 53 shows the aerosol mass concentration, estimated CeO₂ NP mass deposited over the exposure time, CeO₂/DPPC mass ratio and collapse *II* for each of these four experiments. Figure 115 shows the effect of the exposure of a DPPC monolayer to four different aerosolised CeO₂ NP masses on the *II*-Mma isotherm. Figure 116 shows the graphical representation of the effect of the exposure to the four different CeO₂ NP deposited masses on the collapse *II*. As can be seen from Table 53, Figure 115 and Figure 116 there was a systematic change in the isotherm with exposure, with the collapse *II* increasing with the CeO₂ NP aerosol mass deposited.

Table 52. Exposure time, average aerosol CMD, GSD and number concentration of four different experiments performed to study the effects of the exposure of a DPPC monolayer to increasing amounts of aerosolised CeO₂ nanoparticles measured in PBS at 37°C.

Exposure time (min)	CMD ± SD (nm)	GSD ± SD	Number concentration ± SD (particles/cm³)
10	110 ± 2	1.7 ± 0.0	1.29E+05 ± 7.49E+04
30	109 ± 9	1.8 ± 0.0	1.96E+05 ± 6.50E+04
60	107 ± 2	1.8 ± 0.0	2.68E+05 ± 4.59E+04
150	115 ± 6	1.8 ± 0.0	2.97E+05 ± 5.00E+04

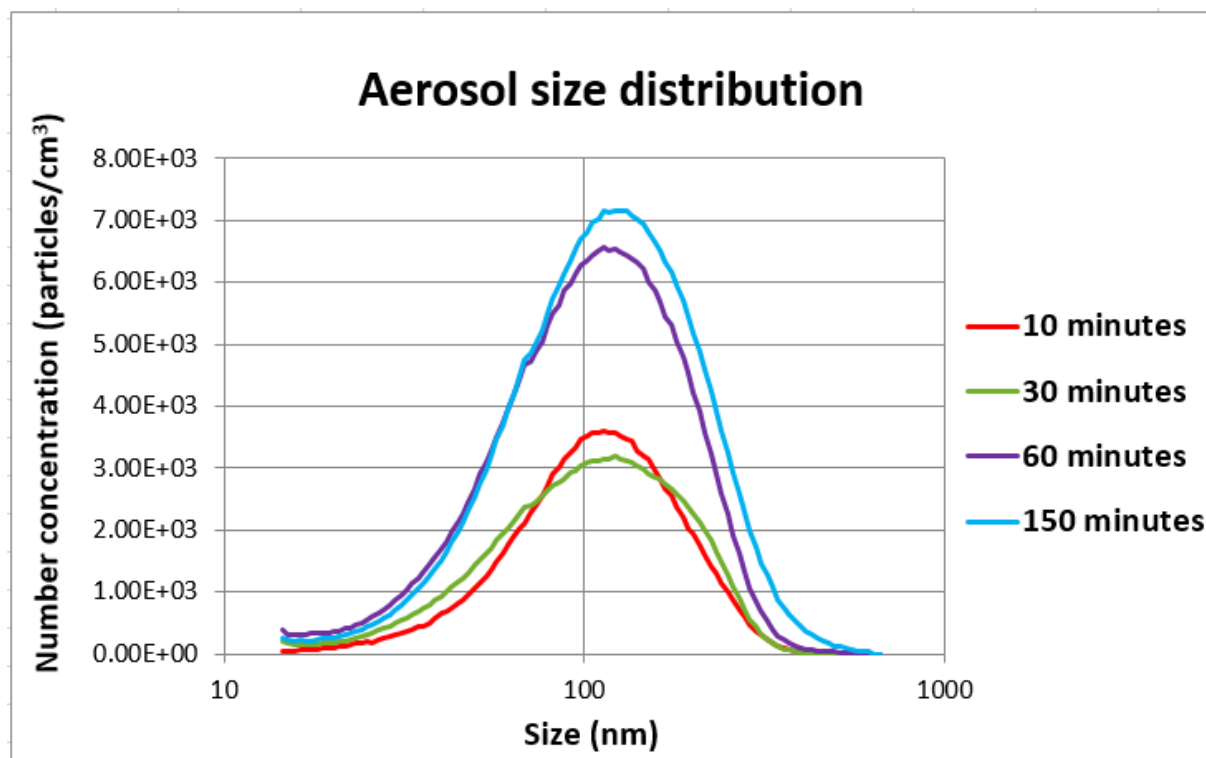


Figure 114. Graphical representation of the CeO₂ aerosol size distribution for each of the four experiments performed to study the effects of the exposure of a DPPC monolayer to increasing amounts of aerosolised CeO₂ nanoparticles measured in PBS at 37°C.

Table 53. Exposure time, aerosol mass concentration, estimated CeO₂ nanoparticle mass deposited, CeO₂/DPPC mass ratio and collapse *II* of the *II*-Mma isotherms for each of the four experiments performed to study the effects of the exposure of a DPPC monolayer to increasing amounts of aerosolised CeO₂ nanoparticles measured in PBS at 37°C.

Exposure time (min)	<i>mc</i> (ng/cm ³)	CeO ₂ NP mass deposited (µg)	CeO ₂ /DPPC mass ratio	Collapse <i>II</i> (mN/m)
10	1.57	1 ± 0.3	0.15/1	44.09
30	3.04	5 ± 2	0.93/1	47.66
60	3.96	13 ± 5	2.98/1	49.89
150	7.17	59 ± 24	13.48/1	56.76

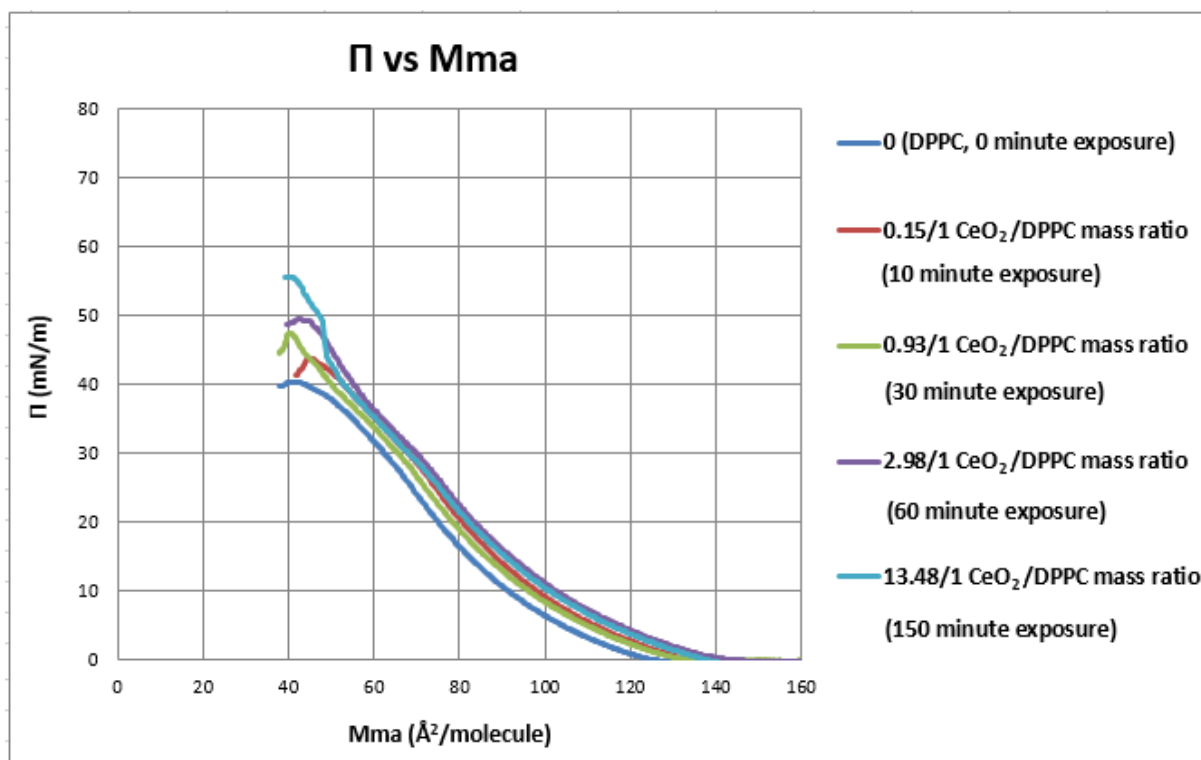


Figure 115. Effect of the exposure of a DPPC monolayer to increasing amounts of aerosolised CeO₂ nanoparticles over increasing exposure times on the Π -Mma isotherm measured in PBS at 37°C. n = 3 experiments for 0 minute exposure experiment and n = 1 experiment for 10, 30, 60 and 150 minute exposure experiments.

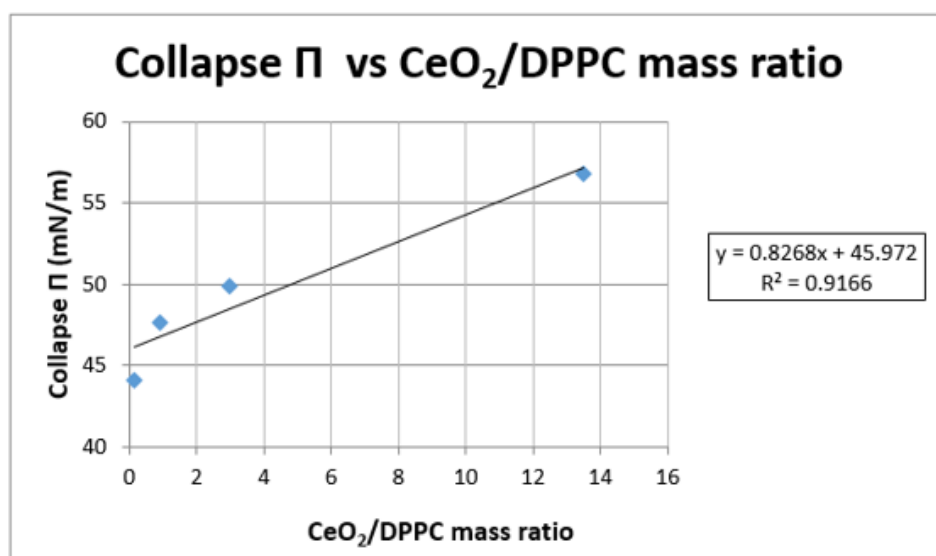


Figure 116. Graphical representation of the effect of the exposure of a DPPC monolayer to increasing amounts of aerosolised CeO₂ nanoparticles (0.15/1, 0.93/1, 2.98/1 and 13.48/1 CeO₂/DPPC mass ratios) on the collapse Π of the Π -Mma isotherms measured in PBS at 37°C.

Finally, a similar set of experiments was performed at 21°C for comparative purposes. In these experiments, a DPPC monolayer was exposed to a CeO₂ NP aerosol for 10 and 90 minutes to produce a ‘low’ and a ‘high’ aerosolised CeO₂ NP mass deposition. Due to time limitations, the experiments were only performed once. Table 54 shows the exposure time, average aerosol CMD, GSD and number concentration for each experiment and Figure 117 shows a graphical representation of the aerosol size distributions. The aerosol size distribution was a uni-modal normal distribution in both experiments. The CMD however was 133 nm for the 10 minute exposure experiment and 167 nm for the 90 minute exposure experiment. The exposure time, aerosol mass concentration, estimated CeO₂ NP mass deposited over the exposure time and CeO₂/DPPC mass ratios for each experiment are shown in Table 55. The number concentration, aerosol mass concentration and estimated CeO₂ NP mass deposited for the 90 minute exposure experiment were higher compared to the 10 minute exposure experiment. Figure 118 shows the effect of the exposure of a DPPC monolayer to aerosolised CeO₂ NPs on the *II*-Mma isotherm for the 10 and 90 minute exposure experiments compared to the *II*-Mma isotherm for CA flow, the control. Table 56 and Table 57 show the C_m for the region 30-45 mN/m and the collapse *II* of the *II*-Mma isotherms for the 10 and 90 minute exposure experiments respectively. As already mentioned, based on the results obtained for the experiment measured at 37°C (Figure 112 and Figure 113), it was decided to focus on the C_m for *II* values above 30 mN/m and the collapse *II*. For both experiments, the corresponding values in each of the parameters measured for CeO₂ NPs were compared with those of CA (control) by calculating the % difference between experiment and control for each of the parameters and dividing them by the reference % change from midpoint values, i.e., assuming similar levels of uncertainties on the parameters to those of the reference isotherms (see section 2.4.1.5). Additionally, the assumption was made that for the reference isotherm, the uncertainty values for the C_m for the region 25-45 mN/m would be similar for the region 30-45 mN/m.

Table 54. Exposure time, average aerosol CMD, GSD and number concentration of two experiments performed to study the effects of the exposure of a DPPC monolayer to increasing aerosolised CeO₂ nanoparticle mass measured in PBS at 21°C.

Exposure time (min)	CMD ± SD (nm)	GSD ± SD	Number concentration ± SD (particles/cm ³)
10	133 ± 9	1.9 ± 0.1	4.10E+05 ± 1.61E+05
90	167 ± 14	2.0 ± 0.0	7.90E+05 ± 1.32E+05

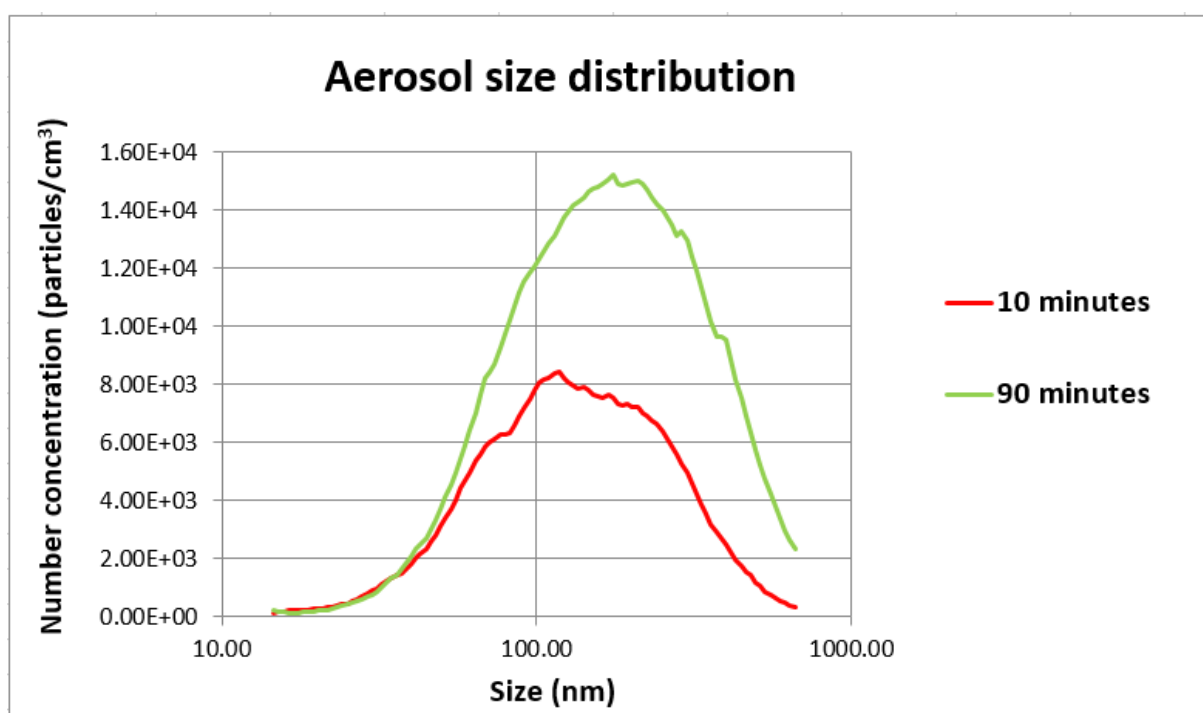


Figure 117. Graphical representation of the CeO₂ aerosol size distribution for the 10 and 90 minute experiments performed to study the effects of the exposure of a DPPC monolayer to increasing aerosolised CeO₂ nanoparticle mass measured in PBS at 21°C.

Table 55. Exposure time, aerosol mass concentration, estimated CeO₂ nanoparticle mass deposited and CeO₂/DPPC mass ratio of two experiments performed to study the effects of the exposure of a DPPC monolayer to increasing aerosolised CeO₂ nanoparticle mass measured in PBS at 21°C.

Exposure time (min)	<i>mc</i> (ng/cm³)	CeO₂ NP mass deposited (µg)	CeO₂/DPPC mass ratio
10	8.27	1 ± 0	0.10/1
90	24.96	21 ± 7	2.31/1

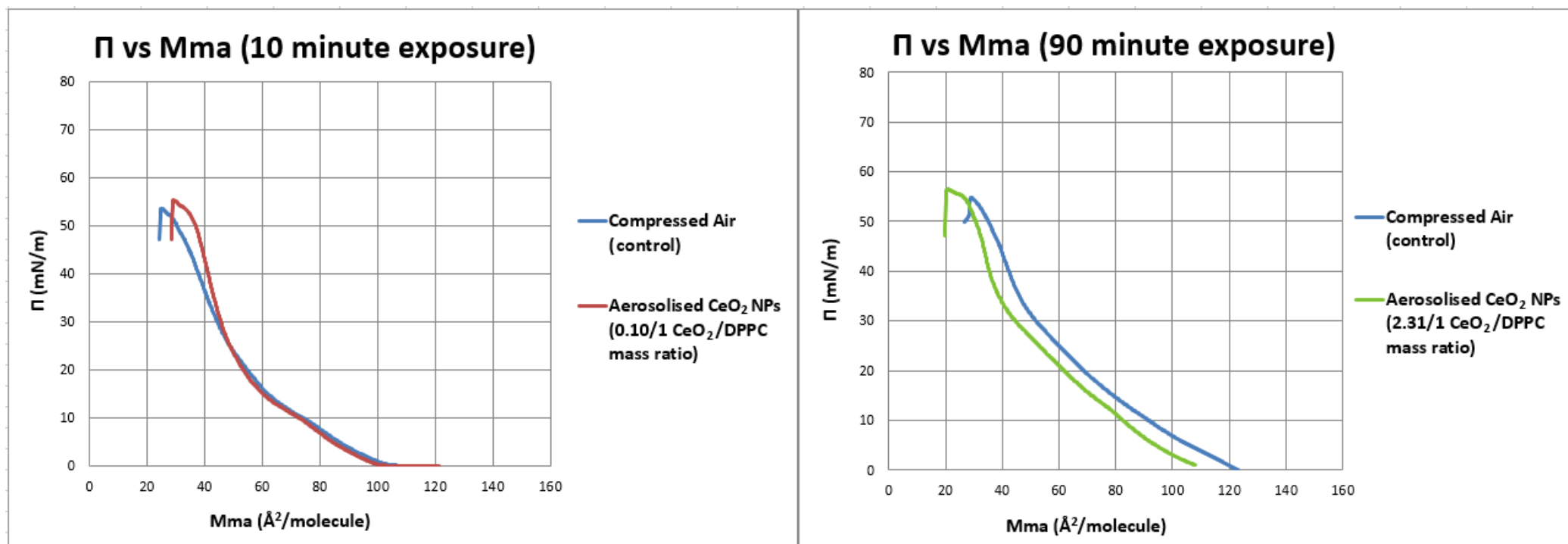


Figure 118. Effect of the exposure of a DPPC monolayer to aerosolised CeO_2 nanoparticles over 10 minutes (0.10/1 CeO_2 /DPPC mass ratio, left image) and over 90 minutes (2.31/1 CeO_2 /DPPC mass ratio, right image) on the Π -Mma isotherm measured in PBS at 21°C. The control isotherm was measured after exposing a DPPC monolayer to compressed air flow for the same duration. $n = 1$ experiment/condition.

Table 56. Effect of the exposure of a DPPC monolayer to aerosolised CeO₂ nanoparticles over 10 minutes (0.10/1 CeO₂/DPPC mass ratio) on the C_m for the region 30-45 mN/m and the collapse Π of the Π -Mma isotherms measured in PBS at 21°C. The corresponding values in each of the parameters measured for CeO₂ nanoparticles were compared with those of compressed air flow (control) by calculating the difference in each of the parameters for the experimental isotherm and the control expressed as a % of the control value and dividing them by the reference % change from midpoint values for the relevant reference isotherm (Table 12). This approach assumes similar levels of uncertainties on the control and experimental isotherm parameters to those of the reference isotherm parameters. Additionally, the assumption was made that for the reference isotherm, the uncertainty values for the C_m for the region 25-45 mN/m would be similar for the region 30-45 mN/m.

10 minute exposure	C_m 30-45 mN/m (mN/m)⁻¹	(% difference experiment and control)/(reference % change from midpoint)	Collapse Π (mN/m)	(% difference experiment and control)/(reference % change from midpoint)
<i>Reference isotherm</i>	0.0063 (25-45 mN/m)	6.0 (% change from midpoint)	57.17	2.0 (% change from midpoint)
CA (control)	0.0141		53.63	
CeO₂	0.0092	5.8	55.31	1.5

Table 57. Effect of the exposure of a DPPC monolayer to aerosolised CeO₂ nanoparticles over 90 minutes (2.31/1 CeO₂/DPPC mass ratio) on the C_m for the region 30-45 mN/m and the collapse Π of the Π -Mma isotherm measured in PBS at 21°C. The corresponding values in each of the parameters measured for CeO₂ nanoparticles were compared with those of compressed air flow (control) by calculating the difference in each of the parameters for the experimental isotherm and the control expressed as a % of the control value and dividing them by the reference % change from midpoint values for the relevant reference isotherm (Table 12). This approach assumes similar levels of uncertainties on the control and experimental isotherm parameters to those of the reference isotherm parameters. Additionally, the assumption was made that for the reference isotherm, the uncertainty values for the C_m for the region 25-45 mN/m would be similar for the region 30-45 mN/m.

90 minute exposure	C_m 30-45 mN/m (mN/m) ⁻¹	(% difference experiment and control)/(reference % change from midpoint)	Collapse Π (mN/m)	(% difference experiment and control)/(reference % change from midpoint)
Reference isotherm	0.0063 (25-45 mN/m)	6.0 (% change from midpoint)	57.17	2.0 (% change from midpoint)
CA (control)	0.0183		54.88	
CeO ₂	0.0141	3.8	56.47	1.5

As indicated above it is difficult to interpret the impact of deposited aerosolised CeO₂ NPs on the DPPC monolayer behaviour because of the significant effect of the CA flow on the monolayer. However, taking this into account there is a clear effect on the final region of the isotherm, in particular the C_m for the region 30-45 mN/m, which decreased with deposited mass and the collapse Π , which increased with deposited mass for both 10 and 90 minute exposure experiments. It is not entirely clear what was causing this effect. SEM images indicated a homogeneous distribution of small agglomerates across the surface (see Figure 101). It is possible that these small agglomerates improved the film containment and therefore prevented surfactant loss from the system, perhaps by protecting the individual DPPC domains. This is further supported by the experiments performed at 37°C shown previously in Figure 112 and Figure 113, as the deposition of aerosolised CeO₂ NPs on the DPPC monolayer clearly decreased the C_m of the isotherm starting at a $\Pi \sim 30$ mN/m compared to the control, which is where the loss of surfactant occurred. Surfactant leakage problems at a subphase temperature

of 37°C were discussed previously in section 2.4.2.3. Moreover, a similar situation would have occurred at 21°C, as the exposure of a DPPC monolayer to CA reduced the nucleation of the LE phases. In fact, the C_m for the region 15-30 mN/m was calculated for the DPPC monolayer exposed to aerosol CeO₂ NPs during 10 and 90 minutes. This value was 0.02 (mN/m)⁻¹ for both experiments. Taking into account experimental values of C_m for the DPPC monolayer phases from the literature (i.e. 0.02-0.1 (mN/m)⁻¹ for LE films, 0.004-0.01 (mN/m)⁻¹ for LC films and < 0.004 (mN/m)⁻¹ for S films (Kodama et al., 2004, Vitovič et al., 2006)), this indicates that the monolayer was in the LE phase in this region instead of the expected LC phase. As monolayers that collapse in the LE phase usually do so at Π_e because of a higher instability of the monolayer (Baoukina et al., 2014), which for DPPC is around 40 mN/m, the loss of material probably started at a $\Pi \sim 30$ mN/m. An improvement in the film containment and reduction of the loss of surfactant should also lead to a higher collapse Π value as discussed previously in sections 2.4.2.3 and 2.4.2.5. These issues could be explored in future studies using different *in situ* imaging techniques including BAM or Fluorescence Microscopy. Finally, results at 21°C were in agreement with those performed at 37°C although the effect on the collapse Π was more pronounced at 37°C described by higher ratios of the % difference between experiment and control to the % change from midpoint in this isotherm parameter. When CeO₂ NPs were deposited using the liquid deposition method 2, the effects of CeO₂ NPs on the DPPC Π -Mma isotherm at 37°C were larger compared to those experiments performed at 21°C (section 3.5.2.2) hence, this could be related to the subphase temperature itself. Nevertheless, future research directed towards examining this in more detail is needed as isotherms were only measured once per exposure time at a subphase temperature of 21°C.

A detailed comparison of the results reported in the present section and those in the literature is included later in this chapter (section 3.6.2).

3.6 Summary discussion and conclusion

3.6.1 Comparison of the three deposition methods

In this chapter, the effect of the method of deposition of CeO₂ NPs (19 nm primary particle size) on the behaviour of a DPPC monolayer located at the air/PBS interface was investigated using a LWB. Three deposition methods were used. In the first method, CeO₂ NPs were suspended in chloroform and deposited onto a DPPC monolayer using a microsyringe. Deposition method 2 consisted of mixing DPPC and CeO₂ NPs in the same chloroform

suspension and depositing the mixture onto a clean PBS subphase using a microsyringe. In the third deposition method, CeO₂ NPs in aerosol form were deposited onto a DPPC monolayer. For this deposition method, an aerosol exposure system was developed which consisted of a device for generating NP aerosols, an exposure chamber where the Langmuir trough was placed and an airflow system that transported the aerosolised NPs into the exposure chamber. To date, there are no other studies of NP deposition onto a surfactant monolayer in aerosol form using a LWB system and thus these data are novel.

For each deposition method, CeO₂ NP properties were characterised both pre and post-administration and the effect of CeO₂ NPs on the Π -Mma isotherm of the DPPC monolayer was investigated. The monolayer was deposited onto a mica substrate and imaged using SEM and ToF-SIMS.

In brief, deposition method 1 had no effect upon the DPPC isotherm during the initial compression of the monolayer at any deposited mass level; deposition method 2 affected a number of parameters of the isotherm, in particular the lift-off Mma, in a mass-dependant manner and deposition method 3 affected the final region of the isotherm, in particular the C_m at Π values above ~ 30 mN/m and the collapse Π value, also in a mass-dependant manner. More details are provided below.

Deposition Method 1

For deposition method 1, CeO₂ NPs suspended in chloroform agglomerated and had a CMD of 158 nm, a hydrodynamic diameter of 220 nm and a zeta potential of -70mV which indicated that NPs were strongly anionic in this medium. CeO₂ NPs suspended in a PBS medium agglomerated and settled at the bottom of the bottle within seconds due to their isoelectric point of 8 (Baalousha et al., 2012b) and the pH of PBS 7. As such, it was not possible to measure the size of the NP agglomerates in this medium. When deposited onto a DPPC monolayer at 37°C and 21°C, CeO₂ NPs did not affect the isotherm at any NP mass deposited (up to 24 μ g at the following NP/DPPC mass ratios: 0.06/1, 1.21/1, 3.64/1 for the experiments performed at 37°C and 0.06/1, 1.16/1, 3.49/1 for the experiments performed at 21°C). One hypothesis for this behaviour was that the CeO₂ NPs rapidly agglomerated into large and dense clusters and entered the subphase as in general, it is suggested that the forces responsible for the interactions between particles in bulk also operate in particle monolayers (Aveyard et al., 2000a, Binks, 2002) and

as already mentioned, CeO₂ NPs were very unstable in PBS, leaving small agglomerates remaining at the interface that were probably insufficient to affect the DPPC isotherm. In fact, when the same experiment was performed using a water subphase, which is a medium in which CeO₂ NPs were much more stable, instead of PBS, CeO₂ NP agglomerates were found to be present across the surface. SEM images of studies performed using a PBS subphase showed only a few small agglomerates of around 3 μm in diameter present at the interface during one compression that could not be chemically identified as cerium in the ToF-SIMS images, which tended to support this hypothesis that, following the loss of large NP agglomerates, only small NP agglomerates remained at the surface whose size was below the minimum detectable size of 300 nm, at levels too low to affect the isotherm. However, after compressing and expanding the interface three times at normal and maximum barrier speed, large and dense CeO₂ NP agglomerates could be visualised at the interface. This could be an indication that DPPC coated the CeO₂ NP agglomerates and increased their wettability, making them more stable at the air/PBS interface. There is evidence that the wettability of particles in a suspending medium can be modified by the adsorption of surfactant to the surface of the particles (Maestro et al., 2012, Maestro et al., 2015). It is difficult to interpret these results further without additional quantitative information on the amount of CeO₂ at the interface. The results of ICP-MS analysis of the subphase were also inconclusive in terms of identifying the presence of the CeO₂ NPs. This potential loss to the subphase is clearly something which needs to be investigated further.

Deposition Method 2

For deposition method 2, three different CeO₂ NP and DPPC mixtures suspended in chloroform were prepared at the following NP/DPPC mass ratios: 0.06/1, 1.25/1, 3.75/1 for the experiments performed at 37°C and 0.05/1, 1.00/1, 3.00/1 for the experiments performed at 21°C. The CMD and hydrodynamic diameters of the CeO₂ NP agglomerates in all of the suspensions (around 40 nm and 134 nm respectively) were lower than those for CeO₂ NPs alone suspended in chloroform and hence, it is believed that DPPC deagglomerated the NP agglomerates. The zeta potential was around + 40 mV which indicated that these mixtures were strongly cationic and stable. When suspended in a PBS medium, these mixtures were more stable compared to CeO₂ NPs alone and had an average size of 2,000 nm.

When the highest CeO₂/DPPC mass ratio mixture was deposited onto a PBS subphase (3.00/1), SEM and ToF-SIMS images showed that NP agglomerates were present at the interface at low

Π values and that the area covered by them as well as the surface concentration increased up to a Π value of 40 mN/m. This indicated that CeO₂ NPs were more stable at the air/PBS interface due to the coating with DPPC as compared to when CeO₂ NPs suspended in chloroform were deposited onto a PBS subphase. With further compression, the area covered by the NP agglomerates as well as the surface concentration decreased suggesting a loss of CeO₂ NP mass from the monolayer. It was hypothesised that large agglomerates had detached from the interface and sedimented into the subphase. However, this could not be confirmed by the ICP-MS results. Nevertheless, after three compression-expansion cycles at normal and maximum barrier speed, there were still some CeO₂ NPs present at the interface.

Π - M_{ma} isotherms showed that the CeO₂ NP agglomerates shifted the isotherm to higher M_{ma} values and, for those experiments performed at 21°C, obscured the LE-LC transition plateau, which became less horizontal with CeO₂ NP mass deposited (i.e. affected the C_m for the region 5-10 mN/m). The lift-off M_{ma} of the isotherms increased with CeO₂ NP mass. It is hypothesised that this was caused by the presence of large and dense CeO₂ NP agglomerates at the interface at early stages of compression that experienced repulsive forces between them when in contact. It is assumed that the presence of CeO₂ NPs in the lipid monolayer could have also reduced the available surface area per surfactant molecule enabling DPPC to increase the Π at an earlier stage of compression. The effect of CeO₂ NP mass on the other parameters of the isotherm (C_m , collapse Π and collapse M_{ma}) was, however, less clear. Effects at 37°C were similar to but more pronounced than those at 21°C.

Finally, these experiments were repeated for the lowest and the highest CeO₂/DPPC mass ratios (0.05/1 and 3.00/1 respectively) at 21°C using a low subphase volume in order to achieve higher Π values not possible using the standard subphase volume because of issues with leakage. Collapse Π was 74 mN/m for both CeO₂/DPPC mass ratios. The collapse M_{ma} was however lower for the higher CeO₂/DPPC mass ratio due to a pronounced increase in the C_m from a Π value of ~ 55 mN/m to ~ 74 mN/m. It is hypothesised that this difference was due to the detachment of CeO₂ NPs from the interface which would have decreased the compression rate per DPPC molecule. These results were in contrast to the situation when working with a normal subphase volume, when the isotherm for the highest CeO₂/DPPC mass ratio collapsed at a higher Π value and M_{ma} than for the other mass ratio experiments.

These results suggest that working with conventional LWB systems in which only low Π are reached due to leakage problems could lead to erroneous conclusions and emphasises the importance of measuring isotherms under conditions as close as possible to those occurring *in vivo*. Measuring the Π -Mma isotherm at a subphase temperature of 37°C and using leak-proof systems in order to reach near zero γ values is key to gaining a better understanding of what happens in the alveoli. Furthermore, mixing DPPC and CeO₂ NPs in chloroform implied that the most important interactions between surfactant and CeO₂ NPs occurred in the suspending medium which modified the wettability of the CeO₂ NPs and therefore influenced their behaviour, rather than at the air/liquid interface.

Deposition Method 3

For deposition method 3, a method to calculate the aerosol mass deposited onto the Langmuir trough was developed based on deriving the deposition velocity of the aerosolised CeO₂ NPs within the exposure chamber. The deposition velocity was estimated using a quartz crystal microbalance (QCM) for experimental conditions applicable to the 37°C experiments and EMFAB filters for those experiments performed at 21°C. The deposition velocities were significantly different for each of the methods. The reason for this difference was not initially clear. Following further experiments using carbon black shown in the next chapter (section 4.5.1.2) it is now thought that this difference was a result of either the different set-up of the experiments performed in the presence of a QCM compared to those using EMFAB filters, or some malfunctioning of the QCM.

Π -Mma isotherms showed that the exposure of a DPPC monolayer to compressed air (CA) flow affected the isotherm by increasing the lift-off Mma and reducing the nucleation of the LE phases with exposure duration. It is not clear exactly what was causing this effect which requires further investigation. For this reason, the isotherm for the DPPC monolayer exposed to aerosol CeO₂ NPs was compared with a control isotherm for the DPPC monolayer exposed to CA flow for the same duration.

The aerosol particle size and number concentration generated by the TSI COA were slightly higher for the experiments performed at 21°C (around 173 nm) compared to those performed at 37°C (around 115 nm) in part because the concentration of the suspension used in each experiment was not identical. The aerosol size distribution was a uni-modal normal distribution.

TEM images also showed limited agglomeration of aerosolised CeO₂ NPs while they were settling from the air onto the trough; for this experiment, the CMD of the airborne CeO₂ NPs was 177 nm whereas the CMD of the CeO₂ aerosol agglomerates upon deposition was 220 nm.

When aerosolised CeO₂ NPs were deposited onto a DPPC monolayer at a NP/DPPC mass ratio of 1.12/1, SEM and ToF-SIMS images indicated the presence of CeO₂ NP agglomerates of a similar size homogeneously spread across the surface during the first compression at Π values of 40 and 70 mN/m. However, images taken for the 2.42/1 mass ratio at a Π value of 20 mN/m showed that agglomerates were not so uniformly distributed. It is possible that this could have been related to aerosol CeO₂ NPs not depositing homogeneously across the trough area in this experiment. Results also showed that the area covered by them as well as the surface concentration increased with compression indicating limited, if any, detachment of material from the interface into the subphase. These results contrast with those obtained for the liquid deposition methods (deposition methods 1 and 2) which indicated a loss of CeO₂ NPs as they became large and dense enough to detach from the interface into the subphase. Compression-expansion cycles promoted the agglomeration of the CeO₂ NP clusters although their size was smaller than for the liquid deposition methods. From these results, it is hypothesised that aerosolised CeO₂ NPs did not agglomerate to the same extent as those CeO₂ NPs deposited from liquid suspensions. One possible explanation for this is that the wettability of the aerosolised CeO₂ NPs was higher than that of CeO₂ NPs deposited from chloroform suspensions which increased the stability of the aerosolised CeO₂ NPs when deposited directly onto a PBS subphase. It is also possible that the use of a spreading solvent, such as chloroform, when depositing CeO₂ NPs onto the air/liquid interface would have induced the agglomeration of the particles to a greater extent compared to the aerosolised CeO₂ NPs as there is evidence that the evaporation of the spreading solvent leads to the formation of particle agglomerates prior to the compression of the monolayer (Huang et al., 2001a, Huang et al., 2001b). Furthermore, the deposition of aerosolised CeO₂ NPs was probably more spatially uniform across the surface compared to the liquid deposition methods which could also have resulted in a reduction in the agglomeration of the aerosolised CeO₂ NPs with compression. This is representative of what happens *in vivo* as deposition of inhaled airborne NPs onto the alveolar surface is spatially uniform (Bahk and Isawa, 1994). It is also expected that NPs will not be able to interact with each other because of the large inter-particle distances. In fact, particles

tend to interact with the fluids, cells and tissues while being retained in the alveolar region (Sturm, 2010).

Regarding the Π - M_{ma} isotherms, CeO₂ NPs were deposited onto a DPPC monolayer at different NP/DPPC mass ratios ranging from 0.15/1 to 13.48/1 for those experiments performed at 37°C and at 0.10/1 and 2.31/1 for those experiments performed at 21°C. It is difficult to interpret the impact of deposited aerosolised CeO₂ NPs on the DPPC monolayer behaviour because of the significant effect of the CA flow on the monolayer. However, taking this into account there was a clear effect on the last region of the isotherm starting at a $\Pi \sim 30$ mN/m by decreasing the C_m and increasing the collapse Π with CeO₂ NP mass deposited. It is hypothesised that a loss of surfactant occurred at a $\Pi \sim 30$ mN/m as the monolayer was in a LE state at Π below this value and that the presence of agglomerates of a similar size homogeneously spread across the surface improved the film containment causing a decrease in the C_m and an increase in the collapse Π . Finally, effects at 37°C were similar but more pronounced than those at 21°C.

Comparison of the three deposition methods

Figure 119 shows a comparison of the effects of the three different CeO₂ NP deposition methods used in the present work on the DPPC isotherm, using the most similar NP/DPPC mass ratios. The subphase was PBS at 37°C. As a summary, the deposition of CeO₂ NPs suspended in chloroform onto a preformed DPPC monolayer (deposition method 1) did not have an effect on the DPPC isotherm for any NP mass deposited. The deposition of mixtures of CeO₂ NPs and DPPC in the same chloroform suspension onto a clean PBS subphase (deposition method 2) shifted the isotherm to higher M_{ma} values and affected the LE-LC transition plateau, which became shorter and less horizontal with CeO₂ NP mass deposited. The deposition of aerosolised CeO₂ NPs onto a preformed DPPC monolayer (deposition method 3) affected the isotherm at Π values above ~ 30 mN/m by decreasing the C_m and increasing the collapse Π . This effect was mass-dependant. An associated table with a summary of the experimental conditions for each deposition method and their effects on the DPPC isotherm is shown in Table 58.

The above results suggest that the manner of deposition of CeO₂ NPs on a monolayer had a clear influence on the monolayer behaviour. Aerosol deposition is the most physiologically realistic approach; delivering NPs onto the air/liquid interface using liquid suspensions is not

representative of *in vivo* deposition of NPs as in the alveoli NPs are primarily deposited from the air onto the surfactant layer by diffusion and it is expected that aerosol NP deposition will be spatially uniform. However, there were issues with the aerosol deposition method, in particular the influence of the carrier gas on the monolayer in the absence of NPs, that needs to be further investigated before such conclusions can be confirmed. Moreover, depositing NPs onto an uncompressed monolayer, as was done in the present work for both the liquid deposition and aerosol deposition, means that the surfactant molecules were not in the same physical state as would be found *in vivo*, which could lead to different NP-surfactant interactions. NPs were deposited onto the air/liquid interface when the DPPC monolayer was in the G phase as opposed to the more ordered phases at the physiologically relevant Π range (i.e., from ~ 45 to ~ 70 mN/m), which would have potential effects on the isotherm. Unfortunately, depositing NPs within the physiologically relevant Π range would have been very challenging when using a conventional LWB system because of leakage artifacts and also in order to be able to operate the LWB within this Π range. However, depositing NPs or investigating NP-lung surfactant interactions at very low Π values is typically done when using a LWB (Ku et al., 2008, Al-Hallak et al., 2010, Harishchandra et al., 2010, Fan et al., 2011, Guzmán et al., 2011) and depositing aerosolised NPs in the same way allowed direct comparison of the results of the present work with those in the literature. Moreover, it is expected that as the aerosol NP projected surface area was much larger than the area per DPPC molecule at the start of an experiment (i.e., when barriers were fully open and Π value was 0 mN/m), aerosol NPs most likely deposited on a surface that was covered with DPPC molecules. For example, the diameter of aerosolised CeO₂ NPs upon deposition was 220 nm (see section 3.5.3.1.2). Thus, the projected surface area was 38,013 nm² whereas the area per DPPC molecule at the start of an experiment performed at 37°C was 1.60 nm² (160 Å²/DPPC molecule, see Figure 112 and Figure 113) or 1.20 nm² when performed at 21°C (120 Å²/DPPC molecule, see Figure 133, Figure 134 and Figure 135). Thus, aerosol NPs probably deposited on top of the DPPC monolayer despite the fact that surfactant molecules were in the G phase.

It is also important to note that although the same CeO₂ primary particle size was used in each case, the size of the agglomerates introduced to the system differed significantly, typically 158 nm for deposition method 1, 40 nm for deposition method 2 and 115 to 173 nm for deposition method 3. It is therefore difficult to establish whether the differences in the effects on the isotherm during an initial compression were due to the deposition method alone or the NP

agglomerate size or a combination of the two factors. Future research directed towards examining this in more detail is needed and could perhaps be explored using different agglomerate sizes as well as different primary particle sizes. In all cases the results indicate that the degree of NP agglomeration is probably one of the most important determining factors of the NP effects on the DPPC isotherm with larger and denser agglomerates having a greater effect on the isotherm compared to smaller homogeneously spread NP clusters. Even if aerosol NPs were not deposited onto a more closely packed lung surfactant layer as occurs *in vivo*, the present work shows that depositing NPs onto the air/liquid interface using liquid suspensions clearly increased the agglomeration of NPs at the interface which is unlikely to occur *in vivo*. Moreover, it is important to use LWBs configured to reflect the alveolar system, e.g. reduce leakage problems and use appropriate environmental factors such as a physiologically relevant temperature and subphase liquids.

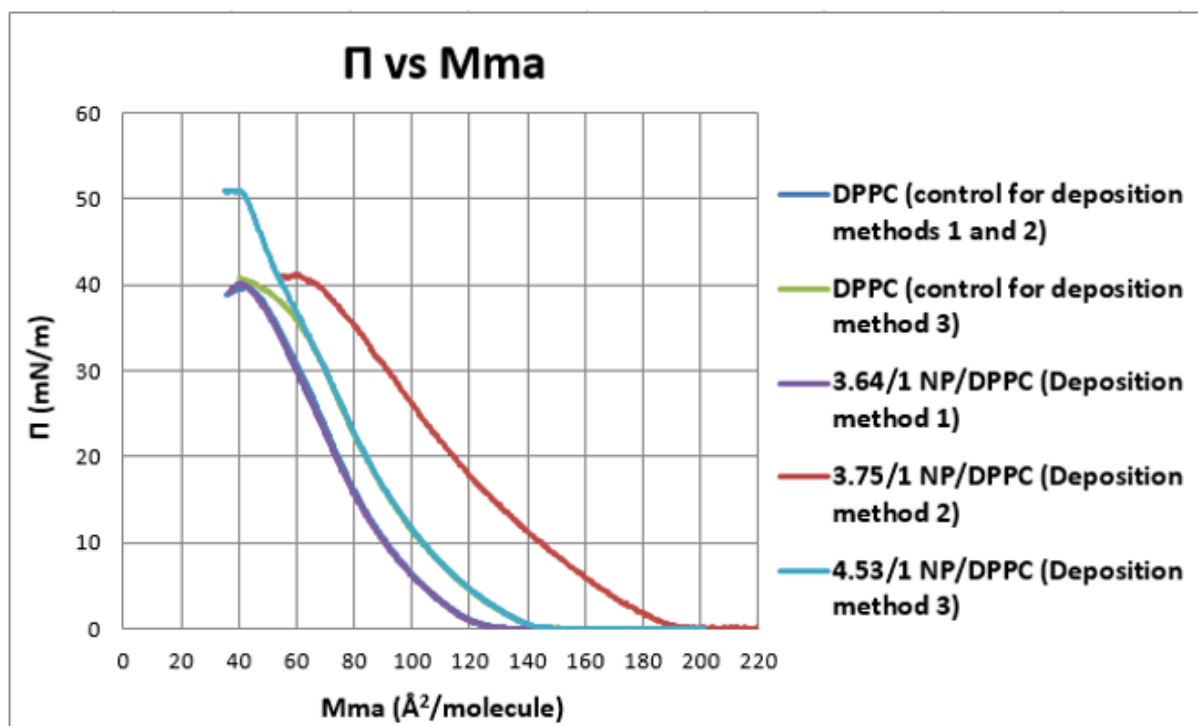


Figure 119. Comparison of the effects of the three different CeO₂ nanoparticle deposition methods used in the present work on the DPPC Π -Mma isotherm, using the most similar NP/DPPC mass ratios. Deposition method 1 refers to the deposition of CeO₂ nanoparticles suspended in chloroform onto a preformed DPPC monolayer. Deposition method 2 refers to the deposition of CeO₂ nanoparticles and DPPC mixtures in the same chloroform suspension onto a clean subphase. Deposition method 3 refers to the deposition of aerosolised CeO₂ nanoparticles onto a preformed DPPC monolayer. The CeO₂ NP/DPPC mass ratios were 3.64/1 for deposition method 1, 3.75/1 for deposition method 2 and 4.53/1 for deposition method 3. For deposition methods 1 and 2, the control isotherm was measured after leaving a DPPC monolayer undisturbed for 15 minutes. For deposition method 3, the control isotherm was measured after exposing a DPPC monolayer to compressed air flow for the same exposure duration as the aerosol CeO₂ nanoparticle experiment. The subphase used was PBS at 37°C.

Table 58. Summary of the experimental conditions for the three different CeO₂ nanoparticle deposition methods used in the present work and their effects on the DPPC isotherm.

Deposition method	CeO₂ NP agglomerate size before deposition*	Deposited CeO₂ NP masses (CeO₂/DPPC mass ratios) for isotherm measurement	Effect on DPPC <i>II</i>-Mma isotherm	Deposited CeO₂ NP masses (CeO₂/DPPC mass ratios) and characteristics and behaviour of CeO₂ NPs at the interface
Liquid 1	TEM (agglomerate projected area) 158 nm DLS (hydrodynamic diameter in chloroform) 222 nm	PBS 37°C 0.35 µg (0.06/1), 7.00 µg (1.21/1), 21.00 µg (3.64/1) PBS 21°C 0.4 µg (0.06/1), 8.0 µg (1.16/1), 24.0 µg (3.49/1)	PBS 37°C: Minimal (Figure 71 and Table 23) PBS 21°C: Minimal (Figure 72 and Table 25)	60 µg (3.20/1) No clear indication of the presence of CeO ₂ NPs during first compression (Figure 73), large NP agglomerates seen on cycling (Figure 74 and Figure 75) It is hypothesised that rapid agglomeration took place and large and dense agglomerates left the monolayer and sedimented out into the subphase leaving small agglomerates remaining at the interface whose size was below the detectable limit
Liquid 2	TEM (agglomerate projected area) ~ 40 nm DLS (hydrodynamic diameter in chloroform) 119-154 nm	PBS 37°C 0.33 µg (0.06/1), 7.00 µg (1.25/1), 13.13 µg (3.75/1) PBS 21°C 0.36 µg (0.05/1), 7.00 µg (1.00/1), 18.75 µg (3.00/1)	PBS 37°C: Lift-off Mma increased with increasing CeO ₂ NP mass. Differences in <i>C_m</i> and collapse <i>II</i> for the two higher ratios only (Figure 87 and Table 31) PBS 21°C: Lift-off Mma, some <i>C_m</i> and collapse <i>II</i> parameters affected at the two higher ratios but no effect for the lowest ratio (Figure 88 and Table 33) Effects at 37°C > 21°C	(3.00/1) Large NP agglomerates clear in SEM and ToF-SIMS images during first compression and after cycling (Figure 82, Figure 83 and Figure 84) SEM and semi-quantitative ToF-SIMS analysis indicated a loss of CeO ₂ NPs from the monolayer during first compression (Table 29 and Figure 85)
Aerosol	SMPS (aerosol mobility size) 107-182 nm	PBS 37°C 1 µg (0.15/1), 5 µg (0.93/1), 13 µg (2.98/1), 14 µg (3.09/1), 25 µg (4.53/1), 59 µg (13.48/1) PBS 21°C 1 µg (0.10/1), 21 µg (2.31/1)	PBS 37°C and 21°C: Clear effect on the last region of the isotherm starting at a <i>II</i> ~ 30 mN/m by decreasing the <i>C_m</i> and increasing the collapse <i>II</i> with CeO ₂ NP mass** (Figure 112 and Table 50; Figure 113 and Table S2; Figure 115 and Table 53; Figure 118 and Table 56 and Table 57) Effects at 37°C > 21°C	36 µg (1.12/1) and 35 µg (2.42/1) Agglomerates of a similar size clear in SEM and ToF-SIMS images during first compression, homogeneously spread across the surface for the 1.12/1 mass ratio. Compression-expansion cycles promoted the agglomeration of the NP clusters (Figure 101, Figure 102, Figure 103, Figure 104) SEM and semi-quantitative ToF-SIMS analysis indicated no or minimal loss of CeO ₂ NPs from the monolayer during first compression (Table 46 and Figure 105)

Notes:

* CeO₂ primary particle size – 19 nm

**Effect of compressed air flow on isotherms made interpretation difficult below a *II* value of ~ 30 mN/m

3.6.2 Comparison of the results with those from other studies

This section includes a comparison of the results reported in the present work and those in the literature that used DPPC as a lung surfactant model, shown previously in chapter 3 (see section 3.2.1.1, studies 1- 6).

As shown previously in section 3.2.1.1, most of the studies in the literature used a water subphase to investigate NP-DPPC interactions. The present work suggests that the effects of NPs on a DPPC isotherm would likely be different when using a more physiologically relevant subphase medium as a greater amount of NPs remained at the interface when using a water subphase compared to PBS. Furthermore, these literature studies were undertaken at subphase temperatures between 20-22°C, again the results from the present study suggest that their findings would have been different if they had used a more physiologically relevant temperature. Even though the DPPC transition from gel phase to liquid crystal phase occurs above body temperature at 41°C, the present work has shown that the isotherm measured at 37°C was different to that at 21°C and that the effects of CeO₂ NPs on the isotherm were more pronounced at 37°C compared to 21°C. This implies that NP doses that do not have an effect when working at 21°C may have significant effects at 37°C.

In the present work, cycling experiments showed that with and without DPPC, compression-expansion cycles promoted the agglomeration of CeO₂ NPs at the interface. These experiments are therefore key to understanding how the system would evolve after several simulated inhalation-exhalation breathing cycles. In the literature, cycling is not usually performed in studies that investigate NP-lung surfactant interactions.

Literature studies on the effect of NPs on the DPPC isotherm have not often measured the Π - A isotherm using a leak-proof system. If this was the case, one would expect the collapse in the pure DPPC isotherm to occur as a horizontal plateau at a Π value \sim 73 mN/m. This is only seen in study 4. In study 6 the DPPC isotherm reached a Π value of \sim 71 mN/m and presumably there was little or no leakage in this system. However, in this study the barrier speed used to compress DPPC alone was higher than that used when DPPC and NPs together were deposited onto the interface as illustrated by the lower number of data points generated to construct the isotherm. The present work shows that a higher barrier speed and a higher compression rate per DPPC molecule led to a higher collapse Π value and vice versa (see sections 2.4.1.6 and

2.4.2.1). In the remaining studies, a kink was recorded for the DPPC isotherm at Π values ~ 50 mN/m followed by an increase in the C_m of the isotherm and a lower collapse Π most likely due to surfactant leakage problems which destabilised the monolayer. It is believed that the presence of NPs at the interface enhanced this destabilisation of the DPPC monolayer by impeding its compression which would generally lead to lower collapse Π values as seen in studies 1, 2, 3, 5 and 6. Study 1 showed that the lower collapse Π might have been caused by the presence of NPs at the interface and the increase in the adhesive forces between NPs and DPPC which would subsequently weaken the cohesive forces between DPPC molecules, reducing the relative packing density of DPPC and thus the collapse Π . Study 2 showed that the NPs accumulated at the interface with no significant squeeze-out; the collapse Π was slightly lower than that of pure DPPC. Study 6 showed that SMWCNTs incorporated into the film reducing the relative packing density of DPPC and increasing the compression resistance which subsequently reduced the collapse Π .

When using a leak-proof system however, collapse Π values of ~ 73 mN/m could be reached at later stages of compression as shown in study 4, and also in the present work when using low subphase volumes (see Figure 92) and in other studies that investigated the effects of NPs on cell membranes using DPPC as a model (Wang et al., 2009). Using leak-proof systems and therefore the possibility of reaching higher Π values could lead to a greater amount of NPs being squeezed-out from the interface and therefore inducing a completely different effect on the last region of the isotherm and the collapse of the monolayer compared to results obtained when using conventional systems as shown in the present work.

One of the biophysical properties that a functional lung surfactant should have for normal respiratory physiology is the ability to reduce surface tension to near zero values upon surfactant film compression during exhalation. Due to the importance of this lung surfactant property, investigators should not ignore surfactant leakage problems when studying effects of NPs on the collapse Π as this could lead to erroneous conclusions on one of the most relevant lung surfactant properties. Moreover, and knowing that the physiologically relevant Π range is confined to between ~ 45 and ~ 70 mN/m, leak-proof systems should be used when investigating NP-lung surfactant interactions.

The present work has clearly indicated the importance of agglomerate size and yet many of the studies provided no information on the size of the agglomerates introduced to the system,

making interpretation of their results and comparison with those from the current study difficult. Some discussion of this in relation to those studies using deposition method 1 and 2 is provided below. Moreover, in the present work, wettability was determined qualitatively by the ability of the CeO₂ NPs to remain at the air/liquid interface and their effect on the surface tension was studied in depth. The study of the wettability of the NPs at the air/liquid interface is a relevant topic to be investigated as, for example, the amount of particles attached to a fluid/fluid interface during the spreading process strongly depends on particle wettability (Horozov et al., 2006, Maestro et al., 2014, Maestro et al., 2015). The most hydrophilic particles will be pushed irreversibly into the liquid phase and the most hydrophobic particles will collapse and form a multilayer, with the particles with intermediate hydrophobicity being the most stable in the system (Binks, 2002). Studies in the literature usually link dose with effects assuming that all the NPs remained at the interface after deposition. In contrast, in the present work, attempts were made to identify loss of CeO₂ NPs into the subphase during the compression, by studying the particles at the interface during the cycle, and determination of particles present in the subphase. This type of analysis is not usually undertaken in studies that investigate NP-lung surfactant interactions.

Only study 1 (Guzmán et al., 2011) deposited the NPs using method 1. Unlike the results of the present work using this method to study CeO₂, which indicated no effect on the isotherm at any deposited mass, Guzmán et al., 2011 found that CB NPs shifted the isotherm to higher areas per molecule of DPPC with increasing deposited mass, interpreting this reasonably as indicating the penetration of the CB NPs into the monolayer. BAM images showed that NPs did not affect the nucleation of the LC domains. CB NPs however increased the C_m of the monolayer at Π values above ~ 10 mN/m and decreased the collapse Π . The deposited masses were similar to those used in the present work and the primary particle sizes were also very similar, although crucially there is no information on subsequent agglomeration or changes in the size of CB particles. There could be a number of reasons why the results differ. One possible explanation is that in the present work, CeO₂ NPs rapidly agglomerated to form large, dense clusters that eventually sedimented into the subphase hence, mainly small agglomerates remained at the interface during one compression that were probably insufficient to affect the DPPC isotherm, due to both their small mass and size. Whereas, in the study by Guzmán et al., 2011 a greater amount of CB NPs might have remained at the air/liquid interface and as such agglomerated with compression and the agglomerates affected the DPPC isotherm. In fact, previous studies suggest that CB NPs do not readily agglomerate in water, whereas they quickly agglomerate

when suspended in PBS, i.e. CB NPs are more stable in water than in PBS. The same group suggests that PBS is not a satisfactory medium to prepare NP suspensions (Sager et al., 2007, Sager, 2008), although as discussed earlier, PBS is more physiologically relevant. It is also possible that CB NPs may have intrinsic properties which make it behave differently from the CeO₂ NPs used in the present work, for example, different surface charge. Finally, and as mentioned above, a difference in agglomerate size might have differentially influenced their effect on the DPPC isotherm. As already mentioned, the θ of particles at the air-liquid-solid interface, and with it the dynamic particle behaviour depends on a number of factors including the chemical nature of both the particles and the fluid phases and the particle size (Maestro et al., 2014).

All of the other studies listed in section 3.2.1.1 used deposition method 2, i.e. the NPs were mixed with DPPC in the same volatile solvent prior to being deposited onto a clean liquid subphase. This implies that interactions between surfactant and NPs probably occurred in the suspending medium by DPPC coating the NPs which might have modified the wettability of the NPs (Maestro et al., 2012, Maestro et al., 2015) as in the present work using this method. The results from these studies were in general somewhat similar to those in the present work for the same deposition method, i.e. increasing NP mass shifted the isotherm to higher M_{ma} values and affected the LE-LC transition plateau which became shorter and less horizontal. The only exceptions were the 12 nm polyorganosiloxane NPs from study 5, which had no effect at any of the concentrations used (although the larger polyorganosiloxane NPs did), as well as the SMWCNTs used in study 6, which did not affect the LE-LC transition plateau. Moreover, some NPs had a large effect at early stages of compression, which suggests the presence of large, denser agglomerates at the interface at the beginning of the experiment (studies 1, 2, 3 and the present work) whereas other NPs had an effect on the isotherm at later stages of compression, which suggests that NPs agglomerated during the compression of the interface to form larger agglomerates (studies 4, 5, 6). At a Π value of ~ 30 mN/m, two different scenarios can be seen. When NPs markedly hindered the nucleation of the LC phase and therefore favoured the expanded phases for example by decreasing the C_m in the LE-LC transition plateau region starting at the onset of the plateau, isotherms shifted to lower areas per molecule at a Π value of ~ 27 mN/m crossing in some cases the control isotherm. This is shown in studies 2, 3, 5 and other studies that investigated the effects of NPs on cell membranes using DPPC as a model (Wang et al., 2009, Stefaniu et al., 2012). This suggests that at least some NPs were squeezed out into the subphase. This process could have been favoured by the higher instability of

monolayers in the LE phase at Π values close to the Π_e (Baoukina et al., 2014). Alternatively, studies 1, 4 and 6 show that NPs did not dramatically hinder the nucleation of the LC phase and accumulated at the interface shifting the isotherm to higher areas per molecule of DPPC with compression. At a Π value of ~ 50 mN/m, and as previously mentioned, the presence of NPs generally destabilised the monolayer which increased the C_m of the isotherm and usually decreased the collapse Π compared to the control. These results contrast with those shown in the present work when CeO₂ NPs were deposited in aerosol form onto a preformed DPPC monolayer as it is believed that the presence of agglomerates of a similar size homogeneously spread across the surface improved the film containment causing a decrease in the C_m starting at a $\Pi \sim 30$ mN/m and an increase in the collapse Π . An improvement in the film containment and reduction of the loss of surfactant should lead to a higher collapse Π as discussed previously in sections 2.4.2.3 and 2.4.2.5.

Finally, the NP doses used in the present work and in most of the studies in the literature are significantly higher than those that would result from inhalation exposure with safe working practices; large NP concentrations are usually needed to induce *in vitro* surfactant inhibition when depositing them as liquid suspensions (Valle et al., 2015). Therefore, drawing conclusions on the impact of CeO₂ NPs on respiratory health based on these studies should be interpreted with caution, addressed later in chapter 5.

CHAPTER 4 – EFFECTS OF THE EXPOSURE OF A DPPC MONOLAYER TO AEROSOLISED CARBON BLACK (CB) NANOPARTICLES

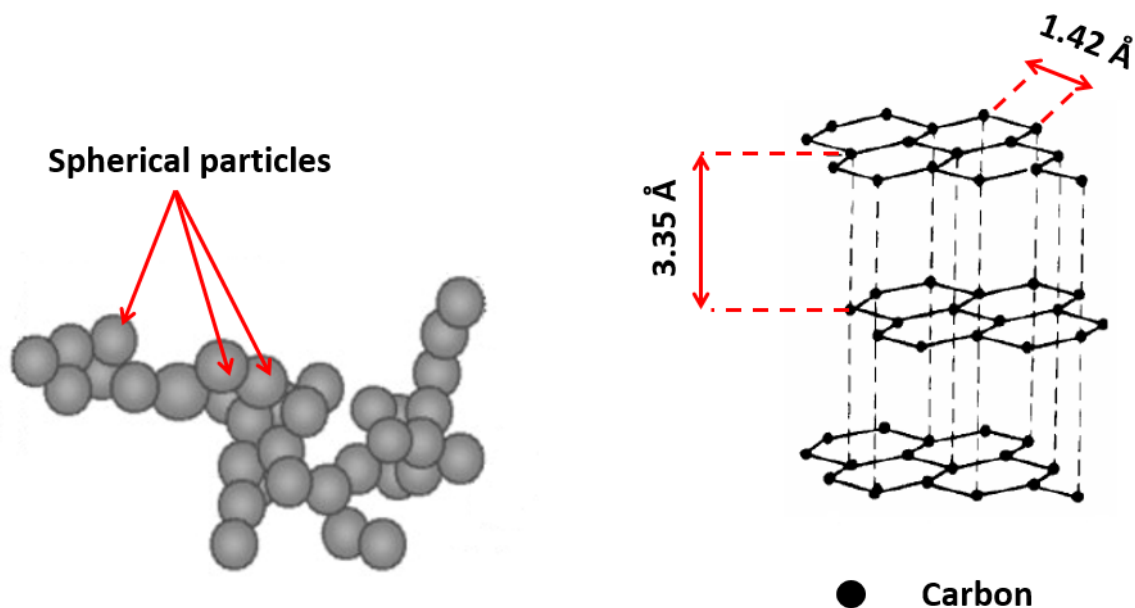
4.1 Rationale

The earlier work supported the hypothesis that an aerosol exposure system is the most appropriate model to investigate inhaled NP interactions with lung surfactant. Thus, this system was used to compare the effects of another common ENP, CB NPs, on the DPPC isotherm with those of aerosolised CeO₂ NPs.

4.2 CB nanoparticles

4.2.1 Properties, structure and uses of CB nanoparticles

Carbon (C) is a non-metallic element. The level of carbon in the crust of the earth is estimated to be ~ 200 ppm being the 15th most abundant element. Carbon black (CB) is a very pure form of carbon that contains more than 97% of elemental carbon. It is produced by incomplete combustion or thermal decomposition of gaseous or liquid hydrocarbons under controlled conditions. In its pure form, it is a black, finely divided pellet or powder (International-Carbon-Black-Association, 2014) with a molar mass of 12.01 g/mol and density of 1.8-2.1 g/cm³. CB occurs in the form of spherical particles with an average size ranging from 15 to 280 nm that fuse together, building agglomerates arranged as a grape-like cluster (aciniform particulate). The particles are made up of layers of carbon atoms similar to the layers in graphite, with atoms situated at the vertices (Figure 120). In each layer, a carbon atom is bonded to three adjacent atoms at 1.42 Å forming a two dimensional hexagonal net. Unlike graphite, however, the layers in CB are curved rather than flat, which accounts for the spherical surfaces of the particles. The space between each layer is 3.35 Å (Houska and Warren, 1954).



Structure of a carbon black agglomerate

Structure of spherical particles

Figure 120. Illustration of the structure of a carbon black agglomerate (left) and spherical carbon black particle (right). Adapted from Deshmukh et al., 2010 and Liu, 2013.

CB is a commonly manufactured ENP, being one of the 14 reference ENMs on the OECD list (Bouwmeester et al., 2011). CB has a wide range of applications including high performance coatings, reinforcement and filling agent in industrial rubber products (especially automotive tyres, which is the largest use of CB), as a black pigment in toners and printing inks and as an electric conductive agent in plastic products due to its specific surface area, particle size and structure, conductivity and colour. It is also a hydrophobic material. CB worldwide production is about £18 billion per year, and hence it is one of the top 50 industrial chemicals manufactured worldwide. CB is different from soot or black carbon which are carbonaceous by-products resulting from the incomplete combustion of carbon-containing materials, such as “oil, fuel oils or gasoline, coal, paper, rubber, plastics and waste material” (Hussain et al., 2009, International-Carbon-Black-Association, 2014).

4.2.2 CB nanoparticle exposure data

The high production volumes of CB have led to its emission into the atmosphere, as well as the workplace during its manufacture. The route of exposure is mostly via inhalation, ingestion or dermal contact (HSS, 1988), inhalation being the most important route in terms of possible health effects (Kim et al., 2011). CB is both an environmental and occupational hazard

(Donaldson et al., 2005). The current US Occupational Safety and Health Administration threshold limit value for CB dust is 3.5 mg/m^3 as a time-weighted average concentration. Nano-sized CB has however higher toxicity compared to its non nano-sized form (IARC, 1996, Lim et al., 2013). Emissions into the atmosphere during its manufacture and due to the wear of automobile tyres also occur (IARC, 1996, Yamashita and Yamanaka, 2013).

A previous study carried out an assessment of the occupational exposure to nano-sized CB during the packaging of CB for shipping in three different industrial plants. Ambient mass concentrations were also measured for comparative purposes. The concentration levels in the work area ranged from $24\text{-}49 \text{ }\mu\text{g/m}^3$. The ambient concentration levels ranged from $12\text{-}14 \text{ }\mu\text{g/m}^3$ (Kuhlbusch et al., 2004). To date, no other studies have been conducted to assess nano-sized CB exposure in the CB industry.

4.2.3 Health effects of CB nanoparticles

CB has been studied extensively regarding its toxicology and so there is a considerable existing database on its toxicity *in vitro* and *in vivo* (Donaldson et al., 2005). In studies performed with lung surfactant, CB NPs in suspension incorporated into DPPC monolayers and affected the phase behaviour and the dynamic response of the monolayer including the collapse conditions (Guzmán et al., 2011). In studies of human umbilical vein endothelial cells (HUVEC) *in vitro*, CB has been shown to cause cytotoxic injury, increase levels of proinflammatory chemokines, inhibit cell growth (Yamawaki and Iwai, 2006), cause oxidative stress, pro-inflammatory gene transcription (Shukla et al., 2000) and stimulation of macrophage phagocytosis at low doses, and inhibition at higher doses (Renwick et al., 2001). In epidemiological as well as experimental studies *in vivo* there is evidence for a role of CB NPs in aggravating pulmonary disorders such as asthma, lung cancer and pulmonary fibrosis as well as systemic cardiovascular disorders (Donaldson et al., 2005). These studies indicate the possible adverse effects that atmospheric CB NPs might have on the respiratory system, which might be particularly important in those with existing respiratory health problems.

4.3 Hypothesis

We hypothesised that the effects of aerosolised CB NPs on the functional activity of DPPC would be similar to those seen for aerosolised CeO_2 NPs.

4.4 Methodology

4.4.1 Reagents and materials

For reagent and materials, see section 2.3.1.

Additional information for this chapter: CB NPs (nominal size < 100 nm) were purchased from Sigma-Aldrich. CB was weighed using a Sartorius M-power balance with a resolution of 0.1 mg. Suspensions of CB NPs were sonicated in an ultrasonic water bath (Ultrawave Ltd, model number F0001602). CB NP samples were collected onto TEM grids (300-mesh copper with carbon support film, purchased from Agar Scientific) and square mica sheets (11 mm x 11 mm, 0.15 mm thick, purchased from Agar Scientific) for imaging using TEM and SEM respectively.

4.4.2 Cleaning of glassware

Glassware was cleaned as described previously (see section 2.3.2).

4.4.3 CB nanoparticles in aerosol form

4.4.3.1 Aerosol exposure system

Aerosolised CB NPs were generated using the aerosol exposure system as described previously (see section 3.4.5.1).

4.4.3.2 Preparation of CB nanoparticle suspensions for the constant output atomiser and samples

CB NPs were suspended in ultrapure water to form stock suspensions with a concentration of 5 mg/mL and stored in the fridge in glass bottles with PP screw caps until use. The suspensions were sonicated for ~ 15 minutes in an ultrasonic water bath before use in the TSI COA. Samples of aerosolised CB NPs were collected onto TEM grids and mica sheets placed on a horizontal surface while performing an experiment, for later characterisation by TEM and SEM imaging respectively.

4.4.3.3 Nanoparticle characterisation pre-CB nanoparticle administration

4.4.3.3.1 Primary particle size, size distribution, number concentration, mass concentration, wettability and surface tension activity of aerosolised CB nanoparticles

CB primary particle size was determined by TEM using a JEM – 2000FX II microscope. Images were taken by Mrs Ecaterina Ware from the Department of Materials, Faculty of Engineering, Imperial College London. TEM images were analysed using the software Image J. The CB primary particle size distribution was described using the CMD of the particle projected area and the GSD. The size distribution, number concentration, mass concentration, wettability and surface tension activity of the aerosolised CB NP agglomerates were determined as described previously (see sections 3.4.3.2.2, 3.4.5.3.1 and 3.4.5.3.2).

4.4.3.3.2 Determination of the mass of aerosolised CB nanoparticles deposited onto a Langmuir trough

An average deposition velocity (dv) for aerosolised CB NPs was calculated by performing 5 and 6 hour experiments in the exposure chamber using four EMFAB[®] filters placed onto the Langmuir trough. This average dv value was used to calculate the aerosol mass deposited onto the Langmuir trough (mdt) in each of the experiments performed in the presence of a DPPC monolayer as described previously (see section 3.4.5.3.3). Two mica sheets and four TEM grids were also placed onto the Langmuir trough for CB NP imaging purposes.

4.4.3.3.3 Measurement of the spatial distribution and size of aerosolised CB nanoparticles upon deposition

The samples collected onto the mica sheets and TEM grids during the 5 and 6 hour experiments were used to determine the spatial distribution and size of aerosol CB NP agglomerates upon deposition. The spatial distribution was determined using SEM and the size was determined using TEM as described previously (see section 3.4.5.3.4).

4.4.3.4 CB nanoparticle deposition

Aerosolised CB NPs were deposited onto a preformed DPPC monolayer over different exposure times. Experiments were performed in PBS at 21°C. Due to time limitations, the experiments were not performed at 37°C.

4.4.4 Measurement of the surface pressure–Mma isotherm

Measurement of Π –Mma isotherms was performed using a LWB system as described previously (see section 2.3.4).

4.4.4.1 Relevant parameters used to describe a surface pressure–Mma isotherm

Due to the significant effect of the CA flow on the DPPC monolayer behaviour, it was decided to focus on two parameters of the isotherm, the C_m for the region 30–45 mN/m and the collapse Π , as it was done for the aerosolised CeO₂ NP experiments (see sections 2.4.1.1 and 3.5.3.2.3).

4.4.4.2 Criteria to compare surface pressure–Mma isotherms measured under different experimental conditions

An experimental isotherm was compared with its associated control isotherm using reference % change from midpoint values as described previously (see section 2.4.1.5).

4.4.5 Interfacial layer characteristics post-CB nanoparticle administration - Langmuir-Blodgett films

LB deposition was performed using a LWB system as described previously (see section 2.3.4). The solid substrate used to produce the LB film was mica (11 mm x 11 mm, 0.15 mm thick, purchased from Agar Scientific). LB films composed of both DPPC and CB NPs could not be analysed using ToF-SIMS as DPPC and CB produced the same carbon signal, and hence the LB film was imaged using SEM only. SEM images were analysed using the software image J.

4.5 Results and discussion

4.5.1 Nanoparticle characterisation pre-CB nanoparticle administration

In this study, a method to calculate the aerosol mass deposited onto the Langmuir trough was developed based on deriving the deposition velocity of the aerosolised CB NPs within the exposure chamber (Equation 19). The size, spatial distribution, wettability and surface tension activity of the aerosolised CB NP agglomerates upon deposition were also determined as well as the size of the CB primary particles.

4.5.1.1 Size of CB primary particles

Figure 121 shows several TEM images of CB primary particles. As can be seen in these images, the shape of these particles was very irregular and different to that of the CeO₂ NPs. The CMD was 65 nm and the GSD was 2.0. The size determined was within the particle size range stated by the manufacturer, i.e., nominal size < 100 nm. This primary particle size was higher than the primary particle size of CeO₂ NPs (CMD was 19 nm and GSD was 1.8).

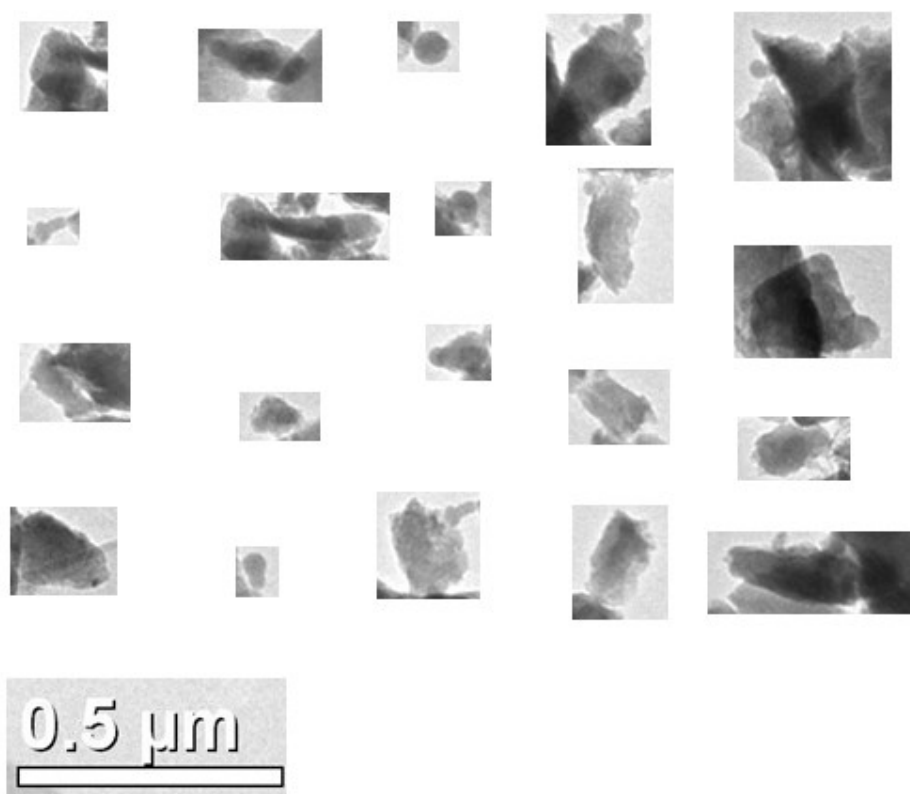


Figure 121. TEM images of CB primary particles.

4.5.1.2 Determination of the mass of aerosolised CB nanoparticles deposited onto a Langmuir trough

Five and six hour experiments were performed in the exposure chamber in the presence of four EMFAB filter membranes. The aerosol mobility size distribution and number concentration were determined using an SMPS Spectrometer which was configured to measure multiple scans each of 3 minutes in length. The average aerosol CMD, GSD and number concentration of all the scans run for each of the experiments are shown in Table 59. Figure 122 shows a graphical representation of the aerosol size distribution for each experiment. Table 60 shows the average

mda value for each experiment. The weight of filter 2 for the six hour experiment was erroneous and *mda* was calculated by averaging the mass of filters 1, 3 and 4.

Table 59. Average aerosol CMD, GSD and number concentration of all the scans run for each of the two experiments performed to calculate an average deposition velocity for aerosolised CB nanoparticles using four EMFAB filters.

Experiment	CMD \pm SD (nm)	GSD \pm SD	Number concentration \pm SD (particles/cm ³)
1 (5 hour)	218 \pm 34	2.6 \pm 0.1	7.92E+05 \pm 8.40E+04
2 (6 hour)	202 \pm 43	2.6 \pm 0.2	5.99E+05 \pm 7.69E+04

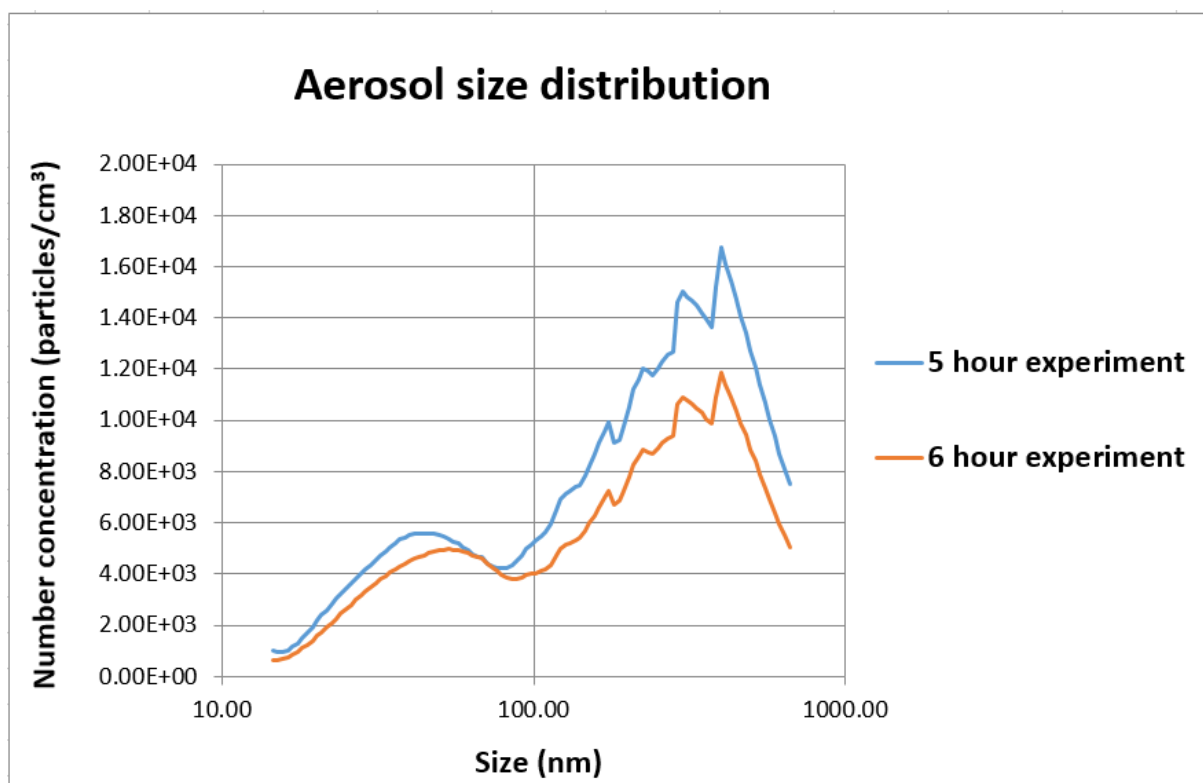


Figure 122. Graphical representation of the CB aerosol size distribution for the 5 and 6 hour experiments performed to calculate an average deposition velocity for aerosolised CB nanoparticles using four EMFAB filters.

Table 60. Calculation of an average *mda* value for each of the two experiments performed to determine an average deposition velocity for aerosolised CB nanoparticles using four EMFAB filters.

Duration (hour)	<i>mda</i> filter 1 (ng/cm²)	<i>mda</i> filter 2 (ng/cm²)	<i>mda</i> filter 3 (ng/cm²)	<i>mda</i> filter 4 (ng/cm²)	Average <i>mda</i> ± SD (RSD, %) (ng/cm²)
5	979.86	1,056.71	1,037.50	730.09	951.04 ± 150.88 (15.86)
6	345.82	-	441.88	1,133.53	640.51 ± 429.74 (67.09)

Figure 122, Table 59 and Table 60 show that the profile of the aerosol size distribution was similar for both experiments, being a bi-modal size distribution including a low peak at ~ 50 nm as opposed to the uni-modal normal size distribution of aerosol CeO₂ NPs (see Figure 111, Figure 114 and Figure 117). The first peak was consistent with the CB primary particle size indicating that probably both aerosol CB primary particles and aerosol CB NP agglomerates were present in the exposure chamber. Using the SMPS data, the CMD for the aerosol was estimated as ~ 210 nm for both experiments, however, it must be recognised that the range of particle sizes present was greater than could be measured using the SMPS, which is significantly less efficient above approximately 400 nm (as is clear from Figure 122). It is likely therefore that the second peak is at a size higher than 400 nm and thus the CMD for the total aerosol may be significantly greater than 200 nm. Because of the bi-modal aerosol size distribution, it was decided to plot the aerosol size distribution in all the remaining experiments. The aerosol number concentration was higher for the 5 hour experiment than the 6 hour experiment.

The variability of the mass deposited per unit area was much greater for the 6 hour experiment, i.e., aerosolised CB NPs did not deposit homogeneously across the trough area in this experiment, possibly due to a less uniform air flow in the system. Results on the spatial distribution of aerosolised CB NP agglomerates upon deposition are shown later in section 4.5.1.4 and indicate that for the 6 hour experiment the number of agglomerates per μm² varied

considerably with the sampling area. Finally, the average aerosol dv was calculated using Equation 20 and is shown in Table 61.

Table 61. Calculation of an average deposition velocity for aerosolised CB nanoparticles by performing two experiments in the exposure chamber using four EMFAB filters.

Experiment	mda (ng/cm ²)	Time (min)	mc (ng/cm ³)	dv (cm/min)
1	951.04 ± 150.88	294	24.26	0.13 ± 0.02
2	640.51 ± 429.74	351	17.22	0.11 ± 0.07
Average dv				0.12
SD				0.06
RSD (%)				46.73

The average dv for aerosolised CB NPs was 0.12 cm/min with a SD of 0.06 cm/min. This value was very similar to the dv value derived for the aerosolised CeO₂ NPs when using EMFAB filter membranes (0.13 ± 0.04 cm/min); this was expected as the experimental set-ups and the aerosol in each case were similar. Having established a value for dv , mdt was estimated in these experiments using the following equation:

$$mdt = 0.12 \pm 0.06 \text{ (cm/min)} \times mc \times t \times \textit{tarea} \quad \text{Equation 23}$$

where mdt is the aerosol mass deposited onto the Langmuir trough (ng); mc is the aerosol mass concentration (ng/cm³); t is the exposure time (min) and \textit{tarea} is the area of the trough (cm²)

4.5.1.3 Size of aerosolised CB nanoparticles upon deposition

In order to determine if aerosolised CB NPs agglomerated while they were settling from the air onto the trough, the average agglomerate size upon deposition was calculated by imaging and analysing two TEM grids used in the 6 hour experiment. Figure 123 shows the aerosol size

distribution for each of the TEM grids and Figure 124 shows several TEM images of the aerosolised CB NP agglomerates upon deposition onto the TEM grid.

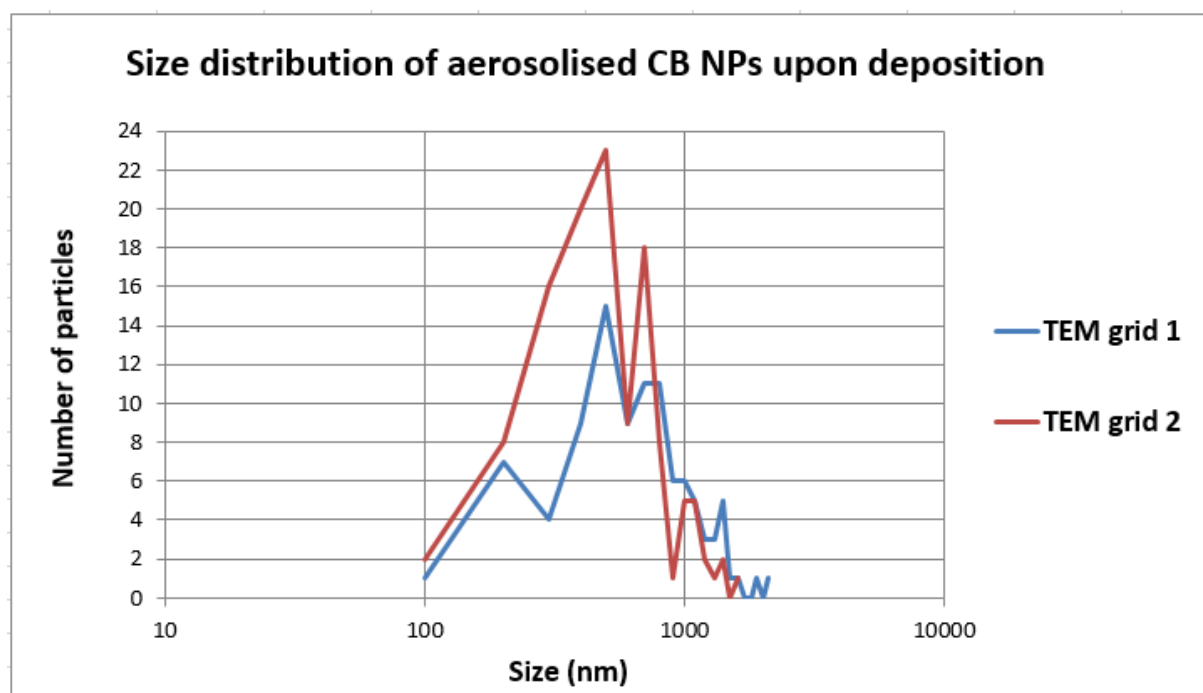


Figure 123. Size distribution of aerosolised CB nanoparticle agglomerates upon deposition onto the Langmuir trough obtained by analysing two TEM grids used in the 6 hour experiment.

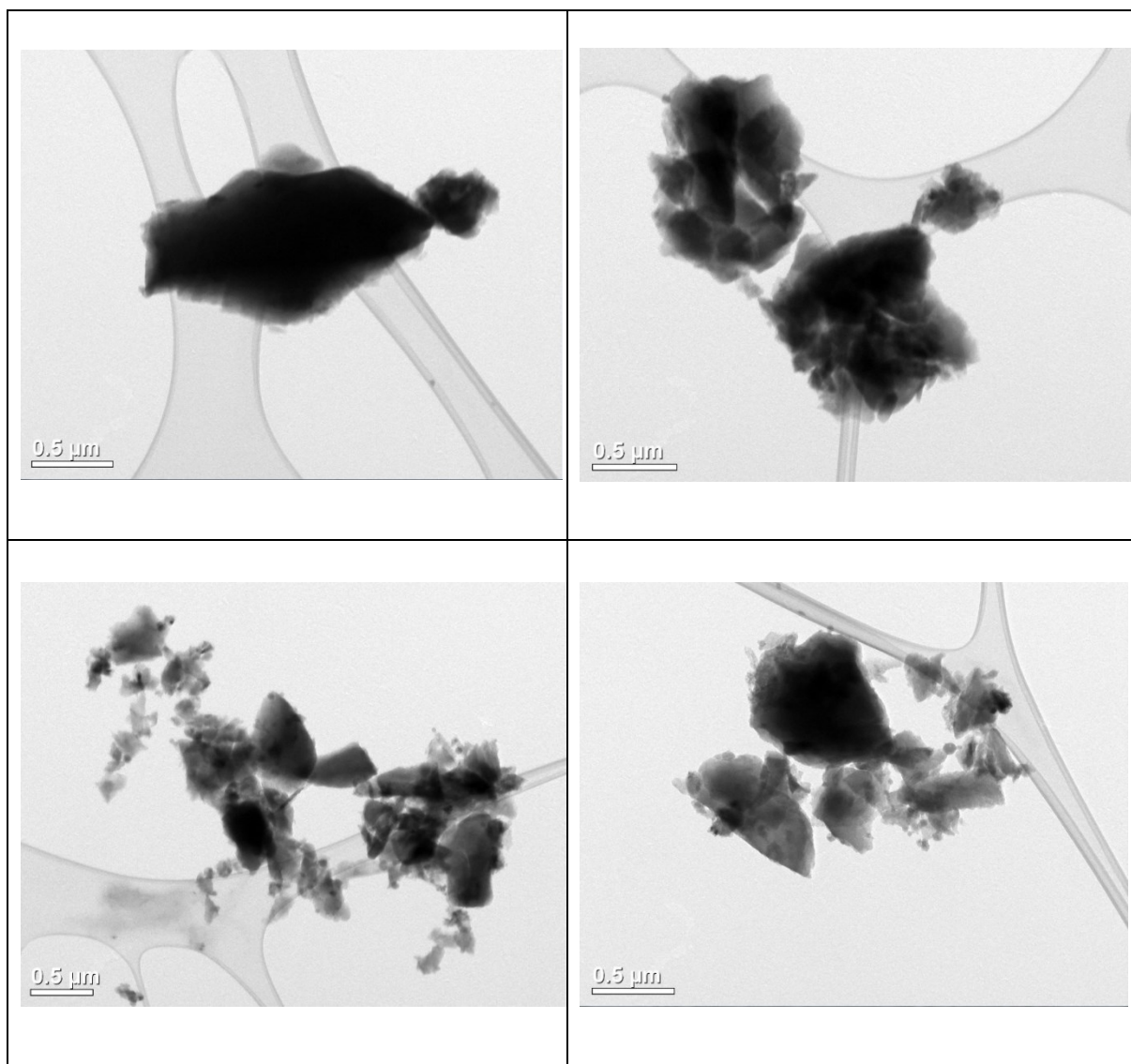


Figure 124. TEM images of aerosolised CB nanoparticle agglomerates upon deposition onto a TEM grid located on the Langmuir trough over 6 hours. The scale bar is 0.5 μm for all the images.

The CMD of these agglomerates upon deposition was 545 nm and the GSD was 1.9. This contrasts with the aerosol size distribution CMD of ca 200 nm, however, as discussed previously, the equipment used to determine this value was not able to measure the full aerosol size range and thus the 200 nm is expected to be a significant underestimate. As the aerosol particle size CMD is not known accurately it was not possible to make a firm judgement as to whether the airborne CB NPs agglomerated during deposition. A CMD of 545 nm is possibly consistent with no or limited agglomeration on deposition, as was seen with the CeO₂ NPs (see section 3.5.3.1.2). Additional experiments using other measurement system would be required to investigate this further.

4.5.1.4 Measurement of the spatial distribution of aerosolised CB nanoparticles upon deposition

The spatial distribution of the aerosol CB NP agglomerates upon deposition, described by the number of agglomerates per μm^2 , was determined for each of the mica sheets placed onto the Langmuir trough during the 5 and 6 hour experiments and is shown in Table 62. Each value was obtained by analysing a minimum of 19 images. The average number of agglomerates per μm^2 as well as the SD and RSD were also calculated.

Table 62. Spatial distribution of the aerosol CB nanoparticle agglomerates upon deposition calculated for each of the mica sheets placed onto the Langmuir trough during the 5 and 6 hour experiments. The average number of agglomerates per μm^2 as well as the SD and RSD are also shown. Number of particles counted per mica sheet: 5 hour experiment mica sheet 1 = 192 particles, 5 hour experiment mica sheet 2 = 127 particles, 6 hour experiment mica sheet 1 = 132 particles, 6 hour experiment mica sheet 2 = 124 particles.

Agglomerate spatial distribution upon deposition (agglomerates/μm^2)	Mica sheet 1	Mica sheet 2
5 hour experiment	0.07 \pm 0.03	0.09 \pm 0.03
6 hour experiment	0.06 \pm 0.02	0.03 \pm 0.01
Average \pm SD (RSD, %)	0.07 \pm 0.01 (14.29)	0.06 \pm 0.04 (66.67)

As can be seen from Table 62, aerosolised CB NP agglomerates deposited uniformly across the trough in the 5 hour experiment but not in the 6 hour experiment. These data are in agreement with Table 60 which shows that the variability on the mass deposited per unit area was much greater for the 6 hour experiment compared to the 5 hour experiment.

4.5.1.5 Wettability and surface tension activity of aerosolised CB nanoparticles

Before showing the results of the wettability of the aerosolised CB NPs when deposited onto a clean PBS subphase it is important to mention that, unlike the CeO₂ NPs, CB NPs were not studied in a PBS medium prior to the LWB experiments, although there is evidence that they

agglomerate and deposit quickly when suspended in PBS (Sager et al., 2007, Sager, 2008). The capacity of aerosolised CB NPs to remain at the air/liquid interface was investigated by depositing approximately 33 μg of aerosolised CB NPs onto a clean PBS subphase over 180 minutes at 21°C and compressing the interface with the barriers to the smallest area technically feasible. To visualise the CB NPs at the interface, a dipping experiment was performed. Table 63 shows the average aerosol CMD, GSD, number concentration, mass concentration and estimated CB NP mass deposited over the exposure time in this experiment. Figure 125 shows a graphical representation of the aerosol size distribution being a bi-modal size distribution with a low peak at a size ~ 50 nm and a high peak at a size ~ 400 nm. As previously mentioned, the CMD is expected to be underestimated as the full aerosol size range could not be measured. Figure 126 shows two SEM images of the surface at two magnifications.

Table 63. Average aerosol CMD, GSD, number concentration, mass concentration and estimated CB nanoparticle mass deposited for an experiment performed to study the wettability and surface tension activity of aerosolised CB nanoparticles when deposited onto a clean PBS subphase at 21°C. Note that the CMD is expected to be underestimated as the full aerosol size range could not be measured.

CMD \pm SD (nm)	GSD \pm SD	Number concentration \pm SD (particles/cm³)	<i>mc</i> (ng/cm³)	CB NP mass deposited (μg)
190 \pm 53	2.6 \pm 0.3	7.13E+05 \pm 3.60E+05	19.71	33 \pm 16

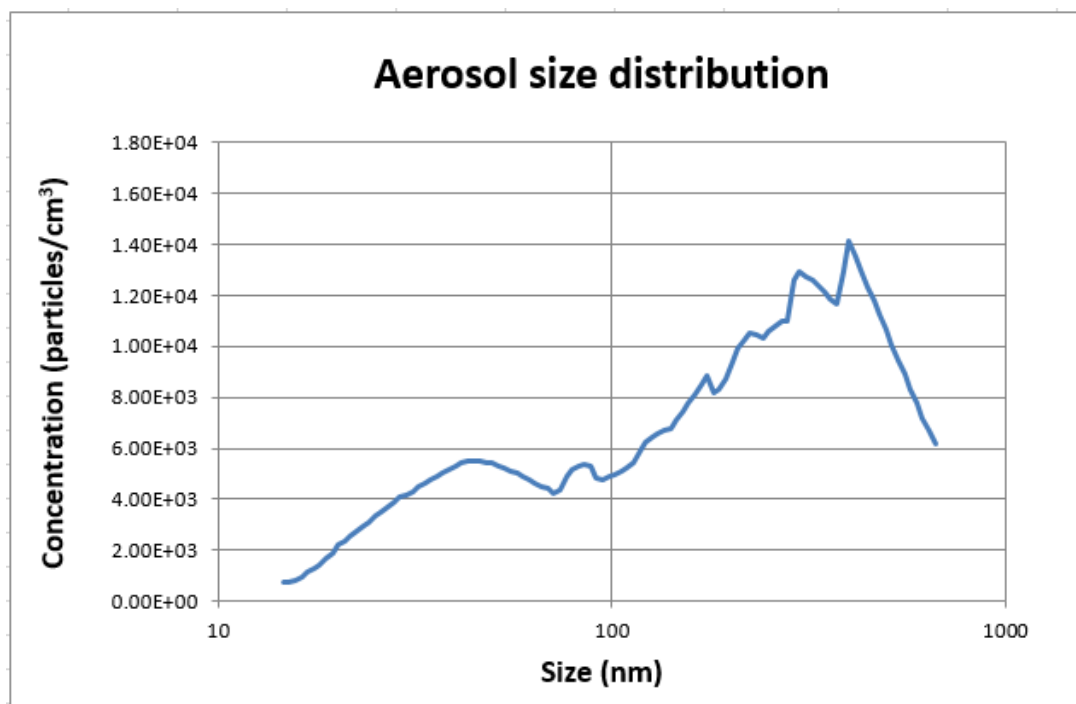


Figure 125. Graphical representation of the CB aerosol size distribution for an experiment performed to study the wettability and surface tension activity of aerosolised CB nanoparticles when deposited onto a clean PBS subphase at 21°C.

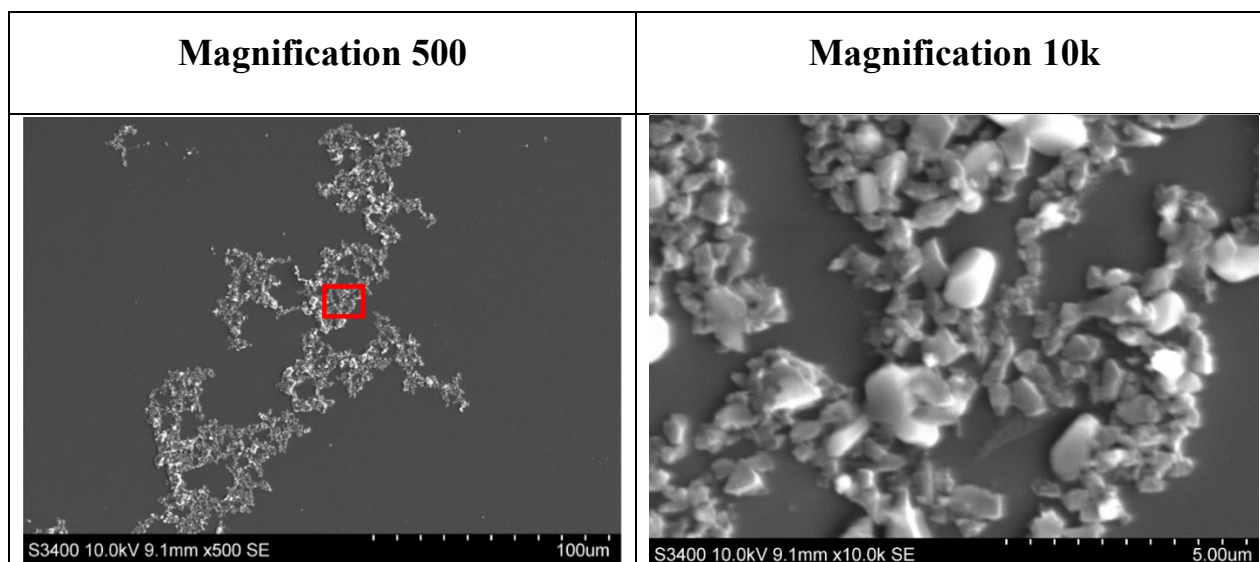
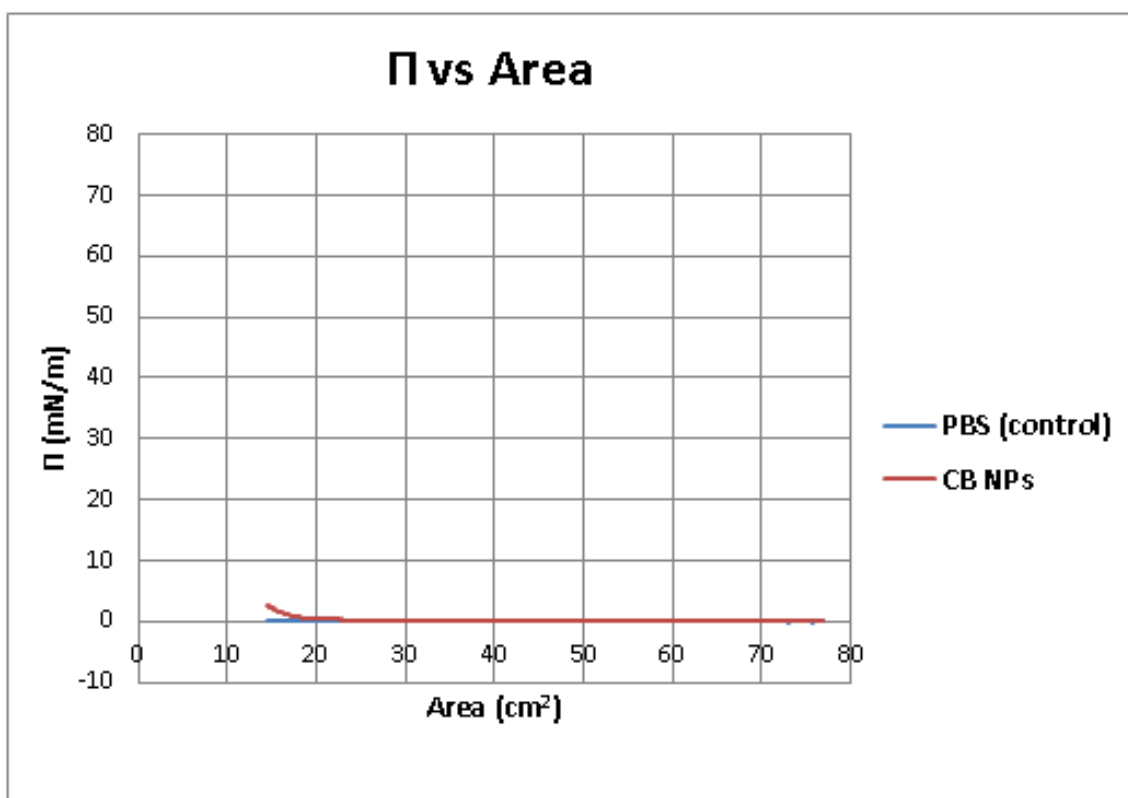


Figure 126. SEM images of the same area at two magnifications of CB nanoparticle agglomerates. The dipping experiment was performed after depositing approximately 33 µg of aerosolised CB nanoparticles onto a PBS subphase at 21°C and compressing the interface to the smallest area technically feasible. The box area in the left image indicates the region displayed in the right image at higher magnification. The dotted scale bar in the left image is 100 µm and in the right image is 5 µm.

Figure 126 shows that some aerosolised CB NPs were present at the interface during one compression. The surface tension activity of the aerosolised CB NPs upon deposition onto the PBS subphase was investigated by recording the Π - A isotherm during the compression of the interface with the barriers to the smallest area technically feasible. This is shown in Figure 127. The Π - A isotherm of PBS was first measured to ensure that the subphase was clean. The isotherms were determined using only one measurement per condition. The table shows the maximum Π value for each isotherm.

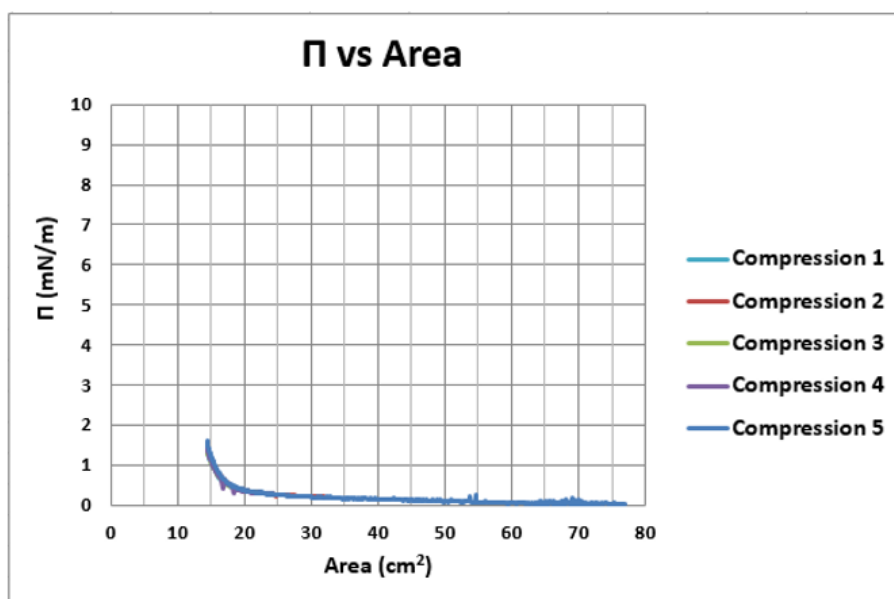


Isotherm	Maximum Π value (mN/m)
PBS (control)	0.22
CB NPs	2.69

Figure 127. Π -A isotherm recorded after depositing approximately 33 μg of aerosolised CB nanoparticles onto a clean PBS subphase at 21°C and compressing the interface to the smallest area technically feasible. The Π -A isotherm of PBS was first measured to ensure that the subphase was clean. The table shows the maximum Π value reached for each isotherm. $n = 1$ experiment/condition.

As can be seen in the previous figure, following application of aerosolised CB NPs, Π only increased slightly at the very late stage of compression from 0.22 to 2.69 mN/m. In order to investigate how these aerosolised CB NPs affected Π after several compression-expansion cycles, the interface was compressed and expanded five times at normal barrier speed. Π -A compression isotherms were measured and the lift-off area and maximum Π reached after each

compression recorded. The isotherms were determined using only one measurement per cycle. These data are shown in Figure 128.



Compression	Lift-off area (cm ²)	Maximum Π (mN/m)
1	17	1.62
2	17	1.53
3	17	1.49
4	17	1.47
5	17	1.41

Figure 128. Π -A compression isotherms measured after depositing approximately 33 μg of aerosolised CB nanoparticles onto a PBS subphase at 21°C and compressing the interface five times to the smallest area technically feasible. The table shows the lift-off area and the maximum Π reached after each compression. n = 1 experiment/cycle.

Figure 128 shows that after five compressions, Π decreased slightly from 1.62 to 1.41 mN/m and the lift-off area remained the same. This suggests limited agglomeration of CB NPs which made them less surface active as larger and denser NP agglomerates would be expected to have

a greater effect on the Π (Huang et al., 2001a, Huang et al., 2001b). Similar results were obtained for the aerosolised CeO₂ NPs (see Figure 100).

4.5.2 Effect of the exposure of a DPPC monolayer to aerosolised CB nanoparticles on the surface pressure– Π isotherm measured in PBS at 21°C and interfacial layer characteristics post-CB nanoparticle administration

4.5.2.1 Effect of the exposure of a DPPC monolayer to compressed air over increasing exposure times on the surface pressure– Π isotherm

Results presented in chapter 3 indicated that exposing the DPPC monolayer to compressed air (CA) flow alone had an effect on the behaviour of the monolayer (see section 3.5.3.2.2). Thus, in the present studies, the isotherms for DPPC monolayers exposed to aerosolised CB NPs for different durations were compared with control isotherms for DPPC monolayers exposed to CA flow for the same duration.

4.5.2.2 Interfacial layer characteristics post-CB nanoparticle administration

In this study, an experiment was performed to investigate the presence of aerosolised CB NPs at the interface during the initial compression of the monolayer and after three compression-expansion cycles performed at maximum barrier speed (270 mm/min). Due to time limitations, a cycling experiment at normal barrier speed was not performed. A DPPC monolayer was exposed to approximately 5 μg of aerosolised CB NPs over 174 minutes. Table 64 shows the average aerosol CMD, GSD, number concentration, mass concentration, estimated CB NP mass deposited over the exposure time and CB/DPPC mass ratio for this experiment. Figure 129 shows a graphical representation of the aerosol size distribution. The aerosol size distribution was a uni-modal right skewed distribution. The estimated CB NP mass deposited in this experiment was smaller than expected for a 174 minute exposure experiment due to the small size of the aerosolised CB NP agglomerates which had a CMD of 70 nm.

A dipping experiment was performed at three different Π values during the initial compression of the monolayer: 20, 40 and 70 mN/m. SEM images of pure DPPC and DPPC exposed to CB NPs are shown in Figure 130. After one compression, the layer was expanded and compressed for a total of three compression-expansion cycles at maximum barrier speed and a dipping

experiment performed at a Γ value of 40 mN/m. SEM images of pure DPPC and DPPC exposed to CB NPs are shown in Figure 130. The areas covered by the CB NPs at the interface at various Γ values during one compression were determined by analysing representative SEM images and expressed as a percentage of the total image area. At least two different sample areas were analysed per Γ . Results are shown in Table 65. As can be seen from these figures, CB NP agglomerates ranging in size from a few hundred nm to a few microns were homogeneously spread across the surface during one compression and after three compression-expansion cycles at maximum barrier speed. SEM images also show that the size of the agglomerates was very similar at the four Γ values at which samples were taken; this suggests limited further agglomeration of the CB NPs with compression. The number of agglomerates present at the interface decreased with compression and with it the area covered by them, although this difference was not statistically significant, as shown in Table 65. This suggests some loss from the monolayer, probably due to the removal of material after each dipping experiment. Experiments for aerosolised CeO₂ NPs were performed in a similar way and indicated limited NP agglomeration during the first compression (see Figure 101) however, three compression-expansion cycles performed at maximum barrier speed promoted the agglomeration of the CeO₂ NP clusters (see Figure 104). Nevertheless, future research directed towards examining this in more detail is needed.

Table 64. Average aerosol CMD, GSD, number concentration, mass concentration, estimated CB nanoparticle mass deposited and CB/DPPC nanoparticle mass ratio for a dipping experiment performed in PBS at 21°C after exposing a DPPC monolayer to aerosolised CB nanoparticles to investigate the presence of CB nanoparticles at the interface during the initial compression of the monolayer and after three compression-expansion cycles at maximum barrier speed.

CMD ± SD (nm)	GSD ± SD	Number concentration ± SD (particles/cm³)	<i>mc</i> (ng/cm³)	CB NP mass deposited (µg)	CB/DPPC mass ratio
70 ± 10	2.2 ± 0.1	8.20E+05 ± 1.19E+05	3.09	5 ± 3	1/3.22

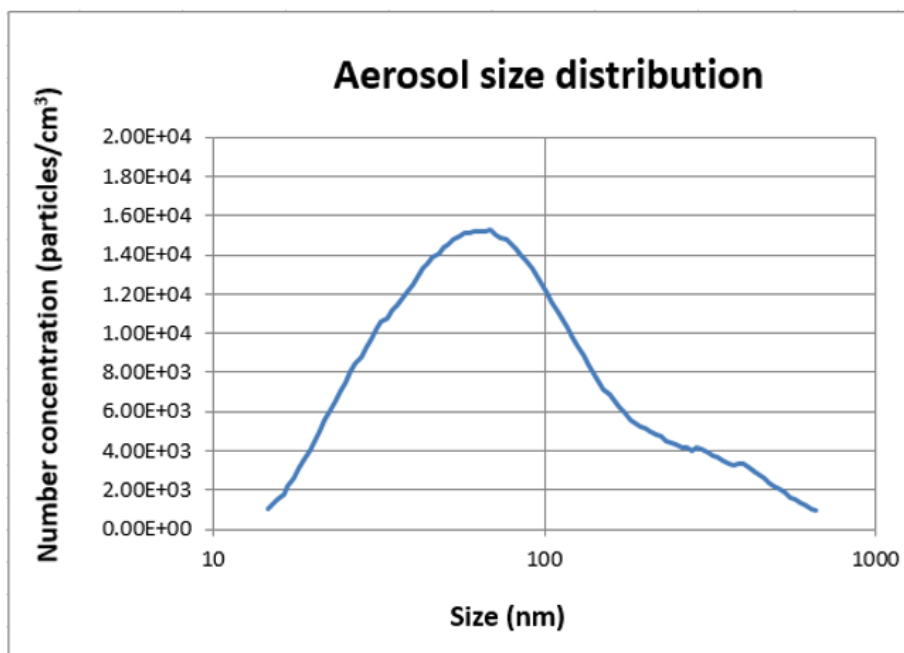


Figure 129. Graphical representation of the CB aerosol size distribution for a dipping experiment performed in PBS at 21°C after exposing a DPPC monolayer to aerosolised CB nanoparticles to investigate the presence of CB nanoparticles at the interface during the initial compression of the monolayer and after three compression-expansion cycles at maximum barrier speed.

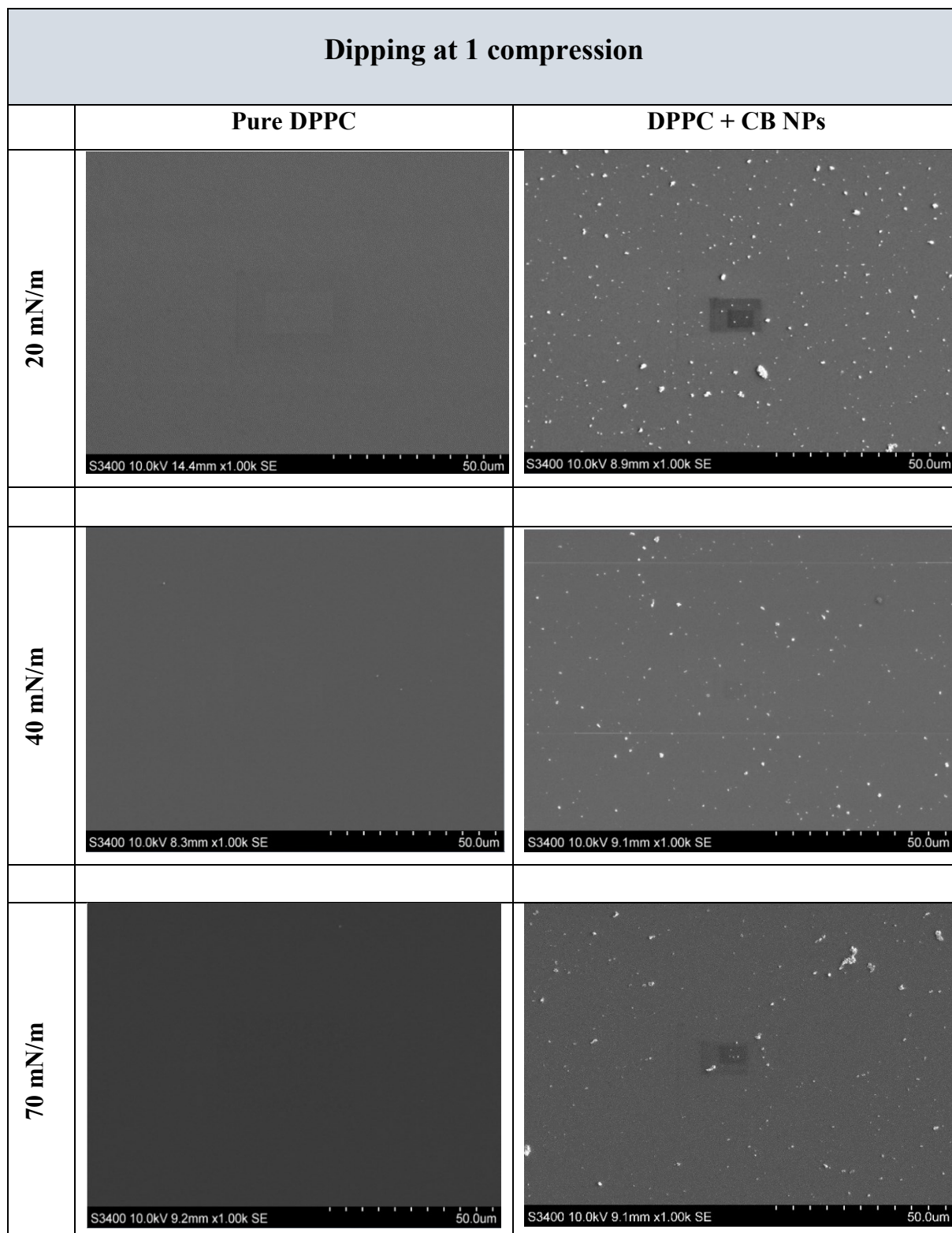


Figure 130. SEM images of LB films of pure DPPC (left) and DPPC exposed to CB nanoparticles (deposited by aerosol, right) at a 1/3.22 CB/DPPC mass ratio, produced in PBS at 21°C during the initial compression of the monolayer at three different Π values: 20, 40 and 70 mN/m. The dotted scale bar is 50 μ m for all the images.

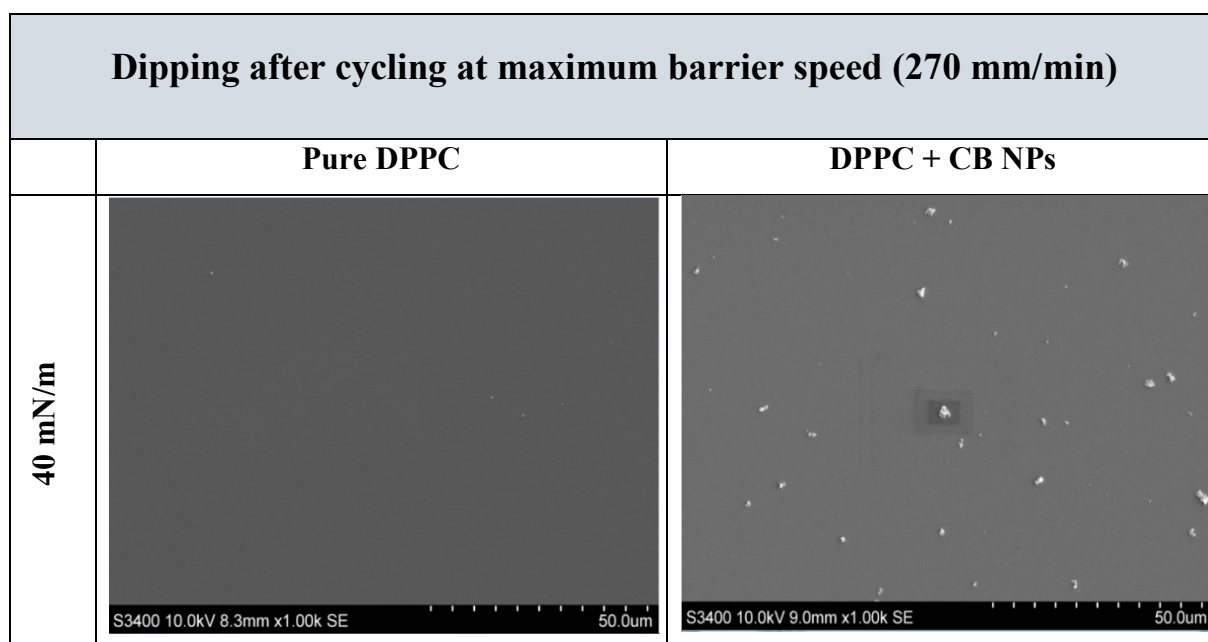


Figure 131. SEM images of LB films of pure DPPC (left image) and DPPC exposed to CB nanoparticles (deposited by aerosol, 1/3.22 CB/DPPC mass ratio, right image) produced at a Π value of 40 mN/m after 3 compression-expansion cycles performed at maximum barrier speed in PBS at 21°C. The dotted scale bar is 50 μm for all the images.

Table 65. Area covered by the CB nanoparticle agglomerates at Π values of 20, 40 and 70 mN/m during the initial compression of the monolayer. The dipping experiment was performed in PBS at 21°C after depositing aerosolised CB nanoparticles onto a DPPC monolayer at a 1/3.22 CB/DPPC mass ratio. The area covered by the CB nanoparticles was determined by analysing representative SEM images and expressed as a percentage of the total image area. At least two different sample areas were analysed per Π .

Surface pressure (mN/m)	Area covered by CB NP agglomerates \pm SD (area covered/total image area, %)
20	1.44 \pm 0.36
40	1.05 \pm 1.19
70	0.85 \pm 0.22

4.5.2.3 Effect of the exposure of a DPPC monolayer to aerosolised CB nanoparticles on the surface pressure–Mma isotherm measured in PBS at 21°C

In these experiments, a DPPC monolayer was exposed to three different aerosolised CB NP masses over 10, 90 and 150 minutes and the Π -Mma isotherm recorded during one compression. Table 66 shows the exposure time, average aerosol CMD, GSD and number concentration for each experiment. Figure 132 shows a graphical representation of the aerosol size distributions. The exposure time, aerosol mass concentration, estimated CB NP mass deposited over the exposure time and CB/DPPC mass ratio for each experiment are shown in Table 67. Figure 133, Figure 134 and Figure 135 show the effect of the exposure of a DPPC monolayer to varying amounts of aerosolised CB NPs on the Π -Mma isotherm for the 10, 90 and 150 minute exposure experiments respectively compared to the Π -Mma isotherm recorded for DPPC exposed to CA only (control) for the same duration. Due to time limitations, the experiments were only performed once. Table 68, Table 69 and Table 70 show the C_m for the region 30-45 mN/m and collapse Π of the Π -Mma isotherms for the 10, 90 and 150 minute exposure experiments respectively. As already mentioned, based on the results obtained for the aerosol CeO₂ NP experiments measured at 37°C (Figure 112 and Figure 113), it was decided to focus on the C_m for Π values above 30 mN/m and the collapse Π . The corresponding values in each of these parameters measured for each CB/DPPC mass ratio were compared with those of CA (control) by calculating the % difference between experiment and control for each of the parameters and dividing them by the reference % change from midpoint values, i.e., assuming similar levels of uncertainties on the parameters to those of the reference isotherms (see section 2.4.1.5). Additionally, the assumption was made that for the reference isotherm, the uncertainty values for the C_m for the region 25-45 mN/m would be similar for the region 30-45 mN/m.

Table 66. Exposure time, average aerosol CMD, GSD and number concentration of three different experiments performed in PBS at 21°C to study the effects of the exposure of a DPPC monolayer to varying amounts of aerosolised CB nanoparticles. Note that the CMD for the 90 and 150 minute exposure experiments are expected to be underestimated as the full aerosol size range could not be measured.

Exposure time (min)	CMD ± SD (nm)	GSD ± SD	Number concentration ± SD (particles/cm ³)
10	52 ± 8	1.9 ± 0.0	4.03E+05 ± 2.70E+05
90	143 ± 31	2.7 ± 0.1	7.17E+05 ± 1.36E+05
150	58 ± 8	2.6 ± 0.1	6.75E+05 ± 1.14E+05

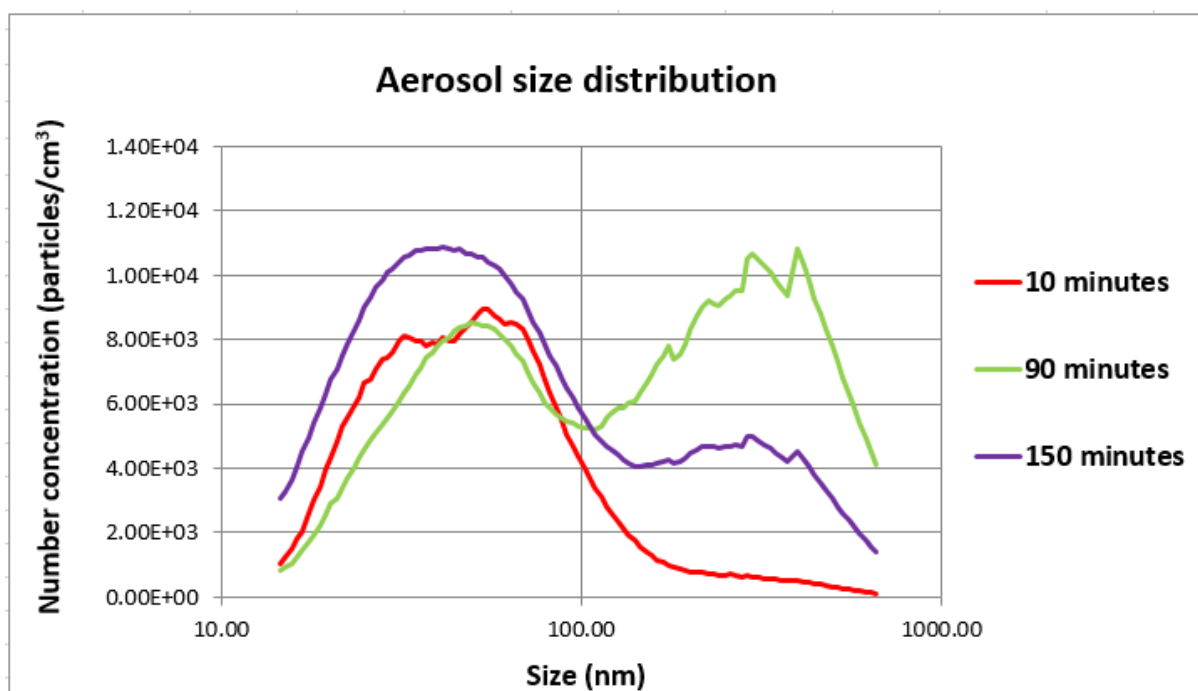


Figure 132. Graphical representation of the CB aerosol size distribution for the 10, 90 and 150 minute experiments performed to study the effects of the exposure of a DPPC monolayer to varying amounts of aerosolised CB nanoparticles.

Table 67. Exposure time, aerosol mass concentration, estimated CB nanoparticle mass deposited and CB/DPPC mass ratio of three different experiments performed in PBS at 21°C to study the effects of the exposure of a DPPC monolayer to varying amounts of aerosolised CB nanoparticles.

Exposure time (min)	mc (ng/cm ³)	CB NP mass deposited (μg)	CB/DPPC mass ratio
10	1.43	0.13 ± 0.07	0.02/1
90	15.20	13 ± 6	1.58/1
150	5.81	8 ± 4	1.01/1

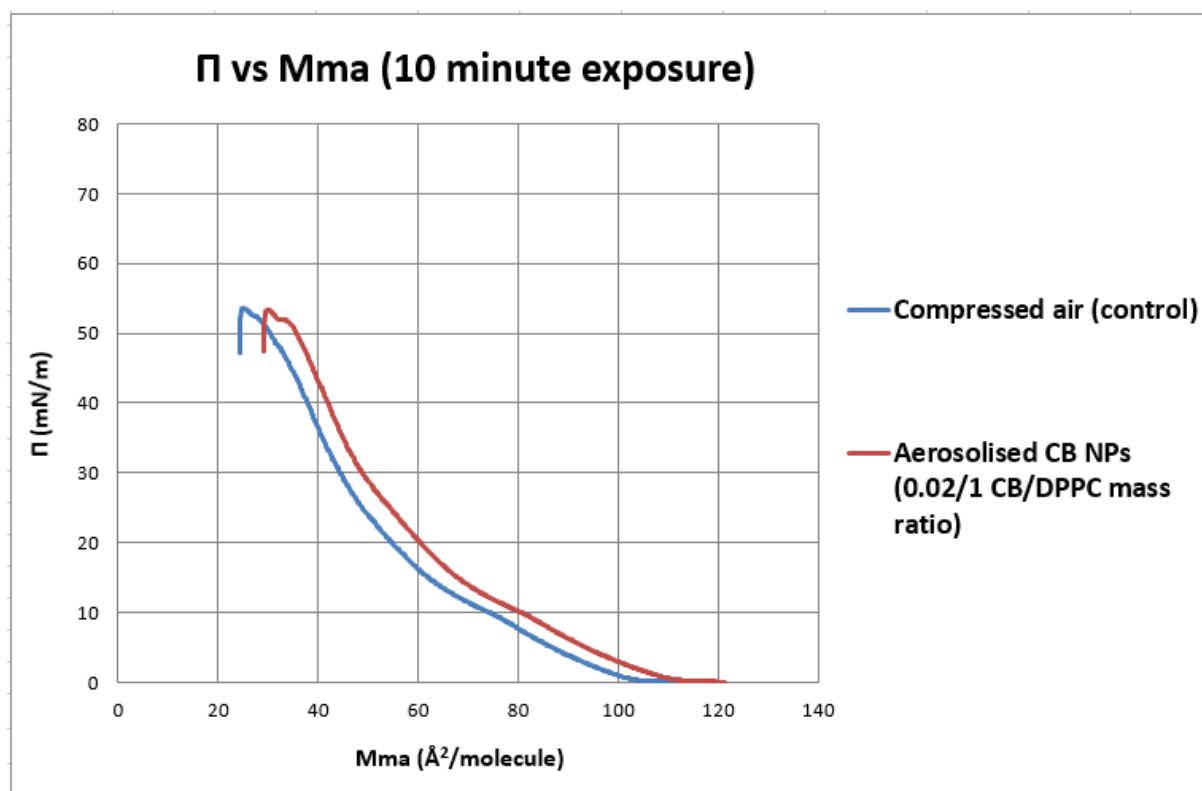


Figure 133. Effect of the exposure of a DPPC monolayer to aerosolised CB nanoparticles over 10 minutes (0.02/1 CB/DPPC mass ratio) on the Π - M_{ma} isotherm measured in PBS at 21°C. The control isotherm was measured after exposing a DPPC monolayer to compressed air flow for the same duration. $n = 1$ experiment/condition.

Table 68. Effect of the exposure of a DPPC monolayer to aerosolised CB nanoparticles over 10 minutes (0.02/1 CB/DPPC mass ratio) on the C_m for the region 30-45 mN/m and the collapse Π of the Π -Mma isotherm measured in PBS at 21°C. The corresponding values in each of the parameters measured for CB nanoparticles were compared with those of compressed air flow (control) by calculating the difference in each of the parameters for the experimental isotherm and the control expressed as a % of the control value and dividing them by the reference % change from midpoint values for the relevant reference isotherm (Table 12). This approach assumes similar levels of uncertainties on the control and experimental isotherm parameters to those of the reference isotherm parameters. Additionally, the assumption was made that for the reference isotherm, the uncertainty values for the C_m for the region 25-45 mN/m would be similar for the region 30-45 mN/m.

10 minute exposure	C_m 30-45 mN/m (mN/m) ⁻¹	(% difference experiment and control)/(reference % change from midpoint)	Collapse Π (mN/m)	(% difference experiment and control)/(reference % change from midpoint)
<i>Reference isotherm</i>	0.0063 (25-45 mN/m)	6.0 (% change from midpoint)	57.17	2.0 (% change from midpoint)
CA (control)	0.0141		53.63	
CB	0.0132	1.1	53.41	0.0

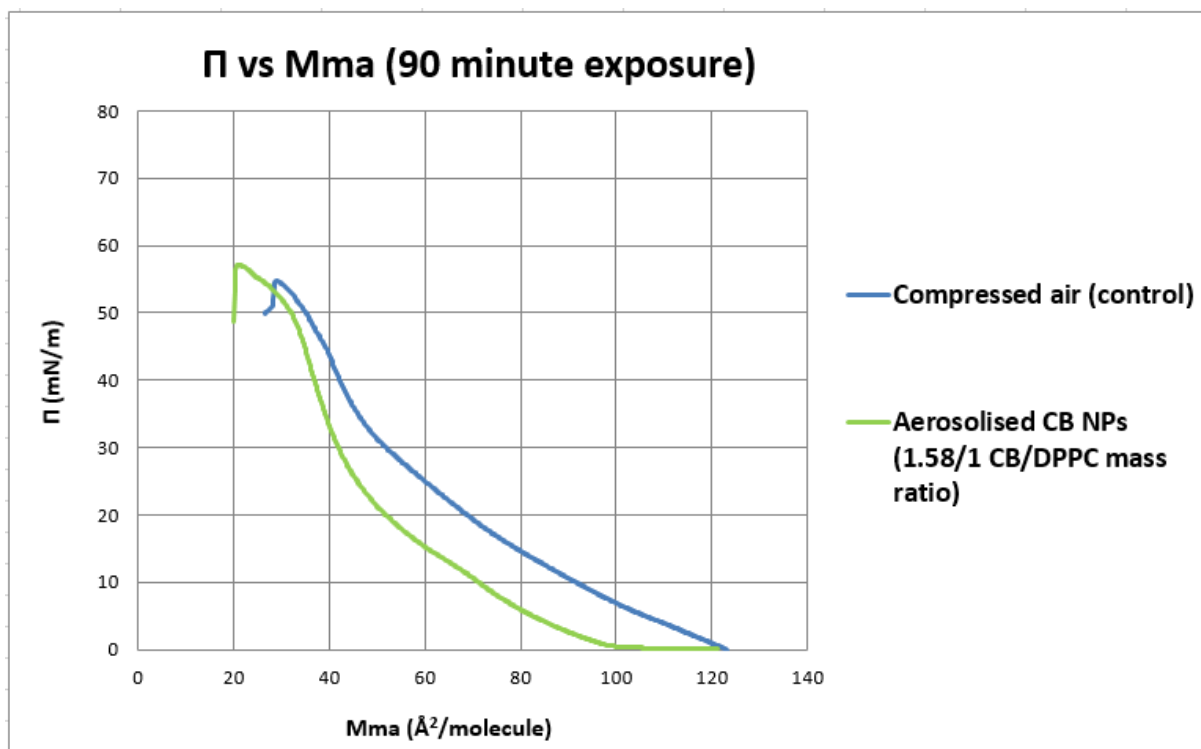


Figure 134. Effect of the exposure of a DPPC monolayer to aerosolised CB nanoparticles over 90 minutes (1.58/1 CB/DPPC mass ratio) on the Π -Mma isotherm measured in PBS at 21°C. The control isotherm was measured after exposing a DPPC monolayer to compressed air flow for the same duration. $n = 1$ experiment/condition.

Table 69. Effect of the exposure of a DPPC monolayer to aerosolised CB nanoparticles over 90 minutes (1.58/1 CB/DPPC mass ratio) on the C_m for the region 30-45 mN/m and the collapse Π of the Π -Mma isotherm measured in PBS at 21°C. The corresponding values in each of the parameters measured for CB nanoparticles were compared with those of compressed air flow (control) by calculating the difference in each of the parameters for the experimental isotherm and the control expressed as a % of the control value and dividing them by the reference % change from midpoint values for the relevant reference isotherm (Table 12). This approach assumes similar levels of uncertainties on the control and experimental isotherm parameters to those of the reference isotherm parameters. Additionally, the assumption was made that for the reference isotherm, the uncertainty values for the C_m for the region 25-45 mN/m would be similar for the region 30-45 mN/m.

90 minute exposure	C_m 30-45 mN/m (mN/m) ⁻¹	(% difference experiment and control)/(reference % change from midpoint)	Collapse Π (mN/m)	(% difference experiment and control)/(reference % change from midpoint)
<i>Reference isotherm</i>	0.0063 (25-45 mN/m)	6.0 (% change from midpoint)	57.17	2.0 (% change from midpoint)
CA (control)	0.0183		54.88	
CB	0.0111	6.6	57.18	2.0

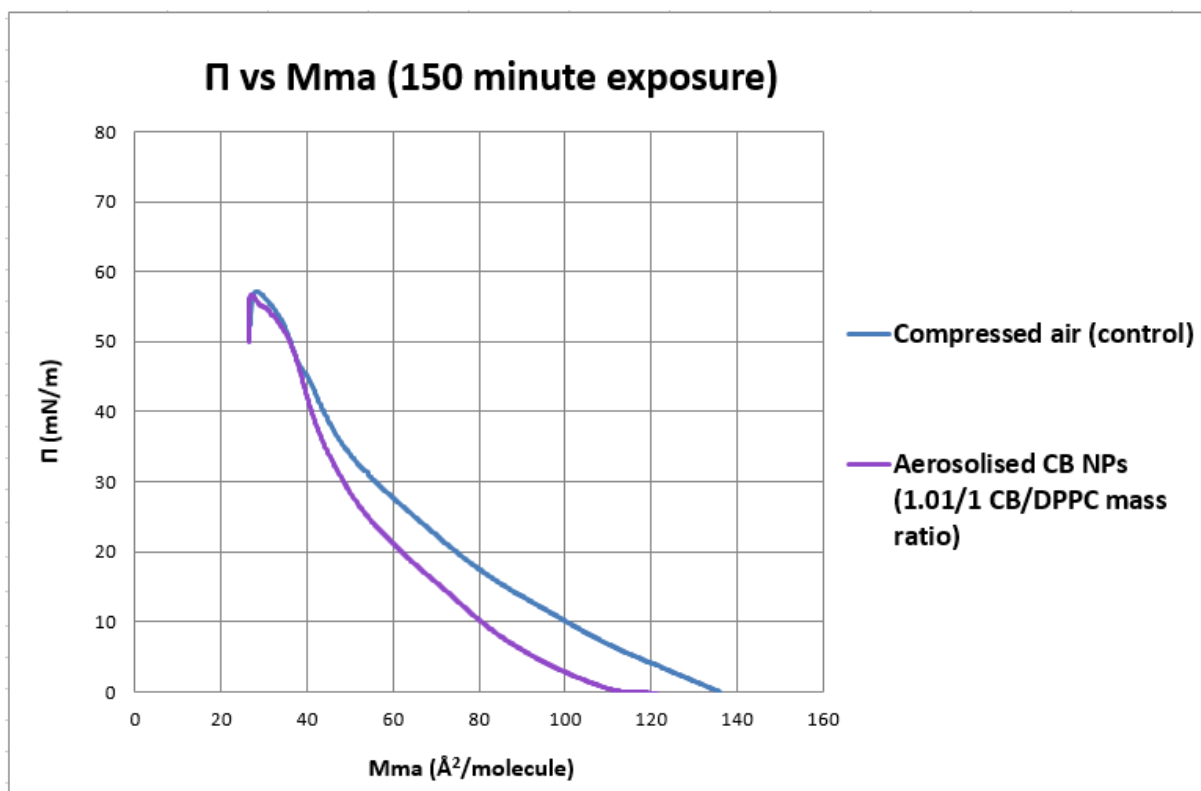


Figure 135. Effect of the exposure of a DPPC monolayer to aerosolised CB nanoparticles over 150 minutes (1.01/1 CB/DPPC mass ratio) on the Π - M_{ma} isotherm measured in PBS at 21°C. The control isotherm was measured after exposing a DPPC monolayer to compressed air flow for the same duration. $n = 1$ experiment/condition.

Table 70. Effect of the exposure of a DPPC monolayer to aerosolised CB nanoparticles over 150 minutes (1.01/1 CB/DPPC mass ratio) on the C_m for the region 30-45 mN/m and the collapse Π of the Π -Mma isotherm measured in PBS at 21°C. The corresponding values in each of the parameters measured for CB nanoparticles were compared with those of compressed air flow (control) by calculating the difference in each of the parameters for the experimental isotherm and the control expressed as a % of the control value and dividing them by the reference % change from midpoint values for the relevant reference isotherm (Table 12). This approach assumes similar levels of uncertainties on the control and experimental isotherm parameters to those of the reference isotherm parameters. Additionally, the assumption was made that for the reference isotherm, the uncertainty values for the C_m for the region 25-45 mN/m would be similar for the region 30-45 mN/m.

150 minute exposure	C_m 30-45 mN/m (mN/m) ⁻¹	(% difference experiment and control)/(reference % change from midpoint)	Collapse Π (mN/m)	(% difference experiment and control)/(reference % change from midpoint)
<i>Reference isotherm</i>	0.0063 (25-45 mN/m)	6.0 (% change from midpoint)	57.17	2.0 (% change from midpoint)
CA (control)	0.0202		57.20	
CB	0.0138	5.3	56.68	0.5

As can be seen in Figure 132, the profile of the aerosol size distribution was different for each experiment. This makes it difficult to directly compare the results for the different exposure durations as they relate not simply to different deposited masses but also to different particle sizes. For the 10 minute exposure experiment, the distribution was a uni-modal right skewed distribution with a peak at a size of ~ 50 nm. For the 90 minute exposure experiment, the distribution was a bi-modal distribution with similar peaks at sizes ~ 50 nm and ~ 300 nm. For the 150 minute exposure experiment, the distribution was a bi-modal distribution with a high peak at a size ~ 50 nm and a low peak at a size ~ 300 nm. Table 67 shows that the lowest CB NP mass deposited corresponded to the 10 minute exposure experiment. The aerosol mass concentration was higher for the 90 minute exposure experiment compared to the 150 minute exposure experiment which was explained by the larger size of the aerosolised CB NP agglomerates for a similar aerosol number concentration. Hence, the CB NP mass deposited onto the trough was higher for the 90 minute exposure experiment compared to the 150 minute exposure experiment.

Regarding the Π -Mma isotherms, it is difficult to interpret the impact of deposited aerosolised CB NPs on the DPPC monolayer behaviour because of the significant effect of the CA flow on the monolayer. This along with the fact that only one isotherm was generated for each exposure duration means that conclusions must be drawn with caution. The lift-off Mma for the 10, 90 and 150 minute exposure experiments were very different compared to the controls. This could have been caused by errors in spreading the monolayer. However, the evidence of a trend of decreasing the C_m for the region 30-45 mN/m with increasing CB NP mass deposited compared to the control isotherm for the three exposure experiments is considered strong.

SEM images indicated a homogeneous distribution of agglomerates of a similar size across the surface during the initial compression of the monolayer (see Figure 130). It is hypothesised that these agglomerates improved the film containment and therefore prevented surfactant loss from the system, perhaps by protecting the individual DPPC domains as is postulated for the experiments performed with aerosol CeO₂ NPs (see section 3.5.3.2.3). However, it is important to note that the aerosol size distribution for the interface visualisation experiment was different from those used for the isotherm investigations, and thus may not be directly comparable. Further work is required to address this.

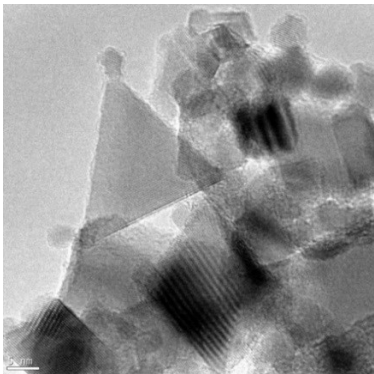
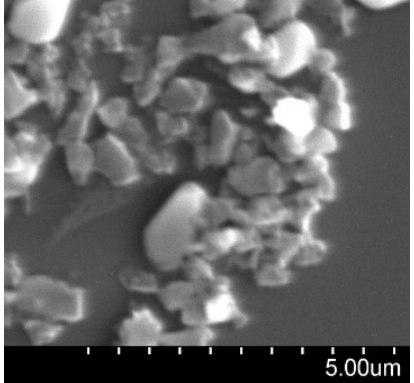
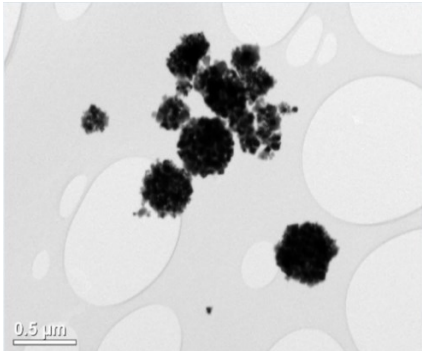
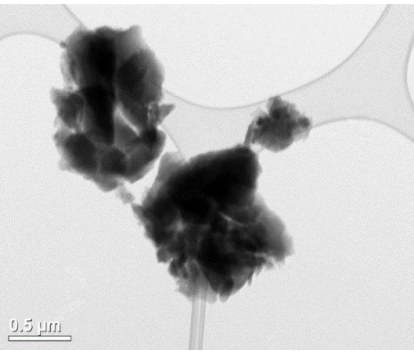
As suggested previously for the aerosol CeO₂ NP experiments, the exposure of a DPPC monolayer to CA flow reduced the nucleation of the LE phases. In fact, the C_m for the region 15-30 mN/m was calculated for the DPPC monolayer exposed to aerosolised CB NPs for the 10, 90 and 150 minute exposure experiments. This value was 0.02 (mN/m)⁻¹ for the three experiments. Taking into account experimental values of C_m for the DPPC monolayer phases from the literature (i.e. 0.02-0.1 (mN/m)⁻¹ for LE films, 0.004-0.01 (mN/m)⁻¹ for LC films and < 0.004 (mN/m)⁻¹ for S films (Kodama et al., 2004, Vitovič et al., 2006)), this indicates that the monolayer was in the LE phase in this region instead of the expected LC phase. As monolayers that collapse in the LE phase usually do so at Π_e because of a higher instability of the monolayer (Baoukina et al., 2014), which for DPPC is around 40 mN/m, the loss of material probably started at a $\Pi \sim 30$ mN/m. An improvement in the film containment and reduction of the loss of surfactant should also lead to a higher collapse Π . The collapse Π value was only higher than the control for the 90 minute exposure experiment. However, the large differences in the lift-off Mma (and thus the lift-off area as the DPPC mass deposited was the same in both the CB NP and control experiments) between the isotherm for the DPPC monolayer exposed to

aerosolised CB NPs and the control could have affected the collapse Π as discussed previously in section 2.4.1.6.

4.5.2.4 Comparison of the similarities and differences between aerosolised CeO₂ nanoparticles and CB nanoparticles and of their effect on the surface pressure–Mma isotherm measured in PBS at 21°C

The table below (Table 71) shows a comparison of the similarities and differences between aerosolised CeO₂ NPs (when used for those experiments performed at a subphase temperature of 21°C) and aerosolised CB NPs.

Table 71. Comparison of the similarities and differences between CeO₂ nanoparticles and CB nanoparticles.

	CeO ₂	CB
Primary particle shape	 <p>* The scale bar is 5 nm</p>	 <p>* The scale bar is 5 μm</p>
NP agglomerate	 <p>* The scale bar is 0.5 μm</p>	 <p>* The scale bar is 0.5 μm</p>
Primary particle size (nm)	19	65

Aerosol size distribution	Uni-modal normal distribution	Bimodal or uni-modal right skewed distribution
Aerosol NP agglomerate size (nm)	~ 177	Peaks at sizes ~ 50 nm or/and ~ 400 nm
Aerosol number concentration (particles/cm³)	~ 7.67E+05	~ 5.99E+05
Deposition velocity (cm/min)	0.13	0.12
NP agglomerate size upon deposition (nm)	220	545
Wettability at the air/PBS interface	Some aerosolised CeO ₂ NPs remained at the interface upon deposition	Some aerosolised CB NPs remained at the interface upon deposition
Surface tension activity at the air/PBS interface	<i>II</i> only increased slightly from 1.22 mN/m to 2.10 mN/m after five compression-expansion cycles	<i>II</i> decreased slightly from 1.62 to 1.41 mN/m after five compression-expansion cycles
Zeta potential in PBS	Very unstable. CeO ₂ NPs agglomerated and settled at the bottom of the bottle within seconds	There is evidence that they agglomerate and deposit quickly when suspended in PBS (Sager et al., 2007, Sager, 2008)

Figure 136 shows a comparison of the effects of the exposure of a DPPC monolayer to aerosolised CeO₂ NPs and CB NPs on the *II*-Mma isotherm measured in PBS at 21°C. In both experiments the aerosol NPs were deposited over 90 minutes and the NP/DPPC mass ratios were 2.31/1 and 1.58/1 for the CeO₂ and CB NP experiments respectively. The aerosol size distribution was a uni-modal normal distribution with a peak at a diameter of 167 nm for the aerosol CeO₂ NP and a bi-modal distribution with similar peaks at sizes ~ 50 nm and ~ 300 nm for the aerosol CB NP. Although the NP deposited mass and size were different in each

experiment, these results indicate that both types of aerosol NPs clearly affected the final region of the isotherm, in particular the C_m at Π values above ~ 30 mN/m, which was lower than the control, and the collapse Π , which was higher than the control. As similar effects were seen with a smaller deposited mass of aerosolised CB NPs, this may suggest that the CB aerosol had a greater effect, possibly as a result of the greater particle size, although this might have been due to other physicochemical characteristics of the two materials. Given the limited number of experiments undertaken using aerosolised CeO₂ and CB NPs and the significant effect of the CA flow on the monolayer further work is required to confirm this findings.

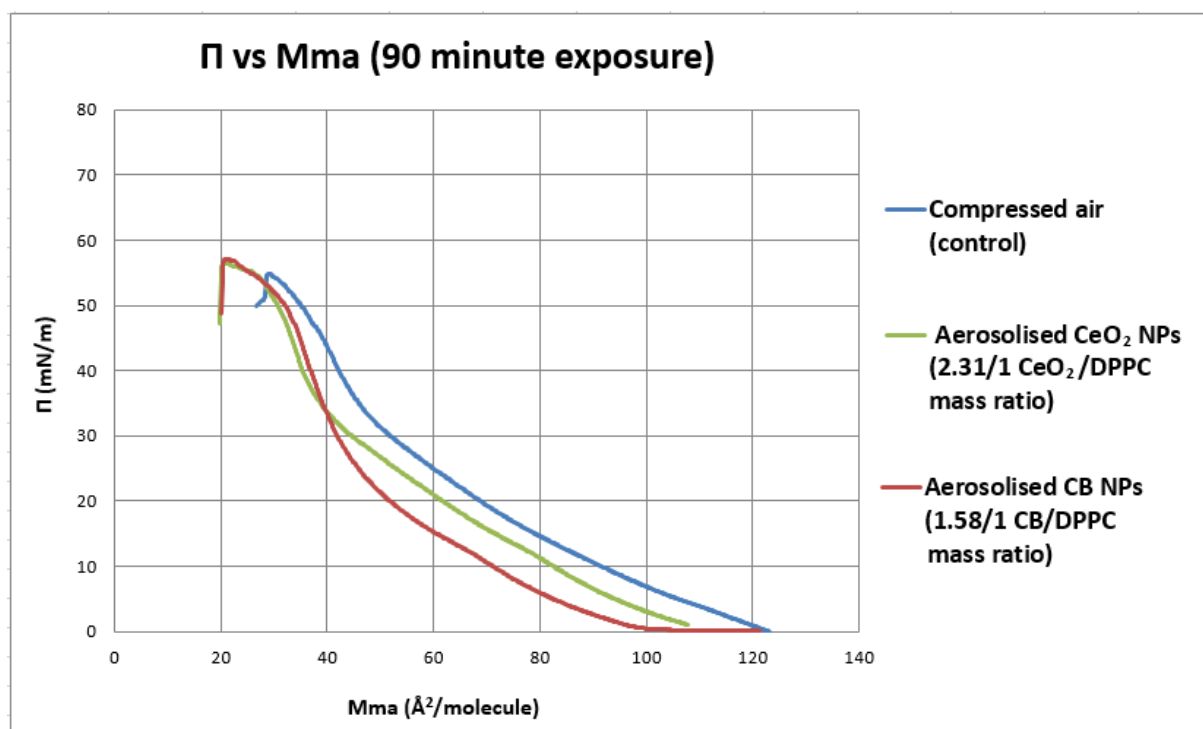


Figure 136. Comparison of the effects of the exposure of a DPPC monolayer to aerosolised CeO₂ and CB nanoparticles on the Π - M_{ma} isotherm. In both experiments the aerosol nanoparticles were deposited over 90 minutes and the NP/DPPC mass ratio was 2.31/1 and 1.58/1 for CeO₂ and CB nanoparticles respectively. The control isotherm was measured after exposing a DPPC monolayer to compressed air flow for the same duration. The subphase used was PBS at 21°C.

4.5.2.5 Comparison of the results of aerosolised CB nanoparticles with those from other studies

In the literature, Guzmán et al., 2011 studied the interactions between DPPC and CB NPs by suspending 15-20 nm CB NPs in chloroform and depositing them onto a preformed DPPC monolayer at DPPC/NP w/w ratios 10/1, 2/1 and 1/3. The subphase used was water at 22°C and

isotherms were recorded during one compression. The authors found that CB NPs shifted the isotherm to higher areas per molecule of DPPC with increasing deposited mass, interpreting this reasonably as indicating the penetration of the CB NPs into the monolayer. BAM images showed that NPs did not affect the nucleation of the LC domains. CB NPs however increased the C_m of the monolayer at Π values above ~ 10 mN/m and decreased the collapse Π value. This suggests the presence of large, dense agglomerates at the interface throughout the compression process. These results contrast with those shown in the present work for similar NP/DPPC mass ratios, as aerosol CB NPs affected the final region of the isotherm, in particular the C_m at Π values above ~ 30 mN/m which decreased with NP mass deposited, possibly due to an improvement in the film containment caused by the presence of CB NP agglomerates of a similar size homogeneously spread across the surface. These results further support the hypothesis that the degree of NP agglomeration is probably one of the most important determining factors of the NP effects on the DPPC isotherm with larger and denser agglomerates having a greater effect on the isotherm compared to smaller homogeneously spread NP clusters. However, as Guzmán et al., 2011 did not provide information on the size of the agglomerates when deposited onto the air/liquid interface, it is difficult to establish a cause for the differences between the studies in the effects on the isotherm. Bearing this in mind, one possible explanation for the current results is that the wettability of the aerosolised CB NPs was higher than that of CB NPs deposited from chloroform suspensions, which in turn increased the stability of the aerosolised CB NPs when deposited onto an air/liquid interface. In fact, the subphase liquid used was different for each experiment. It is also possible that the use of chloroform when depositing CB NPs onto the air/liquid interface increased the agglomeration of the particles to a greater extent compared to the aerosolised CB NPs (Huang et al., 2001a, Huang et al., 2001b). Furthermore, compared to the liquid deposition method, the deposition of aerosolised CB NPs was probably more spatially uniform across the surface resulting in less agglomeration of the aerosolised CB NPs with compression. This agrees well with what happens *in vivo* as inhaled airborne NPs deposit homogeneously onto the alveolar region (Bahk and Isawa, 1994).

4.6 Summary discussion and conclusion

The earlier work supported the hypothesis that an aerosol exposure system is the most appropriate model to investigate inhaled NP interactions with lung surfactant. Thus, this system was used to compare the effects of another common ENP, CB NPs, on the DPPC isotherm with

those of aerosolised CeO₂ NPs. To date, there are no other studies of CB NP deposition onto a surfactant monolayer in aerosol form using a LWB, thus, these data are novel.

In the first instance, the particle characteristics were determined for comparative purposes. CB primary particles were irregular in shape with a CMD of 65 nm and a GSD of 2.0. This size was within the particle size range stated by the manufacturer, i.e., nominal size < 100 nm. This primary particle size was higher than the primary particle size of CeO₂ NPs (CMD was 19 nm and GSD was 1.8).

The aerosol mass deposited onto the Langmuir trough was estimated based on deriving the deposition velocity of the aerosolised CB NPs within the exposure chamber using EMFAB filters and was found to be very similar for CB NPs (0.12 cm/min) compared to that for aerosolised CeO₂ NPs (0.13 cm/min); this was expected as the experimental set-ups and the aerosol in each case were similar.

The aerosol size distribution was generally a bi-modal distribution (see Figure 122, Figure 125, Figure 129 and Figure 132), probably indicating the presence of both aerosol CB primary particles and aerosol CB NP agglomerates as opposed to the uni-modal normal size distribution of aerosol CeO₂ NPs (see Figure 111, Figure 114 and Figure 117). However, there were difficulties in measuring the full size range of the aerosol particles due to limitations of the instrumentation, which made interpretation of the results complex.

In an experiment performed to determine if aerosolised CB NPs agglomerated while they were settling from the air onto the trough, TEM images (Figure 124) showed that the CMD of these agglomerates upon deposition was 545 nm and the GSD was 1.9. This contrasted with the aerosol size distribution CMD of ca 200 nm, however, the equipment used to determine this value was not able to measure the full aerosol size range and thus the 200 nm was expected to be a significant underestimate. As the aerosol particle size CMD was not known accurately it was not possible to make a firm judgement as to whether the airborne CB NPs agglomerated during deposition. A CMD of 545 nm was possibly consistent with no or limited agglomeration on deposition, as was seen with the aerosolised CeO₂ NPs (see section 3.5.3.1.2). Additional experiments using other measurement system would be required to investigate this further.

When 5 μg of aerosolised CB NP agglomerates with a CMD of 70 nm were deposited onto a DPPC monolayer at a NP/DPPC mass ratio of 1/3.22, SEM images indicated the presence of CB NP agglomerates ranging in size from a few hundred nm to a few microns homogeneously spread across the surface during the first compression and after three compression-expansion cycles performed at maximum barrier speed. SEM images also showed that the size of the agglomerates was very similar at the four Π values at which samples were taken; this suggests limited further agglomeration of the CB NPs with compression. Additionally, the number of agglomerates present at the interface decreased with compression and with it the area covered by them, probably due to the removal of material after each dipping experiment. Experiments for aerosolised CeO_2 NPs were performed in a similar way and indicated limited NP agglomeration during the first compression (see Figure 101) however, three compression-expansion cycles performed at maximum barrier speed promoted the agglomeration of the CeO_2 NP clusters (see Figure 104). Nevertheless, future research directed towards examining this in more detail is needed.

Regarding the Π - M_{ma} isotherms, a DPPC monolayer was exposed to three different aerosol CB NP masses at 0.02/1, 1.01/1 and 1.58/1 NP/DPPC mass ratios and the isotherm recorded during one compression. It was difficult to interpret the impact of deposited aerosolised CB NPs on the DPPC monolayer behaviour because of the significant effect of the CA flow on the monolayer. However, taking this into account there was a clear effect on the last region of the isotherm by decreasing the C_m for the region 30-45 mN/m compared to the control in a mass-dependant manner. As the effects seen affected the last region of the isotherm starting at a $\Pi \sim 30$ mN/m, which is where a loss of surfactant probably occurred as the isotherm was in a LE state below this Π value, it is hypothesised that the presence of CB NP agglomerates of a similar size homogeneously spread across the surface improved the film containment in a similar way to aerosolised CeO_2 NPs. The effects of aerosolised CeO_2 NPs and CB nanoparticles on the DPPC isotherm were compared for the 90 minute exposure experiment. As similar effects were seen with a smaller deposited mass of CB NPs (the NP/DPPC mass ratios were 2.31/1 and 1.58/1 for the CeO_2 and CB NP experiments respectively), this may suggest that the CB aerosol had a greater effect compared to aerosolised CeO_2 NPs, possibly as a result of the greater particle size (the aerosol size distribution was a uni-modal normal distribution with a peak at a diameter of 167 nm for the aerosol CeO_2 NP and a bi-modal distribution with similar peaks at sizes ~ 50 nm and ~ 300 nm for the aerosol CB NP), although this might have been due to other physicochemical characteristics of the two materials. Given the limited number of experiments

undertaken using aerosolised CeO₂ and CB NPs further work is required to confirm this findings.

These results further support the hypothesis that the degree of NP agglomeration is probably one of the most important determining factors of the NP effects on the DPPC isotherm with larger and denser agglomerates having a greater effect on the isotherm compared to smaller homogeneously spread NP clusters.

CHAPTER 5 – SUMMARY CONCLUSION, RECOMMENDATIONS AND FUTURE STUDIES

5.1 Summary conclusion

The rapid development of nanotechnology, and the associated production and use of engineered nanomaterials, represents a potential source for human exposure to ENPs (Schleh et al., 2009), with inhalation being a significant exposure route (Oberdörster et al., 2005). Concerns, based on findings from research into the health effects of air pollutants, asbestos and other particulate matter, have been raised about the potential impact of ENPs on human health. When inhaled, a high proportion of ENPs can reach the alveolar region where the first biological barrier is lung surfactant, which consists of a mixture of phospholipids and proteins and covers the entire alveolar region at the air/liquid interface (Peters et al., 2006, Schleh and Hohlfeld, 2009, Schleh et al., 2011). The main physiological function of lung surfactant is to reduce γ during exhalation to near zero values in order to prevent the collapse of the lungs and, thus, it is absolutely essential for life. Several studies have shown that NPs interact with lung surfactant components and impede the ability of surfactant to reduce γ (Bakshi et al., 2008, Schleh et al., 2009, Valle et al., 2014). This interaction may also modify the NP properties and therefore, any toxic effects or bioreactivity (Maynard, 2002, Maier et al., 2006, Harishchandra et al., 2010, Hu et al., 2013). In addition to this, some studies indicate that surfactant displaces particles into the alveolar subphase fluid where they can come into contact with the alveolar epithelium and associated macrophages (Schürch et al., 1990, Geiser et al., 2003, Hu et al., 2013). Some *in vivo* studies indicate that a low percentage of some types of NPs have the potential to translocate across the alveolar epithelium and into the lymphatic and circulatory system and cause damage to respiratory, cardiovascular, neurological, hepatic and gastrointestinal tissues (Oberdörster et al., 2002, Kreyling et al., 2002, Xia et al., 2009). Little is known of the interactions between ENPs and lung surfactant but this is crucial to gain a full understanding of how inhaled airborne NPs might enter the body and cause systemic health problems.

The aim of these studies was to elucidate if the interaction of two commonly used ENPs – CeO₂ and CB – with monolayers of the most abundant component of lung surfactant, DPPC, altered its functional activity, by measuring the Π -Mma isotherm using a LWB. In addition, the effect of DPPC on particle behaviour was studied using a range of imaging techniques in parallel with particle characterisation before and during the individual experiments.

This work was unique in that it involved: (a) the development of a realistic air-to-surfactant particle deposition system using a LWB and (b) the investigation of the effect of different NP deposition methods on the DPPC isotherm. In other reported studies, NPs have been delivered onto the air/liquid interface using liquid suspensions, mostly for ease of application. This is not representative of *in vivo* deposition of NPs, as in the alveoli NPs are primarily deposited from the air onto the surfactant layer by diffusion. Comparison of the effects of the different NP deposition techniques allows an assessment of the adequacy of the liquid deposition methods as models for investigating the effects of inhaled NPs on lung surfactant function.

Initial studies were undertaken to optimise the experimental set-up and procedures, including an investigation of the impact on the DPPC isotherm of using conditions more physiologically relevant than those frequently employed in the literature.

There are a number of parameters that can be used to describe isotherms. On the basis of a consideration of those used in other studies in the literature, in this work, DPPC *II*-Mma isotherms were systematically described in terms of four different characteristics of the curve: the lift-off Mma, the two-dimensional compressibility (C_m) of different regions of the isotherm, the collapse *II* and the collapse Mma. We established a rule to reject or accept measured isotherms to calculate an average DPPC isotherm.

An accurate lift-off Mma for the DPPC isotherm for the most common experimental conditions was determined using a well characterised DPPC solution (i.e. concentration determined by enzymatic-colorimetric assay). These were 99 and 100 Å²/molecule for the DPPC isotherm measured in water and PBS at 21°C respectively and 112 and 123 Å²/molecule for the DPPC isotherm measured in water and PBS at 37°C respectively. These accurate ‘reference’ lift-off Mma values were then used to estimate the amount of DPPC material deposited onto the air/liquid interface using other solutions for which the DPPC concentration was not known so accurately by using the lift-off area of the isotherm.

Typically in the literature results for similar studies are presented without an associated indication of the uncertainty/variability and consequently comparisons between isotherms for different experimental conditions are discussed in a descriptive, broadly qualitative manner rather than quantitatively (Bringezu et al., 2002, Harishchandra et al., 2010, Tatur and Badia, 2011, Guzmán et al., 2011). We wanted to establish criteria to compare an experimental

isotherm with the control in a more quantitative and consistent way that could be used for all experiments. We determined the expected variability on measured ‘reference’ DPPC isotherms, and criteria to compare an experimental isotherm with its associated control isotherm in a quantitative and consistent way for all experiments based on use of the reference isotherm uncertainty values. The assumption was made that the variability on both the control and experiment isotherm parameter values was approximately the same as that evaluated for the reference DPPC isotherm.

Results indicated that isotherms produced at body temperature (37°C) differed from those produced at temperatures typically used in the literature (21°C), and those produced with a PBS subphase differed from those using a water subphase. Thus our hypothesis, that a DPPC isotherm measured under conditions similar to those occurring in the alveoli would differ from that measured under more common experimental conditions, was confirmed except for the case of the ambient relative humidity; the DPPC isotherm was the same under ambient and high relative humidity. Based on this data, when investigating NP-DPPC interactions the DPPC isotherm was typically measured under conditions close to those occurring *in vivo* by using a PBS subphase at 37°C, and reaching near zero γ values in some LB monolayer deposition experiments. For comparative purposes, additional experiments using PBS at 21°C were undertaken and for one of the NP deposition methods some experiments were also performed in PBS and water. Results showed that CeO₂ NPs behaved differently at the air/liquid interface for each subphase composition.

A LWB system requires low barrier speeds to allow the monolayer to reorganise itself but also to avoid the creation of waves at the interface which may interfere with the Π measurements (Zuo et al., 2008c). As such, a barrier speed of 5 mm/min (2.5 cm²/min) was chosen in all the experiments in the present studies when performed in a small trough (unless otherwise specified). Nevertheless, even if the monolayer had been compressed at maximum barrier speed (270 mm/min) it would still have been much slower than the situation *in vivo*; the frequency of the inhalation-exhalation breathing cycle is 10-15 times per minute whereas with a small Langmuir trough it is only possible to complete 2 full cycles per minute.

Our overarching hypothesis anticipated that the method of delivery of NPs to the DPPC monolayer would differentially affect the nature and profile of the DPPC isotherm. Three deposition methods were used. In the first method, CeO₂ NPs were suspended in chloroform

and deposited onto a DPPC monolayer using a microsyringe. Deposition method 2 consisted of mixing DPPC and CeO₂ NPs in the same chloroform suspension and depositing the mixture onto a clean liquid subphase using a microsyringe. In the third deposition method, CeO₂ NPs in aerosol form were deposited onto a DPPC monolayer. For this method a novel aerosol exposure system was developed which consisted of a TSI COA, which is a device that generates NP aerosols, an exposure chamber where the Langmuir trough was placed and an airflow system that distributed the aerosolised NPs through the chamber.

In brief, deposition method 1 had no effect upon the DPPC isotherm during the initial compression of the monolayer at any deposited mass level. Based on SEM and ToF-SIMS images, one hypothesis for this behaviour was that the CeO₂ NPs rapidly agglomerated into large and dense clusters and entered the subphase. This is supported by initial studies which indicated that CeO₂ NPs were very unstable in PBS, rapidly agglomerating and sedimenting out, due to their isoelectric point of 8 (Baalousha et al., 2012b) and the pH of PBS 7. Hence, only small CeO₂ NPs agglomerates remained at the surface at levels too low to affect the isotherm.

Deposition method 2 shifted the isotherm to higher Π values and, for those experiments performed at 21°C, obscured the LE-LC transition plateau, which became less horizontal with CeO₂ NP mass deposited. Based on SEM and ToF-SIMS images, it was hypothesised that this was caused by the presence of agglomerates of CeO₂ NPs at the interface at early stages of compression large and dense enough to experience repulsive forces between them (Huang et al., 2001a, Huang et al., 2001b) and subsequently affect the isotherm. It was assumed that the presence of CeO₂ NPs in the lipid monolayer would also have reduced the available surface area per surfactant molecule enabling DPPC to increase the Π at an earlier stage of compression. Agglomerates increased in surface concentration up to a Π value of 40 mN/m and then decreased with further compression probably due to the formation of larger and denser agglomerates with compression that detached from the interface and sedimented into the subphase. The results indicated that CeO₂ NPs were more stable at the air/PBS interface due to the coating with DPPC as compared to CeO₂ NPs in chloroform deposited onto a PBS subphase.

Deposition method 3 only affected the final region of the isotherm starting at a $\Pi \sim 30$ mN/m by decreasing the C_m and increasing the collapse Π , also in a mass-dependant manner. Based on SEM and ToF-SIMS images, it was hypothesised that the presence of CeO₂ NP agglomerates

of a similar size homogeneously spread across the surface improved the surfactant film containment. Agglomerates increased in surface concentration up to a Π value of 70 mN/m, indicating minimal if any losses to the subphase, which was probably a result of the low degree of agglomeration of CeO₂ NPs.

For each of the deposition methods, experiments were performed at body temperature (37°C) and compared with those at 21°C, which is the temperature most commonly used in studies in the literature. Results showed that the effects on the isotherm were similar but more pronounced when working at body temperature compared to 21°C. This would imply that NP doses that did not have an effect when working at 21°C might have an effect at 37°C. Based on these results, our study hypotheses were confirmed, in that the method of depositing NPs onto the air/liquid interface differentially affected the DPPC isotherm and the effects of NPs on the DPPC isotherm were mass-dependant and modified by the subphase temperature.

The deposition of NPs in aerosol form is considered the most physiologically realistic model of inhaled NP interactions with lung surfactant; the use of liquid suspensions to deliver NPs onto the air/liquid interface is not representative of *in vivo* deposition of inhaled NPs as in the alveoli the main mechanism for deposition of airborne NPs is diffusion and it is expected that aerosol NP deposition will be spatially uniform (Bahk and Isawa, 1994) and that NPs will not be able to interact with each other because of the large inter-particle distances. However, this deposition method had several limitations: for example, there were issues with the influence of the carrier gas on the monolayer in the absence of NPs in this study that need to be further investigated before such conclusions can be confirmed. Moreover, depositing NPs when the DPPC monolayer was in a G phase, as was done in the present work for all the deposition methods, implies that surfactant molecules were not in the same physical state as would be found *in vivo* where molecules are more closely packed to generate a more ordered phase. This could lead to different NP-lung surfactant interactions and different effects on the isotherm. It is also important to note that although CeO₂ NPs of the same primary particle size were used in each case, the size of the agglomerates introduced to the system differed significantly, and it is therefore difficult to establish whether the differences in the effects on the isotherm during an initial compression were due to the deposition method alone or the agglomerate size or a combination of the two factors. Future research directed towards examining this in more detail is needed. In all cases the results indicate that the degree of NP agglomeration is probably one of the most important determining factors of the NP effects on the DPPC isotherm with larger

and denser agglomerates having a greater effect on the isotherm compared to smaller homogeneously spread NP clusters. Even if aerosol NPs were deposited onto a DPPC monolayer at very low Π values instead of a more physiologically relevant Π range (i.e., from ~ 45 to ~ 70 mN/m), the present work shows that the use of liquid suspension to deposit NPs onto the air/liquid interface increased the agglomeration of NPs at the interface which is unlikely to occur *in vivo*.

The present work also addressed the hypothesis that the effects of aerosolised CB NPs on the functional activity of DPPC would be similar to those seen for aerosolised CeO₂ NPs. The results, although somewhat less clear, supported this hypothesis; showing a clear trend of decreasing C_m for the region 30-45 mN/m with CB NP mass deposited compared to the control isotherm. Based on the SEM images, it was hypothesised that the presence of CB NP agglomerates of a similar size homogeneously spread across the surface improved the film containment in a similar way to aerosolised CeO₂ NPs.

5.2 Potential effects of the inhalation of nanoparticles on lung surfactant function *in vivo*

Regarding the potential effects of the inhalation of NPs on lung surfactant function *in vivo*, only the effects of the aerosol CeO₂ NPs on the DPPC isotherm will be taken into consideration, as the other two deposition methods were not considered realistic air-to-surfactant particle deposition models. As already mentioned, aerosol CeO₂ NPs affected the DPPC isotherm by decreasing the C_m and increasing the collapse Π , suggesting improved monolayer stability. It is however difficult to interpret these results in terms of a physiological impact at the lung level for a number of reasons.

In normal healthy lungs, γ is reduced to near zero values at the end of exhalation, but this was not reached when using a conventional Langmuir trough due to leakage problems. How NPs would have affected lung surfactant function if a leak-proof system and a natural lung surfactant had been used is not clear. One possibility is that at some point during the compression of the interface and due to the presence of NPs, the reduction in the area available would aid lung surfactant to reach near zero γ values at higher areas than normal. This may affect the mechanics of breathing. It is also possible that these small agglomerates present at the interface may not have an important effect on the isotherm at the masses involved. However, this would need to

be investigated further using techniques such as AFM, BAM or Fluorescence Microscopy as the lung surfactant domains may still be affected by the presence of the NPs. For individuals with compromised lungs, e.g. patients with lung surfactant dysfunction, γ at the end of exhalation may be higher than zero. This would mean that exposure to aerosol NPs could potentially be beneficial by decreasing the minimum γ at the end of exhalation and with it decreasing the likelihood of alveolar collapse, increasing functional residual capacity and increasing lung compliance. However, such conclusions are highly speculative and clearly controversial and require significant further investigation using a leak-proof system in order to reach lower γ values (see section 5.3).

Finally, the CeO₂ NP doses used in the present work were significantly higher than those that would result from inhalation exposure at current airborne concentration levels. For example, in the present work, masses varying from 1 μg to 59 μg were deposited onto a liquid surface area of 76 cm². However, and as already mentioned in section 3.2.3.2, the CeO₂ NP dose that would be retained in the lungs, based on data from an airborne monitoring site in Newcastle, was predicted to be 230 ng over a period of 20 years (7h/day, 7 days/week) (Park et al., 2008). This would mean an exposure of 0.03 ng per day for a total alveolar surface area of 70 m², equivalent to a dose of $3 \cdot 10^{-6}$ ng per trough area (76 cm²). The concentrations used in the present work were between $3 \cdot 10^8$ and $2 \cdot 10^{10}$ times higher than the estimated environmental exposures. It is however important to note that large NP concentrations are usually needed to induce *in vitro* surfactant inhibition when depositing them as liquid suspensions (Valle et al., 2015). Moreover, CeO₂ NPs and other NPs may be present at higher concentrations, particularly in industrial and occupational settings. At least one study (Valle et al., 2015) has demonstrated effects on surfactant properties of aerosol concentrations comparable to those defined in international occupational exposure limits (OELs). This study will be further discussed in the next section.

5.3 Recommendations and future studies

The present work has provided critical information on the importance of both the method of delivery of NPs to the DPPC monolayer and the use of physiologically relevant experimental conditions when studying NP-lung surfactant interactions. However, in addressing our hypotheses, a number of further questions and recommendations were raised; we believe addressing these should take precedence in any future studies related to the present work.

The present work showed that the LWB system was a very sensitive apparatus and it was difficult to obtain reproducible results primarily due to leakage problems. The amount of surfactant lost from the interface should be proportionally lower in a medium trough (238 cm²) compared to a small trough (76 cm²) which would improve the reproducibility of the isotherm measurements. Additionally, it was found that working with a medium trough allowed the monolayer to reach a higher collapse Π . Therefore, a recommendation for future studies would be to work with larger trough sizes as described elsewhere (Tchoreloff et al., 1991, Klopfer and Vanderlick, 1996, Toimil et al., 2010, Zhang et al., 2011b).

With respect to the subphase volume, and as mentioned earlier, it was discovered in the present studies that reducing the volume from 62 mL to 50 mL considerably improved the monolayer containment, leading to the achievement of near zero γ values. Thus it would be very useful to repeat some experiments from the present work using this low subphase volume to gain a better understanding of how NPs would affect the DPPC isotherm in a reduced leakage environment. For example, and as already mentioned, aerosol CeO₂ NPs increased the collapse Π of the DPPC isotherm when working with normal subphase volumes. It is not clear how NPs would have affected the isotherm if a leak-proof system had been used. Moreover, a recommendation for future studies would be to always use this low subphase volume when working with conventional Langmuir troughs.

The present work also showed that, for the aerosol NP experiments, the exposure of a DPPC monolayer to the carrier gas flow in the absence of NPs had a remarkable effect on the DPPC isotherm, which increased with the exposure duration. It is not clear exactly what was causing this effect and thus it requires further investigation, possibly by exploring the effects of systematically changing the flow rate and/or the air flow path within the exposure chamber. It would also be relevant to investigate if the airflow modified the phase behaviour of the monolayer, as the effect of aerosol NPs on the DPPC isotherm would have been different if the airflow had not affected the surfactant film. Without a better understanding of this effect it is difficult to interpret the aerosol NP effect on the DPPC isotherm and subsequently compare it with the other deposition methods. Moreover, such studies would help to optimise the aerosol exposure system.

We also discovered that the manner of deposition of CeO₂ NPs on a monolayer had a clear influence on the monolayer behaviour. However, the agglomerate size introduced into the

system differed significantly depending on the mode of delivery. This raises the question of whether the effects seen were driven by the agglomerate size, the deposition method alone or a combination of the two factors. This requires further research and could be explored using different agglomerate sizes as well as different primary particle sizes.

In the present work we investigated the capacity of CeO₂ NPs to remain at the air/liquid interface during one compression and after several compression-expansion cycles in the presence of DPPC. For deposition methods 1 and 2, it was hypothesised that CeO₂ NPs detached from the interface and sedimented into the subphase at some point during the compression whereas for deposition method 3 it was believed that CeO₂ NPs remained at the interface increasing in surface concentration with compression. Unfortunately, although comparative quantitative data were discussed, no absolute quantitative analysis of the ToF-SIMS images was undertaken to estimate the CeO₂ NP mass present and whether this changed with the number of compression cycles. This would have been challenging as the detection limit of this technique is ~ 300 nm and CeO₂ NP agglomerates had a lower size before administration. The results of ICP-MS analysis of the subphase were also inconclusive in terms of identifying the presence of the CeO₂ NPs. This potential loss to the subphase is clearly something which needs to be investigated further, by, for example, using different *in situ* imaging techniques, including BAM or Fluorescence Microscopy, to explore how CeO₂ NP agglomerates grow with compression. Further development of the application of ICP-MS to this system would also be useful to enable quantification of CeO₂ in the subphase.

As previously mentioned, for deposition method 1 and deposition method 2 some experiments were performed in both PBS and water. SEM and ToF-SIMS images showed that CeO₂ NPs behaved differently at the air/liquid interface for each subphase composition, with and without the presence of DPPC, with a greater amount of NPs remaining at the interface when using a water subphase compared to PBS. The effect of CeO₂ NPs on the *II*-Mma isotherm when using a water subphase was not studied in the present work but is clearly something that needs to be explored further especially as most of the literature studies that investigate NP-lung surfactant interactions use a water subphase.

In the present work, the effect of NPs on the DPPC domains was not investigated as the only technique available to us at the time to study the structure of films at the air/PBS interface, including those incorporating NPs, was AFM. This technique gives information about the

topography of the film surface with a nanometre scale resolution, however it was not suitable for the present study as NPs could not be clearly differentiated from salt crystals formed during the evaporation of PBS and the presence of salt across the surface made it difficult to visualise the domains. However, it would be useful to study the DPPC domains using other *in situ* imaging techniques including BAM or Fluorescence Microscopy, as other literature studies have shown that even if the NPs did not have an effect on the isotherm, they did on the nucleation, growth and morphology of the DPPC domains (Tatur and Badia, 2011, Dwivedi et al., 2014). These techniques could also be used to explore how aerosol NPs were capable of improving the film containment or stability of the DPPC monolayer.

As the physiologically relevant Π range in healthy lungs is confined to between Π_e and the collapse Π of the film, i.e., from ~ 45 to ~ 70 mN/m (Piknova et al., 2002, Zuo et al., 2008c), ideally, NP and lung surfactant interactions should be studied in this Π range. Unfortunately working within this Π range would be very challenging for a conventional LWB system because of leakage issues, however, this could usefully be explored further (see, for example, earlier comments on the use of lower subphase volume). Moreover, depositing NPs or investigating NP-lung surfactant interactions at very low Π values, as is typically done when using a LWB, means that the surfactant molecules are not in the same physical state as would be found *in vivo*, which could lead to different NP-lung surfactant interactions. For example, in the present work and other studies that have used DPPC as a model lung surfactant, NPs were deposited onto the air/liquid interface when the monolayer was in the G phase (Stuart et al., 2006, Harishchandra et al., 2010, Tatur and Badia, 2011, Guzmán et al., 2011). In this phase the molecules are widely separated and move independently like a two-dimensional gas. Compressing from this phase could enable DPPC molecules to pack around the NPs or rearrange themselves to fit in whatever space is available. At Π values between 45-70 mN/m, however, DPPC molecules are more closely packed to generate a more ordered phase and the layer is more rigid. In fact, physiological evidence suggests that the natural lung surfactant film must have a very low compressibility contributing to lung recoil (Valle et al., 2015). Depositing NPs onto a DPPC monolayer whilst in this range might thus result in a different effect upon the isotherm. The possibility of undertaking such studies using a LWB could usefully be investigated further, or the use of alternative systems, such as a constrained drop surfactometer (Valle et al, 2015), which also has the advantage of a fast cycle time that more closely mimics the breathing cycle, could be considered. It is important to note in this context that although the LE-LC transition

plateau is studied in depth in the literature when investigating DPPC-NP interactions, it has limited physiological relevance for the aforementioned reasons.

As previously mentioned in chapter 2, DPPC was chosen in the present work as a model lung surfactant as it is a low γ stabiliser and there is evidence that it is the only lung surfactant phospholipid capable of forming a LC phase and reaching a near zero γ on compression with a LWB (Smith and Berg, 1980, Zhang et al., 2011b). DPPC monolayer properties and phase states have also been widely investigated for many years for lung surfactant and other biological system studies (Tatur and Badia, 2011, Guzmán et al., 2011, Melbourne et al., 2015). Moreover, it is expected that as DPPC is the major component of lung surfactant, alteration in its phase behaviour would consequently cause alteration in the phase behaviour of the lung surfactant (Dwivedi et al., 2014). However, in the present work, at normal operating conditions, DPPC could not reach near zero γ due to leakage problems associated with the LWB apparatus. DPPC is also incapable of adsorbing and re-spreading quickly into the air/liquid interface (Walters et al., 2000). From a surface activity perspective, there are three biophysical properties that a functional lung surfactant should have for normal respiratory physiology (King and Clements, 1972, Notter, 2000, Serrano and Pérez-Gil, 2006): (a) rapid film formation through adsorption of surface molecules from the alveolar subphase fluid into the air/liquid interface; (b) γ reduction to near zero values upon film compression during exhalation and (c) effective re-spreading of the surface active material to cover the expanded area during inhalation in order to maintain the low γ . Moreover, experimental evidence and morphological observations have shown that at least part of the lung surfactant film consists of a multilayer (Schürch et al., 2001, Zuo et al., 2008c). In fact, the human surfactant monolayer has not yet been successfully demonstrated (Veldhuizen et al., 1998, Schürch et al., 2001). Due to the multilayer nature of the lung surfactant the concepts of LE and LC phases defined for monolayers are not directly applicable (Zuo et al., 2008a).

For all the above reasons, and in view of the highly complex and dynamic nature of the natural lung surfactant film, other studies have investigated lung surfactant and NP interactions using lung surfactant models other than DPPC such as mixtures of DPPC and cholesterol (Guzmán et al., 2013), DOPC and mixtures of DOPC and DPPC (Guzmán et al., 2012a), mixtures of DPPC and palmitic acid (Guzmán et al., 2012c), mixtures of DPPC, DPPG and SP-C (Harishchandra et al., 2010, Sachan et al., 2012, Dwivedi et al., 2014), Infasurf (Fan et al., 2011, Hu et al., 2013, Valle et al., 2014) and Survanta (Tatur and Badia, 2011). Some of these studies

compared the effects of the same NP on the DPPC monolayer and on other model lung surfactant mixtures. For example, Tatur and Badia, 2011 showed that hydrophobic alkylated gold NPs altered the nucleation, growth and morphology of the condensed domains in monolayers of DPPC but not of those of Survanta. It would therefore be very interesting to investigate, in future studies, the effects of aerosolised NPs on other more complex lung surfactant preparations such as those obtained from animal sources or human samples obtained by bronchoalveolar lavage.

As stressed earlier, the investigation of NP-lung surfactant interactions should be done under conditions as close as possible to those occurring *in vivo*. Other studies have shown that the investigation of lung surfactant under conditions not found in the human lungs has led to erroneous conclusions about the intrinsic properties of lung surfactant, and something similar could happen when investigating NP-lung surfactant interactions. For example, studies have shown that cholesterol alters the surfactant film by the variation of the collapse mechanism (Zhang et al., 2011a). There is however some evidence that this finding may be related to the experimental methodology, particularly to leakage artifacts of the devices used to measure Π . Leakage may have been more likely in relatively more fluid cholesterol containing films, which would have produced a film collapse at a Π value lower than expected for the same film without cholesterol (Blanco and Pérez-Gil, 2007, Zhang et al., 2011a). Another example is that, for many years it was believed that DPPC was the only constituent capable of reaching near zero γ on compression with a LWB (Smith and Berg, 1980, Zhang et al., 2011b) and as such, it was assumed that less stable fluidising non-DPPC components were selectively removed from the interfacial monolayer during compression, which would result in a pure DPPC monolayer at very low γ values (Watkins, 1968, Clements, 1977). This theoretical model has been challenged as other studies have shown that some fluid non-DPPC phospholipids can reach near zero γ values on compression at very high speeds with a captive bubble surfactometer (Crane and Hall, 2001, Smith et al., 2003). Such rates have never been achieved with a LWB. Therefore, a monolayer of DPPC is not required for reaching near zero γ values. Consequently, the investigation of NP and lung surfactant interactions under conditions not found in the human lung could lead to erroneous conclusions about the effects of NPs on lung surfactant function.

The above serves to re-inforce earlier comments on the need in future experimental studies to investigate the effect of NPs on the surface tension properties of lung surfactant, for careful

consideration of the appropriate experimental techniques, conditions and lung surfactant model to use.

To date, few studies have systematically investigated the physicochemical properties that govern the deposition of NPs onto lung surfactant, the displacement of NPs into lung surfactant and the translocation of NPs across lung surfactant. This is crucial to gain a full understanding of how NPs might impact on surfactant function, and potentially enter the body and cause systemic health problems. Moreover, future studies should also focus on investigating the effects of NPs on the other two key biophysical properties that a functional lung surfactant should have for normal respiratory physiology: (a) rapid film formation through adsorption of surface active molecules from the alveolar subphase fluid into the air/liquid interface and (b) effective re-spreading of the surface active material to cover the expanded area during inhalation in order to maintain the low γ . To date, however, there are a limited number of studies that have investigated the effects of NPs on lung surfactant properties using biophysical techniques and much remains to be explored in this area.

5.4 Scientific results for publication in peer-reviewed journals

Notwithstanding some methodological issues which require further investigation (for example the effect of the carrier gas flow on the monolayer or the deposition of NPs on compressed monolayers), the need to use other techniques to understand the underlying mechanisms/monolayer changes in relation to NPs (for example the study of the effects of NPs on the DPPC domains using in situ imaging techniques including BAM or Fluorescence Microscopy) and the need to repeat some experiments using more complete lung surfactant models, the following has been successfully accomplished:

- Development of a novel system for the deposition of well characterised aerosols onto monolayers using a LWB with associated methodologies for determining deposition levels and spatial distribution. This has not previously been addressed/published. This is of importance as it mimics deposition by aerosol within the lung and it provides details of an approach that could be adopted by other workers in the field. Other papers have referred to the importance of looking at aerosol deposition (Stuart et al., 2006, Valle et al., 2015).

- Undertaken a comparison of the effect of the method of NP deposition on the surface tension behaviour of DPPC monolayers using 3 different techniques. This included the two major techniques used in literature studies (NPs suspended in a volatile solvent and deposited onto a preformed surfactant monolayer and NPs mixed with the surfactant in a volatile solvent prior to being deposited onto a liquid subphase) as well as the deposition of NPs by aerosol onto a surfactant monolayer. Such a comparison, even between the two most common techniques, has not been published before. The results suggest that the method of deposition can have a marked effect on subsequent monolayer behaviour. This is an important conclusion for researchers in this area and for the interpretation of results from other studies.
- Undertaken a study of the effect of CeO₂ NPs on the surface tension behaviour of DPPC. This is the only study we are aware of that has studied the effect of CeO₂ NPs on the surface tension behaviour of a lung surfactant model.
- Undertaken a study of the effect of CB NPs on the surface tension behaviour of DPPC for comparison with CeO₂ NPs. There are very few papers in which the effects of different NPs have been compared with each other.
- Imaged the interface after performing three compression-expansion cycles for each of the deposition experiments rather than focusing on one compression only, to investigate how the system would evolve after several simulated inhalation-exhalation breathing cycles. In the literature very few studies have performed recycling when investigating NP-lung surfactant interactions.
- Undertaken a comparison of the results (a) when using a PBS and a water subphase, (b) when working with subphase temperatures of 21°C and 37°C and (c) when using a low and a normal subphase volume and thus, achieving and not achieving near zero surface tension values respectively. Such comparisons have not previously been performed. The present work has shown that for each variable (subphase composition, subphase temperature and subphase volume), each condition led to different results. Moreover, in the literature, most of the studies used a water subphase, a subphase temperature of 21°C and conventional Langmuir troughs to investigate NP-DPPC interactions. The results shown in the present studies emphasise the importance of measuring isotherms under conditions as close as

possible to those occurring *in vivo*; performing experiments under unrealistic conditions makes it difficult to interpret the results in terms of a physiological impact at the lung level.

- Semi-quantitative assessment of the amount of NPs in the monolayer and of the agglomerate size. Of the approximately 20 published studies on the effect of NPs on lung surfactant surface tension behaviour using a LWB system (from 2006-2016) a number have failed to use any imaging techniques. The remainder have typically used only one technique: BAM, Fluorescence Microscopy or AFM, while advanced X-ray scattering approaches were only used in one study (You et al., 2016). The present work used a combination of techniques, ToF-SIMS and SEM imaging, to try to determine the amount of NPs remaining in the monolayer in a semi-quantitative manner.

Based on the information above, papers that could be prepared for publication in peer-reviewed journals such as Langmuir, Journal of Colloid and Interface Science and Biochimica et Biophysica Acta are as follows:

- The method for deposition of CeO₂ nanoparticles onto the air/liquid interface using DPPC as model lung surfactant and how this differentially affects lung surfactant function.
- Comparison of the effects of aerosolised CeO₂ nanoparticles with those of aerosolised CB nanoparticles using a Langmuir-Wilhelmy Balance.

REFERENCES

- ABD-ELHADY, M., ZAYED, S. & RINDT, C. Removal of dust particles from the surface of solar cells and solar collectors using surfactants. International Conference on Heat Exchanger Fouling and Cleaning, 2011. 5-10.
- ADEWUMI, M. 2016. *PV Diagram for Pure Systems* [Online]. Available: https://www.e-education.psu.edu/png520/m3_p3.html [Accessed].
- AKINO, T. T. 1992. Biochemical and Clinical Aspects of Pulmonary Surfactant Proteins. *Nihon Kyōbu Shikkan Gakkai zasshi* 30, 5-14
- AL-HALLAK, M. K., AZARMI, S., SUN, C., LAI, P., PRENNER, E. J., ROA, W. H. & LÖBENBERG, R. 2010. Pulmonary toxicity of polysorbate-80-coated inhalable nanoparticles; in vitro and in vivo evaluation. *The AAPS journal*, 12, 294-299.
- ALA'A, F., BRUNET, S. M. & PAIGE, M. F. 2012. A comparison of atomic force microscopy, confocal fluorescence microscopy and Brewster angle microscopy for characterizing mixed monolayer surfactant films.
- ALBRECHT, O., CUMMING, W., KREUDER, W., LASCHEWSKY, A. & RINGSORF, H. 1986. Monolayers of rod-shaped and disc-shaped liquid crystalline compounds at the air-water interface. *Colloid and Polymer Science*, 264, 659-667.
- ALIAS, A. K. 2013. *Emulsion stability* [Online]. Available: <http://www.slideshare.net/akarim717/emulsion-stability> [Accessed].
- ALONSO, C., WARING, A. & ZASADZINSKI, J. A. 2005. Keeping lung surfactant where it belongs: protein regulation of two-dimensional viscosity. *Biophysical journal*, 89, 266-273.
- ALVES, S., FERREIRA JR, S. & MARTINS, M. 2008. Strategies for optimize off-lattice aggregate simulations. *Brazilian Journal of Physics*, 38, 81-86.
- ATKINSON, R. W., FULLER, G. W., ANDERSON, H. R., HARRISON, R. M. & ARMSTRONG, B. 2010. Urban Ambient Particle Metrics and Health. A Time-series Analysis. *Epidemiology*, 21, 501-511.
- AUFFAN, M., ROSE, J., BOTTERO, J. Y., LOWRY, G. V., JOLIVET, J. P. & WIESNER, M. R. 2009a. Towards a definition of inorganic nanoparticles from an environmental, health and safety perspective. *Nature nanotechnology*, 4, 634-641.
- AUFFAN, M., ROSE, J., WIESNER, M. R. & BOTTERO, J. Y. 2009b. Chemical stability of metallic nanoparticles: A parameter controlling their potential cellular toxicity in vitro. *Environmental Pollution*, 157, 1127-1133.
- AVEYARD, R., CLINT, J. H., NEES, D. & PAUNOV, V. N. 2000a. Compression and structure of monolayers of charged latex particles at air/water and octane/water interfaces. *Langmuir*, 16, 1969-1979.

- AVEYARD, R., CLINT, J. H., NEES, D. & QUIRKE, N. 2000b. Structure and collapse of particle monolayers under lateral pressure at the octane/aqueous surfactant solution interface. *Langmuir*, 16, 8820-8828.
- AZIMI, G., DHIMAN, R., KWON, H.-M., PAXSON, A. T. & VARANASI, K. K. 2013. Hydrophobicity of rare-earth oxide ceramics. *Nature materials*, 12, 315-320.
- BAALOUSHA, M., JU-NAM, Y., COLE, P. A., GAISER, B., FERNANDES, T. F., HRILJAC, J. A., JEPSON, M. A., STONE, V., TYLER, C. R. & LEAD, J. R. 2012a. Characterization of cerium oxide nanoparticles part 1: size measurements. *Environmental Toxicology and Chemistry*, 31, 983-993.
- BAALOUSHA, M., JU-NAM, Y., COLE, P. A., HRILJAC, J. A., JONES, I. P., TYLER, C. R., STONE, V., FERNANDES, T. F., JEPSON, M. A. & LEAD, J. R. 2012b. Characterization of cerium oxide nanoparticles part 2: nonsize measurements. *Environmental Toxicology and Chemistry*, 31, 994-1003.
- BACHOFEN, H. & SCHÜRCH, S. 2001. Alveolar surface forces and lung architecture. *Comparative Biochemistry and Physiology Part A: Molecular & Integrative Physiology*, 129, 183-193.
- BACHOFEN, H., SCHURCH, S., URBINELLI, M. & WEIBEL, E. 1987. Relations among alveolar surface tension, surface area, volume, and recoil pressure. *Journal of Applied Physiology*, 62, 1878-1887.
- BAHK, Y. W. & ISAWA, T. 1994. Radioaerosol imaging of the lung. An IAEA [CRP] group study. International Atomic Energy Agency.
- BAILEY, M. R. & PUNCHER, M. R. B. 2007. *Uncertainty Analysis of the ICRP Human Respiratory Tract Model Applied to Interpretation of Bioassay Data for Depleted Uranium*, Health Protection Agency.
- BAILEY, S. 1984. Classification and structures of the micas. *Reviews in Mineralogy and Geochemistry*, 13, 1-12.
- BAKAND, S., HAYES, A. & DECHSAKULTHORN, F. 2012. Nanoparticles: a review of particle toxicology following inhalation exposure. *Inhalation toxicology*, 24, 125-135.
- BAKSHI, M. S., ZHAO, L., SMITH, R., POSSMAYER, F. & PETERSEN, N. O. 2008. Metal Nanoparticle Pollutants Interfere with Pulmonary Surfactant Function In Vitro. *Biophysical Journal*, 94, 855-868.
- BAOUKINA, S., MONTICELLI, L., RISSELADA, H. J., MARRINK, S. J. & TIELEMAN, D. P. 2008. The molecular mechanism of lipid monolayer collapse. *Proceedings of the National Academy of Sciences*, 105, 10803-10808.
- BAOUKINA, S., ROZMANOV, D., MENDEZ-VILLUENDAS, E. & TIELEMAN, D. P. 2014. The mechanism of collapse of heterogeneous lipid monolayers. *Biophysical journal*, 107, 1136-1145.

- BARNES, G. T. & GENTLE, I. R. 2011. *Interfacial science: an introduction*, New York, Oxford University Press.
- BEAUMONT, J. 2005. *The Potential of Nanotechnology* [Online]. Available: [www.researchgate.net/publications.PublicPostFileLoa](http://www.researchgate.net/publications/PublicPostFileLoa) [Accessed].
- BENSON, B., WILLIAMS, M., SUEISHI, K., GOERKE, J. & SARGEANT, T. 1984. Role of calcium ions in the structure and function of pulmonary surfactant. *Biochimica et Biophysica Acta (BBA)-Lipids and Lipid Metabolism*, 793, 18-27.
- BERNHARD, W., MOTTAGHIAN, J., GEBERT, A., RAU, G. A., VON DER HARDT, H. & POETS, C. F. 2000. Commercial versus native surfactants: surface activity, molecular components, and the effect of calcium. *American Journal of Respiratory and Critical Care Medicine*, 162, 1524-1533.
- BINDER, H. & ZSCHÖRNIG, O. 2002. The effect of metal cations on the phase behavior and hydration characteristics of phospholipid membranes. *Chemistry and physics of lipids*, 115, 39-61.
- BINKS, B. P. 2002. Particles as surfactants—similarities and differences. *Current opinion in colloid & interface science*, 7, 21-41.
- BLANCHETTE, C. D., ORME, C. A., RATTO, T. V. & LONGO, M. L. 2008. Quantifying growth of symmetric and asymmetric lipid bilayer domains. *Langmuir*, 24, 1219-1224.
- BLANCO, O. & PÉREZ-GIL, J. 2007. Biochemical and pharmacological differences between preparations of exogenous natural surfactant used to treat Respiratory Distress Syndrome: Role of the different components in an efficient pulmonary surfactant. *European journal of pharmacology* 568, 1-15
- BLAUDEZ, D., TURLET, J.-M., DUFOURCQ, J., BARD, D., BUFFETEAU, T. & DESBAT, B. 1996. Investigations at the air/water interface using polarization modulation IR spectroscopy. *Journal of the Chemical Society, Faraday Transactions*, 92, 525-530.
- BORM, P. J. A., ROBBINS, D., HAUBOLD, E., KUHLBUSCH, T., FISSAN, H., DONALDSON, K., SCHINS, R., STONE, V., KREYLING, W., LADEMANN, J., KRUTMANN, J., WARHEIT, D. & OBERDÖRSTER, E. 2006. The potential risks of nanomaterials: a review carried out for ECETOC. *Particle and Fibre Toxicology* 3, 11.
- BOTHE, D. & PRÜSS, J. 2015. On the Interface Formation Model for Dynamic Triple Lines. *arXiv preprint arXiv:1504.04758*.
- BOULPAEP, E. L., BORON, W. F., CAPLAN, M. J., CANTLEY, L., IGARASHI, P., ARONSON, P. S. & MOCZYDLOWSKI, E. G. 2009. Medical Physiology a Cellular and Molecular Approach. *Signal Transduction*, 48, 27.
- BOURBON, J. R. 1991. *Pulmonary Surfactant: Biochemical, Functional, Regulatory, and Clinical Concepts*, Taylor & Francis.

- BOUWMEESTER, H., LYNCH, I., MARVIN, H. J., DAWSON, K. A., BERGES, M., BRAGUER, D., BYRNE, H. J., CASEY, A., CHAMBERS, G. & CLIFT, M. J. 2011. Minimal analytical characterization of engineered nanomaterials needed for hazard assessment in biological matrices. *Nanotoxicology*, 5, 1-11.
- BRADBURY, R. & NAGAO, M. 2016. Effect of charge on the mechanical properties of surfactant bilayers. *Soft Matter*, 12, 9383-9390.
- BRINGEZU, F., DING, J. Q., BREZESINSKI, G., WARING, A. J. & ZASADZINSKI, J. A. 2002. Influence of Pulmonary Surfactant Protein B on Model Lung Surfactant Monolayers. *Langmuir*, 18, 2319-2325
- BROWN, D. L. & PATTISHALL, E. N. 1993. Other uses of surfactant. *Clinics in perinatology*, 20, 761-789.
- BURNS, D. B. & ZYDNEY, A. L. 2000. Buffer effects on the zeta potential of ultrafiltration membranes. *Journal of membrane science*, 172, 39-48.
- CASILLAS-ITUARTE, N. N., CHEN, X., CASTADA, H. & ALLEN, H. C. 2010. Na⁺ and Ca²⁺ Effect on the Hydration and Orientation of the Phosphate Group of DPPC at Air–Water and Air–Hydrated Silica Interfaces. *The Journal of Physical Chemistry B*, 114, 9485-9495.
- CASSEE, F. R., VAN BALEN, E. C., SINGH, C., GREEN, D., MUIJSER, H., WEINSTEIN, J. & DREHER, K. 2011. Exposure, health and ecological effects review of engineered nanoscale cerium and cerium oxide associated with its use as a fuel additive. *Critical Reviews in Toxicology*, 41, 213-229.
- CAUSES-OF-COLOR. 2015. *Estimating bubble lifetimes* [Online]. Available: <http://www.webexhibits.org/causesofcolor/15E.html> [Accessed].
- CHATTORAJ, D. 2012. *Adsorption and the Gibbs surface excess*, Springer Science & Business Media.
- CHIPFUNHU, D., ZANIN, M. & GRANO, S. 2011. The dependency of the critical contact angle for flotation on particle size–Modelling the limits of fine particle flotation. *Minerals Engineering*, 24, 50-57.
- CHOI, S. Q., KIM, K., FELLOWS, C. M., CAO, K. D., LIN, B., LEE, K. Y. C., SQUIRES, T. M. & ZASADZINSKI, J. A. 2014. Influence of molecular coherence on surface viscosity. *Langmuir*, 30, 8829-8838.
- CHOU, T.-H. & CHANG, C.-H. 2000. Thermodynamic behavior and relaxation processes of mixed DPPC/cholesterol monolayers at the air/water interface. *Colloids and Surfaces B: Biointerfaces*, 17, 71-79.
- CHU, J., CLEMENTS, J., COTTON, E., KLAUS, M., SWEET, A. & TOOLEY, W. 1967. Neonatal Pulmonary Ischemia Part I: Clinical and Physiological Studies. *Pediatrics*, 40, 709-782.

- CHUNG, J. H., KITAICHI, M., HAM, E. K. & SEO, J. W. 1998. Immunohistochemical localization of surfactant apoproteins in usual interstitial pneumonia associated with pulmonary carcinoma. *Microscopy research and technique*, 42, 234-238.
- CLEMENTS, J. A. 1977. Functions of the Alveolar Lining 1, 2. *American Review of Respiratory Disease*, 115, 67-71.
- CLINT, J. H. & TAYLOR, S. E. 1992. Particle size and interparticle forces of overbased detergents: a Langmuir trough study. *Colloids and surfaces*, 65, 61-67.
- CLOGSTON, J. D. & PATRI, A. K. 2011. Zeta potential measurement. *Characterization of nanoparticles intended for drug delivery*. Springer.
- COLACICCO, G., BASU, M. K. & SCARPELLI, E. M. 1976. pH, temperature, humidity and the dynamic force-area curve of dipalmitoyl lecithin. *Respiration physiology*, 27, 169-186.
- COOK, G. J. R., MAISEY, N., BRITTON, K. E. & CHENGAZI, V. 2006. *Clinical Nuclear Medicine Fourth Edition*, Taylor & Francis.
- CRANE, J. M. & HALL, S. B. 2001. Rapid compression transforms interfacial monolayers of pulmonary surfactant. *Biophysical journal*, 80, 1863-1872.
- CRANE, J. M., PUTZ, G. & HALL, S. B. 1999. Persistence of phase coexistence in disaturated phosphatidylcholine monolayers at high surface pressures. *Biophysical journal*, 77, 3134-3143.
- CRANE, M., HANDY, R. D., GARROD, J. & OWEN, R. 2008. Ecotoxicity test methods and environmental hazard assessment for engineered nanoparticles. *Ecotoxicology*, 17, 421-437.
- CRAPO, J. D., BARRY, B. E., GEHR, P., BACHOFEN, M. & WEIBEL, E. R. 1982. Cell Number and Cell Characteristics of the Normal Human Lung 1-3. *American Review of Respiratory Disease*, 126, 332-337.
- CREUWELS, L., VAN GOLDE, L. & HAAGSMAN, H. 1997. The pulmonary surfactant system: biochemical and clinical aspects. *Lung*, 175, 1-39.
- CRUZ, A., VÁZQUEZ, L., VÉLEZ, M. & PÉREZ-GIL, J. 2004. Effect of pulmonary surfactant protein SP-B on the micro- and nanostructure of phospholipid films. *Biophysical journal*, 86, 308-320.
- DE GENNES, P.-G., BROCHARD-WYART, F. & QUÉRÉ, D. 2004. *Capillarity and wetting phenomena: drops, bubbles, pearls, waves*, Springer Science & Business Media.
- DE LA SERNA, J. B., PEREZ-GIL, J., SIMONSEN, A. C. & BAGATOLLI, L. A. 2004. Cholesterol Rules DIRECT OBSERVATION OF THE COEXISTENCE OF TWO FLUID PHASES IN NATIVE PULMONARY SURFACTANT MEMBRANES AT PHYSIOLOGICAL TEMPERATURES. *Journal of Biological Chemistry*, 279, 40715-40722.

- DEL RÍO, O. & NEUMANN, A. 1997. Axisymmetric drop shape analysis: computational methods for the measurement of interfacial properties from the shape and dimensions of pendant and sessile drops. *Journal of colloid and interface science*, 196, 136-147.
- DEPARTMENT-OF-INTERFACIAL-PHENOMENA. 2013. *Methods of surface tension measurements* [Online]. Available: <http://zsm.umcs.lublin.pl/Wyklad/FGF-Ang/2A.F.G.F.%20Surface%20tension.pdf> [Accessed].
- DEVRIES, C. A., HAYCRAFT, J. J., HAN, Q., NOOR-E-AIN, F., RAIBLE, J., DUSSAULT, P. H. & ECKHARDT, C. J. 2011. Reversible collapse of the Langmuir films of a series of triphenylsilyl ether-terminated amphiphiles. *Thin Solid Films*, 519, 2430-2437.
- DILLOW, A. & LOWMAN, A. 2002. *Biomimetic Materials and Design: Biointerfacial Strategies, Tissue Engineering and Targeted Drug Delivery*, CRC Press.
- DING, J. J., TAKAMOTO, D. Y., VON NAHMEN, A., LIPP, M. M., LEE, K. Y., WARING, A. J. & ZASADZINSKI, J. A. 2001. Effects of Lung Surfactant Proteins, SP-B and SP-C, and Palmitic Acid on Monolayer Stability. *Biophysical journal* 80, 2262-2272
- DONALDSON, K., STONE, V., SEATON, A. & MACNEE, W. 2001. Ambient Particle Inhalation and the Cardiovascular System: Potential Mechanisms. *Environmental Health Perspectives*, 109, 523-527.
- DONALDSON, K., TRAN, L., JIMENEZ, L. A., DUFFIN, R., NEWBY, D. E., MILLS, N., MACNEE, W. & STONE, V. 2005. Combustion-derived nanoparticles: a review of their toxicology following inhalation exposure. *Particle and fibre toxicology*, 2, 10.
- DORLAND'S-MEDICAL-DICTIONARY-FOR-HEALTH-CONSUMERS. 2007. *Alveolar sacs* [Online]. Available: <http://medical-dictionary.thefreedictionary.com/alveolar+sacs> [Accessed].
- DUNCAN, J. S. 1980. *Introduction to colloid and surface chemistry*, London, Butterworths.
- DUNCAN, S. L. & LARSON, R. G. 2008. Comparing experimental and simulated pressure-area isotherms for DPPC. *Biophysical journal*, 94, 2965-2986.
- DWIVEDI, M. V., HARISHCHANDRA, R. K., KOSHKINA, O., MASKOS, M. & GALLA, H.-J. 2014. Size influences the effect of hydrophobic nanoparticles on lung surfactant model systems. *Biophysical journal*, 106, 289-298.
- EEMAN, M. & DELEU, M. 2010. From biological membranes to biomimetic model membranes. *Base*.
- ERDEMLI, G. 2015. Lecture notes on human respiratory system physiology Available: http://www.liv.ac.uk/~gdwill/hons/gul_lect.pdf.
- EUROPEAN-COMMISSION. 2011. *Definition of a nanomaterial* [Online]. Available: http://ec.europa.eu/environment/chemicals/nanotech/faq/definition_en.htm [Accessed].

- FAHY, E., SUBRAMANIAM, S., BROWN, H. A., GLASS, C. K., MERRILL, A. H., MURPHY, R. C., RAETZ, C. R., RUSSELL, D. W., SEYAMA, Y. & SHAW, W. 2005. A comprehensive classification system for lipids. *Journal of lipid research*, 46, 839-862.
- FAN, Q., WANG, Y. E., ZHAO, X., LOO, J. S. & ZUO, Y. Y. 2011. Adverse biophysical effects of hydroxyapatite nanoparticles on natural pulmonary surfactant. *ACS nano*, 5, 6410-6416.
- FARRÉ, M., SANCHÍS, J. & BARCELÓ, D. 2011. Analysis and assessment of the occurrence, the fate and the behavior of nanomaterials in the environment. *Trends in Analytical Chemistry*, 30, 517-527.
- FENWICK, N., BRESME, F. & QUIRKE, N. 2001. Computer simulation of a Langmuir trough experiment carried out on a nanoparticulate array. *The Journal of Chemical Physics*, 114, 7274-7282.
- FIRST-TEN-ÅNGSTROMS. 2015. *USB 2 Camera Images* [Online]. Available: <http://www.firsttenangstroms.com/faq/USB2CameraImages.html> [Accessed].
- FLANDERS, B. N., VICKERY, S. A. & DUNN, R. C. 2002. Divergent Fluctuations in the Molar Area of a Model Lung Surfactant. *Journal of Physical Chemistry*, 106, 3530-3533
- FOLLOWS, D., TIBERG, F., THOMAS, R. & LARSSON, M. 2007. Multilayers at the surface of solutions of exogenous lung surfactant: direct observation by neutron reflection. *Biochimica et Biophysica Acta (BBA)-Biomembranes*, 1768, 228-235.
- FOX, G. F. & SOTHINATHAN, U. 2005. The choice of surfactant for treatment of respiratory distress syndrome in preterm infants: A review of the evidence. *Infant*, 1, 8-12.
- FRERKING, I., GÜNTHER, A., SEEGER, W. & PISON, U. 2001. Pulmonary surfactant: functions, abnormalities and therapeutic options. *Intensive care medicine*, 27, 1699-1717.
- GEHR, P., GREEN, F., GEISER, M., HOF, V. I., LEE, M. & SCHÜRCH, S. 1996. Airway surfactant, a primary defense barrier: mechanical and immunological aspects. *Journal of aerosol medicine*, 9, 163-181.
- GEISER, M., SCHÜRCH, S. & GEHR, P. 2003. Influence of surface chemistry and topography of particles on their immersion into the lung's surface-lining layer. *J Appl Physiol*, 94, 1793-1801.
- GHOSH, P. 2009. *Colloid and interface science*, PHI Learning Pvt. Ltd.
- GOERKE, J. 1998. Pulmonary surfactant: functions and molecular composition. *Biochimica et Biophysica Acta (BBA)-Molecular Basis of Disease*, 1408, 79-89.

- GOERKE, J. & GONZALES, J. 1981. Temperature dependence of dipalmitoyl phosphatidylcholine monolayer stability. *Journal of Applied Physiology*, 51, 1108-1114.
- GOTO, T. E. & CASELI, L. 2013. Understanding the collapse mechanism in Langmuir monolayers through polarization modulation-infrared reflection absorption spectroscopy. *Langmuir*, 29, 9063-9071.
- GOTTSCHLICH, M. M. 2001. *The Science and Practice of Nutrition Support: A Case-based Core Curriculum*, Kendall/Hunt Publishing Company.
- GRABAR, K. C., BROWN, K. R., KEATING, C. D., STRANICK, S. J., TANG, S.-L. & NATAN, M. J. 1997. Nanoscale characterization of gold colloid monolayers: a comparison of four techniques. *Analytical chemistry*, 69, 471-477.
- GRIESE, M. 1999. Pulmonary surfactant in health and human lung diseases: state of the art. *European Respiratory Journal*, 13, 1455-1476.
- GUMKOWSKI, G., GRAND ISLAND, N. & STEINMAN, A. 2014. Mitigating Electrostatic Effects on Measurement Accuracy.
- GUNASEKARA, L., SCHÜRCH, S., SCHOEL, W. M., NAG, K., LEONENKO, Z., HAUFS, M. & AMREIN, M. 2005. Pulmonary surfactant function is abolished by an elevated proportion of cholesterol. *Biochimica et Biophysica Acta (BBA)-Molecular and Cell Biology of Lipids*, 1737, 27-35.
- GUPTA, M., HERNANDEZ-JUVIEL, J., WARING, A. & WALTHER, F. 2001. Function and inhibition sensitivity of the N-terminal segment of surfactant protein B (SP-B1-25) in preterm rabbits. *Thorax*, 56, 871-876.
- GUZMÁN, E., LIGGIERI, L., SANTINI, E., FERRARI, M. & RAVERA, F. 2011. Effect of hydrophilic and hydrophobic nanoparticles on the surface pressure response of DPPC monolayers. *The Journal of Physical Chemistry C*, 115, 21715-21722.
- GUZMÁN, E., LIGGIERI, L., SANTINI, E., FERRARI, M. & RAVERA, F. 2012a. DPPC–DOPC Langmuir monolayers modified by hydrophilic silica nanoparticles: Phase behaviour, structure and rheology. *Colloids and Surfaces A: Physicochemical and Engineering Aspects*, 413, 174-183.
- GUZMÁN, E., LIGGIERI, L., SANTINI, E., FERRARI, M. & RAVERA, F. 2012b. Influence of silica nanoparticles on dilational rheology of DPPC–palmitic acid Langmuir monolayers. *Soft Matter*, 8, 3938-3948.
- GUZMÁN, E., LIGGIERI, L., SANTINI, E., FERRARI, M. & RAVERA, F. 2012c. Influence of silica nanoparticles on phase behavior and structural properties of DPPC–Palmitic acid Langmuir monolayers. *Colloids and Surfaces A: Physicochemical and Engineering Aspects*, 413, 280-287.

- GUZMÁN, E., LIGGIERI, L., SANTINI, E., FERRARI, M. & RAVERA, F. 2013. Mixed DPPC–cholesterol Langmuir monolayers in presence of hydrophilic silica nanoparticles. *Colloids and Surfaces B: Biointerfaces*, 105, 284-293.
- HAITSMA, J. J., PAPADAKOS, P. J. & LACHMANN, B. 2004. Surfactant therapy for acute lung injury/acute respiratory distress syndrome. *Current opinion in critical care*, 10, 18-22.
- HALL, S. B., VENKITARAMAN, A. R., WHITSETT, J. A., HOLM, B. A. & NOTTER, R. H. 1992. Importance of hydrophobic apoproteins as constituents of clinical exogenous surfactants. *Am Rev Respir Dis*, 145, 24-30.
- HALLIDAY, H. 2008. Surfactants: past, present and future. *Journal of perinatology*, 28, S47-S56.
- HANLY, G., FORNASIERO, D., RALSTON, J. & SEDEV, R. 2011. Electrostatics and metal oxide wettability. *The Journal of Physical Chemistry C*, 115, 14914-14921.
- HARBOTTLE, R. R., NAG, K., MCINTYRE, N. S., POSSMAYER, F. & PETERSEN, N. O. 2003. Molecular organization revealed by time-of-flight secondary ion mass spectrometry of a clinically used extracted pulmonary surfactant. *Langmuir*, 19, 3698-3704.
- HARISHCHANDRA, R. K., SALEEM, M. & GALLA, H.-J. 2010. Nanoparticle interaction with model lung surfactant monolayers. *J. R. Soc. Interface*, 7, 15-26.
- HARKINS, W. D. 1952. *The physical chemistry of surface films*, Reinhold.
- HARKINS, W. D. & BROWN, F. 1919. The determination of surface tension (free surface energy), and the weight of falling drops: The surface tension of water and benzene by the capillary height method. *Journal of the American Chemical Society*, 41, 499-524.
- HASSELLÖV, M., READMAN, J. W., RANVILLE, J. F. & TIEDE, K. 2008. Nanoparticle analysis and characterization methodologies in environmental risk assessment of engineered nanoparticles. *Ecotoxicology*, 17, 344-361.
- HAWGOOD, S. & CLEMENTS, J. A. 1990. Pulmonary surfactant and its apoproteins. *Journal of Clinical Investigation*, 86, 1.
- HEATH, J. R., KNOBLER, C. M. & LEFF, D. V. 1997. Pressure/temperature phase diagrams and superlattices of organically functionalized metal nanocrystal monolayers: the influence of particle size, size distribution, and surface passivant. *The Journal of Physical Chemistry B*, 101, 189-197.
- HELLAND, A., KASTENHOLZ, H., THIDELL, A., ARNFALK, P. & DEPPERT, K. 2006. Nanoparticulate materials and regulatory policy in Europe: an analysis of stakeholder perspectives. *Journal of Nanoparticle Research*, 8, 709-719.

- HELM, C., MÖHWALD, H., KJAER, K. & ALS-NIELSEN, J. 1987. Phospholipid monolayer density distribution perpendicular to the water surface. A synchrotron x-ray reflectivity study. *EPL (Europhysics Letters)*, 4, 697.
- HERRMANN, T. R., JAYAWEERA, A. R. & SHAMOO, A. E. 1986. Interaction of europium (III) with phospholipid vesicles as monitored by laser-excited europium (III) luminescence. *Biochemistry*, 25, 5834-5838.
- HIFEDA, Y. & RAYFIELD, G. 1992. Evidence for first-order phase transitions in lipid and fatty acid monolayers. *Langmuir*, 8, 197-200.
- HINDS, W. C. 2012. *Aerosol technology: properties, behavior, and measurement of airborne particles*, John Wiley & Sons.
- HOHELLA, M. F., LOWER, S. K., MAURICE, P. A., PENN, R. L., SAHAI, N., SPARKS, D. L. & TWINING, B. S. 2008. Nanominerals, mineral nanoparticles, and earth systems. *science*, 319, 1631-1635.
- HOET, P. H., BRÜSKE-HOHLFELD, I. & SALATA, O. V. 2004. Nanoparticles—known and unknown health risks. *Journal of nanobiotechnology*, 2, 12.
- HORIE, T. & HILDEBRANDT, J. 1971. Dynamic compliance, limit cycles, and static equilibria of excised cat lung. *Journal of applied physiology*, 31, 423-430.
- HOROZOV, T. S., AVEYARD, R., BINKS, B. P. & CLINT, J. H. 2005. Structure and stability of silica particle monolayers at horizontal and vertical octane-water interfaces. *Langmuir*, 21, 7405-7412.
- HOROZOV, T. S., BINKS, B. P., AVEYARD, R. & CLINT, J. H. 2006. Effect of particle hydrophobicity on the formation and collapse of fumed silica particle monolayers at the oil–water interface. *Colloids and Surfaces A: Physicochemical and Engineering Aspects*, 282, 377-386.
- HOTZE, E. M., PHENRAT, T. & LOWRY, G. V. 2010. Nanoparticle aggregation: challenges to understanding transport and reactivity in the environment. *Journal of environmental quality*, 39, 1909-1924.
- HOUSKA, C. & WARREN, B. 1954. X-Ray Study of the Graphitization of Carbon Black. *Journal of Applied Physics*, 25, 1503-1509.
- HSS. 1988. *Occupational safety and health guideline for carbon black potential human carcinogen*. [Online]. Available: <http://www.cdc.gov/niosh/docs/81-123/pdfs/0102.pdf> [Accessed].
- HU, G., JIAO, B., SHI, X., VALLE, R. P., FAN, Q. & ZUO, Y. Y. 2013. Physicochemical properties of nanoparticles regulate translocation across pulmonary surfactant monolayer and formation of lipoprotein corona. *ACS nano*, 7, 10525-10533.

- HUANG, S., MINAMI, K., SAKAUE, H., SHINGUBARA, S. & TAKAHAGI, T. 2004. Effects of the surface pressure on the formation of Langmuir-Blodgett monolayer of nanoparticles. *Langmuir*, 20, 2274-2276.
- HUANG, S., TSUTSUI, G., SAKAUE, H., SHINGUBARA, S. & TAKAHAGI, T. 2001a. Experimental conditions for a highly ordered monolayer of gold nanoparticles fabricated by the Langmuir-Blodgett method. *Journal of Vacuum Science & Technology B*, 19, 2045-2049.
- HUANG, S., TSUTSUI, G., SAKAUE, H., SHINGUBARA, S. & TAKAHAGI, T. 2001b. Formation of a large-scale Langmuir-Blodgett monolayer of alkanethiol-encapsulated gold particles. *Journal of Vacuum Science & Technology B*, 19, 115-120.
- HUSSAIN, S., BOLAND, S., BAEZA-SQUIBAN, A., HAMEL, R., THOMASSEN, L. C., MARTENS, J. A., BILLON-GALLAND, M. A., FLEURY-FEITH, J., MOISAN, F. & PAIRON, J.-C. 2009. Oxidative stress and proinflammatory effects of carbon black and titanium dioxide nanoparticles: role of particle surface area and internalized amount. *Toxicology*, 260, 142-149.
- IARC 1996. *Printing Processes and Printing Inks, Carbon Black and Some Nitro Compounds: The Evaluation of Carcinogenic Risks to Humans*, World Health Organization.
- IBRAHIM, A. Y. 2000. *A study of DPPC and DMPC monolayers at different temperatures using epifluorescence surface balance*. Memorial University of Newfoundland.
- ICRP 1994. *ICRP Publication 66: Human Respiratory Tract Model for Radiological Protection*, Elsevier Health Sciences.
- INGENITO, E. P., MORA, R. & MARK, L. 2000. Pivotal role of anionic phospholipids in determining dynamic behavior of lung surfactant. *American journal of respiratory and critical care medicine*, 161, 831-838.
- INTERNATIONAL-CARBON-BLACK-ASSOCIATION. 2014. *What is carbon black?* [Online]. Available: <http://www.carbon-black.org/index.php/what-is-carbon-black> [Accessed].
- IONTOF. 2016. *TOF-SIMS* [Online]. Available: <https://www.iontof.com/tof-sims-secondary-ion-mass-spectrometry.html> [Accessed].
- IUPAC. 2001. *Definitions, Terminology and Symbols in Colloid and Surface Chemistry* [Online]. Available: http://old.iupac.org/reports/2001/colloid_2001/manual_of_s_and_t/manual_of_s_and_t.html [Accessed].
- JOHANS, C., PALONEN, I., SUOMALAINEN, P. & KINNUNEN, P. 2005. *Making Surface Tension Measurement a Practical Utility for Modern Industrial R&D* [Online]. Available: <http://americanlaboratory.com/914-Application-Notes/36139-Making-Surface-Tension-Measurement-a-Practical-Utility-for-Modern-Industrial-R-D/> [Accessed].

- JOHANSSON, J., CURSTEDT, T. & ROBERTSON, B. 1994. The proteins of the surfactant system. *European Respiratory Journal*, 7, 372-391.
- JOHANSSON, J., GUSTAFSSON, M., PALMBLAD, M., ZALTASH, S., ROBERTSON, B. & CURSTEDT, T. 1998. Synthetic surfactant protein analogues. *Neonatology*, 74, 9-14.
- JONAS, D. U. 2009. *What is a Surface / Interface?* [Online]. Available: http://esperia.iesl.forth.gr/~ujonas/Master_Surf_Chem/lecture_IntroSurfChem_1a.pdf [Accessed].
- JYOTI, A., PROKOP, R., LI, J., VOLLHARDT, D., KWOK, D., MILLER, R., MÖHWALD, H. & NEUMANN, A. 1996. An investigation of the compression rate dependence on the surface pressure-surface area isotherm for a dipalmitoyl phosphatidylcholine monolayer at the air/water interface. *Colloids and Surfaces A: Physicochemical and Engineering Aspects*, 116, 173-180.
- KAGANER, V. M., MÖHWALD, H. & DUTTA, P. 1999. Structure and phase transitions in Langmuir monolayers. *Reviews of Modern Physics*, 71, 779.
- KALUZA, S., BALDERHAAR, J. K., ORTHEN, B., HONNERT, B., JANKOWSKA, E., PIETROWSKI, P., ROSELL, M. G., TANARRO, C., TEJEDOR, J. & ZUGASTI, A. 2009. *Workplace exposure to nanoparticles* [Online]. European Agency for Safety and Health at Work. Available: http://osha.europa.eu/en/publications/literature_reviews/workplace_exposure_to_nano_particles [Accessed].
- KEATING, E., RAHMAN, L., FRANCIS, J., PETERSEN, A., POSSMAYER, F., VELDHUIZEN, R. & PETERSEN, N. O. 2007. Effect of cholesterol on the biophysical and physiological properties of a clinical pulmonary surfactant. *Biophysical journal*, 93, 1391-1401.
- KEATING, E., WARING, A. J., WALTHER, F. J., POSSMAYER, F., VELDHUIZEN, R. A. & PETERSEN, N. O. 2011. A ToF-SIMS study of the lateral organization of lipids and proteins in pulmonary surfactant systems. *Biochimica et Biophysica Acta (BBA)-Biomembranes*, 1808, 614-621.
- KEMPSON, I. M., BARNES, T. J. & PRESTIDGE, C. A. 2010. Use of TOF-SIMS to study adsorption and loading behavior of methylene blue and papain in a nano-porous silicon layer. *Journal of the American Society for Mass Spectrometry*, 21, 254-260.
- KENN, R., BÖHM, C., BIBO, A., PETERSON, I., MÖHWALD, H., ALS-NIELSEN, J. & KJAER, K. 1991. Mesophases and crystalline phases in fatty acid monolayers. *The Journal of Physical Chemistry*, 95, 2092-2097.
- KIM, J.-K., KANG, M.-G., CHO, H.-W., HAN, J.-H., CHUNG, Y.-H., RIM, K.-T., YANG, J.-S., KIM, H. & LEE, M.-Y. 2011. Effect of nano-sized carbon black particles on lung and circulatory system by inhalation exposure in rats. *Safety and health at work*, 2, 282-289.

- KING, R. J. & CLEMENTS, J. A. 1972. Surface active materials from dog lung. II. Composition and physiological correlations. *American Journal of Physiology--Legacy Content*, 223, 715-726.
- KLEIN, G., REUTTER, B., HO, M., REED, J. & HUESMAN, R. 1998a. Real-time system for respiratory-cardiac gating in positron tomography. *Nuclear Science, IEEE Transactions on*, 45, 2139-2143.
- KLEIN, J. M., MCCARTHY, T. A., DAGLE, J. M. & SNYDER, J. M. 2002. Antisense inhibition of surfactant protein A decreases tubular myelin formation in human fetal lung in vitro. *American Journal of Physiology-Lung Cellular and Molecular Physiology*, 282, L386-L393.
- KLEIN, J. M., THOMPSON, M. W., SNYDER, J. M., GEORGE, T. N., WHITSETT, J. A., BELL, E. F., MCCRAY, P. B. & NOGEE, L. M. 1998b. Transient surfactant protein B deficiency in a term infant with severe respiratory failure. *The Journal of pediatrics*, 132, 244-248.
- KLEINMAN, M. T., ARAUJO, J. A., NEL, A., SIOUTAS, C., CAMPBELL, A., CONG, P. Q., LI, H. & BONDY, S. C. 2008. Inhaled ultrafine particulate matter affects CNS inflammatory processes and may act via MAP kinase signaling pathways. *Toxicology Letters* 178, 127-130
- KLOPFER, K. & VANDERLICK, T. 1996. Isotherms of dipalmitoylphosphatidylcholine (DPPC) monolayers: features revealed and features obscured. *Journal of colloid and interface science*, 182, 220-229.
- KODAMA, M., SHIBATA, O., NAKAMURA, S., LEE, S. & SUGIHARA, G. 2004. A monolayer study on three binary mixed systems of dipalmitoyl phosphatidyl choline with cholesterol, cholestanol and stigmaterol. *Colloids and Surfaces B: Biointerfaces*, 33, 211-226.
- KOTOV, N., MELDRUM, F., WU, C. & FENDLER, J. 1994. Monoparticulate layer and Langmuir-Blodgett-type multiparticulate layers of size-quantized cadmium sulfide clusters: a colloid-chemical approach to superlattice construction. *The Journal of Physical Chemistry*, 98, 2735-2738.
- KREYLING, W. G., HIRN, S. & SCHLEH, C. 2010. Nanoparticles in the lung. *Nature biotechnology*, 28, 1275-1276.
- KREYLING, W. G., SEMMLER, M., ERBE, F., MAYER, P., TAKENAKA, S., SCHULZ, H., OBERDÖRSTER, G. & ZIESENIS, A. 2002. Translocation of ultrafine insoluble iridium particles from lung epithelium to extrapulmonary organs is size dependent but very low. *J. Toxicol Environ Health A.*, 20, 1513-1530.
- KRISHNAKUMAR, P. 2010. Wetting and spreading phenomena.
- KRÜSS. 2017. *Dynamic contact angle* [Online]. Available: <https://www.kruss.de/services/education-theory/glossary/dynamic-contact-angle/> [Accessed].

- KSV-NIMA 2010. Software Manuals of Langmuir and Langmuir-Blodgett devices. Revision 1.0. Finland.
- KSV-NIMA 2012. KSV NIMA Langmuir & Langmuir-Blodgett Ribbon Barrier Trough.
- KSV-NIMA. 2014. *Accesories and Modules. Langmuir and Langmuir-Blodgett Deposition Troughs* [Online]. Available: http://www.biolinscientific.com/zafepress.php?url=%2Fpdf%2FKSV%20NIMA%2FProducts%2FLangmuir%20%26%20Langmuir-Blodgett%2FKN_P_All_LLB_Accessoryandmodules_23-8-2013.pdf [Accessed].
- KU, T., GILL, S., LÖBENBERG, R., AZARMI, S., ROA, W. & PRENNER, E. J. 2008. Size dependent interactions of nanoparticles with lung surfactant model systems and the significant impact on surface potential. *Journal of nanoscience and nanotechnology*, 8, 2971-2978.
- KUHLBUSCH, T., NEUMANN, S. & FISSAN, H. 2004. Number size distribution, mass concentration, and particle composition of PM1, PM2.5, and PM10 in bag filling areas of carbon black production. *Journal of Occupational and environmental Hygiene*, 1, 660-671.
- KULKARNI, P., BARON, P. A. & WILLEKE, K. 2011. *Aerosol measurement: principles, techniques, and applications*, John Wiley & Sons.
- LALCHEV, Z., TODOROV, R. & EXEROWA, D. 2008. Thin liquid films as a model to study surfactant layers on the alveolar surface. *Current Opinion in Colloid & Interface Science*, 13, 183-193.
- LANONE, S., ROGERIEUX, F., GEYS, J., DUPONT, A., MAILLOT-MARECHAL, E., BOCZKOWSKI, J., LACROIX, G. & HOET, P. 2009. Comparative toxicity of 24 manufactured nanoparticles in human alveolar epithelial and macrophage cell lines. *Particle and Fibre Toxicology*, 6, 14.
- LEE, K. Y. C. 2008. Collapse mechanisms of Langmuir monolayers. *Annu. Rev. Phys. Chem.*, 59, 771-791.
- LEE, Y.-L., LIN, J.-Y. & CHANG, C.-H. 2006. Thermodynamic characteristics and Langmuir–Blodgett deposition behavior of mixed DPPA/DPPC monolayers at air/liquid interfaces. *Journal of colloid and interface science*, 296, 647-654.
- LENZ, A. G., KARG, E., LENTNER, B., DITTRICH, V., BRANDENBERGER, C., ROTHEN-RUTISHAUSER, B., SCHULZ, H., FERRON, G. A. & SCHMID, O. 2009. A dose-controlled system for air-liquid interface cell exposure and application to zinc oxide nanoparticles. *Part Fibre Toxicol*, 6, b16.
- LEO, B. F., CHEN, S., KYO, Y., HERPOLDT, K.-L., TERRILL, N. J., DUNLOP, I. E., MCPHAIL, D. S., SHAFFER, M. S., SCHWANDER, S. & GOW, A. 2013. The stability of silver nanoparticles in a model of pulmonary surfactant. *Environmental science & technology*, 47, 11232-11240.

- LEONENKO, Z., GILL, S., BAOUKINA, S., MONTICELLI, L., DOEHNER, J., GUNASEKARA, L., FELDERER, F., RODENSTEIN, M., ENG, L. M. & AMREIN, M. 2007. An elevated level of cholesterol impairs self-assembly of pulmonary surfactant into a functional film. *Biophysical journal*, 93, 674-683.
- LEWIS, J. F. & VELDHUIZEN, R. The future of surfactant therapy during ALI/ARDS. *Seminars in respiratory and critical care medicine*, 2006. 377-388.
- LIM, C.-H., KANG, M., HAN, J.-H. & YUN, H.-I. 2013. Effects of nano-sized carbon black on the lungs of high fat-diet induced overweight rats. *Environmental health and toxicology*, 28.
- LIN, E. K., SOLES, C. L., GOLDFARB, D. L., TRINQUE, B. C., BURNS, S. D., JONES, R. L., LENHART, J. L., ANGELOPOULOS, M., WILLSON, C. G. & SATIJA, S. K. Measurement of the spatial evolution of the deprotection reaction front with nanometer resolution using neutron reflectometry. SPIE's 27th Annual International Symposium on Microlithography, 2002. International Society for Optics and Photonics, 313-320.
- LIN, X., LI, Y. & GU, N. 2011. Molecular dynamics simulations of the interactions of charge-neutral PAMAM dendrimers with pulmonary surfactant. *Soft Matter*, 7, 3882-3888.
- LIPP, M., LEE, K., TAKAMOTO, D., ZASADZINSKI, J. & WARING, A. 1998. Coexistence of buckled and flat monolayers. *Physical Review Letters*, 81, 1650.
- LIPP, M. M., LEE, K. Y., WARING, A. & ZASADZINSKI, J. A. 1997. Fluorescence, Polarized Fluorescence, and Brewster Angle Microscopy of Palmitic Acid and Lung Surfactant Protein B Monolayers. *Biophysical journal* 72, 2783-2804
- LIU, J.-L., FENG, X.-Q. & WANG, G.-F. 2007. Buoyant force and sinking conditions of a hydrophobic thin rod floating on water. *Physical Review E*, 76, 066103.
- LIU, J. L. & BASHIR, S. 2015. *Advanced Nanomaterials and Their Applications in Renewable Energy*, Elsevier.
- LIU, M. 2013. Coating technology of nuclear fuel kernels: a multiscale view. *Modern surface engineering treatments. InTech, Rijeka*, 159-184.
- LIU, X., WANG, X., LIANG, Y. & ZHOU, F. 2009. Floating behavior of hydrophobic glass spheres. *Journal of colloid and interface science*, 336, 743-749.
- LOWER, S. 2015. *Liquids and their Interfaces* [Online]. Available: <http://www.chem1.com/acad/webtext/states/liquids.html> [Accessed].
- LU, J. J., YU, L. M. Y., CHEUNG, W. W. Y., POLICOVA, Z., LI, D., HAIR, M. L. & NEUMANN, A. W. 2003. The effect of concentration on the bulk adsorption of bovine lipid extract surfactant. *Colloids and Surfaces B: Biointerfaces*, 29, 119-130
- MA, P.-C. & KIM, J.-K. 2011. *Carbon nanotubes for polymer reinforcement*, CRC Press.
- MACRITCHIE, F. 2012. *Chemistry at interfaces*, Elsevier.

- MAESTRO, A., BONALES, L., RITACCO, H., RUBIO, R. & ORTEGA, F. 2010. Effect of the spreading solvent on the three-phase contact angle of microparticles attached at fluid interfaces. *Physical Chemistry Chemical Physics*, 12, 14115-14120.
- MAESTRO, A., GUZMÁN, E., ORTEGA, F. & RUBIO, R. G. 2014. Contact angle of micro- and nanoparticles at fluid interfaces. *Current Opinion in Colloid & Interface Science*, 19, 355-367.
- MAESTRO, A., GUZMÁN, E., SANTINI, E., RAVERA, F., LIGGIERI, L., ORTEGA, F. & RUBIO, R. G. 2012. Wettability of silica nanoparticle–surfactant nanocomposite interfacial layers. *Soft Matter*, 8, 837-843.
- MAESTRO, A., SANTINI, E., ZABIEGAJ, D., LLAMAS, S., RAVERA, F., LIGGIERI, L., ORTEGA, F., RUBIO, R. G. & GUZMAN, E. 2015. Particle and Particle-Surfactant Mixtures at Fluid Interfaces: Assembly, Morphology, and Rheological Description. *Advances in Condensed Matter Physics*, 2015.
- MAGNUSSON, Y. K., FRIBERG, P., SJÖVALL, P., MALM, J. & CHEN, Y. 2008. TOF-SIMS Analysis of Lipid Accumulation in the Skeletal Muscle of ob/ob Mice. *Obesity*, 16, 2745-2753.
- MAIER, M., HANNEBAUER, B., HOLLDORFF, H. & ALBERS, P. 2006. Does Lung Surfactant Promote Disaggregation of Nanostructured Titanium Dioxide? *J Occup Environ Med.*, 48, 1314-1320.
- MALCHAREK, S., HINZ, A., HILTERHAUS, L. & GALLA, H.-J. 2005. Multilayer structures in lipid monolayer films containing surfactant protein C: effects of cholesterol and POPE. *Biophysical journal*, 88, 2638-2649.
- MALVERN-INSTRUMENTS. 2015. *Zeta potential - An introduction in 30 minutes* [Online]. Available: <http://www.malvern.com/es/support/resource-center/technical-notes/TN101104ZetaPotentialIntroduction.aspx> [Accessed].
- MALVERN-INSTRUMENTS. 2016. *Zeta Potential Measurements of Non-Aqueous Particulate Suspensions* [Online]. Available: <http://www.malvern.com/en/pdf/secure/AN101104ZetaPotentialMeasurements.pdf> [Accessed].
- MAN, S., ADAMS, G. & PROCTOR, D. 1979. Effects of temperature, relative humidity, and mode of breathing on canine airway secretions. *Journal of Applied Physiology*, 46, 205-210.
- MÁTÉ, M., FENDLER, J. H., RAMSDEN, J. J., SZALMA, J. & HÓRVÖLGYI, Z. 1998. Eliminating surface pressure gradient effects in contact angle determination of nano- and microparticles using a film balance. *Langmuir*, 14, 6501-6504.
- MAYNARD, A. D. 2002. Experimental Determination of Ultrafine TiO₂ Deagglomeration in a Surrogate Pulmonary Surfactant: Preliminary Results. *Ann. occup. Hyg.*, 46, 197-202.

- MCCONLOGUE, C. W. & VANDERLICK, T. K. 1997. A close look at domain formation in DPPC monolayers. *Langmuir*, 13, 7158-7164.
- MCCONNELL, H. M. 1991. Structures and transitions in lipid monolayers at the air-water interface. *Annual Review of Physical Chemistry*, 42, 171-195.
- MEDLINEPLUS. 2012. *Lower respiratory tract* [Online]. Available: <http://www.nlm.nih.gov/medlineplus/ency/imagepages/19379.htm> [Accessed].
- MEHTA, S. C., SOMASUNDARAN, P., MALDARELLI, C. & KULKARNI, R. 2006. Effects of functional groups on surface pressure-area isotherms of hydrophilic silicone polymers. *Langmuir*, 22, 9566-9571.
- MELBOURNE, J., CLANCY, A., SEIFFERT, J., SKEPPER, J., TETLEY, T. D., SHAFFER, M. S. & PORTER, A. 2015. An investigation of the carbon nanotube–Lipid interface and its impact upon pulmonary surfactant lipid function. *Biomaterials*, 55, 24-32.
- MELIKOV, A. & KACZMARCZYK, J. 2007. Measurement and prediction of indoor air quality using a breathing thermal manikin. *Indoor air*, 17, 50-59.
- MERRITT, T. A., HALLMAN, M., BLOOM, B. T., BERRY, C., BENIRSCHKE, K., SAHN, D., KEY, T., EDWARDS, D., JARVENPAA, A.-L. & POHJAVUORI, M. 1986. Prophylactic treatment of very premature infants with human surfactant. *New England Journal of Medicine*, 315, 785-790.
- MESSING, M. E., DICK, K. A., WALLENBERG, L. R. & DEPPERT, K. 2009. Generation of size-selected gold nanoparticles by spark discharge – for growth of epitaxial nanowires. *Gold Bulletin*, 42, 20-26
- MILLER, C., BUSATH, D., STRONGIN, B. & MAJEWSKI, J. 2008. Integration of ganglioside GT 1b receptor into DPPE and DPPC phospholipid monolayers: an X-ray reflectivity and grazing-incidence diffraction study. *Biophysical journal*, 95, 3278-3286.
- MILLER, C., MAJEWSKI, J., FALLER, R., SATIJA, S. & KUHL, T. 2004. Cholera toxin assault on lipid monolayers containing ganglioside GM 1. *Biophysical journal*, 86, 3700-3708.
- MOHAMMAD-AGHAIE, D., MACÉ, E., SENNOGA, C. A., SEDDON, J. M. & BRESME, F. 2009. Molecular dynamics simulations of liquid condensed to liquid expanded transitions in DPPC monolayers. *The Journal of Physical Chemistry B*, 114, 1325-1335.
- MÖLLER, W., HÄUBINGER, K., WINKLER-HEIL, R., STAHLHOFEN, W., MEYER, T., HOFMANN, W. & HEYDER, J. 2004. Mucociliary and long-term particle clearance in the airways of healthy nonsmoker subjects. *Journal of Applied Physiology*, 97, 2200-2206.
- MONTGOMERY, S. W., FRANCKEK, M. A. & GOLDSCHMIDT, V. W. 2000. Analytical dispersion force calculations for nontraditional geometries. *Journal of colloid and interface science*, 227, 567-584.

- MOU, J., CZAJKOWSKY, D. M., ZHANG, Y. & SHAO, Z. 1995. High-resolution atomic-force microscopy of DNA: the pitch of the double helix. *FEBS letters*, 371, 279-282.
- MOURITSEN, O. G. & ZUCKERMANN, M. J. 2004. What's so special about cholesterol? *Lipids*, 39, 1101-1113.
- MUNKHOLM, M. & MORTENSEN, J. 2014. Mucociliary clearance: pathophysiological aspects. *Clinical physiology and functional imaging*, 34, 171-177.
- NAG, K. 2005. *Lung Surfactant Function and Disorder*, Taylor & Francis.
- NAG, K., BOLAND, C., RICH, N. & KEOUGH, K. M. 1991. Epifluorescence microscopic observation of monolayers of dipalmitolophosphatidylcholine: dependence of domain size on compression rates. *Biochimica et Biophysica Acta (BBA)-Biomembranes*, 1068, 157-160.
- NAKAHARA, H., LEE, S., SUGIHARA, G., CHANG, C.-H. & SHIBATA, O. 2008. Langmuir monolayer of artificial pulmonary surfactant mixtures with an amphiphilic peptide at the air/water interface: comparison of new preparations with Surfacten (Surfactant TA). *Langmuir*, 24, 3370-3379.
- NALWA, H. S. 2001. *Handbook of Surfaces and Interfaces of Materials: Surface and interface phenomena*, Academic Press.
- NANOSCIENCE-INSTRUMENTS. 2016. *How and SEM Works* [Online]. Available: <http://www.nanoscience.com/technology/sem-technology/how-sem-works/> [Accessed].
- NASA. 2011. *Surface Tension-Driven Flow* [Online]. Available: <http://quest.nasa.gov/space/teachers/microgravity/6surf.html> [Accessed].
- NAVE, S. 2001. Phase behaviour and interfacial properties of double-chain anionic surfactants.
- NG, A. W., BIDANI, A. & HEMING, T. A. 2004. Innate Host Defense of the Lung: Effects of Lung-lining Fluid pH. *Lung*, 182, 297-317
- NIELSON, D., GOERKE, J. & CLEMENTS, J. 1981. Alveolar subphase pH in the lungs of anesthetized rabbits. *Proceedings of the National Academy of Sciences*, 78, 7119-7123.
- NIST-CENTER-FOR-NEUTRON-RESEARCH. 1999. *Neutron Reflectometry* [Online]. Available: http://www.ncnr.nist.gov/programs/reflect/NR_article/ [Accessed].
- NOGEE, L. M., DEMELLO, D. E., DEHNER, L. P. & COLTEN, H. R. 1993. Deficiency of pulmonary surfactant protein B in congenital alveolar proteinosis. *New England Journal of Medicine*, 328, 406-410.
- NOTTER, R. & MORROW, P. 1975. Pulmonary surfactant: a surface chemistry viewpoint. *Annals of biomedical engineering*, 3, 119-159.

- NOTTER, R., TAUBOLD, R. & MAVIS, R. 1982. Hysteresis in saturated phospholipid films and its potential relevance for lung surfactant function in vivo. *Experimental lung research*, 3, 109-127.
- NOTTER, R. H. 2000. *Lung surfactants: basic science and clinical applications*, CRC Press.
- NOWACK, B. & BUCHELI, T. D. 2007. Occurrence, behavior and effects of nanoparticles in the environment. *Environmental Pollution*, 150, 5-22.
- NURAJE, N., KHAN, W. S., LEI, Y., CEYLAN, M. & ASMATULU, R. 2013. Superhydrophobic electrospun nanofibers. *Journal of Materials Chemistry A*, 1, 1929-1946.
- O'LENICK, A. J. 2009. *Comparatively Speaking: Static vs. Dynamic Measurement of Surface Tension* [Online]. Available: <http://www.cosmeticsandtoiletries.com/research/chemistry/78318722.html> [Accessed].
- OBERDÖRSTER, G. 2001. Pulmonary effects of inhaled ultrafine particles. *Int Arch Occup Environ Health*, 74, 1-8.
- OBERDÖRSTER, G., OBERDÖRSTER, E. & OBERDÖRSTER, J. 2005. Nanotoxicology: An Emerging Discipline Evolving from Studies of Ultrafine Particles. *Environmental Health Perspectives*, 113, 823-839.
- OBERDÖRSTER, G., SHARP, Z., ATUDOREI, V., ELDER, A., GELEIN, R., LUNTS, A., KREYLING, W. & COX, C. 2002. Extrapulmonary translocation of ultrafine carbon particles following whole-body inhalation exposure of rats. *Journal of toxicology and environmental health*, 65, 1531.
- ORGEIG, S., BERNHARD, W., BISWAS, S. C., DANIELS, C. B., HALL, S. B., HETZ, S. K., LANG, C. J., MAINA, J. N., PANDA, A. K. & PEREZ-GIL, J. 2007. The anatomy, physics, and physiology of gas exchange surfaces: is there a universal function for pulmonary surfactant in animal respiratory structures? *Integrative and comparative biology*, 47, 610-627.
- PALLAS, N. & HARRISON, Y. 1990. An automated drop shape apparatus and the surface tension of pure water. *Colloids and Surfaces*, 43, 169-194.
- PARENT, R. A. 1992. *Treatise on Pulmonary Toxicology: Comparative biology of the normal lung*, CRC Press.
- PARENT, R. A. 2015. *Comparative Biology of the Normal Lung*, Elsevier Science.
- PARK-SYSTEMS. 2016. *How AFM works* [Online]. Available: <http://www.parkafm.com/index.php/medias/nano-academy/how-afm-works> [Accessed].

- PARK, B., DONALDSON, K., DUFFIN, R., TRAN, L., KELLY, F., MUDWAY, I., MORIN, J.-P., GUEST, R., JENKINSON, P. & SAMARAS, Z. 2008. Hazard and risk assessment of a nanoparticulate cerium oxide-based diesel fuel additive—a case study. *Inhalation toxicology*, 20, 547-566.
- PATTLE, R. E. 1966. Surface tension and the lining of the lung alveoli. *In: CARO, C. G. (ed.) Advances in Respiratory Physiology*. London: Edward Arnold Ltd.
- PENG, J., BARNES, G. & GENTLE, I. 2001. The structures of Langmuir–Blodgett films of fatty acids and their salts. *Advances in Colloid and Interface Science*, 91, 163-219.
- PÉREZ-MORALES, M., PEDROSA, J. M., MUÑOZ, E., MARTÍN-ROMERO, M. T., MÖBIUS, D. & CAMACHO, L. 2005. Ellipsometric study of a phospholipid monolayer at the air–water interface in presence of large organic counter ions. *Thin Solid Films*, 488, 247-253.
- PETERS, A., VERONESI, B., CALDERÓN-GARCIDUEÑAS, L., GEHR, P., CHEN, L. C., GEISER, M., REED, W., ROTHEN-RUTISHAUSER, B., SCHURCH, S. & SCHULZ, H. 2006. Translocation and potential neurological effects of fine and ultrafine particles a critical update. *Part Fibre Toxicol*, 3, 1-13.
- PETTY, M. C. 1996. *Langmuir-Blodgett films: an introduction*, Cambridge University Press.
- PIKNOVA, B., SCHIEF, W. R., VOGEL, V., DISCHER, B. M. & HALL, S. B. 2001. Discrepancy between phase behavior of lung surfactant phospholipids and the classical model of surfactant function. *Biophysical journal*, 81, 2172-2180.
- PIKNOVA, B., SCHRAM, V. & HALL, S. 2002. Pulmonary surfactant: phase behavior and function. *Current opinion in structural biology*, 12, 487-494.
- PISON, U., HEROLD, R. & SCHÜRCH, S. 1996. The pulmonary surfactant system: biological functions, components, physicochemical properties and alterations during lung disease. *Colloids and Surfaces A: Physicochemical and Engineering Aspects*, 114, 165-184.
- POLIN, R. A., FOX, W. W. & ABMAN, S. H. 2011. *Fetal and neonatal physiology*, Elsevier Health Sciences.
- POPE III, C. A., BURNETT, R. T., THUN, M. J., CALLE, E. E., KREWSKI, D., ITO, K. & THURSTON, G. D. 2002. Lung cancer, cardiopulmonary mortality, and long-term exposure to fine particulate air pollution. *Jama*, 287, 1132-1141.
- POSSMAYER, F. 1988. A proposed nomenclature for pulmonary surfactant-associated proteins. *American Review of Respiratory Disease*, 138, 990-998.
- POSSMAYER, F., HALL, S. B., HALLER, T., PETERSEN, N. O., ZUO, Y. Y., DE LA SERNA, J. B., POSTLE, A. D., VELDHUIZEN, R. A. & ORGEIG, S. 2010. Recent advances in alveolar biology: some new looks at the alveolar interface. *Respiratory physiology & neurobiology*, 173, S55-S64.

- POSSMAYER, F., NAG, K., RODRIGUEZ, K., QANBAR, R. & SCHÜRCH, S. 2001. Surface activity in vitro: role of surfactant proteins. *Comparative Biochemistry and Physiology Part A: Molecular & Integrative Physiology*, 129, 209-220.
- POWELL, C., FENWICK, N., BRESME, F. & QUIRKE, N. 2002. Wetting of nanoparticles and nanoparticle arrays. *Colloids and Surfaces A: Physicochemical and Engineering Aspects*, 206, 241-251.
- POWERS, K. W., BROWN, S. C., KRISHNA, V. B., WASDO, S. C., MOUDGIL, B. M. & ROBERTS, S. M. 2006. Research strategies for safety evaluation of nanomaterials. Part VI. Characterization of nanoscale particles for toxicological evaluation. *Toxicological Sciences*, 90, 296-303.
- PROKOP, R. M. & NEUMANN, A. W. 1996. Measurement of the interfacial properties of lung surfactant. *Current Opinion in Colloid & Interface Science*, 1, 677-681.
- PUAH, L. S., SEDEV, R., FORNASIERO, D., RALSTON, J. & BLAKE, T. 2010. Influence of surface charge on wetting kinetics. *Langmuir*, 26, 17218-17224.
- PURVES, W. K., ORIAN, G. H., SADAVA, D. & HELLER, H. C. 2003. *Life: The Science of Biology: Volume III: Plants and Animals*, Macmillan.
- PUTZ, G., GOERKE, J., TAEUSCH, H. & CLEMENTS, J. 1994. Comparison of captive and pulsating bubble surfactometers with use of lung surfactants. *Journal of Applied Physiology*, 76, 1425-1431.
- PUTZ, G., WALCH, M., VAN EIJK, M. & HAAGSMAN, H. P. 1998. A spreading technique for forming film in a captive bubble. *Biophysical journal*, 75, 2229-2239.
- QI, S., ROSER, S. J., DEUTSCH, D., BARKER, S. A. & CRAIG, D. Q. 2008. A laser imaging and neutron reflection investigation into the monolayer behaviour of fatty acids used for taste masking microspheres. *Journal of pharmaceutical sciences*, 97, 1864-1877.
- RAMÉ-HART-INSTRUMENT-COMPANY. 2015. *ramé-hart contact angle goniometers and tensiometers* [Online]. Available: <http://www.ramehart.com/contactangle.htm> [Accessed].
- RENWICK, L., DONALDSON, K. & CLOUTER, A. 2001. Impairment of alveolar macrophage phagocytosis by ultrafine particles. *Toxicology and applied pharmacology*, 172, 119-127.
- RENWICK, L. C., BROWN, D., CLOUTER, A. & DONALDSON, K. 2004. Increased inflammation and altered macrophage chemotactic responses caused by two ultrafine particle types. *Occup Environ Med*, 61, 442-447.
- RICHTER, A., GUICO, R. & WANG, J. 2001. Calibrating an ellipsometer using x-ray reflectivity. *Review of Scientific Instruments*, 72, 3004-3007.
- ROBERTS, G. 2013. *Langmuir-blodgett films*, Springer Science & Business Media.

- ROBERTSON, B. & HALLIDAY, H. L. 1998. Principles of surfactant replacement. *Biochimica et Biophysica Acta (BBA)-Molecular Basis of Disease*, 1408, 346-361.
- ROBILLARD, E., ALARIE, Y., DAGENAIS-PERUSSE, P., BARIL, E. & GUILBEAULT, A. 1964. Microaerosol administration of synthetic β - γ -dipalmitoyl-L- α -lecithin in the respiratory distress syndrome: a preliminary report. *Canadian Medical Association Journal*, 90, 55.
- ROBINSON, D. & EARNSHAW, J. 1992a. Experimental study of colloidal aggregation in two dimensions. I. Structural aspects. *Physical Review A*, 46, 2045.
- ROBINSON, D. & EARNSHAW, J. 1992b. Experimental study of colloidal aggregation in two dimensions. II. Kinetic aspects. *Physical Review A*, 46, 2055.
- ROCO, M. C. 2005. Environmentally responsible development of nanotechnology. *Environmental science & technology*, 39, 106A-112A.
- ROSOFF, M. 2001. *Nano-surface chemistry*, CRC Press.
- ROSS, M., KROL, S., JANSHOFF, A. & GALLA, H.-J. 2002. Kinetics of phospholipid insertion into monolayers containing the lung surfactant proteins SP-B or SP-C. *European Biophysics Journal*, 31, 52-61.
- ROSSI, E. M., PYLKKÄNEN, L., KOIVISTO, A. J., VIPPOLA, M., JENSEN, K. A., MIETTINEN, M., SIROLA, K., NYKÄSENOJA, H., KARISOLA, P., STJERNVALL, T., VANHALA, E., KIILUNEN, M., PASANEN, P., MÄKINEN, M., HÄMERI, K., JOUTSENSAARI, J., TUOMI, T., JOKINIEMI, J., WOLFF, H., SAVOLAINEN, K., MATIKAINEN, S. & ALENIOUS, H. 2010. Airway Exposure to Silica-Coated TiO₂ Nanoparticles Induces Pulmonary Neutrophilia in Mice. *Toxicological Sciences*, 113, 422-433.
- ROTH, C., FERRON, G. A., KARG, E., LENTNER, B., SCHUMANN, G., TAKENAKA, S. & HEYDER, J. 2004. Generation of Ultrafine Particles by Spark Discharging. *Aerosol Science and Technology*, 38, 228-235.
- SACHAN, A. K., HARISHCHANDRA, R. K., BANTZ, C., MASKOS, M., REICHEL, R. & GALLA, H.-J. 2012. High-resolution investigation of nanoparticle interaction with a model pulmonary surfactant monolayer. *ACS nano*, 6, 1677-1687.
- SAGER, T. M. 2008. *An in Vivo Examination of the Pulmonary Toxicity of Ultrafine and Fine Carbon Black and Titanium Dioxide: Defining the Role of Particle Surface Area*, ProQuest.
- SAGER, T. M., PORTER, D. W., ROBINSON, V. A., LINDSLEY, W. G., SCHWEGLER-BERRY, D. E. & CASTRANOVA, V. 2007. Improved method to disperse nanoparticles for in vitro and in vivo investigation of toxicity. *Nanotoxicology*, 1, 118-129.
- SALAGER, J.-L. 2002. Surfactant's types and uses. *Fire p booket-E300-attaching aid in surfactant science and engineering in English. Merida Venezuela*, 2, 3.

- SALGIN, S., SALGIN, U. & BAHADIR, S. 2012. Zeta potentials and isoelectric points of biomolecules: the effects of ion types and ionic strengths. *Int. J. Electrochem. Sci*, 7, 12404-12414.
- SATAKE, M., HAYASHI, Y., MIDO, Y., IQBAL, S. & SETHI, M. 2003. Colloidal and Surface Chemistry. Discovery Publishing House, New Delhi.
- SCHLEH, C. & HOHLFELD, J. M. 2009. Interaction of nanoparticles with the pulmonary surfactant system. *Inhalation toxicology*, 21, 97-103.
- SCHLEH, C., MÜHLFELD, C., PULSKAMP, K., SCHMIEDL, A., NASSIMI, M., LAUENSTEIN, H. D., BRAUN, A., KRUG, N., ERPENBECK, V. J. & HOHLFELD, J. M. 2009. The effect of titanium dioxide nanoparticles on pulmonary surfactant function and ultrastructure. *Respiratory Research*, 10, 90.
- SCHLEH, C., ROTHEN-RUTISHAUSER, B. & KREYLING, W. G. 2011. The influence of pulmonary surfactant on nanoparticulate drug delivery systems. *European Journal of Pharmaceutics and Biopharmaceutics*, 77, 350-352.
- SCHNEEMILCH, M. & QUIRKE, N. 2010. Molecular dynamics of nanoparticle translocation at lipid interfaces. *Molecular Simulation*, 36, 831-835.
- SCHÜRCH, D., OSPINA, O. L., CRUZ, A. & PÉREZ-GIL, J. 2010. Combined and independent action of proteins SP-B and SP-C in the surface behavior and mechanical stability of pulmonary surfactant films. *Biophysical journal*, 99, 3290-3299.
- SCHÜRCH, S. 1982. Surface tension at low lung volumes: dependence on time and alveolar size. *Respiration physiology*, 48, 339-355.
- SCHÜRCH, S., BACHOFEN, H. & POSSMAYER, F. 2001. Surface activity in situ, in vivo, and in the captive bubble surfactometer. *Comparative Biochemistry and Physiology Part A: Molecular & Integrative Physiology*, 129, 195-207.
- SCHÜRCH, S., GEHR, P., IM HOF, V., GEISER, M. & GREEN, F. 1990. Surfactant displaces particles toward the epithelium in airways and alveoli. *Respiration physiology*, 80, 17-32.
- SCHÜRCH, S., GOERKE, J. & CLEMENTS, J. A. 1978. Direct determination of volume- and time-dependence of alveolar surface tension in excised lungs. *Proceedings of the National Academy of Sciences*, 75, 3417-3421.
- SCHÜRCH, S., POSSMAYER, F., CHENG, S. & COCKSHUTT, A. M. 1992. Pulmonary SP-A enhances adsorption and appears to induce surface sorting of lipid extract surfactant. *American Journal of Physiology-Lung Cellular and Molecular Physiology*, 263, L210-L218.
- SCOTT, B. R. 2015. *How Particles Deposit in the Respiratory Tract* [Online]. Available: <http://www.radiation-scott.org/deposition/particles.htm> [Accessed].

- SEATON, A., MACNEE, W., DONALDSON, K. & GODDEN, D. 1995. Particulate air pollution and acute health effects. *The Lancet*, 345, 176-178.
- SEIFERT, M., BREITENSTEIN, D., KLENZ, U., MEYER, M. & GALLA, H.-J. 2007. Solubility versus electrostatics: what determines lipid/protein interaction in lung surfactant. *Biophysical journal*, 93, 1192-1203.
- SEN, S., BANERJEE, A. & ACHARJEE, A. 1999. Nanotechnology: Shaping the world atom by atom.
- SERRANO, A. G. & PÉREZ-GIL, J. 2006. Protein–lipid interactions and surface activity in the pulmonary surfactant system. *Chemistry and physics of lipids*, 141, 105-118.
- SHAFRIN, E. G. & ZISMAN, W. A. 1960. Constitutive relations in the wetting of low energy surfaces and the theory of the retraction method of preparing monolayers I. *The Journal of Physical Chemistry*, 64, 519-524.
- SHAPOVALOV, V. 1998. Interaction of DPPC monolayer at air–water interface with hydrophobic ions. *Thin Solid Films*, 327, 599-602.
- SHARIFI, S., BEHZADI, S., LAURENT, S., FORREST, M. L., STROEVE, P. & MAHMOUDI, M. 2012. Toxicity of nanomaterials. *Chemical Society Reviews*, 41, 2323-2343.
- SHINODA, K., NAKAGAWA, T. & TAMAMUSHI, B.-I. 2013. *Colloidal surfactants: some physicochemical properties*, Elsevier.
- SHUKLA, A., TIMBLIN, C., BERUBE, K., GORDON, T., MCKINNEY, W., DRISCOLL, K., VACEK, P. & MOSSMAN, B. T. 2000. Inhaled Particulate Matter Causes Expression of Nuclear Factor (NF)- κ B–Related Genes and Oxidant-Dependent NF- κ B Activation In Vitro. *American journal of respiratory cell and molecular biology*, 23, 182-187.
- SIDES, P. J., FARUQUI, D. & GELLMAN, A. J. 2009. Dynamics of charging of muscovite mica: measurement and modeling. *Langmuir*, 25, 1475-1481.
- SIEGRIST, M., WIEK, A., HELLAND, A. & KASTENHOLZ, H. 2007. Risks and nanotechnology: the public is more concerned than experts and industry. *Nature Nanotechnology*, 2, 67.
- SINNAMON, B., DLUHY, R. & BARNES, G. 1999. Reflection–absorption FT-IR spectroscopy of pentadecanoic acid at the air/water interface. *Colloids and Surfaces A: Physicochemical and Engineering Aspects*, 146, 49-61.
- SMITH, E. C., CRANE, J. M., LADERAS, T. G. & HALL, S. B. 2003. Metastability of a supercompressed fluid monolayer. *Biophysical journal*, 85, 3048-3057.
- SMITH, R. D. & BERG, J. C. 1980. The collapse of surfactant monolayers at the air—water interface. *Journal of Colloid and Interface Science*, 74, 273-286.

- SODHI, R. N. 2004. Time-of-flight secondary ion mass spectrometry (TOF-SIMS):— versatility in chemical and imaging surface analysis. *Analyst*, 129, 483-487.
- SOVAGO, M., WURPEL, G. W., SMITS, M., MÜLLER, M. & BONN, M. 2007. Calcium-induced phospholipid ordering depends on surface pressure. *Journal of the American Chemical Society*, 129, 11079-11084.
- STANKIEWICZ, J., VÍLCHEZ, M. A. C. & ALVAREZ, R. H. 1993. Two-dimensional aggregation of polystyrene latex particles. *Physical Review E*, 47, 2663.
- STEFANIU, C., BREZESINSKI, G. & MÖHWALD, H. 2012. Polymer-capped magnetite nanoparticles change the 2D structure of DPPC model membranes. *Soft Matter*, 8, 7952-7959.
- STOFFER, P. 2013. *Chapter 8 - Weathering, Mass Wasting, and Erosion* [Online]. Available: <http://geologycafe.com/class/chapter8.html> [Accessed].
- STONE, V., JOHNSTON, H. & CLIFT, M. J. D. 2007. Air Pollution, Ultrafine and Nanoparticle Toxicology: Cellular and Molecular Interactions. *IEEE Transactions on Nanobioscience*, 6, 331-340.
- STUART, D., LOEBENBERG, R., KU, T., AZARMI, S., ELY, L., ROA, W. & PRENNER, E. J. 2006. Biophysical Investigation of Nanoparticle Interactions with Lung Surfactant Model Systems. *Journal of Biomedical Nanotechnology* 2, 245-252
- STURM, R. 2010. Deposition and cellular interaction of cancer-inducing particles in the human respiratory tract: Theoretical approaches and experimental data. *Thoracic Cancer*, 1, 141-152.
- SU, W., WANG, L., WENG, S., WANG, H., DU, L., LIU, Y., YANG, L. & CHEN, W. 2008. [Effect of humidity and temperature on filter and gravimetric measurement of ambient particulate matter in a balance room]. *Zhonghua lao dong wei sheng zhi ye bing za zhi= Zhonghua laodong weisheng zhiyebing zazhi= Chinese journal of industrial hygiene and occupational diseases*, 26, 198-202.
- TABAK, S. & NOTTER, R. 1977. Modified technique for dynamic surface pressure and relaxation measurements at the air–water interface. *Review of Scientific Instruments*, 48, 1196-1201.
- TADMOR, R. & PEPPER, K. G. 2008. Interfacial tension and spreading coefficient for thin films. *Langmuir*, 24, 3185-3190.
- TAKAMOTO, D., LIPP, M., VON NAHMEN, A., LEE, K. Y. C., WARING, A. & ZASADZINSKI, J. 2001. Interaction of lung surfactant proteins with anionic phospholipids. *Biophysical Journal*, 81, 153-169.
- TAMAM, L., MENAHEM, T., MASTAI, Y., SLOUTSKIN, E., YEFET, S. & DEUTSCH, M. 2009. Langmuir films of chiral molecules on mercury. *Langmuir*, 25, 5111-5119.

- TATUR, S. & BADIA, A. 2011. Influence of hydrophobic alkylated gold nanoparticles on the phase behavior of monolayers of DPPC and clinical lung surfactant. *Langmuir*, 28, 628-639.
- TCHORELOFF, P., GULIK, A., DENIZOT, B., PROUST, J. E. & PUISIEUX, F. 1991. A structural study of interfacial phospholipid and lung surfactant layers by transmission electron microscopy after Blodgett sampling: influence of surface pressure and temperature. *Chemistry and physics of lipids* 59, 151-165
- TELESFORD, D.-M. L.-A. 2012. *Langmuir Trough and Brewster Angle Microscopy Study of Model Lung Surfactant Monolayers at the Air/Aqueous Interface*. The Ohio State University.
- THE ROYAL SOCIETY & THE ROYAL ACADEMY OF ENGINEERING. 2004. *Nanoscience and nanotechnology: Opportunities and uncertainties* [Online]. Available: <http://www.nanotec.org.uk/report/Nano%20report%202004%20fin.pdf> [Accessed].
- THEODOROU, I. G., BOTELHO, D., SCHWANDER, S., ZHANG, J., CHUNG, K. F., TETLEY, T. D., SHAFFER, M. S., GOW, A., RYAN, M. P. & PORTER, A. E. 2015. Static and Dynamic Microscopy of the Chemical Stability and Aggregation State of Silver Nanowires in Components of Murine Pulmonary Surfactant. *Environmental science & technology*, 49, 8048-8056.
- THERMOFISHER-SCIENTIFIC. 2015. *Introduction to FTIR spectroscopy* [Online]. Available: <https://www.thermofisher.com/uk/en/home/industrial/spectroscopy-elemental-isotope-analysis/spectroscopy-elemental-isotope-analysis-learning-center/molecular-spectroscopy-information/ftir-information/ftir-basics.html> [Accessed].
- THERMOPEDIA. 2015. *Surface and interfacial tension* [Online]. Available: <http://www.thermopedia.com/content/30/?tid=104&sn=1312> [Accessed].
- THIES, R., BEESLEY, R. C., PERSON, R. J., BLAIR, R. W., FARBER, J. P., FOREMAN, R. D., KLING, O. R., MCHALE, P. A., PERSON, R. J. & STITH, R. D. 2012. *Physiology*, Springer New York.
- TOIMIL, P., PRIETO, G., MIÑONES JR, J. & SARMIENTO, F. 2010. A comparative study of F-DPPC/DPPC mixed monolayers. Influence of subphase temperature on F-DPPC and DPPC monolayers. *Physical Chemistry Chemical Physics*, 12, 13323-13332.
- TORRANO, A. A., PEREIRA, A. S., OLIVEIRA, O. N. & BARROS-TIMMONS, A. 2013. Probing the interaction of oppositely charged gold nanoparticles with DPPG and DPPC Langmuir monolayers as cell membrane models. *Colloids and Surfaces B: Biointerfaces*, 108, 120-126.
- TORTORA, G. J. & DERRICKSON, B. H. 2011. *Principles of anatomy and physiology*, Wiley.
- TREFALT, G., SZILAGYI, I. & BORKOVEC, M. 2013. Measuring particle aggregation rates by light scattering.

- TRICOT, Y.-M. 1997. Surfactants: Static and Dynamic Surface Tension. *In*: KISTLER, S. F. & SCHWEIZER, P. M. (eds.) *Liquid Film Coating: Scientific principles and their technological implications*. Dordrecht: Springer Netherlands.
- TSI. 2005. *Model 3076 Constant Output Atomizer. Instruction Manual*. [Online]. Available: <http://www.wmo-gaw-wcc-aerosol-physics.org/files/Atomizer-TSI-3076.pdf> [Accessed].
- UR-HEALING-CONNECTION. 2015. *Natural Health & Wellness* [Online]. Available: <http://www.holisticnutritionhealing.com/index.html> [Accessed].
- VALLE, R. P., HUANG, C. L., LOO, J. S. & ZUO, Y. Y. 2014. Increasing hydrophobicity of nanoparticles intensifies lung surfactant film inhibition and particle retention. *ACS Sustainable Chemistry & Engineering*, 2, 1574-1580.
- VALLE, R. P., WU, T. & ZUO, Y. Y. 2015. Biophysical influence of airborne carbon nanomaterials on natural pulmonary surfactant. *ACS nano*, 9, 5413-5421.
- VARGAFTIK, N., VOLKOV, B. & VOLJAK, L. 1983. International tables of the surface tension of water. *Journal of Physical and Chemical Reference Data*, 12, 817-820.
- VAYRYNEN, O. 2003. *Proinflammatory cytokines modify the expression of surfactant proteins: Study in perinatal rabbit lung*. University of Oulu.
- VELDHUIZEN, R., NAG, K., ORGEIG, S. & POSSMAYER, F. 1998. The role of lipids in pulmonary surfactant. *Biochimica et Biophysica Acta (BBA)-Molecular Basis of Disease*, 1408, 90-108.
- VITOVIC, P., NIKOLELIS, D. & HIANIK, T. 2006. Study of calix [4] resorcinarene–dopamine complexation in mixed phospholipid monolayers formed at the air–water interface. *Biochimica et Biophysica Acta (BBA)-Biomembranes*, 1758, 1852-1861.
- VYAS, S. 2005. *Simulation of Ceria: Bulk and Surface Defects*. Doctor of Philosophy, Imperial College London.
- WALTERS, R. W., JENQ, R. R. & HALL, S. B. 2000. Distinct steps in the adsorption of pulmonary surfactant to an air-liquid interface. *Biophysical journal*, 78, 257-266.
- WALTON, A. J. 1983. *Three phases of matter*, Oxford University Press.
- WANG, Z., GUREL, O., WEINBACH, S. & NOTTER, R. H. 1997. Primary importance of zwitterionic over anionic phospholipids in the surface-active function of calf lung surfactant extract. *American journal of respiratory and critical care medicine*, 156, 1049-1057.
- WANG, Z., LI, X. & YANG, S. 2009. Studies of dipalmitoylphosphatidylcholine (DPPC) monolayers embedded with endohedral metallofullerene (Dy@ C82). *Langmuir*, 25, 12968-12973.

- WARE, L. B. & MATTHAY, M. A. 2000. The acute respiratory distress syndrome. *New England Journal of Medicine*, 342, 1334-1349.
- WATKINS, E., MILLER, C., MULDER, D., KUHL, T. & MAJEWSKI, J. 2009. Structure and orientational texture of self-organizing lipid bilayers. *Physical review letters*, 102, 238101.
- WATKINS, J. 1968. The surface properties of pure phospholipids in relation to those of lung extracts. *Biochimica et Biophysica Acta (BBA)-Lipids and Lipid Metabolism*, 152, 293-306.
- WAUER, R. R. 1998. *Surfactant therapy: basic principles, diagnosis, therapy*, Georg Thieme Verlag.
- WEAVER, T. E. & CONKRIGHT, J. J. 2001. Function of surfactant proteins B and C. *Annual Review of Physiology*, 63, 555-578.
- WEIR, R. D. & DE LOOS, T. W. 2005. *Measurement of the thermodynamic properties of multiple phases*, Gulf Professional Publishing.
- WEN, G., CHUNG, B. & CHANG, T. 2006. Effect of spreading solvents on Langmuir monolayers and Langmuir–Blodgett films of PS-b-P2VP. *Polymer*, 47, 8575-8582.
- WEN, X. & FRANCES, E. I. 2001. Role of subsurface particulates on the dynamic adsorption of dipalmitoylphosphatidylcholine at the air/water interface. *Langmuir*, 17, 3194-3201.
- WEST, J. B. 2012. *Respiratory Physiology: The Essentials*, Wolters Kluwer Health/Lippincott Williams & Wilkins.
- WIESNER, M. R., LOWRY, G. V., ALVAREZ, P., DIONYSIOU, D. & BISWAS, P. 2006. Assessing the Risks of Manufactured Nanomaterials. *Environmental science & technology* 40, 4336-4345
- WILDEBOER-VENEMA, F. 1980. The influences of temperature and humidity upon the isolated surfactant film of the dog. *Respiration physiology*, 39, 63-71.
- WRIGHT, J. R. 2005. Immunoregulatory functions of surfactant proteins. *Nature Reviews: Immunology*, 5, 58-68.
- XIA, T., LI, N. & NEL, A. E. 2009. Potential health impact of nanoparticles. *Annual review of public health*, 30, 137-150.
- XIE, Y., WILLIAMS, N. G., TOLIC, A., CHRISLER, W. B., TEEGUARDEN, J. G., MADDUX, B. L., POUNDS, J. G., LASKIN, A. & ORR, G. 2012. Aerosolized ZnO nanoparticles induce toxicity in alveolar type II epithelial cells at the air-liquid interface. *Toxicological Sciences*, 125, 450-461.

- YAMADA, H., NARITA, S., ONODERA, H., SUZUKI, H., TANAKA, N., NYUI, T. & USHIROZAWA, T. 2003. Analysis by time-of-flight secondary ion mass spectroscopy for nuclear products in hydrogen penetration through palladium. *Proceedings of ICCF-10, Cambridge, Aug, 24-29.*
- YAMASHITA, M. & YAMANAKA, S. 2013. Dust Resulting from Tire Wear and the Risk of Health Hazards.
- YAMAWAKI, H. & IWAI, N. 2006. Mechanisms underlying nano-sized air-pollution-mediated progression of atherosclerosis carbon black causes cytotoxic injury/inflammation and inhibits cell growth in vascular endothelial cells. *Circulation Journal*, 70, 129-140.
- YOKEL, R. A., HUSSAIN, S., GARANTZIOTIS, S., DEMOKRITOU, P., CASTRANOVA, V. & CASSEE, F. R. 2014. The yin: an adverse health perspective of nanoceria: uptake, distribution, accumulation, and mechanisms of its toxicity. *Environmental Science: Nano*, 1, 406-428.
- YOU, S. S., HEFFERN, C. T., DAI, Y., MERON, M., HENDERSON, J. M., BU, W., XIE, W., LEE, K. Y. C. & LIN, B. 2016. Liquid Surface X-ray Studies of Gold Nanoparticle-Phospholipid Films at the Air/Water Interface. *arXiv preprint arXiv:1603.09024.*
- YU, S.-H. & POSSMAYER, F. 2003. Lipid compositional analysis of pulmonary surfactant monolayers and monolayer-associated reservoirs. *Journal of lipid research*, 44, 621-629.
- YU, Z.-W., JIN, J. & CAO, Y. 2002. Characterization of the liquid-expanded to liquid-condensed phase transition of monolayers by means of compressibility. *Langmuir*, 18, 4530-4531.
- YUAN, C. & JOHNSTON, L. 2002. Phase evolution in cholesterol/DPPC monolayers: atomic force microscopy and near field scanning optical microscopy studies. *Journal of microscopy*, 205, 136-146.
- YUAN, Y. & LEE, T. R. 2013. Contact angle and wetting properties. *Surface science techniques*. Springer.
- YUN, H., CHOI, Y.-W., KIM, N. J. & SOHN, D. 2003. Physicochemical properties of phosphatidylcholine (PC) monolayers with different alkyl chains, at the air/water interface. *Bulletin-Korean Chemical Society*, 24, 377-383.
- ZAITSEV, S. Y., VERESCHETIN, V., ZUBOV, V., ZEISS, W. & MÖBIUS, D. 1996. Ionic selectivity of valinomycin in the dipalmitoylphosphatidylcholine monolayers. *Thin solid films*, 284, 667-670.
- ZHANG, C. & CARLONI, P. 2012. Salt effects on water/hydrophobic liquid interfaces: a molecular dynamics study. *Journal of Physics: Condensed Matter*, 24, 124109.

- ZHANG, H., FAN, Q., WANG, Y. E., NEAL, C. R. & ZUO, Y. Y. 2011a. Comparative study of clinical pulmonary surfactants using atomic force microscopy. *Biochimica et biophysica acta* 1808, 1832-1842
- ZHANG, H., WANG, Y. E., FAN, Q. & ZUO, Y. Y. 2011b. On the Low Surface Tension of Lung Surfactant. *Langmuir : the ACS journal of surfaces and colloids* 27, 8351-8358
- ZHANG, J.-P., WANG, Y.-L., WANG, Y.-H., ZHANG, R., CHEN, H. & SU, H.-B. 2004. Prophylaxis of neonatal respiratory distress syndrome by intra-amniotic administration of pulmonary surfactant. *Chinese medical journal*, 117, 120-124.
- ZHAO, G.-X., ZHU, B.-Y., DOU, Z.-P., YAN, P. & XIAO, J.-X. 2008. Effect of charge distribution along surfactant molecules on physico-chemical properties of surfactant systems. *Colloids and Surfaces A: Physicochemical and Engineering Aspects*, 327, 122-126.
- ZUO, Y. Y., ACOSTA, E., POLICOVA, Z., COX, P. N., HAIR, M. L. & NEUMANN, A. W. 2006. Effect of humidity on the stability of lung surfactant films adsorbed at air–water interfaces. *Biochimica et Biophysica Acta (BBA)-Biomembranes*, 1758, 1609-1620.
- ZUO, Y. Y., GITIAFROZ, R., ACOSTA, E., POLICOVA, Z., COX, P. N., HAIR, M. L. & NEUMANN, A. W. 2005. Effect of Humidity on the Adsorption Kinetics of Lung Surfactant at Air-Water Interfaces. *Langmuir : the ACS journal of surfaces and colloids* 21, 10593-10601
- ZUO, Y. Y., KEATING, E., ZHAO, L., TADAYYON, S. M., VELDHUIZEN, R. A., PETERSEN, N. O. & POSSMAYER, F. 2008a. Atomic Force Microscopy Studies of Functional and Dysfunctional Pulmonary Surfactant Films. I. Micro- and *Biophysical journal* 94, 3549-3564
- ZUO, Y. Y., TADAYYON, S. M., KEATING, E., ZHAO, L., VELDHUIZEN, R. A., PETERSEN, N. O., AMREIN, M. W. & POSSMAYER, F. 2008b. Atomic Force Microscopy Studies of Functional and Dysfunctional Pulmonary Surfactant Films, II. *Biophysical journal* 95, 2779-2791
- ZUO, Y. Y., VELDHUIZEN, R. A., NEUMANN, A. W., PETERSEN, N. O. & POSSMAYER, F. 2008c. Current perspectives in pulmonary surfactant—inhibition, enhancement and evaluation. *Biochimica et Biophysica Acta (BBA)-Biomembranes*, 1778, 1947-1977.

APPENDICES

APPENDIX 1 - Surface tension: key concepts

A. The Laplace equation for spherical interfaces

This equation is named after Pierre-Simon Laplace (1749-1827). A fluid surface remains flat when no force acts perpendicular to the surface. But if the pressure on one side of the surface is different from the pressure on the other side, the pressure difference results in a force acting along the normal to the interface at each point which curves the surface of the fluid. For example, in a bubble immersed in a fluid, the pressure inside the bubble is greater than the pressure outside the bubble. The force of surface tension acts tangentially at all points around the perimeter of the bubble and tends to collapse the bubble (Figure S1).

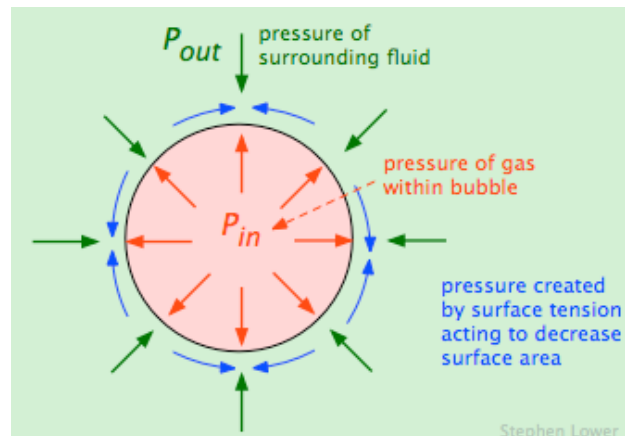


Figure S1. Bubble immersed in a fluid. The pressure outside the bubble is different from the pressure inside the bubble which curves the surface of the fluid. The force of surface tension acts tangentially at all points around the perimeter of the bubble (Lower, 2015).

The pressure inside the bubble must be sufficient to oppose the pressure outside of it and the surface tension force. This is expressed in the Laplace equation (Equation S1) which says that the pressure required to sustain a spherical surface is directly dependent on the surface tension and inversely dependent on its radius. Thus, smaller bubbles have the greatest internal gas pressures.

$$P_{in} = P_{out} + \frac{2\gamma}{r}$$

Equation S1

where P_{in} is the pressure inside the bubble; P_{out} is the pressure outside the bubble; r is the radius of the sphere and γ is the surface tension

For a bubble with two surfaces (an inner surface and an outer surface) such as a soap bubble, the value of the force due to surface tension is the double: $4\gamma/r$ (Figure S2). A spherical droplet of liquid has one surface only.



Figure S2. Illustration of the inner and the outer surfaces of a soap bubble. Adapted from Causes-of-Color, 2015.

B. Contact angle

Surface tension is a property of a fluid's interface with another medium. When a drop of liquid is placed onto a solid, three different interfaces are formed: an interface between the liquid and the surrounding atmosphere (referred to as vapour), an interface between the liquid and the solid and an interface between the vapour and the solid. Each interface has a value of surface tension which is usually different. The point where the three interfaces meet is called triple interface and it will move in response to the horizontal component of the forces arising from the three surface tensions until an equilibrium position is reached. At this point, the geometry must be such that all forces balance (De Gennes et al., 2004). The angle between the solid surface and the tangent to the liquid surface at the line of contact with the solid is known as wetting contact angle or contact angle (θ). By convention, it is measured in the liquid phase (Figure S3).

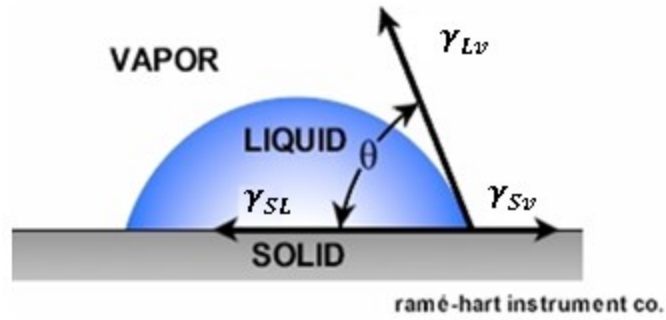


Figure S3. Schematic of the surface tension forces at equilibrium and contact angle of a drop of liquid placed onto a solid. γ^{sv} is the surface tension force at the solid-vapour interface. γ^{sl} is the surface tension force at the solid-liquid interface. γ^{lv} is the surface tension force at the liquid-vapour interface. θ is the wetting contact angle. Adapted from Ramé-hart-instrument-company, 2015.

The relationship between the various surface tensions and the contact angle at the equilibrium situation when the surface tension forces balance each other is given by the Young equation (Equation S2) (Krishnakumar, 2010):

$$\gamma^{sv} = \gamma^{sl} + \gamma^{lv} \cos\theta \quad \text{Equation S2}$$

where γ^{sv} is the surface tension force at the solid-vapour interface; γ^{sl} is the surface tension force at the solid-liquid interface; γ^{lv} is the surface tension force at the liquid-vapour interface and θ is the wetting contact angle measured in the liquid phase

A static contact angle is measured when the liquid droplet is standing on the surface and the three-phase contact line is not moving. When the three phase boundary is moving, dynamic contact angles are measured. In particular, the contact angles formed by expanding (wetting) and contracting (de-wetting) the liquid are referred to as the advancing and receding contact angle respectively. Dynamic contact angles can be measured at various rates of speed. At a low speed, the contact angle should be close or equal to a properly measured static contact angle (Yuan and Lee, 2013). Dynamic processes such as coating are better modelled by means of dynamic measurements whereas static contact angles are often more meaningful for assessing quasi-static processes such as bonding in semiconductor technology (KRÜSS, 2017).

C. Wetting

If the adhesive forces between a solid and a liquid are stronger than the cohesive forces between the liquid molecules, the liquid spreads across the solid surface. On the contrary, if cohesive forces within the liquid are stronger than adhesive forces between a solid and a liquid, the liquid will not spread and remains as a droplet on the solid to avoid contact with the surface or in some cases, it will even try to leave the surface (Krishnakumar, 2010). Wetting is the ability of a liquid to maintain contact with a solid surface. It is determined principally by the forces acting at the relevant interfaces and quantified by the contact angle at equilibrium: since the tendency of a liquid to spread over a solid surface increases as the contact angle decreases, the contact angle is an inverse measure of wettability (Shafrin and Zisman, 1960). If $\theta = 0^\circ$ there is complete or perfect wetting; if $\theta < 90^\circ$ the liquid partially wets the solid; if $90^\circ < \theta < 180^\circ$ the liquid does not wet the solid. Contact angles above 180° are not found as there is always some interaction between the liquid and the solid.

If the liquid is water, the solid surface is called superhydrophilic when $\theta < 5^\circ$; hydrophilic when $\theta < 90^\circ$; hydrophobic when $90^\circ < \theta < 150^\circ$ and superhydrophobic when $150^\circ < \theta < 180^\circ$ (Figure S4) (Nuraje et al., 2013). A hydrophilic solid surface has primarily polar groups on the surface which have a good affinity for water and therefore, strong adhesive forces and a low contact angle. A hydrophobic surface is made up of non-polar groups which do not have affinity for water and therefore weak adhesive forces and a large contact angle. When the liquids are different from water, the terms used are lyophilic (solvent loving) and lyophobic (solvent hating) (Barnes and Gentle, 2011).

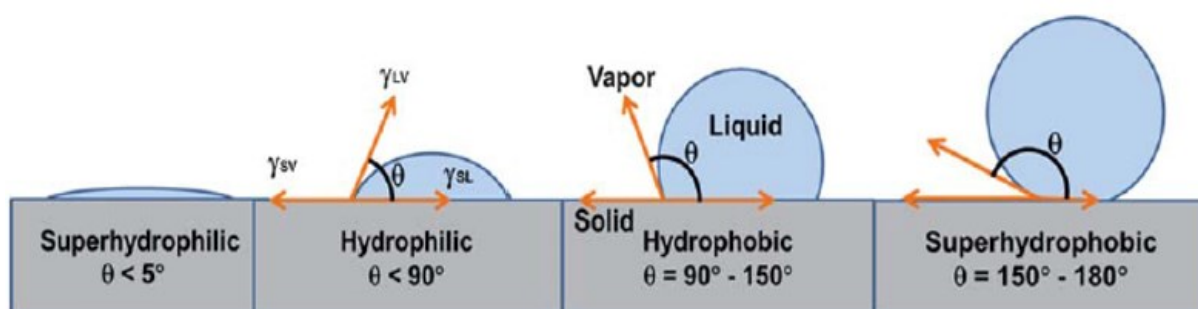


Figure S4. Schematic view of superhydrophilic, hydrophilic, hydrophobic and superhydrophobic solid surfaces. γ^{sv} is the surface tension force at the solid-vapour interface. γ^{sl} is the surface tension force at the solid-liquid interface. γ^{lv} is the surface tension force at the liquid-vapour interface. θ is the wetting contact angle (Nuraje et al., 2013).

D. Spreading coefficient

The spreading coefficient, also called work of spreading, measures the spreading of a liquid as a film per unit surface of a solid or another liquid. During the spreading of the liquid onto a solid surface, two interfaces are created (liquid-vapour and liquid-solid) and one is destroyed (solid-vapour). The spreading coefficient at equilibrium is equal to the surface tension at the solid-vapour interface minus the surface tension at the liquid-vapour interface minus the surface tension at the solid-liquid interface as shown in the following equation (Equation S3) (Tadmor and Pepper, 2008):

$$S^{LS} = \gamma^{Sv} - (\gamma^{Lv} + \gamma^{SL}) \quad \text{Equation S3}$$

where S^{LS} is the spreading coefficient at equilibrium; γ^{Sv} is the surface tension force at the solid-vapour interface; γ^{Lv} is the surface tension force at the liquid-vapour interface and γ^{SL} is the surface tension force at the solid-liquid interface

The value of the spreading coefficient can be positive or negative. If the spreading coefficient is positive the liquid will spread completely whereas if the spreading coefficient is negative, the liquid will not spread and form a drop on the surface with a definite wetting contact angle.

E. Floating

Archimedes' principle states the following:

Any object, wholly or partially immersed in a fluid, is buoyed up by a force equal to the weight of the fluid displaced by the object

In simple terms, the principle states that the buoyancy force on an object is equal to the weight of the fluid displaced by the object. This means that if an object is fully submerged in a fluid and its density is lower than the density of the fluid, it will experience a buoyancy force greater than its own weight and it will float. If the object has the same density as the fluid, the buoyancy force will equal its weight and will remain suspended in the fluid, neither sinking nor floating. If the density of the object is higher than the density of the fluid, the weight of the object will be greater than the buoyancy force and the object will sink.

Archimedes' principle does not consider the surface tension force acting on the body. However, the surface tension of a liquid can provide a buoyant force large enough to float small objects denser than the liquid (Liu et al., 2007). Surface tension modifies only the amount of fluid displaced so the principle *Buoyant force = weight of the displaced fluid* remains valid.

APPENDIX 2 - Methods to measure surface tension

There are several ways of measuring the surface tension of a liquid (Duncan, 1980, Barnes and Gentle, 2011).

a) Capillary rise method. This method is the oldest method and one of the most accurate one to determine surface tension. It consists of the dipping of a thin circular capillary into the tested liquid. If the interaction forces of the liquid with the capillary walls (adhesion) are stronger than those between the liquid molecules (cohesion), the liquid wets the walls and rises up the capillary until an equilibrium position is attained (Figure S5).

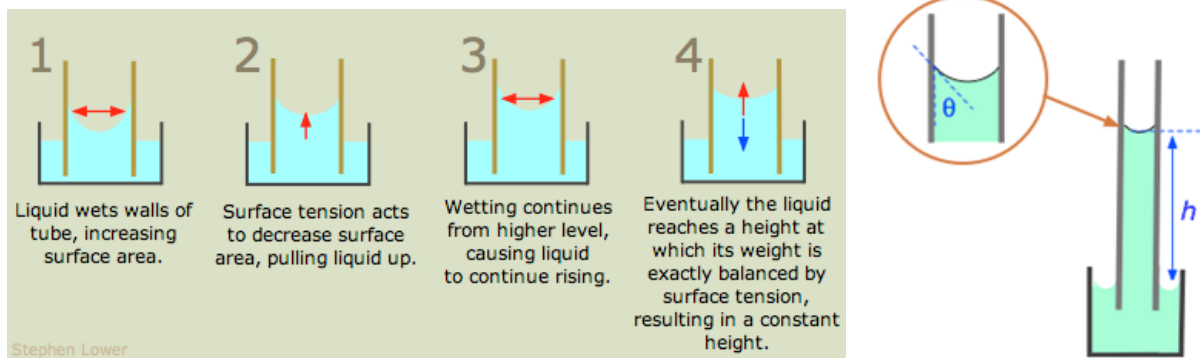


Figure S5. Schematic of the phenomenon of capillary rise. h is the height the liquid reaches in the capillary. θ is the contact angle. Adapted from Lower, 2015.

At this point, it can be considered that the liquid column in the capillary is supported by the surface tension. The surface tension of the liquid is related to the height the solution reaches inside the capillary as shown in the following equation:

$$h = \frac{2\gamma \cos\theta}{\rho g r}$$

Equation S4

where h is the height the liquid reaches in the capillary; γ is the surface tension at the air/liquid interface; θ is the contact angle; ρ is the density of the liquid; g is the gravitational constant and r is the radius of the capillary

To accurately determine surface tension of a pure liquid, it is essential that the capillary is perfectly clean so that the contact angle is zero, due to the uncertainty in measuring contact angles in a capillary.

b) Wilhelmy plate. This method is based on a rectangular thin plate named after the scientist Ludwig Ferdinand Wilhelmy (1812-1864) who first used it as a device to measure surface tension. The plate is hanging vertically from the arm of a balance, partially immersed in a liquid subphase and perfectly wetted by the liquid (Figure S6).

Three forces act on the plate (Figure S7): gravity and surface tension downward and buoyancy due to the displaced liquid upward (Duncan, 1980, Petty, 1996, Weir and de Loos, 2005, KSV-Nima, 2010, Barnes and Gentle, 2011). The net force acting on the plate is given by the following equation:

$$F = \rho_P g l_P w_P t_P + 2\gamma(t_P + w_P)(\cos\theta) - \rho_L g t_L w_L d_L \quad \text{Equation S5}$$

where ρ_P is the density of the plate; g is the gravitational constant; l_P is the length of the plate; w_P is the width of the plate; t_P is the thickness of the plate; γ is the surface tension at the air/liquid interface; θ is the contact angle; ρ_L is the density of the liquid and $t_L w_L d_L$ is the volume of the displaced liquid due to the immersion of the plate in the liquid, being d the depth the plate is immersed

The Π is calculated by measuring the change in the net force that acts on the plate when the air/liquid interface is clean and when the same interface has a surfactant monolayer. The gravity and buoyancy force will be the same in each situation. If we assume that the plate is perfectly wetted by the liquid ($\theta = 0^\circ$ and therefore $\cos\theta = 1$), Π is obtained from the following equation:

$$F - F_0 = 2(t_p + w_p)(\gamma - \gamma_0)$$

$$\Delta\gamma = \Pi = -[\Delta F/2(t_p + w_p)]$$

Equation S6

where F_0 and γ_0 are the net force and surface tension in the absence of the monolayer respectively; F and γ are the net force and surface tension with the monolayer present respectively; Π is the surface pressure ($\gamma_0 - \gamma$); t_p is the thickness of the plate and w_p is the width of the plate

If the plate used is very thin ($w_p \gg t_p$), the difference on the net force acting on the plate is determined by measuring the changes in the mass of the plate by a balance to which the plate is coupled.

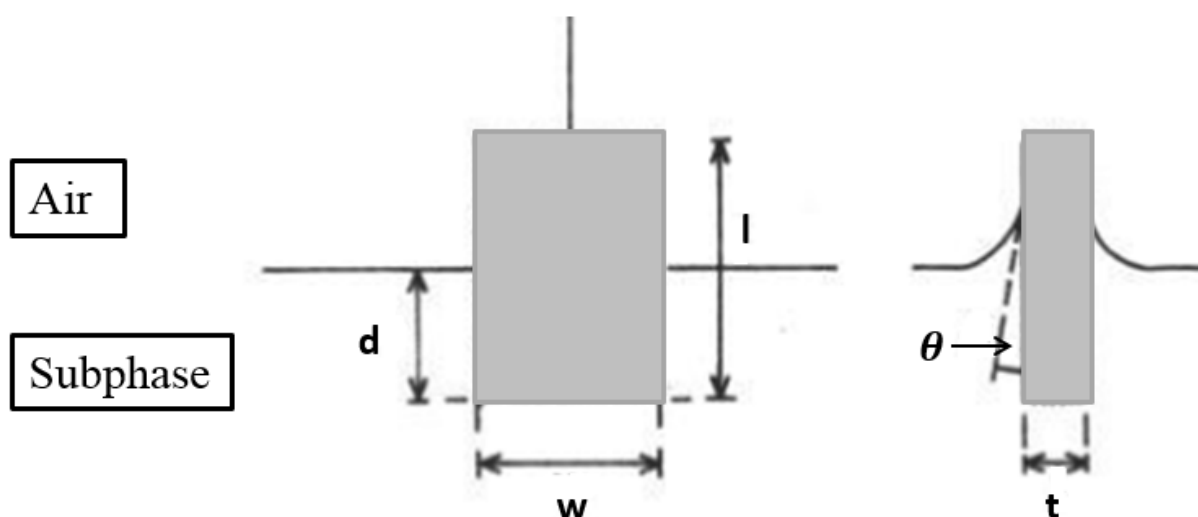


Figure S6. Schematic of a Wilhelmy plate partially immersed in a liquid subphase. w , l , t are the plate width, length and thickness respectively. d is the depth the plate is immersed in the liquid subphase. θ is the contact angle. Adapted from KSV-Nima, 2010.

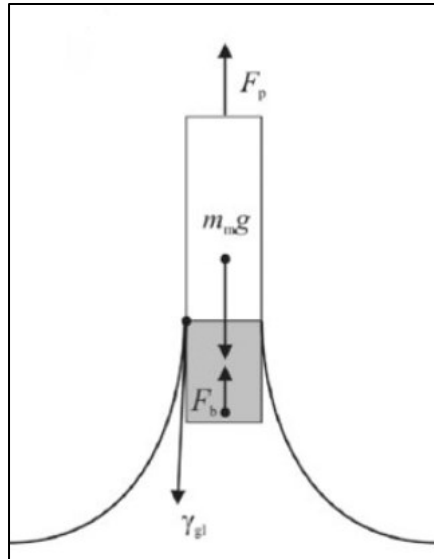


Figure S7. Schematic of the forces acting on a Wilhelmy plate partially immersed in a liquid subphase. Three forces act on the plate: gravity ($m_m g$) and surface tension (γ_{gl}) downward and buoyancy due to the displaced liquid upward (F_b). F_p is the net force acting on the plate (Johans et al., 2005).

c) **Drop weight or volume.** This method is based on the fact that a drop of a liquid hanging from the tip of a capillary is supported by the surface tension of the liquid (Figure S8).



Figure S8. Schematic of the detachment sequence of a drop hanging from the tip of a capillary (Thermopedia, 2015).

The pendant drop at the tip starts to detach when the downward force due to its weight (volume) is balanced by the upward force due to the surface tension at the line of contact with the tube tip. Drops detach slowly from the tip of the vertical narrow tube and can be either weighed or their volume measured as shown in the following equation:

$$\gamma = \frac{\emptyset mg}{2\pi r} = \frac{\emptyset V \rho g}{2\pi r}$$

Equation S7

where γ is the surface tension of the liquid; m is the mass of the drop; V is the volume of the drop; g is the gravitational constant; ρ is the density of the liquid; r is the radius of the capillary tube and \emptyset is a correction factor

A correction factor is required as up to 40% of the drop volume may remain attached to the tip and therefore, the weight measured would not be the total weight of the drop. This correction factor has been determined empirically by Harkins and Brown and is a function of the drop volume, the capillary tip radius and a constant which is characteristic of a given capillary tube (Harkins and Brown, 1919).

d) Maximum bubble pressure. This method is also called the bubble pressure method. In this method, a bubble of an inert gas is blown at a constant rate through a capillary which is submerged in the tested liquid. The maximum value of pressure inside the gas bubble is reached when the radius of the bubble is equal to the radius of the capillary as the radius of the bubble reaches its minimum value (Figure S9).

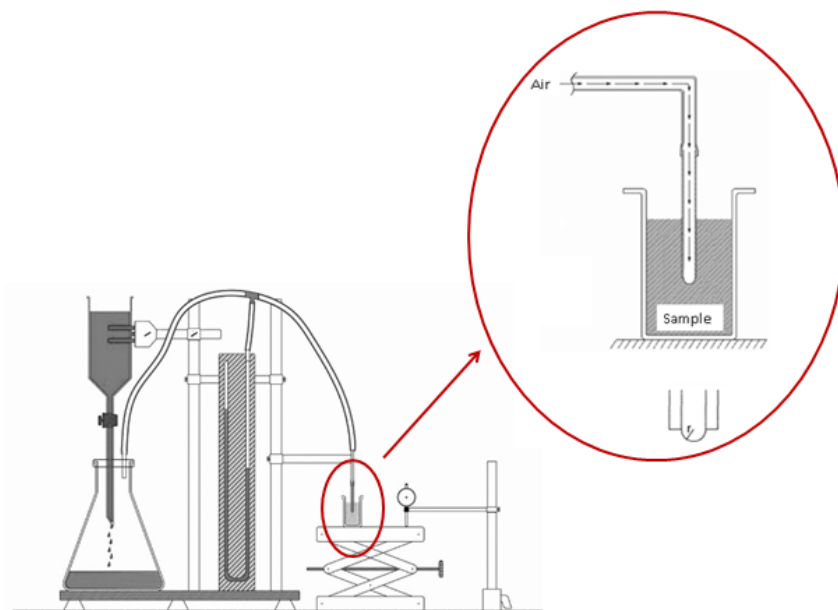


Figure S9. Schematic of the device used to measure the surface tension of a liquid by the maximum bubble pressure method. Adapted from De Gennes et al., 2004.

Surface tension can be calculated from the Laplace equation as follows:

$$\Delta P = \frac{2\gamma}{r}$$

Equation S8

where ΔP is the difference between the pressure applied to the capillary and atmospheric pressure; γ is the surface tension and r is the radius of the capillary. ΔP needs to be corrected for the small hydrostatic pressure arising from the depth of immersion

e) Pendant and sessile drop profile method. In this method, drops are suspended from the end of a tube (pendant drop) or formed on a flat surface (sessile drop) (Figure S10). The drop of liquid is photographed or its image projected onto graph paper. Axisymmetric drop shape analysis (ADSA) computing techniques can be used to determine the surface tension by fitting the shape and dimensions of pendant and sessile drops to theoretical profiles given by the Laplace equation (Del Río and Neumann, 1997). This method requires small volumes of liquid which is very convenient when measuring surface tension of expensive liquids (De Gennes et al., 2004).

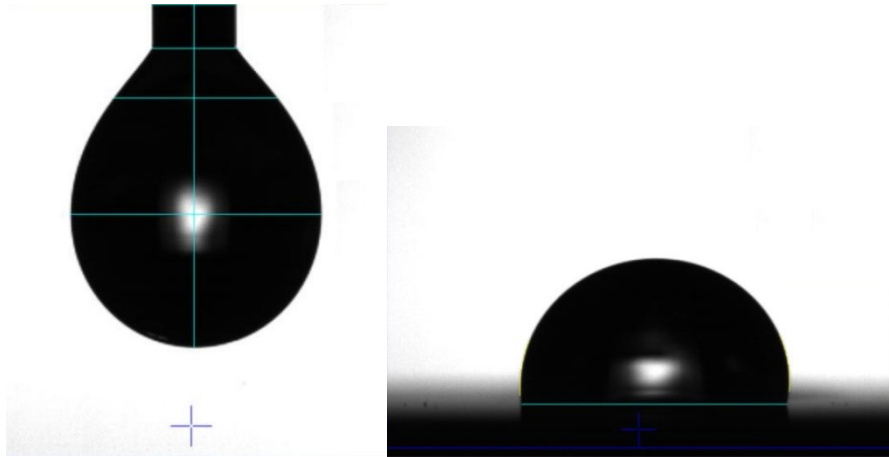


Figure S10. Camera images of pendant (left) and sessile (right) drops. Adapted from First-Ten-Ångstroms, 2015.

f) Indicator oils. These are employed in situations where the use of laboratory instrumentation is not feasible. This method is normally used to detect the presence of a surface film onto a subphase liquid and to estimate the change in surface tension caused by the film by observing the spreading of drops of various indicator oils with different spreading coefficients on the surface of the liquid.

APPENDIX 3

A *II*-Mma isotherm is analogous to a pressure-volume (P-V) diagram for a pure component when the temperature is held constant. In fact, the monolayer phases bear some resemblance to the gaseous, liquid and solid states in the three-dimensional matter (Duncan, 1980, Satake et al., 2003, Shinoda et al., 2013). In a P-V diagram such as that shown in Figure S11, a gas undergoes an isothermal compression process which results in a significant reduction in volume, going from a starting point A to a point B where the gas is saturated. In this region, the ideal gas law describes the relationship between the pressure and volume of the substance as shown in equation S9:

$$P = \frac{nRT}{V} = \frac{\text{constant}}{V}$$

Equation S9

where P is pressure; n is the number of moles of gas present; R is the ideal gas constant; T is temperature and V is volume. The product PV is a constant if the gas is kept at isothermal conditions

If the isothermal compression process continues, the first liquid droplet appears and thus liquid and vapour coexist in equilibrium. In this situation, the pressure of the system remains constant until all the vapour becomes liquid (path B - C). At point C, a rapid increase in pressure occurs with compression as indicated by the steep slope in the P-V diagram. This is caused by the high incompressibility of the liquid state in where a great deal of pressure is needed to cause a small reduction in volume.

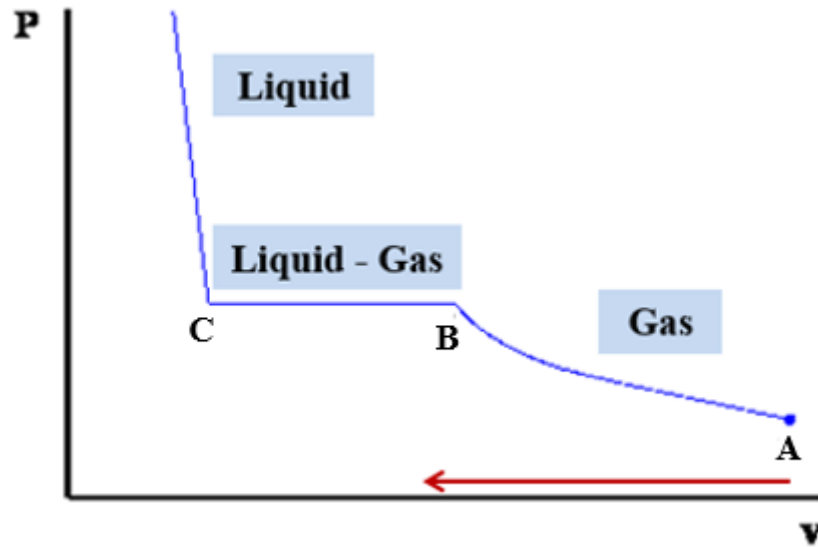


Figure S11. Graphical representation of the theoretical pressure-volume diagram obtained by isothermal compression or volume reduction of a pure gaseous component. The red arrow shows the direction of isotherm formation. Letters A, B and C refer to different key points in the isotherm. Adapted from Adewumi, 2016.

APPENDIX 4

The main function of the respiratory system in humans is the process of breathing or gas exchange. Most of the organs and structures help the system to distribute air downstream but only the alveoli are responsible for gas exchange (Parent, 2015). Gas exchange occurs on the surface of each alveolus by a network of capillaries that surround the walls of the alveoli and that carry blood that has come through veins from other parts of the body (MedlinePlus, 2012).

In addition to gas exchange and air distribution, the respiratory system filters the incoming air and clears it from trapped pathogens and particles (Möller et al., 2004). It also warms and humidifies the air when passing through the conducting airways to achieve a temperature of 37°C and 100% relative humidity at the alveoli (Man et al., 1979).

Organs in the respiratory system also play a role in speech and the sense of smell.

The process of breathing

The process of breathing refers to the delivery of oxygen from the lungs to the bloodstream and the elimination of carbon dioxide from the bloodstream to the lungs. Apart from the organs and structures of the lower and the upper respiratory tract, there are other important structures and muscles that play a role in the breathing process. These are the external intercostal muscles, the pleura and the diaphragm (Figure S12):

- **External intercostal muscles:** These are muscles that connect adjacent ribs.

- **Pleura:** It is a two layered-membrane structure that lines the lungs and the chest cavity. The inner pleura, which covers the lungs, is called the visceral pleura whereas the outer pleura, which covers the chest wall, is called the parietal pleura. The space between the two pleura is called pleural cavity. Intrapleural pressure refers to the pressure within the pleural cavity and is lower than the atmospheric pressure in healthy lungs, what is known as negative pressure. Transpulmonary pressure is the difference between the alveolar pressure (pressure held within the alveoli of the lungs) and the intrapleural pressure. In healthy lungs, transpulmonary pressure is positive.

- **Diaphragm:** It is the principal muscle of respiration in the human body located at the bottom of the rib cage.

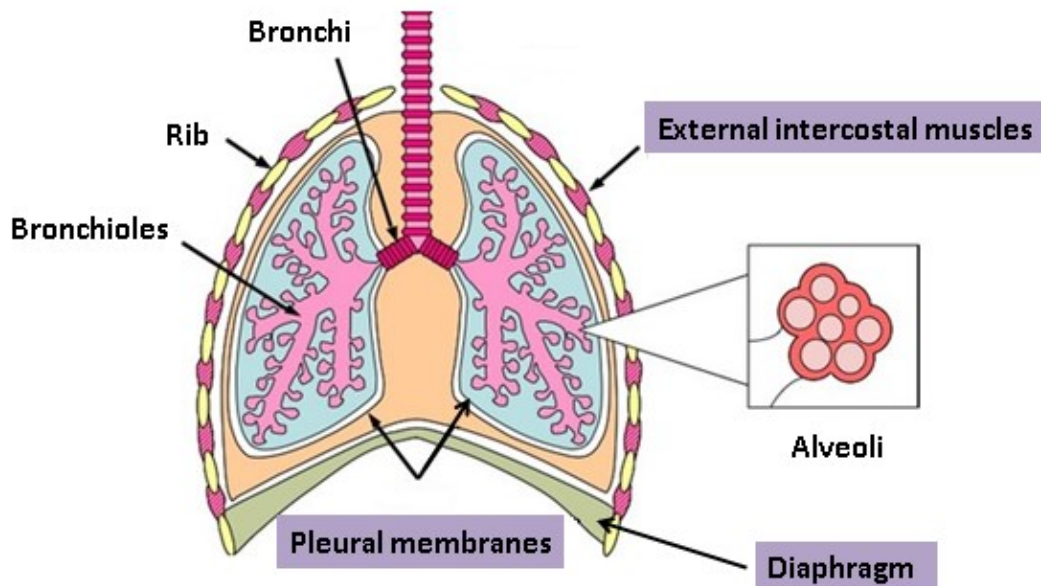


Figure S12. Schematic diagram of the positioning of the pleural membranes, the diaphragm and the external intercostal muscles within the respiratory system. Adapted from UR-Healing-Connection, 2015.

In the process of breathing, the lungs expand to take in air (inhalation) and then contract passively to expel it (exhalation). The volume of air inspired or expired per breath is called tidal volume and is approximately 500 mL at rest (Tortora and Derrickson, 2011). Air moves in and out of the lungs in response to differences in pressure. The inhalation-exhalation cycle of breathing occurs about 10-15 times per minute (Klein et al., 1998a, Melikov and Kaczmarczyk, 2007). Gas exchange occurs by diffusion. The process of breathing consists of three phases (Thies et al., 2012, Erdemli, 2015):

- **Inspiration or inhalation:** Inspiration is the process of drawing air into the lungs and is the active part of the breathing process. It is initiated by the contraction of the external intercostal muscles, which move the sternum upwards and outwards and thus, the width of the chest increases. The diaphragm also contracts and descends, which increases the depth of the chest. This leads to a reduction in the intrapleural pressure. The lungs expand to fill the thoracic cavity and the elastic tissue of the lungs is stretched. The space enclosing lung air increases and thus, there is less air per unit volume of the lungs which causes the alveolar pressure to be lower than the atmospheric pressure. Thus, air is drawn into the alveoli from

the atmosphere until alveolar pressure equals atmospheric pressure. The average person inhales about 10,000 litres of gas per day (Wright, 2005).

- **Expiration or exhalation:** Expiration is the process of releasing air from the lungs. It is a passive event in where the external intercostal muscles relax, which moves the sternum downwards and inwards and thus, the width of the chest diminishes. The diaphragm also relaxes and ascends, which decreases the depth of the chest. This leads to an increase in the intrapleural pressure. The elastic tissue of the lungs recoils. The space enclosing lung air decreases and hence, there is more air per unit volume of the lungs which causes the alveolar pressure to be higher than the atmospheric pressure. Thus, air is exhaled from the alveoli into the atmosphere until alveolar pressure equals atmospheric pressure at the original lung volume. Functional residual capacity is the volume of air present in the lungs at the end of passive expiration. There is always some air remaining to prevent the lungs from collapsing.
- **Gas exchange:** Gas exchange occurs by diffusion. Diffusion occurs when molecules move from an area of high concentration to an area of low concentration. During inhalation, the blood in the capillaries surrounding the alveoli has a lower oxygen concentration than the air in the alveoli which has just been inhaled and oxygen diffuses from the alveoli to the capillaries. The same happens with carbon dioxide which is a by-product of cellular and metabolic reactions. The blood in the surrounding capillaries has a higher concentration of carbon dioxide than the inspired air. Therefore carbon dioxide diffuses from the capillaries into the alveoli where it is exhaled. The total surface area for gas exchange is around 80 m² per adult human lung (Cook et al., 2006). Hence, the lungs have the largest surface of the body in contact with the environment (West, 2012).

The elastic recoil of the lungs

Elastic recoil is a static property that refers to the resistance to change in shape and the tendency to return to the original shape or resting position once deformed and upon removal of an opposing force. The lungs resist stretch and have a tendency to collapse because of their elastic recoil. This phenomenon occurs because of two factors (Boulpaep et al., 2009):

- a) **The elasticity of pulmonary cells and the extracellular matrix in the connective tissue of the lungs**

- b) **The surface tension of the liquid that lines the alveoli at the air/liquid interface.** Surface tension accounts for two-thirds of the lung elastic recoil (Tortora and Derrickson, 2011). Because the attractive forces between adjacent molecules of the liquid are much stronger than those between the liquid and the gas, there is a pressure difference at both sides of the air/water interface which makes the interface to contract as much as possible and form the smallest possible surface area: a sphere. The force of surface tension acts tangentially at all points around the interface and tends to collapse the alveoli (Erdemli, 2015). According to the Laplace equation for spherical interfaces, surface tension is inversely proportional to the radius of the sphere. This means that surface tension changes with the surface alveolar area: the larger the radius of the alveoli, the larger the area and the smaller the surface tension force (Erdemli, 2015).

Lung compliance refers to the effort required to stretch the lungs and chest wall. High compliance means that lungs and chest will expand easily whereas low compliance means that they will resist expansion. Thus, elastic recoil is inversely related to lung compliance (Tortora and Derrickson, 2011).

Two factors prevent the lungs from collapsing (Boulpaep et al., 2009):

- a) **The transpulmonary pressure.** In healthy lungs, the intrapleural pressure is lower than the alveolar pressure. This positive transpulmonary pressure tends to pull the thoracic cage outwards and with it the lungs due to the pleural membranes that are connected to both the chest wall and the lungs. Both pleural membranes are normally kept in close proximity due to a layer of fluid located in the pleural cavity.

- b) **The alveolar lung surfactant or pulmonary surfactant.** It reduces the surface tension of the liquid that lines the alveoli at the air/liquid interface.

APPENDIX 5 - Chemical structure of lung surfactant components

A. Neutral lipids

a) **Free fatty acids:** A fatty acid consists of a hydrocarbon chain with a carboxylic acid at one end. There are two types of fatty acids:

- **unsaturated:** there is at least one double bond in the hydrocarbon chain of the fatty acid
- **saturated:** no double or triple bond in the hydrocarbon chain of the fatty acid. Thus, carbon atoms are “saturated” with hydrogen atoms. The most abundant free fatty acid found in lung surfactant is palmitic acid (Veldhuizen et al., 1998). Palmitic acid is a 16 carbon acyl chain with no double bonds (Figure S13).

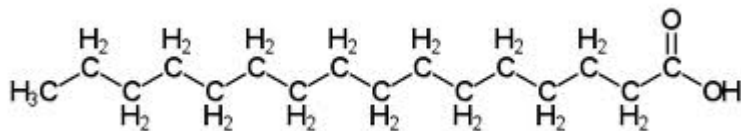


Figure S13. Chemical structure of palmitic acid.

b) **Acylglycerol:** Acylglycerols or glycerides consist of a molecule of glycerol linked to fatty acids by an ester bond. Depending on the numbers of fatty acids bounded to glycerol we have (Figure S14):

- **Monoacylglycerol or monoglyceride:** 1 fatty acid bounded to glycerol
- **Diacylglycerol or diglyceride:** 2 fatty acids bounded to glycerol
- **Tryacylglycerol or tryglyceride:** 3 fatty acids bounded to glycerol

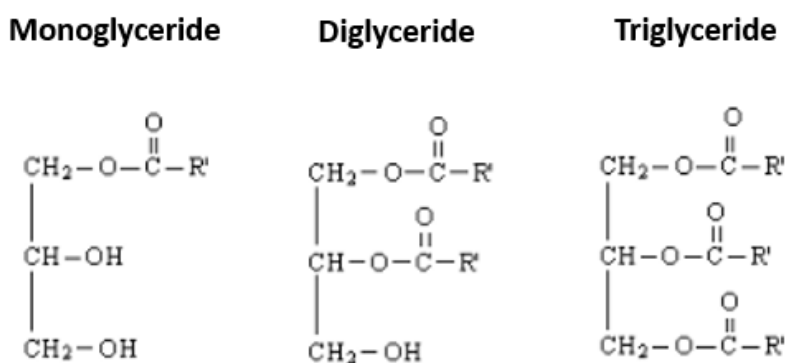


Figure S14. General chemical structure of a monoglyceride, diglyceride and triglyceride. Fatty acids are designated with an “R”.

c) Cholesterol: It comprises the major part of neutral lipids (59.9% weight of the neutral lipid content, 6% weight of the lung surfactant content). The molecule of cholesterol has three regions: a hydrocarbon tail, a ring structure region with 4 hydrocarbon rings and a hydroxyl group (Figure S15). Both the tail and ring region are non-polar whereas the hydroxyl group is polar and therefore, cholesterol is an amphiphilic molecule.

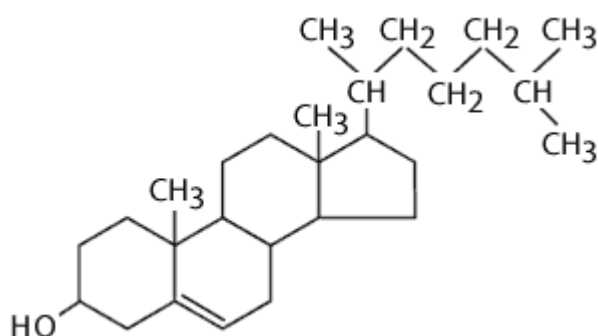


Figure S15. Chemical structure of cholesterol.

d) Cholesterol ester: It consists of a molecule of cholesterol where the hydroxyl group is linked to the carboxylate group of a fatty acid by an ester bond (Figure S16). They are much less polar and more hydrophobic than free cholesterol.

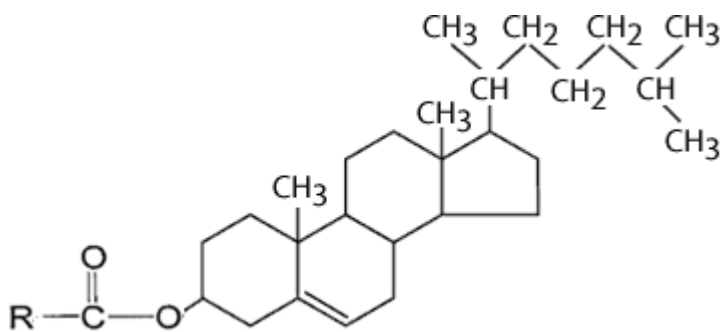


Figure S16. General chemical structure of cholesterol ester. The fatty acid is designated with an “R”.

B. Phospholipids

Lung surfactant phospholipids belong to three main types of phospholipids:

- a) **Glycerophosphatides:** These are the most common types of phospholipids and are derived from glycerol. The hydrophobic part of the molecule consists of two fatty acids and a molecule of glycerol whereas the hydrophilic part consists of a phosphate group and a simple organic molecule (Figure S17).

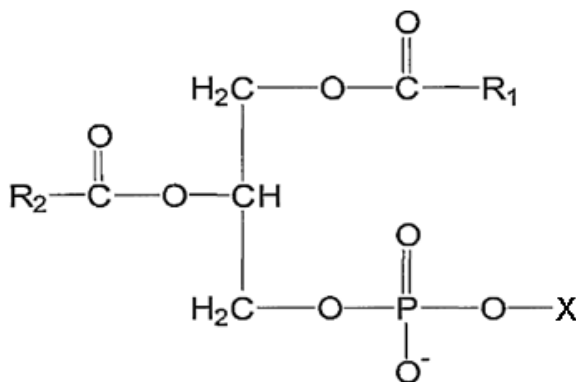


Figure S17. General chemical structure of a glycerophosphatide. Fatty acids are designated with an “R” and the simple organic molecule with an “X”.

Lung surfactant contains the following glycerophosphatides:

- **Phosphatidylcholine:** It is the most abundant phospholipid (67.5% weight of the phospholipid content and 54% weight of the lung surfactant content). The organic molecule in the head group is choline (Figure S18).

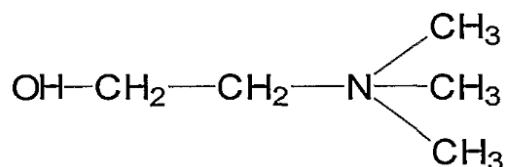


Figure S18. Chemical structure of choline.

There are two types of phosphatidylcholine: saturated (no double or triple bonds in the hydrocarbon chain of the fatty acid) and unsaturated (there is at least one double bond in the hydrocarbon chain of the fatty acid).

- **Phosphatidylglycerol:** It is the second most abundant phospholipid. The organic molecule in the head group is glycerol (Figure S19).

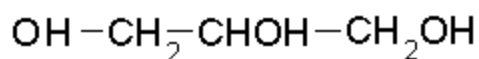


Figure S19. Chemical structure of glycerol.

- **Phosphatidylethanolamine:** The organic molecule in the head group is ethanolamine (Figure S20).

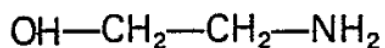


Figure S20. Chemical structure of ethanolamine.

- **Phosphatidylinositol:** The organic molecule in the head group is inositol (Figure S21).

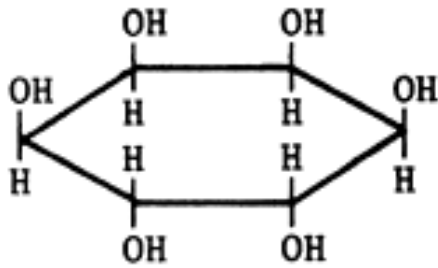


Figure S21. Chemical structure of inositol.

- **Lysobisphosphatidic acid:** The organic molecule in the head group is acylglycerol.
- **Phosphatidylserine:** The organic molecule in the head group is serine (Figure S22).

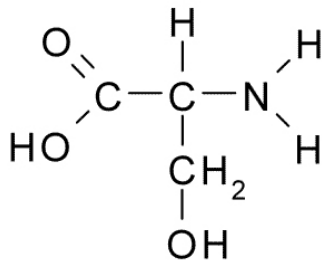


Figure S22. Chemical structure of serine.

- **Cardiolipin:** The organic molecule in the head group is phosphatidylglycerol.
- b) Sphingosyl phosphatides:** These types of phospholipids are derived from sphingosine instead of glycerol. Lung surfactant contains sphingomyelin: the hydrophobic part of the molecule consists of a fatty acid and a sphingosine and the hydrophilic part consists of a phosphate group and choline (Figure S23).

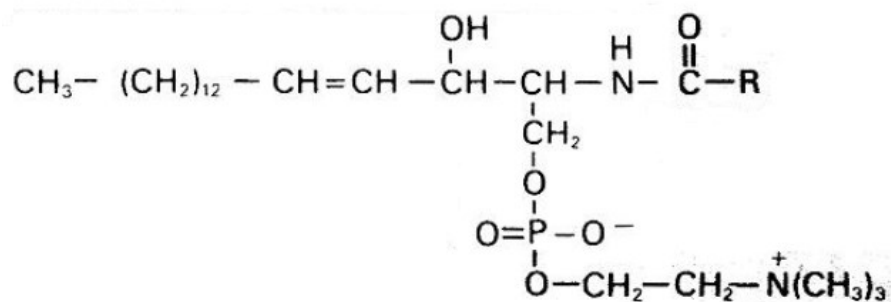


Figure S23. General chemical structure of sphingomyelin. The fatty acid is designated with an “R”.

- c) **Lisoglycerophosphatides:** These types of phospholipids are derived from phosphatidylcholine. They result from the removal of one of the fatty acids of phosphatidylcholine by hydrolysis. Lung surfactant contains lysophosphatidylcholine: the hydrophobic part of the molecule consists of a fatty acid and a molecule of glycerol and the hydrophilic part of a phosphate group and choline (Figure S24).

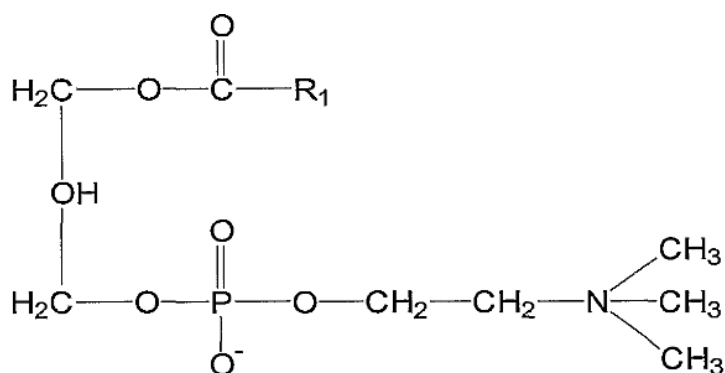


Figure S24. General chemical structure of lysophosphatidylcholine. The fatty acid is designated with an “R”.

C. Surfactant proteins (SP)

Table S1. Summary of the molecular mass and the structure of pulmonary surfactant proteins (Akino, 1992).

Apoprotein		Molecular mass	Primary structure	Macromolecular structure
Hydrophilic	SP-A	26-38 kDa	N-linked glycoprotein short segment at N-terminal collagenous structure at N-terminal region (formation of triple helical trimer) C-type lectin structure at C-terminal region (formation of two intramolecular disulfide bonds ; formation of globular head) hydrophobic region between collagenous structure and C-type lectin structure	six trimers assemble to form macromolecules ; flower bucket structure like Clq and mannose binding protein
	SP-D	43 kDa	N-linked glycoprotein collagenous structure at N-terminal region (formation of triple helical trimer) C-type lectin structure at C-terminal region (formation of two intramolecular disulfide bonds ; formation of globular head)	four trimers assemble to form macromolecules ; cruciform structure like conglutinin
Hydrophobic	SP-B	8 kDa	7 cysteine residues in 79 amino acids highly hydrophobic	formation of polymers
	SP-C	3.7 kDa	12 valine residues in 36 amino acids highly hydrophobic palmitic acids bound at two cysteine residues	present as monomer

APPENDIX 6 - *In vitro* methods to investigate the properties of exogenous lung surfactant

A. Langmuir-Wilhelmy balance (LWB)

The LWB measures the Π of a liquid held in a trough with a surfactant monolayer spread onto its surface during the compression or expansion of the monolayer by two barriers using a Wilhelmy plate (Figure S25).

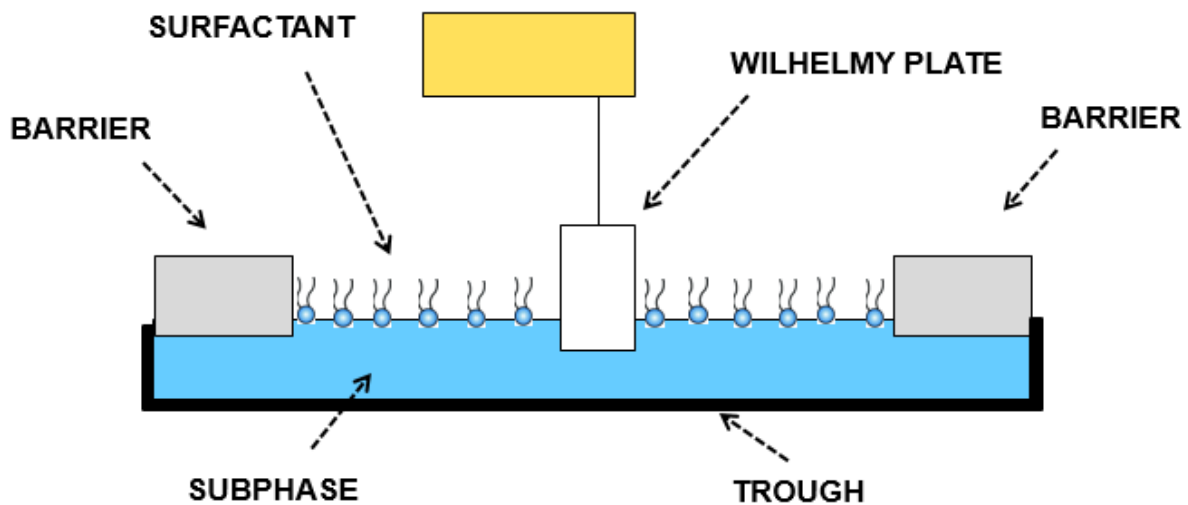


Figure S25. Schematic diagram of a Langmuir-Wilhelmy balance.

Advantages of the Langmuir-Wilhelmy balance:

- It is simple to use.
- The surface area per surfactant molecule can be precisely calculated as there is a strong control over the amount of surfactant spread and the available surface area for spreading.
- The composition and structure of the monolayer can be further examined *in situ* or transferred to a solid substrate using a variety of microscopic and spectroscopic techniques including BEM, AFM, SEM, X-ray diffraction or ToF-SIMS.

Disadvantages of the Langmuir-Wilhelmy balance:

- It is not ideal for studying surfactant adsorption from the subphase as high volumes of surfactant liquid sample are required, usually tens of millilitres.
- Slow cycle rate which does not simulate the inhalation-exhalation cycle of breathing.

- The Wilhelmy plate requires a $\theta = 0^\circ$. This condition is difficult to maintain especially in experiments involving compression and expansion, as some of the surfactant material deposits onto the plate on compression which means that the subphase liquid will not completely wet the plate.
- Trough overflow and barrier leakage problems.
- The flat geometry of the trough is not realistic.
- Difficult to isolate from the environment with regards to temperature and impurities.
- A constant Π can only be maintained by continuously compressing the film which does not simulate the film stability found *in situ*.

B. Pulsating bubble surfactometer

It is a variation of the maximum bubble pressure method. It consists of a polyacrylamide chamber that contains a surfactant liquid with a capillary submerged in it. A bubble is formed at the end of the capillary by drawing air from the atmosphere through the capillary. The surfactant film adsorbs at the bubble surface and changes in surface tension are measured during dynamic oscillation of the air bubble by a pulsator (Figure S26).

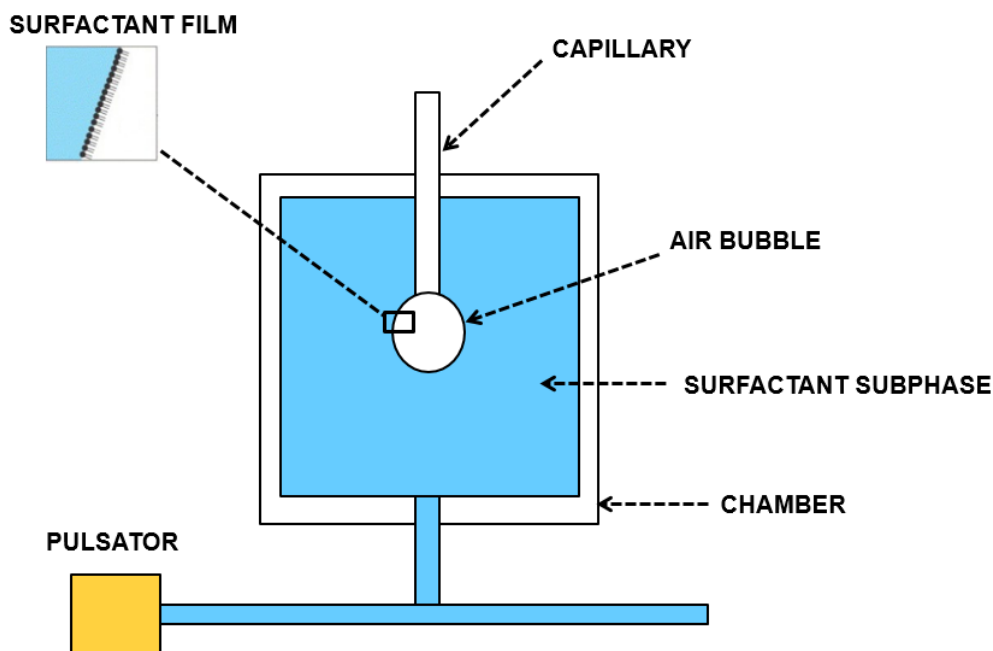


Figure S26. Schematic diagram of a pulsating bubble surfactometer.

Advantages of the pulsating bubble surfactometer:

- Highly efficient and time effective. One measurement can be completed in 5 minutes.
- Quick cycle rate which simulates the inhalation-exhalation cycle of breathing.
- Low sample volume for studying surfactant adsorption from the subphase, usually ~ 20 μL .
- Easy to change samples: it is very useful for comparing the surface activity of different surfactant samples.

Disadvantages of the pulsating bubble surfactometer:

- No control over the amount of surfactant at the surface.
- Measurements at low surface tension values are not reliable as the bubble deforms from spherical shape due to gravity or hydrodynamic effects.
- Leakage at low surface tension values is a serious problem. It can happen at the inner and outer surface of the capillary.
- It can require repeated cycling to reach low surface tension values.
- The film area must be reduced by 50-80% to reach low surface tension values. Lung surfactant however achieves this value by only a slight film compression, particularly by no more than 20-30% alveolar area reduction.

C. Captive bubble surfactometer

It is a technique invented to address some of the problems of the pulsating bubble surfactometer. In this system the bubble floats against a hydrophilic roof coated with 1% agar gel. Dynamic oscillation of the bubble is controlled by varying the pressure in the sample chamber with a pressure piston (Figure S27).

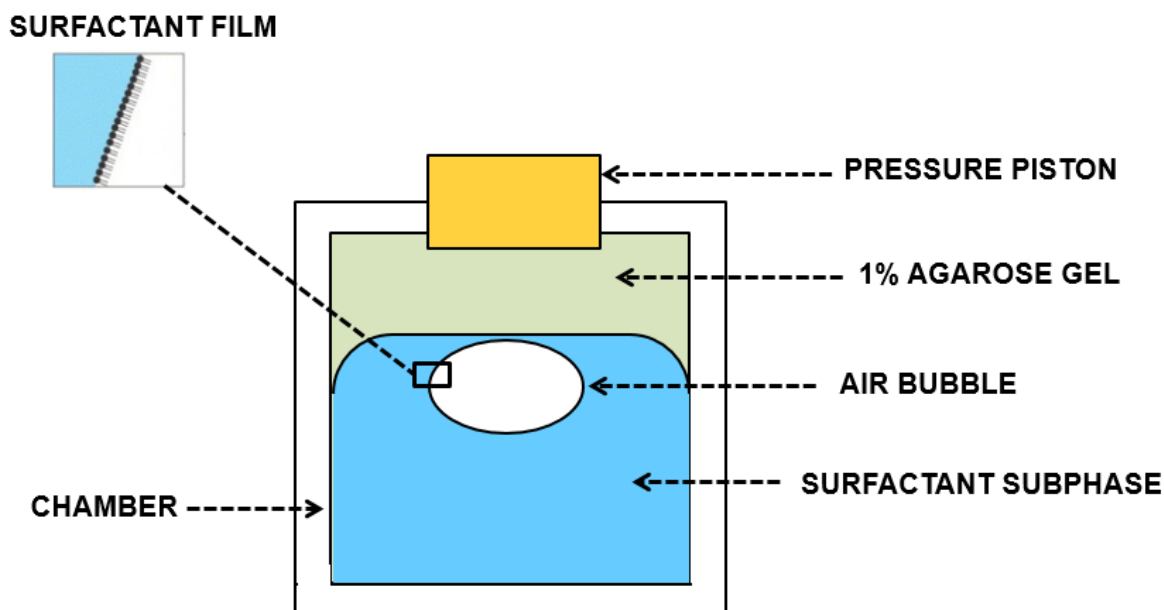


Figure S27. Schematic diagram of a captive bubble surfactometer.

Advantages of the captive bubble surfactometer:

- Leak-proof system at physiological and higher temperatures. Thus, it is capable of reproducing the stability of lung surfactant films and reach near zero γ values.
- Quick cycle rate which simulates the inhalation-exhalation cycle of breathing.
- Low sample volume for studying surfactant adsorption from the subphase.

Disadvantages of the captive bubble surfactometer:

- Control over the amount of surfactant at the surface is not easy.
- For adsorption studies, the maximum surfactant concentration is 3 mg/ml due to visibility issues as surfactant suspensions become opaque.
- It is difficult to operate and clean.
- Complex data analysis which is relatively time-consuming. This problem can however be solved using ADSA.

APPENDIX 7

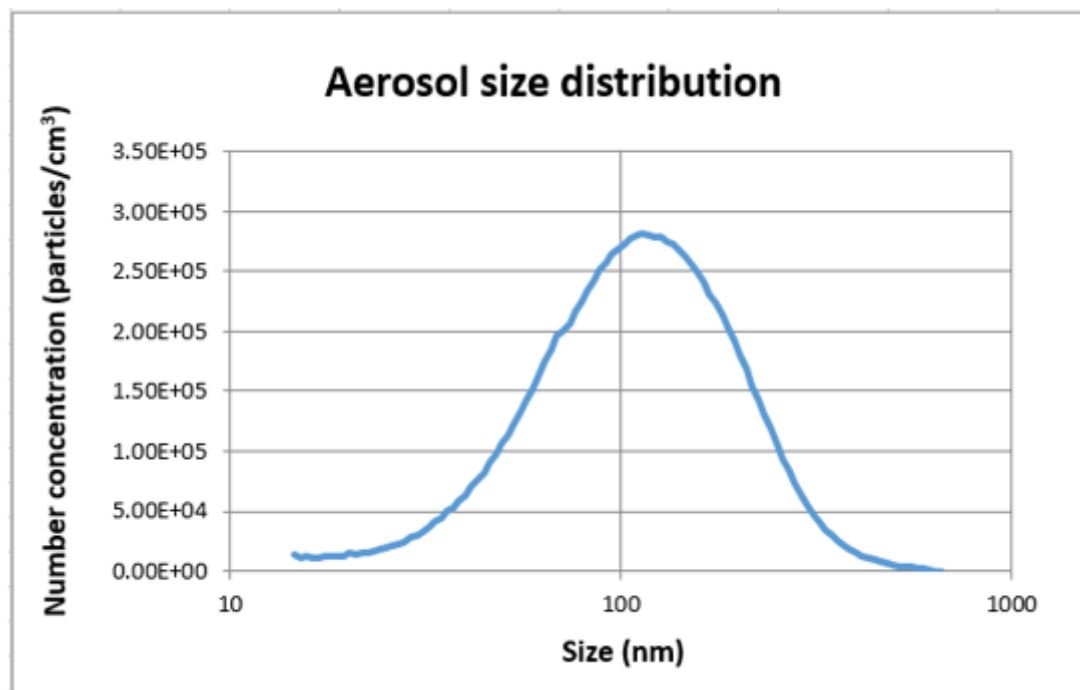


Figure S28. Graphical representation of the CeO₂ aerosol size distribution of an experiment performed to study the effect of the exposure of a DPPC monolayer to aerosolised water, compressed air flow and aerosolised CeO₂ nanoparticles over 45 minutes measured in PBS at 37°C.

Table S2. Effect of the exposure of a DPPC monolayer to aerosolised water, compressed air flow and aerosolised CeO₂ nanoparticles over 45 minutes (3.09/1 CeO₂/DPPC mass ratio) on the lift-off Mma, C_m , collapse Π and collapse Mma of the Π -Mma isotherms measured in PBS at 37°C. The corresponding values in each of these parameters measured for water and CeO₂ nanoparticles were compared with those of compressed air flow (control) by calculating the difference in each of the parameters for the experimental isotherm and the control expressed as a % of the control value and dividing them by the reference % change from midpoint values for the relevant reference isotherm (Table 11). This approach assumes similar levels of uncertainties on the control and experimental isotherm parameters to those of the reference isotherm parameters.

Deposition	Lift-off Mma (Å ² /molecule)	(% difference experiment and control)/(reference % change from midpoint)	C_m 1-5 mN/m (mN/m) ⁻¹	(% difference experiment and control)/(reference % change from midpoint)	C_m 10-25 mN/m (mN/m) ⁻¹	(% difference experiment and control)/(reference % change from midpoint)
<i>Reference isotherm</i>	123	1.0 (% change from midpoint)	0.0298	3.0 (% change from midpoint)	0.0150	2.0 (% change from midpoint)
CA (control)	141		0.0332		0.0171	
Water	136	4.0	0.0331	0.0	0.0169	0.5
CeO₂ NPs	138	2.0	0.0328	0.3	0.0172	1.0

Deposition	C_m 31 mN/m – lowest collapse Π (mN/m) ⁻¹	(% difference experiment and control)/(reference % change from midpoint)	Collapse Π (mN/m)	(% difference experiment and control)/(reference % change from midpoint)	Collapse Mma (Å ² /molecule)	(% difference experiment and control)/(reference % change from midpoint)
<i>Reference isotherm</i>	0.0294	15.0 (% change from midpoint)	39.40	2.0 (% change from midpoint)	49	4.0 (% change from midpoint)
CA (control)	0.0440		39.67		44	
Water	0.0373	1.0	40.86	1.5	42	1.3
CeO₂ NPs	0.0226	3.3	50.70	14.0	40	2.3

APPENDIX 8

Table S3. Exposure time, average aerosol CMD, GSD and number concentration of eight different experiments performed to study the effects of the exposure of a DPPC monolayer to increasing amounts of aerosolised CeO₂ nanoparticles measured in PBS at 37°C.

Exposure time (min)	CMD ± SD (nm)	GSD ± SD	Number concentration ± SD (particles/cm³)
30	99 ± 4	2.0 ± 0.1	9.81E+04 ± 3.34E+04
60	114 ± 5	1.8 ± 0.0	2.76E+05 ± 7.68E+04
75	113 ± 4	1.8 ± 0.0	2.81E+05 ± 6.09E+04
75	110 ± 4	1.8 ± 0.0	2.75E+05 ± 7.32E+04
90	Not available	Not available	Not available
90	106 ± 4	1.8 ± 0.0	2.62E+05 ± 4.68E+04
120	113 ± 5	1.8 ± 0.0	3.39E+05 ± 3.04E+05
120	117 ± 2	1.8 ± 0.0	3.19E+05 ± 5.06E+04

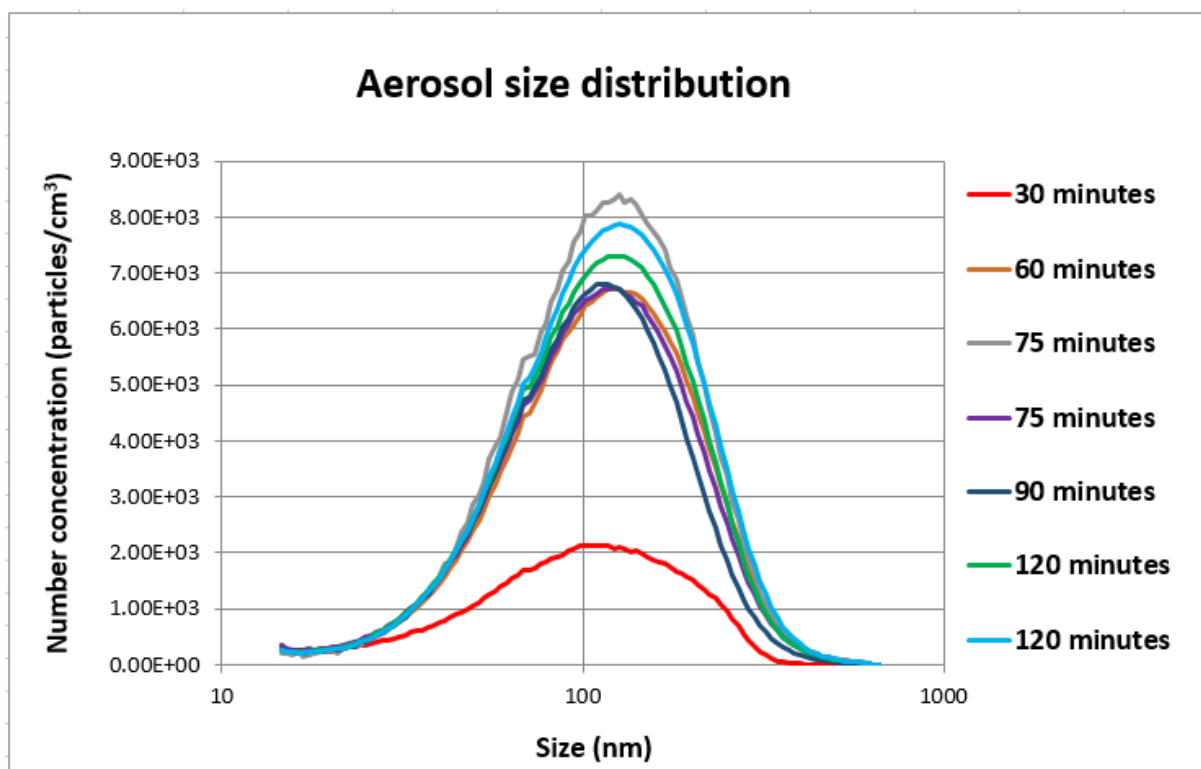


Figure S29. Graphical representation of the CeO₂ aerosol size distribution for each of the experiments performed to study the effects of the exposure of a DPPC monolayer to increasing amounts of aerosolised CeO₂ nanoparticles measured in PBS at 37°C.

Table S4. Exposure time, aerosol mass concentration, estimated CeO₂ nanoparticle mass deposited, CeO₂/DPPC mass ratio and collapse Π of the Π -Mma isotherms for each of the eight experiments performed to study the effects of the exposure of a DPPC monolayer to increasing amounts of aerosolised CeO₂ nanoparticles measured in PBS at 37°C.

Exposure time (min)	<i>mc</i> (ng/cm³)	CeO₂ NP mass deposited (μg)	CeO₂/DPPC mass ratio	Collapse Π (mN/m)
30	Not available	Not available	Not available	44.89
60	6.76	22 \pm 9	5.09/1	50.59
75	5.72	23 \pm 9	5.38/1	47.79
75	5.31	22 \pm 9	4.99/1	50.46
90	4.61	23 \pm 9	5.21/1	50.43
90	5.03	25 \pm 10	5.68/1	51.85
120	6.93	46 \pm 18	10.43/1	50.71
120	8.02	53 \pm 21	12.07/1	51.07

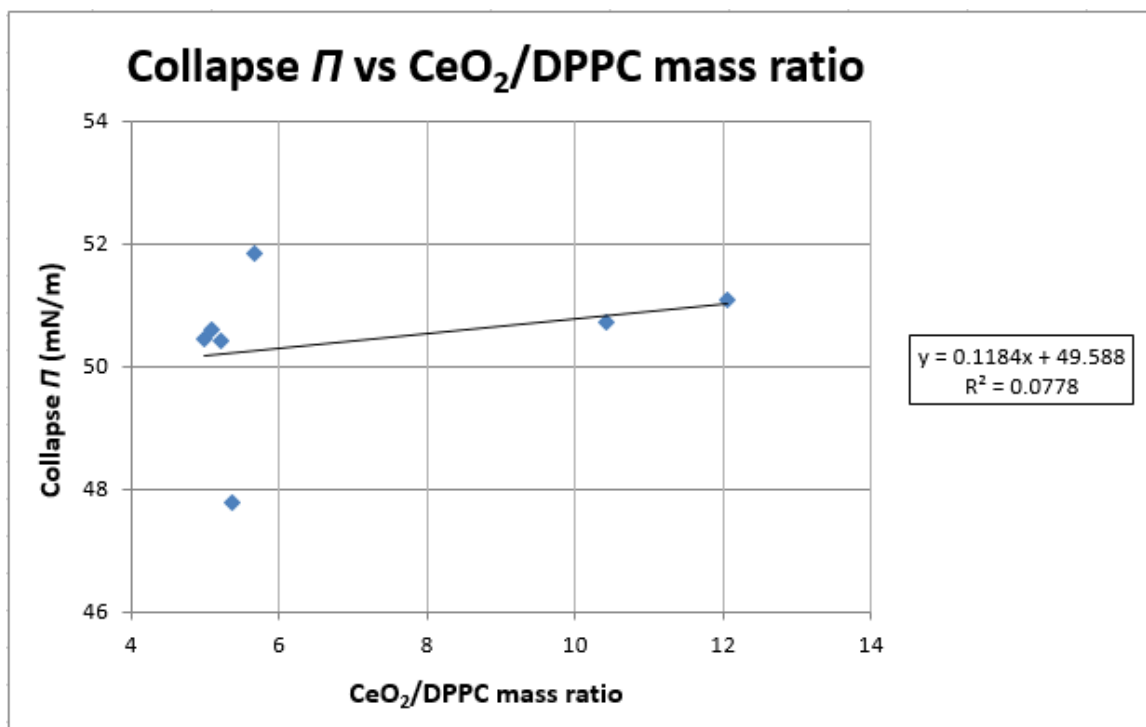


Figure S30. Graphical representation of the effect of the exposure of a DPPC monolayer to increasing amounts of aerosolised CeO_2 nanoparticles (4.99/1, 5.09/1, 5.21/1, 5.38/1, 5.68/1, 10.43/1 and 12.07/1 CeO_2/DPPC mass ratios) on the collapse Π of the Π -Mma isotherms measured in PBS at 37°C.

